Dynamic nonlinear soil-structure interaction

Esteban Saez Robert

THÈSE
présentée par

Esteban Patricio SAEZ ROBERT

pour l'obtention du

GRADE DE DOCTEUR

Spécialité : Modélisation numérique, Dynamique des Sols

Laboratoire d'accueil : Mécanique des Sols, Structures et Matériaux

SUJET: DYNAMIC NONLINEAR SOIL-STRUCTURE INTERACTION

Soutenue le: 20 mars 2009

devant un jury composée de:

M. BISCH Philippe	Président
Mme. MODARESSI Arézou	Directrice de Thèse
M. PAOLUCCI Roberto	Rapporteurs
M. PITILAKIS Kyriazis	
Mme. FOERSTER Evelyne	Examinateurs
M. LOPEZ-CABALLERO Fernando	
M. CLOUTEAU Didier	Invité

Avant-propos

Abstract

The dynamic interaction of the soil with a superstructure (DSSI) has been the subject of numerous investigations assuming elasticity of both, superstructure and soil foundation behavior. Nevertheless, the effect of DSSI may differ between elastic and inelastic systems. Thus, the current interaction methodologies based on elastic response studies could not be directly applicable to structures expected to behave inelastically during severe earthquakes. Additionally, the soil is known to exhibit inelastic behavior even for relatively weak to moderate ground motions. Consequently, ignoring these characteristics in studying DSSI could lead to erroneous predictions of structural damage.

The main purpose of this work is to develop a general strategy to address the full DSSI problem in the context of the seismic vulnerability analysis of structures. Thus, realistic Finite Elements models are constructed and applied in a practical way to deal with these issues. These models cover a large range of soil conditions and structural typologies under several earthquake databases. Some modeling strategies are introduced and validated in order to reduce the computational cost. Therefore, an equivalent 2D model is developed, implemented in *GEFDyn* and used in the large parametric study conducted. Several indicators for both structural and soil responses are developed in order to synthesize their behavior under seismic loading. Additionally, a vulnerability assessment strategy is presented in terms of measures of information provided by a ground motion selection.

According to the investigation conducted in this work, there is in general a reduction of seismic demand or structural damage when non-linear DSSI phenomenon is included. This reduction can be associated fundamentally to two phenomena: radiative damping and hysteretic damping due to non-linear soil behavior. Both effects take place simultaneously during the dynamic load and it is extremely difficult to separate the contribution of each part in reducing seismic demand. Indeed, effective motion transmitted to the superstructure does not correspond to the free field motion because of the geometrical and inertial interactions as well as the local modification of soil behavior, specially due to the supplementary confinement imposed by the superstructure's weight. A series of strong-motion severity measures, structural damage measures and energy dissipation indicators have been introduced and studied for this purpose. Nevertheless, results are erratic and consequently, generalization was extremely difficult.

Despite these difficulties, the results illustrate the importance of accounting for the inelastic soil behavior. The major part of the studied cases show beneficial effects such as the decrease of the maximum seismic structural demand. However, the non-linear DSSI could increase or decrease the expected structural damage depending on the type of the structure, the input motion, and the dynamic soil properties. Furthermore, there is an economic justification to take into account the modification effects due to inelastic soil behavior.

Keywords: *dynamic soil-structure interaction, non-linear behavior, finite elements, coupled formulation, structural damage, ductility demand, seismic vulnerability*

Résumé

L'interaction dynamique entre le sol et les structures (IDSS) a fait l'objet de nombreuses études sous l'hypothèse de l'élasticité linéaire, bien que les effets de l'IDSS puissent être différents entre un système élastique et un système inélastique. De fait, les méthodologies usuelles développées à partir des études élastiques peuvent ne pas être adaptées aux bâtiments conçus pour dissiper de l'énergie par de l'endommagement lors de séismes sévères. De plus, il est bien connu que la limite d'élasticité du sol est normalement atteinte même pour de séismes relativement faibles. En conséquence, si les effets inélastiques de l'ISS sont négligés, les études d'endommagement sismique des bâtiments peuvent être très inexactes.

L'objectif de ce travail est de développer une stratégie générale pour l'étude du problème de l'IDSS non-linéaire dans le contexte de l'analyse de la vulnérabilité sismique des bâtiments. Ainsi, des modèles d'éléments finis réalistes sont développées et appliquées à des problèmes d'IDSS non-linéaires. Les modèles couvrent une large gamme des conditions pour le sol et des typologies de bâtiments soumis à plusieurs base de données sismique. Une stratégie de modélisation a été développée et validée afin de réduire significativement le coût numérique. Pour cela, un modèle 2D équivalent a été développé, implanté dans *GEFDyn* et utilisé pour effectuer un importante étude paramétrique. De nombreux indicateurs de comportement non-linéaire de la structure et du sol ont été proposés pour synthétiser leur fonctionnement lors du chargement sismique. De surcroît, une stratégie d'évaluation de la vulnérabilité sismique basée sur l'information apportée par une base des données sismiques a été développée.

De façon, générale, les résultats ont mis en évidence une réduction de la demande sismique lorsque les effets inélastiques de l'IDSS sont pris en compte. Cette réduction est liée fondamentalement à deux phénomènes : l'amortissement par radiation et l'amortissement hystérétique du sol. Ces deux effets ont lieu simultanément pendant le mouvement sismique. Il est alors très difficile d'isoler l'influence de ces deux phénomènes. En effet, le mouvement effectif transmis à la structure n'est pas le même que celui en champs libre du aux effets d'interaction, ainsi qu'à la modification locale du comportement du sol fortement lié aux poids du bâtiment. Une série de mesures de sévérité sismique et des mécanismes de dissipation d'énergie au niveau du sol et du bâtiment a été introduite dans le but d'analyser ces effets. Cependant, ces résultats sont en général très irréguliers et leur généralisation à été très difficile.

Néanmoins, ces résultats mettent en évidence l'importance de la prise en compte des effets du comportement inélastique du sol. La plupart des cas étudiés ont montré un effet favorable de l'IDSS non-linéaire. Mais, en général, l'IDSS peut augmenter ou diminuer la demande sismique en fonction de la typologie de la structure, des caractéristiques du mouvement sismique et des propriétés du sol. Tout de même, il y a une justification économique pour étudier les effets du comportement non-linéaire du sol sur la réponse sismique.

Mots-clés: *interaction dynamique sol-structure, comportement non-linéaire, éléments finis, formulation couplé, endommagement, demande en ductilité, vulnérabilité sismique*

Contents

Notations

f	frequency
f_0	fixed base fundamental frequency
f_c	concrete resistance to compressive stresses (Appendix I)
f_c	corner frequency (Chapter 5)
f_k, f_{iso}	yield surfaces
f_{soil}	first elastic frequency of the soil deposit
f_{s_u}	ultimate stress of steel
f_y	yield stress of steel
F	probability of success on each trial
F_k	factorial axis k
$\underline{g}$	gravity acceleration
G	shear modulus
G_{max}	maximum shear modulus
G_{ref}	maximum shear modulus under the reference pressure
h	vertical dimension of beam sections
$\bar{h}$	equivalent height of single-degree-of-freedom systems
H	hardening modulus of interface
i	imaginary unit
$\underline{\underline{I}}$	second-order unit tensor
i_{soil}	local soil energy dissipation index
I_{soil}	global soil energy dissipation index
I_{str}	indicator of energy dissipated by the superstructure
$ISD_{max,\%}$	normalized maximum inter-story drift
k_0	earth pressure coefficient
k_s	one-dimensional permeability
$\underline{k}$	geometrical permeability tensor
$\underline{\underline{K}}$	permeability tensor
K_f	compressibility of the fluid phase
K_{ref}	bulk modulus under the reference pressure
K_s	compressibility of the solid skeleton
l_a	width of the soil slide considered in equivalent 2D plane-strain approach
M	slope of the critical stat line in the plane $(q - p')$
M_{act}^p	set of activated mechanisms
M_{pact}^p	set of potentially activated mechanisms
M_p^k	bending moment in plastic component at plastic hinge k
n	porosity or number of samples
n_e	exponent of non-linear elastic laws
n_h	total number of plastic hinges
n_p	exponent of deviatoric hardening law
$\underline{n}$	normal vector
N_α^I	shape function for the variable α of the node I
p'	effective mean stress
p_c	critical mean stress
p_{co}	initial critical mean stress
p'_{ref}	effective reference pressure
Pa	instantaneous average power
PGA	peak ground acceleration

PS	spectrogram
PSa	acceleration response spectrum
PS_τ	power spectral density
Q	mean liquefaction index
$r_k^m,\ r_k^c$	friction mobilization degree
$r_k^{ela},\ r_k^{hys},\ r_k^{mob}$	threshold domains parameters
R_u	pore pressure ratio
S	Fourier spectra
t	time
$\underline{t}$	stress vector
T_0	fundamental fixed base period
T_e	reference fundamental period
T_m	mean period according to Rathje et al. (1998)
T_{soil}	first elastic period of the soil deposit
T_{SR}	significant duration according to Trifunac and Brady (1975)
$\underline{u}_b$	displacement field in the superstructure domain
$\underline{u}_d$	displacement field due to diffracted waves
$\underline{u}_i$	displacement incident field
$\underline{u}_f$	foundation displacement field
$\ddot{u}_g$	seismic base acceleration
$[u_N]$	normal interface jump
$\underline{u}_{rf}$	relative displacement field between solid and fluid phases
$\underline{u}_s$	displacement field of solid phase
$[\underline{u}_T]$	tangent interface jump vector
U_c	coefficient of uniformity
$V_{s,30}$	average shear wave velocity in the upper 30[m]
$\underline{w}_b,\ \underline{w}_s$	virtual displacement fields
W	weight of the single-degree-of-freedom system
$\underline{x}$	material point coordinates
y	realization of the random variable Y
Y	Poisson random variable

Greek Alphabet and other symbols

α	parameter defining position of fragility curves (Chapter 5)
α	hardening evolution function (Appendix E)
β	Newmark integration parameter (Chapter 1)
β	parameter describing slope of fragility curves (Chapter 5)
β	plastic compressibility (Appendix E)
Δt	time step
$\underline{\underline{\varepsilon}}$	strain tensor
$\bar{\underline{\underline{\varepsilon}}}$	deviatoric strain tensor
ε_v	volumetric strain
ε_v^p	volumetric plastic strain
γ	Newmark integration parameter (Chapter 1)
γ	distortion
γ^p	plastic deviatoric strain
Γ_s, Γ_b	mechanical boundaries of soil and superstructure domains
Γ_{s_σ}, Γ_{b_σ}	parts of boundaries where stresses are imposed
Γ_{s_u}, Γ_{b_u}	parts of boundaries where displacements are imposed
Γ_{s_p}	part of boundary where pore pressures are imposed
Γ_{s_φ}	part of boundary where flow is imposed
$\mathcal{I}_{i,j}$	Fisher information matrix
λ	Lamé coefficient
λ_1, λ_2	eigenvalues of $\mathcal{I}_{i,j}$
$\dot{\lambda}^p$	plastic multiplier
$\mathcal{L}$	likelihood function
μ	coefficient of Lamé (Chapter 1)
μ	ductility ratio (Chapter 4)
ω	angular frequency
ρ	total specific mass
ρ_b	superstructure's mean density
ρ_s	solid phase density
ρ_f	fluid phase density
Ω_b, Ω_s	superstructure and soil domains
ϕ	friction angle for interfaces
ϕ'_{pp}	friction angle at critical state
$\underline{\phi}_j$	fixed base mode j
Φ	standard normal distribution function
ψ	dilatancy angle for interfaces (Appendix B)
ψ	characteristic angle (Appendix E)
$\underline{\psi}_n$	rigid body mode n
$\underline{\underline{\Psi}}$	plastic flow direction
$\underline{\underline{\sigma}}'$	effective stress tensor
$\underline{\underline{s}}$	deviatoric stress tensor
σ_I, σ_{II}, σ_{III}	principal stresses
Σ_{bs}, Σ	interfaces between domains
τ	shear stress
θ_1, θ_2	directions of eigenvectors of $\mathcal{I}_{i,j}$

Tensorial notation and operators

$[\cdot]$	jump of a quantity
$\cdot$	scalar product
$\otimes,\ \otimes_s$	tensorial products
$:$	contracted product
$\underline{a}$	vector a
$\underline{\underline{a}}$	second-order tensor a
$\underline{\underline{\underline{\underline{a}}}}$	fourth-order tensor a
$\lvert\,\cdot\,\rvert$	absolute value of a scalar
$\lVert\cdot\rVert$	modulus of a vector
a_N	normal component of vector $\underline{a}$
$\underline{a}_T$	tangential projection of vector $\underline{a}$
$tr(\cdot)$	tensor trace
$\mathrm{grad}(\cdot)$	gradient operator
$\mathrm{div}(\cdot)$	divergence operator
$\mathrm{rot}(\cdot)$	rotation operator
$\triangle(\cdot)$	Laplace operator
$E[\cdot]$	expectation
$\mathrm{Var}[\cdot]$	variance operator
$\mathrm{Cov}[\cdot]$	covariance operator

Abbreviations

ATC	Applied Technology Council
BE	Boundary Elements approach
bd	soil-bedrock interface
BEM	Boundary Elements Method
C1L	low-rise reinforced concrete moment frame type SDOF
C1M	mid-rise reinforced concrete moment frame type SDOF
CPU	Central Processing Unit
CSM	Capacity Spectrum Method
DCS	Drained Cyclic Shear test
DOF	Degree Of Freedom
DSSI	Dynamic Soil-Structure-Interaction
ECP	Ecole Centrale Paris
FE	Finite Elements approach
FEM	Finite Elements Method
FEMA	Federal Emergency Management Agency
ff	free field
ff/bd	spectral ratio amplitude between free field and soil-bedrock interface
GEFDyn	Géomécanique Elements Finis DYNamique
HAZUS-MH	Hazards United States Multi-Hazard
MISS-3D	Modélisation de l'Interaction Sol-Structure 3D
PCA	Principal Component Analysis
PP	Performance Point
SDOF	Single-Degree Of Freedom
SDT	Structural Dynamic Toolbox
SPT	Standard Penetration Test
SSI-FE	Soil-Structure Interaction analysis using a Finite Element model
SSI-E	Soil-Structure Interaction analysis using a Finite Element model assuming non-linear elastic soil
SSI-N	Soil-Structure Interaction analysis using a Finite Element model assuming inelastic soil
tp	top of the structure
tp/ff	spectral ratio amplitude between the top of the structure and the free field
T-S	Two-Step analysis
TS-E	Two-Step analysis assuming non-linear elastic soil
TS-N	Two-Step analysis assuming inelastic soil
UCS	Undrained Cyclic Shear test

List of Figures

Introduction

Motivation

During the last years, significant advances in comprehensive strategies for seismic risk assessment have been developed in Earthquake Engineering. Indeed, elaborated methods have been proposed to quantify structural and non-structural damage, to estimate the number of casualties or to predict the rehabilitation cost after major earthquakes. In this way, powerful analysis methods have been developed to accurately analyze structural models and estimate the demands for different levels of shaking. Nevertheless, the major part of these methods do not incorporate explicitly the foundation conditions. Thus, the structure is supposed to be clumped on the foundation medium and local soil conditions are solely included by selecting adequate ground motions compatible with the characteristics of the soil deposit.

Both, research and practice, have shown that a structure founded on a deformable soil could respond differently compared to a fixed base situation. Indeed, in flexible supported case, mutual interaction between structure and adjacent soil takes place inducing modifications in the dynamic response. The interaction of the soil with a superstructure has been the subject of numerous investigations assuming linearity of both, superstructure and soil foundation. Nevertheless, the effect of dynamic soil-structure interaction (DSSI) may differ between elastic and inelastic systems. Thus, the current interaction methodologies based on elastic response studies could not be directly applicable to structures expected to behave inelastically during severe earthquakes. Additionally, the soil is known to exhibit non-linear behavior even for relatively weak to moderate ground motions. Consequently, ignoring the non-linear characteristics of the DSSI phenomenon could lead to erroneous predictions of structural damage.

In every day engineering practice, static, dynamic or incremental dynamic, non-linear structural seismic analysis procedures become more and more frequent. In contrast, full non-linear dynamic soil-structure analysis is still out of the usual practice, and is restricted because of the high computational cost of this kind of analysis. Consequently, it is a challenge for researchers to identify configurations where the structural response is highly affected by the non-linear DSSI. As a general rule, the soil-structure interaction effects are assumed beneficial and ignored. Nevertheless, a more precise knowledge of the expected structural seismic response including DSSI effects could allow reduce the cost of new structures with the same reliability and improve the earthquake engineering practice.

Objectives and scope

The goal of this work is to develop a general strategy to address the full non-linear DSSI problem. This strategy includes:

- the construction of an appropriate numerical model taking into account realistically the physical phenomena encountered such as the wave propagation and the non-linear behavior of both superstructure and soil, as well the soil-foundation contact problem

- the selection of an adequate strong motion database

- the identification of a set of suitable measures describing the earthquake, the soil and the structure dynamic responses

- the inclusion of non-linear DSSI effects into a seismic vulnerability assessment

This work aims to show how realistic Finite Elements (FE) models can be constructed and applied in a practical way to deal with the issues associated to non-linear DSSI. Some modeling strategies are introduced and validated in order to reduce the computational cost for a given configuration. Several indicators for both structural and soil responses are developed in order to summarize their behavior under seismic loading. Additionally, a vulnerability assessment strategy is presented in terms of measures of information provided by a ground motion selection.

Several single-degree-of-freedom (SDOF) and multiple-degree-of-freedom (MDOF) structures founded on several soils are studied. In addition, two hydraulic conditions are considered: dry and fully saturated. Conclusions, as general as possible, are derived for each case. General tendencies are identified in several configurations.

The ultimate goal is to encourage practice towards the inclusion of DSSI phenomena in order to improve the prediction of the structural response under weak to moderate ground motions. The near to soil-failure case has been intentionally excluded from the scope of the present work.

Organization and outline

All chapters are written to be autonomous, each planned as a future publication. Some information regarding theoretical formulation of used constitutive models, considered structures' details and selected strong motions, have been placed in appendices to simplify the lecture of the document.

Chapter 1 establishes and defines the basic principles of the time-domain dynamic soil-structure interaction problem. The theoretical strong formulation and the corresponding weak formulation for a FE modeling are presented. Generalities about the time and the non-linear integration strategies adopted in the used tool *GEFDyn* are also provided. The final part of this chapter describes in detail the adopted criteria to model the DSSI problem by FE, and presents numerical validations of the used models compared to the results obtained by a coupled BE-FE approach.

Chapter 2 summarizes the earliest stage of this work. The general strategy to define a set of comparable data including and neglecting DSSI effects is presented in this chapter. Implications of the non-linear DSSI in standard non-linear static procedures for seismic demand assessment are investigated. The influence of the DSSI on the seismic structural demand is summarized in terms of fragility curves. Three major issues are detected at this stage of the work: limitations associated to a 2D plane-strain approach, contribution of the elastic part of the DSSI and influence of the seismic database on the obtained fragility curves. These issues are explored in detail in Chapters 3, 4 and 5, respectively.

Chapter 3 proposes a modified plane-strain approach to model the non-linear DSSI problem for regular buildings. Multiple validations are provided to highlight the accuracy of the introduced approach. A strong motion selection strategy is presented. An energy oriented analysis is introduced to evaluate the response of the soil and the building. Two buildings founded on three different soils are studied.

Chapter 4 explores the contribution of the elastic DSSI to the complete non-linear DSSI problem. With this purpose, a set of 3D analyses are carried out for two SDOF structures laid on two soils. General tendencies in terms of influence on the ductility demand are presented. Situations where elastic DSSI considerations give an erroneous prediction are identified.

Chapter 5 introduces a vulnerability assessment strategy in terms of measures of the information provided by a ground motion selection. The strategy is applied to a target building over a soil profile composed of a mix of sandy and clayey soils. Full 3D and 2D modified plane-strain computations are carried out. A strategy to construct an equivalent 2D model starting from a 3D regular enough building is introduced. A detailed analysis of the influence of the motion database size on the vulnerability assessment for the studied case is presented.

Chapter 1

Numerical modeling of non-linear dynamical SSI

Contents

1.1 Introduction

The assessment of the dynamical soil-structure interaction phenomenon demands the study of several aspects of the problem, among others: the definition of the seismic hazard, site topography and ground water level, the non-linear soil behavior of the soil under cyclic loading, the spatial variation of the soil properties, the non-linear dynamic soil response of the superstructure and the wave pattern modification due to neighboring structures. Nevertheless, several simplifications must be done in order to formulate a problem which can be solved with the today's state of the art earthquake engineering numerical methods.

In §1.2 a brief review of the governing equations of the dynamical soil-structure problem in view of a material non-linear finite element numerical implementation is presented. Afterwards, some simplifications introduced for the numerical modeling in earthquake engineering practice will be presented. Section 1.3 presents the theoretical formulation and the implementation of the different constitutive models used to take into account the material non-linear behavior of the different constituents of the problem. Finally, §1.4 presents some special aspects of the numerical resolution of the dynamical non-linear soil-structure interaction problem using the Finite Element Method. Some numerical validation of the used finite element tool (*GEFDyn*) under linear elastic behavior assumption is also presented in this section.

1.2 Definition of the problem

1.2.1 Governing equations

To derive the basic motion governing equations, it is sufficient to examine a generic structure embedded in soil under an incoming earthquake excitation $\underline{u}_i(\underline{x}, t)$ (Fig. 1.1). The dynamic system consists of two sub-domains, the superstructure Ω_b (bounded by Γ_b) and the soil (unbounded half-space). As it is impossible to cover the unbounded domain with a finite element discretization, an artificial boundary Γ_s has to be introduced for modeling purposes. In addition, appropriate boundary conditions must be introduced to represent the missing soil (§1.2.3). Depending on the type of boundary condition enforced, the location of the artificial boundary is a function of the level of material damping of the soil, the frequency range of interest, the wave velocity, and the duration of the excitation (Wolf, 1985). Therefore, the total domain can be decomposed in two bounded sub-domains: the soil Ω_s (two-phases) and the superstructure Ω_b (one-phase). These domains are separated by an interface Σ_{bs}. Hereafter, the displacements in the Ω_s and Ω_b due to a dynamic loading are denoted by $\underline{u}_s(\underline{x}, t)$ and $\underline{u}_b(\underline{x}, t)$ respectively. The mechanical problem consists in computing the stress field $\underline{\underline{\sigma}}_s(\underline{u}_s)$ on the soil and $\underline{\underline{\sigma}}_b(\underline{u}_b)$ on the superstructure domain verifying the momentum conservation.
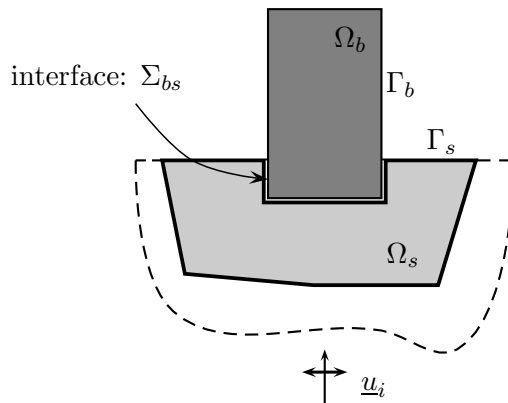
Figure 1.1: Definition of the global system

Assuming a fully saturated soil domain (Ω_s), the total stress tensor $\underline{\underline{\sigma}}_s$ can be decomposed into an effective stress tensor $\underline{\underline{\sigma}}'_s$ and the pore pressure p, according with the Therzaghi's principle:

$$\underline{\underline{\sigma}}_s = \underline{\underline{\sigma}}'_s - p.\underline{\underline{I}} \tag{1.1}$$

where $\underline{\underline{I}}$ is the second-order identity tensor. In (1.1) the continuum mechanic's sign convention is assumed, i.e. tractions are positive. This decomposition is strictly correct only if the increment of pore pressure for a constant effective stress does not deforms the soil's skeleton. The complete formulation of the problem for the soil domain includes the conservation relations, the constitutive model, the boundary and the initial conditions. Biot (1962) formulated for the first time the dynamic behavior of saturated porous media. The latter author generalized the consolidation theory to three dimensional case and introduced the inertia forces and the compressibility of pore water, but did not include the Terzaghi's principle in his formulation. The mathematical formulation of the complete problem can be done using several choices of dependant variables. Either, the absolute displacements of the solid and of the fluid and the pressure ($\underline{u}_s$, $\underline{u}_f$, p) (Zienkiewicz and Shiomi, 1984) or the absolute displacements of the solid, the relative displacement of the fluid and the pressure ($\underline{u}_s$, $\underline{u}_{rf}$, p) (Modaressi, 1987; Aubry and Modaressi, 1992b) can be used. These approaches are interesting for higher frequencies. However, for the frequency range suited in earthquake engineering some simplifications are possible. Zienkiewicz et al. (1980) proposed a simplified formulation of Biot's equation in dynamics ($\underline{u}_s - p$ formulation) for low-frequency range. In this approach, the relative acceleration of the fluid to the solid phase is neglected resulting in a reduction of unknowns. In this case, the momentum conservation may be written as:

$$\operatorname{div} \underline{\underline{\sigma}}'_s - \operatorname{grad} p + \rho \, \underline{g} = \rho \, \underline{\ddot{u}}_s \tag{1.2}$$

where $\underline{\ddot{u}}_s$ is the absolute acceleration vector of the solid skeleton and ρ is the mean soil's specific mass:

$$\rho = (1 - n) \, \rho_s + n\rho_f \tag{1.3}$$

where n is the porosity, ρ_s the density of the solid phase and ρ_f the density of the fluid.

The movement of one phase with respect to the other is controlled by the flow equation (generalized Darcy's law) for the simplified $\underline{u}_s - p$ approach:

$$\underline{\dot{u}}_{rf} = \underline{\underline{K}}. \left(-\operatorname{grad} p + \rho_f \left(\underline{g} - \rho \, \underline{\ddot{u}}_s \right) \right) \tag{1.4}$$

where $\underline{\dot{u}}_{rf}$ is the relative velocity vector between the solid phase and the fluid: $\underline{u}_{rf} = n \left(\underline{u}_f - \underline{u}_s \right)$ and $\underline{\underline{K}}$ is the permeability tensor:

$$\underline{\underline{K}} = \frac{\underline{\underline{k}}}{\rho_f . g} \tag{1.5}$$

in which $\underline{\underline{k}}$ is the kinematic permeability tensor.

The combination of the mass conservation for each phase gives the following expression:

$$\operatorname{div} \underline{\dot{u}}_{rf} + \operatorname{div} \underline{\dot{u}}_s = -n \frac{\dot{p}}{K_f} - (1 - n) \frac{\dot{p}}{K_s} \tag{1.6}$$

where K_f and K_s are the compressibility of the fluid and the solid skeleton, respectively. Using (1.4) the relative displacement of the fluid may be eliminated:

$$\operatorname{div} \underline{\dot{u}}_s - \operatorname{div} \left(\underline{\underline{K}}.\operatorname{grad} \left(p - \rho_f \underline{g}.\underline{x} \right) \right) - \operatorname{div} \left(\underline{\underline{K}}.\rho_f \underline{\ddot{u}}_s \right) + \frac{\dot{p}}{Q} = 0 \tag{1.7}$$

so that the solid phase displacement and the pore pressure are the only unknown variables. The compressibility parameter Q is given by:

$$\frac{1}{Q} = \frac{n}{K_f} + (1 - n) \frac{1}{K_s} \tag{1.8}$$

The main advantage of the simplified model is related to the reduction of the numerical cost. For example, for a 3D finite element model the number of degrees of freedom at each node, in the soil domain Ω_s, is reduced from 6 to 4. The inaccuracies of the $\underline{u}_s - p$ simplified approach are pronounced only in high-frequency, short-duration phenomena (Zienkiewicz et al., 1999). The limits of validity of this approach are extensively studied by Zienkiewicz et al. (1980, 1999) following a comparative one-dimensional analysis between the complete and the approximative formulation and the undrained case assuming linear elastic soil's skeleton behavior.

In summary, the two sets of equations which describe together with the initial and boundary conditions (§1.2.2) the $\underline{u}_s - p$ formulation for the two-phases soil domain Ω_s are given by:

$$\underline{\operatorname{div}} \, \underline{\sigma}_s' - \underline{\operatorname{grad}} \, p + \rho \, \underline{g} \; = \; \rho \ddot{\underline{u}}_s \quad \forall \underline{x} \in \Omega_s \tag{1.9}$$

$$\operatorname{div} \dot{\underline{u}}_s - \operatorname{div} \left(\underline{\underline{K}} . \underline{\operatorname{grad}} \left(p - \rho_f \underline{g} . \underline{x} \right) \right) - \operatorname{div} \left(\rho_f \underline{\underline{K}} . \ddot{\underline{u}}_s \right) + \frac{\dot{p}}{Q} \; = \; 0 \quad \forall \underline{x} \in \Omega_s \tag{1.10}$$

to this one should add the constitutive model (§1.3.4) for the soil skeleton.

It is also necessary to take into account the interaction between the two deformable domains by writing the conditions of compatibility over the interface Σ_{bs} (§1.2.2).

The equilibrium equation for the superstructure domain (Ω_b) can be written as:

$$\underline{\operatorname{div}} \, \underline{\sigma}_b + \rho_b \, \underline{g} = \rho_b \ddot{\underline{u}}_b \quad \forall \underline{x} \in \Omega_b \tag{1.11}$$

where $\underline{g}$ is the acceleration of gravity and ρ_b the specific mass of the superstructure material.
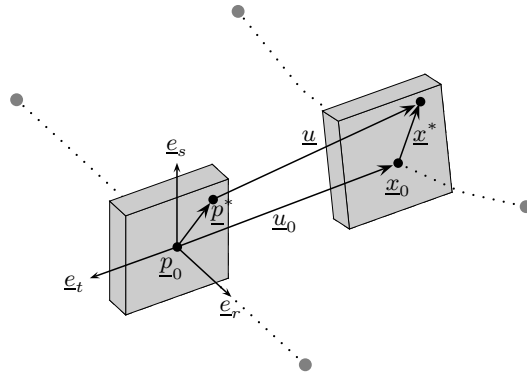
Figure 1.2: Notation for continuous beam geometry and section

Concerning this domain (Ω_b), we assume a Mindlin kinematics which describes the displacement by two independent fields of translations and rotations. In this formulation the plane sections originally normal to the mindlin axis remain plane and undistorted under deformation but not necessarily normal to this axis. This assumption does not allow warping effects in torsion and corresponds to the Bernouilli beam theory. The parametric description in the undeformed configuration of the domain Ω_b is noted as:

$$\underline{p}(r, s, t) = \underline{p}_0(r) + s\underline{e}_s + t\underline{e}_t = \underline{p}_0 + \underline{p}^* \tag{1.12}$$

where $\underline{p}_0(r)$ is the position on the middle line and $\underline{p}^*$ is the vector describing the section. After the loading, the deformed configuration can be written under the assumption of a rigid section as:

$$\underline{x}(r, s, t) = \underline{x}_0(r) + s\underline{\underline{R}}(s, t)\underline{e}_s + t\underline{\underline{R}}(s, t)\underline{e}_t = \underline{x}_0 + \underline{x}^* \tag{1.13}$$

where $\underline{\underline{R}}$ specifies the rotation of the section. If the rotation is small, it can be approached by:

$$\underline{\underline{R}} = \underline{\underline{I}} + \underline{\underline{U}}_1 \tag{1.14}$$

where $\underline{\underline{U}}_1$ is antisymmetric. The displacement field in Ω_b is given by:

$$\underline{u}_b = \underline{x} - \underline{p} \tag{1.15}$$

so that:

$$\underline{u}_b(r,s,t) = \underline{u}_0(r) + s\,\underline{\underline{U}}_1(r)\underline{e}_s + t\,\underline{\underline{U}}_1(r)\underline{e}_t = \underline{u}_0 + \underline{\underline{U}}_1\underline{x}^* \tag{1.16}$$

Therefore, the kinematic of the Ω_b domain is dependent of only two variables, the vector field $\underline{u}_0(r)$ along the displacement axis and the small rotations antisymmetric operator $\underline{\underline{U}}_1(r)$. The operator $\underline{\underline{U}}_1$ is associated to a rotation vector $\underline{u}_1$ by a wedge product:

$$\underline{u}_b = \underline{u}_0 + \underline{u}_1 \wedge \underline{x}^* \tag{1.17}$$

The gradient of the displacement field can be computed as:

$$\underline{\underline{\mathrm{grad}}}\,\underline{u}_b = \partial_r \underline{u}_b \otimes \underline{e}_r + \partial_s \underline{u}_b \otimes \underline{e}_s + \partial_t \underline{u}_b \otimes \underline{e}_t \tag{1.18}$$

According to the kinematics defined by (1.16), the gradient can be written as:

$$
\begin{aligned}
\underline{\underline{\mathrm{grad}}}\,\underline{u}_b &= \left(\partial_r \underline{u}_0 + \partial_r \underline{\underline{U}}_1 . \underline{x}^*\right) \otimes \underline{e}_r + \underline{\underline{U}}_1\left(\underline{e}_s \otimes \underline{e}_s\right) + \underline{\underline{U}}_1\left(\underline{e}_t \otimes \underline{e}_t\right)\\
&= \left(\partial_r \underline{u}_0 + \partial_r \underline{\underline{U}}_1 . \underline{x}^*\right) \otimes \underline{e}_r + \underline{\underline{U}}_1\left(\underline{\underline{I}} - \underline{e}_r \otimes \underline{e}_r\right)\\
&= \left(\partial_r \underline{u}_b - \underline{u}_1 \wedge \underline{e}_r\right) \otimes \underline{e}_r + \underline{\underline{U}}_1
\end{aligned}
\tag{1.19}
$$

The strain tensor $\underline{\underline{\varepsilon}}$ is related to $\underline{u}_b$ by:

$$\underline{\underline{\varepsilon}}\,(\underline{u}_b) = \frac{1}{2}\left(\underline{\underline{\mathrm{grad}}}\,\underline{u}_b + \underline{\underline{\mathrm{grad}}}\,\underline{u}_b^t\right) \tag{1.20}$$

Using the previous definitions, and using the antisymmetric property of $\underline{\underline{U}}_1$, the strain tensor becomes:

$$\underline{\underline{\varepsilon}}\,(\underline{u}_b) = \left(\partial_r \underline{u}_b - \underline{u}_1 \wedge \underline{e}_r\right) \otimes_s \underline{e}_r = \left(\partial_r \underline{u}_0 - \underline{\underline{U}}_1 \underline{e}_r + \partial_r \underline{\underline{U}}_1 \underline{x}^*\right) \otimes_s \underline{e}_r \tag{1.21}$$

Expanding the previous expression, we obtain:

$$
\begin{aligned}
\underline{\underline{\varepsilon}}\,(\underline{u}_b) &= \left(\partial_r u_{0_r} + \left(\partial_r \underline{\underline{U}}_1 \underline{x}^*\right).\underline{e}_r\right)\underline{e}_r \otimes \underline{e}_r + \left(\partial_r \underline{u}_0.\underline{e}_s - \left(\underline{\underline{U}}_1\underline{e}_r\right).\underline{e}_s + \left(\partial_r \underline{\underline{U}}_1 \underline{x}^*\right).\underline{e}_s\right)\underline{e}_s \otimes_s \underline{e}_r\\
&\quad + \left(\partial_r \underline{u}_0.\underline{e}_t - \left(\underline{\underline{U}}_1\underline{e}_r\right).\underline{e}_t + \left(\partial_r \underline{\underline{U}}_1 \underline{x}^*\right).\underline{e}_t\right)\underline{e}_t \otimes_s \underline{e}_r
\end{aligned}
\tag{1.22}
$$

We verify that $\varepsilon_{ss} = \varepsilon_{tt} = \varepsilon_{st} = 0$, which means that no deformation within each transverse section exist. It is possible to identify the following terms

$$\partial_r u_{0_r} \quad : \quad \text{axial strain}$$

$$\partial_r \underline{u}_0.\underline{e}_\alpha - \left(\underline{\underline{U}}_1\underline{e}_r\right).\underline{e}_\alpha \quad \text{with} \quad \alpha = s,t \quad : \quad \text{transverse shear strain}$$

$$\left(\partial_r \underline{\underline{U}}_1 \underline{x}^*\right).\underline{e}_r = \left(\partial_r \underline{u}_1 \wedge \underline{x}^*\right).\underline{e}_r \quad : \quad \text{bending strain}$$

$$\left(\partial_r \underline{\underline{U}}_1 \underline{x}^*\right).\underline{e}_\alpha = \left(\partial_r \underline{u}_1 \wedge \underline{x}^*\right).\underline{e}_\alpha \quad \text{with} \quad \alpha = s,t \quad : \quad \text{torsional strain}$$

The hypothesis of Bernouilli is adopted, i.e. it is assumed the orthogonality of the section with respect to the deformed midline. This assumption implies that the transverse shear is zero:

$$\partial_r \underline{u}_0.\underline{e}_\alpha - \left(\underline{\underline{U}}_1\,\underline{e}_r\right).\underline{e}_\alpha = 0 \quad \text{with} \quad \alpha = s,t \tag{1.23}$$

In this case, the rotation associated with the bending can be expressed from the displacement of the axis:

$$\underline{e}_r \wedge \left(\partial_r\left(\underline{u}_0.\underline{e}_s\right)\underline{e}_s + \partial_r\left(\underline{u}_0.\underline{e}_t\right)\underline{e}_t\right) = \underline{e}_r \wedge \left(\underline{u}_1 \wedge \underline{e}_r\right) = \underline{u}_1 - u_{1_r}\underline{e}_r \tag{1.24}$$

from which:

$$\underline{u}_1 = \underline{e}_r \wedge \left(\partial_r\left(\underline{u}_0.\underline{e}_s\right)\underline{e}_s + \partial_r\left(\underline{u}_0.\underline{e}_t\right)\underline{e}_t\right) + u_{1_r}\underline{e}_r \tag{1.25}$$

Replacing in the bending strain expression:

$$\begin{aligned}
\partial_r\underline{\underline{U}}_1\underline{x}^* &= \partial_r\underline{u}_1 \wedge \underline{x}^* \\
&= \left(\underline{e}_r \wedge \left(\partial_{rr}\left(\underline{u}_0.\underline{e}_s\right)\underline{e}_s + \partial_{rr}\left(\underline{u}_0.\underline{e}_t\right)\underline{e}_t\right) + \partial_r u_{1_r}\underline{e}_r\right) \wedge \underline{x}^* \\
&= -\left(\underline{x}^*.\left(\partial_{rr}\left(\underline{u}_0.\underline{e}_s\right)\underline{e}_s + \partial_{rr}\left(\underline{u}_0.\underline{e}_t\right)\underline{e}_t\right)\right)\underline{e}_r + \partial_r u_{1_r}\underline{e}_r \wedge \underline{x}^*
\end{aligned} \tag{1.26}$$

And finally, the strain tensor can be written as:

$$\begin{aligned}
\underline{\underline{\varepsilon}}\left(\underline{u}_b\right) &= \left(\partial_r u_{0_r}\underline{e}_r + \partial_r\underline{u}_1 \wedge \underline{x}^*\right) \otimes_s \underline{e}_3 \\
&= \left(\left(\partial_r u_{0_r} - \underline{x}^*.\left(\partial_{rr}\left(\underline{u}_0.\underline{e}_s\right)\underline{e}_s + \partial_{rr}\left(\underline{u}_0.\underline{e}_t\right)\underline{e}_t\right)\right)\underline{e}_r + \partial_r u_{1_r}\underline{e}_3 \wedge \underline{x}^*\right) \otimes_s \underline{e}_r
\end{aligned} \tag{1.27}$$

Therefore, the movement can be described by the vector field $\underline{u}_0$ and the twisting component u_{1_r}, both function of the spatial variable r.

1.2.2 Boundary and Interface Conditions

The boundary conditions for the soil domain Ω_s will be more complex than for the superstructure domain Ω_b because they must be decomposed into boundary conditions relative to the solid phase and in fluid flow.

For the superstructure, a traction boundary condition is applied (free surface in dynamics):

$$\underline{t}_b\left(\underline{x},t\right) = \underline{\underline{\sigma}}_b.\underline{n} = \underline{0} \quad \forall \underline{x} \in \Gamma_{b_\sigma} = \Gamma_b \tag{1.28}$$

where $\underline{t}_b$ is the stress vector following the exterior normal direction $\underline{n}$ of Γ_b. For some static computations, this boundary condition is slightly modified using prescribed values for tractions $\underline{t}^*$ over a portion of the boundary $\Gamma_{b_\sigma}^*$ ($\Gamma_{b_\sigma}^* \cap \Gamma_{b_\sigma} = \emptyset$ and $\Gamma_{b_\sigma}^* \cup \Gamma_{b_\sigma} = \Gamma_b$):

$$\begin{aligned}
\underline{t}_b\left(\underline{x}\right) &= \underline{0} \quad \forall \underline{x} \in \Gamma_{b_\sigma} \\
\underline{t}_b\left(\underline{x}\right) &= \underline{t}^*\left(\underline{x}\right) \quad \forall \underline{x} \in \Gamma_{b_\sigma}^*
\end{aligned} \tag{1.29}$$

Because of the equations (1.9) and (1.10), the boundary Γ_s of the domain Ω_s is decomposed into two types of partitioning. First (1.9) into two parts (mechanical boundary): Γ_{s_σ} and Γ_{s_u}. On Γ_{s_u} the displacement is imposed while the total traction boundary condition is retaining on Γ_{s_σ} ($\Gamma_{s_u} \cap \Gamma_{s_\sigma} = \emptyset$ and $\Gamma_{s_u} \cup \Gamma_{s_\sigma} = \Gamma_s$). For the fluid flow boundary conditions, another partition is considered: Γ_{s_p} and Γ_{s_φ} ($\Gamma_{s_p} \cap \Gamma_{s_\varphi} = \emptyset$ and $\Gamma_{s_p} \cup \Gamma_{s_\varphi} = \Gamma_s$). On Γ_p there is a pore pressure boundary condition while on Γ_{s_φ} there is a condition on the flux:

$$\underline{\dot{u}}_{rf}\left(\underline{x},t\right).\underline{n} = \varphi^*\left(\underline{x},t\right) \quad \forall \underline{x} \in \Gamma_{s_\varphi} \tag{1.30}$$

where $\underline{n}$ is the exterior normal vector over Γ_{s_φ} and φ^* the prescribed value of the flux.

Over the interface Σ_{bs} between both domains, the condition on the fluid can be either restricted to the nullity of the fluid flow through the interface:

$$\left(\underline{\underline{K}} \cdot \underline{\text{grad}}\, p(\underline{x}, t) \right) \cdot \underline{n} = 0 \quad \forall \underline{x} \in \Sigma_{bs} \tag{1.31}$$

or the atmospheric pressure. $\underline{n}$ is the exterior normal vector of Ω_s over the interface Σ_{bs}. The continuity of the stress vector must be verified over the interface (even if uplift appears):

$$\underline{t}_b\left(\underline{x}, t\right) + \underline{t}_s\left(\underline{x}, t\right) = \underline{0} \quad \forall \underline{x} \in \Sigma_{bs} \tag{1.32}$$

in which $\underline{t}_s$ is the stress vector applied on Γ_s. Concerning the displacement, discontinuities are allowed between Ω_s and Ω_b over the interface Σ_{bs}. If $[\cdot]$ represents the jump of a quantity, the jump of displacements between the superstructure and the soil on the interface Σ_{bf} can written as:

$$[\underline{u}(\underline{x}, t)] = \underline{u}_b(\underline{x}, t) - \underline{u}_s(\underline{x}, t) \quad \forall \underline{x} \in \Sigma_{bs} \tag{1.33}$$

1.2.3 Earthquake input and dynamic boundary conditions

The specification of the earthquake input motion for a fixed base structure problem is usually done by prescribing the base displacement $u_g(t)$ or base acceleration $\ddot{u}_g(t)$. In this approach, the problem is usually formulated in terms of the displacement relative to this base movement, but can be also formulated in terms of the total displacements.
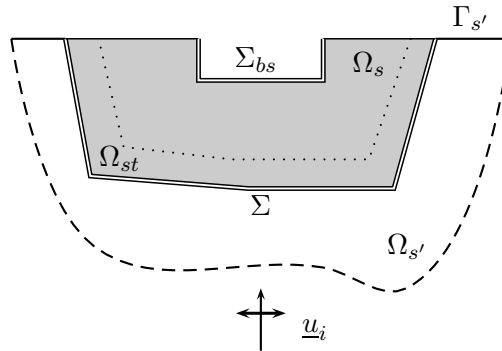
Figure 1.3: Domain decomposition for dynamic boundary conditions

In the case of an earthquake non-linear SSI problem treated by a finite elements approach, where a truncated portion of the surrounding soil is added to the problem, the fixed base procedure is strictly not applicable. In this case, the soil truncation boundary must allow the incoming seismic wave to enter to the model, as well as to ensure that the outgoing waves are transmitted. In order to formulate an appropriate absorbing/incident boundary model, the total unbounded soil domain can be divided in two distinct sub-domains Ω_s and $\Omega_{s'}$ (Fig. 1.3). The domain Ω_s is non-linear and two phase, and obeys the equations of the previous sections. The domains $\Omega_{s'}$ is assumed to be elastic, homogenous, isotropic, monophasic and unbounded. The behavior of this last will be modelled by the paraxial approximation of the elastodynamics equations (Modaressi, 1987; Engquist and Majda, 1977). If the displacement field in $\Omega_{s'}$ is denoted by $\underline{u}_{s'}$, the equation of elastodynamics in time domain can be written as:

$$(\lambda + \mu)\,\underline{\text{grad}}\,(\text{div}\underline{u}_{s'}) + \mu \triangle \underline{u}_{s'} = \rho_{s'}\ddot{\underline{u}}_{s'} \quad \forall \underline{x} \in \Omega_{s'} \tag{1.34}$$

where λ and μ are the Lamé elastic constants and $\rho_{s'}$ the mass density. Free field conditions are supposed on the boundary $\Gamma_{s'}$ of $\Omega_{s'}$. The displacement field $\underline{u}_{s'}$ must tend to incident field $\underline{u}_i$ far enough from the interface Σ between Ω_s and $\Omega_{s'}$:

$$\lim_{\|\underline{x}\| \to \infty} \underline{u}_{s'} = \underline{u}_i \tag{1.35}$$

The stress tensor on $\Omega_{s'}$ can be decomposed in a static part $\underline{\underline{\sigma}}_{s'}^0$ due to gravity and static loads, and a dynamic part due to $\underline{u}_{s'}$:

$$\underline{\underline{\sigma}}_{s'} = \underline{\underline{\sigma}}_{s'}^0 + \underline{\underline{\sigma}}_{s'}\left(\underline{u}_{s'}\right) \tag{1.36}$$

At the interface Σ, the continuity of the displacements and the stress vector must be respected:

$$\underline{u}_{s'} = \underline{u}_s \quad \text{and} \quad \underline{t}_s + \underline{t}_{s'}\left(\underline{u}_{s'}\right) = \underline{0} \tag{1.37}$$

It is assumed that an elastic monophasic transition soil portion Ω_{st} exists between Σ and Ω_s (Fig. 1.3). This sub-domain obeys the elastodynamics equations. Finally, the initial conditions for unbounded domain $\Omega_{s'}$ are:

$$
\begin{aligned}
\underline{u}_{s'}(0) &= \underline{0} \\
\underline{\underline{\sigma}}_{s'}(0) &= \underline{\underline{\sigma}}_{s'}^0 \\
\underline{\dot{u}}_{s'}(0) &= \underline{0}
\end{aligned}
\tag{1.38}
$$

Several authors have proposed perfectly boundary conditions for general classes of wave propagation problems. Unfortunately, these boundary conditions are necessarily nonlocal in both space and time, and thus are not useful for practical calculations in time domain. In time domain, the simpler solution is to use viscous dampers, but the efficacy of this approach decays when the outgoing wave is not perfectly normal to the damper orientation. Additionally, a total displacement splitting in an incoming wave and the displacement relative to the incoming displacement must be done for earthquake incident fields problems (Zienkiewicz et al., 1988). The paraxial approximation (Engquist and Majda, 1977), allows to develop a local dynamic impedance in time and space on the interface Σ. This kind of boundary approximation can be easily extended to be used simultaneously as an absorbing boundary and as a tool to impose an incident field (Modaressi, 1987). Details about the derivation of the paraxial approximation implemented in *GEFDyn* are provided in the Appendix A.

1.2.4 Variational formulation

The weak form of the governing equations can be obtained using a variational formulation. The set of kinematically acceptable displacement fields $\mathbb{V}_b$ for the Ω_b domain is defined as:

$$\mathbb{V}_b = \{\underline{w}_b \,|\, \underline{w}_b \text{ regular in } \Omega_b\,,\; \underline{w}_b(\underline{x}) = \underline{0} \text{ on } \Gamma_{b_u}\}$$

Similarly, for the Ω_s domain a set of acceptable kinematically displacement fields $\mathbb{V}_s$ and a set of admissible pressure fields $\mathbb{Q}$ can be defined:

$$
\begin{aligned}
\mathbb{V}_s &= \{\underline{w}_s \,|\, \underline{w}_s \text{ regular in } \Omega_s\,,\; \underline{w}_s(\underline{x}) = \underline{0} \text{ on } \Gamma_{s_u}\} \\
\mathbb{Q} &= \{q \,|\, q \text{ regular in } \Omega_s\,,\; q(\underline{x}) = \underline{0} \text{ on } \Gamma_{s_p}\}
\end{aligned}
$$

Considering the previous definitions, the variational formulation of (1.11) can be written as:

$$\int_{\Omega_b} \underline{\underline{\sigma}}_b : \underline{\underline{\varepsilon}}_b\left(\underline{w}_b\right) dV + \int_{\Omega_b} \rho_b \underline{\ddot{u}}_b.\underline{w}_b dV = \int_{\Omega_b} \rho_b\, \underline{g}.\underline{w}_b dV + \int_{\Sigma_{bs}} \underline{t}_b.\underline{w}_b dS + \int_{\Gamma_{b_\sigma}} \underline{t}_b.\underline{w}_b dS \tag{1.39}$$

using the Stoke's formula and the boundary conditions described in the previous section. According to (1.28), the last term vanishes for the dynamic case. $\underline{\underline{\varepsilon}}_b$ is the strain tensor associated to the virtual displacement field $\underline{w}_b$. Using the kinematics imposed for the displacement field:

$$\underline{w}_b(r, s, t) = \underline{w}_0(r) + \underline{w}_1(r) \wedge \underline{x}_{s'}^* \tag{1.40}$$

the inertia term in (1.39) can be computed as:

$$
\int_{\Omega_b} \rho_b \, \underline{\ddot{u}}_b . \underline{w}_b \, dV = \int_L \int_S \rho_b \left(\underline{\ddot{u}}_0 + \underline{\ddot{u}}_1 \wedge x^* \right) . \left(\underline{\ddot{w}}_0 + \underline{\ddot{w}}_1 \wedge \underline{x}^* \right) dS dl
$$

$$
= \int_L \bar{\rho} \, \underline{\ddot{u}}_0 . \underline{w}_0 + \bar{\rho}\underline{\bar{x}} . \left(\underline{\ddot{u}}_0 \wedge \underline{w}_1 - \underline{\ddot{u}}_1 \wedge \underline{w}_0 \right) + \left(\underline{\underline{J}} \, \underline{\ddot{u}}_1 \right) . \underline{w}_1 \, dl \tag{1.41}
$$

where dl and dS indicates integration following the midline and over the section, respectively. The mass density per unit of length ($\bar{\rho}$), the center of inertia of the section $\bar{x}$ and the inertia operator of the section ($\underline{\underline{J}}$) are defined by:

$$
\bar{\rho} = \int_S \rho_b \, dS \quad ; \quad \bar{\rho}\underline{\bar{x}} = \int_S \rho_b \underline{x}^* \, dS \quad \text{and} \quad \underline{\underline{J}} = \int_S \rho \left(|\underline{x}^*|^2 \, \underline{\underline{I}} - \underline{x}^* \otimes \underline{x}^* \right) dS
$$

If the inertia center of the section is not on the midline, coupling effects appears between axial and bending fields. The integration of internal force term can be also decomposed into the axial direction and over the section. Using the imposed kinematics and the symmetry of the stress tensor, it can be written as:

$$
\int_{\Omega_b} \underline{\underline{\sigma}}_b : \underline{\underline{\varepsilon}} \left(\underline{w}_b \right) dV = \int_L \int_S \left(\underline{\underline{\sigma}}_b \, \underline{e}_r \right) . \left(\partial_r \underline{w}_b - \underline{w}_1 \wedge \underline{e}_r \right) dS dl
$$

$$
= \int_L \int_S \left(-\underline{e}_r \wedge \left(\underline{\underline{\sigma}}_b \, \underline{e}_r \right) \right) . \underline{w}_1 + \left(\underline{\underline{\sigma}}_b \, \underline{e}_r \right) . \partial_r \underline{w}_b \, dS dl
$$

$$
= \int_L \left(-\underline{e}_r \wedge \underline{q} \right) . \underline{w}_1 + \underline{q} . \partial_r \underline{w}_0 + \underline{m} . \partial_r \underline{w}_1 \, dl \tag{1.42}
$$

where $\underline{q}$ and $\underline{m}$ are the resultant force and the bending moment over the section:

$$
\underline{q} = \int_S \underline{\underline{\sigma}}_b \, \underline{e}_r \, dS \quad \text{and} \quad \underline{m} = \int_S \underline{x}^* \wedge \left(\underline{\underline{\sigma}}_b \, \underline{e}_r \right) dS
$$

The body forces can be computed by a similar way:

$$
\int_{\Omega_b} \rho_b \underline{g} . \underline{w}_b \, dV = \int_L \int_S \rho \underline{g} . \left(\underline{w}_0 + \underline{w}_1 \wedge \underline{x}^* \right) dS dl
$$

$$
= \rho \int_L \int_S \underline{g} . \underline{w}_0 + \left(\underline{x}^* \wedge \underline{g} \right) . \underline{w}_1 \, dS dl
$$

$$
= \int_L \underline{q}_g . \underline{w}_0 + \underline{m}_g . \underline{w}_1 \, dl \tag{1.43}
$$

where $\underline{q}_g$ and $\underline{m}_g$ are the section equivalent forces and moments due to body forces:

$$
\underline{q}_g = \int_S \rho_b \, \underline{g} \, dS \quad \text{and} \quad \underline{m}_g = \int_S \rho_b \, \underline{x}^* \wedge \underline{g} \, dS
$$

Similarly, the variational formulation for the soil domain (1.10) is given by:

$$\int_{\Omega_s} \rho \, \underline{\ddot{u}}_s . \underline{w}_s \, dV + \int_{\Omega_s} \underline{\underline{\sigma}}'_s : \underline{\underline{\varepsilon}}_s \left(\underline{w}_s \right) dV - \int_{\Omega_s} p.\mathrm{div} \left(\underline{w}_s \right) dv = \int_{\Omega_s} \rho \, \underline{g} . \underline{w}_s dV +$$

$$\int_{\Gamma_{s_\sigma}} \underline{t}_s . \underline{w}_s dS + \int_{\Sigma_{bs}} \underline{t}_s . \underline{w}_s dS \quad (1.44)$$

$$-\int_{\Omega_s} \rho_f \, \mathrm{div} \left(\underline{\underline{K}} . \underline{\ddot{u}}_s \right) .q dV + \int_{\Omega_s} \mathrm{div} \, \underline{\dot{u}}_s . q \, dV + \int_{\Omega_s} \frac{\dot{p}}{Q} . q \, dV$$

$$+ \int_{\Omega_s} \left(\underline{\underline{K}} . \underline{\mathrm{grad}} \, p \right) . \underline{\mathrm{grad}} \, q \, dV = \int_{\Gamma_\varphi} \varphi^* . q \, dS$$

$$- \int_{\Omega_s} \left(\underline{\underline{K}} . \underline{\mathrm{grad}} \left(\rho_f \underline{g} . \underline{x} \right) \right) . \underline{\mathrm{grad}} \, q \, dV$$

$$(1.45)$$

where $\underline{\underline{\varepsilon}}_s$ is the strain tensor associated to the virtual displacement field, $\underline{w}_s$, in the soil domain. The terms over the interface Σ_{bs} in (1.39) and (1.45) can be related using the relation between the jump of the displacement $[\underline{u}]$ ($[\underline{w}]$ in the variational formulation) and the continuity of the stress vector ($\underline{t}_s = -\underline{t}_b$), introducing coupling between the soil and the superstructure.

$$\int_{\Sigma_{bs}} \underline{t}_b . \underline{w}_b dS + \int_{\Sigma_{bs}} \underline{t}_s . \underline{w}_s dS = \int_{\Sigma_{bs}} \underline{t}_{bs} . [\underline{w}] \, dS \quad (1.46)$$

where $[\underline{w}] = \underline{w}_b - \underline{w}_s$ denotes the jump of the virtual displacements fields between both domains and $\underline{t}_{bs}$ the stress vector over the interface Σ_{bs}.

When a deformable bedrock condition is considered, the first equation of the variational formulation for the soil domain (1.44) can be slightly modified in order to introduce the paraxial approximation at the boundary Σ:

$$\int_{\Omega_s} \rho \, \underline{\ddot{u}}_s . \underline{w}_s \, dV + \int_{\Omega_s} \underline{\underline{\sigma}}'_s : \underline{\underline{\varepsilon}}_s \left(\underline{w}_s \right) dV$$

$$- \int_{\Omega_s} p.\mathrm{div} \left(\underline{w}_s \right) dV = \int_{\Omega_s} \rho \, \underline{g} . \underline{w}_s dV + \int_{\Sigma_{bs}} \underline{t}_{bs} . [\underline{w}] \, dS$$

$$+ \int_{\Gamma_{s_\sigma}} \underline{t}_s . \underline{w}_s dS + \int_{\Sigma} \underline{t}_s . \underline{w}_s dS \quad (1.47)$$

where $\Gamma_s = \Gamma_{s_\sigma} \cup \Sigma_{bs} \cup \Sigma$, $\Gamma_{s_\sigma} \cap \Sigma_{bs} = \emptyset$, $\Gamma_{s_\sigma} \cap \Sigma = \emptyset$ and $\Sigma_{bs} \cap \Sigma = \emptyset$. Introducing the zero-order paraxial approximation (A.36) in the variational formulation:

$$\int_{\Omega_s} \rho \, \underline{\ddot{u}}_s . \underline{w}_s \, dV + \int_{\Omega_s} \underline{\underline{\sigma}}'_s : \underline{\underline{\varepsilon}}_s \left(\underline{w}_s \right) dV$$

$$- \int_{\Omega_s} p.\mathrm{div} \left(\underline{w}_s \right) dV + \int_{\Sigma} \underline{\underline{A}}_0 \left(\underline{\dot{u}}_s \right) . \underline{w}_s dS = \int_{\Omega_s} \rho \, \underline{g} . \underline{w}_s dV + \int_{\Sigma_{bs}} \underline{t}_{bs} . [\underline{w}] \, dS + \int_{\Gamma_{s_\sigma}} \underline{t}_s . \underline{w}_s dS$$

$$+ \int_{\Sigma} \left(-\underline{t}_s \left(\underline{u}_i \right) + \underline{\underline{A}}_0 \left(\underline{\dot{u}}_i \right) \right) . \underline{w}_s dS \quad (1.48)$$

The discretization in space will be treated by finite elements and the discretization in time by a Newmark method. The corresponding matrices are developed below.

1.2.5 Space discretization

A finite element approximation of $\underline{u}_b$, $\underline{u}_s$ and p defined by $\underline{u}_b^h$, $\underline{u}_s^h$ and p^h should be computed by restricting the shape functions to finite dimensional spaces for the displacement and rotations of the superstructure, displacements of the solid phase of the soil and the pressure.

In the superstructure domain Ω_b, we introducing the following finite element approximation $\underline{u}_0^h$ and $\underline{u}_1^h$ for the field displacement $\underline{u}_0$ and the rotations $\underline{u}_1$:

$$
\begin{aligned}
\underline{u}_0^h(\underline{x}, t) &= \sum_{i=1}^{3} \sum_{I=1}^{n_b} N_0^I(\underline{x}) \, \underline{e}_i u_{0_{Ii}}(t) \quad \forall \underline{x} \in \bar{\Omega}_b \\
\underline{u}_1^h(\underline{x}, t) &= \sum_{i=1}^{3} \sum_{I=1}^{n_b} N_1^I(\underline{x}) \, \underline{e}_i u_{1_{Ii}}(t) \quad \forall \underline{x} \in \bar{\Omega}_b
\end{aligned}
\tag{1.49}
$$

where n_b are the total node numbers where displacements and/or rotation are defined, $\bar{\Omega}_b$ denotes the discretized domain and $u_{0_{Ii}}$ and $u_{1_{Ii}}$ are the nodal values. The index I stands for the nodes and i for the DOFs associated to each node. It can be noticed that is not necessary to assume the same shape functions for transverse and extensional displacement N_1^I or for bending and torsional rotations N_0^I.

In the soil domain Ω_s, the finite element spaces have the usual finite element shape functions $N_s^J(\underline{x}).\underline{e}_j$ and $N_p^J(\underline{x})$ where J stands for a node number and, $\underline{e}_j$ is the unit basis vector of the Euclidean space. Therefore the following expansion may be written:

$$
\begin{aligned}
\underline{u}_s^h(\underline{x}, t) &= \sum_{i=1}^{3} \sum_{I=1}^{n_s} N_s^I(\underline{x}) \, \underline{e}_i \, u_{Ii}(t) \quad \forall \underline{x} \in \bar{\Omega}_s \\
p^h(\underline{x}, t) &= \sum_{I=1}^{n_p} N_p^I(\underline{x}) \, p_I(t) \quad \forall \underline{x} \in \bar{\Omega}_s
\end{aligned}
\tag{1.50}
$$

where n_s and n_p are the total node numbers, where solid phase displacement and fluid pressure are defined, respectively; $\bar{\Omega}_b$ and $\bar{\Omega}_s$ are the discretized domains; $u_{Ii}(t)$ and $p_I(t)$ are the nodal values of displacements and pressures. For a 3D case, four degrees of freedom (3 displacements and 1 pore pressure) can be defined in the discretized soil domain $\bar{\Omega}_s$, but for the superstructure up to six degrees of freedom can be required for each node (three displacements and three rotations).

The shape functions for the displacements or the pore pressures may be chosen differently and this choice can influence the quality of the results. So, according to the previous space discretization, the virtual test functions for variational formulation can be chosen successively equal to each member unit basis, that is (Galerkin's method):

$$
\underline{w}_0^{h,J} = \sum_{j=1}^{3} N_0^J \underline{e}_j \quad ; \quad \underline{w}_1^{h,J} = \sum_{j=1}^{3} N_1^J \underline{e}_j \quad ; \quad \underline{w}_s^{h,J} = \sum_{j=1}^{3} N_b^J \underline{e}_j \quad ; \quad p^{h,J} = N_p^J
\tag{1.51}
$$

Using the variational formulation of the equilibrium equation for the superstructure (1.39) and the previous space discretization, the governing equation in the matrix form becomes:

$$
[M_{bb}] \{\ddot{u}_b\} + \{B\sigma_b\} + \{B\sigma_b\}^{bs} = \{f_b\}
\tag{1.52}
$$

The matrix terms are defined by:

$$
\begin{aligned}
[M_{bb}]_{IiJj} &= \int_{\bar{L}} \bar{\rho} N_0^I \underline{e}_i . N_0^J \underline{e}_j + \bar{\rho}\underline{\bar{x}}. \left(N_0^I \underline{e}_i \wedge N_1^J \underline{e}_j - N_1^I \underline{e}_i \wedge N_0^J \underline{e}_j \right) + \left(\underline{J}.N_1^I \underline{e}_i\right).N_1^J \underline{e}_j \, dl \\
\{B\sigma_b\}_{Jj} &= \int_{\bar{L}} \left(-\underline{e}_r \wedge \underline{q}\right).N_1^J \underline{e}_j + \underline{q}.\partial_r N_0^J \underline{e}_j + \underline{m}.\partial_r N_1^J \underline{e}_j \, dl \\
\{B\sigma_b\}_{Jj}^{bs} &= -\int_{\bar{\Sigma}_{bs}} \underline{t}_b. \left(N_0^J \underline{e}_j + N_1^J \underline{e}_j \wedge \underline{x}^*\right) dS \\
\{f_b\}_{Jj} &= \int_{\bar{L}} \underline{q}_g.N_0^J \underline{e}_j + \underline{m}_g.N_1^J \underline{e}_j dl + \int_{\Gamma_{b_\sigma}} \underline{t}_b. \left(N_0^J \underline{e}_j + N_1^J \underline{e}_j \wedge \underline{x}^*\right) dS
\end{aligned}
$$

All the nodal unknowns in $\bar{\Omega}_b$ are regrouped into the vector $\{\ddot{u}_b\}$. Similarly, the corresponding matrix system for the set of equations (1.48) can be written as:

$$[M_{ss}]\{\ddot{u}_s\} + [C_{ss}]\{\dot{u}_s\} + \{B\sigma_s\} + \{B\sigma_s\}^{bs} + [K_{sp}]\{p\} = \{f_s\}$$
$$[M_{ps}]\{\ddot{u}_s\} + [C_{ps}]\{\dot{u}_s\} + [C_{pp}]\{\dot{p}\} + [K_{pp}]\{p\} = \{f_p\}$$

where the vectors $\{\ddot{u}_s\}$, $\{\dot{u}_s\}$, $\{\dot{p}\}$ and $\{p\}$ regroup the nodal accelerations, velocities, pressure time evolution and fluid pressures in the soil domain, respectively. The matrix terms are defined by:

$$[M_{ss}]_{IiJj} = \delta_{ij} \int_{\bar{\Omega}_s} \rho\, N_s^I . N_s^J\, dV$$

$$\{B\sigma_s\}_{Jj} = \int_{\bar{\Omega}_s} \underline{\underline{\sigma}}'_s : \underline{\underline{\varepsilon}}_s \left(N_s^J \underline{e}_j\right)\, dV$$

$$\{B\sigma_s\}_{Jj}^{bs} = -\int_{\bar{\Sigma}_{bs}} \underline{t}_s . \left(N_s^J \underline{e}_j\right)\, dS$$

$$[C_{ss}]_{IiJj} = \int_{\bar{\Sigma}} \underline{\underline{A}}_0 \left(N_s^I \underline{e}_i\right) . N_s^J \underline{e}_j\, dS$$

$$[K_{sp}]_{IJj} = -\int_{\bar{\Omega}_s} N_p^I . \text{div} \left(N_s^J \underline{e}_j\right)\, dV$$

$$\{f_s\}_{Jj} = \int_{\bar{\Omega}_s} \rho\, \underline{g} . \left(N_s^J \underline{e}_j\right)\, dV + \int_{\Sigma_{s\sigma}} \underline{t}_s . \left(N_s^J \underline{e}_j\right)\, dS + \int_{\bar{\Sigma}} \left(-\underline{t}_s(\underline{u}_i) + \underline{\underline{A}}_0(\underline{\dot{u}}_i)\right) . \left(N_s^J \underline{e}_j\right)\, dS$$

$$[M_{ps}]_{IiJ} = \int_{\bar{\Omega}_s} \rho_f \left(\underline{\underline{K}} . \left(N_s^I \underline{e}_i\right)\right) . \underline{\text{grad}}\, N_s^J\, dV$$

$$[C_{ps}]_{IiJ} = \int_{\bar{\Omega}_s} \text{div} \left(N_s^I \underline{e}_i\right) . N_p^J\, dV$$

$$[C_{pp}]_{IJ} = \int_{\bar{\Omega}_s} \frac{1}{Q} N_p^I . N_p^J\, dV$$

$$[K_{pp}]_{IJ} = \int_{\bar{\Omega}_s} \left(\underline{\underline{K}} . \underline{\text{grad}}\, N_p^I\right) . \underline{\text{grad}}\, N_p^J\, dV$$

$$\{f_p\}_J = \int_{\bar{\Gamma}_\varphi} \varphi^* . N_p^J\, dS - \int_{\bar{\Omega}_s} \left(\underline{\underline{K}} . \underline{\text{grad}} \left(\rho_f \underline{g} . \underline{x}\right)\right) . \underline{\text{grad}}\, N_p^J\, dS$$

where δ_{ij} denotes the Kronecker's symbol. In the previous expressions $[M.]$ have the structure of mass matrix, whereas $[K.]$ and $[C.]$ have the structure of stiffness matrix. The vectors $\{f.\}$ correspond to external forces over the system. The vectors $\{B\sigma_b\}$ and $\{B\sigma_s\}$ are associated to internal forces and are non-linearly dependent of the deformations of the system by the material constitutive model. Because of the continuity of the stress vector over the interface Σ_{bs} (1.46):

$$\{B\sigma_b\}_{Jj}^{bs} + \{B\sigma_s\}_{Jj}^{bs} = \int_{\bar{\Sigma}_{bs}} \underline{t}_{bs} . \left[N^J \underline{e}_j\right]\, dS = \{B\sigma_{bs}\}_{Jj} \qquad (1.53)$$

1.2.6 Time discretization

For mechanical systems characterized by components with very different characteristic periods, a numerical effective strategy for transient integration, is to partition the finite elements into implicit/explicit groups (Hughes and Liu, 1977b,a; Hughes et al., 1979). The first step for an implicit/explicit time integration is the definition of an implicit method. The predictor-corrector Newmark scheme with standard parameters β and γ is used separating the unknown values into two sets: let $(\{u\}_n, \{v\}_n, \{a\}_n)$ a series of approximative nodal values of displacements, velocities, accelerations

at time step n (Ω_s and Ω_b domains), and similarly another series ($\{p\}_n$, $\{s\}_n$) of nodal pressures and pressure time evolution at a time n (only Ω_s domain). The Newmark predictor is then given by:

$$
\begin{aligned}
\{\tilde{u}\}_{n+1} &= \{u\}_n + \Delta t\,\{v\}_n + \Delta t^2 \left(\frac{1}{2} - \beta\right)\{a\}_n \\
\{\tilde{v}\}_{n+1} &= \{v\}_n + \Delta t\,(1-\gamma)\,\{a\}_n \\
\{\tilde{p}\}_{n+1} &= \left(\frac{1}{2} + \frac{1}{\beta}\right)\{p\}_n + \left(\frac{1}{2} - \frac{1}{\beta}\right)\{\tilde{p}\}_n + \Delta t\,\{s\}_n \\
\{\tilde{s}\}_{n+1} &= \frac{1}{\gamma}\{s\}_n + \left(1 - \frac{1}{\gamma}\right)\{\tilde{s}\}_n
\end{aligned}
\tag{1.54}
$$

where Δt is the time step, $\{\tilde{u}\}_{n+1}$, $\{\tilde{v}\}_{n+1}$, $\{\tilde{p}\}_{n+1}$ and $\{\tilde{s}\}_{n+1}$ are the predictor values. The Newmark corrector values $\{u\}_{n+1}$, $\{v\}_{n+1}$ and $\{s\}_{n+1}$ are given by:

$$
\begin{aligned}
\{u\}_{n+1} &= \{\tilde{u}\}_{n+1} + \Delta t^2 \beta \{a\}_{n+1} \\
\{v\}_{n+1} &= \{\tilde{v}\}_{n+1} + \Delta t\,\gamma \{a\}_{n+1} \\
\{s\}_{n+1} &= \{\tilde{s}\}_{n+1} + \frac{\gamma}{\Delta t \beta}\left(\{p\}_{n+1} - \{\tilde{p}\}_{n+1}\right)
\end{aligned}
\tag{1.55}
$$

Using the previous expressions, the accelerations and velocities vectors, at time step $n+1$, can only be written in terms of the nodal displacements, pressures and the corresponding predictor values:

$$
\begin{aligned}
\{a\}_{n+1} &= \frac{1}{\beta\,\Delta t^2}\left(\{u\}_{n+1} - \{\tilde{u}\}_{n+1}\right) \\
\{v\}_{n+1} &= \{\tilde{v}\}_{n+1} + \frac{\gamma}{\beta\,\Delta t}\left(\{u\}_{n+1} - \{\tilde{u}\}_{n+1}\right) \\
\{s\}_{n+1} &= \{\tilde{s}\}_{n+1} + \frac{\gamma}{\beta\,\Delta t}\left(\{p\}_{n+1} - \{\tilde{p}\}_{n+1}\right)
\end{aligned}
\tag{1.56}
$$

The matrix form of the variational formulation of each domain (1.39) and (1.45) can be rewritten by partitioning the domains into an explicit group of elements (superscript $\mathbb{E}$) and an implicit group (superscript $\mathbb{I}$) at a time step $n+1$, by eliminating accelerations and velocities using the expressions (1.56). For the superstructure domain, the corresponding matrix form is given by:

$$
\frac{1}{\beta\,\Delta t^2}\,[M_{bb}]\,\{u_b\}_{n+1} + \{B\sigma_b\}^{\mathbb{I}}_{n+1} + \{B\sigma_{bs}\}^{\mathbb{I}}_{n+1} = \{f_b\} + \frac{1}{\beta\,\Delta t^2}\,[M_{bb}]\,\{\tilde{u}_b\}_{n+1} - \{B\sigma\}^{\mathbb{E}}_{n+1}
\tag{1.57}
$$

where:

$$
\begin{aligned}
\{B\sigma_b\}^{\mathbb{I}}_{n+1_{Jj}} &= \int_{\bar{L}^{\mathbb{I}}} \left(-\underline{e}_r \wedge \underline{q}\left(\{u_b\}_{n+1}\right)\right).N_1^J \underline{e}_j + \underline{q}\left(\{u_b\}_{n+1}\right).\partial_r N_0^J \underline{e}_j + \underline{m}\left(\{u_b\}_{n+1}\right).\partial_r N_1^J \underline{e}_j\, dl \\
\{B\sigma_b\}^{\mathbb{E}}_{n+1_{Jj}} &= \int_{\bar{L}^{\mathbb{E}}} \left(-\underline{e}_r \wedge \underline{q}\left(\{\tilde{u}_b\}_{n+1}\right)\right).N_1^J \underline{e}_j + \underline{q}\left(\{\tilde{u}_b\}_{n+1}\right).\partial_r N_0^J \underline{e}_j + \underline{m}\left(\{\tilde{u}_b\}_{n+1}\right).\partial_r N_1^J \underline{e}_j\, dl \\
\{B\sigma_{bs}\}^{\mathbb{I}}_{n+1_{Jj}} &= \int_{\bar{\Sigma}_{bs}} \underline{t}_{bs}\left(\{\tilde{u}_b\}_{n+1}\right).\left[N^J \underline{e}_j\right]\, dS
\end{aligned}
$$

In (1.57) it is assumed that the interface elements are integrated implicitly. Similarly, the corresponding matrix system for the set of equations (1.53) can be written as:

$$\frac{1}{\beta\,\Delta t^2}\,[M_{ss}]\,\{u_s\}_{n+1}+\{B\sigma_s\}^{\mathbb{I}}_{n+1}$$

$$+[K_{sp}]^{\mathbb{I}}\{p\}_{n+1}\;=\;\{f_s\}+\frac{1}{\beta\,\Delta t^2}\,[M_{ss}]\,\{\tilde{u}_s\}_{n+1}-\{B\sigma_s\}^{\mathbb{E}}_{n+1}$$

$$-[K_{sp}]^{\mathbb{E}}\{\tilde{p}\}_{n+1}-\underline{[C_{ss}]\,\{\tilde{v}_s\}_{n+1}} \tag{1.58}$$

$$\frac{\gamma}{\beta\,\Delta t}\,[C_{ps}]^{\mathbb{I}}\{u_s\}_{n+1}+\frac{\gamma}{\beta\,\Delta t}\,[C_{pp}]^{\mathbb{I}}\{p\}_{n+1}$$

$$+[K_{pp}]^{\mathbb{I}}\{p\}_{n+1}\;=\;\{f_p\}+\frac{\gamma}{\beta\,\Delta t}\,[C_{ps}]^{\mathbb{E}}\{\tilde{u}_s\}_{n+1}-[C_{ps}]\{\tilde{v}\}_{n+1}$$

$$+\frac{\gamma}{\beta\,\Delta t}\,[C_{pp}]^{\mathbb{E}}\{\tilde{p}\}_{n+1}-[C_{pp}]\{\tilde{s}\}_{n+1}-[K_{pp}]^{\mathbb{E}}\{\tilde{p}\}_{n+1}$$

$$\underline{-\frac{1}{\beta\,\Delta t^2}\,[M_{ps}]\,\{u_s\}_{n+1}+\frac{1}{\beta\,\Delta t^2}\,[M_{ps}]\,\{\tilde{u}_s\}_{n+1}}$$

$$\tag{1.59}$$

where:

$$\{B\sigma_s\}^{\mathbb{I}}_{n+1\,Jj}\;=\;\int_{\bar{\Omega}^{\mathbb{I}}_s}\underline{\underline{\sigma}}'_s\left(\{u_s\}_{n+1}\right):\underline{\underline{\varepsilon}}_s\left(N^J_s\underline{e}_j\right)\,dV$$

$$[K_{sp}]^{\mathbb{I}}_{IJj}\;=\;-\int_{\bar{\Omega}^{\mathbb{I}}_s}N^I_p.\mathrm{div}\left(N^J_s\underline{e}_j\right)\,dV$$

$$\{B\sigma_s\}^{\mathbb{E}}_{n+1\,Jj}\;=\;\int_{\bar{\Omega}^{\mathbb{E}}_s}\underline{\underline{\sigma}}'_s\left(\{\tilde{u}_s\}_{n+1}\right):\underline{\underline{\varepsilon}}_s\left(N^J_s\underline{e}_j\right)\,dV$$

$$[K_{sp}]^{\mathbb{I}}_{IJj}\;=\;-\int_{\bar{\Omega}^{\mathbb{I}}_s}N^I_p.\mathrm{div}\left(N^J_s\underline{e}_j\right)\,dV$$

$$[C_{ps}]^{\mathbb{I}}_{IiJ}\;=\;\int_{\bar{\Omega}^{\mathbb{I}}_s}\mathrm{div}\left(N^I_s\underline{e}_i\right).N^J_p\,dV$$

$$[C_{ps}]^{\mathbb{E}}_{IiJ}\;=\;\int_{\bar{\Omega}^{\mathbb{E}}_s}\mathrm{div}\left(N^I_s\underline{e}_i\right).N^J_p\,dV$$

$$[C_{pp}]^{\mathbb{I}}_{IJ}\;=\;\int_{\bar{\Omega}^{\mathbb{I}}_s}\frac{1}{Q}N^I_p.N^J_p\,dV$$

$$[C_{pp}]^{\mathbb{E}}_{IJ}\;=\;\int_{\bar{\Omega}^{\mathbb{E}}_s}\frac{1}{Q}N^I_p.N^J_p\,dV$$

$$[K_{pp}]^{\mathbb{I}}_{IJ}\;=\;\int_{\bar{\Omega}^{\mathbb{I}}_s}\left(\underline{\underline{K}}.\underline{\mathrm{grad}}\,N^I_p\right).\underline{\mathrm{grad}}\,N^J_p\,dV$$

$$[K_{pp}]^{\mathbb{E}}_{IJ}\;=\;\int_{\bar{\Omega}^{\mathbb{E}}_s}\left(\underline{\underline{K}}.\underline{\mathrm{grad}}\,N^I_p\right).\underline{\mathrm{grad}}\,N^J_p\,dV$$

In order to preserve a symmetrical system, the underlined term in (1.59) is treated explicitly, i.e. this value is computed using the displacement values at time step n and included in the right-hand side evaluation. This term can also be neglected. The effect of this omission has been reported as insignificant by several authors (Zienkiewicz and Shiomi, 1984; Chan, 1988).

The incident field appears explicitly at the right-hand side of (1.58) in $\{f_s\}$. The underlined term in (1.58) can be treated, explicitly or implicitly in general. In the current implementation in *GEFDyn* this term is treated explicitly. A detailed study of the influence of this term in the numerical stability depending on the adopted time integration scheme is presented in Aubert (1997). This work is conducted using the zero-order monophasic formulation treated explicitly. With these assumptions, the following conditions must be satisfied (Hughes and Liu, 1977b):

$$\gamma \geq \frac{1}{2}$$

and if $[M]$ is defined as:

$$[M] = [M]^{\mathbb{E}} - \frac{\Delta t}{2}[C]^{\mathbb{E}} - \frac{\Delta t^2 \gamma}{2}[K]^{\mathbb{E}}$$

$[M]$ must be positive-definite, where $[\cdot]^{\mathbb{E}}$ denotes symbolically the system mass matrix, the system stiffness matrix and the system damping matrix associated to explicitly treated element groups. Nevertheless, the convergence of the explicit elements must be treated case to case, and usually will control the maximum allowed time step Δt for the global numerical stability.

The incident displacement and velocity field needed for computation are obtained by numerical integration of the input accelerogram with respect to time. This integration requires initial values, which are often unknown, due to recording techniques. A bad initial information leads to a purely numerical drift on displacements when the numerical simulations are carried out. In order to avoid this kind of numerical effect, one of the various base-line correction techniques available in the literature must be used over the incident field.

1.2.7   Resolution of non-linear system

The system defined by the equations (1.57) and (1.59) is in general non-linear. Therefore, the resolution of the implicit terms must be carried out using an iterative algorithm. The iterative procedure implemented in *GEFDyn* is a variation of the method of Newton, using a linearized version of the non-linear system. If the total DOFs of the model are regrouped into a single vector $\{x\}$, the entire non-linear system for a time step $n+1$ can be written as:

$$\{G(\{x\}_{n+1})\} = \{R(\{x\}_{n+1})\} - \{F(\{x\}_{n+1})\} = \{0\} \quad ; \quad \{x\}_{n+1} = \begin{Bmatrix} \{u_b\}_{n+1} \\ \{u_s\}_{n+1} \\ \{p\}_{n+1} \end{Bmatrix} \quad (1.60)$$

where $\{R\}_{n+1}$ regroups the implicit terms and $\{F\}_{n+1}$ the explicit terms and the external loading. The strategy consists to replace $\{G\}_{n+1}$ for the current iteration $k+1$ by its linearization around the previous iteration k ($\{x\}_{n+1}^k$ is known) following the incremental direction $\{\delta x\}$. The truncated Taylor's series (first order) is:

$$\left\{ G\left(\{x\}_{n+1}^{k+1}\right) \right\} = \left\{ G\left(\{x\}_{n+1}^{k}\right) \right\} + \left[\frac{\{\partial G\}_{n+1}^k}{\{\partial x\}} \right] \cdot \left(\{x\}_{n+1}^{k+1} - \{x\}_{n+1}^{k} \right) \quad (1.61)$$

with the definition of the unknown vector:

$$\{\delta x\}_{n+1}^{k+1} = \{x\}_{n+1}^{k+1} - \{x\}_{n+1}^{k} \quad (1.62)$$

The matrix $\left[\frac{\{\partial G\}_{n+1}^k}{\{\partial x\}} \right]$ corresponds to the tangent stiffness matrix $[K]_{n+1}^k$ for the iteration k and load step (or time step) $n+1$. Assuming that the stiffness matrix is not singular, the equation (1.60) can be rewritten as:

$$\{\delta x\}_{n+1}^{k+1} = \left([K]_{n+1}^k\right)^{-1} \left(\{F\}_{n+1} - \{R\}_{n+1}^k \right) \quad (1.63)$$

The exact Jacobian matrix is used as stiffness matrix for the iterative procedure. The computed incremental correction $\{\delta x\}_{n+1}^{k+1}$ is used to evaluate the new approximation of displacements and pressures:

$$\{x\}_{n+1}^{k+1} = \{x\}_{n+1}^{k} + \{\delta x\}_{n+1}^{k+1} \quad (1.64)$$

The total time consumption for a complete analysis is strongly dependent on the construction and factorization of the Jacobian matrix. The classic implementation of Newton method updates the tangent stiffness matrix at each iteration, but for large systems this strategy can be excessively time consuming. The modified Newton method keeps the initial tangent matrix $[K]_0$ during the complete analysis. This strategy can increase significantly the number of iterations required to attempt the convergence. The strategy adopted in *GEFDyn* is allows the user to select the number of loading steps (or time steps) during which the tangent stiffness matrix is kept, then:

$$[K]_q \cdot \{\partial x\}_{n+1}^{k+1} = \{F\}_{n+1} - \{R\}_{n+1}^k \quad \text{with} \quad q < n+1 \qquad (1.65)$$

Additionally, the coefficients of the matrix $[K]_q$ can be given by the user (auxiliary stiffness values), in order to improve the converge. The detailed expressions of $\{F\}_{n+1}$ and $\{R\}_{n+1}^k$ can be derived straightforward combining the incremental form of the unknowns for the time step $n+1$ at iteration $k+1$:

$$
\begin{aligned}
\{\delta u_b\}_{n+1}^{k+1} &= \{u_b\}_{n+1}^{k+1} - \{u_b\}_{n+1}^k \\
\{\delta u_s\}_{n+1}^{k+1} &= \{u_s\}_{n+1}^{k+1} - \{u_s\}_{n+1}^k \\
\{\delta p\}_{n+1}^{k+1} &= \{p\}_{n+1}^{k+1} - \{p\}_{n+1}^k \\
\{\delta \tilde{u}_b\}_{n+1} &= \{\tilde{u}_b\}_{n+1} - \{u_b\}_{n+1}^k \\
\{\delta \tilde{u}_s\}_{n+1} &= \{\tilde{u}_s\}_{n+1} - \{u_s\}_{n+1}^k \\
\{\delta \tilde{p}\}_{n+1} &= \{\tilde{p}\}_{n+1} - \{p\}_{n+1}^k
\end{aligned}
\qquad (1.66)
$$

with the equations (1.57) and (1.59). Concerning the convergence, the iterative procedure stops when the relative norms of the displacements $\{u\}$, pressures $\{p\}$ and the corresponding unbalanced forces or right-hand side values of (1.60) $\{G(\{u\})\}$ and $\{G(\{p\})\}$ reach a defined tolerance value (u_{tol}, p_{tol}, Ru_{tol} and Rp_{tol}):

$$
\begin{aligned}
\frac{\|\{u\}_{n+1}^{k+1} - \{u\}_{n+1}^k\|}{\|\{u\}_{n+1}^{k+1} - \{u\}_n\|} &< u_{tol} \\[2mm]
\frac{\|\{p\}_{n+1}^{k+1} - \{p\}_{n+1}^k\|}{\|\{p\}_{n+1}^{k+1} - \{p\}_n\|} &< p_{tol} \\[2mm]
\frac{\|\{G(\{u\})\}_{n+1}^{k+1}\|}{\|\{G(\{u\})\}_{n+1}^0\|} &< Ru_{tol} \\[2mm]
\frac{\|\{G(\{p\})\}_{n+1}^{k+1}\|}{\|\{G(\{p\})\}_{n+1}^0\|} &< Rp_{tol}
\end{aligned}
\qquad (1.67)
$$

where the norm is defined by:

$$\|\{a\}\| = \sqrt{\{a\}^t \cdot \{a\}}$$

Usually, tolerance values near to 10^{-3} for displacements and pressures, and 10^{-2} for the right-hand side terms give satisfactory results.

1.3   Non-linear constitutive models

The main sources of non-linearities in an earthquake SSI problem are related to material behavior and second order geometrical effects, for instance $P - \Delta$ effects of the superstructure. This work is focused on the role of non-linear behavior of the soil and its effect on the non-linear dynamical soil-structure interaction. According with this purpose, geometrical non-linearities are neglected and the

small-strain assumption is kept for the formulation of the non-linear behavior of each component of the complete model. The next sections describe the main aspects of each used non-linear constitutive model for the soil, the interface and the superstructure.

1.3.1   Mechanical interfaces

The contact problem between the soil and the foundation was treated by interface elements. The original formulation proposed by Aubry et al. (1990) was adapted for this work, using the same general hypothesis and making the necessary modifications to integrate an initial thickness. Additionally, the numeric integration quadrature was modified from Gauss to Newton-Cotes, in order to reduce number of iterations. This numerical integration approach introduces a lumped stiffness matrix for the interface, reducing the interaction with the opening or closing state of neighboring elements. As the superstructure domain Ω_b is assumed to be monophasic, the used interface model is purely mechanic imposing a null normal flux from the soil domain Ω_s. Details regarding the formulation, numerical integration and model parameters are given in Appendix B.

The main purpose of introducing joint elements in this work is to improve the numerical treatment of the stress concentration zone between the foundation and the soil, i.e. prevent the apparition of traction in the soil. In fact, the stress concentration at the corners of the foundation can be reduced allowing the sliding between the two solids. The problem of the uplift during the dynamic loading appears usually for tall and slender structures, such as bridge piers, antennas or elevated water tanks. As the focus of this work is the role of non-linear soil behavior in the dynamic response of medium regular buildings, the set of parameters for the joint elements is selected in order to obtain sliding but not uplift.

1.3.2   Continuous non-linear beam model

According to kinematic assumption presented in §1.2, the superstructure domain Ω_b is modeled by Bernouilli beams. The main assumption is related to the thinness of the beam element (transverse section size compared to beam length) which allows to consider these elements as lines rather than volumes.

The first version of continuous Bernoulli beam was developed and included by Aubry and Modaressi (1996) in *GEFDyn* on the basis of the implementation proposed by Bathe (1996) for general curved beam elements. Later, Pianka (1998) extends the formulation to thick beams. In this work, the first formulation was used with some modifications and improvements concerning the consistent mass matrix computation, the internal forces calculation and the integration of the constitutive model. Details about the formulation and numerical integration of the used constitutive model are given in Appendix C.

The integrals defining mass and stiffness matrices and body and external forces, are computed numerically using a Newton-Cotes quadrature. The implementation in *GEFDyn* allows to choose different order of integration following each local axis of the element r, s and t (Fig.1.2). When a non-linear constitutive model is used, the order of integration must be high enough to assess the evolution of the plastic zone during the load. For earthquake loading, the plastic zones are concentrated at the ends of beams and columns, i.e. an elevated order of integration (over the spam and the flexural direction) is required in these zones. A low order of integration can be used for mid spam elements or for foundation beams.

1.3.3   Plastic hinges beam model

As previously noted, during an earthquake loading the nonlinearities of structural elements are concentrated near to ends of horizontal spam or extreme section of the columns. The beam element developed in the previous section integrates a constitutive model across the entire element, i.e. over some sections that remain essentially elastic during the dynamic response. The non-linear behavior is expressed in terms of a strain-stress constitutive model, that is a suitable approach for example

for steel structural elements. For reinforced concrete elements, this kind of approach is complex and requires the definition of multi-fiber elements, including constitutive relation for concrete and steel fibers that are integrated simultaneously using appropriate compatibility relations. As the emphasis of this work is on the non-linear soil behavior, a more global approach is desirable to asses the non-linear behavior of reinforced-concrete structural elements. According to this purpose, a concentrated plastic hinge beam-column element has been introduced in *GEFDyn* during this work (Sáez, 2007).

The beam model added to *GEFDyn* has nonlinear hysteretic bending moment-end rotation characteristics. The model is based on the two-component model presented by Giberson (1969) and the modifications included in DRAIN-2DX (Prakash et al., 1993) and PC-ANSR (Maison, 1992) softwares to take into account axial force and bending moment interaction. The basic DRAIN-2DX (2D) and PC-ANSR (3D) model was extended to some features of *GEFDyn* : elementary body forces, consistent and lumped elementary mass, sequential construction availability, etc. Details about the model are provided in Appendix D.

1.3.4   Constitutive modeling of the soil

The ECP elastoplastic multi-mechanism model (Aubry et al., 1982; Hujeux, 1985), commonly called Hujeux model is used to represent the soil behavior. This model can take into account the soil behavior in a large range of deformations. The model is written in terms of effective stress. The representation of all irreversible phenomena is made by four coupled elementary plastic mechanisms: three plane-strain deviatoric plastic deformation mechanisms in three orthogonal planes and an isotropic one. The model uses a Coulomb type failure criterion and the critical state concept. The evolution of hardening is based on the plastic strain (deviatoric and volumetric strain for the deviatoric mechanisms and volumetric strain for the isotropic one). To take into account the cyclic behavior a kinematical hardening based on the state variables at the last load reversal is used. The soil behavior is decomposed into elastic, pseudo-elastic, hysteretic and mobilized domains. In the Appendix E, the ECP elastoplastic multi-mechanism model in its generic formulation is presented. A general description of the numerical integration procedure is also provided in this Appendix.

In a general way, the number of parameters of a constitutive model is related to the number of physical phenomena described by the model. Thus, for a very complex material behavior such as the soil, we must accept an elevated number of parameters. In a practical point of view, we need to be able to identify the model parameters in a simple way adapted to standard available data. According to this goal, several works have been conducted at ECP in order to define sets of parameters for diverse materials under different loading paths for the different versions of multimechanism model. These parameters collections have been tested and validated in order to verify the performance in modeling realistic soil behavior.

The numerical simulation of laboratory tests has been extensively studied by Hujeux (1979), Hajal (1984), Rahma (1988), Michalski and Rahma (1989), Piccuezzu (1991), Hicher and Rahma (1994), Michali (1994), Kordjani (1995) and Modaressi and Lopez-Caballero (2001), among others. Studies on the accuracy of the model in applications related to earthquake engineering have been carried out by Hujeux (1985), Modaressi (1987), Aubry and Modaressi (1989), Modaressi and Aubry (1989), Aubry and Modaressi (1992b), Benzenatti (1992), Modaressi et al. (1995), Mellal (1997), Sica (2001) and Lopez-Caballero and Modaressi (2002) among others. Other than Hujeux (1985) and Kordjani (1995), the major part of these studies were oriented to monotonic loading. Recently, Lopez-Caballero (2003) and Modaressi (2003) presented a strategy for parameters identification oriented to cyclic behavior.

A particular aspect of the multimechanism model presented in Appendix E is that it was written for a large range of deformation. According to this, even if laboratory data is available, there are practical difficulties to explode these results for very large deformation (near to critical state) or for very small deformations (elastic range). In order to encompass these difficulties, the strategy proposed by Lopez-Caballero and Modaressi-Farahmand Razavi (2008) takes into account several results of different studies that highlight correlations between intrinsic characteristics of the soils (e.g. elastic modulus or critical states parameters) to well-known properties traditionally used in soil mechanics

(e.g. Atterberg's limits or granulometry properties). These correlations and considerations on the representation of physical aspects of the soil by the constitutive model are combined with several reference curves in order to define a practical strategy to set-up the model parameters.

Concerning the identification of parameters for cyclic loading, the proposed strategy is based on the numerical simulation of laboratory tests with special emphasis on modulus degradation $G - \gamma$ and damping $D - \gamma$ curves. The goal is to identify a set of parameters using a minimum of laboratory data and a maximum of information available from correlations. According with this purpose, a first parameter classification can be done in terms of the role of each parameter in the model:

- Elasticity: K, G, p'_{ref} and n_e

- Plasticity and critical state: ϕ'_{pp}, β, b and d

- Hardening: ψ, a_1, a_2, n_p and c

- Threshold domain: r_k^{el}, r_k^{hys}, r_k^{mob} and r_{iso}^{el}

- Initial state: p_{c_0}

Table 1.1: Classification of the Elastoplastic model parameters

	Stiffness	State	Hardening
Directly measured	G, K and β	ϕ'_{pp}, ψ and d	
Non-Directly measured	a_1 and a_2	b	r_k^{ela}, r_k^{hys}, r_k^{mob}, n_p, c, r_{iso}^{el} and c

Concerning the role of each parameter related to soil behavior, the parameters can be separated into three categories: parameters related to the stiffness (strain-stress relation), those associated to the state independent of the loading history (e.g. ϕ'_{pp} or b) and those related to the evolution of hardening variables. Finally, the strategy proposed by Lopez-Caballero and Modaressi-Farahmand Razavi (2008) proposes a separation related to the estimation method: those that can be directly measured from either in-situ or laboratory test results as elastic or perfect plasticity parameters, and those which cannot be directly measured (Table 1.1). The initial state parameter p_{c_0} is directly measurable. The reader is addressed to references for further details concerning the parameter identification strategy. The numerical used values for each soil are given in the Appendix H. This appendix shows several soil mechanics test simulations used to verify the accuracy of each parameter set.

1.3.5 General remarks

The general monophasic and/or two phase dynamic formulation, some specific elements and the constitutive models used for the numerical modeling of the dynamical SSI problem were presented in the previous sections and annexes. The *GEFDyn* code was enhanced by adding a new plastic-hinge beam column element model. Other improvements have been done concerning the numerical integration of interface elements and the dynamic formulation of continuous beam elements. A specific formulation for the modeling of dynamical SSI problem for regular buildings by a modified plane-strain approach is presented in Chapter 3. A large amount of work has been devoted to develop pre and post-treatment tools required to perform numerically-costly applications presented in next chapters. In this way, several improvements in run time and numerical capacity of *GEFDyn* have been performed during this work.

Next section is devoted to some specific aspects of the numerical modelization of dynamical SSI concerning damping considerations and the treatment of the boundary conditions under dynamical loading for the non-linear behavior case. With this purpose, some theoretical and numerical validations are presented.

1.4   Special aspects of the numerical resolution of the dynamic SSI problem with Finite Elements

As previously discussed in §1.2.3, when the dynamic SSI problem is treated by finite elements some special considerations must be included in order to ensure that the truncated domain model be compatible with the unbounded nature of the real problem. If the soil remains elastic under dynamic loading, the use of absorbing elements such as paraxial elements described in Appendix A provides a relative simple way to modeling the unbounded soil domain. Even if several other forms of radiation boundary conditions have been developed last years as discussed by Wolf and Song (1996), or more recently by Basu and Chopra (2003), these forms are suitable only for linear elastic materials. As the scope of this work is the non-linear material behavior, a tied lateral boundary approach (Zienkiewicz et al., 1988, 1999) or repeatable approach is retained as modeling strategy (Fig.1.4).
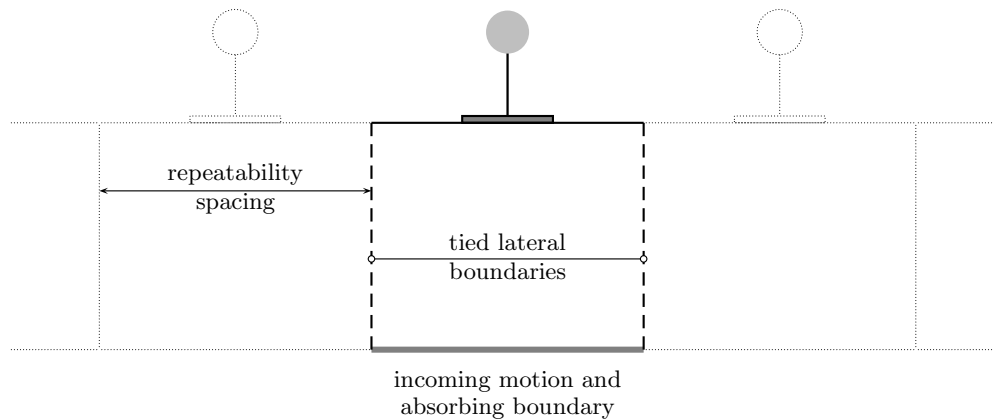
Figure 1.4: Tied lateral boundary approach

In a general way, if we consider a horizontally stratified soil with an incoming seismic input propagating following the vertical direction, a superstructure can be interpreted as a perturbation to the one-dimensional wave propagation problem. Due to this perturbation, the waves are reflected not only in the vertical direction. Assuming that the model truncation is deep enough to verify elastic behavior at the bottom, the last can be treated by previously described paraxial approximation. Thus, the only additional problem arises from the appropriate treatment of the vertical lateral boundaries. In these boundaries, it is necessary to allow the radiation of the waves caused by the superstructure. These radiated waves can be expressed in terms of the difference between the free field solution (i.e. the solution of the one-dimensional wave propagation problem) and the total field associated to the soil-structure problem. Zienkiewicz et al. (1988) propose to write the equilibrium equations in terms of the relative displacements to the incoming displacement field at the bottom truncation level and add a fictitious transmitting layer interpreted as the last layer of elements along the lateral boundaries of the mesh. These transmitting layers are used to transmit the perturbed motion caused by the superstructure. The numerical procedure involves the parallel resolution of the main mesh and the one-dimensional column, the resolution of the transmitting layer and the application of the obtained difference field as nodal prescribed displacements to main mesh. Additionally, this approach requires that the region near to truncation lateral boundary remains elastic and homogenous under the loading.

A simpler alternative to the treatment suggested by Zienkiewicz et al. (1988) is the tied lateral boundary approach or repeatable boundary conditions which is illustrated in Fig.1.4. In this approach, the periodic nature of the surface perturbation is assumed, thus a sequence of superstructures is placed

at regular intervals (repeatability spacing). Consequently, the values of displacements, stresses, etc. are identical on both vertical sections. This condition is explicitly imposed in *GEFDyn* by an equivalent node concept including displacements and hydraulic DOFs. Of course, correct results must be obtained if sufficiently large repeatability space is adopted. As the soil undergoes plastic deformation under seismic excitation, the material damping ensures the decrease of the amplitude of the radiated waves from the soil-foundation interface. As will be explained in following sections, a criterion associated to spectral amplitudes of the radiated waves has been adopted to define an adequate repeatability spacing case for each case. This approach is fully applicable to the non-linear earthquake analysis, where the only maintained linear elastic material domain is the portion of soil above the arbitrary bottom truncation level of the model.

Next sections present application of this approach to one-dimensional, bi-dimensional and three-dimensional cases. The first example corresponds to the solution of the one-dimensional wave propagation problem of a homogenous soil column. This example is validated with the theoretical solution and it is used to discuss the numerical or algorithmic damping considerations retained in this work. The second example shows the effectiveness of the tied lateral boundary strategy by comparing a full three-dimension time domain finite element computation with a coupled boundary-finite element computation in frequency domain for the same soil-structure interaction problem. Finally, the third example presents a discussion about the repeatability spacing required for bi-dimensional FE computations in order to explore other strategies to treat the model truncation boundaries using the paraxial implementation described in §1.2.3.

1.4.1   One-dimensional ground amplification problem and numerical damping

The transfer function modulus $|T(\omega)|$ of a homogenous elastic soil layer overlying a half-space bedrock is defined as the ratio of the ground movement amplitude to a hypothetic outcrop bedrock outcrop amplitude:

$$|T(\omega)| = \frac{1}{\sqrt{\cos^2 \frac{i\omega}{c_s}h + \alpha^2 \sin^2 \frac{i\omega}{c_s}h}} \tag{1.68}$$

where h is the soil depth, α is the impedance ratio between the elastic soil and the half-space bedrock, c_s is the shear wave velocity of the soil and ω the circular frequency. Details regarding the derivation of this expression are provided in Appendix F.

The previous expression does not take into account material damping and only radiation damping introduced by the unbounded bedrock is evaluated. A linear hysteretic damping independent of the frequency can be introduced into the solution when working in the frequency domain by using the correspondence principle (Wolf, 1985). According to this principle, the damped solution can be obtained from the elastic one by replacing the elastics constants by the corresponding complex ones. Thus, a complex shear wave velocity c_s^* can be obtained from a frequency-independent complex shear modulus μ^*:

$$c_s^* = \sqrt{\frac{\mu^*}{\rho}} = \sqrt{\frac{\mu\left(1 + 2i\zeta\right)}{\rho}} \approx \sqrt{\frac{\mu}{\rho}}\left(1 + i\zeta\right) = c_s\left(1 + i\zeta\right) \tag{1.69}$$

for small ζ damping ratio. Using the complex shear wave velocities in the previous expressions, an equivalent viscous material damping can be introduced. This kind of equivalent viscous material is often used in structural mechanics as a simple way to introduce material energy dissipation satisfying linear elastic hypothesis. As the focus of this work is the material damping related to non-linear behavior (hysteretic damping), we do not use an explicit equivalent viscous damping. However, the use of equivalent viscous damping permits to obtain some attenuation with time even at very small amplitudes. It is desirable to plot time response curves, specially in order to obtain decreasing amplitude after the main shock when the response is near to free-oscillations. With this purpose, we introduce

an algorithmic damping by the choice of the integration parameters β and γ of the predictor-corrector Newmark scheme presented in §1.2.6.

In a general way, one of the purposes to introduce numerical damping is to remove the participation of the high-frequency modes of the FE model. For Newmark method, a value of $\gamma > \frac{1}{2}$ is required to introduce high-frequency dissipation. For a fixed value of $\gamma > \frac{1}{2}$, the goal is to select the value of β that maximizes the high-frequency dissipation. Conditions are derived from a stability analysis, according to Hughes (2000) they can be summarized as:

- Unconditional:

$$0 \le \zeta < 1 \quad ; \quad \gamma \ge \frac{1}{2} \quad ; \quad \beta \ge \frac{\left(\gamma + \frac{1}{2}\right)^2}{4}$$

- Conditional:

$$0 \le \zeta < 1 \quad ; \quad \gamma \ge \frac{1}{2} \quad ; \quad \Omega < \Omega_{bif}$$

where Ω_{bif} is the so-called sample bifurcation frequency. This value is related to eigenvalues of the matrix associated to corresponding modal first order differential linear system equivalent to modal second order differential system integrated by Newmark method. Ω_{bif} is the value of sample frequency of the system $\Omega = \omega^h \Delta t$ at which complex conjugate eigenvalues bifurcate into real distinct eigenvalues. ω^h is the maximum natural frequency of the system and Δt is the integration time step. The value of ω^h can be bounded by the maximum frequency of the smallest element of the mesh (Hughes, 2000), thus $\frac{2c}{h}$ for solid elements. For the undamped case (i.e. without viscous damping), this bifurcation frequency can be computed by:

$$\Omega_{bif} = \frac{1}{\sqrt{\frac{\left(\gamma + \frac{1}{2}\right)^2}{4} - \beta}} \tag{1.70}$$

According to the previous expression, the most effective high-frequency filtering is achieved by selecting $\beta = \frac{\left(\gamma + \frac{1}{2}\right)^2}{4}$. Choosing β value larger than the optimum value reduces the high-frequency damping. Selecting a value of β inferior to optimum value (but larger than $\frac{\gamma}{2}$ to keep unconditional stability), the high-frequency damping vanishes for sampling frequency larger than Ω_{bif}. Thus, by selecting β larger than the optimum some high-frequency damping is ensured.

By selecting a value of $\gamma > \frac{1}{2}$ some high-frequency dissipation is introduced, but unfortunately, the accuracy of the numerical method drops to first-order in the low modes. In order to measure the numerical dissipation and dispersion introduced by the algorithm when a value of $\gamma > \frac{1}{2}$ is used, Hughes (1983) uses $\bar{\zeta}$ and $\bar{\omega}^h$ as the numerical counterparts of the viscous damping ζ and fundamental frequency ω^h of the system. This author proposes the algorithmic damping ratio $\bar{\zeta}$ and the relative period error $\frac{\bar{T}-T}{T}$ ($\bar{T} = \frac{2\pi}{\bar{\omega}^h}$ and $T = \frac{2\pi}{\omega^h}$) as measures of numerical dissipation and dispersion. It is difficult to obtain a general expression for these measures, but this author proposes:

$$\begin{aligned}
\bar{\zeta} &= \zeta + \frac{1}{2}\left(\gamma - \frac{1}{2}\right)\left(\Omega + \mathcal{O}\left(\Omega^2\right)\right) \\
\frac{\bar{T}-T}{T} &= \mathcal{O}\left(\Omega^2\right)
\end{aligned} \tag{1.71}$$

from some analytical results. These expressions illustrate that the first-order error created by choosing $\gamma > \frac{1}{2}$ induces numerical dissipation but no period errors.

In order to choose a set of values for Newmark's γ and β parameters and to evaluate the associated numerical dissipation, we perform a simple one dimensional wave propagation test of a single elastic 30[m] depth homogenous layer overlying an elastic half-space bedrock. The material properties and the used mesh are shown in Fig.1.5. Different colors displayed in the mesh indicate different vertical mesh refinements, starting from a vertical space of 1[m] to 2.5[m] over the bedrock. This variable vertical

mesh spacing is useful to increase the precision near to surface, thus near to the zone that concentrates significative stress variations due to surface perturbations (superstructures for SSI application conducted in this work) or free surface. When a non uniform mesh is used in a FE wave propagation problem, some numerical wave dispersion can appear due to wave reflection over the interface between elements of different size. If the wave-length is larger than the length of some elements of the mesh, a variation of size creates numerical dispersion. In a general way, numerical reflection is not important if the wave-length is 10 times larger than the biggest element of the mesh. If the variation of size of elements is progressive and the size ratio between neighboring element is no largen than 0.5, no significative numerical reflection will appear. Additionally, the use of consistent mass matrices instead of lumped mass matrices also reduces the numerical dispersion. These guidelines have been followed during mesh generation for each problem studied in this work.
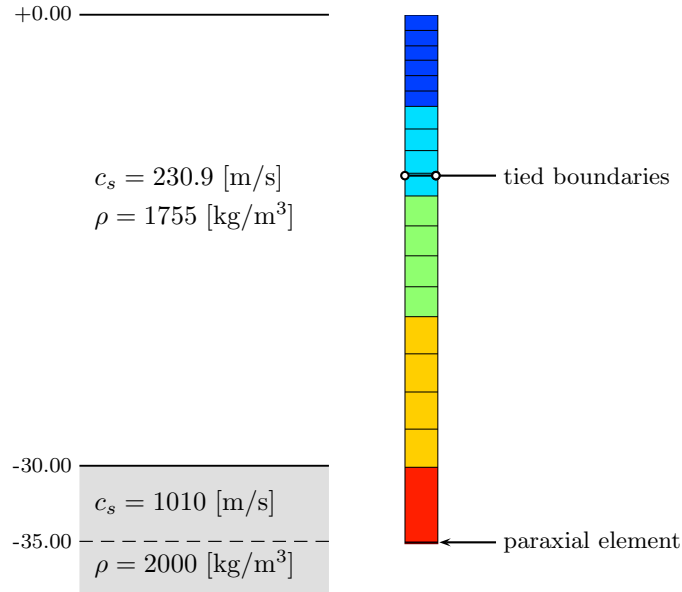
Figure 1.5: FE element mesh of a homogenous elastic soil layer overlying a half-space bedrock used to calibrate Newmark integration parameters γ and β

The one-dimensional nature of the problem is ensured by introducing lateral tied boundary conditions over the depth. Only the first 5[m] of the bedrock are modelled by a single element. At the bottom of the mesh, a single paraxial element is used to impose the incident field and ensure the radiation condition for the outgoing vertical waves. Fig.1.5 shows relevant information concerning material properties of both soil and bedrock. A Ricker pulse is assumed as input motion at outcrop using paraxial elements (Fig.1.6a). Computations are carried out in time domain assuming linear elastic behavior using two sets of integration parameters:

1. Second-order accuracy values (no numerical dissipation): $\gamma = \frac{1}{2}$ and $\beta = \frac{1}{4}$

2. First-order accuracy values (numerical dissipation induced): $\gamma = 0.625$ and $\beta = 0.375$

The first set is defined starting with $\gamma = \frac{1}{2}$ and computing the corresponding β as the optimum value for high-frequency filtering. The second set of parameters is calibrated imposing $\gamma > \frac{1}{2}$ and β larger or equal to the optimum value to ensure some high-frequency filtering. In this case, the values are selected by comparison with the theoretical transfer function (F.12) for some viscous damping characterized by the damping ratio ζ. The total duration of the analysis is 10 seconds in both cases, using a time step $\Delta t = 1 \times 10^{-3}$[s] and consistent mass operator.

Fig.1.6b displays the first 4[s] of the acceleration response obtained at free field using both sets of time integration parameters. As expected, it can be noticed that no significant variation is obtained in period characteristic of the response. A slight reduction in peak amplitudes can be observed when numerical dissipation is induced.
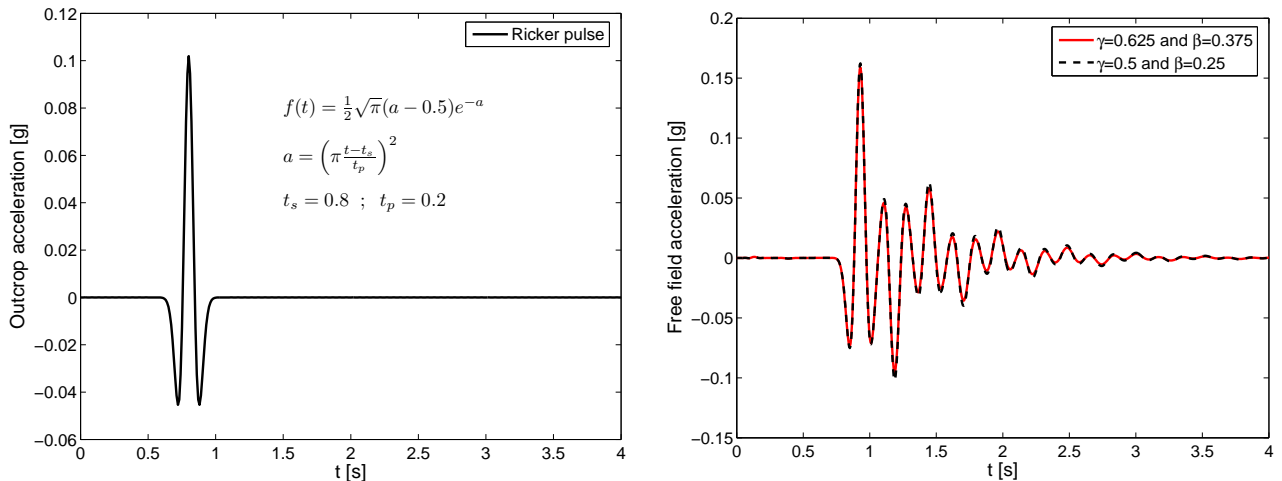
(a) Ricker wavelet used as input acceleration motion at outcrop

(b) Free field acceleration response using different values of time integration parameters γ and β

Figure 1.6: Input acceleration motion and computed free field responses for an elastic homogeneous soil overlying an elastic bedrock

Fig.1.7 shows the comparisons between the theoretical transfer function and the computed one, defining the transfer function amplitude as the ratio between the observed free field acceleration and a hypothetic bedrock outcrop (F.12). Fig.1.7a corresponds to second-order accuracy parameters, with only high-frequency filtering as some numerical dispersion is present. This curve is compared to analytical viscous undamped case ($\zeta = 0$) where the only damping is related to wave radiation. In this case, the amplitude and the frequency of the fundamental mode of deposit agree, but the quality of the computation decays for the second mode. The reduction of the amplitude of the computed second mode can be associated to numerical dispersion due to wave reflections, time and space discretizations. It can be also noticed that the quality of the computation decays for very-low frequency. This range of frequency is extremely sensitive to integration time step, thus a reduction in Δt improves the computation but increases significantly the numerical cost. As the FE models used in this work are numerically costly, reduction in Δt increases significantly the computing time. In a general way, a value of $\Delta t = 1 \times 10^{-3}$ is kept as general rule and it is reduced only if strong non-linearities, specially related to superstructure, are detected during the analysis.

Fig.1.7b shows the same comparison but including some viscous damping in the analytical solution and numerical dissipation induced by the integration parameters. After a calibration procedure, we obtain that $\gamma = 0.625$ and $\beta = 0.375$ values agree satisfactorily with a viscous damping of $\zeta = 0.8\%$. The selected value of β is not optimum, but satisfies the condition to ensure high-frequency damping. It can be concluded by comparison between the computed curves for numerically damped and undamped cases that only a part of the reduction of the transfer function amplitude can be associated to numerical dissipation. The amplitude of the first mode remains unchanged for practical purposes, and only a reduction of the amplitude of the second mode can be observed. Indeed, the computed reduction of the second mode transfer function amplitude is a combination of algorithmic dissipation, waves dispersion and other effects associated to numerical resolution. Nevertheless, the value of $\zeta = 0.8\%$ gives an indicator of the total amount of damping associated to diverse numeric phenomena. The main purpose of including some numerical dissipation in this work is to obtain an attenuation of the time responses after the strongest part of each used earthquake, when the response is essentially in free oscillations.

This total numerical damping depends on the problem and the used FE mesh. Other tests using 2D and 3D meshes for the same problem were conducted giving similar values for an equivalent viscous damping. According to expressions provided by Hughes (2000) to estimate the algorithmic damping ratio $\bar{\zeta}$ (1.71), the used mesh, the numerical values of integration parameters and used time step, may introduce an algorithmic damping ratio near to $\bar{\zeta} \approx 0.028$ as upper bound, i.e. three times larger than
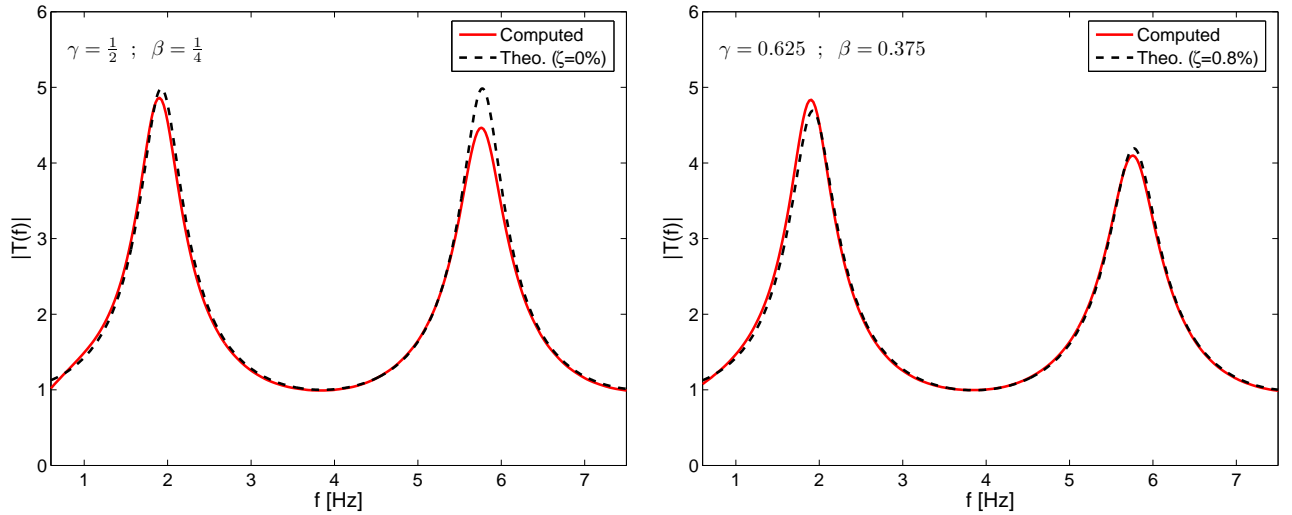
(a) Computed transfer function obtained using second-order accuracy Newmark parameters, i.e. without numerical dissipation

(b) Obtained transfer function using first-order accuracy Newmark parameters $\gamma = 0.625$ and $\beta = 0.375$, inducing numerical dissipation

Figure 1.7: Comparison between computed transfer function and theoretical solution of the one-dimensional shear wave propagation problem including some viscous damping (ζ)

the obtained value by curve matching. The calibrated values of $\gamma = 0.625$ and $\beta = 0.375$ inducing numerical dissipation will be used for all the computations conducted in this work.

1.4.2 3D linear elastic SSI numerical validation

This section describes a comparative test performed for a linear elastic dynamic SSI problem conducted following time-domain FE and frequency-domain boundary-elements (BE) approaches. The problem consists in a rigid base mat SDOF superstructure over two different 30 [m] depth soil profiles. The problem will be treated by the substructure method in frequency domain using MISS-3D code (Clouteau, 2000, 2003), and by the direct method in time domain using *GEFDyn* FE software. Appendix G presents a brief overview of the substructure approximation implemented in MISS-3D, valid in the small elastic deformation range. The studied problem and both, BE and FE models, are presented in §1.4.2.1. Finally, comparative results are presented and discussed in §1.4.2.2.

1.4.2.1 Soil-foundation-structure system and models

In order to study the accuracy of the tied-lateral boundary approach to simulate 3D dynamical soil-structure interaction problems, we use a simple SDOF structure over two different soil profiles. The dynamic properties for the SDOF were defined from mean values for low-rise concrete moment frames proposed in HAZUS-MH MR3 (2003) (see §4.2.1 for more details). According to this document, a typical low-rise concrete moment frame might be characterized by an equivalent SDOF of $\bar{h} = 6$[m] of height, $W = 1080$[kN] of weight and a fundamental period $T_0 = 0.4$[s]. Assuming a lumped mass model (Fig.1.8) and using a Young modulus of $E = 50 \times 10^9$[Pa], we can solve for a suitable equivalent transversal square section. The foundation is supposed to be shallow, rigid and square of side $a = 6$[m].

Two elastic soil profiles were studied:

1. Homogenous soil profile of 30[m] depth overlying an elastic bedrock (Fig.1.8a)

2. Horizontally stratified soil of 30[m] depth overlying an elastic bedrock (Fig.1.8b)

These soil profiles are not arbitrary. The first one is selected with the purpose to obtain a fundamental soil frequency f_{soil} larger than the fixed base frequency of the structure $f_0 = \frac{1}{T_0} = 2.5$[Hz], where according to our experience on this subject the DSSI effects are not significant. The second

<div style="text-align:center">(a) Homogenous soil profile   (b) Horizontally stratified soil profile</div>
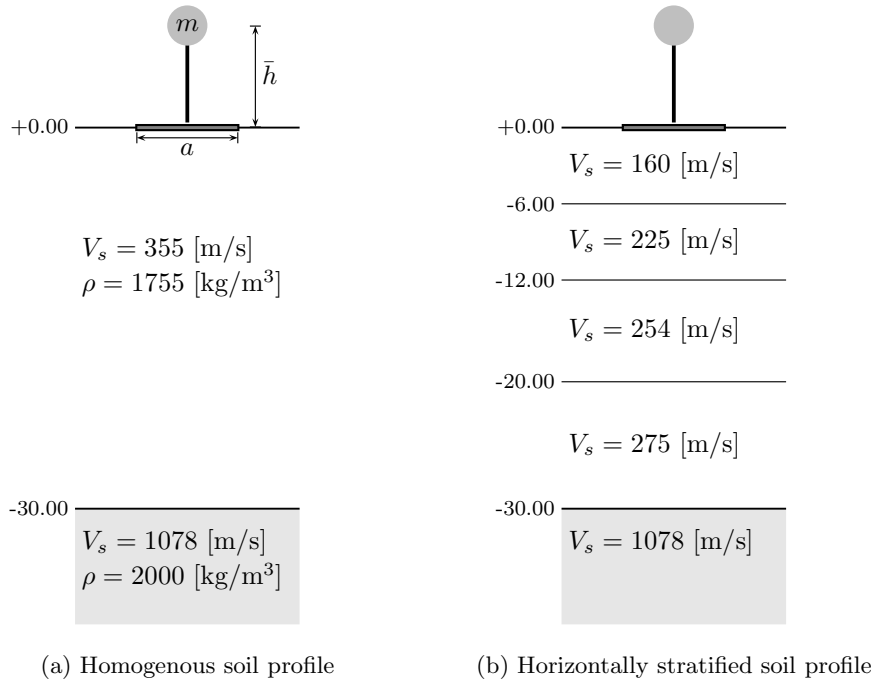
Figure 1.8: Schema of both soil-structure systems used for the linear elastic comparative analysis

profile corresponds to a simplification of a homogenous dry sand profile studied in chapters 2 and 3. As it is explained in these chapters, when non-linear soil behavior is taken into account the initial state of soil confinement is a key issue. The variation of initial confinement with effective vertical stress is modeled by a non-linear elastic approach (E.4) in the multimechanism model. This vertical variation produces a gradually increasing shear wave velocity profile with the depth. The soil profile in Fig.1.8b correspond to a discretization of this vertical variation, assuming constant shear wave velocity in each layer. In this case, the fundamental frequency of the soil f_{soil} is close to the fixed base frequency of the superstructure f_0. In this condition, resonance phenomena between soil and structure produce significative soil-structure interaction. Densities of the soil and the bedrock are the same for both profiles, they are omitted in Fig.1.8b for sake of simplicity.

Modeling assumptions and characteristics of each numerical model depends on the used code and are detailed in the following. As MISS3D code requires linear elasticity, we used linear elastic constitutive models for both soil and superstructure. We also impose that loss of contact between soil and foundation do not take place, thus we assume continuity of displacement and stress over the soil-structure interface Σ_{bs}.

1.4.2.1.1   Substructure approach   As mentioned in §G, in this approach the unbounded soil subdomain is modeled with BEM and its response is disjointed from the solution of the superstructural subdomain. The superstructure is a FE model constructed using vertical beam elements and lumping the mass at 6[m] hight above the foundation level. The foundation is modeled using a regular mesh of solid 3D massless elements and imposing a kinematical constraint to ensure its rigidness. The surface meshes required for the boundary of the soil over the soil-structure interface is deduced from the finite element mesh of the superstructure. The coupling between FEM and BEM is conducted using a modal reduction technique. We use the Craig-Bampton reduction technique to export the FE superstructure model to MISS3D code accounting the six rigid body modes (3 translations and 3 rotations) and the first fixed base mode (Fig.1.9). We add a very stiff foundation beam following the load direction y, in order to avoid relative rotation between column and foundation.

Concerning the damping, we use two different values: the first one ζ_0 is related to the superstructure and the second one β_s is assumed for the soil and the bedrock. The superstructure damping ratio ζ_0
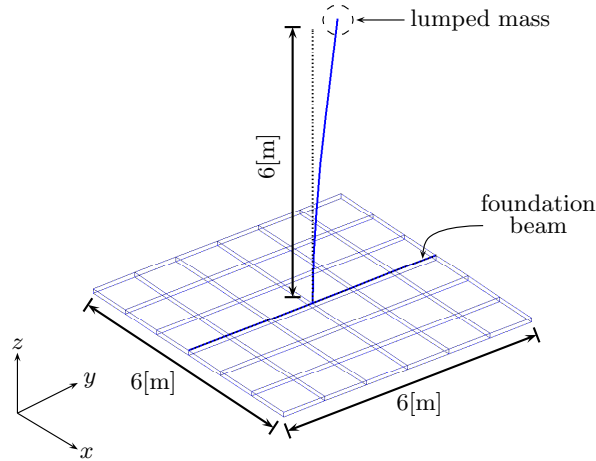
Figure 1.9: FE superstructure model and its first fixed base mode used for the modal decomposition

is used to construct a damping matrix as a linear combination of stiffness and mass matrix following traditional Rayleigh method. The value of β_s representing the hysteretic soil damping, is introduced into equations using the correspondence principle in frequency domain over the Lamé's coefficients λ_s and μ_s of the soil and bedrock:

$$
\begin{aligned}
\lambda_s^* &= \lambda_s \left(1 + i\beta_s\right) \\
\mu_s^* &= \mu_s \left(1 + i\beta_s\right)
\end{aligned}
$$

These modified values account approximately for average energy dissipation by hysteresis in soil and bedrock. The standard damping ratio ζ commonly used in structural mechanics is related to the damping coefficient β through:

$$
\zeta = \frac{\beta}{2} \tag{1.72}
$$

Both, ζ_0 and β_s are computed by calibration, matching the obtained response with the one from direct approach described below. In the later case, the damping is controlled by numerical integration parameters as described in §1.4.1. BEM approach incorporates in its formulation radiation damping associated to outgoing waves, thus no special consideration must be added to account for this phenomenon. As mentioned, computations are carried out in frequency domain.

1.4.2.1.2 Direct approach In this case, we need to construct a complete FE model of both soil and structure. The same properties described before are retained for the superstructure and its foundation. Thus, the structure is modeled by traditional beam elements, lumping the structural mass at the top of the higher vertical beam element. The foundation is also modeled by solid 3D elements with no mass. Beams in foundation are used to ensure rotation continuity between foundation and structural beams. Between soil and foundation, continuity of both displacement and stresses are ensured over the soil-structure interface, as no uplift or sliding is possible. The complete used mesh is shown in Fig.1.10a. In this figure colors are related to diffrent group of elements required for the second soil profile. For the homogenous deposit, the same mesh is used keeping the same material properties for each soil element group.

Similarly to the one dimensional wave propagation case studied in §1.4.1, we include only the first 5[m] of the bedrock in the mesh. At the bottom of the model, paraxial elements ensure the radiation condition and impose the incident field. The incident motion is imposed following the y direction. This orientation defines the boundary conditions of the mesh. Imposing tied lateral boundaries described before, we are assuming periodicity in x and y direction. As the motion will be imposed in y direction, the mesh will be deformed as a shear-beam in $y - z$ plane, but no significant deformation will be

(a) FE model used for GEFDYN computations   (b) Boundary conditions, plane $x-y$
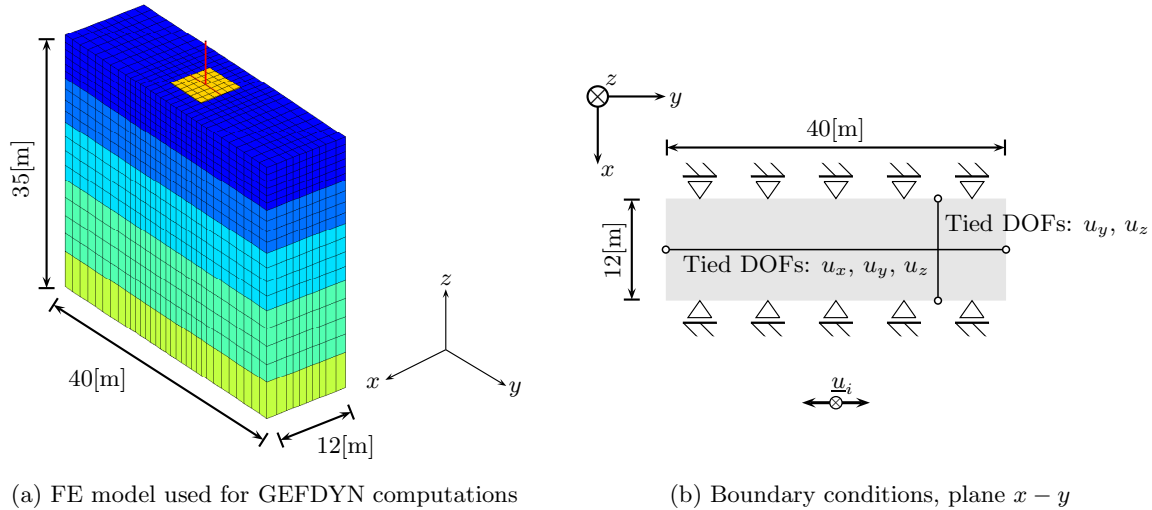
Figure 1.10: Finite element mesh and schematic representation of boundary conditions for direct approach

obtained across x direction if the lateral limits following this direction are selected far enough to eliminate border effects. In the y direction, the limits of the mesh must be selected far enough to minimize the effects of reflected waves. As numerical dissipations are included by numerical integration parameters, the reflection can be controlled with the dimension of the mesh along y direction. Indeed, the wave front outgoing from the soil-structure interaction is approximately half-spherical, thus some reflections also appear in x borders. By choosing a box-type mesh, the reflection of the same wave-front on the x border occurs at different instants. Thus, the coherence of the waves are destructed producing a favorable effect over the total wave reflections.

The lateral dimension across x and y has been selected by an iterative procedure, analyzing wave reflections by Fourier transform over time responses on different meshes. The study presented in this section supposes linear elastic behavior for both soil and structure. The major part of computations carried out in this work include non-linear behavior, thus a significative damping is added by non-linear hysteretic stress-strain responses. In these conditions, the attenuation of waves is significantly increased reducing the problem of wave reflection over lateral borders of the mesh. For each studied configuration, we choose the limits of the correspondent mesh under linear elastic hypothesis controlling wave reflections, knowing that these reflections will be reduced in the target non-linear computation. Of course, some concessions were done in order to obtain a satisfactory accuracy with a reasonable numerical-cost.

The retained boundary conditions are illustrated in Fig.1.10. We accept that x dimension is large enough to eliminate border effects, thus u_x DOFs are removed over lateral sides (in $x = 6$ and $x = -6$ planes). In order to satisfy the periodicity across this direction, lateral nodes are tied for y and z displacement directions. For lateral borders on y direction ($y = -20$ and $y = 20$ planes), three spatial translations are kept but opposite nodes are tied in order to ensure periodicity and shear-beam type deformation (standard 1D shear wave propagation). These boundary conditions will be used for all 3D dynamical analyses conducted in this work. Some additional conditions will be added for two-phase cases presented in next chapters.

As the soil is elastic in this case, no special considerations are required to initialize soil state and the dynamic computation can be directly launched. For non-linear computations presented in next chapters, dynamical phase is preceded by a static initialization of the stress and internal variables fields of the soil model, and eventually the simulation of the sequential construction of the superstructure. This initialization phase will be followed by a pre-dynamic analysis in some cases. The static phase is specially delicate for two-phase cases, where the soil permeability controls the initialization procedure. The boundary conditions represented in Fig.1.10 apply only for dynamic loading and are different of

those imposed at static phase.

Numerical integration parameters derived from one dimensional wave propagation problem described in §1.4.1 are kept, so that the a time step $\Delta t = 0.001[s]$, $\gamma = 0.625$ and $\beta = 0.375$. The induced numerical damping for this case will be discusses regarding the calibration parameters obtained for ζ_0 and β_s for the substructure approach.

1.4.2.2 Linear elastic SSI responses

The comparative results presented in this section are given in terms of different spectral ratio moduli, corresponding to ratio between displacements computed at different points in frequency domain. We define three key control points: the top of the structure (**tp**), a point on the free field (**ff**) and the vertical projection of this free field point over the soil-bedrock interface (**bd**). Fig.1.11 shows schematically the position of these control points. Some precisions must be given about the free field control point. Indeed this point is defined as far as possible in the FE model, thus at 1[m] of the border following y direction, at the center of the mesh in x direction from the superstructure. This point can be selected arbitrarily far in MISS3D model, but in order to compare the response in the same place we kept the same coordinates for the free field control point and the corresponding vertical projection on the bedrock. We compute two different spectral ratios, between the top and the free field control points (**tp/ff**) and between the free field and the bedrock (**ff/bd**). The purpose of the tp/ff spectral ratio is to illustrate the degree of interaction between the superstructure and the soil. For an infinitely rigid soil, this ratio gives the fixed base transfer function commonly used in earthquake engineering. The second spectral ratio ff/bd permits to identify the relative position of the structure compared to the soil and illustrate the clearness of the free field response, thus for a perfect free field condition we might not find evidences of the neighboring superstructure. The clearness of this spectral ratio is controlled by the generation and the attenuation of superficial waves, and its eventual reflections at the border for the FE approach.
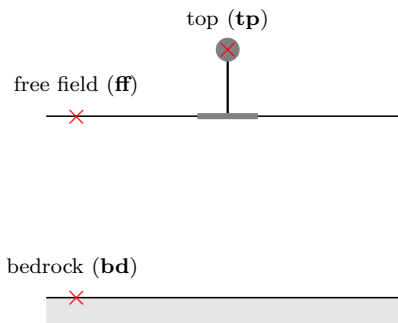
Figure 1.11: Spectral ratio definitions

In order to obtain these spectral ratios we impose different input signals depending on the model. For substructure approach, as the computation is conducted in frequency domain we do not need a particular time input motion. In this case, it is possible to use a unitary SH wave input for the entire studied frequency range. We obtain the displacements at different control points and the modal participation factors that allow to reconstruct the response of the superstructure due to this unitary input. On the contrary, for the direct approach we need the chronology of the input signal in order to carry out the computation in time domain. As the comparison will be done in frequency domain, we choose the Ricker wavelet used in the previous section (Fig.1.6a) for sake of simplicity. The MISS3D computation is conducted several times in order to calibrate parameters ζ_0 and β_s controlling the damping at the structure and soil, respectively, which math with the FE response obtained for the selected integration parameters.

Fig.1.12a shows the comparison between the spectral ratio obtained for both computations and the transfer function of the fixed base model. The agreement between both computations is excellent in frequency and modulus. As expected, the relative value of the fixed base frequency $f_0 = 2.5[Hz]$
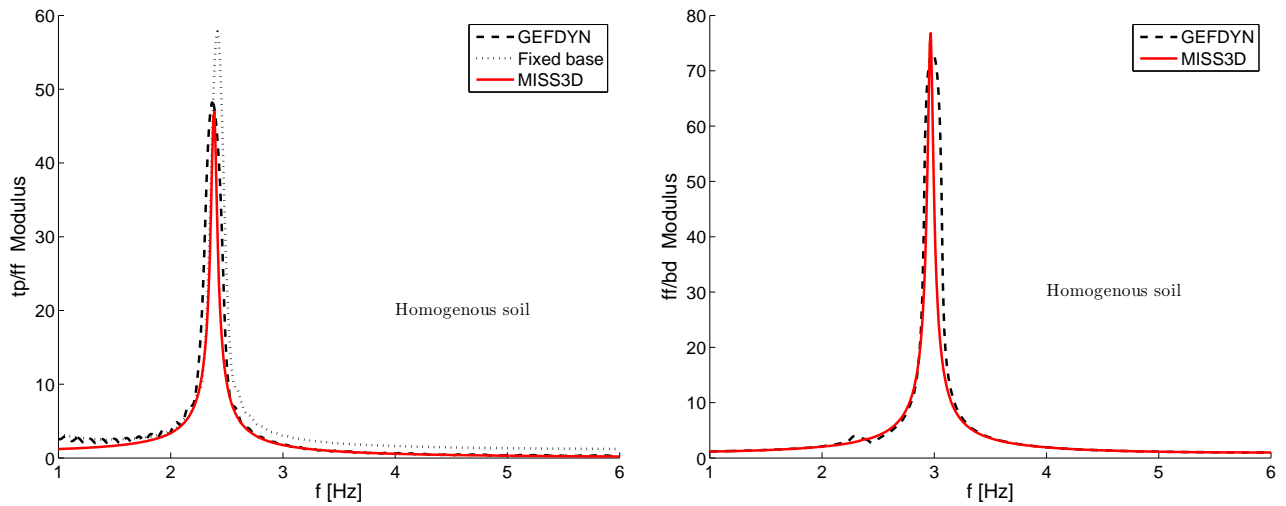
(a) Computed spectral ratios tp/ff for the homogenous soil compared to fixed base transfer function

(b) Obtained spectral ratios ff/bd for the homogenous soil

Figure 1.12: Comparison between computed spectral ratio moduli obtained with substructure and direct method for the homogenous deposit

compared to the soil layer frequency $f_{soil} \approx 3$[Hz] explains the relatively low soil-structure interaction. Indeed, a little shift of the frequency is found and some reduction of amplitude can be noticed. The agreement between ff/bd spectral ratio is also satisfactory in frequency and amplitude as can be deduced from Fig.1.12b. In this plot, a little evidence of the structure is found near to its fixed base resonance frequency on *GEFDyn* computed curve. This perturbation might be related to wave reflections over the mesh border. Nevertheless, these little reflections are negligible for practical purposes. The plots on Fig.1.12 were computed with a structural damping ratio of $\zeta_0 = 0.1\%$ and soil damping coefficient $\beta_s = 0.15\%$. Regarding the soil damping coefficient, this value agrees with the critical damping ratio $\zeta = 0.8\%$ obtained by curve matching for the 1D wave propagation test presented before, considering that by definition the soil damping coefficient is two times the usually critical damping ratio. These values of damping are kept for MISS3D computation of the horizontally stratified case.
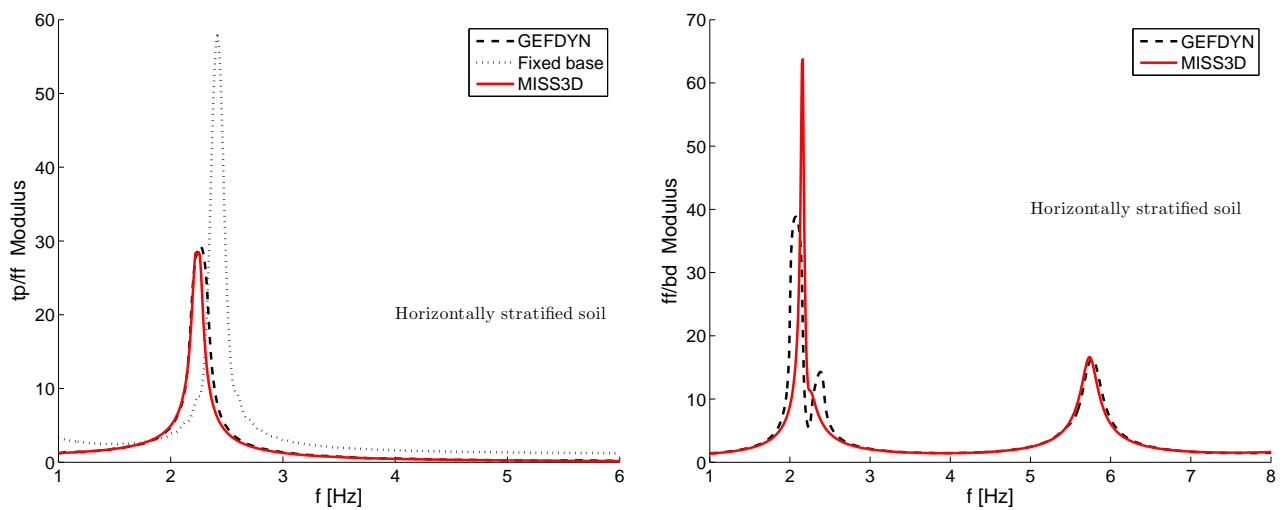
(a) Computed spectral ratios tp/ff for the horizontally stratified soil compared to fixed base transfer function

(b) Obtained spectral ratios ff/bd for the homogenous soil

Figure 1.13: Comparison between computed spectral ratios modulus between substructure and direct method for the horizontally stratified deposit

Fig.1.13a displays the obtained response for the horizontally stratified soil using the damping parameters defined above. It can be noticed that the agreement is still satisfactory in frequency and modulus for this case. As the fixed base frequency of the superstructure and the soil are close ($f_0 \approx f_{soil} \approx 2.5$[Hz]), soil-interaction effects are bigger compared to those of the previous case. In this curve, the shift on the fundamental frequency and the reduction of amplitude related to radiation damping are significantly larger compared to the homogenous soil case. The quality of the agreement between both computations decays for the ff/bd spectral ratio as can be noted from Fig.1.13b. According to this curve, the superstructure is significantly more visible for the FE computation than for substructure one. The agreement is still excellent for the second resonance frequency. The differences between both curves might be related to multiple wave reflections between both superficial layers and the resonance condition between soil and soil profile. Even if some differences exist in frequency and amplitude for the first mode of the soil profile, the spectral ratio involving the structure is quite satisfactory for practical purpose. Indeed, the wave reflections should reduce by including hysteretic damping associated to material non-linear behavior.

1.4.3   Investigation of boundary conditions modeling for elastic 2D SSI problem

Early stage of this work was devoted to define the better strategy to model the SSI problem following a direct approach by FE. This investigation was conducted under linear elastic condition for both, soil and structure, neglecting other possible sources of non-linear behavior as uplift over the soil-foundation interface. A summary of this study is presented in this section.

We use the elastic homogenous soil profile defined in Fig.1.14a overlying an elastic bedrock. Numerical integration parameters selected in §1.4.1 are kept in order to ensure some numerical dissipation. As the bedrock is elastic, radiation damping is present. The test structure is selected following criteria described in Chapter 2. We use only the structure of fundamental fixe base period $T_0 = 0.4$[s] in the following. This structure is used due to the value of its fundamental frequency $f_0 = 2.5$[Hz] compared to the first mode of the soil profile $f_{soil} \approx 2$[Hz]. As previously indicated and showed in Chapter 2, for structures of f_0 between first and second modes of the soil profile, some soil-structure interaction effects appear. The used superstructure corresponds approximately to an equivalent SDOF for a regular moment-frame structure of 3 or 4 levels (Fig.1.14b).

The study was focussed on different boundary condition configurations in order to minimize the wave reflection at the borders of the mesh. We assume a plane-strain model for the soil, thus a bidimensional mesh is used for each tested configuration. As it will be largely discussed in Chapters 3, when non-linear soil-behavior is take into account, the hypothesis relative to load transfer between soil and structure plays a key role in the numerical modeling of the SSI problem. For this example, the soil is supposed to be elastic, thus no important effects related to over stress transmission are expected. However, by modeling the problem using a 2D dimensional approach we are implicity assuming a periodicity of 1[m] following the direction normal to the plane of the model. An extension of this plane-strain approach for more general regular buildings will be presented in Chapter 3.

We study three different configurations. The first one corresponds to lateral tied boundaries describes before (**Tied**). The second one, corresponds to the approach suggested by Modaressi (1987) to study the effects of geometrical irregularities on the wave propagation in valleys (**Inc.**). Finally, in the third configuration we include absorbing elements in lateral boundaries (**Lat.**).

Lateral tied approach (**Tied**) has the advantages of its simplicity and that it is suitable for general non-linear soil models. The model is constructed in yz plane. In this case, tied DOFS are nodal displacement u_y and u_z, across y and z respectively. For saturated case, if a simplified Biot formulation is used, nodal pressure DOF p is also tied between lateral boundaries. Similarly to previous models, we include only the first 5[m] of the bedrock adding a paraxial element at the bottom to satisfy radiation condition and impose incoming waves. The total mesh has 200[m] width in y horizontal direction. This dimension is chosen exceptionally big in order to make possible the comparison with the other studied configurations. The used mesh is shown in Fig.1.15a, where colors are used to illustrate the variation of vertical size of elements. This vertical variation is the same illustrated in Fig.1.5, the

(a) Homogenous elastic soil profile of 30[m] overlying elastic bedrock

(b) Superstructure model of fundamental fixed base period $T_0 = 0.4$[s]
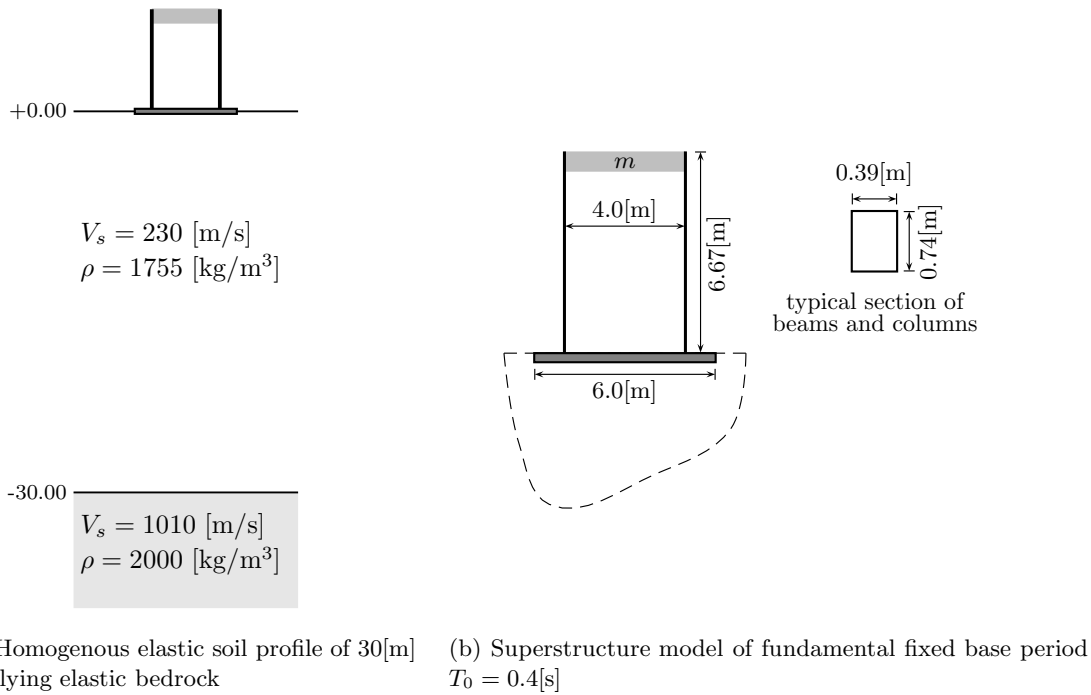
Figure 1.14: Schema of both soil profile and superstructure used for the investigation of boundary conditions for elastic 2D SSI problems

horizontal spacing is regular and equal to 1[m].

In the second tested approach, the main difference is related to the incident field (**Inc.**). In this case, we introduce the incoming wave across the entire boundary using paraxial elements with two functions, to absorb the outgoing waves and to impose the incident field. As described in §1.2.3, paraxial elements require locally elasticity condition. Thus, we need to use elastic solid elements at least in the first range of elements neighbor to the boundary. This condition represents a limitation for the non-linear case. In this situation, lateral limits must be chosen far enough of the superficial perturbation to ensure elasticity behavior (Fig.1.15b). This conditions explains the large horizontal dimension required for this model. Even if for this investigation we use elasticity condition we need test configurations suitable for the general non-linear case. The same vertical discretization is kept. Horizontal discretization is also the same in the center of the mesh and it is modified gradually toward the borders to impose valley type geometry. Two layers of horizontal elements with 5[m] of width are used adjacent to inclined paraxial elements. Lateral borders correspond to segments of circumferences. We also test a mesh configuration including the complete circumferential region, but we found equivalent responses with an important numerical-cost increase.

The third configuration studied has exactly the same mesh as tested with tied lateral approach, but the tied border condition is removed and vertical paraxial elements are added (**Lat.**). Horizontal paraxial elements at the bottom of the mesh are kept. Nevertheless, lateral paraxial elements are used only as absorbing elements and no incident field is imposed laterally. Similarly to the previous case, this approach requires elastic behavior close to lateral mesh borders, even if a non-linear computation is conducted. Consequently, it also requires a relatively large mesh in the horizontal direction. The use of lateral absorbing boundaries is often suggested in literature, but their use must be conducted carefully. Their use is straightforward when the source is interior to the mesh and the displacement field reaching the border must be completely absorbed. For earthquake engineering application, this kind of lateral absorbing devices must be able to separate the incident field and the outgoing field, and absorb only the last one. In this case, one option is to reformulate the problem separating fields and solving the problem in two steps as suggested by Zienkiewicz et al. (1988). Both solutions are combined to obtain the total response. For this test, lateral vertical absorbing boundaries are assumed

(a) Tied lateral boundaries approach (**Tied**)

(b) Valley type approach (**Inc.**)

(c) Lateral absorbing boundaries (**Lat.**)
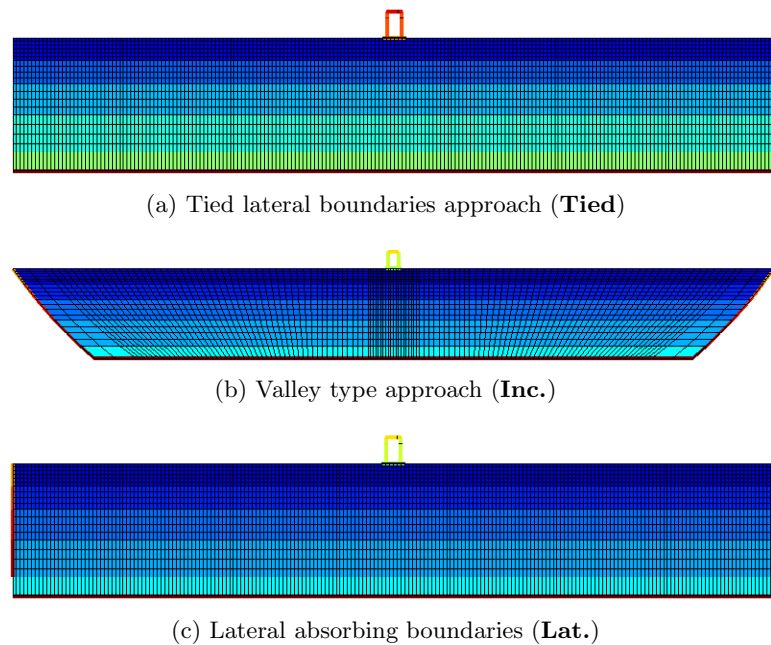
Figure 1.15: Different 2D meshes studied in order to define the better strategy to treat lateral boundaries in FE modeling approach

to be far enough in order to not perturb the incident field and to absorb essentially radiated wave field. Therefore, the computation is carried out in total displacements directly.
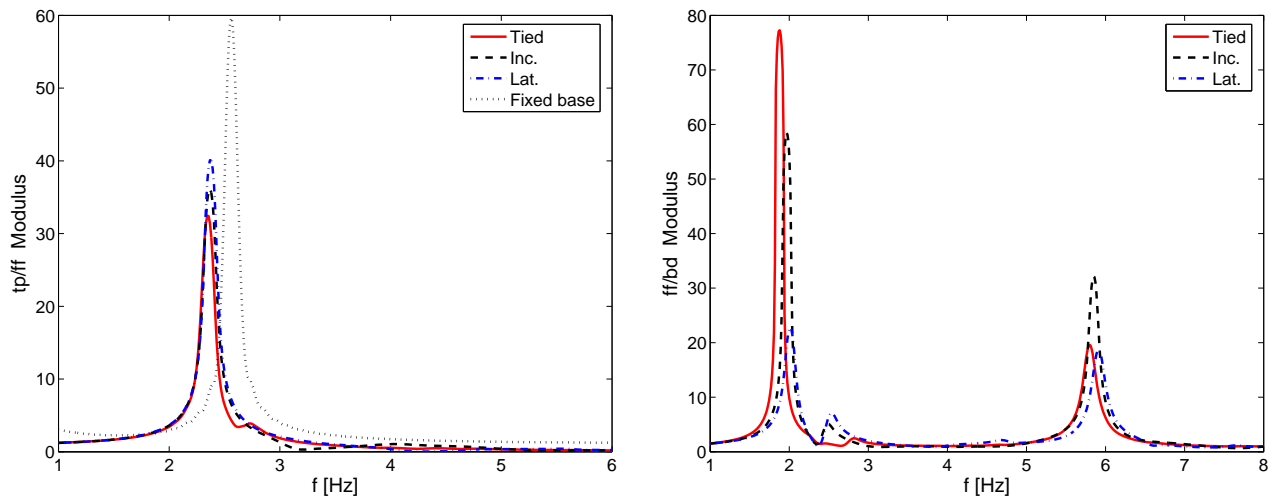
(a) Computed spectral ratios tp/ff for three studied configurations

(b) Obtained spectral ratios ff/bd for three cases

Figure 1.16: Comparison between computed spectral ratio moduli for three configurations of boundary conditions for the SSI 2D elastic case

The three computations are conducted with *GEFDyn* in time domain using numerical dissipative time integration parameters. The Ricker wavelet of the Fig.1.6 is used as the incident field in all cases. The response will be compared firstly in frequency domain in terms of both spectral ratios tp/ff and ff/bd defined in previous section (Fig.1.11). Fig.1.16 shows the obtained spectral ratio modulus for three modelled configurations compared to fixed base transfer function amplitude. As expected, significant SSI effects are visible in frequency and in amplitude. The predicted shift in the fundamental period of the structure agrees for all three computations, but some differences appear concerning the amplitude. Tied approach predicts a larger reduction of amplitude, whereas Inc. and Lat. approaches

give approximately the same amplitude. This differences might be related to confinement effect of the lateral paraxial elements. Indeed, absorbing feature of paraxial elements introduces a normal stress to the boundary similarly to a dashpot. This lateral stress contributes to relatively stiffening of the soil deposits. This increase of stiffness might explain the relative reduction of the interaction and the shift to high frequency of the fundamental mode of the deposit noticed in Fig.1.16b.

(a) First 6[s] of the obtained top displacement response

(b) First 4[s] of the computed free field acceleration
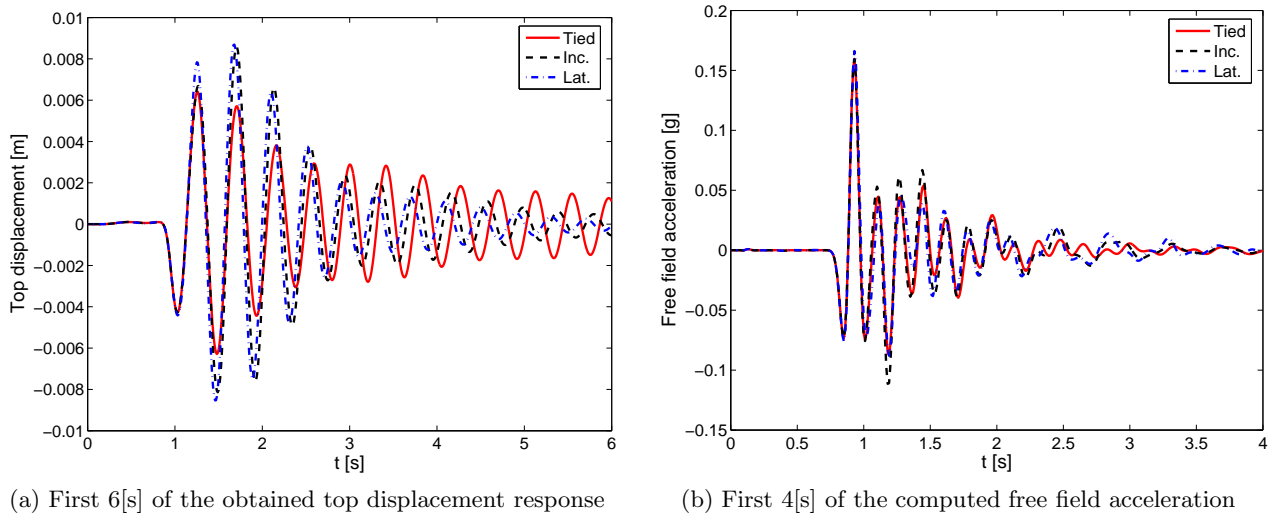
Figure 1.17: Time responses obtained at top of the structure and free field for the three studied configuration

Fig.1.16b shows that including lateral dissipative elements does not improve the solution at free field. On the contrary, free field response of Inc. or Lat. models show a perturbation around the fixed base frequency of the structure. This perturbation might be related to reflections of the surface waves on the border of the mesh. Tied approach gives the cleaner spectral ratio function at free field. Concerning the amplitudes, as expected, lateral absorbing strategy gives the minor amplitude values. In this case, lateral paraxial elements provide supplementary radiation damping and consequently the amplitudes diminish. Lateral incident approach provides an intermediary prediction in terms of the amplitudes for the first mode, but the larger amplitude for the second mode. These free field estimations were taken as far as possible from the structure for Tied and Lat. approaches. For the Inc. case, free field condition was taken at the end of the rectangular part of the mesh, thus before reaching the circumferential zone in order to prevent local effects due to relatively near incident field.

In order to illustrate the effects of these differences in time domain, Fig.1.17a shows computed structural top displacement responses and Fig.1.17b the obtained accelerations at free field. The differences of modulus noticed on computed tp/ff spectral ratio agrees with the variations of the displacement amplitudes found at the top of the structure. Thus, the amplitude of displacement obtained following Tied approach are slightly less than those obtained for other two strategies. No significant variations on frequency are detected, but some differences related to decay of the curves appear. Indeed, the reduction of top displacement of the structure seems to be low for the Tied approach. This result might be related to the radiation damping. In fact Inc. and Lat. approaches provide lateral absorption that increases the damping of the system. Variations depending upon the adopted model are not significative in the observed free field acceleration (Fig.1.17). In this plot, differences between three approaches are negligible for practical purposes.

In summary, no significant differences were found between three strategies studied here. In frequency domain, Tied approach gives the cleaner solution. In time domain, obtained responses are equivalent in acceleration but some differences were found in displacement responses. Nevertheless, Tied approach has important advantages. In this approach lateral elastic elements are not required, thus the size of the mesh can be significantly reduced. This feature is specially important for large non-linear 3D models. Of course periodicity hypothesis implicit to Tied approach must be compatible

with the problem studied. For more complicated geometrical situations, Inc. approach will be more suitable. The use of lateral absorbing elements is adequate when the source is interior to the mesh or if a rigid base relative-displacement approach is conducted. When the motion is imposed as incident field, absorbing boundaries must be treated carefully using decomposition techniques as suggested by Zienkiewicz et al. (1988).

1.5   Concluding remarks

The general dynamic soil-structure interaction problem was presented theoretically by the definition of the related governing equations in the soil and structure domains, as well as conditions over their interface. Special emphasis was put on dynamic boundary conditions concerning the truncation of the unbounded domain for a finite element modeling.

The constitutive models used for the numerical modeling of soil, interface and structural components were presented. These non-linear constitutive models take into account some important aspects of the dynamic non-linear behavior of different involved materials. The used FE code *GEFDyn* was enhanced by the implementation of a three dimensional plastic-hinge beam model, and the improvement of several other available features related to interfaces, continuous beams, sequential construction ability, among others. Special developments will be done, in order to increase the numerical capacity of the code to run costly models as presented in next chapters.

Some special aspects of the numerical modeling of the dynamical SSI problems were presented. As was mentioned, major issues are the treatment of the lateral boundaries and damping. These aspects were presented in the form of 1D, 2D and 3D validations, in order to justify different modeling choices adopted in this work.

The numerical simulations presented in this chapter were conducted in linear elasticity for both, soil and structure. Next chapters are devoted to present several non-linear applications, including some specific developments.

Chapter 2

Effects of non-linear soil behaviour on the seismic performance evaluation of structures [1]

Contents

2.1 Introduction

In the present earthquake engineering practice, the capacity spectrum method is widely used for seismic performance evaluation of existing and new structures. Nevertheless, usually the effects of dynamic soil-structure interaction (SSI) and the non-linear behaviour of the surrounding ground are neglected.

Some simplified procedures taking into account the dynamic SSI effects on the determination of the design earthquake forces and the corresponding displacements exist. For instance, FEMA 356 (2000) and ATC 40 (1996) documents give some provisions to include ground flexibility in the structural analysis model. Recently, FEMA 450 (2003) draft document proposes some techniques to improve the traditional non-linear static seismic analysis. Concerning soil-structure interaction effects, this document presents procedures to take into account kinematical effects as well as foundation damping effects. Kinematical effects are related to filtering the ground shaking transmitted to the structure i.e. a modification factor is applied to the input motion. Foundation damping is combined with the structural damping to obtain a revised damping for the system. All these procedures are based on traditional soil-structure interaction expressions with linear-elastic soil behaviour assumption. However, it is well-known that the limit of linear-elastic soil behaviour is very low ($\gamma < 10^{-5}$). This strain limit is normally exceeded during a real motion.

In this work the influence of SSI effects on the seismic performance evaluation is investigated. For this purpose, numerical simulations of pushover tests and non-linear dynamic analyses (i.e. non-linearity of the soil and the structure behaviour) are performed in order to study the role of several parameters on the seismic performance evaluation. This parametric study concerns the mechanical properties of the soil foundation (e.g. $V_{s,30}$ and fundamental soil deposit frequency) and the structure (i.e. fundamental period, effective height and mass) as well as the characteristics of the input motion (i.e. amplitude and frequency content). Thus, several 2D finite element computations are carried out using non-linear elastoplastic models to represent both the soil and the structure behaviour. Results obtained by simplified computations performed following a two-step approach (which will be described below), are compared with the ones obtained from fully non-linear time-history finite element modelling analyses.

These results allow to identify and to quantify the differences between the two approaches. Thus, it is possible to establish the situations for which the approximate techniques might tend to overestimate or underestimate the displacement demand. We present a summary of the main findings including some recommendations to consider in a performance evaluation following the Capacity Spectrum Method (CSM).

2.2 Proposed approaches

In order to investigate the effect of non-linear soil behaviour on seismic demand evaluation, a comparative dynamic analysis is carried out. First, a complete finite element model including soil and structural non-linear behaviour is used to asses the effect of non-linear dynamic soil-structure interaction on the structural response. Secondly, a two-step approach is carried out where: a non-linear 1D wave propagation problem is solved for a soil column of the foundation soil. Next, the obtained free field motion is imposed as the ground motion to a fixed base structural model. The two approaches are sketched in Fig.2.1.

The analysis is carried out for several non-linear SDOF models, with fundamental period varying from 0.1[s] to 0.4[s]. The mass and height of each SDOF is obtained with typical weight and height values, relating its fundamental period to the number of levels of the structure. The same infinitely rigid shallow foundation is considered for all SDOF models.

In order to simulate the soil foundation, two non-linear homogenous dense sandy soil deposits were used. The first one is in dry condition and the second one is fully saturated. The bedrock is placed at the depth of 30[m]. Four Europeans earthquakes are considered, scaled to different maximum outcropping acceleration values.
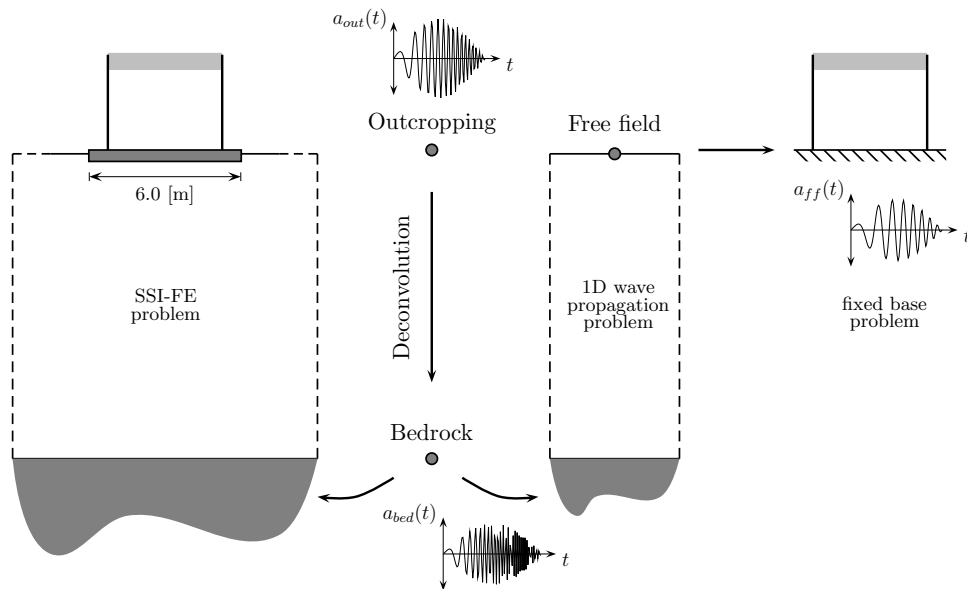
Figure 2.1: Summary of proposed approaches

2.2.1 Soil constitutive model

The ECP's elastoplastic multi-mechanism model (Aubry and Modaressi, 1992a; Hujeux, 1985) , commonly called Hujeux model is used to represent the soil behaviour. This model can take into account the soil behaviour in a large range of deformations. The model is written in terms of effective stress. The representation of all irreversible phenomena is made by four coupled elementary plastic mechanisms: three plane-strain deviatoric plastic deformation mechanisms in three orthogonal planes and an isotropic one. The model uses a Coulomb type failure criterion and the critical state concept. The evolution of hardening is based on the plastic strain (deviatoric and volumetric strain for the deviatoric mechanisms and volumetric strain for the isotropic one). To take into account the cyclic behaviour a kinematical hardening based on the state variables at the last load reversal is used. The soil behaviour is decomposed into pseudo-elastic, hysteretic and mobilized domains.

The model's parameters of the soil are obtained using the methodology suggested by Lopez-Caballero et al. (2003); Lopez-Caballero et al. (2007). In order to verify the model's parameters, the behaviour of the sand must be studied by simulating drained (DCS) and undrained cyclic shear tests (UCS). The Fig.2.2a shows the response of a DCS test obtained by the model of the sand at an effective stress of 100[kPa]. The test results are compared with the reference curves given by Iwasaki et al. (1978).

In saturated conditions, the evolution of shear strain and pore pressure can be observed during the UCS. The Fig.2.2c and Fig.2.2d shows the test simulation for a stress controlled shear test with the same model's parameters. The generation of pore pressure reduces the effective stress inducing cyclic mobility without liquefaction.

Two levels of water table were considered: deeper than the model (dry) and at surface level (saturated or wet). The shear wave velocity of the soil increases with depth (Fig.2.6a). The shear wave velocity profile gives an average shear wave velocity in the upper 30[m] ($V_{s,30}$) of 232.8[m/s] for dry conditions and 204.3[m/s] for saturated condition. This soil profile corresponds to a category C site of Eurocode 8 (deep deposit of dense or medium dense soil) in both cases.

2.2.2 Structural model

The typical one-story frame chosen to represent each SDOF structure is shown in Fig.2.3a. The mass of the building is assumed to be uniformly distributed along beam elements and the columns are supposed massless. Non-linear material behaviour is taken into account through an elastic-perfect plastic strain-stress relation. Fig.2.3b shows a normalized moment-curvature ($M - \Psi$) diagram obtained from the

(a) DCS test results

(b) DCS test results

(c) UCS test results
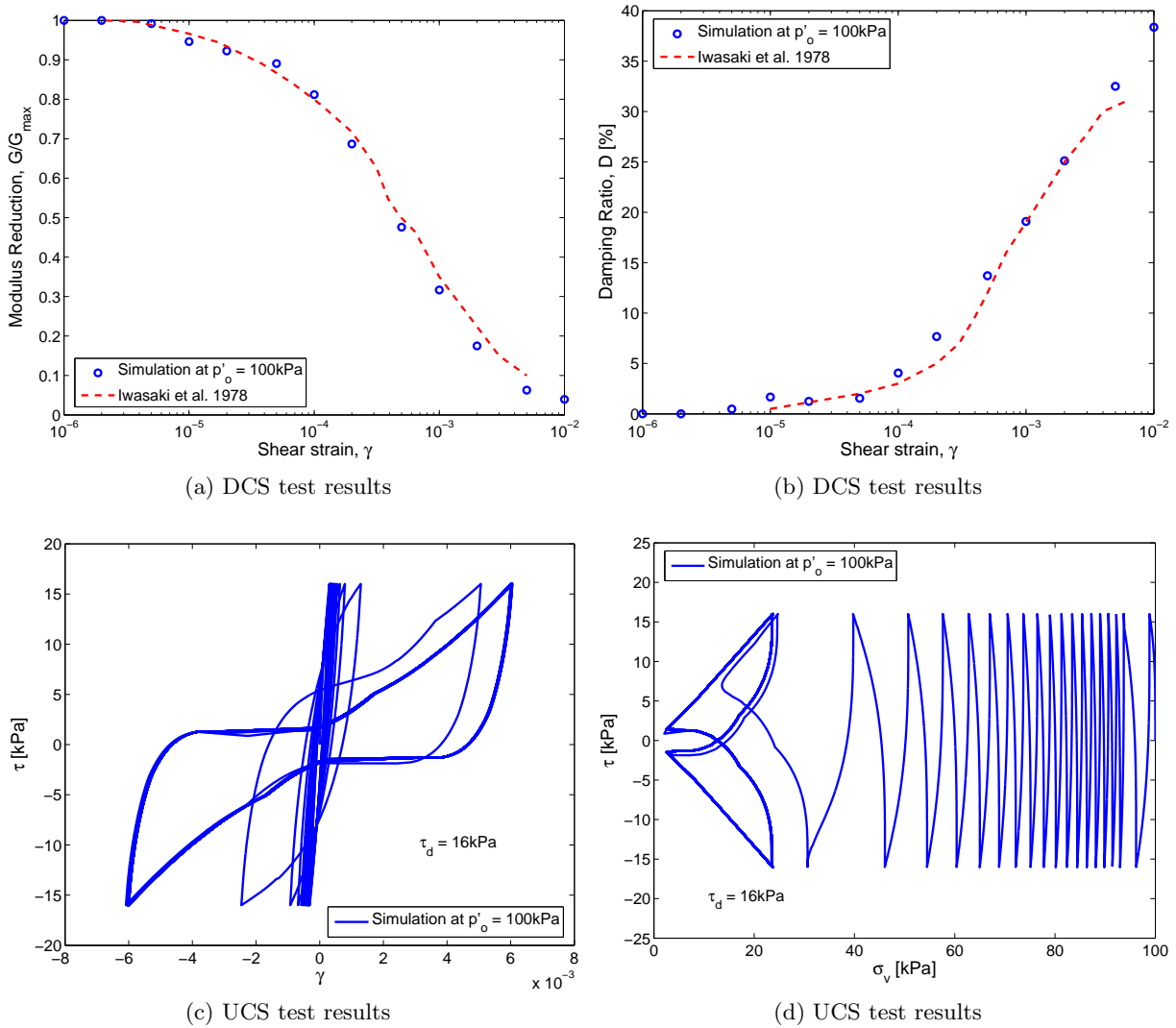
(d) UCS test results

Figure 2.2: Simulated drained (DCS) and undrained (UCS) cyclic shear test results obtained with the soil's constitutive model.

computation of a simply fixed beam with this behaviour model. As it can be noticed, the stiffness decreases when the elastic limit is reached (at M_y or Ψ_y), and under load reversal the curve forms hysteresis loops. The maximum resisting moment remains constant under increasing deformation and the member rotates as a hinge with this constant resisting moment. The value of stress yield is supposed to be the same for all computations.

The elastic modulus (E) and the yielding stress (σ_y) of structural elements are 25.5[GPa] and 18[MPa], respectively. The mass and height of each SDOF is obtained with typical weight and height values. A typical value of 20000[kg] is assumed for each level. A constant value of 2.5[m] is considered for each interstory height. Thus, the equivalent SDOF corresponding to a building of n levels is computed assuming a mass of $20000n$[kg], a fixed base period of $T_0 = \frac{n}{10}$[s] and equivalent height $H = \frac{2}{3} \times 2.5n$[m], and finally solving for b and h (lateral stiffness). The Table 2.1 shows the basic properties for the used SDOF.

A viscous damping of $\beta_i = 0.02$ was considered for all computations. The same infinitely rigid shallow foundation with a characteristic length of 6[m] was used for alls SDOF.
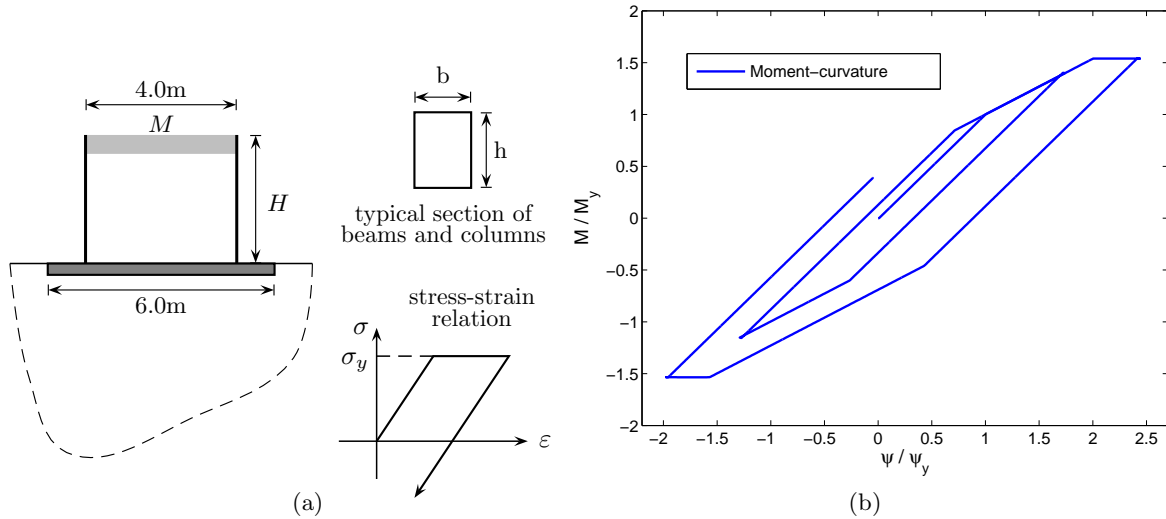
Figure 2.3: Structural model description

Table 2.1: Properties of equivalent SDOF

T_0[s]	Mass [kg]	Equivalent height [m]	b [m]	h [m]
0.10	20000	1.66	0.20	0.43
0.15	30000	2.50	0.23	0.50
0.20	40000	3.33	0.25	0.56
0.25	50000	4.17	0.30	0.61
0.30	60000	5.00	0.34	0.65
0.40	80000	6.67	0.39	0.74

2.2.3   Input earthquake motion

The used seismic input motions are the acceleration records of Friuli earthquake - San-Rocco site (Italy-1976), Superstition Hills earthquake - Supers. Mountain site (USA-1987), Kozani earthquake (Greece - 1995) and Aegion earthquake (Greece - 1995). The frequency content was characterized with the mean period (T_m) Rathje et al. (1998) (Table 2.2). All signals are consistent with the response spectra of Type A soil of Eurocode8.

Table 2.2: Used input earthquake motions

Earthquake Records	$T_{m,out}(s)$	Symbol for plots
Kozani (Greece)	0.28	◯
Superstition Hill (USA)	0.38	☐
Friuli (Italy)	0.46	◇
Aegion (Greece)	0.56	▽

Each motion will be used as the outcropping motion and scaled to different values ranging from $0.15g$ to $0.30g$ linearly increased by an increment of $0.05g$, resulting in a total of 16 events for each frame on dry soil. For frames exhibiting important non-linear structural behavior, this range will be extended to $0.35g$ (see section 2.4).

2.2.4   Finite element approach (SSI-FE)

The Finite Element model is composed of: the structure, the soil foundation and a part of the bedrock. The considered structure is a one-story, one bay frame. The 30[m] thick homogenous soil deposit is modelled by 4 node linear elements. In the bottom, a layer of 5[m] of elastic bedrock ($V_s = 1000$[m/s] and $\rho = 2000$[kg/m3]) is added to the model. The finite element mesh used for modelling this problem is showed in Fig.2.4. Plane strain condition is assumed for the soil deposit and the bedrock.

   As the main purpose of this paper is to investigate the role of the general parameters as T_0, T_m, a_{out},etc. in order to establish general tendencies of the results and identify when the non-linear SSI is a major issue, the set of SDOFs analysed for this paper does not correspond to a specific set of structures. They are idealizations of typical values of height, mass and fundamental periods. The effect of the structural weight on the effective stress in the soil is neglected in this paper and will be extensively treated in further works.
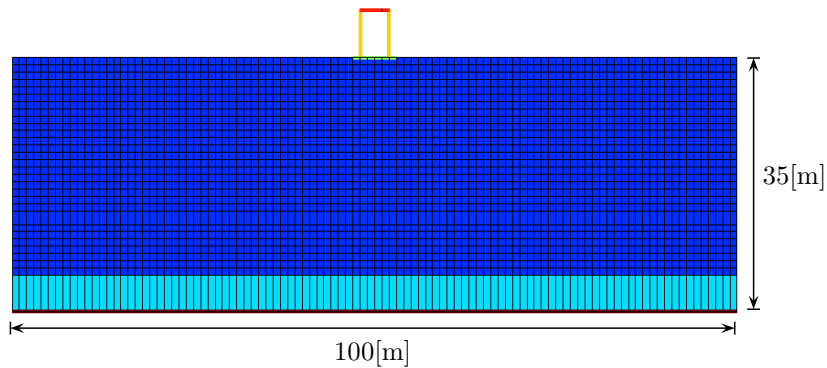
Figure 2.4: Finite element mesh

For the bedrock's boundary condition, paraxial elements simulating a *deformable unbounded bedrock* have been used. The incident waves, defined at the outcropping bedrock are introduced into the base of the model after deconvolution. In the analysis, as the lateral limits of the problem are considered to be far enough periodic conditions are verified. Then, only vertically propagating shear waves are studied resulting in the free field response. Thus, equivalent boundaries have been imposed on the nodes of these boundaries (i.e. the normal stress on these boundaries remains constant and the displacements of nodes at the same depth in two opposite lateral boundaries are the same in all directions). Thus, the obtained movement at the bedrock is composed of the incident waves and the reflected signal. The computations are carried-out in the time domain. The simulations are performed with the Finite Element tool GEFDYN (Aubry et al., 1985; Aubry and Modaressi, 1996).

2.2.5   Numerical tool Validation

Before proceeding to the non-linear analysis effects, a validation of the soil-structure interaction phenomenon assuming linear elasticity behaviour for both the soil and the structure is performed (i.e. a sample seismic signal is imposed at very low amplitude to ensure linear-elastic soil behaviour). A two-story frame taken from Saez et al. (2006) (fixed base fundamental frequency of 4.25[Hz]) is supposed to lie on the studied soil profile under dry condition. Fig.2.5 shows the obtained response of spectral ratio amplitude between the displacements at the top and at the base (*top/base*) of the structure compared with the response calculated using the numerical BE-FE tool MISS3D (Clouteau, 2003) for the dry soil case. Fig.2.5 also shows the spectral ratio amplitude between the free field and the bedrock motion (*ff/bedrock*) and the fixed base transfer function of the structure. For coupled BE-FE computations, the analysis is directly carried out in the frequency domain.

   For linear elastic SSI computations, the first two natural frequencies of the soil profile are 2.2 (T_{soil} = 0.46[s]) and 6.15[Hz] (Fig.2.5). Thus, due to the value of the fixed base fundamental frequency of the structure compared to the one of elastic soil deposit (i.e. $f_{str} > f_{soil}$), it is expected that SSI phenomena appears.
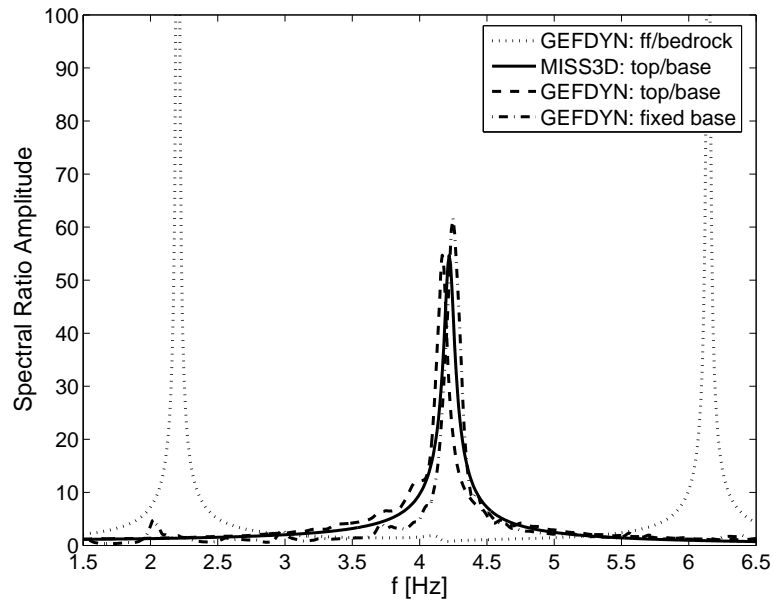
Figure 2.5: Spectral ratio amplitudes obtained with the coupled BE-FE linear elastic tool MISS3D compared to FE computations with GEFDYN for an elastic domain.

From the comparative results, it can be seen that the two different results obtained by the tools are in perfect agreement. The shift of the main frequency of the structure to 4.17[Hz] results from the flexibility of the foundation soil, whereas the change in the amplitude results from the material soil and radiation damping added. The numerical value of period shifting is compatible with the standard simple expression to compute linear-elastic soil-structure interaction provided in design codes.

2.2.6   Two-step approach

The first step is to solve a non-linear one-dimensional wave propagation problem for a soil column. The mesh consists of one column of solid elements obeying the same constitutive model as in the SSI-FE approach. The same boundary conditions have been imposed. The incident waves, defined at the outcropping bedrock, are introduced into the base of the model after deconvolution. In the second step, the obtained free field motion is imposed as the ground motion to a fixed base structural model. This two-step approach neglects all SSI effects, but takes into account the effect of non-linearity behaviour of both soil and structure.

2.3   Soil analysis and results

In order to define the input motion for the two-step approach, a free field dynamic analysis of the soil profile is performed. The response of the free field soil profile is analysed for the four earthquake records (Tab.2.2) as outcropping input with amplitudes increased with an increment of $0.05g$ from $0.1g$ to $0.5g$. The Fig.2.6b shows the obtained values and a tendency curve for the PGA (Peak Ground Acceleration) with respect to maximum acceleration on the bedrock ($a_{max,bedrock}$). These results are compared with the one for an AB deep soil profile according to the classification proposed by Dickenson and Seed (1996). It is possible to see that for weak base acceleration, the behaviour of both dry and saturated soil deposits is similar and thus the reduction in the effective stress due the water has not evident effect. It is noted that an amplification of the ground response for moderate range of $a_{max,bedrock}$ is obtained. For strong base acceleration the soil weakening attenuates the seismic motion. In saturated conditions, the pore pressure build-up acts as a frequency filter and the soil de-amplifies the input motion for large $a_{max,bedrock}$ values (Ghosh and Madabhushi, 2003; Lopez-Caballero and Modaressi-Farahmand Razavi, 2008).
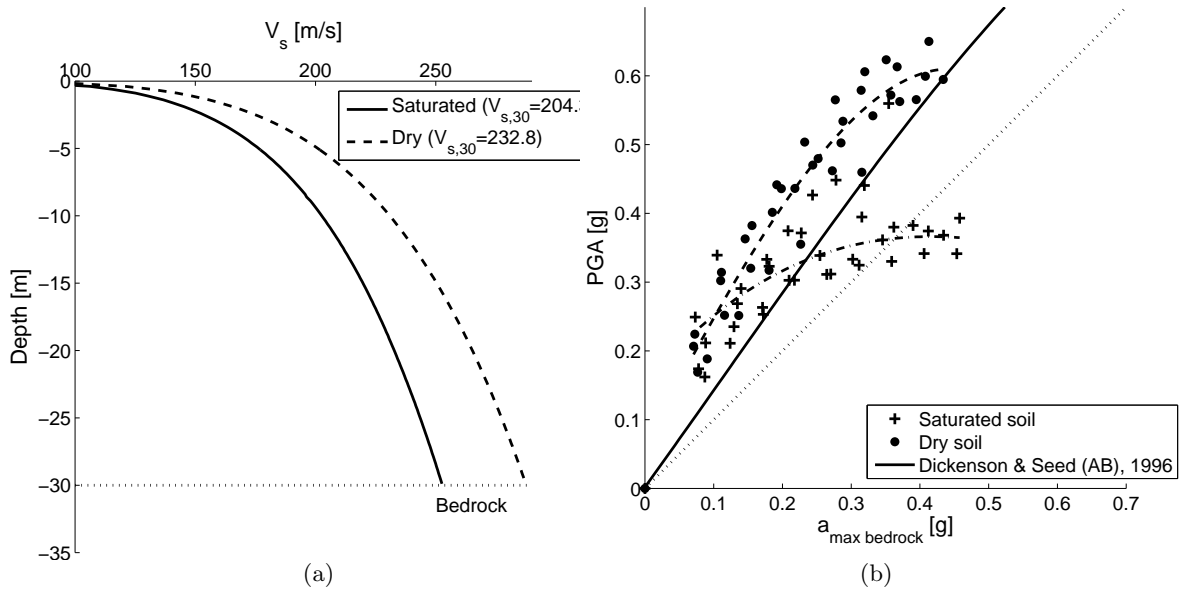
Figure 2.6: Effect of the presence of water on soil response

The influence of the inelastic behaviour of the soil deposit on the structural response can be directly related to 2% damped pseudo-acceleration response spectra (PSA) at the free field. The comparison between outcropping and obtained free field normalized PSA for different acceleration levels using Friuli earthquake scaled to $0.10g$ (Fig.2.7a) and $0.35g$ (Fig. 2.7b) are shown in Fig.2.7. For weak acceleration ($a_{out} = 0.1g$), the computed PSA is similar for both dry and saturated cases showing that the modification in the initial effective stress due to the presence of water has not a significant influence.
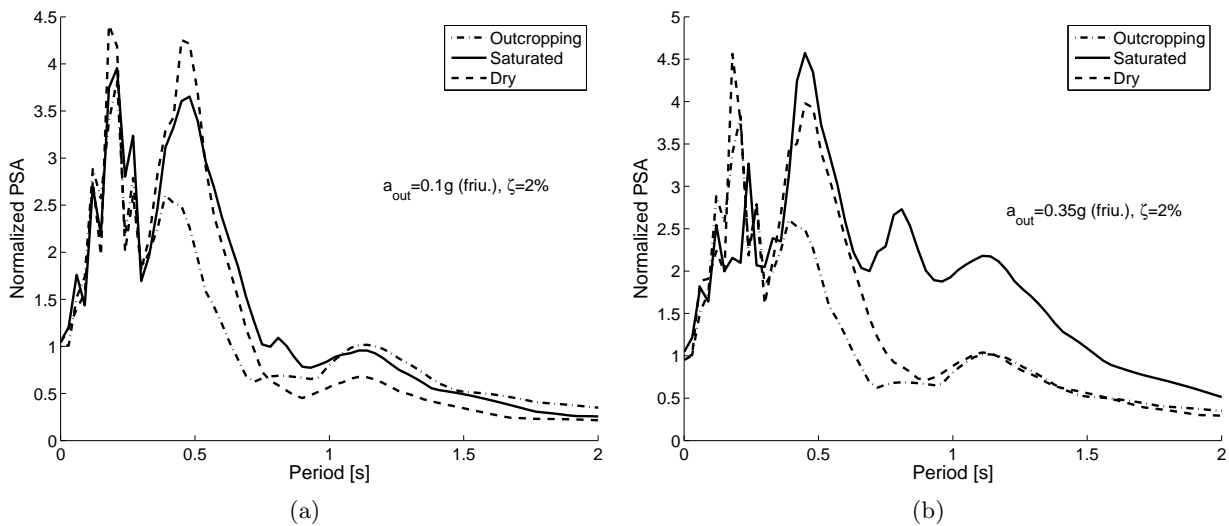
Figure 2.7: Effect of the water on PSA

According to Fig.2.7b ($a_{out} = 0.35g$), the spectral amplitude of saturated soil is greater than that of dry soil for large periods. This amplification of the PSA for the saturated soil with respect to dry soil can be explained by the pore water pressure built up (Fig.2.8) phenomenon properly simulated by the soil constitutive model (Lopez-Caballero and Modaressi-Farahmand Razavi, 2008). For short periods, the spectral amplitude of saturated soil is smaller than that of dry soil. It can be noted that it is not possible to identify this feature of soil behaviour using a simplified approach such as equivalent

linear method.
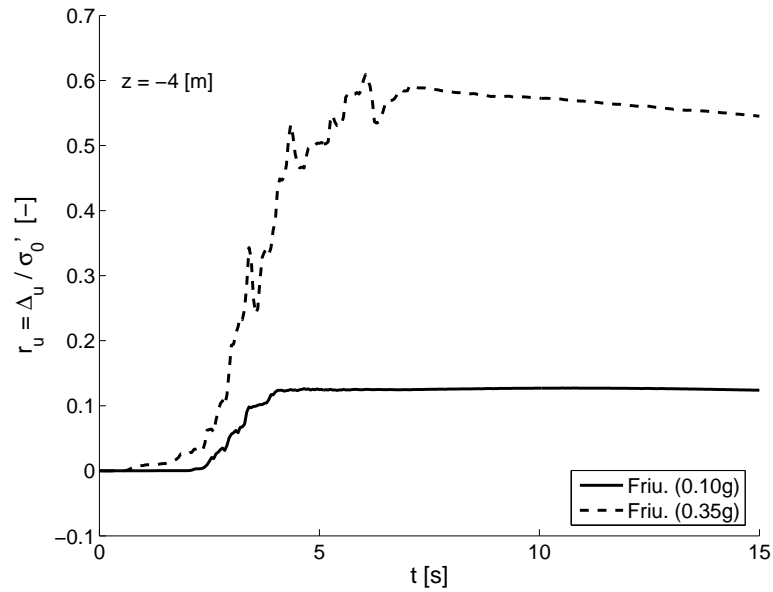
Figure 2.8: Pore pressure ratio r_u at 4[m] depth for two earthquake amplitudes.

2.4 Non-linear SSI analysis and results

Concerning the seismic demand evaluation, the maximum top displacement D (top drift) and its corresponding base shear, in terms of spectral acceleration A, are plotted for each studied SDOF structure following the two approaches for dry soil. For each SDOF, the corresponding capacity curve obtained by modelling the pushover test is also plotted (dashed lines in Fig.2.9a).
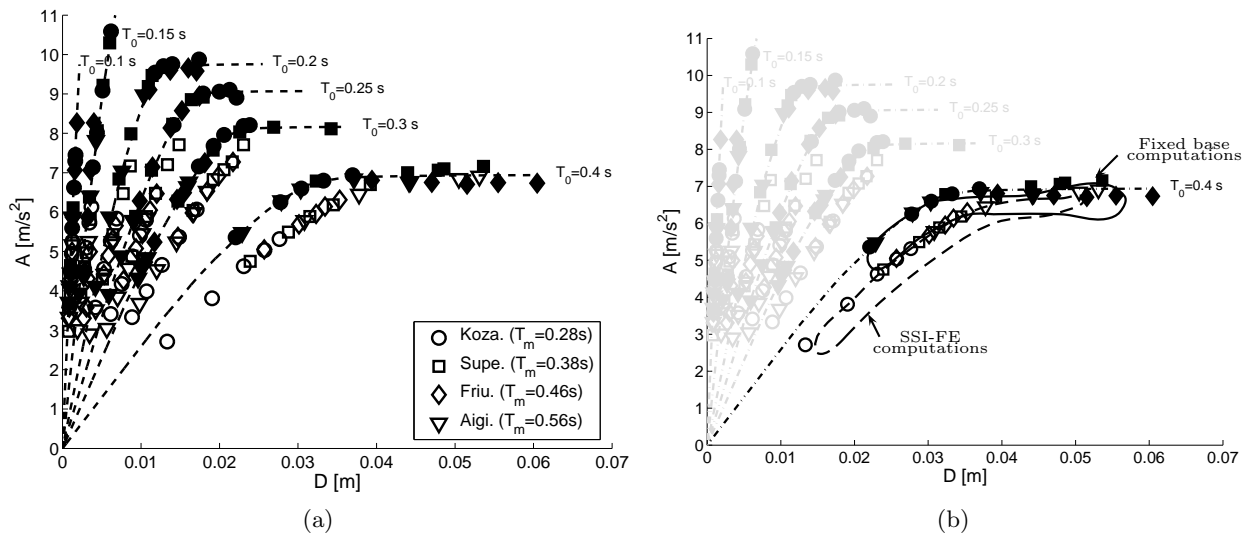
Figure 2.9: Summary of computations

In the SSI-FE approach, the obtained structural response for SDOFs with $T_0 \leq 0.25$[s] is approximately elastic even for high acceleration levels. The purpose of the paper is to investigate the role of the non-linear soil behaviour on the computed structural damage (i.e. structural non-linear behaviour). In order to focus the analysis of the results on the SDOFs exhibiting non-linear behaviour, the $T_0 = 0.3$[s] and $T_0 = 0.4$[s] SDOFs were studied for a slightly larger range of outcropping acceleration levels ($0.1g - 0.35g$) compared to $0.1g - 0.3g$ range used for the other SDOFs. Similarly, the

saturated soil case is carried out only for $T_0 = 0.3$[s] and $T_0 = 0.4$[s] frames.

To visualize the SSI effect on seismic demand evaluation, it is possible to take for example the $T_0 = 0.4\,(s)$ fundamental period SDOF (Fig.2.9b). Solid symbols correspond to the two-step approach, while the hollow ones are obtained by the SSI-FE approach. Each point represents a response obtained by one input motion scaled to a specific value.

The effect of the non-linear SSI on the seismic response can be represented by the ratio $D_{two-step}/D_{SSI-FE}$ between the computed top drift obtained following the two-step approach ($D_{two-step}$) and the computed value from the SSI-FE approach (D_{SSI-FE}) for the same outcropping motion. Fig.2.10a and 2.10b show this ratio in terms of the outcropping accelaration imposed (a_{out}) for the four used motions, with amplitudes varying from $0.1g$ to $0.35g$ with an increment of $0.05g$.
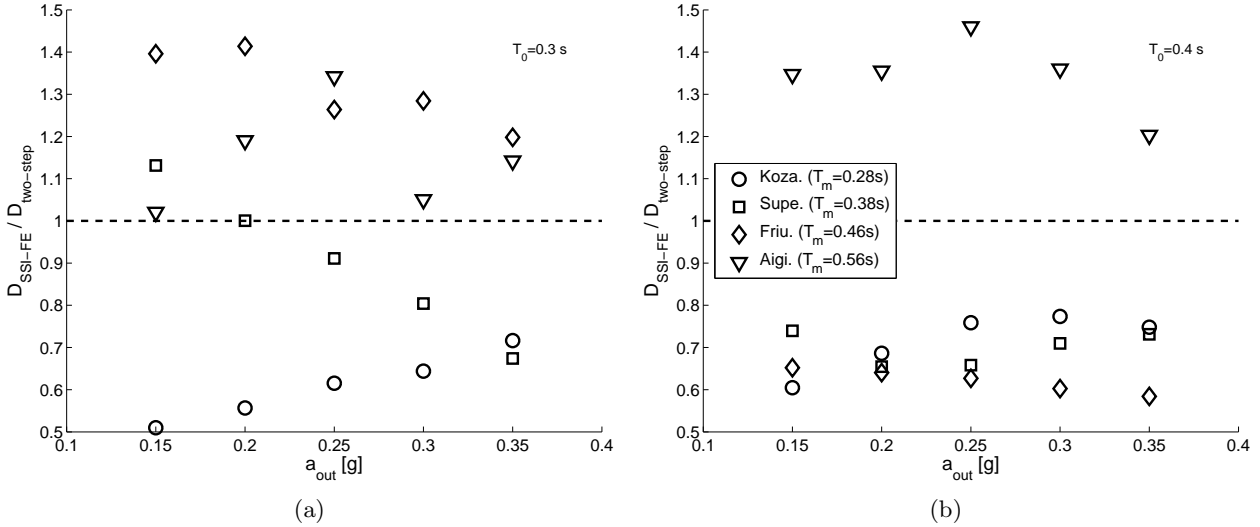
Figure 2.10: Top drift ratio between two-step computation ($D_{two-step}$) and SSI-FE approach D_{SSI-FE} for $T_0 = 0.3$s (a) and 0.4s (b) frames in terms of the maximum imposed outcropping acceleration a_{out}.

It is well-known that the stiffness degradation of the soil of the foundation introduces additional damping in the system, modifying the structural response. Additionally, radiation damping appears. According to our computations, the predicted top displacement obtained by the two-step approach is conservative, i.e. larger than the one obtained in the SSI-FE approach if $T_m \lesssim 1.3T_0$. On the contrary, for mean periods T_m larger than approximately 1.3 times the fixed base fundamental period of the frame T_0, the two-step computations give smaller values compared to non-linear SSI approach. Furthermore, the evolution of this ratio with the amplitude depends on the frame. For the $T_0 = 0.4$[s], the values of the ratio $DI_{two-step}/DI_{SSI-FE}$ vary between 0.6 and 0.8 for motions with $T_m \lesssim 1.3T_0$, but for the $T_0 = 0.3$[s] the ratio varies between $0.5 - 1.1$ for the same range of T_m.

Fig.2.9a shows that, even for relatively weak motion, the SSI-FE dynamic response of the structure (hollow symbols)is not placed on the pushover curve. Then, the non linear soil behaviour and the SSI effect induce a significant variation of the effective period (T_{eff}) of the structure and can decrease/increase the top displacement depending on the motion characteristics (T_m and a_{out}) and the structure properties (T_0 and m). In order to explain this behaviour, it is possible to see the distribution of principal strains in the neighboring soil of the structure during the Friuli earthquake scaled to $0.25g$ at outcropping (Fig.2.11a).

Fig.2.11b and 2.11c show the the principal strains distribution in two different steps of the analysis (Fig.2.11a). After the first part of strong motion ($t = 3.6s$) the soil is extensively deformed, then for the subsequent part of the motion its stiffness and damping differ considerably from their initial values. After the strong motion ($t = 12s$), an asymmetrical distribution of irreversible deformations is found. Permanent settlements are also generated. This soil deformation induces a high material soil damping. This damping has a direct influence on the seismic response of the structure and it cannot

(a)

(b)

(c)
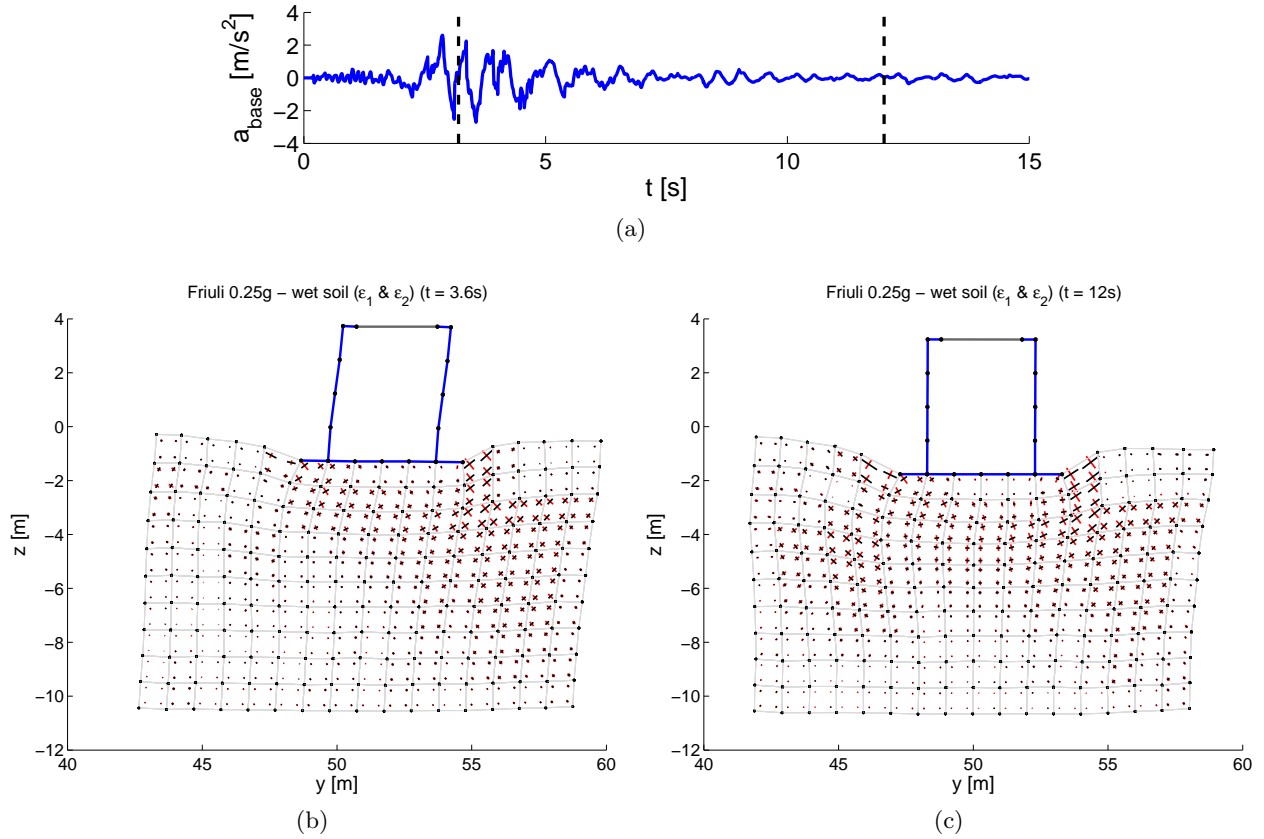
Figure 2.11: Principal strains and the deformed mesh (scaled ×50) in the neighboring saturated soil for two different steps of analysis for the $T_0 = 0.3s$ SDOF.

be properly evaluated following a fixed based approach or even if elastic SSI is taken into account. Therefore, the total seismic demand is highly controlled by the surrounding non-linear soil behaviour. For motions able to induce damage into a structure, the soil behaviour will be certainly non-linear.

To complete the previous analysis, the saturated soil results are also included in Fig.2.12a for the $T_0 = 0.4[s]$ SDOF. The tendency of the results is the same. The computed results are clearly aligned following an effective period. This value of Teff can be calculated from a linear fitting. After this approximately linear portion, the computed values of seismic demand approach asymptotically the fixed base capacity curve. The plateau of the curve does not change because it depends only upon the strength of structural elements. For a given motion, it can be noticed that the Performance Point (P.P.) from the two-step dynamic computation is approximately placed on the capacity curve; this indicates that capacity spectrum method is adequate for fixed base analysis. However, when SSI effects are taken into account, the P.P. from SSI-FE dynamic computation is placed approximately on the modified capacity spectrum with T_{eff} (Fig.2.12b).

2.4.1   Period lengthening due to SSI

The computed effective period (T_{eff}) may be related to the height (h), mass (m) and foundation characteristic length (a) (Fig.2.13) of the SDOF structure by traditional linear elastic soil-structure interaction expressions for rigid shallow foundations. With these expressions, an effective shear wave velocity can be computed ($V_{s,eff}$):

$$\left(\frac{T_0 V_{s,eff}}{2\pi h}\right)^2 = \frac{\frac{a^2(2-\nu)}{h^2} + 3(1-\nu)}{\frac{8\rho a^3}{m}\left(\left(\frac{T_{eff}}{T_0}\right)^2 - 1\right)} \tag{2.1}$$

where ν is the Poisson ratio and ρ is the mass per unit volume of the soil.
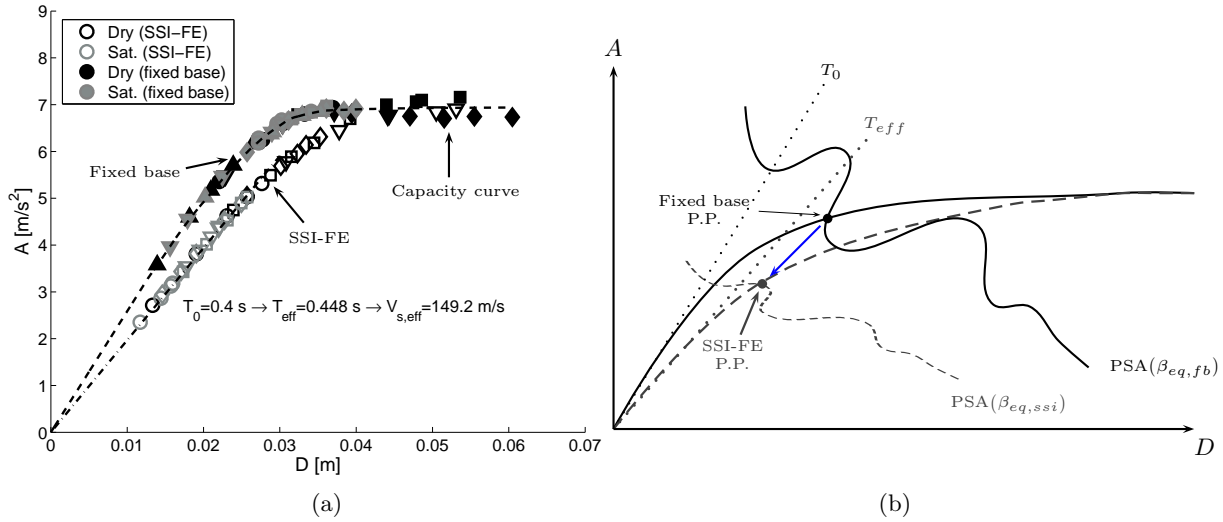
Figure 2.12: Summary of results
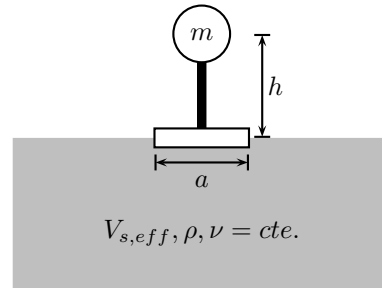
Figure 2.13: Geometrical scheme

It is possible to obtain for each SDOF, the variation of effective period and effective shear wave velocity.

According to Fig.2.14a, soil-structure interaction effects seem important only for structures with elastic periods placed between the two first elastic periods of the soil deposit (T_{soil}^1 and T_{soil}^2). For periods smaller than the second period of soil, the effective periods approach quickly that of the fixed base value. The ratio between the fixed base value and effective value is near to 90% for this type of soil.

From Fig.2.14b, it can be noticed that the effective shear wave velocity is approximately constant for structures with fundamental periods between the two first ones of the soil. This value can be considered like approximately constant and equal to two third of $V_{s,30}$ Eurocode 8's parameter in this case. Then, according to our results, a typical value of $\frac{2}{3}V_{s,30}$ into traditional elastic SSI relations can be used to compute an effective period for the used SDOFs.

2.4.2 Structural damping quantification

The application of the CSM procedure implies the computation of an equivalent viscous damping coefficient at the performance point (β_{eq}). This parameter includes the inherent structural damping (β_i) and the damping related to the damage of the structure (β_0).

A bilinear representation of the capacity spectrum is constructed following ATC-40 guidelines to estimate β_0 (Fig.2.15a). The values of β_0 are computed using fixed base capacity spectrum. Fig.2.15b show the computed values of damping as a function of the peak ground acceleration at the free field ($a_{max,ff}$) (solid symbols on Fig.2.15b). For SSI-FE computations, the capacity spectrum curve fitted using the obtained results of the dynamic SSI computations was used. With this capacity spectrum, the equivalent viscous damping β_0 values are also computed using the bilinear approximation suggested by ATC-40 (hollow symbols on Fig.2.15b). Some cases exhibiting structural linear behaviour have been
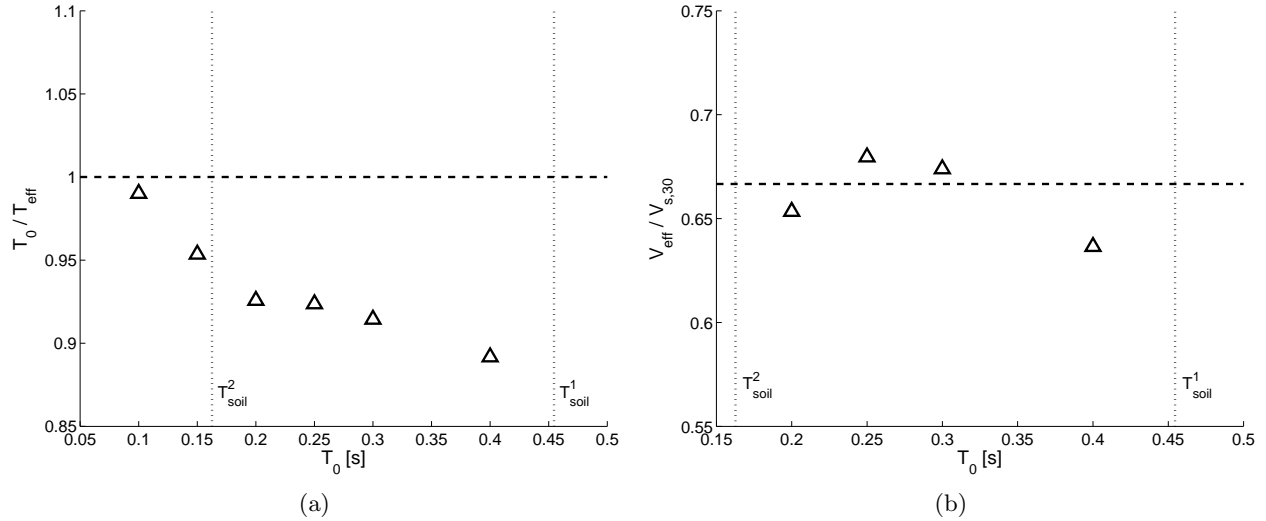
Figure 2.14: Effective period and shear wave velocity values

omitted in Fig.2.15b: outcropping accelerations of $0.1g$ and Aegion earthquake.
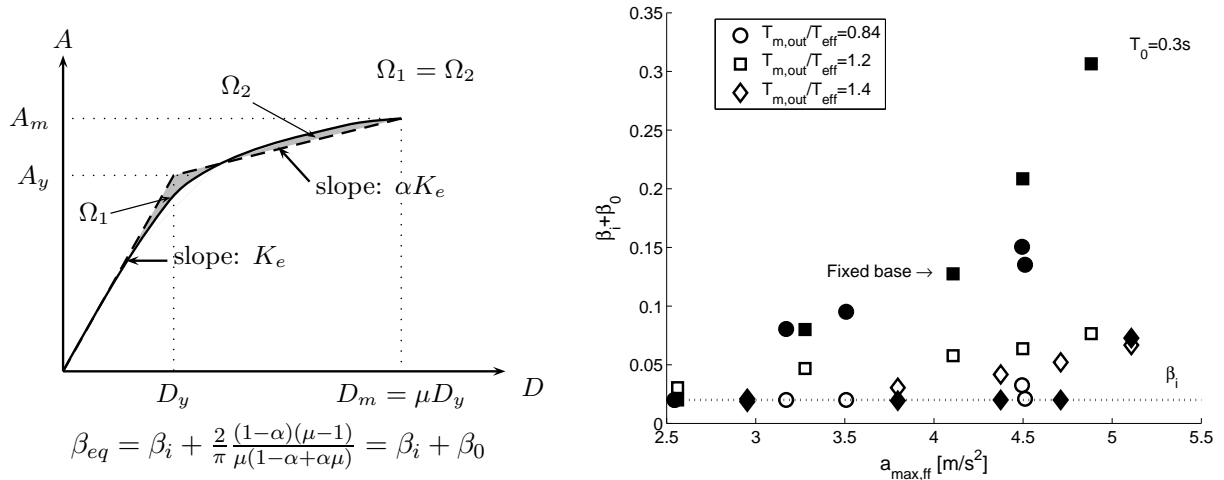
(a) Bilinear representation of the capacity curve: α is the ratio of post-yield stiffness to effective elastic stiffness (K_e) and μ is the ductility factor.

(b) $\beta_i + \beta_0$ values for $T_0 = 0.3s$ SDOF. Solids symbols refer to fixed base computation while hollow symbols are for SSI-FE approach. Earthquake notation according to Tab.2.2.

Figure 2.15: Equivalent damping computation.

It can be noticed that the damping developed in the structure is significantly reduced when SSI effects are included in computations. According to our results, for motions with a frequency content near to the fundamental period of the fixed base structure (i.e. $\frac{T_{m,out}}{T_0} \approx 1$) the damping attains a maximum, i.e. a higher level of damage. The damping added to the system by nonlinear soil behaviour increases the energy dissipation mechanisms, then the expected damage in the structure is reduced. When the ratio $\frac{T_{m,out}}{T_{eff}}$ is near to 1.4, the structural behaviour for fixed based condition is approximately elastic. But, when SSI effects are taken into account, the structure develops nonlinear behaviour and undergoes damage. In this case, the lengthening of fundamental period approaches the effective period value to resonance condition and induces plasticity in the structure for moderate values of acceleration thus increasing the damping.

2.4.3 Damage index

The damage index used in this paper to evaluate the structural damage of the structures is based on the Park & Ang damage model (Park and Ang, 1985) for reinforced concrete. The Park & Ang damage model accounts for damage due to maximum inelastic excursions, as well as damage due to the history of deformations. Both components of damage are linearly combined.

Two damage indices are computed using this damage model:

- Local element damage index (DI_{loc}): columns and beams.

- Overall structure damage (DI_{ov}).

Since the inelastic behaviour is confined to plastic zones near the ends of some members, the relation between element and overall structure integrity is not direct. According to the used structural non-linear model, for each element section i, it is possible to compute a local index of damage (Fig.2.16a):

$$DI_{loc,i} = \frac{\Psi_{m,i}}{\Psi_u} + \frac{\lambda_p}{\Psi_u M_y} \int dE_i \tag{2.2}$$

where $\Psi_{m,i}$ is the maximum curvature reached during the load history, Ψ_u is the ultimate curvature capacity of the section, M_y is the yield moment and E_i is the energy dissipated in the section. λ_p is a model constant parameter. For nominal strength deterioration of reinforced concrete sections a value of 0.1 for this parameter has been suggested by the same author (Park and Ang, 1985). The value of M_y is computed for a simple fixed beam with the used structural non-linear model (Fig.2.3b). Finally, the Ψ_u value corresponds to the most plastified section at the end of pushover test.

The overall damage index is computed using weighting factors based on dissipated hysteretic energy at each component section i:

$$DI_{ov} = \sum_i \lambda_i DI_{loc,i} \quad ; \quad \lambda_i = \frac{E_i}{\sum_i E_i} \tag{2.3}$$

where λ_i are the energy weighting factors of the section i.

(a) Shematic representation of the used damage index

(b) Overall damage index for the $T_0 = 0.3s$ SDOF on dry soil.
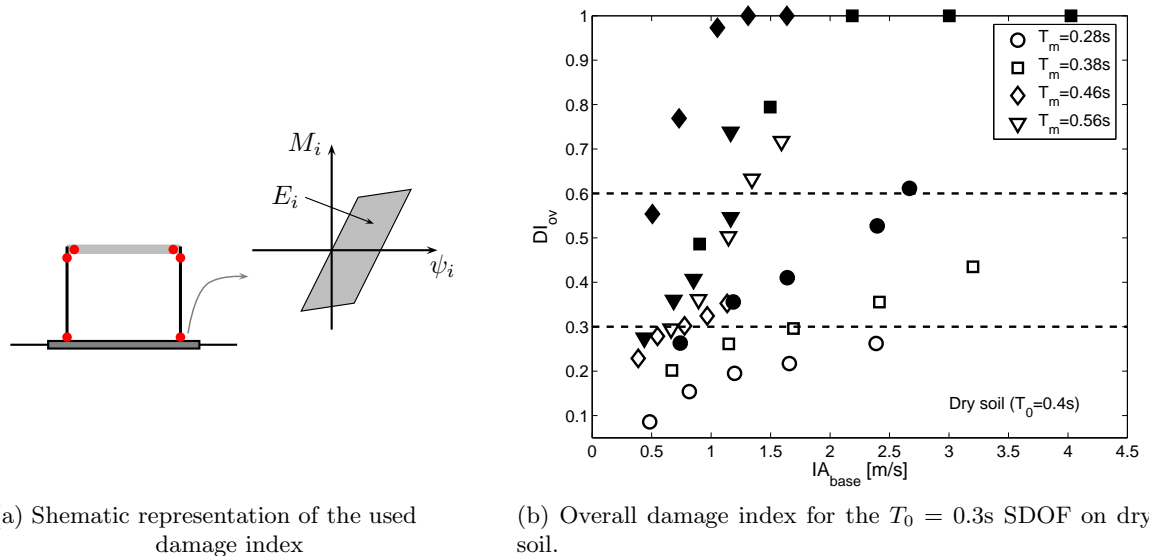
Figure 2.16: Damage index computation

Fig.2.16b displays the computed overall damage index of the $T_0 = 0.4s$ SDOF on dry soil for SSI-FE computations (hollow symbols) and two-step approach (solid symbols) in terms of the Arias intensity at the base of the structure (IA_{base}). When SSI effects are taken into account, in general a

reduction of damage index is found. Assuming that a threshold limit for slight damage can be fixed at $DI_{ov} < 0.3$, the SSI-FE computations shows that this limit is reached only if T_m is larger than the SDOF's effective fundamental period T_{eff}. If $T_m < T_{eff}$, the non-linear soil behavior avoids the structural damage. Furthermore, only for fixed-based computation the total collapse is found, i.e. a DI_{ov} near to 1.

2.5   Vulnerability Assessment

According to the results of the previous section, the dynamic non-linear soil-structure interaction can significantly modify the structural damage induced by an earthquake, then a variation of seismic vulnerability is expected. In order to investigate the effect of non-linear SSI on the vulnerability assessment, a fragility curve approach is followed in terms of more representative index of structural damage rather than an equivalent viscous damping coefficient β_{eq}.

The likelihood of structural damage due to different levels of seismic ground motion can be expressed by a fragility curve. The fragility curve describes the damage probability corresponding to specific damage state, for various earthquakes. If it is assumed that the fragility curve can be expressed in the form of two-parameters lognormal distribution function, the corresponding analytical form $(F(a))$ is:

$$F(a) = \Phi\left(\frac{\log\frac{a}{\alpha}}{\beta}\right) \tag{2.4}$$

where a represents the Arias Intensity (I_{Arias}) (Arias, 1970) and Φ is the standardized normal distribution function. The distribution parameters α and β can be obtained following the maximum likelihood method treating each event of damage as a realization from a Bernouilli experiment (Shinozuka, 1998). The likelihood function is expressed as:

$$M = \prod_{k=1}^{N} (F(a_k))^{y_k} (1 - F(a_k))^{1-y_k} \tag{2.5}$$

where a_k is the Arias Intensity of the $k-$th set of acceleration time histories to which each structure is subjected, y_k represents the realization of the Bernouilli random variable Y_k with $y_k = 1$ or 0 depending on whether or not the structure sustains the specific state of damage under the I_{Arias} equal to a_k, and N is the total number of sets of time histories for which the structure is analyzed. The computation is performed numerically using a standard optimization algorithm.

Two different damage levels are defined in terms of the overall damage index DI_{ov}. The first one, corresponds to a none to slight damage, and it is assumed for a value of $DI_{ov} < 0.3$. The second one, associated with a moderate damage, is defined for a value of $0.3 \leq DI_{ov} < 0.6$.

For problems involving stiffness degradation, the duration and the frequency content of strong motion (i.e. severity intensity) have a great effect on the response of the system. A measure characterizing the severity intensity of an earthquake can be the Arias Intensity.

Fig.2.17a and 2.17b displays the computed fragility curves for the damage states related to the damage index defined below. Fig.2.17a shows the computed fragility curves by following the two-step approach for the $T_0 = 0.4$[s] SDOF. The fragility curves obtained for the second approach (SSI-FE) for the same structure are showed in Fig.2.17b. The fragility curves reflect the variations of the computed damage index obtained for each case (Fig.2.16b). In Fig.2.17a and 2.17b, black cross are used to plot the corresponding values of y_k (2.5) for slight damage levels and grey circles the corresponding values of y_k for moderate damage.

In the case when the SSI is taken into account directly, (SSI-FE) a significantly higher level of seismic energy is required to induce a damage.

(a) Two-step approach   (b) complete FE approach
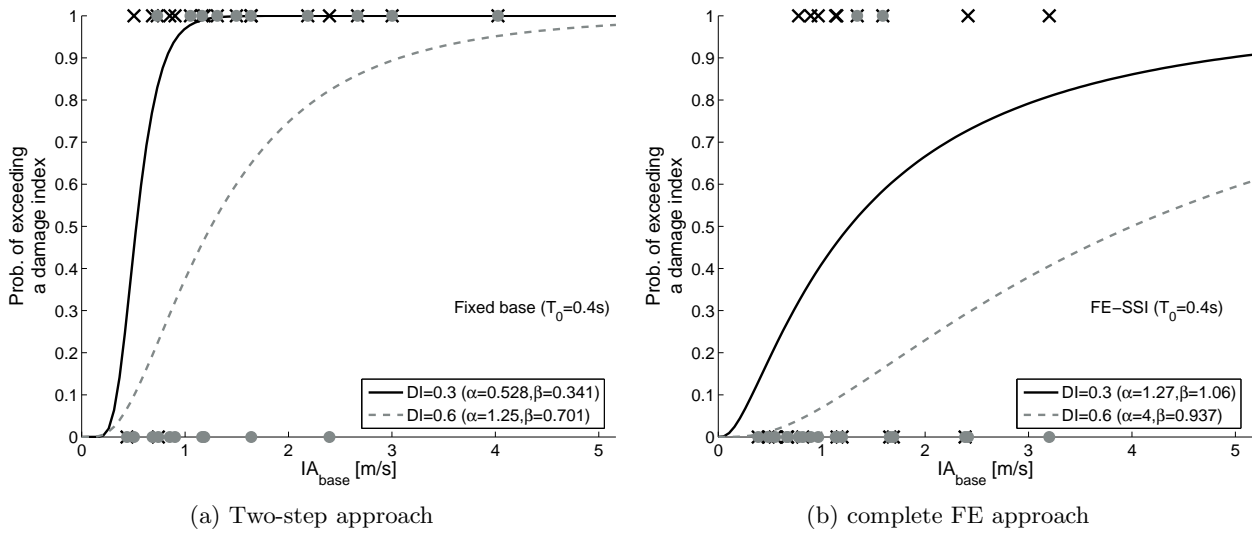
Figure 2.17: Computed fragility curves

2.6 Conclusions

Non-linear dynamic soil-structure interaction analysis is a complex problem were several phenomena take place and interact with each other. Some of these aspects have been studied in this paper in order to highlight the influence of some parameters concerning the structure, the input signal and the soil. The main conclusion of this study is that the soil-structure interaction with a non-linear soil model varies significantly the response of the studied structure set with respect to the one with fixed base condition.

It is well-known that the soil exhibits an elastic behaviour only in a very small range of distortion. This range is certainly exceeded for a motion able to induce inelastic deformations in a structure. Thus, a coupled approach using non-linear structural behaviour with linear soil hypothesis is not consistent. In fact, the results show that when non-linear SSI is properly taken into account, the seismic demand is not on the capacity curve.

According to our computations and for the studied cases, a first approximation for T_{eff} may be obtained with $\frac{2}{3}V_{s,30}$ and with traditionally elastic SSI expressions. Nevertheless, the major challenge to quantify the non-linear SSI effects in seismic demand evaluation is to predict an accurate global damping, able to be related to a simpler approach.

Concerning the vulnerability assessment, according to our computations, if the SSI is taken into account, a higher level of seismic energy is required to exceed a moderate damage level (DI_{ov}) for a given likelihood. For none to slight damage level, the type of followed approach seems not to be important for vulnerability evaluation purposes.

The results of the study illustrate clearly the importance of accounting for the non-linear soil behaviour. In this case, the non-linear SSI has a favourable effect related to decreasing the maximum top displacements and the base forces. However, the non-linear SSI could increase or decrease the seismic demand depending on the type of the structure (e.g. m, h and T_0), the input motion (e.g. T_m), and the dynamic soil properties (e.g. T_{soil}, $V_{s,30}$). Furthermore, there is an economic justification to take into account the modification effects due to non-linear soil behaviour. Further investigations in this way will be needed in order to obtain more general conclusions for diverse structure and soil typologies.

Chapter 3

Non-linear SSI effects on regular buildings

Contents

3.1   Introduction

In general, under earthquake loading, the soil reaches the limit of its elastic behavior before the structural elements. Thus, an earthquake analysis approach assuming nonlinear structural behavior under fixed base condition or with linear soil-structure interaction (SSI) hypothesis is not consistent. In practice, there are several approaches to estimate the effect of the nonlinear soil behavior on the seismic response of structures. As a non linear 3D analysis is costly, usually, 2D finite element computations assuming plane-strain condition for the soil can be carried out in order to asses the role of the non-linear soil behavior on the superstructure response. However, for this type of approach, special assumptions related to the soil condition, the orientation of the seismic input and the superstructure must be considered.

In this chapter, the influence of SSI effects on the response of regular multistory frames is investigated. For this purpose, a modified version of standard plane-strain model taking into account the out-of-plane width of the soil is presented. Mathematical formulation and numerical validations are provided in order to highlight the advantages of the proposed approach on a CPU time consumption point of view.

Numerical simulations of fully non-linear dynamic analysis (i.e. non-linearity of the soil and the structure behavior) are performed in order to study the role of the dynamic soil behavior on the seismic response of buildings. Thus, several 2D plane-strain finite element computations are carried out using non-linear elastoplastic models to represent both the soil and the structure behavior. Results obtained by simplified computations performed following a two-step approach (it will be described below), are compared with the ones obtained from fully SSI non-linear time-history finite element modeling analyses. Two reinforced concrete moment resisting frame buildings are studied on a homogenous sandy soil profile in two hydraulic conditions: dry and fully saturated. A strategy of earthquake selection intended to maximize the information provided is presented. A detailed analysis of the structural maximum responses is carried out in terms of several strong-motion parameters.

A set of energy measures are introduced in order to study the role of different energy dissipation mechanisms when the non-linear SSI effects are considered. Structural and soil energy dissipation indicators are introduced for this purpose. The structural energy dissipation indicator provides a general measure of the hysteretic behavior developed in the superstructure, thus it can be used as a structural damage measure. The effect of the superstructure over the initial state of the soil under the foundation and during the earthquake motion is studied in detail in order to define the extension of the soil influenced by the SSI phenomena.

Finally, the specific case of liquefiable soils is investigated. The same buildings placed over a liquefiable soil deposit are studied using some motions of the selection triggering liquefaction. Ground and structural responses are studied in terms of strong-motion parameters, standard liquefaction parameters and energy dissipation indicators.

Results presented in this chapter show the advantages of the proposed approach and allow to identify situations when neglecting dynamical SSI effects is highly conservative. Additionally, they contribute to the understanding of both, the influence of the soil on the superstructure's seismic response, and the influence of the superstructure on the dynamic non-linear behavior of the soil around the foundation.

3.2   Modified plane-strain approach

Assuming a standard 3D regular multistory building as sketched in Fig.3.1a, an equivalent 2D model for the superstructure can be constructed straightforward for the shorter dimension. For this purpose, a simple assumption is to take a typical transverse resistant axis (equally separated by l_a) loaded by tributary weight/mass over the distance l_a in order to preserve approximately the internal forces in structural elements. The stiffness contributions of the transverse elements across x axis (longer direction) are neglected as shown if Fig.3.2.
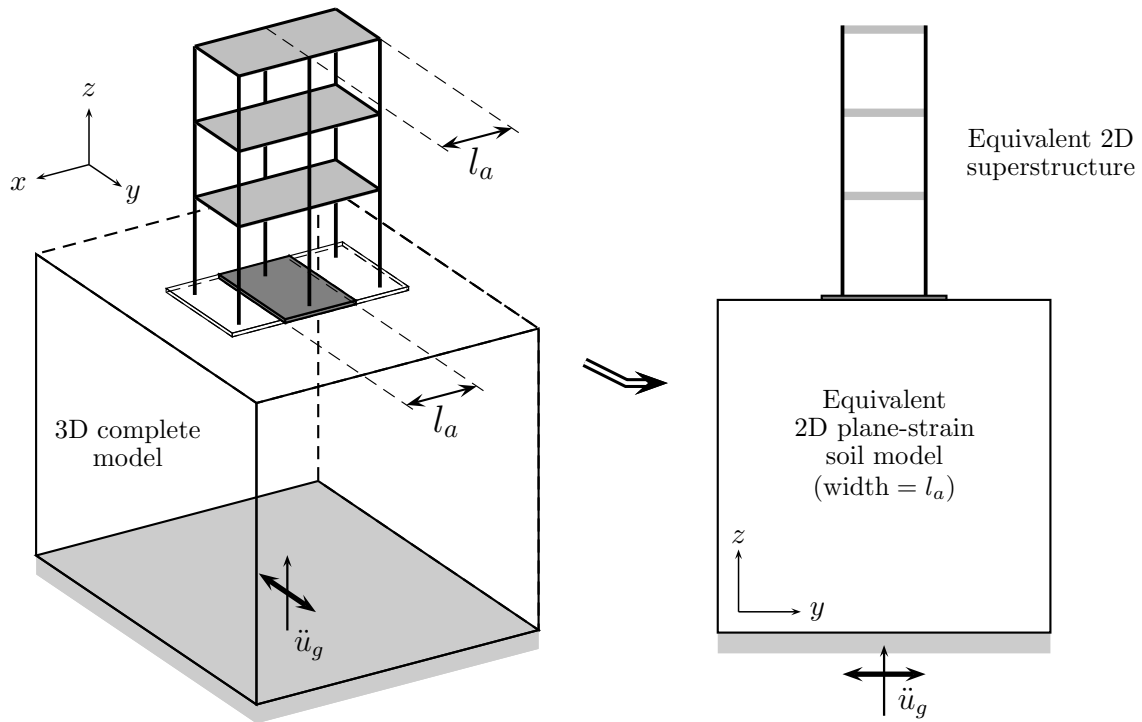
Figure 3.1: Typical regular multistory building model

If the foundation is supposed to be infinitely rigid for bending in xz plane, an equivalent plane-strain foundation-soil model is still valid for periodic loading along x axis (Fig.3.2), typically static body forces or seismic motion in yz plane. Consequently, for an arbitrary horizontal plane xy in the soil, stress state following x direction is constant. Thus, standard plane strain-state is verified:

$$\varepsilon_{xx}(\underline{x},t) = \gamma_{xz}(\underline{x},t) = \gamma_{xy}(\underline{x},t) = 0 \quad \forall \, \underline{x} \in \Omega_s \cup \Omega_f \tag{3.1}$$

according to definitions of domains presented in Fig.G.1 (pp.191). The same condition applies for the soil-foundation interface and the foundation itself. More precisely, due to the fact that the superstructure motion is prescribed to yz, this condition also applies to its stress state. However, as this domain is modelled by one-dimensional elements, no additional considerations are required.
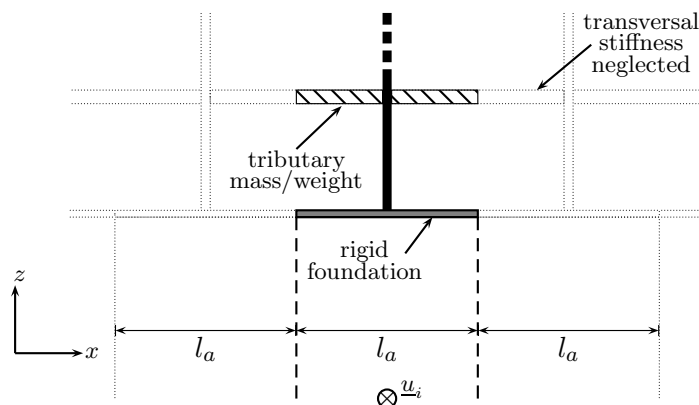
Figure 3.2: Typical axis showing out-of-plane periodicity

In order to properly take into account the SSI interaction effects between superstructure and the plane-strain domain (soil, foundation and interface), the width l_a must be taken into account in the equations for the soil-foundation part of the model. If this out-plane dimension is not included, the stress state of the plane strain-domain will be $l_a/1[-]$ times over or sub estimated depending on

the numeric value of l_a compared to traditional unit length plane-strain formulation. This effect is not important for the linear elastic case, but under non-linear material assumption, neglecting this correction can considerably alter the soil behavior and thus the obtained response.

The variational formulation presented in §1.2.4 is still valid. We repeat here the expression (1.39) for the superstructure domain Ω_b for convenience:

$$\int_{\Omega_b} \underline{\underline{\sigma}}_b : \underline{\underline{\varepsilon}}_b \left(\underline{w}_b\right) dV + \int_{\Omega_b} \rho_b \underline{\ddot{u}}_b . \underline{w}_b dV = \int_{\Omega_b} \rho_b \, \underline{g} . \underline{w}_b dV + \int_{\Sigma_{bf}} \underline{t}_b . \underline{w}_b dS + \int_{\Gamma_{b_\sigma}} \underline{t}_b . \underline{w}_b dS \tag{3.2}$$

It can be noticed that the soil-structure interface Σ_{bs} in Eq.1.39 has been changed by structure-foundation interface Σ_{bf}. In the foundation domain Ω_f, integration of the weak formulation over the domain must take into account the width l_a. In the previous expression, Ω_b corresponds to a 3D domain, even if it is constituted by one-dimensional elements. The corresponding weak formulation for the foundation domain can be written as:

$$l_a \int_{\Omega_f} \rho_f \underline{\ddot{u}}_f . \underline{w}_f dS = l_a \int_{\Omega_f} \rho_f \, \underline{g} . \underline{w}_f dS + \int_{\Sigma_{bf}} \underline{t} . \underline{w}_f dl + l_a \int_{\Sigma_f} \underline{t} . \underline{w}_{sf} dl \tag{3.3}$$

In (3.3), foundation domain is assumed rigid along x direction and one-phase. The correction factor l_a appears in the volumetric integration of inertial and body forces. On the soil-foundation interface, the width l_a must be also included. Free field condition is assumed over Γ_{f_σ} boundary. The modified weak-formulation for the soil domain is given by the following momentum conservation equation:

$$
\begin{aligned}
l_a \int_{\Omega_s} \rho \, \underline{\ddot{u}}_s . \underline{w}_s \, dS + l_a \int_{\Omega_s} \underline{\underline{\sigma}}'_s : \underline{\underline{\varepsilon}}_s \left(\underline{w}_s\right) dS & \\
-l_a \int_{\Omega_s} p . \mathrm{div} \left(\underline{w}_s\right) dS \;&=\; l_a \int_{\Omega_s} \rho \, \underline{g} . \underline{w}_s dS + \\
& \qquad l_a \int_{\Gamma_{s_\sigma}} \underline{t} . \underline{w}_s dl + l_a \int_{\Sigma_{sf}} \underline{t} . \underline{w}_s dl
\end{aligned}
\tag{3.4}
$$

and the mass conservation:

$$
\begin{aligned}
- l_a \int_{\Omega_s} \rho_f \, \mathrm{div} \left(\underline{\underline{K}} . \underline{\ddot{u}}_s\right) . q \, dS + l_a \int_{\Omega_s} \mathrm{div} \, \underline{\dot{u}}_s . q \, dS & \\
+ l_a \int_{\Omega_s} \frac{\dot{p}}{Q} . q \, dS + l_a \int_{\Omega_s} \left(\underline{\underline{K}} . \underline{\mathrm{grad}} \, p\right) . \underline{\mathrm{grad}} \, q \, dS \;&=\; l_a \int_{\Gamma_\varphi} \varphi^* . q \, dl \\
& \qquad - l_a \int_{\Omega_s} \left(\underline{\underline{K}} . \mathrm{grad} \left(\rho_f \underline{g} . \underline{x}\right)\right) . \underline{\mathrm{grad}} \, q \, dS
\end{aligned}
$$
$$\tag{3.5}$$

where the width l_a is included. The integration over Γ_{s_σ} must be conducted carefully for the part corresponding to soil domain truncation. As discussed in the previous chapter, in a part of this boundary, dynamic conditions are used to ensure radiation condition and impose incident motion (paraxial elements described in §1.2.3). The equilibrium equation of the global system is obtained by the addition of equations (3.2), (3.3) and (3.4), where discontinuity of displacements between foundation and soil are introduced.

Assembling procedure, mesh partitions and resolution schema remain unchanged. These modifications have been implemented and tested in *GEFDyn* code for solid 2D, interface and paraxial elements. Validations comparing results obtained by this approach with full 3D computations are described in the following sections. These validations have been also used to define some properties for the models described below, more precisely, the required stiffness for the shallow foundation to ensure the validity of plane-strain approach presented in this section.

3.3   Proposed approaches

In order to investigate the effect of non-linear soil behavior on seismic demand evaluation, a comparative dynamical analysis is carried out:

1. A complete finite element model including soil and structural non-linear behavior is used to asses the effect of non-linear dynamic soil-structure interaction on the structural response (**SSI-FE**).

2. A two-step approach (**T-S**) is carried out in which:

   (a) A non-linear 1D wave propagation problem is solved for a simple soil column of the foundation soil.

   (b) The obtained free field motion is imposed as ground motion to a fixed base structural model.

   The two approaches are presented schematically in Fig.3.3. SSI-FE takes into accounts all material non-linearities of soil, superstructure and interface, associated to seismic soil-structure interaction problem. T-S approach takes into account non-linear behavior of soil and superstructure, but neglects all interaction effects. This comparative approach was developed in order to provide two groups of consistent responses. The simple comparison of the SSI-FE approach with the fixed base response imposing outcropping bedrock input motion is not adequate, because site effects will be neglected. It is well known that modifications of the input motion due to soil conditions play a decisive role on the dynamic response of the superstructure.
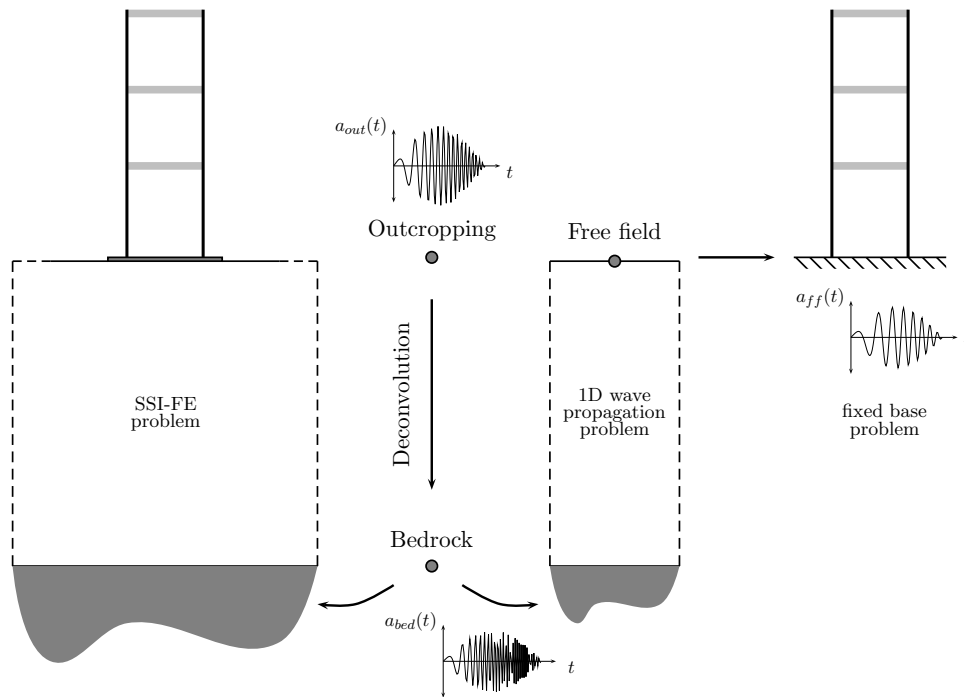
Figure 3.3: Proposed approaches

   T-S approach corresponds to the state of the practice in earthquake engineering. In this work, wave propagation part of the T-S approach is achieved using the elastoplastic soil constitutive model presented in Appendix E. However, this step can be performed through the widely used equivalent-liner approach (Schnabel et al., 1972), or by employing 1D constitutive models (Mellal, 1997; Modaressi and Foerster, 2000) among others. The computed free field response can be injected later as input for any commercial non-linear structural dynamic code. On the contrary, a complete non-linear dynamic soil-structure interaction is still out of the today's engineering practice. Nevertheless, some simplified methods for taking into account the nonlinear soil behavior in the DSSI problem through an equivalent

linear approach have been developed (Pitilakis, 2006). The comparison presented in this chapter provides some guidelines about the importance of taking into account SSI effects, thus defines some general situations when a T-S approach is too conservative or eventually unsafe.

3.3.1 Studied buildings

The analysis is conducted for two concrete multistory frames: **b01** (2 levels) and **b02** (7 levels). The purpose of selecting two test buildings of very different sizes is to asses the role of the initial state of the soil. Indeed, one of the differences between SSI-FE and T-S approaches is related to the initial stress field in the soil model. For T-S case, effective stress distribution in the soil column is due only to body forces, i.e. gravity. In the SSI-FE approach, overstress appears in the neighborhood of the foundation due static forces applied by the superstructure. This loading modifies the soil confinement and the initial density for the dynamic analysis.

Both reinforced concrete buildings were taken from Marante et al. (2005). Details of geometry and transversal sections are given in Appendix I. Main characteristics are listed in Tab.3.1. The last column in this Table shows the assumed out-of-plane spacing l_a required for the plane-strain SSI-FE approach. This dimension can or not be included in the first step of T-S approach according to (3.5). Indeed, the inclusion of this dimension in the soil column has no effect on the free field response.

Table 3.1: Properties of the buildings

Building	Mean interstory height [m]	Total height [m]	Total Mass [Ton]	First fixed base period T_0[s]	Length of found. [m]	Out-of-plane spacing l_a[m]
b01	2.10	4.20	40	0.24	6.0	4.0
b02	2.60	20.12	390	0.76	10.0	6.0

The concrete structural elements are modeled by plastic hinge beam-column elements presented in §1.3.3. The model is based on the two-component model presented by Giberson (1969) and the modifications introduced by Prakash et al. (1993) to take into account axial force and bending moment interaction. This model has been implemented and enhanced in *GEFDyn* by introducing lumped and consistent mass formulations, body forces and sequential construction ability (Sáez, 2007).

3.3.2 Soil profiles

In a first stage, we consider a homogenous medium dense ($D_r = 38\%$) Toyoura sand soil profile of 30[m] depth, overlying an elastic bedrock. Two hydraulic conditions are studied: dry and fully saturated. The effect of the stiffness increasing with the confinement is taken into account by a non-linear elastic approach (E.4). Thus the low-strain shear wave profile increases with the depth as is shown in Fig.3.4a. The shear wave velocity profile gives an average shear wave velocity in the upper 30[m] $V_{s,30}$ of 232.8[m/s] for dry condition and of 204.3[m/s] for saturated condition, corresponding to a site category C of EUROCODE 8 (2003) (deep deposit of dense or medium dense soil) in both cases. The low-strain frequency analysis gives a first elastic period T_{soil} of 0.46[s] for the dry case and 0.54[s] for the fully saturated case (Fig.3.4b).

According to non-linear elastic approach, the reduction of effective stress due to pore water pressure reduces the stiffness of the soil and consequently increases the elastic periods of the soil deposit. The corresponding shift in frequency is noticed on Fig.3.4b, but no significant variation of damping is found for low-strain response. As will be discussed later, strong variations in soil material damping will be found in non-linear behavior range.

Relative positions of fixed base frequency f_0 of both studied buildings are also shown in Fig.3.4b. The fixed base frequency of b01 ($f_0 = 4.17$[Hz]) is larger than the first mode of both studied profiles f_{soil}. Thus, according to our experience, significant soil-structure interaction effects are expected. For the b02 building, its fixed base frequency $f_0 = 1.32$[Hz] is less than the fundamental frequency of both

(a) Obtained low-strain shear wave velocity profile

(b) Computed spectral ratio amplitudes between free field and bedrock (ff/bd)
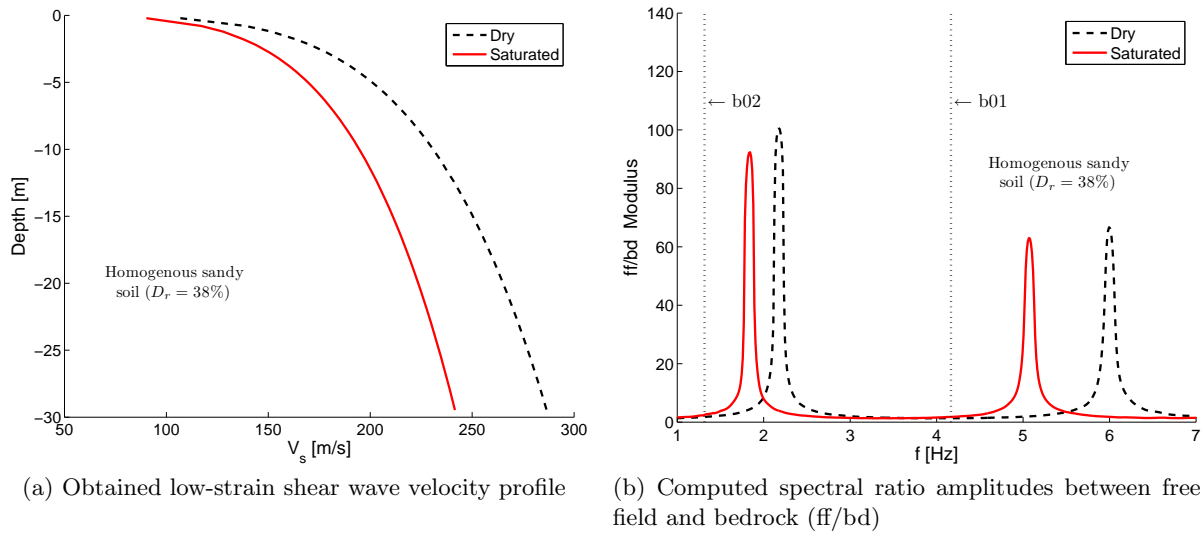
Figure 3.4: Low-strain characteristics of studied medium dense sand profile in dry and fully saturated conditions

soil deposits. Thus no important SSI effects will take place. However, due to its relative big weight, the initial state of the soil is altered producing strong modifications of the effective motion transmitted to the structure as will be shown later.

3.3.3 Finite element (SSI-FE) and Two-Step (T-S) models

The Finite Element model is composed of: the structure, the soil foundation and a part of the bedrock. The finite element meshes used for modeling this problem are shown in Fig.3.5. In dry condition, soil is modelled by four node quadrilateral elements with two DOFs by node (displacements). In saturated condition, ground water level is assumed at surface ($z = 0$[m]). The soil is idealized as a two-phase porous material and discretized into four-node quadrilateral continuum two-phase porous elements with three DOFs per node (two for solid phase displacement and one for water pressure). At the bottom, a layer of 5[m] of elastic bedrock is added to the model. For the bedrock's boundary condition, paraxial elements simulating a deformable unbounded bedrock have been used (§1.2.3). The incident waves, defined at the outcropping bedrock are introduced into the base of the model after deconvolution. In the analysis, the lateral limits of the problem are considered to be far enough from the structure so that periodic conditions are verified on them. Thus, tied conditions or equivalent node condition have been imposed on the nodes of these boundaries. The definition of required horizontal dimension of meshes has been carried-out following a similar procedure as that described in §1.4.3, thus controlling the cleanness of the response at approximate free field location. As expected, for the large building associated to a bigger mass, lateral limits must be extended to obtain a satisfactory free field condition.

Colors in Fig.3.5 are associated to different vertical size of elements. A finer mesh is used in the neighbor of the foundation to improve the approximation of strong non-linear behavior expected for this neighborhood zone. The dark region below the superstructure will be used to compute some soil non-linear behavior indicators associated to dissipated energy by hysteresis (§3.8) and pore pressure built up for the saturated case. In order to prevent the apparition of traction between the foundation and the surrounding soil, Mohr-Coulombs type interface elements have been positioned at the soil-foundation interface.

Concerning the Two-Step approach, the first step is to solve a non-linear one-dimensional wave propagation problem for a soil column. The mesh consists of one column of solid elements using the same vertical spacing of SSI-FE meshes. The same tied boundary conditions have been imposed to ensure 1D shear wave propagation kinematics. In the second step, the obtained free field motion is imposed as ground motion to the fixed base structural model.

(a) Used mesh for b01 building ($l_a = 4$[m])

(b) Used mesh for b02 building ($l_a = 6$[m])
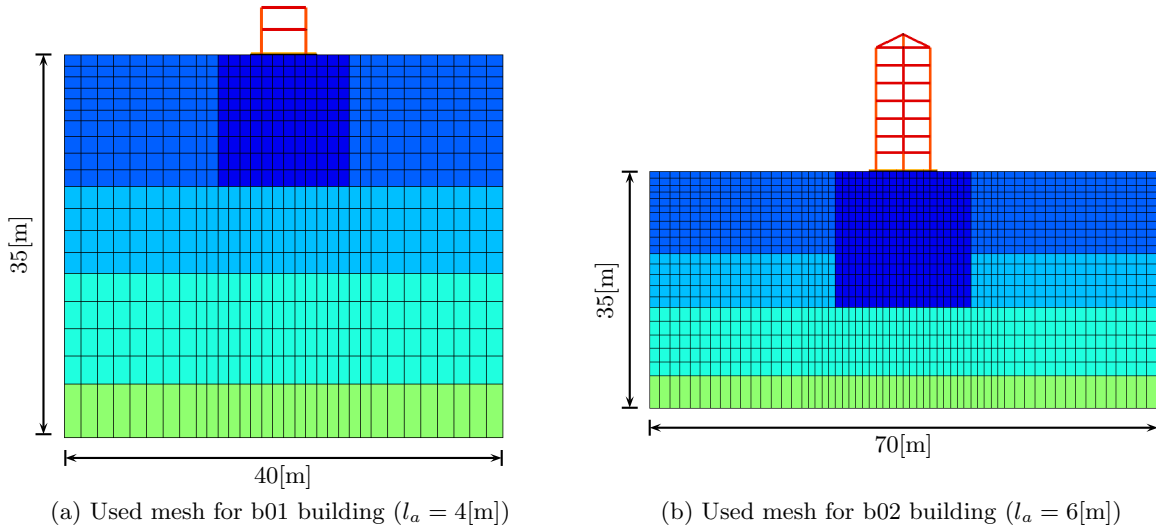
Figure 3.5: Finite element meshes (SSI-FE approach)

Numerical computation of SSI-FE and column are carried out in two sequential steps:

1. Static computation that permits to initialize the stresses and the internal variables of both soil and superstructure's constitutive models.

2. Dynamic perturbation analysis around the stress state and internal material memory obtained in the static computation.

For SSI-FE approach, the static computation includes initialization of stresses (and internal variables) in the soil deposit and sequential level-by-level construction of the superstructure. This sequential construction is numerically performed by consecutive global assembling of matrices and force vectors, but using penalization over non-existent finite elements. This whole step is extremely delicate for saturated case, in which time intervals must be carefully selected in order to allow to dissipate pore pressure build up due to overload imposed by the superstructure. The apparition of tensile stresses near to foundation corners is controlled by selecting appropriate parameters for the soil-foundation interface, thus allowing some sliding.

Dynamic computation is conducted starting from the equilibrated state found at static initialization. Stresses, forces and constitutive models' internal variables are stored in order to obtain only the perturbations part due to dynamic loading. Consequently, strains, distortions, displacements and accelerations given below are relative to initial static displacement field and its associated strain field which has been put to zero at the beginning of the dynamic computation.

3.3.4 Materials parameters

3.3.4.1 Soil

The ECP's elastoplastic cyclic multi-mechanism model (Aubry et al., 1982; Hujeux, 1985) is used to represent the soil behavior. Theoretical formulation and physical interpretations of different parameters was extensively treated in Appendix E. The soil model's parameters are obtained using the methodology suggested by Lopez-Caballero et al. (2003) and Lopez-Caballero et al. (2007) described briefly in §1.3.4. In order to verify the model's parameters, the behavior of the sand has been studied by simulating isotropically consolidated undrained monotonic triaxial test (CUD), drained (DCS) and undrained cyclic shear tests (UCS). The tests results are compared with the reference curves given by Ishihara (1993) for monotonic paths and by Iwasaki et al. (1978) for cyclic loading (Appendix H). The set of parameters calibrated for a confinement of $p' = 100$[kPa] in Tab.H.1 is used for the entire soil

profile, for both, dry and saturated case. Thus, variation of initial critical pressure p_{c0} and hardening variables with the in-situ density are neglected for sake of simplicity. Soil density is assumed constant and equal to $\rho = 1755[\mathrm{kg/m3}]$, the initial earth pressure coefficient is fixed to $k_0 = 0.5$.

In saturated conditions three additional parameters must be selected, the porosity n, the permeability tensor $\underline{\underline{K}}$ and the water compressibility K_f. A porosity of $n = 0.54$ is selected, in order to keep approximately the same mean soil density as that of the dry case for grain's mass of $\rho_s = 2700[\mathrm{kg/m3}]$. The permeability is calibrated by imposing that the generation of pore pressure under seismic loading does not induce liquefaction. The water bulk modulus is chosen small enough to prevent near to incompressible behavior for approximate undrained behavior obtained for quick dynamic loading. Of course, the calibration of the last two parameters must be performed together. An isotropic value of $k_y = k_z = 10^{-4}[\mathrm{m/s}]$ is assumed for permeability and a value of $\beta_f = 9.38 \times 10^{-8}[\mathrm{1/Pa}]$ for fluid compressibility.

Bedrock is assumed to behave elastically. A Young's modulus of $E = 5305[\mathrm{MPa}]$ and a Poisson's ratio of $\nu = 0.3$ is used. For both soil cases, bedrock is assumed to be a one-phase medium with a density of $\rho = 2000[\mathrm{Kg}]$. Paraxial elements placed at the bottom to simulate the half-space condition use the same set of parameters.

3.3.4.2 Structure

Parameters for the plastic-hinge beams constituting superstructure models are derived directly from material properties of concrete, reinforcement steel and reinforcement disposition in terms of axial force-moment interaction diagrams. Numerical values of transverse section and materials properties are given in Appendix I. Additionally, the hardening parameter $\tilde{p}$ that governs the stiffness distribution between elastic and plastic components is fixed to $\tilde{p} = 0.05$ for both buildings.

Foundation models are composed of the base mat and foundation beams that ensure zero relative rotation between foundation and columns. In order to ensure the validity of modified plane strain formulation, it must be rigid for out-plane bending. One option is to impose kinematical constraint to ensure this condition, but another possibility is to use very stiff material parameters to impose rigidness. We choose the second option in this work. These values are calibrated by comparison with 3D analysis results used for testing the implementation, as described below.

3.3.4.3 Interface

Interface between foundation and soil is used with the main purpose being to prevent apparition of tensile stress in the soil at static initialization phase allowing sliding between soil and foundation. A detailed study of the uplift problem is out of the scope of this work. In order to reduce stress concentration at foundation corners but not to alter the dynamic response by uplift or excessive sliding, we use a relatively large value for joint thickness e_{ini} combined with an elevated penalization parameters E and G (Appendix B). No dilatancy is also imposed. Used values are shown in Tab.3.2. These values were calibrated by controlling the stress state near to foundation after static initialization and by comparing responses in dynamic condition with a no loss of contact case in frequency and time domain.

3.4 Numerical validation

The pertinence of the proposed approach described in §3.2 is verified by comparison with a complete 3D model for the same problem. This verification also permits to define the required stiffness value to be used for the foundation in order to ensure plane strain condition for the soil. Computations are carried-out for both buildings and soil conditions, for static initialization phase and for a test dynamic loading. Meshes used in 3D cases included explicitly the out-of-plane dimension l_a that is incorporated in equations of the proposed plane-strain approach. Each couple of 2D and 3D meshes have the same projection on $y - z$ plane, thus the same size and number of elements. 3D mesh is constructed by

Table 3.2: Parameters for soil-foundation interface model

Parameter	Description
E	$9 \times 10^{10}[\text{Pa}]$
G	$4 \times 10^{10}[\text{Pa}]$
ϕ	23°
ψ	0°
e_{ini}	$0.01[\text{m}]$
c	$6 \times 10^3[\text{Pa}]$

extruding the 2D $y - z$ plane mesh following x direction, a distance $l_a/2$, symmetrically from the superstructure (Fig.3.6). Naturally, the numerical cost of the 3D model is increased several times due to the number of elements and by including u_x DOF. The time-consumption ratio is near to 5 times for b01 building and near to 8 times for the bigger one, that proves the usefulness of the proposed 2D formulation.

(a) 3D mesh for b01 building

(b) 3D mesh for b02 building
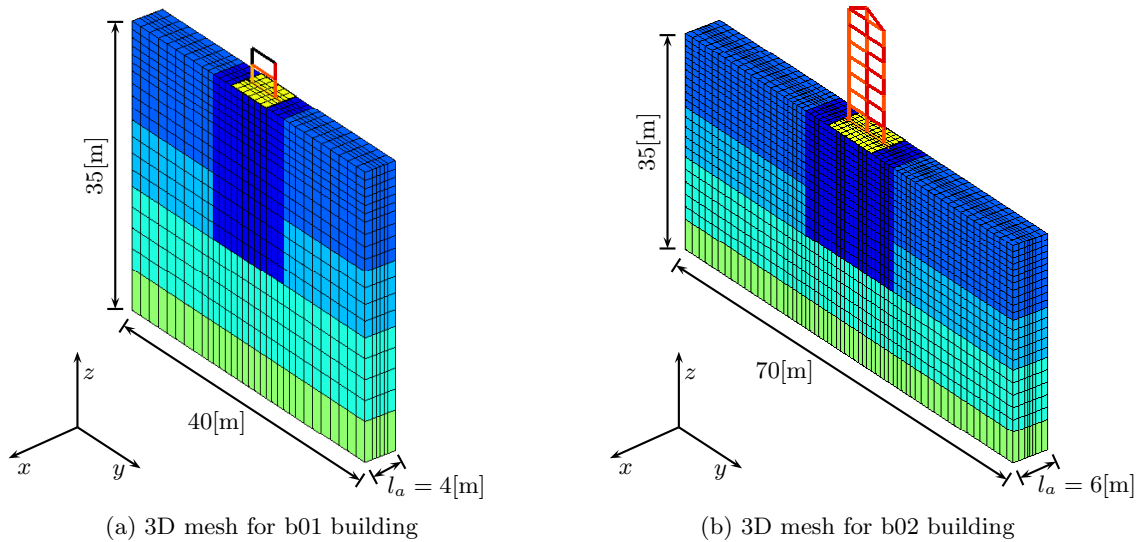
Figure 3.6: Three-dimensional FE meshes for numerical validation

For the 3D model, displacements following x direction are allowed for all interior nodes. Nodes on vertical planes at $x = \frac{l_a}{2}$ and $x = -\frac{l_a}{2}$ have u_x DOF blocked. This kinematic assumption is only valid if the superstructure is regular and periodic and if the incident field is independent of x coordinate. For an input motion with components out of the yz plane, a complete 3D model including torsional effects is required. Symmetry with respect to the frame axis is also imposed, thus u_x DOF is also blocked over $x = 0$ plane. Dynamical kinematic constraints sketched in Fig.1.10b are still valid for this case.

3.4.1   Static initialization

The static initialization is conducted simulating the sequential level-by-level construction of each building. Time step increment is not important for dry case, but is a critical aspect for saturated soil. For this latter case, the time step is selected by controlling the required time to dissipate the instantaneous generated pore pressure and to obtain the vertical overstress $\Delta\sigma'_{zz}$ associated to the last level added to the building, thus to let the load transmit from fluid phase to solid skeleton. Stabilized

values of overstress distribution are shown in Fig.3.7 for b01 on dry soil and for b02 on saturated soil in Fig.3.8. Both FE models are displayed in each figure.

(a) Vertical overstress $\Delta\sigma'_{zz}$[kPa] distribution for 2D modified plane-strain approach

(b) Vertical overstress $\Delta\sigma'_{zz}$[kPa] distribution for full 3D model
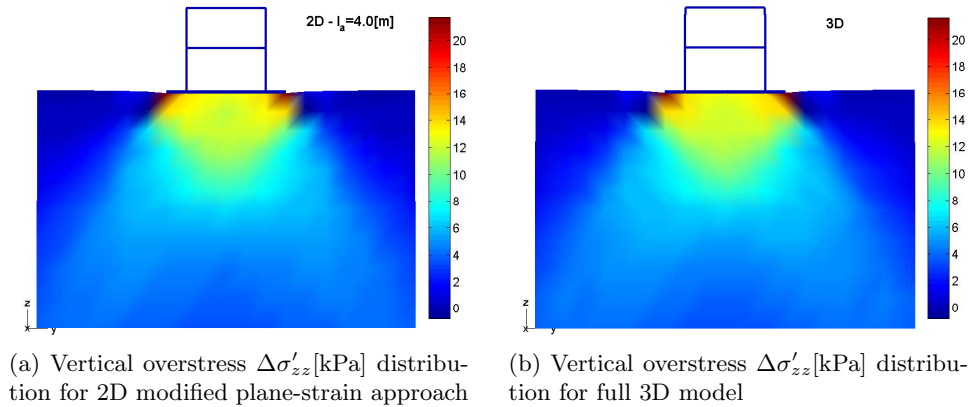
Figure 3.7: Vertical overstress distribution due to superstructure for b01 on dry soil. Window of 20×12[m] under foundation. Deformation magnification factor=100

According to Fig.3.7, vertical overstress distribution for the 2D plane-strain proposed approach is identical to the distribution of $\Delta\sigma'_{zz}$ obtained in any vertical yz plane cut over the 3D model. This observation is associated to the rigidness of the foundation of the superstructure, thus it must be stiff enough to avoid relative vertical displacement across x axis. Rigid foundation condition across y axis is not required, but we use a complete rigid foundation for sake of simplicity. For b01 building on dry soil, the maximum vertical overstress obtained is approximately 20[kPa] near the foundation corners. Foundation-soil joint elements were introduced to reduce this stress concentration and avoid tensile stresses in the soil, however some small traction stresses up to 0.7[kPa] were found at shallow integration points near the foundation border. These local traction stresses have a negligible effect on the accuracy of the complete model. After superstructure's sequential construction simulation, a maximum settlement of 2.7[mm] is found in this case. Dynamic response will be computed as a perturbation around this initial deformation.

(a) Vertical overstress $\Delta\sigma'_{zz}$[kPa] distribution for 2D modified plane-strain approach

(b) Vertical overstress $\Delta\sigma'_{zz}$[kPa] distribution for full 3D model
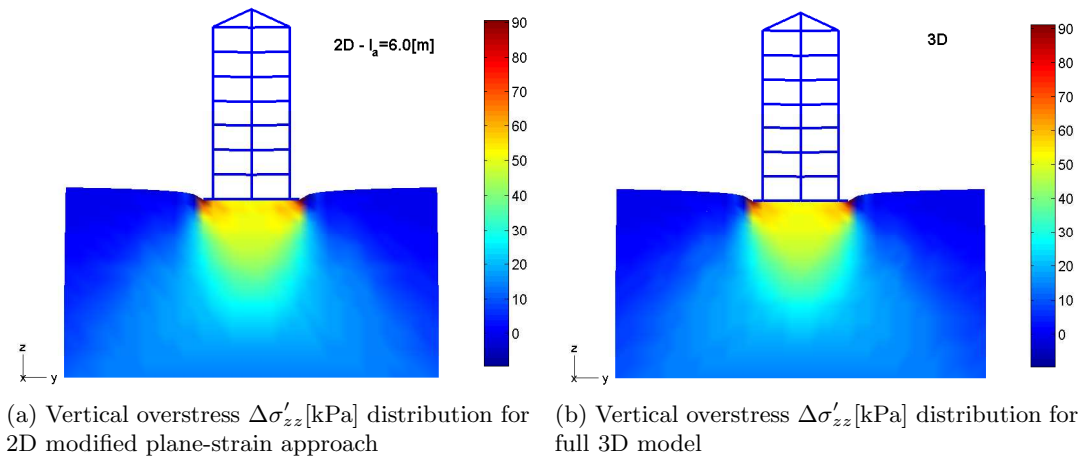
Figure 3.8: Vertical overstress distribution due to superstructure for b02 on saturated soil. Window of 40×20[m] under foundation. Deformation magnification factor=100

Fig.3.8 shows stabilized effective overstress distribution for the b02 building on saturated soil. This is the critical case in terms of soil deformations, because water reduces effective stresses under self weight and consequently the initial confinement and b02 is the heavier building studied. In this case, stabilized effective overstress values are up to 90[kPa]. The obtained settlement in this case is of 1.5[cm]. As this settlement is uniform, these soil deformations do not induce additional forces in the superstructure. Differential settlements found under dynamic loading will be treated later. In spite

of introducing sliding between soil and foundation, some tensile stress up to 4[kPa] appears in the neighborhood of foundation corners. No convergency problems were found for this level of shallow traction stresses in this configuration.

(a) Monotonic ray r_{yz}^m distribution for 2D modified plane-strain approach

(b) Monotonic ray r_{yz}^m distribution for full 3D model
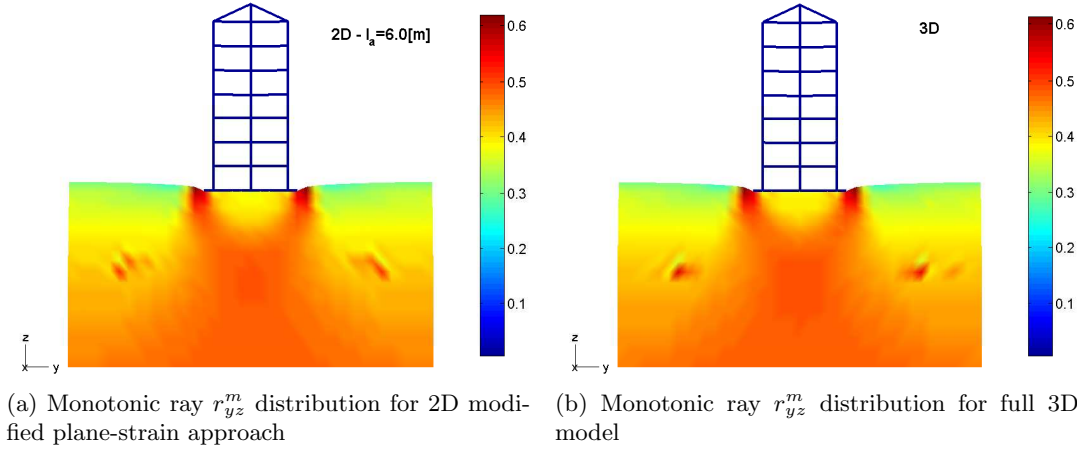
Figure 3.9: Degree of mobilization of yz deviatoric mechanism for b02 on dry soil. Window of 40×20[m] under foundation. Deformation magnification factor=100

For the dynamic non-linear soil behavior studied in this work, initial state plays a key role on the seismic response of the problem. In order to verify the accuracy of the implemented approach, internal hardening variable of the soil's constitutive model was also checked. Fig.3.9 shows the mobilization of plasticity in deviatoric plane yz characterized by the monotonic radius r_{yz}^m, according to model formulation described in §1.3.4. According to this figure, both plasticity mobilization distributions are equivalent. Due to the geometry of the studied problem, this deviatoric plane will control the overall non-linear soil response. The characteristic failure mechanism of shallow foundations can be noticed, thus an active wedge formation under the structure and the transition to passive wedges. However, this state is far from failure. Maximum plastic mobilization is approximately of 0.6 in stress concentration zones, reminding that 1 means perfect plasticity state.

(a) Tangential stress σ_s distribution due to relative sliding

(b) Normal stress σ_n distribution
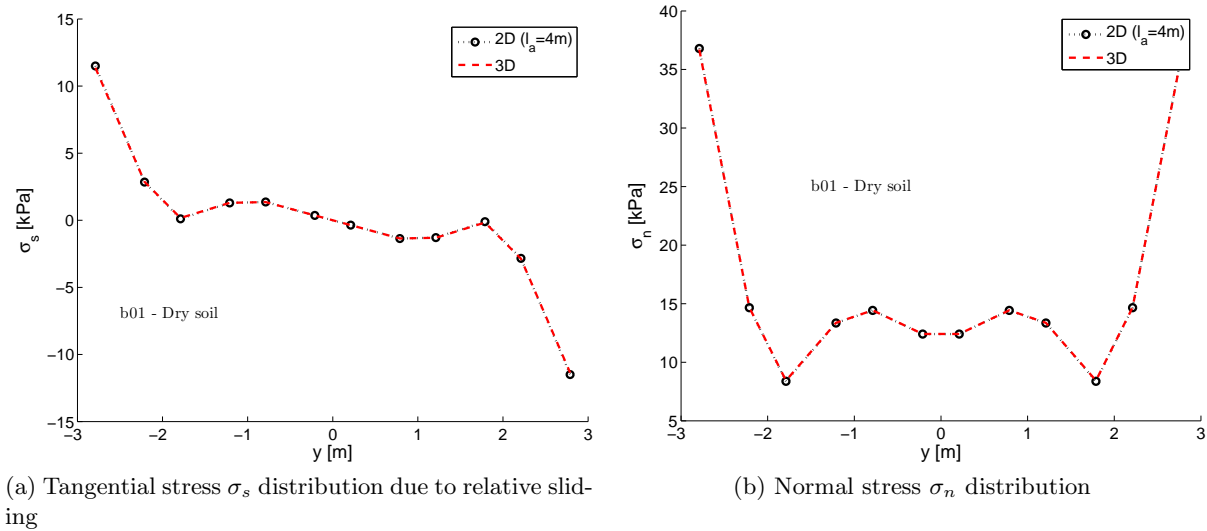
Figure 3.10: Interface stresses for b01 building on dry soil using modified plane-strain approach and 3D model

According to expression (3.3), interface elements must be also modified to take into account soil out-of-plane width. Fig.3.10 show distribution of tangential stresses σ_s and normal stresses σ_n over the interface for b01 building on dry soil. The obtained curves for the 2D case and for any longitudinal

cut over the foundation for 3D case agree perfectly. Under the columns, at $y = 2$[m] and $y = -2$[m], tangential stress vanishes. Large sliding, or tangential displacement jump, takes place along the interface between the foundation and the soil. Normal stress distribution coincides with the standard normal pressures distribution under a rigid shallow foundation. As expected, stress concentration takes place near the corners of the foundation despite relative soil-foundation displacements.

3.4.2   Comparative dynamic analysis

Dynamic comparative analysis is conducted using Friuli earthquake record at San Rocco site (Italy, 1976) as input acceleration. It is scaled to very-low amplitude to ensure elastic soil response. Obtained spectral amplitude modulus ratios between the free field (ff) and its vertical projection over the bedrock (bd), and between the top of the structure (tp) and the ff according to definitions of Fig.1.11 are shown in Fig.3.11 for b01 building on dry soil. An excellent agreement between both computations is found, for both ff/bd and tp/ff spectral ratios. Nevertheless, spectral ratios displayed in Fig.3.11a present some frequency component arising from the structure for their two frequency modes (near to 4.1 and 5.7[Hz]). Some small amplitude differences are also found for the fundamental frequency of the soil profile. For tp/ff spectral ratio (Fig.3.11), the agreement between both computations is quite satisfactory. The predicted shift on fixed base frequency due to SSI effects coincides in both models.
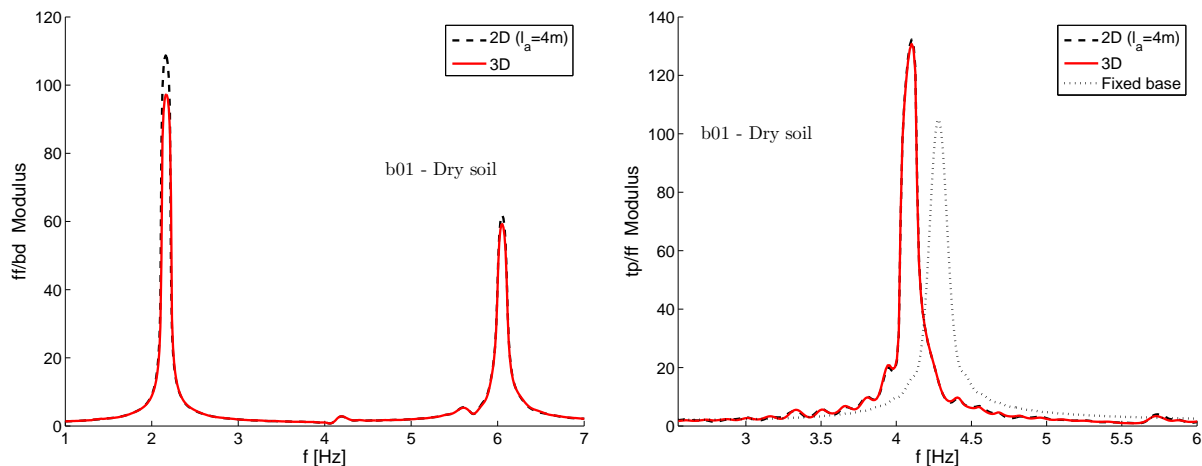
(a) Spectral ratio modulus between free field and bedrock

(b) Spectral ratio modulus between top of the structure and free field

Figure 3.11: Frequency domain responses for b01 building on dry soil using modified plane-strain approach and 3D model

Time domain responses at the top of the building and at free field are shown in Fig.3.12. It can be noticed that small differences on soil amplification found in frequency analysis have a negligible effect over the structural time response. Nevertheless, major differences are found at free field time responses as is displayed in Fig.3.12. Indeed, even if stress field and other responses are properly simulated by this approach, some differences persist concerning wave reflections over the mesh boundary. For 3D model, front-wave pattern emitted by superstructure vibration is approximately a half-sphere. Thus, reflection of waves takes places over both lateral boundaries. As these reflections occur at different times over x limits of the mesh, successive reflections destroy the coherency of the wave producing a beneficial effect over lateral wave reflection issue. This effect vanishes in 2D plane-strain condition. In this case, the front-wave patterns outgoing the superstructure are approximately half-cylinders with longitudinal axis across x. Thus, reflections takes places only in y borders of the mesh and no destructive effect appears. Nevertheless, according to Fig.3.12, this effect does not affect computed structural time response. Additionally, hysteretic damping due to non linear soil behaviour under strong motion will contribute to attenuation of radiated waves before reaching mesh borders.

Finally, Fig.3.13 shows the computed distortion for an arbitrary point at 4[m] under one of the columns of the b01 building on dry soil. Fig.3.13a displays the obtained shear strain for Friuli earth-

(a) Top building displacement

(b) Free field displacement
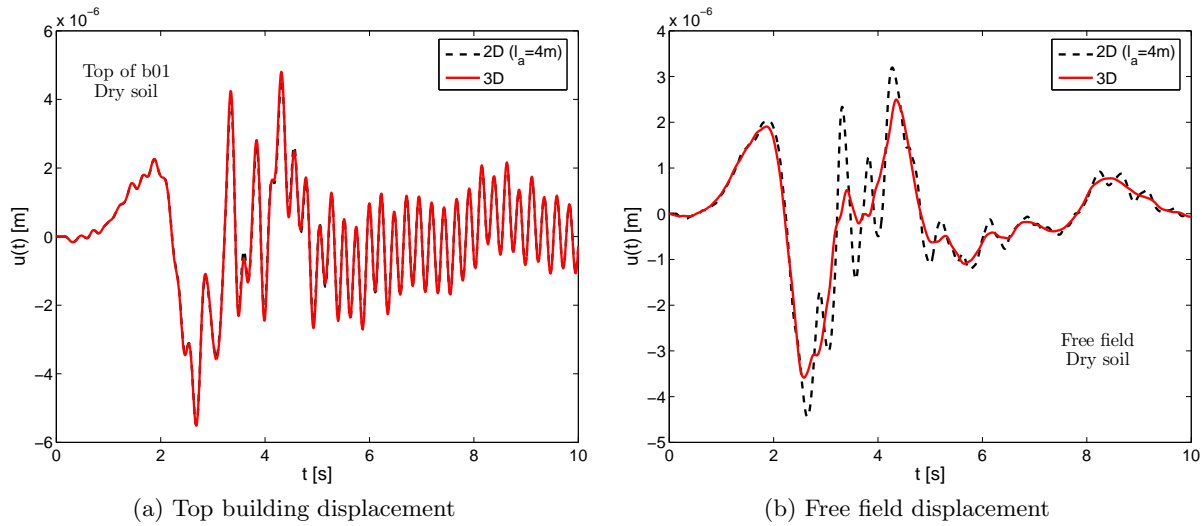
Figure 3.12: Time domain responses for b01 building on dry soil using modified plane-strain approach and 3D model

quake imposed at very low-amplitude to ensure globally elastic response, and Fig.3.13b the corresponding response for the original amplitude of this ground motion. In both cases a satisfactory agreement is found, that proves accuracy of the proposed approach in elastic or inelastic range. In Fig.3.13b the apparition of permanent deformations due to the fact that soil behaves in a non-linear manner should be noted. Indeed, the predicted co-seismic settlement at the center of the foundation is 2.2[cm].

(a) Response to low-amplitude input (elastic)

(b) Non-linear response to Friuli earthquake
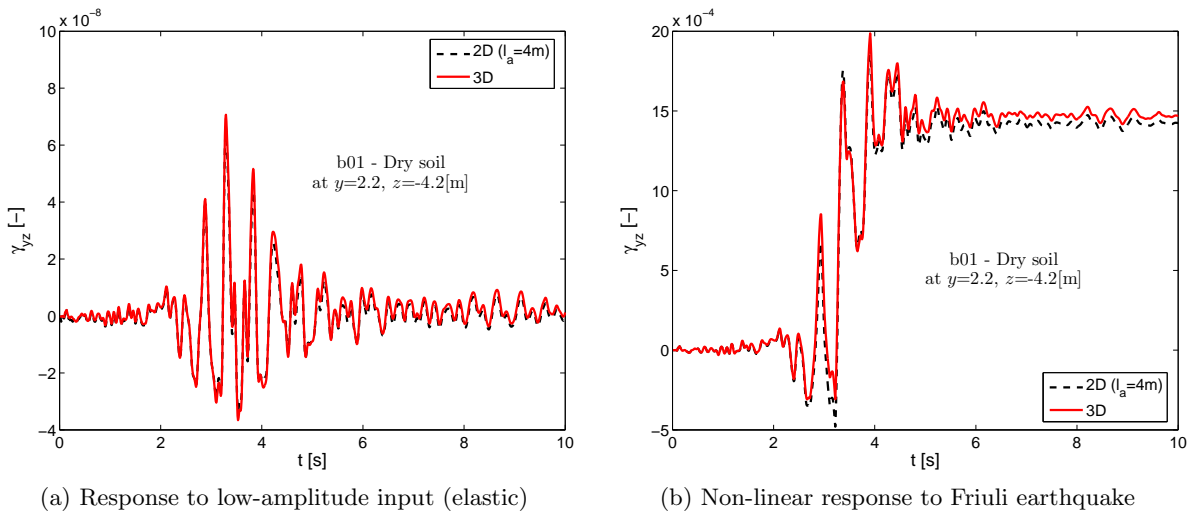
Figure 3.13: Time domain shear strain γ_{yz} evolution for b01 building on dry soil using modified plane-strain approach and 3D model

Similar comparisons have been done for other combinations used in this work, thus for b02 building in dry or saturated soil, as well as the liquefiable soil profile analyzed in §3.10. For all cases similar agreement is found. Consequently, it can be conclude that the proposed modified plane-strain approach gives equivalent results with a significative reduction in computational cost.

3.5   Earthquake selection

The purpose of this section is to describe the methodology used to select strong-motion records that will be used as input in the computations. The adopted strategy is based on the methodology proposed by Douglas (2006) in the framework of the VEDA (Seismic Vulnerability of structures: a Damage

mechanics Approach) research project in which a part of this work was done.

At present there are many sources of earthquake strong-motion records that could provide thousands of records as input to the structural models (Seekins et al., 1992; Ambraseys et al., 2004) or other Internet databases. However, as the studied FE models are complex and consequently take time to run, it is important that a small selection of strong-motion records be chosen in order to cut down the number of runs required but allowing to obtain general tendencies. In order to select an efficient set of input accelerograms some ideas from the theory of Design of Experiments (**DOE**) are employed (NIST/SEMATECH, 2006). In the terminology of DOE, the FE model is the process and the estimated responses from these models are the outputs. The controlled inputs (factors) are split into the parameters defining the FE model (soil and superstructure properties) and the input ground motions.

Since there is an infinite variety of possible earthquake ground motions it is useful to characterize them using a number of scalar strong-motion parameters that approximately measure different properties of the motions (amplitude, frequency content, duration, etc.). Hence the set of strong-motion parameters becomes the controlled inputs to the process. Unfortunately these strong-motion parameters do not perfectly characterize the ground motions, thus the use of strong-motion parameters introduces uncontrolled factors (co-factors) due to the complexity of the motions not measured by the strong-motion parameters chosen.

The geographical scope of this study is France. Metropolitan France has a seismic hazard that is thought to be characterized by earthquakes of magnitudes (M_L) less than or equal to 6.3 with an average focal depth less than or equal to 12[km] (Marin et al., 2004). In view of this, the database of strong-motion records developed by Ambraseys et al. (2004) has been chosen as the source of data for this work since it provides a large set of data mainly from moderate ($M_w < 6.5$) shallow ($h < 30$[km]) earthquakes that occurred within Europe and the Middle East.

We select a full factorial design in two levels, thus each input factor set is split in two levels. These levels are called high and low. A design with all possible high/low combinations of all the input factors is a full factorial design in two levels. We consider a two-level of factorial design for three factors (strong-motion parameters). This implies eight runs. Graphically, we can represent this design by the cube shown in Fig.3.14. The arrows show the direction of increase of the factors. The numbers 1 to 8 at the corners of the design box reference correspond to non-randomized order of runs or standard order according to NIST/SEMATECH (2006). One record is chosen to be at each corner of the cube. Running the entire design more than once permits to obtain average values of the responses as well as some ideas about the dispersion or variability due to uncontrolled factors.

run	AI	T_m	T_{SR}
1	-	-	-
2	+	-	-
3	-	+	-
4	+	+	-
5	-	-	+
6	+	-	+
7	-	+	+
8	+	+	+
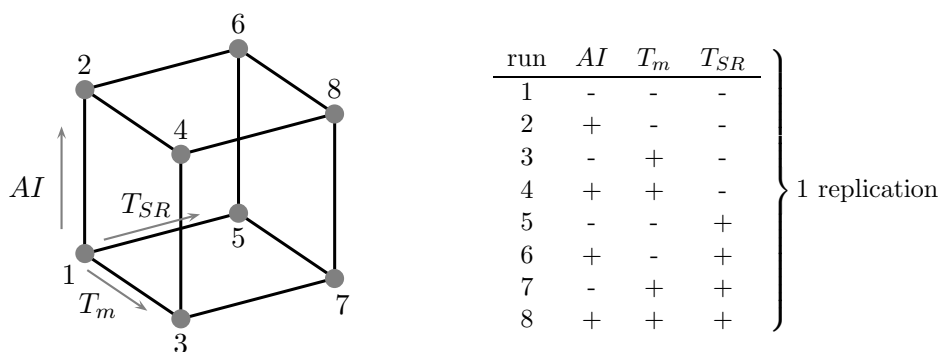
Figure 3.14: Illustration of two-level full factorial design with factors T_{SR}, AI and T_m (adapted from NIST/SEMATECH (2006)).

An earthquake can be characterized by measures of its frequency content, duration and severity/intensity measures. It is generally accepted that pure amplitude measures as PGA are not ideal measures of the severity/intensity of earthquakes, as they do not contain any information about the duration and the frequency content of strong ground motion, especially for problems involving stiffness degradation (Koutsourelakis et al., 2002). Consequently, using parameters of severity/intensity includ-

ing duration and frequency content information to characterize earthquake ground motions could lead to an improved prediction of earthquake damage. According to this, we choose three strong-motion parameters: significant duration T_{SR} (Trifunac and Brady, 1975); Arias intensity AI (Arias, 1970) and the mean period T_m (Rathje et al., 1998), associated to duration, energy and frequency content, respectively. Additionally, as site effects are explicitly included in the FE model, only records on rock or stiff soil ($V_{s,30} > 400$[m/s]) were considered. The ranges of the low and high bins were chosen close to mean values of selection strong-motion parameters of motions available in database satisfying the geographical scope and recording conditions requirements. Selection bins range were adjusted in order to have sufficient numbers of records within each bin category (Tab.3.3).

Table 3.3: Strong-motion parameters and ranges of low and high bins used for selecting records.

Parameter	Low bin range	High bin range
T_{SR}	≤ 10[s]	> 10[s]
AI	≤ 0.07[m/s]	> 0.07[m/s]
T_m	≤ 0.5[s]	> 0.5[s]

An experiment is constituted by $2^3 = 8$ records (or runs). Each experiment was repeated four times (4 earthquakes selection), thus a total of 32 runs were conducted for each building on each soil type. Details about strong-parameters for the 32 used records are listed in Appendix J.1.

In order to study the earthquake selection on a statistical point of view, we use principal component analysis technique (PCA), one of the mostly used tools in exploratory data analysis. In mathematical terms, PCA is as an orthogonal linear transformation that transforms the n data to a new small k-dimensional coordinate system. PCA is theoretically the optimum transform for a given data in least square terms. Thus, it is obtained by maximization of projected inertia of n data over the sub-space axis F_k. PCA involves the calculation of the eigenvalue decomposition of a data covariance matrix or singular value decomposition of a data matrix, usually after mean centering the data for each attribute. A detailed description of PCA is out of the scope of this presentation and can be found in Lebrat et al. (2004) or Saporta (2006).

PCA is thus used to identify correlations in the data. According to selection criteria previously defined, each record can be interpreted as a sample of three selection variables T_m, AI and T_{SR}. In order to maximize the information provided by the earthquake selection, selection variables must be as independent as possible. A high correlation between two or more variables means that these variables might be redundant for describing non-linear SSI effects studied here. Fig.3.15a presents a graphical vector approach to verify correlations. In this representation, each selection variable is displayed as a vector in the space of first and second principal components F_1 and F_2, respectively. Thus, the variation of the variables across selected motions is indicated by the length and direction of the vector. In this representation, vectors that are as right angles mean that their variation is independent. Vectors pointed at similar direction, mean that they vary together. Vectors that are oppositely directed are related and have inverse variation. According with these interpretations for relative orientations, it can be noticed that selection variables AI and T_{SR} are approximately independent of T_m, and AI and T_{SR} are inversely related. Consequently, these variable are not redundant to describe earthquake hazard.

Next step in PCA analysis is to study data points, thus the 32 selected records in this case. Fig.3.15b is generated by projecting data points on the plane spanned by first and second principal components. Percents indicated in these axis mean that F_1 and F_2 are associated to 40.3% and 33.8% of data inertia, thus 74.1% of the data information together. Representation of samples over the principal component plane gives information about the distribution of data in order to detect zones of different density. In this case, a small set of motions are slightly out of the global tendency (records 2, 12, 13, 21 and 28). These records have an excessive contribution to principal components and might be a factor of instability, thus removing them might significantly alter result of the analysis.

(a) Correlation circle of selection variables

(b) Projection of records on principal component plane
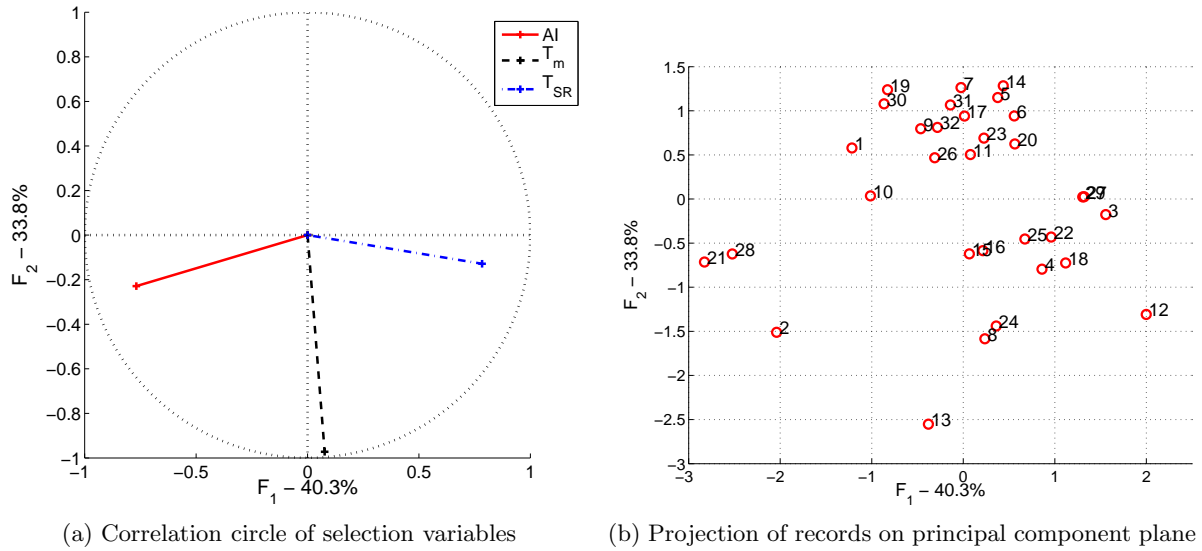
Figure 3.15: ACP analysis of selected input

Their relative position might also indicate some incoherency, for instance different geological recording conditions. Therefore, runs corresponding to these motions must be carefully analyzed.

3.6 Soil analysis and results

In order to define the input motion for the T-S approach (corresponding to the first step), a free field dynamic analysis of the soil profile, was performed. The response of the free field soil profile was analyzed for the earthquake records selected for the outcropping bedrock as described in §3.5.

The Fig.3.16 shows the simulation results representing the peak ground acceleration (PGA) obtained at free field with respect to maximum acceleration amplitude at outcropping (a_{out}) for both, dry and saturated soil conditions. It is possible to see that for weak base acceleration the behavior of both soil deposits is similar: the amplification is near to 2.5 times the acceleration recorded at outcropping. In this range, the reduction in the effective stress due to the water has not an evident effect. It is noted that due to soil non-linearity the amplification of the ground response decays with the input amplitude.

(a) Computed PGA for dry and saturated soil

(b) Obtained Arias intensity AI_{ff} at free field
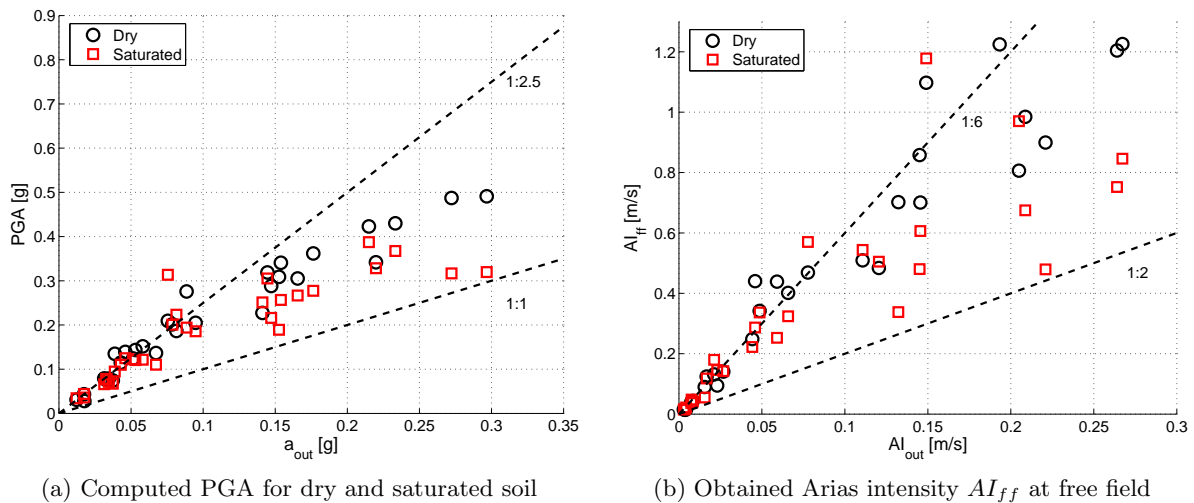
Figure 3.16: Non-linear behavior of the column subjected to the selected earthquakes

The effect of the soil non-linearity over the input motion can be also studied in terms of the energy

associated to each motion. The Arias intensity AI computed at outcropping (AI_{out}) and computed at free field (AI_{ff}) are plotted in Fig.3.16b for both soil profiles. In this case, the amplification behavior is similar compared to acceleration amplitude scheme. For weak AI, the amplification is approximately constant and near to six times the outcropping value (low-strain domain). For AI_{out} larger than 0.1[m/s], the amplification diminishes due to the hysteresis energy dissipation in the soil. In this range, in general terms, the amplification of the saturated soil is lower than the obtained one for the dry case but it is more than two times the value computed at outcropping bedrock.

(a) Obtained pore pressure excess in the soil profile for different used records

(b) Comparisons between dry and saturated response spectra computed at free field
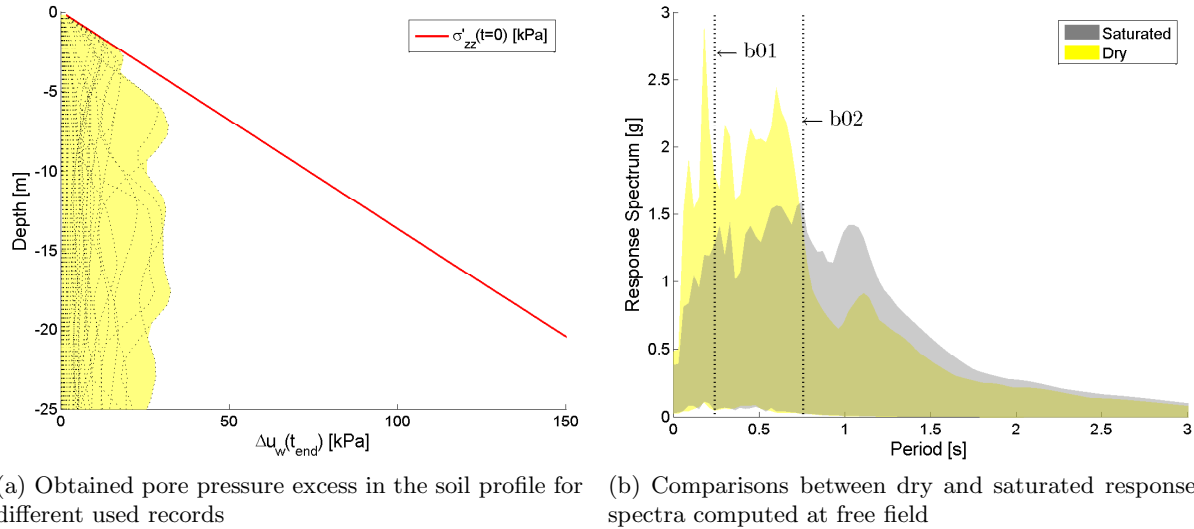
Figure 3.17: Effect of overburden pressure in free field response

In order to highlight differences between dry and saturated soil responses to be used as the input motion to the structure's, it is interesting to compare the induced pore pressure excess distribution Δu_w with depth for different input motions. Fig.3.17a displays the Δu_w profile at the end of each strong motion signal t_{end} and the initial vertical effective stress σ'_{zz} profile. Envelope of these profiles is presented in yellow. According to this figure, liquefaction takes places in the first 3[m] for some motions, but for the major part of records liquefaction state is not reached. Only one motion is close to induce liquefaction at 7[m] depth. There are, however, significant pore-water pressure build-up and subsequent rigidity degradation at free field. Due to this coseismic softening, the signal might be attenuated depending on its frequency content and its energy.

In order to illustrate the rigidity degradation effect over the effective input for T-S approach, Fig.3.17b displays computed response spectrum envelopes at free field for dry and saturated condition. For weak motions (inferior limit of the envelope), no significant non-linear effects take place and obtained envelopes coincide. In this case, soil behaves approximately elastic and no significant pore pressure is generated. As both soil profiles have similar transfer functions in elastic range, responses at low-amplitude are equivalent. For strong motions, majors differences can be noticed. In saturated conditions, for large Arias intensity the pore-pressure build-up acts as a frequency filter for the high frequency component (Ghosh and Madabhushi, 2003; Lopez-Caballero and Modaressi-Farahmand Razavi, 2008). In the present analysis, this phenomenon takes place for periods up to 0.7[s] approximately. For periods larger than 0.7[s], the computed response spectra indicates that a large amount of seismic energy is transmitted to the structure in saturated condition compared to dry situation. In terms of analyzed buildings, this means that significant differences might be found for b01 building under strong-motions due to its fixed base period value. For b02 building, we expect to find minor variations between dry and saturated soil conditions. These free field accelerations are then used as the input of the dynamic fixed-base structural analysis of the T-S approach. The results are then compare to the ones off SSI-FE computations in the next section.

3.7   Effect of SSI on the dynamic response

The same set of input motions listed in Appendix J.1, are used in the SSI-FE simulations. In order to assess the influence of the SSI effects on the dynamic non-linear structural response, the results of the two approaches for each building and for each soil are shown in Figures 3.18, 3.19, 3.22 and 3.23. Results are presented in the form of scatter plots of the maximum value of the computed inter-story drift normalized by the corresponding inter-story height ($ISD_{max,\%}$) for each record as a function of the strong-motion parameters of the earthquakes. In order to use a common reference for both T-S and SSI-FE approaches, severity measures computed at outcropping or free field might be used for these figures on the x-axis. In general, it is accepted that acceleration amplitude as the measure of severity of earthquakes is not ideal because it does not contain information about the duration and frequency content. This aspect is critical for systems involving stiffness degradation, where the duration and frequency content of strong motion have a profound effect on the response of the system (Koutsourelakis et al., 2002). Correlations between several strong-motion parameters and the observed responses will be discussed in the following.

(a) Computed $ISD_{max,\%}$ in terms of outcrop acceleration amplitude a_{out}

(b) Obtained $ISD_{max,\%}$ in terms of outcrop Arias's intensity AI_{out}
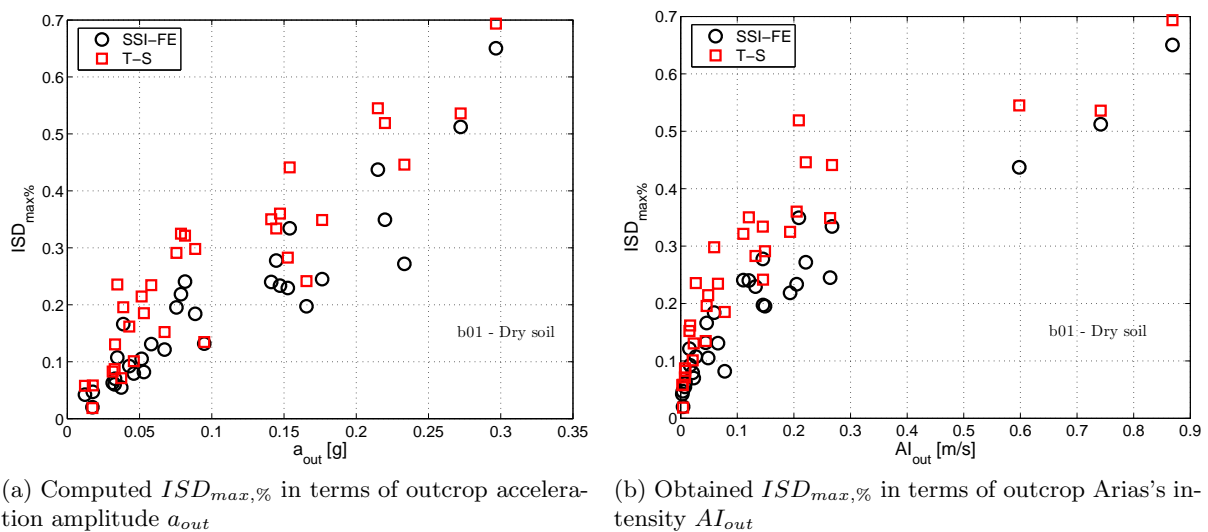
Figure 3.18: Scatter plots of maximum inter-story drift for b01 building on dry soil

Figures 3.18a and 3.18b provide scatter plots of the maximum response of $ISD_{max\%}$ in terms of a_{out} and AI_{out}, respectively, for the b01 building on dry soil. According to these figures in a general way, including non-linear SSI effects in the dynamic computation reduces the obtained maximum inter-story drift. However, results present dispersion, thus for approximately the same value of input severity large variation of $ISD_{max,\%}$ is found. In order to define the more suitable strong-motion parameter to describe the computed seismic demand, correlation coefficients $\rho_{X,Y}$ between $ISD_{max,\%}$ and the maximum amplitude of the acceleration at outcropping bedrock (a_{out}) and at free field (PGA), the Arias intensity at outcropping bedrock (AI_{out}) and at free field (AI_{ff}), the mean period T_m and the predominant period of the ground motion T_g (Miranda and Vertero, 1994), for each studied case are listed in Tab.3.4.

According to Tab.3.4, correlation coefficients between free field or outcropping bedrock severity measures are equivalent, thus corresponding $\rho_{X,Y}$ values for a_{out} compared to PGA or AI_{out} compared to AI_{ff} are similar. As computed values at outcropping bedrock depends only of the input motion characteristics, we select outcropping measures to simplify the interpretation of results. Consequently, hereinafter two alternative of measures are considered: the maximum amplitude of the acceleration at outcropping bedrock a_{out} and the corresponding Arias intensity AI_{out}. According to values of $\rho_{X,Y}$ listed in Tab.3.4 for a_{out} and AI_{out}, depending on the building and the soil considered, one of them might be better than the other to describe the expected maximum structural response. Indeed, values of correlations coefficients are in general of the same order for both parameters. As a general rule,

Table 3.4: Correlation coefficient $\rho_{X,Y}$ between $ISD_{max,\%}$ and several strong-motion parameters

Building	Soil	Approach	a_{out}	PGA	AI_{out}	AI_{ff}	T_m	T_g
b01	Dry	T-S	0.92	0.92	0.86	0.89	-0.06	-0.17
b02	Dry	T-S	0.73	0.68	0.93	0.89	0.20	0.16
b01	Sat.	T-S	0.72	0.82	0.51	0.61	-0.30	0.21
b02	Sat.	T-S	0.64	0.68	0.66	0.79	0.08	0.55
b01	Dry	SSI-FE	0.93	0.92	0.94	0.94	-0.08	0.16
b02	Dry	SSI-FE	0.71	0.66	0.90	0.87	0.25	0.14
b01	Sat.	SSI-FE	0.84	0.85	0.70	0.71	-0.24	0.31
b02	Sat.	SSI-FE	0.68	0.65	0.77	0.89	0.26	0.71

we will use AI_{out} to describe the severity/intensity of the used motions because this measure takes into account the duration and the frequency content of the ground motion. Nevertheless, similar conclusions can be derived in terms of a_{out}. Concerning the frequency content measures T_m and T_g, in general a poor correlation is found. Indeed, this kind of measures are not adequate because they do not cause a monotonic increase in structural response with increasing values of the measure. However, T_m will be used below to identify some close to structure-earthquake or soil-earthquake resonance situations.
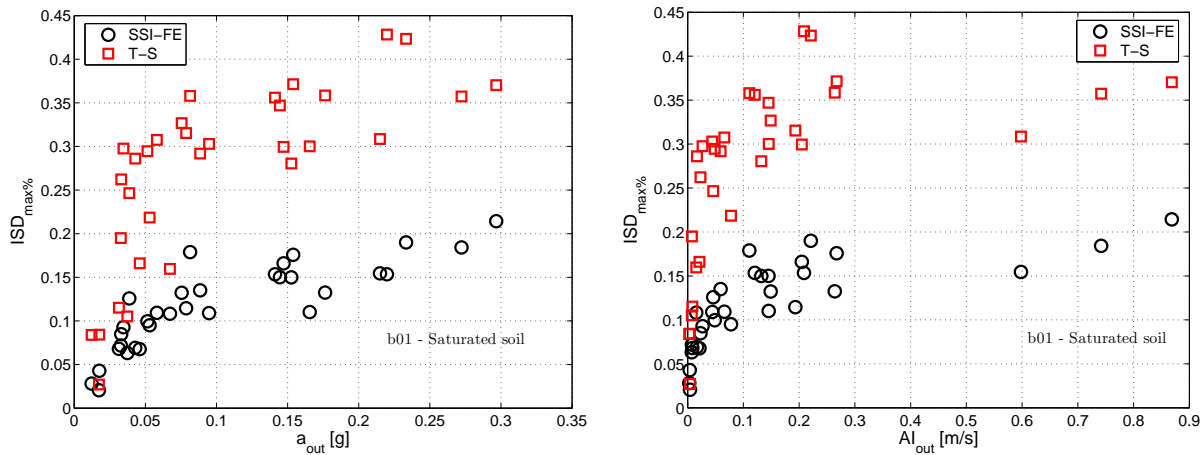
(a) Computed $ISD_{max,\%}$ in terms of outcrop acceleration amplitude a_{out}

(b) Obtained $ISD_{max,\%}$ in terms of outcrop Arias's intensity AI_{out}

Figure 3.19: Scatter plots of maximum inter-story drift for b01 building on saturated soil

For the saturated case (Fig.3.19a), the difference between both approaches is relatively constant over the acceleration amplitude of the input motion. It can be noted that in all cases the structures on the saturated soil are less damage ($ISD_{max\%} = 0.7$ in dry soil and $ISD_{max\%} = 0.45$ in saturated soil). Additionally, this difference is larger than the dry case. This variation can be related to the different deformations induced during the shaking in the soil. As the imposed shear stress is approximately the same for both soils for the same motion, but the degree of confinement for the saturated case is less than one for the dry case, thus the induced strains are larger and the obtained damping increases. If the energy dissipation in the soil grows, the seismic demand of superstructure diminishes. In the saturated case, approximately parallel curves are found for $a_{out} > 0.04$[g] or $AI_{out} > 0.05$[m/s], thus when the energy of the input motion is high enough to induce inelastic behavior in soil.

The variations on computed responses can be partially explained by computing response spectra of the effective motion imposed to superstructure, thus of the free field response for T-S approach or

(a) Envelopes of response spectra for dry soil   (b) Envelopes of response spectra for saturated case
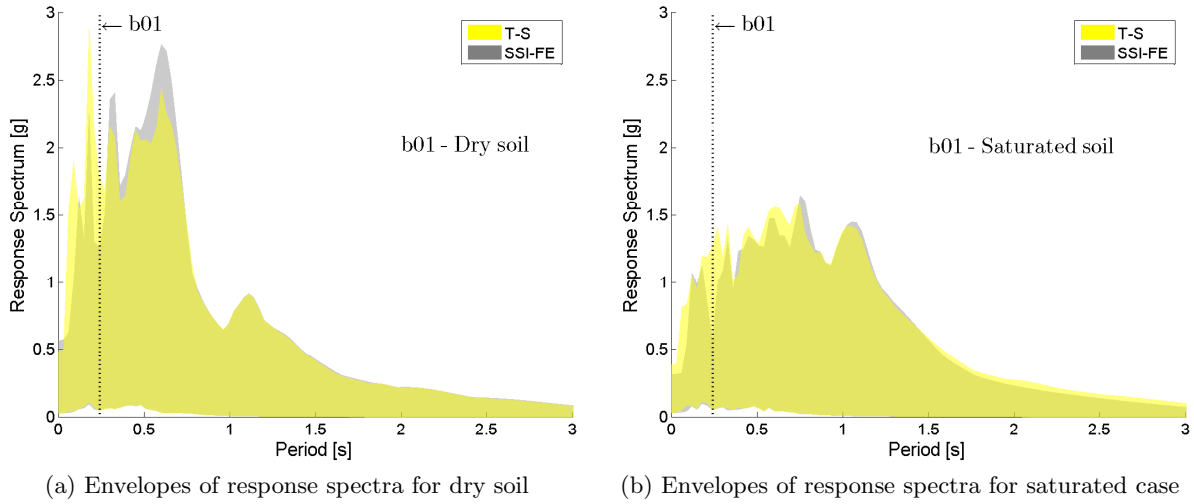
Figure 3.20: Comparison between response spectra at the base of the superstructure following T-S and SSI-FE approaches for b01 building

at the structure base level for the SSI-FE case. Fig.3.20a and b show the envelope of response spectra computed at base level for the 32 considered records. The fixed base structural fundamental period is also displayed in these figures. In both situations, dry or saturated soil, response spectra is reduced when SSI effects are included. This attenuation might be related to initial state of the soil. When the weight of superstructure is included, effective stress under foundation grows resulting into an increase of the soil stiffness. But, at the same time, internal soil friction is mobilized altering the initial state of the soil. Additionally, during the dynamic loading, soil dissipates energy by both radiation and material damping reducing the effective energy transmitted to the superstructure. These soil's energy dissipation mechanisms will be explored in section §3.8.

(a) Computed settlements for b01 building   (b) Obtained settlements for b02 building
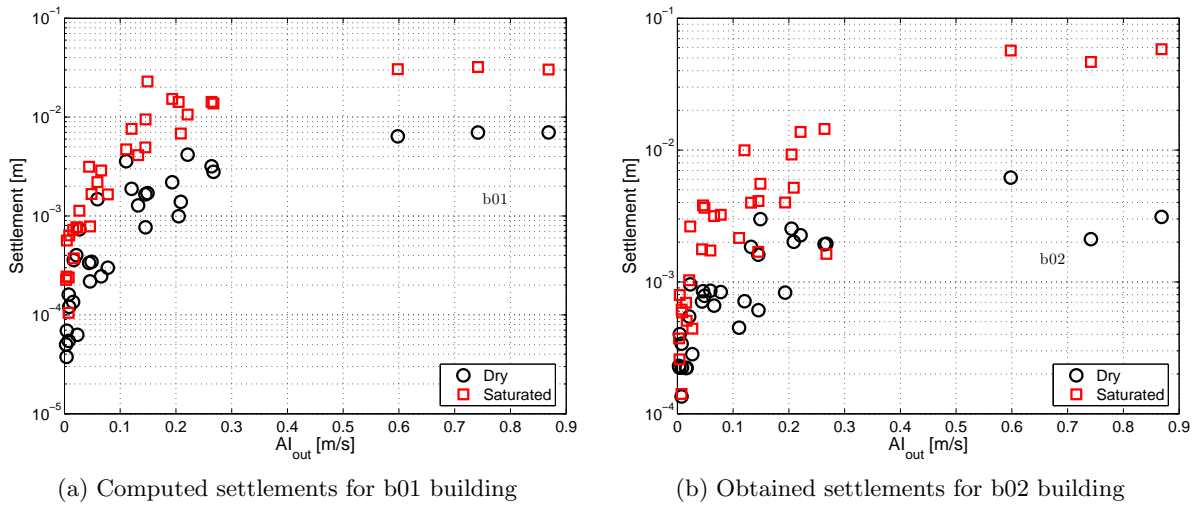
Figure 3.21: Scatter plots of maximum foundation co-seismic settlement

The attenuation of the motion due to soil stiffness degradation effect is evident comparing dry and saturated soil spectra in Fig.3.20. Spectral ordinates for saturated case are significantly smaller than dry situation. A reduction of the spectral ordinates around the fixed base period can be also noticed for the saturated case, that explains the reduction of the computed $ISD_{max,\%}$. Nevertheless, this reduction of the superstructure displacement is accompanied by an increase up to four times of the foundation co-seismic settlement as is depicted in Fig.3.21a. In this figure, we use logarithmic y-axis due to large variability on the predicted coseismic settlement. These co-seismic settlements

were computed with respect to the corresponding free field settlements.

(a) Computed $ISD_{max,\%}$ in terms of outcrop accelera-   (b) Obtained $ISD_{max,\%}$ in terms of outcrop Arias's in-
tion amplitude a_{out} tensity AI_{out}
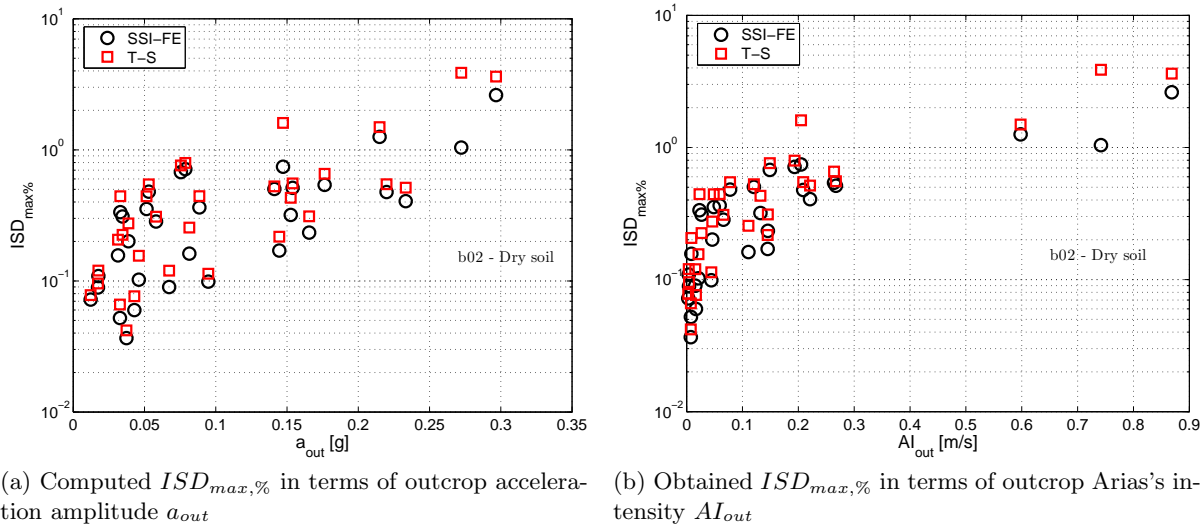
Figure 3.22: Scatter plots of maximum inter-story drift for b02 building on dry soil

In this study, superstructures are symmetric and the soil is supposed homogenous, thus differ-
ential settlements can be generated only by asymmetry of the record. Computed permanent tilts
are negligible in this case, but in more general situations for multi-supported irregular buildings in
non-homogeneous soils, large coseismic tilt might control the structural damage.

Figures 3.22a and b show the same comparison for the b02 building. As it can be noticed, the
effects of the SSI are less significant than for the b01 building. In this case, the fundamental period
of the superstructure is larger than the fundamental period of the soil $(T_0 > T_{soil})$. According to our
experience, in this condition the SSI effects can be generally neglected.

(a) Computed $ISD_{max,\%}$ in terms of outcrop accelera-   (b) Obtained $ISD_{max,\%}$ in terms of outcrop Arias's in-
tion amplitude a_{out} tensity AI_{out}
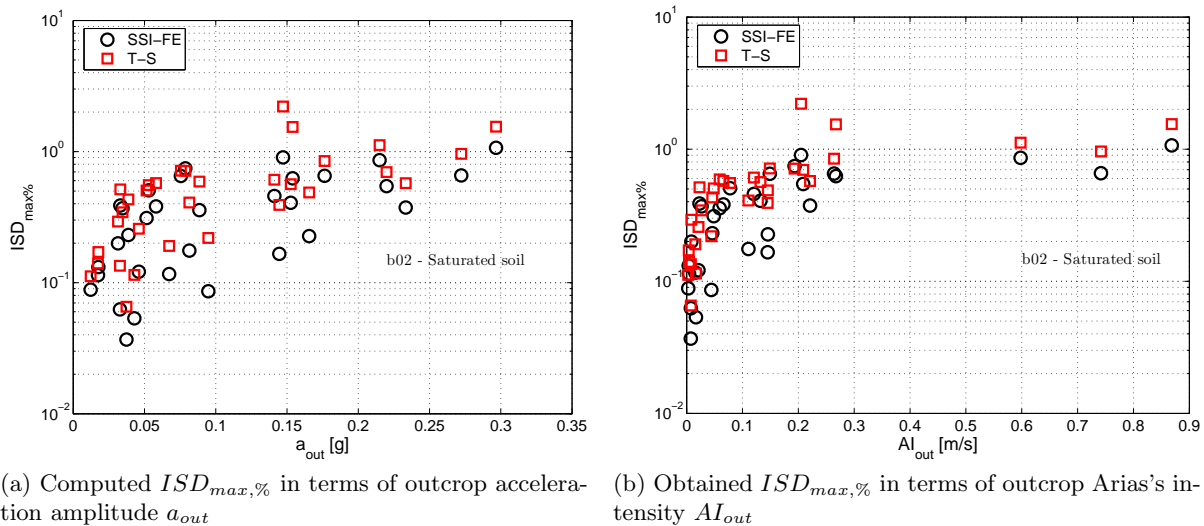
Figure 3.23: Scatter plots of maximum inter-story drift for b02 building on saturated soil

Again, obtained scatter plots of the computed response spectra at free field (T-S approach) or
structural base (SSI-FE) agree. Fig.3.23a and b display the envelope of these spectra for both, dry
and saturated situations. It can be noticed that for dry soil, response spectra envelope remains
relatively unchanged around the fundamental fixed base period of b02 building. This means, that
amplitude and frequency content are approximately the same for both approaches. Consequently,
reductions displayed in scatter plots Fig.3.22 might be associated to added damping by radiation and
non-linear hysteretic soil behavior. The variations on hysteretic soil damping will be depicted below.

(a) Envelopes of response spectra for dry soil

(b) Envelopes of response spectra for saturated soil
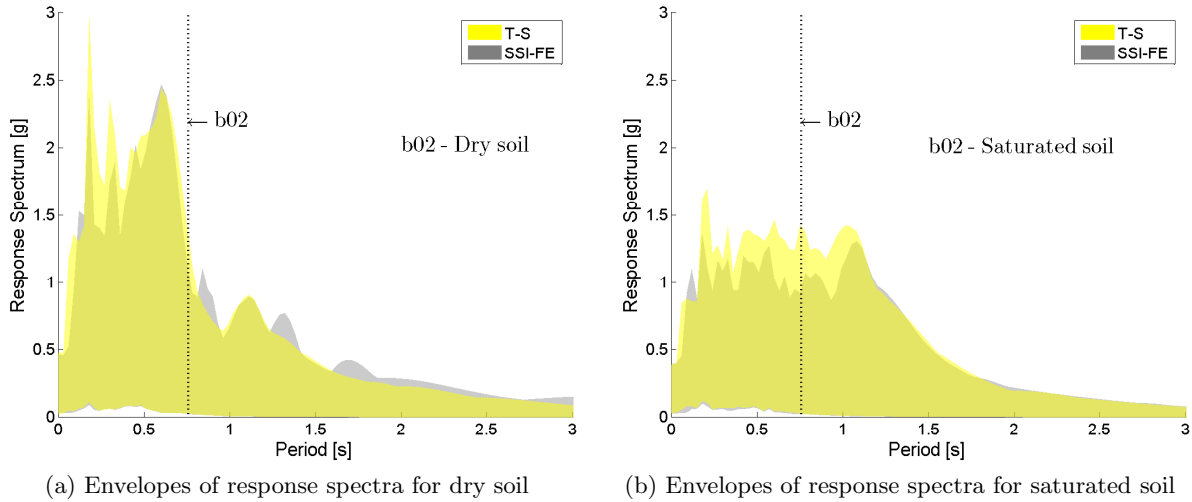
Figure 3.24: Comparison between response spectra at the base of the superstructure following T-S and SSI-FE approaches for b02 building

In saturated condition, similar reductions in maximum inter-story drift are found compared to the dry case. However, the effect over the effective response spectra is quite different. For saturated case, a general reduction in spectral amplitudes is found for periods between 0.2[s] and 1.2[s] approximately. As the fixed base fundamental period of b02 lies in this interval, this means that a significant variation of the effective amplitude is found in this case. However, not so large differences are obtained for this building. This behavior might be related to the fact that the building responds essentially in elastic range and no significant SSI effects takes place.

Similarly to b01 building, an increase of foundation settlements can be noticed for b02 building on saturated soil according to Fig.3.21b. Again, this augmentation is related to reduction in soil stiffness due to pore water pressure generation. Coseismic settlements are for both buildings of the same order, and they are well correlated with Arias intensity. Increases of foundation settlements in saturated condition are also approximately of the same order for b01 and b02, thus they are not a relevant effect of the initial overstress over the coseismic settlement in this configuration, considering that initial vertical overstress is approximately four times larger for b02 compared to b01. Therefore, large inertial forces are compensated by the increase of soil stiffness due to effective stress in this case.

3.8   Energy oriented analysis of results

In order to identify the role of the different energy dissipation mechanisms in the problem and asses the effects of the non-linear SSI, two energy dissipation indicators can be computed.

For the superstructure, the material non-linearity is concentrated in plastic hinges of beam-column elements. Thus, an indicator of the amount of energy dissipated on the superstructure I_{str} can be defined as:

$$I_{str} = \frac{1}{m} \sum_{k=1}^{n_g} \int_t M_p^k (t) \, d\theta_p^k (t) + 1 \times 10^{-3} \quad [\text{J/m3}] \tag{3.6}$$

where M_p^k is the bending moment in plastic component and θ_p^k the corresponding hinge rotation. The superscript k corresponds to potential plastic hinge k of the superstructure. The total number of potential plastic hinges is denoted n_g and m corresponds to the total mass of the superstructure (Tab.3.1). According to this definition, I_{str} corresponds to the average energy dissipated by unit of volume. Other authors have proposed measures of dissipated energy normalized by ultimate values of rotation and bending moment to compute a damage index (Park and Ang, 1985). A direct measure

of energy is selected here in order to facilitate comparisons with soil energy dissipation measures introduced below.

Interpretation of structural responses can be completed by including some measures about the non-linear response of the soil. In particular, the analysis of the energy dissipated in soil by its no-linear hysteretic behavior might give additional information on different damping mechanisms and their interactions. For the soil, a normalized energy dissipation index can be computed by:

$$I_{soil} = \frac{1}{\Omega} \int_{\Omega} \int_t \underline{\underline{\Delta\sigma'}} \, (\underline{x}, t) : d\underline{\underline{\varepsilon}} \, (\underline{x}, t) \; dV \quad [\text{J/m3}] \tag{3.7}$$

where $\underline{\underline{\Delta\sigma'}}$ and $\underline{\underline{\varepsilon}}$ are the shear and strain tensors dynamic perturbations induced in the soil during the dynamic loading at an interior material point $\underline{x}$. This integration is performed over a control volume Ω. The criterion adopted for the definition of the extension of this control volume is detailed in §3.8.2. For the modified plane-strain approach in yz plane explored in this chapter, the previous expression takes the form:

$$I_{soil} = \frac{1}{\Omega} \int_{\Omega} \int_t \left[\Delta\sigma'_{yy} \, d\varepsilon_{yy} + \Delta\sigma'_{zz} \, d\varepsilon_{zz} + \Delta\tau_{yz} \, d\gamma_{yz} \right] (\underline{x}, t) \; dV \quad [\text{J/m3}] \tag{3.8}$$

The contribution of each term to the total value of I_{soil} depends on the characteristics of the loading. As a result of the horizontal seismic motion (in yz plane) imposed in this case, the contribution of $\Delta\sigma'_{yy} \, d\varepsilon_{yy}$ is negligible. According to our computations, the shear term $\Delta\tau_{yz} \, d\gamma_{yz}$ represents approximately the 98% and 95% of the total value of I_{soil}, for b01 and b02 respectively. Indeed, for the weighter building, relatively larger variations of vertical stress and strains are induced by the superstructure rocking. Consequently, the contribution of the vertical term $\Delta\sigma'_{zz} \, d\varepsilon_{zz}$ increases.

3.8.1 Energy dissipated by the superstructure

Fig.3.25 shows computed structural indicator for b01 building, in both dry and saturated soil conditions. In these plots, values of $I_{str} = 1 \times 10^{-3}$ means that no plastic rotations are induced in any potential hinge for the corresponding motion.

(a) Computed I_{str} for b01 on dry soil   (b) Obtained I_{str} for b01 on saturated soil
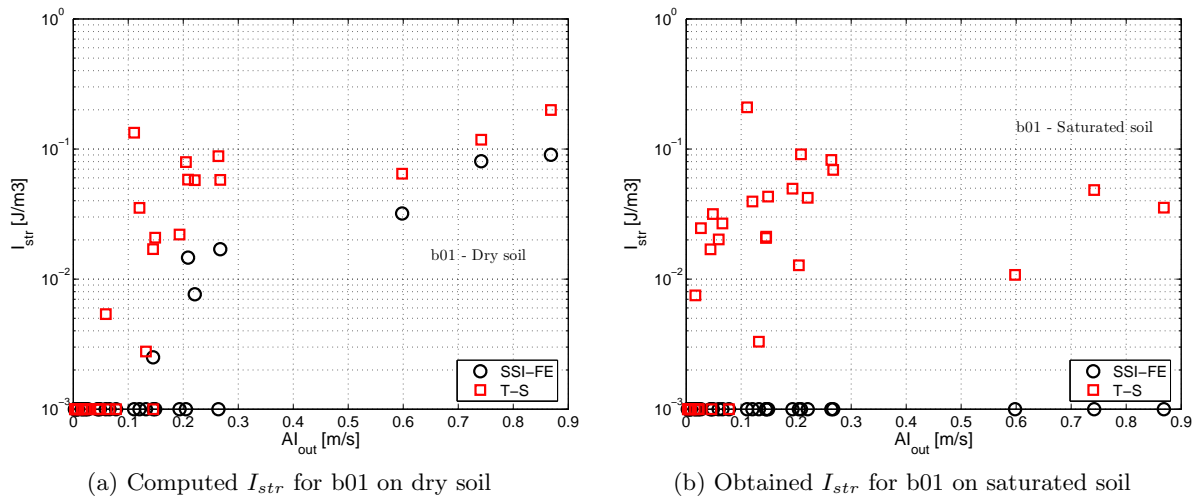
Figure 3.25: Scatter plots of energy dissipated by the superstructure for b01 building

According to Fig.3.25a, structural responses is in general elastic for $AI_{out} < 0.1[\text{m/s}]$. For larger input severity values, SSI effects reduce the energy dissipated by the structure, thus the coseismic structural damage. Large differences between T-S and SSI-FE approaches are found for moderate motions ($0.1 < AI_{out} < 0.3[\text{m/s}]$). For strong motions, the energies dissipated in the structure following both approaches are closer. It can be noticed that for T-S case input severity larger than $AI_{out} > 0.1[\text{m/s}]$ is enough to induce inelastic structural behaviour. This threshold grows to 0.2[m/s]

when SSI effects are included, thus for some records T-S predicts inelastic behavior whereas SSI-FE gives structural elastic response. This variation on predicted I_{str} indicator becomes dramatic for the saturated soil case. According to Fig.3.25b, structural damage vanishes when SSI effects are taken into account. In opposition to dry case, superstructure undergoes plastic deformations for several weak motions ($AI_{out} < 0.1[\mathrm{m/s}]$) in T-S approach. However for strong motions, the numerical values of computed energy indicators of dry case are larger than the obtained ones for saturated condition. These differences can be explained by the decreasing in amplification observed for severe motion in saturated case (Fig.3.16b). It can be concluded that neglecting SSI effects for b01 building case give conservative predictions of structural response.

(a) Computed I_{str} for b02 on dry soil   (b) Obtained I_{str} for b02 on saturated soil
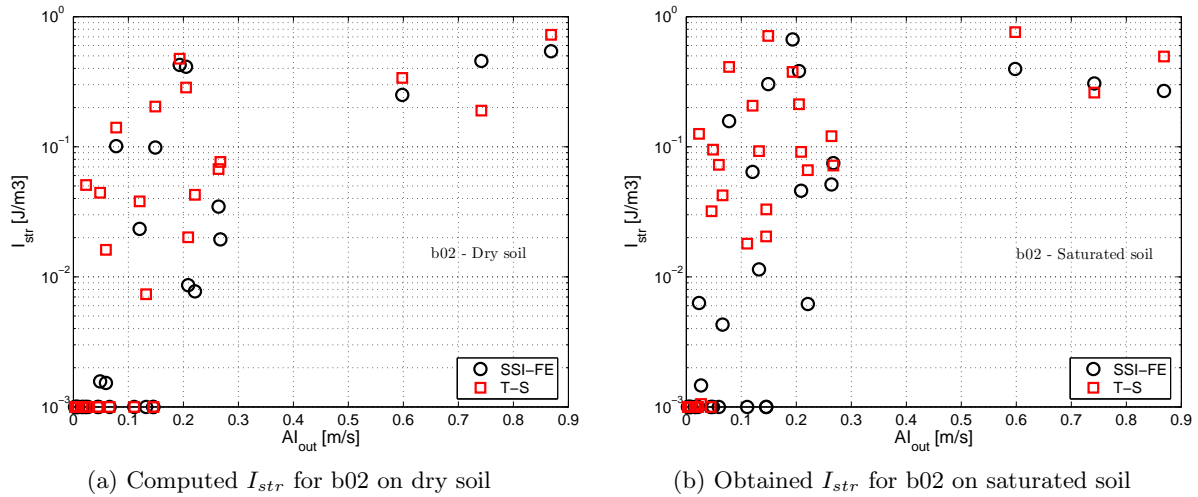
Figure 3.26: Scatter plots of energy dissipated by the superstructure for b02 building

Variations between T-S and SSI-FE approaches are in general terms less important for b02 building. In Fig.3.26a and b, large differences are found only for some cases associated to weak motions ($AI_{out} < 0.1[\mathrm{m/s}]$). For large values, inelastic structural indicators are relatively close. Similarly to b01 building, it can be noticed that there are more cases of moderate severity ($0.1 < AI_{out} < 0.3[\mathrm{m/s}]$) exhibiting inelastic behavior for T-S approach in saturated condition than dry one. Thus, dry non-linear soil effect in this range is benefic compared to saturated condition. They are two cases at approximately $AI_{out} = 0.18$ and $0.65[\mathrm{m/s}]$ showing larger responses for SSI-FE than T-S approach. Despite these two cases, the general tendency is that SSI effects reduce superstructure damage. However, the relative reduction of I_{str} for b02 building is not as large as the corresponding for b01 building. Relative position of fixed base frequency of the structure compared to modes of the soil profile will explain this response.

3.8.2   Energy dissipated by the soil

In order to define a suitable control volume Ω, the variation of the I_{soil} index in terms of the integration depth z over a unit with soil column according to schema of Fig.3.27a is studied.

Figures 3.27b and c show the evolution of I_{soil} index with z for dry and saturated conditions, respectively, when studying the dynamic response of the soil column only. It can be noticed that for weak motions relative larger values are found for saturated case. Under saturated condition soil stiffness decreases. Assuming that the imposed shear stress field is approximately the same for both soils, larger shear strains are obtained in saturated case. Stabilized values of I_{soil} are obtained for depths below 10 or 15[m] in both cases. For depth lower than this level, the value of I_{soil} decays. This means that the major part of non-linear soil behavior is in the top layers. In this zone, inelastic response is highly affected by the degree of confinement. Deeper soil is stiffer due to larger effective stress, and consequently damping associated to hysteretic behavior decreases.

Dynamic hysteretic behavior of soil is depicted in Fig.3.28a and b, for dry and saturated conditions

(a) Unitary col-
umn of depth z

(b) Evolution of I_{soil} with z for dry soil

(c) Evolution of I_{soil} with z for saturated soil
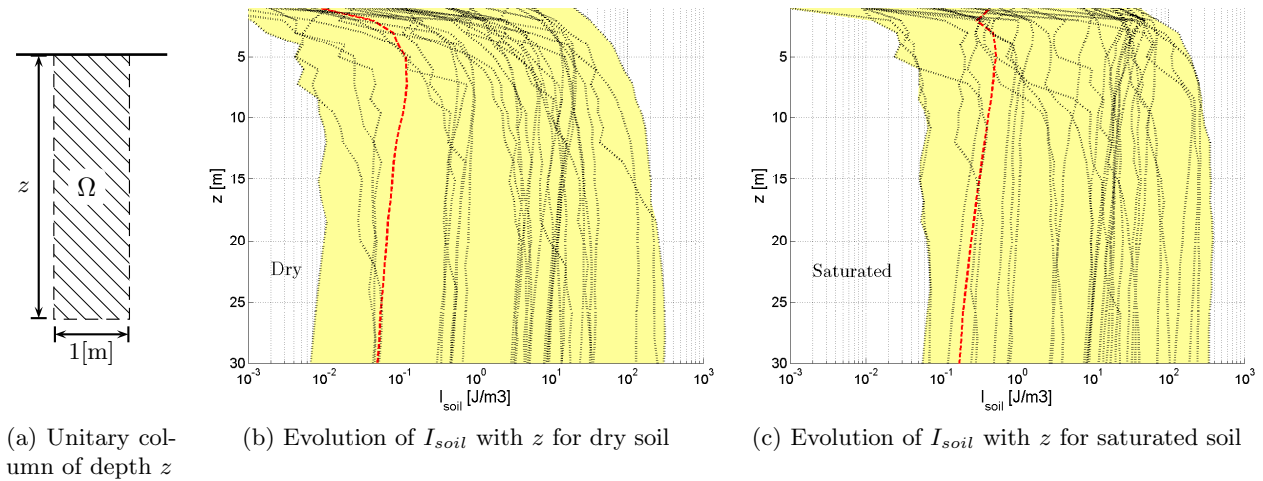
Figure 3.27: Definition of the integration volume Ω to compute normalized energy dissipation index I_{soil}

(a) $\tau - \gamma$ curve for dry soil

(b) $\tau - \gamma$ curve for saturated soil
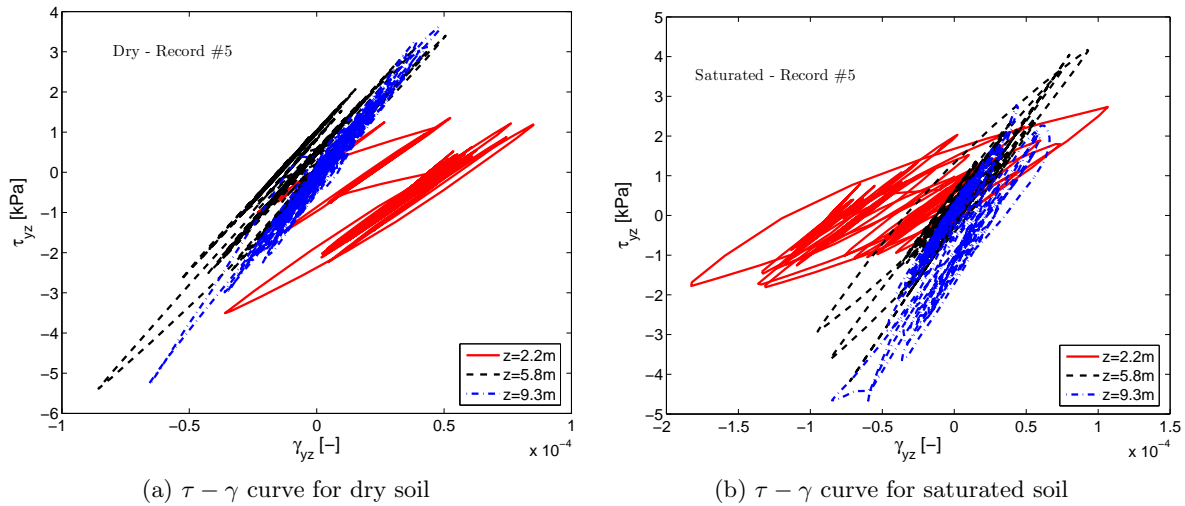
Figure 3.28: Time domain shear stress-strain responses at three different depths for record number 5

respectively. These figures shows $\tau_{yz} - \gamma_{yz}$ curves at three different depths, computed for record number 5. The evolution of I_{soil} with the control volume for this motion is displayed in red on Fig.3.27. These figures illustrate clearly the reduction of hysteretic damping with depth, associated to increase of soil stiffness with the effective stress. It can be noticed that bigger loops are obtained for saturated case, thus larger damping is induced but also larger permanent deformations are developed.

The definition of the volume of integration to compute I_{soil} for the SSI-FE is more complicated due to horizontal and vertical variation of non-linear soil behavior near the superstructure. Far enough from soil-structure interface following horizontal direction, equivalent behavior to one dimensional column approach is reached. In order to highlight spatial variation of hysteretic damping in soil, Fig.3.29 shows distribution of i_{soil}:

$$i_{soil}\left(\underline{x}\right) = \int_t \underline{\underline{\sigma}}'\left(\underline{x}, t\right) : d\underline{\underline{\varepsilon}}\left(\underline{x}, t\right) \quad [\text{J/m3}] \tag{3.9}$$

for cases where b01 and b02 buildings lay on saturated soil subjected to record number 5.

The effect of the increase of the effective stresses due to the over stress imposed by the super-structure's weight is evident in Fig.3.29. For b02 building, large augmentation of confinement due to superstructure self weight reduces inelastic behavior of soil below the foundation. Far from the foundation, confinement effect vanishes and soil undergoes plastic deformation inducing large hysteretic

(a) Spatial distribution of i_{soil}[J/m3] for b01 building   (b) Spatial distribution of i_{soil}[J/m3] for b02 building
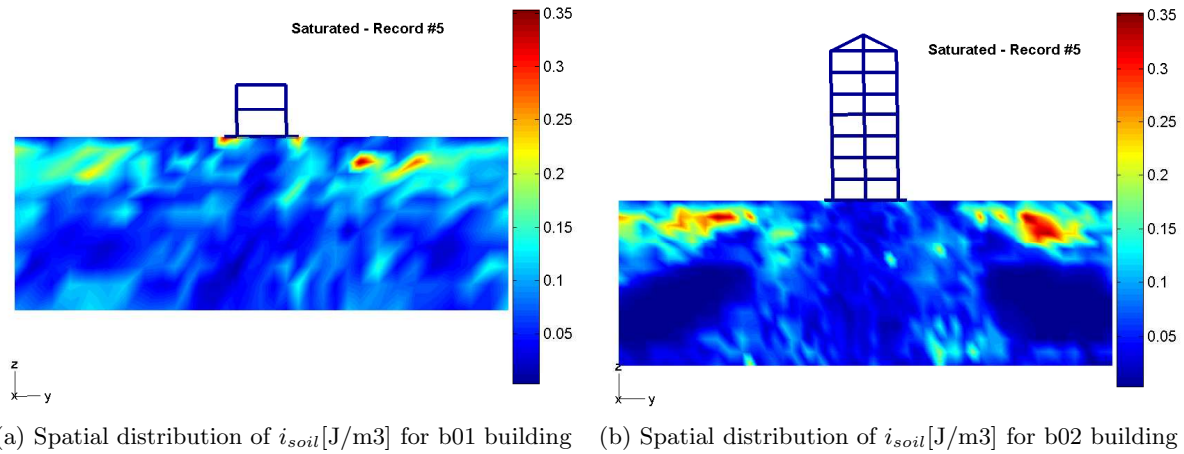
Figure 3.29: Spatial distribution of hysteretic damping in saturated soil subjected to record number 5

damping. As b01 building is relatively light, the over stress effect is less significative and hysteretic damping near the foundation corners induced by stress concentration is approximately of the same order as the free field inelastic material damping. These figures correspond to a single record, but the same tendency is obtained for other motions considered in this work.

In order to take into account local modification in hysteretic damping induced by the superstructure, the index I_{soil} is computed over a variable volume of soil $\Omega(z)$ in terms of depth z from the foundation level. Due to regular mesh used and with the purpose to make compatible the obtained index with the computation conducted for the one dimensional column, a square control volume of side z is assumed (Fig.3.30a).

(a) Square region of integration in   (b) Adopted criterion to define Ω
terms of depth z in terms of characteristic length a
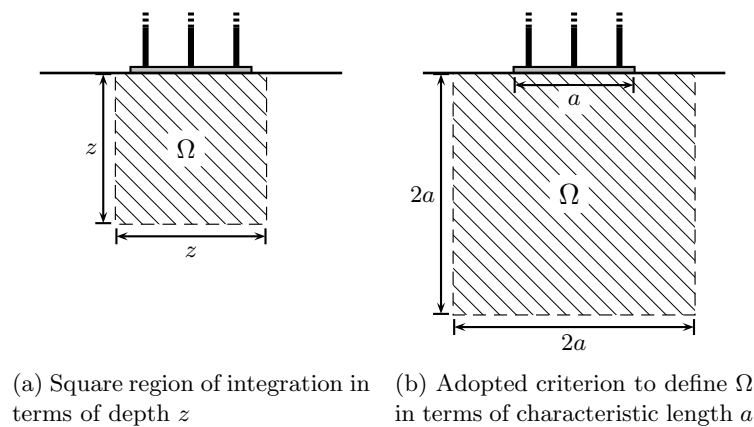
Figure 3.30: Definition of the integration volume Ω to compute normalized energy dissipation index I_{soil} for SSI-FE approach

The dependency of I_{soil} with the volume of integration Ω for the b01 is depicted in Fig.3.31a and b, for dry and saturated case, respectively. In general terms, similarly to free field case, hysteretic damping for weak records increases in saturated condition. However, stabilization of I_{soil} indicator with the depth z is faster compared to one-dimensional cases displayed in Fig.3.27. Indeed, according to Fig.3.31 the value of I_{soil} does not change significantly for $z > 8$[m] approximately. Numerical values of the indicator are equivalent as well. The effect of over stress imposed by the superstructure is evident comparing the shape of $I_{soil} - z$ curves for record number 5 highlighted in red in the plots. The concentration of hysteretic damping near the surface is reduced when b01 is added to the model, thus the maximum value of I_{soil} reached near to $z = 5$[m] for free field case disappears.

Similar behavior is found for b02 building (Fig.3.32). In this case, the high over stress imposed under the foundation increases significantly the degree of confinement which results into reducing

(a) B01 building on dry soil

(b) B01 building on saturated soil
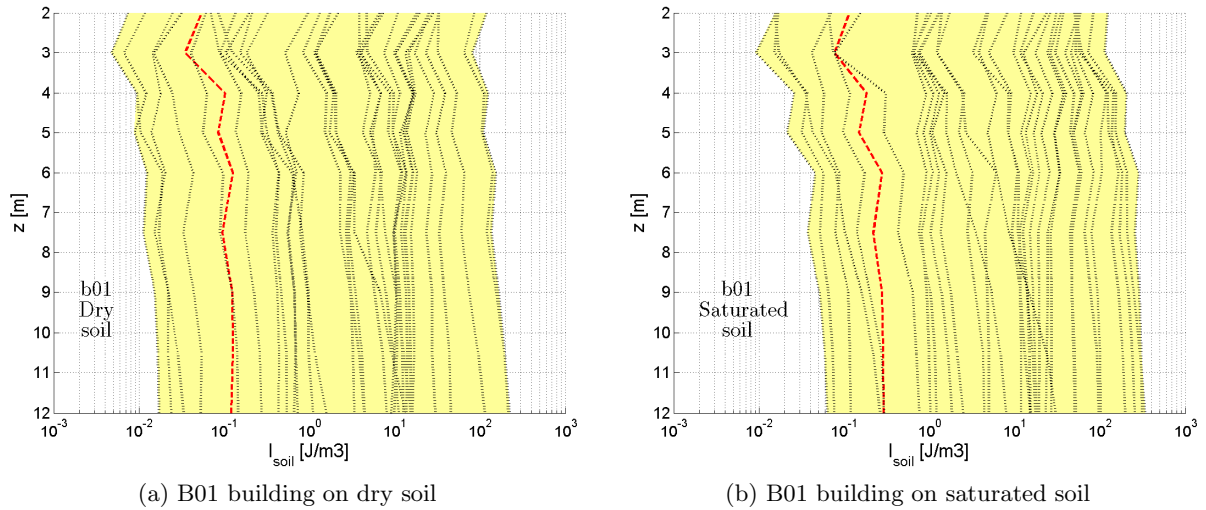
Figure 3.31: Variation of I_{soil}[J/m3] with the square volume of integration depending on depth z

coseismic deformations and the associated hysteretic damping. For both dry and saturated cases, the computed value of I_{soil} is approximately constant for depths below 14[m]. Again, high values of I_{soil} are obtained in saturated case because of the stiffness reduction induced by pore pressure build-up.

(a) B02 building on dry soil

(b) B02 building on saturated soil
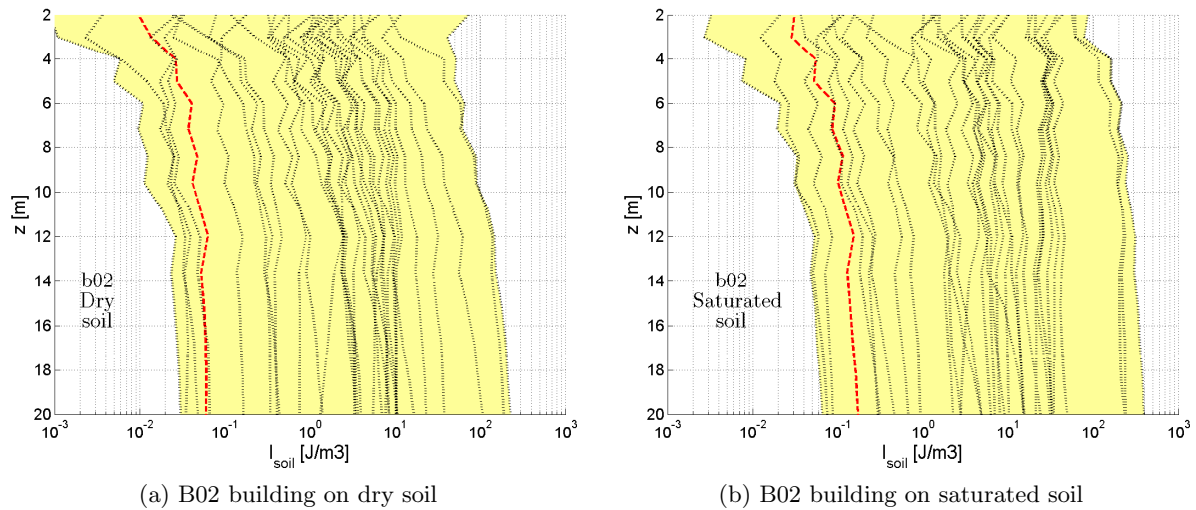
Figure 3.32: Variation of I_{soil}[J/m3] with the square volume of integration depending on depth z

In order to define a general criteria to define the control volume of the soil in which I_{soil} is computed, two general aspects should be considered. We have decided to express this volume in terms of a the characteristic length of the shallow foundation. According to the discussion above, by choosing a square volume of side $2a$ local effects due to superstructure interaction are globally included in the computation of I_{soil}. Of course, this criterion is purely geometric and clearly the superstructure's weight plays a key role in defining this influenced region. However, in practice both variables a and superstructure's weight are not completely independent for regular buildings. Thus, in this study, we define the volume Ω in terms of only the characteristic length a for sake of simplicity (Fig.3.30b). Characterizing the control zone in this way agrees satisfactorily with the author's previous studies concerning the definition of the surrounding soil that concentrates non-linear effects due to dynamic soil-structure interaction (Sáez, 2005; Saez et al., 2007). These studies were conducted using an equivalent-linear approach implemented in the coupled BE-FE code MISS3D (Clouteau and Aubry, 2001), defining an influence criteria in terms of the variation of the amplitude of computed shear strain in frequency domain. Square regions of 12×12[m] and 20×20[m] defined below the foundation were

used for b01 and b02 structures, respectively. They are shown in dark color in Fig.3.5a and b.

(a) Computed I_{soil} for b01 on dry soil

(b) Obtained I_{soil} for b01 on saturated soil
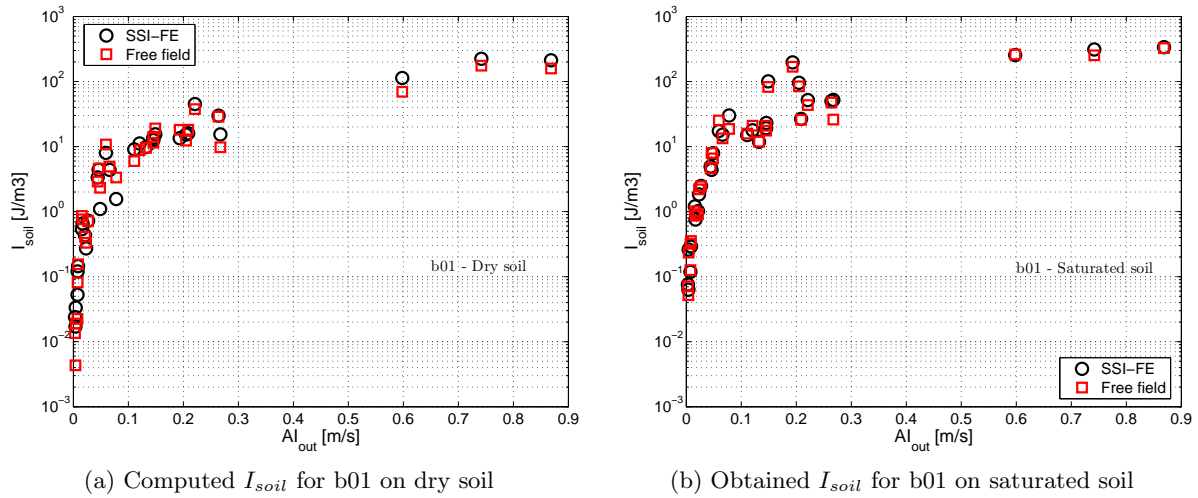
Figure 3.33: Scatter plots of energy dissipated by the soil in terms of I_{soil}[J/m3] for b01 building

The computed values of I_{soil} over the control volume Ω for the b01 building on dry and saturated soil are presented in scatter plots, on Fig.3.33a and b, in terms of AI_{out} for each used record. According to previous lines, the change in the initial state of soil below foundation and dynamic interaction effects are not enough to alter significantly the hysteretic behavior of foundation's neighboring soil. In both, saturated and dry conditions, I_{soil} values in free field or in SSI-FE approach are similar. Thus, differences found for the maximum interstory drift or structural dissipated energy measured by I_{str} are related to the whole soil-structure interaction phenomena, and not only to material damping induced by soil. This means that radiation damping, kinematical and inertial dynamical soil-structure interaction neglected in the T-S approach explains the major part of variations obtained for b01 building. In other words, the effect of b01 building on the non-linear behavior of soil does not alter enough the effective motion transmitted to the superstructure to influence the non-linear response of the structure. Thus, strong differences found in structural response of b01 building must be associated to radiative damping and support flexibility. Of course, other aspects such as frequency content of the motion compared to the soil first elastic frequency and the superstructure also play a key role on the structural response. Additionally, it can be noticed that for strong motions the soil energy dissipation indicator is slightly larger for SSI-FE than those obtained in the free field (T-S approach). This might indicate that for strong inputs, inertial SSI effects are large enough to increase significantly strains in some regions inside the integration region Ω, probably near to the foundation corners and in the transition zones between active and passive wedges below the structure.

Similarly, Fig.3.34a and b show the corresponding responses for b02 building. In this case, a general reduction of the coseismic hysteretic damping is found for SSI-FE approach except for very strong motions. These results are coherent with previous observations related to soil confinement induced by the superstructure below the foundation. However, for very strong motions, inertial SSI effects seem to be strong enough to induce large strains that compensate differences in initial state. As fixed base frequency of b02 building is shorter than the fundamental frequency of soil profile, dynamic SSI effects are not important. This explains relative small differences of structural responses obtained between T-S and SSI-FE approaches. As the obtained I_{soil} for SSI-FE are smaller than those obtained in T-S approach, variation of hysteretic non-linear behavior can not explain the general reduction tendency found in the structural response. Thus, variations of $ISD_{max,\%}$ or I_{str} between two conducted approaches might be related to radiative damping and modification of fundamental frequency due to soil flexibility.

(a) Computed I_{soil} for b02 on dry soil   (b) Obtained I_{soil} for b02 on saturated soil
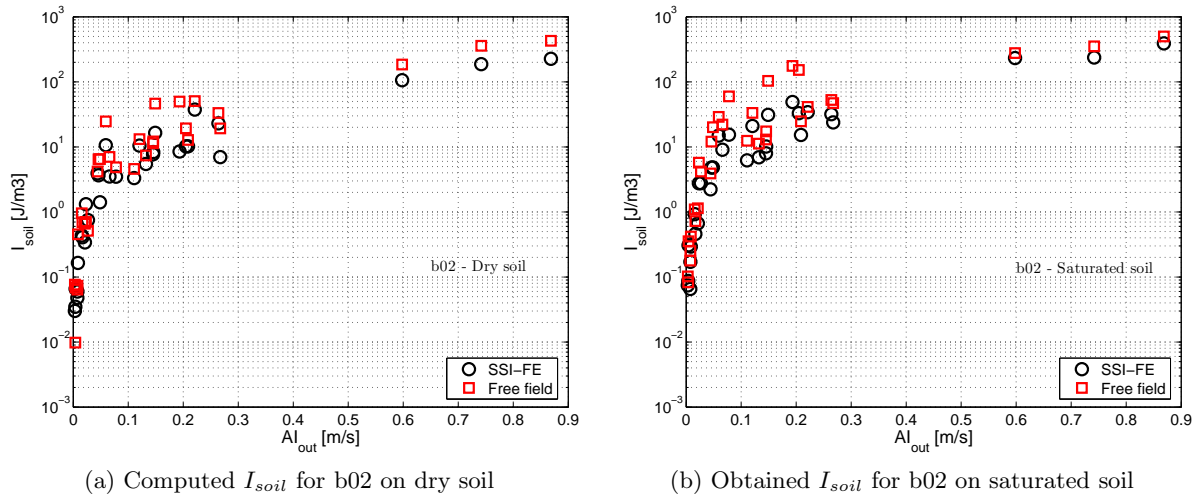
Figure 3.34: Scatter plots of energy dissipated by the soil in terms of I_{soil}[J/m3] for b02 building

3.9   Results exploration

This section is devoted to the exploration of obtained results, in order to identify parameters that might explain differences computed between T-S and SSI-FE approaches. The influence of SSI phenomenon on the structural response will be measured in terms of relative variation of the computed maximum interstory drift following both presented approaches according to:

$$\Delta ISD = \frac{ISD_{max,\%}^{T-S} - ISD_{max,\%}^{SSI-FE}}{ISD_{max,\%}^{T-S}} \tag{3.10}$$

where the superscript $T-S$ or $SSI-FE$ indicates the approach followed to obtain the value of $ISD_{max,\%}$. According to results presented in previous sections, the measure ΔISD is positive except for very few records. Thus, a positive value of $ISD_{max,\%}$ means a beneficial effect of the non-linear dynamical SSI.

(a) B01 on dry and saturated soil   (b) B02 on dry and saturated soil
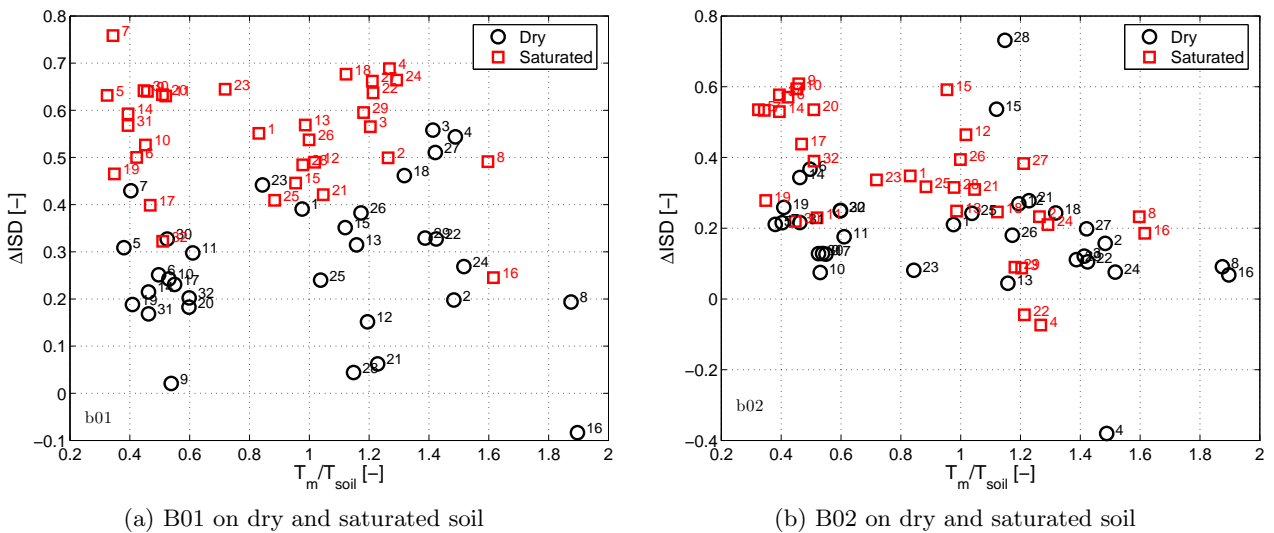
Figure 3.35: Variation of $ISD_{max,\%}$ as a function of ratio $\frac{T_m}{T_{soil}}$ for both studied buildings

Firstly, the influence of the frequency content of the input motion is studied in terms of the ratios between mean period of each motion T_m and fundamental period of both, soil profile (T_{soil}) and fixed base structure (T_0). Variation of the computed $ISD_{max,\%}$ in terms of $\frac{T_m}{T_0}$ is depicted in Fig.3.35, for b01 and b02 buildings. Record numbers are also displayed on scatter plots in Fig.3.35 near the

corresponding point. For b01 on dry soil the $ISD_{max,\%}$ variation lies approximately between 0.15 and 0.55, whereas for saturated case the range is between 0.4 and 0.7. No particular tendency can be detected between ΔISD and the period ratio $\frac{T_m}{T_{soil}}$. The only motion that exhibits a negative ΔISD value for the b01 building is the motion number 16, however there is a second motion (number 8) with approximately the same ratio $\frac{T_m}{T_{soil}}$ with a positive ΔISD. For b02 building on dry soil, records number 15 and 28 exhibit an exceptionally large variation of $ISD_{max,\%}$. These records have a ratio $\frac{T_m}{T_{soil}}$ value near to unity, thus resonance between soil and input motion might have taken place. Negative values of ΔISD for some records of b02 building seem not to be related to $\frac{T_m}{T_{soil}}$ ratio. Nevertheless, it can be noticed that less dispersion is found for b02 building compared to b01. This reduction of dispersion might be related to SSI. Indeed, as previously noted, due to its fixed base frequency is smaller than the first fundamental frequency of the soil profile, reduced SSI effects take place in this case.

(a) B01 on dry and saturated soil (b) B02 on dry and saturated soil
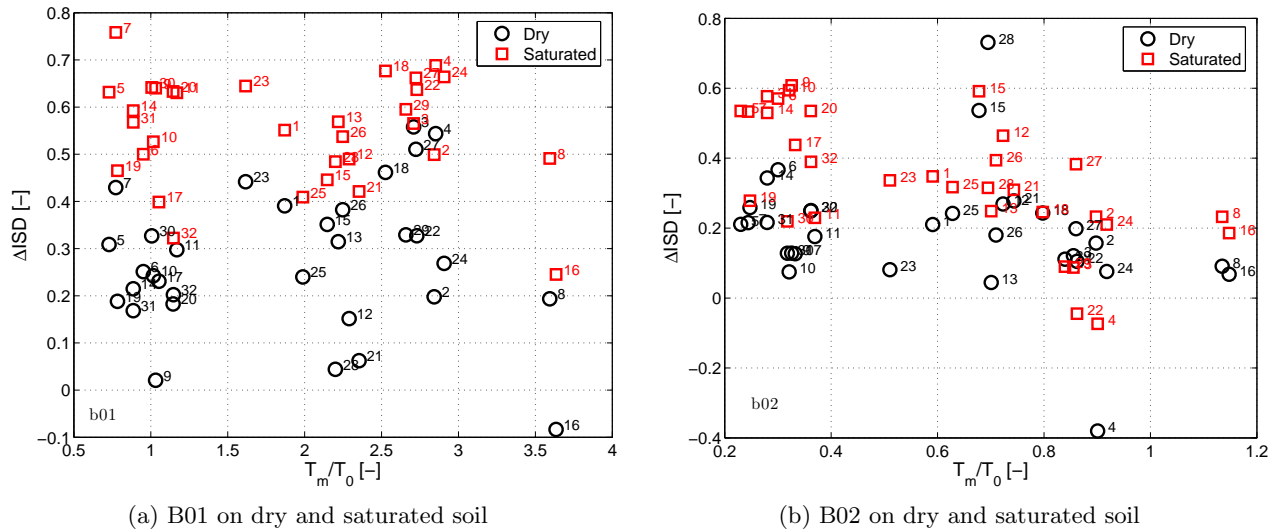
Figure 3.36: Variation of $ISD_{max,\%}$ as a function of ratio $\frac{T_m}{T_0}$ for both studied buildings

Computed ΔISD in terms of the ratio between mean period of the motion and the structures fundamental period $\frac{T_m}{T_0}$ are depicted in Fig.3.36. Similarly to previous analysis, no evident dependency between the effect of the SSI and this frequency ratio can be detected. No particular behavior is found near to the superstructure-motion resonance frequency, thus when $\frac{T_m}{T_0}$ approaches to one. Particular behavior found for some motions giving negative values of ΔISD (number 16 for dry soil case and 16 on saturated soil case) seems not to be related with the motion frequency content compared to fixed base fundamental period.

Table 3.5: Correlation coefficient $\rho_{X,Y}$ between ΔISD and several severity/intensity measures

Building	Soil	a_{out}	PGA	AI_{out}	AI_{ff}
B01	Dry	-0.27	-0.23	-0.33	-0.28
B02	Dry	-0.10	0.04	-0.18	-0.18
B01	Sat.	0.39	0.38	0.40	0.40
B02	Sat.	0.07	0.16	-0.08	-0.08

Finally, we explore the motion severity as an explanatory variable of dynamic non-linear SSI phenomena. In order to identify a suitable explanatory severity/intensity earthquake measure, Tab.3.5 displays the computed correlation coefficients between ΔISD and a_{out}, PGA, AI_{out} and AI_{ff}. In a general way, obtained values of $\rho_{X,Y}$ are significantly inferior to those obtained for $ISD_{max,\%}$ (Tab.3.4). Thus, the variation on the maximum structural response is not well described by severity/intensity measures. Nevertheless, a graphic representation of ΔISD in terms of a severity measure can provide

some information about the influence of the soil condition (dry or saturated) on the effect of the SSI. Among the parameters listed in Tab.3.5, AI_{out} show the better correlation with ΔISD, expect for b02 building on saturated soil. Hence, we will use this measure to describe the variations of ΔISD as a function of the motion severity (Fig.3.37).

(a) B01 on dry and saturated soil   (b) B02 on dry and saturated soil
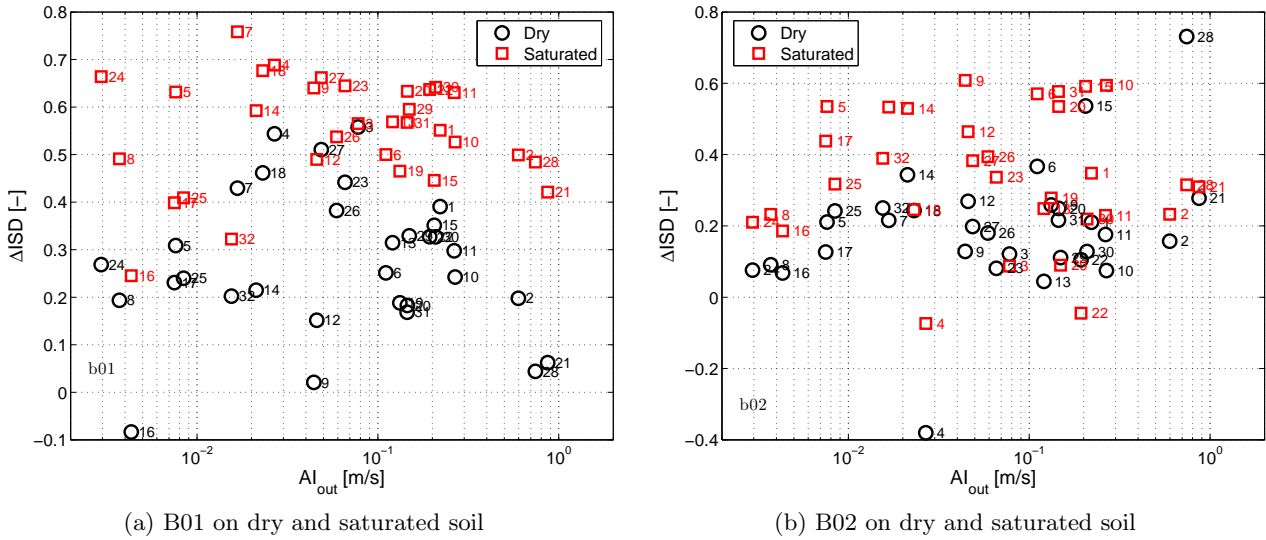
Figure 3.37: Variation of $ISD_{max,\%}$ as a function of ratio AI_{out} for both studied buildings

As expected, no evident relation between SSI effects and AI_{out} is detected in Fig.3.37. Nevertheless, exceptional reduction found for b02 in dry soil using record number 28 might be related to its frequency content compared to the first elastic frequency of the soil profile ($\frac{T_m}{T_{soil}} \approx 1$) in combination with the large severity of this motion. Additionally, according to this Figure, large variations of $ISD_{max,\%}$ are obtained in saturated soil compared to dry one, for both studied buildings independently of the severity of the motion.

In general terms, no evident relation between the input signals characteristics and non-linear SSI effects was found. Statistical studies of obtained results were carried out without success. Poor correlations were computed between ΔISD and several strong-motion parameters (AI_{out}, PGA, etc.). Nevertheless, it is interesting to study particular cases detected in this study. Fig.3.38 shows some response spectrum computed at free field (input for second step of T-S approach) and at the base of the b01 building for the SSI-FE approach, thus the effective motion transmitted to the superstructure for the dry soil condition. Fig.3.38a an b correspond to records number 8 and 16, respectively. Both records have approximatively the same severity (AI_{out}) and frequency content (T_m), nevertheless a beneficial effect of SSI is obtained for record 8 ($\Delta ISD \approx 0.2$) while for record 16 a detrimental effect is obtained ($\Delta ISD \approx -0.1$). As both motions are relatively weak, no structural damage is obtained for these motions. Thus, the fundamental structural period lengthening is only related to soil support flexibility. For small period lengthening, spectral ordinates of T-S approach are larger than SSI-FE spectrum for record number 8, that is consistent with the positive value of ΔISD found. Whereas, ordinates of response spectra of SSI-FE approach for record number 16 are larger than that at free field near the b01 building fixed base period. Consequently, detrimental effect of SSI in this case is related to the characteristic of the motion in the period range of the b01 building (low amplitudes in this case around the fixed base fundamental period T_0).

Similar comparison is presented in Fig.3.39 for the two records where a negative value of ΔISD was obtained, thus a detrimental effect of SSI. Fig.3.39 presents the response spectrum obtained for the dry soil condition using the record number 4. In this case, due to the severity of the motion and to the high superstructure mass affecting both initial stress state and inertial soil-structure interaction, large differences are found between computed spectra at free field and that obtained at the structure base in SSI-FE case. For motion number 4, an increase of spectral ordinates is obtained near the b02 fixed base period. Consequently, earthquake displacement demand rises for SSI-FE approach. For motion

(a) Record number #8 ($\Delta ISD > 0$)   (b) Record number #16 ($\Delta ISD < 0$)
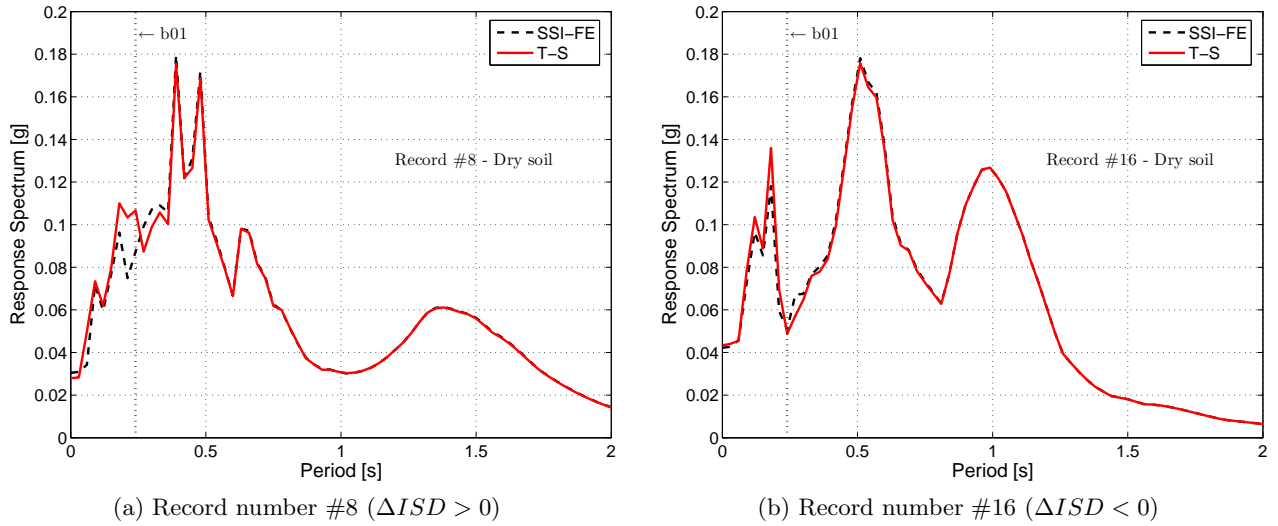
Figure 3.38: Comparison between response spectra in the dry soil condition at the free field (T-S) and at the base (SSI-FE) of the b01 building

number 22 in saturated condition, variation of spectral ordinate is also evident. Nevertheless, near the b02 fixed base period spectral ordinate is reduced in this case. However, record number 22 is a strong motion that induces large inelastic deformations in both, superstructure and soil. Structural damage contributes to its period lengthening due to the degradation of its elements stiffness. Surrounding soil stiffness degradation contributes to the period shift due to induced foundation soil flexibility. The combination of both phenomena introduces a large period shift. This large period lengthening might drive the system to spectral zone where spectral ordinates of SSI-FE are slightly larger than T-S approach.

(a) Record number #4 ($\Delta ISD < 0$) on dry soil   (b) Record number #16 ($\Delta ISD < 0$) on saturated soil
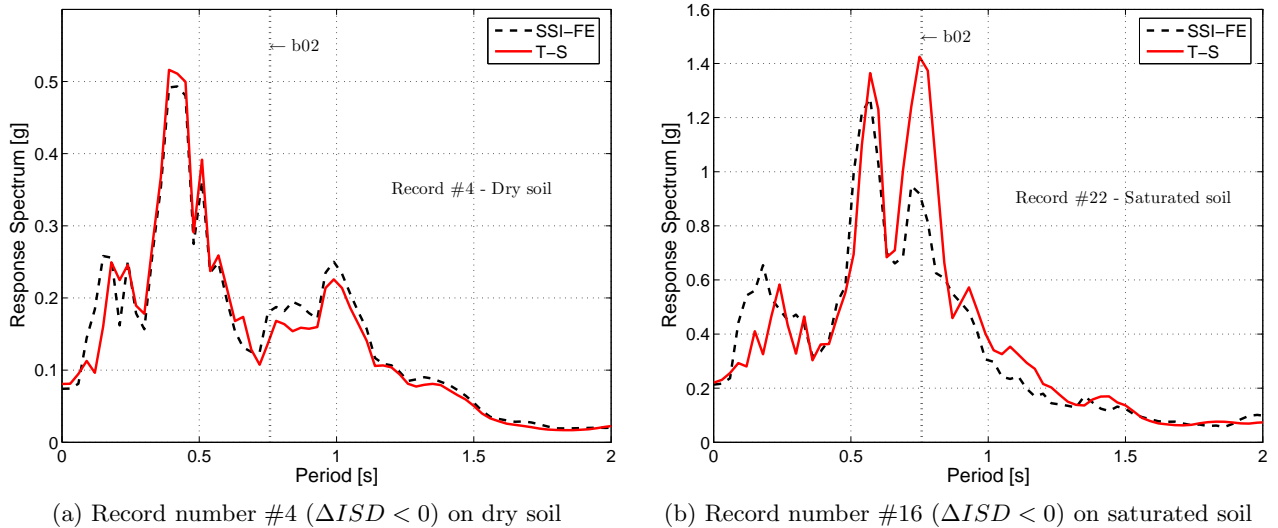
Figure 3.39: Comparison between response spectra at the free field (T-S) and at the base (SSI-FE) of the b02 building

3.9.1   Concluding remarks

The influence of the inelastic behavior of the soil deposit on the soil-structure interaction effects has been highlighted. Those effects result in a variation of the computed structural response compared to that obtained with fixed base condition, even if the non-linear behavior of the soil is taken into account in the study of the wave propagation in the soil deposit to estimate the free field motion.

Evaluation of the dissipated energies has shown that the initial state modification induced by the self weight of the superstructure contributes to increase the stiffness of the soil below the foundation. This additional confinement reduces hysteretic behavior under dynamic loading, compensating strain field generated by the superstructure's oscillations. However, for strong motions, this compensation seems to be surpassed by SSI inertial effects for low-rise buildings.

Generalization of SSI effects on displacement demand for a given building on a defined soil was unsuccessful. Large dispersion of results can be associated to the complexity of natural earthquakes, where spectral-amplitude characteristics can modify significantly the global response of the superstructure. This phenomenon was highlighted comparing response spectra of records showing detrimental SSI effects.

The next section is devoted to apply the presented modified plane-strain approach to the particular case of liquefiable soil. With this purpose, both studied buildings are analyzed on a locally liquefiable profile following the same approaches presented before and using the same record database.

3.10   Liquefiable soil

This section is devoted to evaluate the influence of soil non-linearity on the soil-foundation-structure interaction phenomena for a liquefiable soil. The purpose of this presentation is to better understand the effect of the liquefaction on the superstructure's response, as well as to investigate the modification introduced in the liquefaction phenomena due to the presence of the superstructure.

This study is an extension of the investigation of Lopez-Caballero and Modaressi-Farahmand Razavi (2008) conducted for three linear-elastic SDOFs on a liquefiable profile. In present study, we introduce non-linear behavior for the superstructure and we apply the modified plane-strain condition described previously. The fist study was conducted for four European earthquakes of very different frequency contents scaled to several outcropping amplitudes. In the present study we take advantage of the Design of Experiments methodology to select a motion database as is described in §3.5. Thus, the analysis is conducted for b01 and b02 non-linear buildings described in appendix I for the 32 records listed in appendix J.

The studied site is composed principally of clay layers overlaid by 22[m] of loose sand, i.e. relative density of $D_r < 50\%$. Site measurement of $SPT_{N_{60}}$ and low-strain shear wave velocities are given in Fig.3.40. According to $SPT_{N_{60}}$ profile, liquefaction phenomenon might take places between 4 and 15[m], where $SPT_{N_{60}}$ value is lower than 10. Soil deeper than 22[m] is constituted mainly of overconsolidated clay. Non-linear behavior is expected only for the first 29[m], thus isotropic linear elastic behavior is assumed for soil deeper than 29[m]. The deformable bedrock is placed at 40[m] depth.
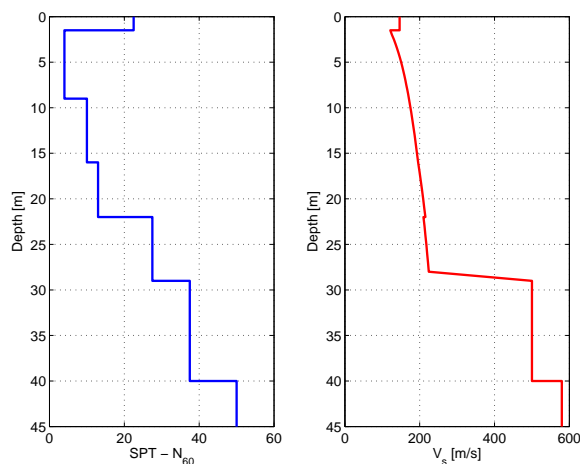
Figure 3.40: SPT and low-strain shear velocity profile of the studied site (after Lopez-Caballero and Modaressi-Farahmand Razavi (2008))

The ECP's elastoplastic cyclic multi-mechanism model Aubry et al. (1982); Hujeux (1985) is used to represent the soil behavior. Theoretical formulation and physical interpretations of different parameters was extensively treated in Appendix E. The soil model's parameters are obtained using the methodology suggested by Lopez-Caballero et al. (2003); Lopez-Caballero et al. (2007) described briefly in §1.3.4. In order to verify the model's parameters and to characterize the liquefaction resistance of sand placed between 3.5 and 9[m] depth, the behavior is studied by simulating drained cyclic shear (DCS) tests and undrained stress controlled cyclic shear test. Parameter sets and comparison of simulations with references curves are provided in appendix H.2.

3.10.1 Ground response

According to approaches described in §3.3, first part of T-S strategy consists in obtaining the free field response associated to record database selected for the analysis. Fig.3.41a presents the variation of peak ground acceleration PGA at free field as function of the imposed peak acceleration at outcropping bedrock a_{out}. It can be noticed that amplification of the peak acceleration takes places for $a_{out} < 0.1$[g]. Maximum amplification reached for this range of a_{out} is approximately up to 2.5 times the amplitude of the imposed motion. For amplitudes larger than 0.1[g], the apparition of the liquefaction phenomenon attenuates strongly seismic motion resulting in a relative de-amplification of acceleration peaks.

(a) Computed PGA for liquefiable soil

(b) Obtained pore pressure excess in the soil profile for different used records
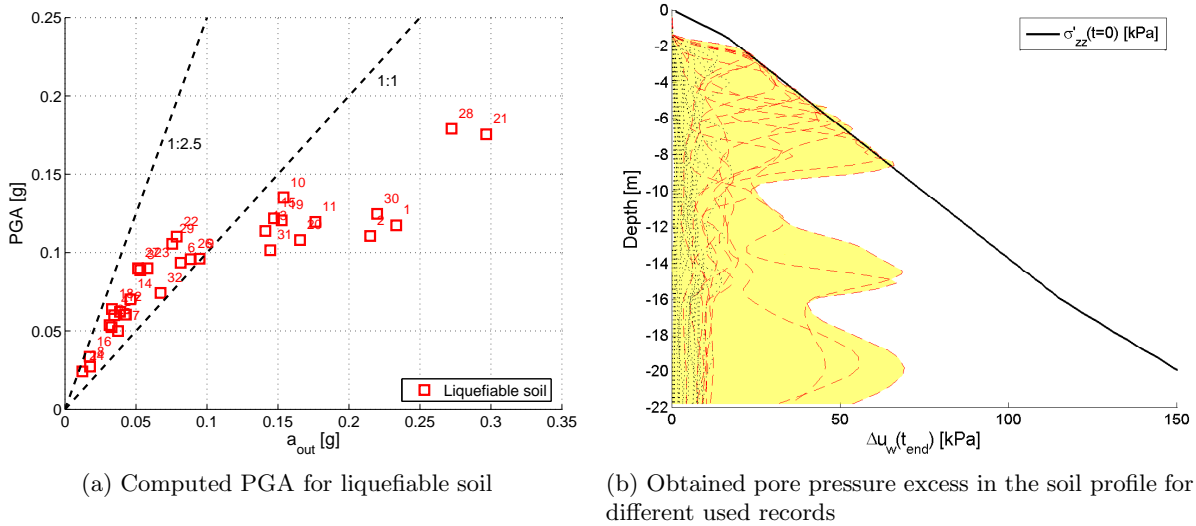
Figure 3.41: Effect of excess pore pressure on free field response

In order to define depth and thickness of zones where liquefaction might take place, Fig.3.41b shows the envelope of induced pore pressure excess Δu_w profile at the end of the analyses (t_{end}). Profiles associated to each motion are displayed in dotted lines. It can be concluded, that depending on the input, liquefaction take places between 2 and 10[m] approximately. However, only strong motions are able to induce liquefaction. In order to study the influence of the frequency content and the severity of the motion on triggering liquefaction, we define the mean liquefaction index $Q(t)$ at a time t as:

$$Q(t) = \frac{1}{\Omega} \int_{\Omega} R_u\left(\underline{x}, t\right) \, dV = \frac{1}{\Omega} \int_{\Omega} \frac{\Delta u_w\left(\underline{x}, t\right)}{\sigma'_{zz}\left(\underline{x}, 0\right)} \, dV \tag{3.11}$$

where $R_u(\underline{x}, t)$ is the pore pressure ratio at a material point $\underline{x}$ at a time t, computed from the pore pressure excess $\Delta u_w(\underline{x}, t)$ and the initial vertical effective stress $\sigma'_{zz}(\underline{x}, 0)$ at the same material point. The control volume Ω is defined as presented in Fig.3.27a in terms of the depth z. According to pore pressure built-up profile on Fig.3.41b, we select a volume of integration between $z = 2$ and $z = 10$[m], where liquefaction phenomenon is expected. Fig.3.42a and b show computed liquefaction index for the 32 used records in terms of a_{out} and AI respectively. It can be noticed that a better correlation

is found for Arias's intensity than for outcrop acceleration amplitude, thus triggering of liquefaction can be better explained by a measure of energy than by a simple amplitude parameter. In this case, for AI_{out} larger than 0.2[m/s] a liquefied zone is found (motions number 1, 2, 10, 11, 15, 21, 22, 28 and 29 highlighted in red dashed lines on Fig.3.41b). The computed $Q(t_{end})$ for these records is larger than 0.3 and the computed PGA is smaller or equal to a_{out}.
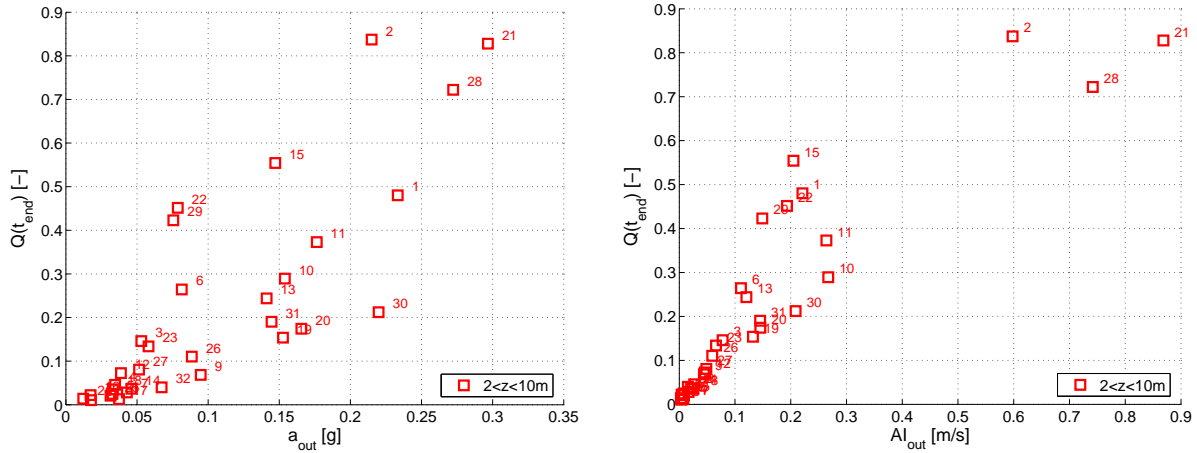
(a) $Q(t_{end})$ in terms of acceleration amplitude at outcrop

(b) Computed $Q(t_{end})$ as a function of Arias'intensity at outcrop

Figure 3.42: Obtained mean liquefaction index at t_{end} in soil profile for different records

Several authors (Koutsourelakis et al., 2002; Popescu, 2002) have suggested that for motions able to induce liquefaction, the liquefaction zone depends on the frequency content of the motion. Tab.3.6 shows soil depths where liquefaction takes places ($R_u(t_{end}) = 1$) and the ratio $\frac{T_m}{T_{soil}}$ between mean period of the input and the first elastic mode of the soil profile T_{soil}. As frequency contents and amplitude change between records, it is difficult to obtain general tendencies. However, these results indicate that liquefaction occurs between $2-3$[m] for records with $T_m < T_{soil}$. When T_m value is near to T_{soil}, a deeper liquefaction zone appears (around 6[m]) in general terms. If $\frac{T_m}{T_{soils}} > 1$, a liquefaction zone is placed near to 5[m]. Theses tendencies agree with the results provided by Lopez-Caballero and Modaressi-Farahmand Razavi (2008) for the same soil profile using scaled natural motions.

Table 3.6: Region of soil where liquefaction is induced

Record	Depth	$\frac{T_m}{T_{soil}}$
1	$3-5$	0.79
2	$3-8$	1.07
6	$2-3$	0.40
10	$5-6$	0.42
11	$2-3$	0.46
15	$2-3$ and $6-7$	0.88
21	$2-5$ and $7-9$	0.95
22	$3-5$	1.07
28	$3-6$	0.95
29	$5-6$	1.05

Very strong motions inducing large liquefaction zones (record number 2, 21 and 28) were recorded in geological conditions corresponding to stiff soil classification according to information available in Ambraseys et al. (2004). This category is associated to a $V_{s,30}$ value larger than 400[m/s]. As concerns these three motions, the range is between $400-450$ [m/s], thus we cannot discard some site effects

related to amplification and frequency modification. These effects might explain exceptionally large values of AI_{out} and large zones of induced liquefaction. We decide not to remove these motions from the database and use them to study high severity behavior.

3.10.2 SSI analysis

The SSI interaction problem on liquefiable soil was studied using the modified plane strain formulation presented in §3.2. Same criteria as described in §3.3.3 were used to construct a suitable FE model for both buildings on liquefiable soil profile. The used FE models are depicted in Fig.3.43. In this case, the soil mesh vertical dimension is increased to 45[m] and a finer mesh is used in potentially liquefiable layers. Total horizontal mesh dimension remains unchanged. Colors displayed in Fig.3.43 are related to different group of elements with different constitutive model parameters. Rectangular regions below foundation correspond to zones where a more refined time step storing was used for detailed post-treatments. As for sandy soil, a soil-foundation interface is included to avoid traction near the foundation corners.

(a) Used mesh for b01 building ($l_a = 4$[m])

(b) Used mesh for b02 building ($l_a = 6$[m])
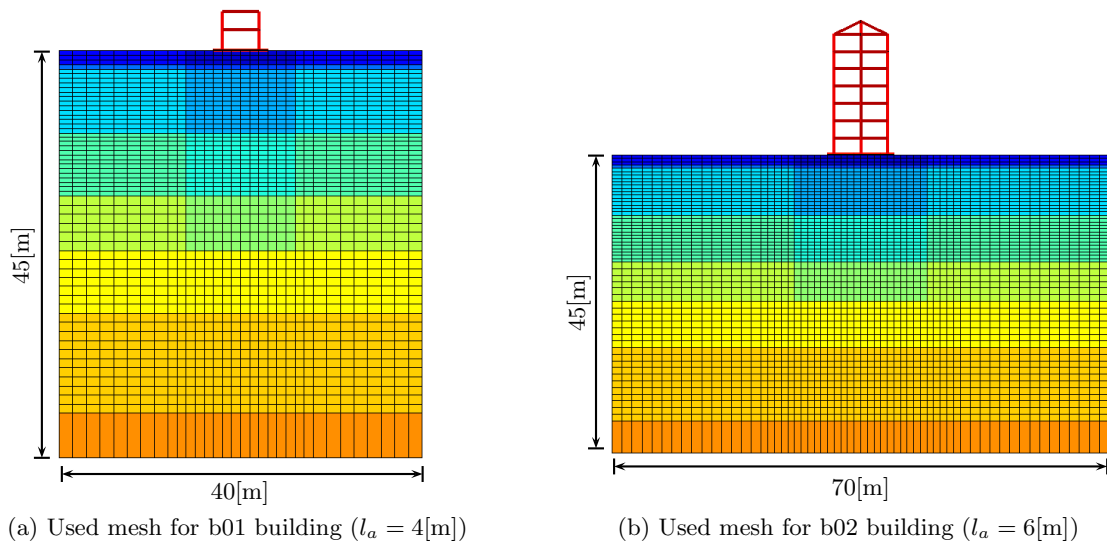
Figure 3.43: Finite element meshes (SSI-FE approach) for liquefaction case

Each analysis is carried out in two steps, starting by a static initialization followed by a dynamical analysis around the computed initial state. Similar validations by comparison with a complete 3D model were carried out to validate the modified plane-strain implementation again. Details concerning these validations are omitted here for sake of simplicity.

3.10.2.1 Dynamic low-strain SSI analysis

Before proceeding to the analysis of liquefaction effects on the non-linear response of the superstructure, a computation of the SSI phenomenon at very low-strain, to ensure elastic behaviour, is performed. Thus, spectral ratios according to schema in Fig.1.11 are computed.

Transfer function modulus of spectral ratios between free field and its vertical projection over the bedrock (ff/bd), between top of the structure and free field (tp/ff) and fixed base are shown in Fig.3.44a for b01 building. First (f_{soil}^1) and second (f_{soil}^2) modal frequencies of the soil profile appear at 1.86 [Hz] and 4.82[Hz], respectively. As the fixed base fundamental frequency of b01 is 4.27[Hz], thus larger than the first mode of the soil profile, SSI effects take place inducing a shift of this frequency to 4.09[Hz] and a reduction of amplitude due to radiation. For b02 building (Fig.3.44b), SSI effects are visible only for the second fixed base mode. In fact, fundamental fixed base frequency of 1.32[Hz] is shorter than f_{soil}^1 and consequently this mode does not interact with soil. A shift of second fixed base frequency from 4.35[Hz] to 4.19[Hz] is evident from this figure. However, this second mode mobilizes
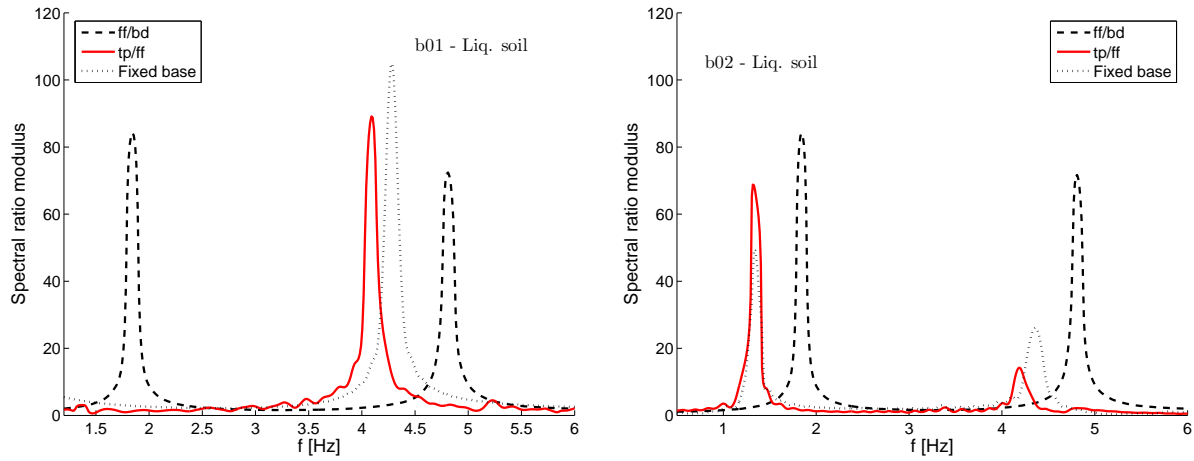
(a) Computed spectral ratios for b01 building on liquefiable soil

(b) Obtained spectral ratios for b02 building on liquefiable soil

Figure 3.44: Computed spectral ratios modulus for liquefiable soil for b01 and b02 building

only 12% of the mass under seismic loading. Even if from low-strain analysis no significant effect of SSI is expected for b02 building, large excess pore pressure generated in the soil alters significantly its non-linear behavior under dynamic loading as will be shown in the next section.

3.10.2.2 Liquefaction below superstructure foundation

The presence of the superstructure imposes an increase in the overburden pressure in the soil below the foundation, thus introduces an additional confinement that modifies the pore pressure build-up under dynamic loading. A variation in extension of the liquefied zone and motion severity required to trigger liquefaction is expected in comparison to free field case.
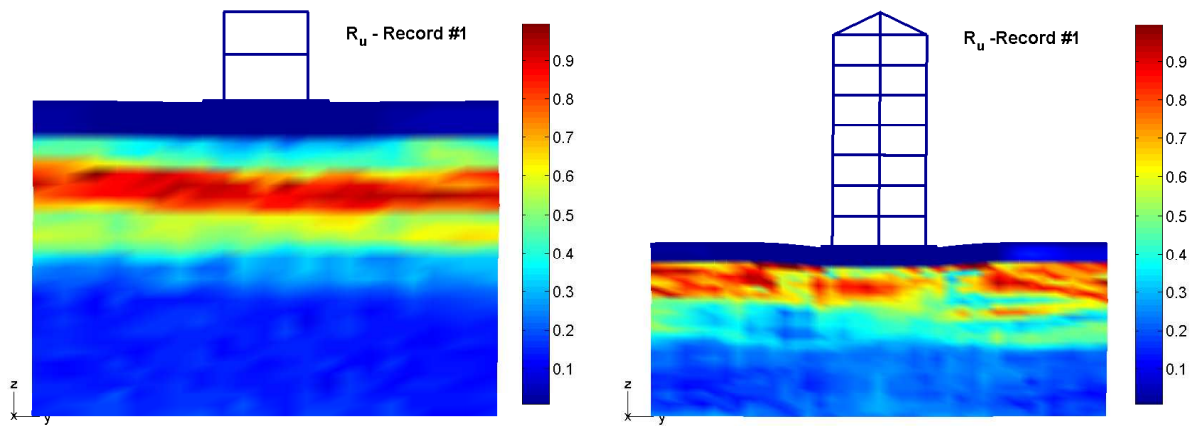
(a) Window of 24×15[m] below foundation for b01

(b) Window of 40×15[m] below foundation for b02

Figure 3.45: Spatial distribution of $R_u(\underline{x}, t_{end})$ for b01 and b02 buildings on liquefiable soil. Deformation magnification factor=5

Contours of $R_u(\underline{x}, t_{end})$ pore pressure ratio with respect to initial effective vertical stress at the end of the analysis for record number 1 are shown in Fig.3.45. For b01 building, it can be noted that the obtained pore pressure excess in the soil below the foundation is not significantly altered. Liquefaction takes place between $3 - 5$[m] as obtained for the free field condition. Nevertheless, for b02 building, the pore pressure ratio is reduced specially near the corners of the foundation. There is, however, significant pore-water pressure build-up and subsequent stiffness degradation below the foundation even for b02 building. This softening generates large coseismic settlements as will be shown later. The

reduction of $R_u(\underline{x}, t_{end})$ is a consequence of the increase of the effective vertical stress σ'_{zz} in Eq.3.11 and the associated reduction of volumetric plastic strains.

(a) $Q(t_{end})$ integrated over a window of 12×8[m] for b01 building

(b) $Q(t_{end})$ integrated over a window of 20×8[m] for b02 building
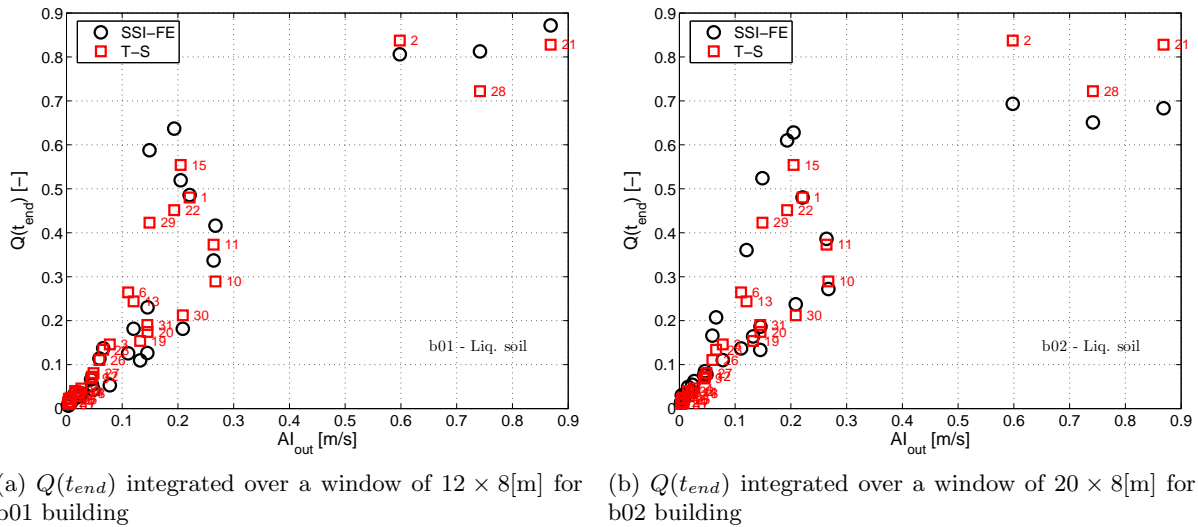
Figure 3.46: Comparison of computed mean liquefaction index at t_{end} for SSI-FE and free field cases.

In order to investigate the effect of the increase of the overburden pressure due to the superstructure's self-weight, Fig.3.46 shows the obtained liquefaction index $Q(t_{end})$ at the end of the analysis for both, SSI-FE and free field compuations. With the purpose to include perturbations below the foundation, the control volume Ω considered for SSI case is defined by 2 times the characteristic length of the foundation ($2a$) in horizontal direction, and from 2 to 10[m] depth in vertical sense. Thus, 12×8[m] for b01 and 20×8[m] for b02 building. According to this figure, not significative difference of $Q(t_{end})$ between the two cases is detected for motions of severity under $AI_{out} < 0.1$[m/s]. In the range of $0.1 \leq AI_{out} \leq 0.3$[m/s], some reductions and increases can be reported depending on the record. In particular the motion number 1 ($AI_{out} = 0.21$[m/s]) displayed in Fig.3.46 shows a very small increase of $Q(t_{end})$ when SSI is taken into account for b01 building and it is approximately constant for b02. Thus, modifications reported in contours of $R_u(t_{end})$ on Fig.3.45 compared to those at free field are not enough to change the value of $Q(t_{end})$. For very strong motions (i.e. $AI_{out} > 0.3$[m/s]), some small increases are obtained for b01 building but large reduction can be noticed for b02 building. It might indicate that for this soil profile, the beneficial effect of overburden pressure on liquefaction appears only for long period strong motions.

Before proceeding to study effect of SSI on liquefiable soil in non-linear structural response, it is interesting to compare obtained response spectra at free field (input for T-S approach) and at the base of the structure. Fig.3.47 shows this comparison for b01 and b02 buildings only for motions inducing liquefaction (listed in Tab.3.6). From Fig.3.47a for b01 building, it can be noticed that no significative variations of amplitude or frequency content is induced by the presence of this superstructure. In this case, some peaks of spectra vanish in short period range and small increase in spectral ordinates is found for large period range. These variations might be associated to modification of initial state and wave radiation from soil-structure interface.

Corresponding comparison for b02 building is presented in Fig.3.47. In this plot, record number 2 has been removed due to some abnormalities detected in dynamic analysis. Accelerations computed for this record at free field and base structure are shown in Fig.3.48. Important peak of accelerations at structural base near to 7[s] can be noticed. It seems that this peak is associated to some failure at soil-structure interface. We decide to remove this motion in the following. Concerning computed response spectra for b02 building, large reduction of spectral ordinates are found around the fundamental fixed base period of b02 probably due to wave radiation around b02 first period. For short period, increase of overburden pressure due to b02 influence reduces pore pressure build-up compared to free field. Thus, attenuation effect at high frequency due to this pore pressure increase is still small. Consequently,

(a) Envelopes of records on Tab.3.6 for b01 building   (b) Envelopes of records on Tab.3.6 for b02 building
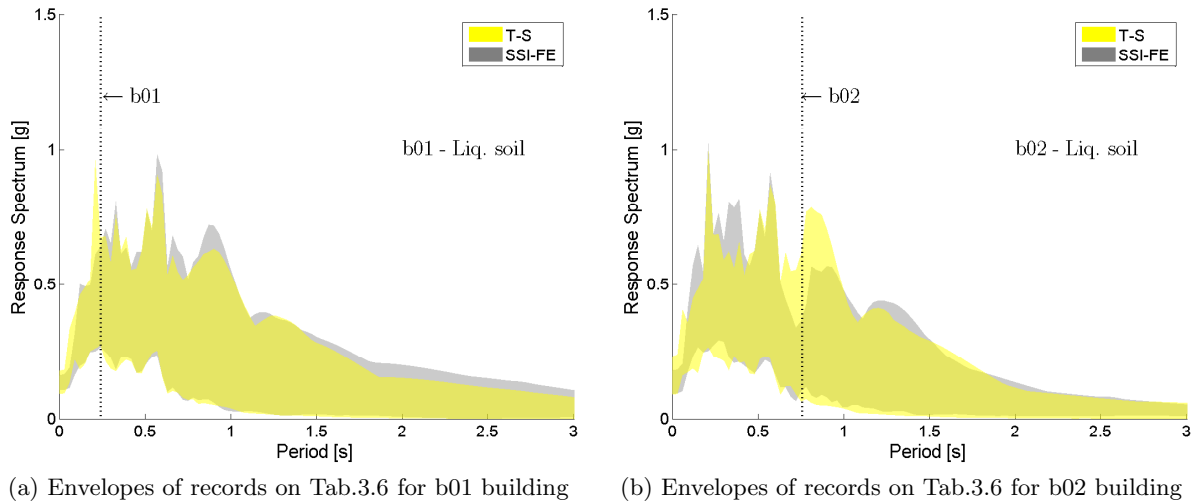
Figure 3.47: Response spectra envelopes at the base of the superstructure for SSI-FE approach and free field for records inducing liquefaction.
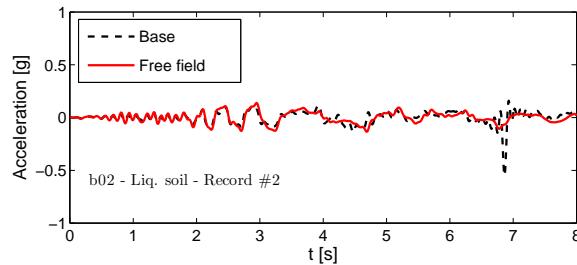
Figure 3.48: Obtained accelerations at free field and base structure level for b02 building on liquefiable soil for record number 2

larger spectral ordinates are found for SSI-FE case compared to free field response.

3.10.2.3   Effect on non-linear structural response

As concerns the influence on seismic structural response of non-linear SSI effects, Fig.3.49 presents the maximum value of the normalized inter-story drift $ISD_{max,\%}$ in the form of scatters plots. According to these results, significative reduction of the computed $ISD_{max,\%}$ are obtained for both b01 and b02 building when the SSI is taken into account. For b01 building, this difference is approximately constant for motions between $0.1 < AI_{out} < 0.3$[m/s]. This difference vanishes for strong motions when liquefaction takes places. For b02 building, similar tendency is observed but with irregular differences.

According to computed response spectra for b01 building (Fig.3.47), these large differences can not be explained by a significant modification of the effective input motion. Thus, large variations found are associated to SSI effects such as radiation damping and fixed base period modification. Nevertheless, differences found for b02 building are partially explained by strong modification of the effective input motion at the structures' base level as highlighted in response spectra envelopes on Fig.3.47.

In order to investigate the effect of SSI on the non-linear behavior of superstructures, Fig.3.50 displays the energy dissipated by the structure (indicator defined in §3.8) as a function of the AI_{out} for both considered buildings. According to responses obtained for b01 building, including non-linear SSI effects in the analysis produces nearly elastic response for the used records database. Thus, damage in b01 building vanishes thanks to additional energy dissipation mechanism introduced by the dynamic soil-structure interaction. For b02 building, a great reduction of the induced damage is noticed, specially for very strong motions. In fact, this remarkable reduction of structural damage
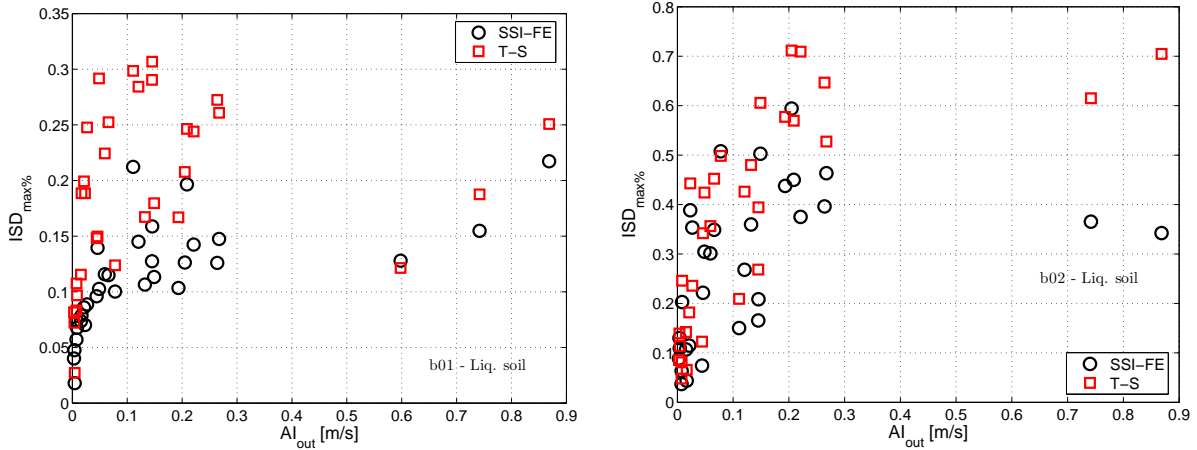
(a) Computed $ISD_{max,\%}$ in terms of outcropping bedrock acceleration amplitude a_{out}

(b) Obtained $ISD_{max,\%}$ in terms of outcropping bedrock Arias's intensity AI_{out}

Figure 3.49: Scatter plots of maximum inter-story drift for b01 and b02 buildings on liquefiable soil
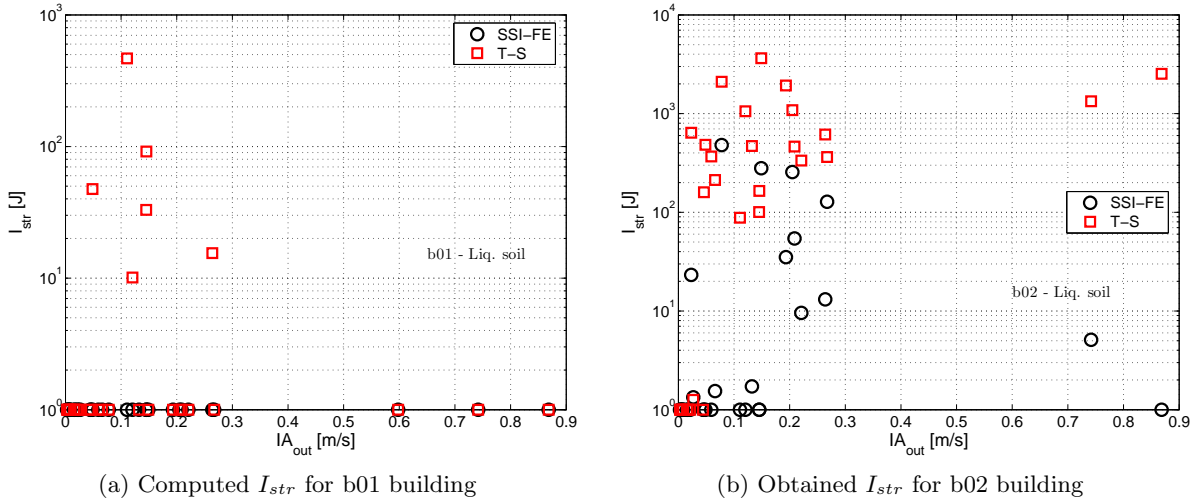
(a) Computed I_{str} for b01 building

(b) Obtained I_{str} for b02 building

Figure 3.50: Scatter plots of energy dissipated by the superstructures on liquefiable soil

is a consequence of massive liquefaction phenomenon at ground level. Due to significant increase in pore-water pressure and subsequent soil stiffness degradation, both structures behave as a rigid block compared to extensively yielded soil. Fig.3.51a illustrates the distribution of the pore pressure increase ratio $R_u(\underline{x}, t_{end})$ at the end of record number 21 for the b02 buildings. According to Fig.3.50, the superstructure behaves elastic for this motion due to the extension of the liquefied soil. This phenomenon is also visible from computed $ISD_{max,\%}$ in Fig.3.49.

Large reduction of structural damage for large Arias intensity should not be misinterpreted as a benefic situation. Even if computed seismic responses are smaller than those obtained for weak motions, large coseismic settlements are associated to severe motions. Computed settlements for b01 and b02 buildings are displayed in Fig.3.51. According to this figure, settlements up to 0.1[m] are computed for very strong motions for b02 building. For this level of deformations, the integrity of the superstructure might be compromised. This phenomenon can explain the response of collapsed structures observed during recent earthquakes, as it is reported by Tokimatsu et al. (1996) or Juang et al. (2005), among others.

(a) Contours of $R_u(t_{end})$ for b02 associated to record # 21. Deformation magnification factor=5

(b) Scatter plot of coseismic settlements for b01 and b02 buildings
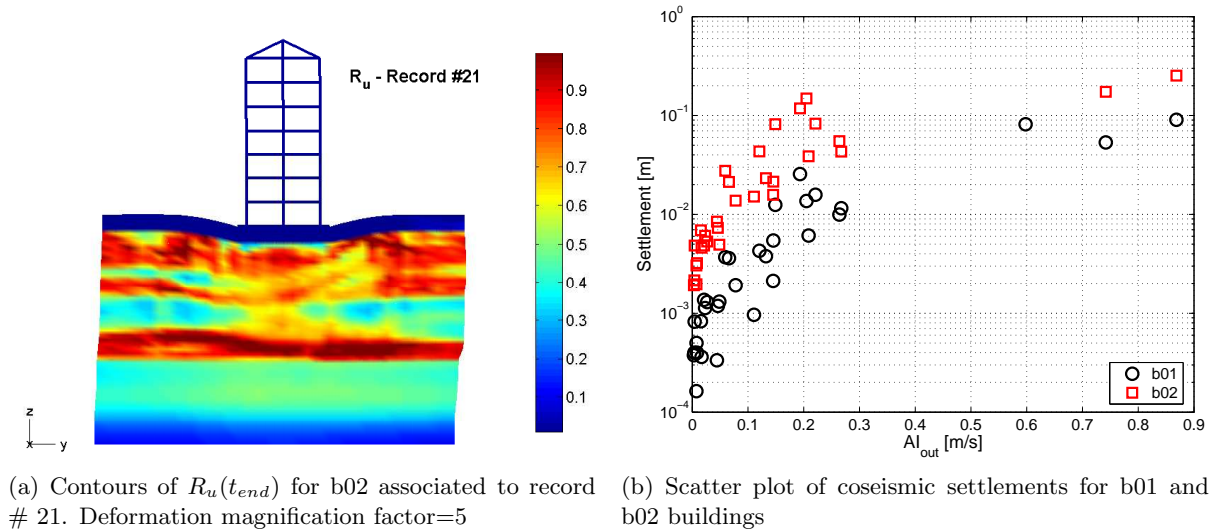
Figure 3.51: Coseismic settlements in liquefiable SSI-FE analysis

3.10.3   Concluding remarks

The results of this section point out the important attenuation of incident field passing through a potentially liquefiable soil region. In free field condition, liquefaction takes places for motions having an Arias intensity larger than 0.2[m/s]. The influence of the frequency content on space distribution of large pore pressure increments has been also highlighted. For strong enough records, the soil profile deamplifies the input motion.

The comparison conducted between free field condition and SSI situation showed that pore water pressure distribution after the stronger part of the motion is significantly modified only for the larger studied superstructure. Effects of the light building seem to be negligible on effective input motion.

Despite relative position of structural fixed base frequency to soil's fundamental modes, large reduction in seismic demand due to SSI effects was found. These significative effects seem to be more related to wave radiation than local soil influence or period lengthening.

In the case of severe motions inducing extensive pore pressure build-up and subsequent liquefaction phenomenon, the superstructure behaves approximately elastic. In this case, structure responds essentially as a rigid block compared to extensive softened soil.

Chapter 4

Effects of elastic and non-linear DSSI on seismic demands of SDOF structures

Contents

4.1 Introduction

The influence of the interaction of the soil with a superstructure on its dynamic behavior has been the subject of numerous investigations assuming linearity of both, superstructure and soil foundation. For elastic systems, first studies for soil-structure interacting systems were conducted by Jennings and Bielak (1973); Veletsos and Meek (1974); Veletsos and Nair (1975) for surface-supported structures. In these works, the effects of the inertial DSSI are summarized by an equivalent SDOF characterizing support ground flexibility and the foundation damping. The effect of the flexible soil is included by modifying the fixed base fundamental period. The foundation damping associated to radiation and soil material damping is introduced by defining an effective damping of the superstructure-foundation system as the sum of a term proportional to viscous damping in the structure plus an equivalent viscous foundation damping. The increase of the natural period and the added foundation damping have been extensively studied by several authors (e.g Veletsos 1977; Luco 1980; Wolf 1985; Avilés and Pérez-Rocha 1996). Nevertheless, this replacement oscillator approach is strictly valid only for elastic superstructure-foundation systems. This aspect is a significant limitation for earthquake engineering, where inelastic superstructure behavior is intentionally accepted. Despite the elastic intrinsic assumption, this approach has been included in several seismic design provisions (e.g. ATC 40 1996; FEMA 356 2000; FEMA 450 2003), using free-field response spectra combined with effective values of both, fundamental period and equivalent viscous damping including elastic DSSI.

In principle, the effect of DSSI may differ between elastic and inelastic systems. Thus, the current interaction provisions based on elastic response studies could not be directly applicable to seismic design of typical buildings, expected to deform considerably beyond the yield limit during severe earthquakes (Avilés and Pérez-Rocha, 2003). According with the works of Veletsos (1977), the yielding of the superstructure can be viewed as a general increase of the relative flexibility between the superstructure and the soil, resulting into a reduction of DSSI effects. Unfortunately, the effects of the DSSI on yielding superstructure systems have not been extensively studied. Theoretical studies conducted by Priestley and Parck (1987) for elastoplastic bridge piers showed that the foundation compliance reduces the ductility capacity of the system. More recently, several other studies using the replacement oscillator technique (Ciampoli and Pinto, 1995; Rodriguez and Montes, 2000; Gazetas and Mylonakis, 2001; Avilés and Pérez-Rocha, 2003), have been conducted in order to elucidate the effect of the DSSI on the maximum required ductility. Similarly, Ghannad and Jahankhah (2007) use the replacement oscillator method to study the effect of DSSI on strength reduction factors of elastoplastic SDOFs. These studies point out some configurations were the DSSI has a considerable effect on the ductility demand of structures.

In the studies listed above, the soil replacement spring and dashpots are selected using frequency-independent approximations of the solutions available for dynamic impedances of rigid footings on elastic soil profiles, using Cone models, or using series of linear springs and dashpots attached to the base foundation. Despite the used method, the numerical values of the soil replacement spring and dashpot are dependent on the shear wave velocity. As shear wave velocity decreases when the soil shear strain increases, some of these authors use degraded shear wave velocity values in their models. Experimental results show that the limit of linear-elastic soil behavior is very low ($\gamma < 10^{-5}$). This shear strain limit is normally exceeded during motions inducing damage of superstructures. Nevertheless, as described in Chapter 3, superstructure's self weight increases the soil confinement under the foundation reducing locally the energy dissipation by hysteresis. Indeed, larger soil energy dissipation takes place in less confined zones. Consequently, the solely modification of the shear wave velocity under the foundation does not seem an appropriate approach to take into account the contribution of the non-linear soil behavior.

Results presented in other chapters of this work highlight the effect of the combined DSSI effects and non-linear soil behavior on the computed structural response, the separation of the contribution of each phenomenon to the total response is not easy to identify due to the complexity of the problem. This chapter describes the investigation conducted in order to compare the contribution of elastic and inelastic DSSI effects on the seismic response.

4.2   Methods of analysis

In order to evaluate the contribution of the elastic DSSI in the modification of the structures' dynamic response studied in previous chapters, two kinds of dynamic time-domain analyses are conducted:

1. Non-linear dynamic fixed base superstructure computations using as input motion the free field acceleration obtained for elastic (TS-E) and non-linear (TS-N) soil columns.

2. Complete dynamic soil-foundation-superstructure FE analyses, considering elastic (SSI-E) and non-linear (SSI-N) soil behavior.

Both, TS-N and TS-E cases take into account non-linear structural behavior but neglect DSSI effects. Complete DSSI analyses, SSI-E or SSI-N, include dynamic interaction effects and superstructure material non-linearities. Details regarding each model, assumptions and parameters are provided in the following.

4.2.1   Superstructure modeling

The superstructures considered in this chapter are modeled by a massless continuous column (§1.3.2) of height h with a single mass m on top. The foundation is assumed square of side a (Fig.4.1a). These superstructures respond as a SDOF system with a fundamental period T_0 in fixed-base condition. Damping is assumed to be hysteretic, controlled by the non-linear constitutive model of the column. Numerical values of properties characterizing each SDOF are selected on the basis of the classification of building types used in HAZUS-MH MR3 (2003).

(a) Schematic representation of superstructure model

(b) Reference capacity curve according to HAZUS-MH MR3 (2003)
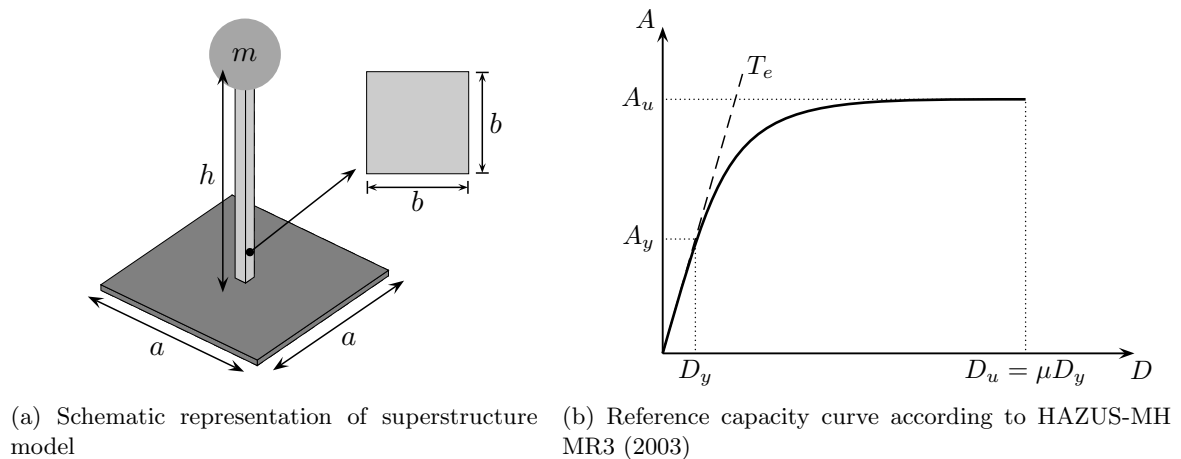
Figure 4.1: Superstructure's SDOF representation and generic capacity curve

According to this document, reinforced concrete moment frame buildings can be classified, as shown in the first four columns of Tab.4.1, in terms of the total height and/or the number of stories. In this work, only C1L (low-rise) and C1M (mid-rise) categories are explored. In order to define the geometric parameters describing the SDOFs, we start assuming a height. The typical height suggested in Tab.4.1 is selected as height of the equivalent SDOF, i.e. 6 and 15[m], for low-rise and mid-rise structures, respectively. The choice of the foundation dimension a is based on the slender ratio $\frac{h}{a}$. As usually the slender ratio increase with the number of stories of a building, we select slender ratios of 1 and 1.5 for C1L and C1M categories, respectively. The total weight/mass is defined assuming a number of levels and a uniform weight distribution of $\rho g = 10$[kN/m3] over each level. Assuming 3 and 5 levels, we obtain a total weight (mg) of 1080 and 5000[kN] for C1L and C1M, respectively.

In the HAZUS-MH MR3 (2003) methodology, some reference parameters are given to develop capacity curves (Fig.4.1b). The value of these parameters depend on the conformity of the studied building to modern seismic design provisions. In this way, four levels are defined: High-Code, Moderate-Code, Low-Code and Pre-Code. Last four columns of Tab.4.1 show the reference fundamental-mode

Table 4.1: Reinforced concrete moment frame classification and capacity parameters according to HAZUS-MH MR3 (2003)

Building type	Description	Stories range	Typical height [m]	T_e [s]	A_y range [g]	A_u range [g]	μ range
C1L	Low-rise	$1-3$	6	0.4	$0.040-0.160$	$0.119-0.479$	$8-5$
C1M	Mid-rise	$4-7$	15.2	0.75	$0.033-0.133$	$0.099-0.399$	$5.3-3.3$
C1H	High-rise	$8+$	36.6	1.45	$0.014-0.055$	$0.042-0.166$	$4-2.5$

period T_e of the building depending on its type, the ranges of the control points of the fragility curve A_y and A_u and the range of ductility μ, defined by different seismic code conformity. In this table, A_y corresponds to the yield capacity representing the true lateral strength of the building and A_u the ultimate capacity when the system reaches the fully plastic state.
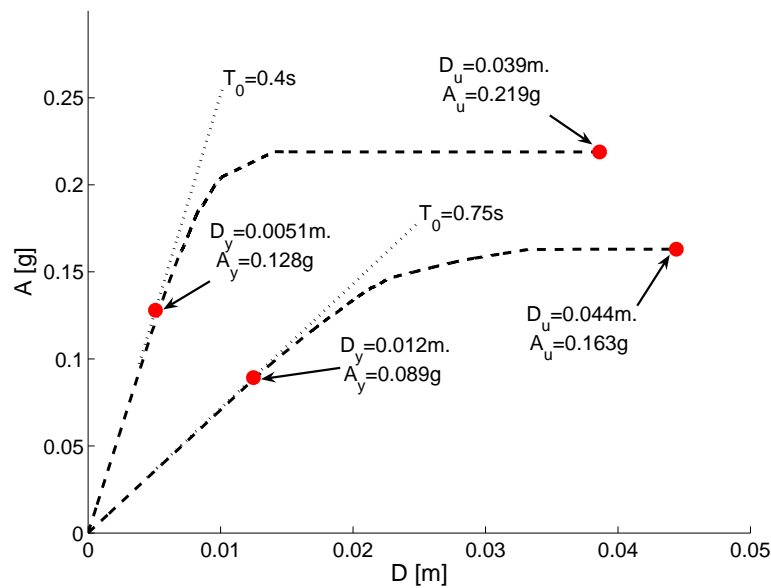
Figure 4.2: Computed capacity curves for C1L and C1M SDOFs

The provided value of T_e is fixed as the target value for T_0. The stiffness of the cantilever column of the SDOF model (Fig.4.1a) is computed using the value of T_0 and m, assuming a constant square transversal section and a fixed value of the Young modulus E. To model the post-yielding behavior, we use the constitutive model described in Appendix C. Thus, the values of the hardening modulus E_t and initial yield stress σ_y are selected in order to obtain a capacity curve compatible with the ranges defined in Tab.4.1. Parameters describing the used geometrical configuration and material properties are listed in Tab.4.2. The corresponding capacity curves are shown in Fig.4.2. It can be noticed that a maximum ductility μ of 7.6 and 3.7 are computed for C1L and C1M, respectively. These values, satisfy the ranges displayed in Tab.4.1 and correspond approximately to a Moderate-Code conformity.

Table 4.2: Properties of studied studied SDOFs

Label	T_0 [s]	h [m]	a [m]	b [m]	E [MPa]	σ_y [MPa]	E_t [Pa]
C1L	0.40	6.0	6.0	0.98	25.5×10^3	6.0	0.1
C1M	0.75	15.0	10.0	2.09	25.5×10^3	5.5	0.1

4.2.2 Soil profiles' description

In this chapter, we consider the same soil profiles as the previous chapter and described in §3.3.2. Thus, a dry and a saturated homogenous dense Toyoura sand profiles of 30[m] depth, overlying an elastic bedrock are used. The effect of the stiffness increasing with depth is shown in Fig.3.4a in terms of free field low-strain shear velocity profile. As discussed in previous chapters, the superstructure's self weight increases locally the confinement below the foundation. This additional confinement increases the low-strain shear wave velocity as shown in Fig.4.3 for both, dry and saturated cases. These profiles were computed at the center of the foundation in the DSSI analyses using FE models described in §4.2.4.

(a) Low-strain shear wave profiles for dry case   (b) Low-strain shear wave profiles for saturated case
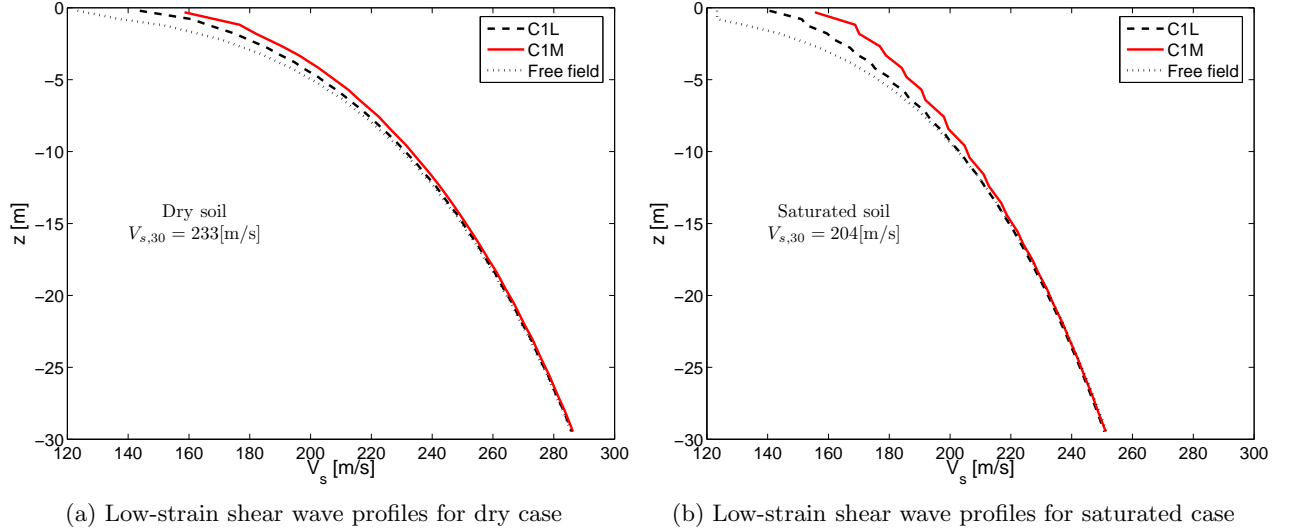
Figure 4.3: Low-strain shear wave velocity profiles of studied medium dense sand profile under dry and fully saturated conditions. Influence of superstructure's self weight

According to Fig.4.3, the influence of the superstructure on the low-strain shear wave velocity reaches approximately 7 and 15[m] depth, for C1L and C1M structures, respectively. Indeed, in the saturated case, as the initial effective stresses are reduced due to the water table, the over stress imposed by the superstructure has a relatively larger influence on the effective confinement and consequently on the soil stiffness. Despite these variations, the spectral ratio amplitudes between free field and bedrock, shown in Fig.3.4b, are not much modified and remain unchanged. The computed values of the average shear wave velocity in the upper 30[m] ($V_{s,30}$) are shown in Fig.4.3 for each soil column. The elastic first periods of the soils (T_{soil}) are 0.46[s] and 0.54[s], for dry and saturated cases, respectively.

As described above, two kind of constitutive models were used for describing the soil's dynamic behavior: a non-linear elastic model and an elasto-plastic one (Appendix E). In both constitutive models, the influence of the soil confinement is taken into account by a non-linear approach governed by the expression (E.4) in terms of reference elastic modulus (K_{ref} and G_{ref}), the mean effective compressive stress (p') and the coefficient n_e defining the degree of non-linearity. As identical values of elastic parameters and n_e coefficient have been used for both constitutive models, the low-strain shear wave profiles shown in Fig.4.3 are valid for both cases. The parameters describing elasto-plastic constitutive model have been calibrated by simulating laboratory soil test (Appendix H) for both dry and saturated condition, using the methodology described in §1.3.4. Variations of initial critical pressure p_{c_0} and hardening variables due to in-situ densities are neglected, thus a homogenous soil profile obeying the set of parameters provided in the second column of Tab.H.1 is assumed. In saturated condition, a porosity n of 0.54 and an isotropic permeability of $k_x = k_y = k_z = 10^{-4}$[m/s] are supposed. A compressibility of the fluid equal to $K_f = 9.38 \times 10^{-8}$[1/Pa] is adopted.

4.2.3   Fixed base two-step analyses: TS-E and TS-N

Similarly to other chapters, the approach consists in solving firstly the shear wave propagation problem for a soil column model obeying the same constitutive model as the full 3D computations. In this case, the corresponding FE model is composed of 3D solid elements using the same vertical discretization as the one used for complete 3D DSSI models. The computed free field motion is imposed afterward as input accelerogram to fixed base models described in §4.2.1. This approach takes into account inelastic behavior of the soil (TS-N) and the superstructure (TS-E and TS-N), but neglects dynamical interaction effects. As the wave propagation part of the problem is solved in free field condition, variations of the low-strain shear wave profile due to over stress imposed by the weight of the superstructure are not considered.

4.2.4   Complete DSSI models: SSI-E and SSI-N

Similarly to FE models described in other chapters, the complete DSSI models are composed of the superstructure, the foundation, the soil and a part of the underlying bedrock. Due to 3D nature of the problem, we use 3D meshes in this case. Indeed, modified-plane strain approach presented in §3.2 requires periodicity across an axis normal to dynamic loading and a rigid foundation. This requirement is not satisfied for a general SDOF model on a finite foundation. This assumption of periodicity was implicitly used in computations presented in Chapter 2. In the study presented in this part of the work we relax this hypothesis analyzing the more general 3D case. Unfortunately, the required time of run in this 3D case increases drastically compared to modified plane-strain approach. For this reason, the number of ground motions considered was reduced.

(a) C1L on dry soil

(b) C1L on saturated soil
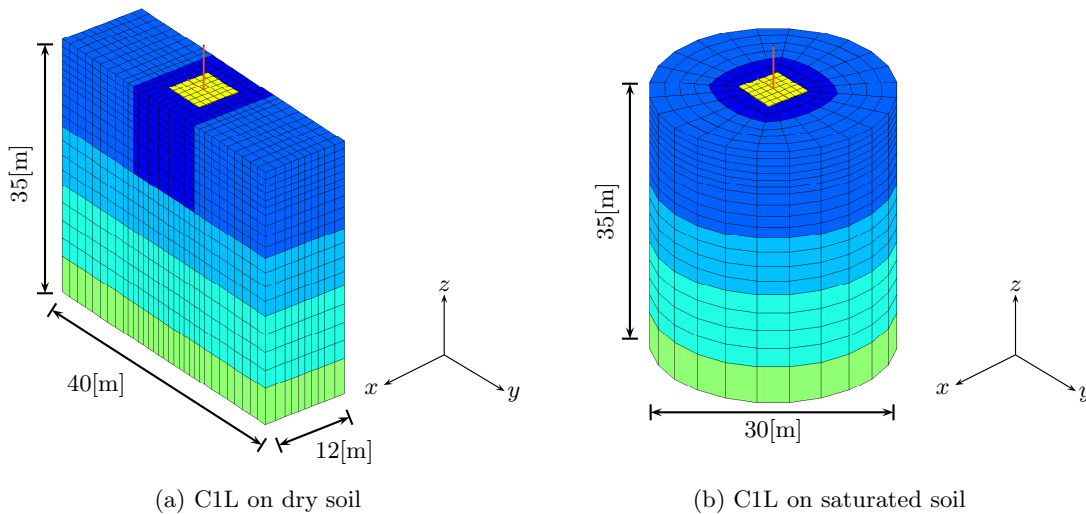
Figure 4.4: Finite element meshes for FE DSSI models corresponding to C1L superstructure

The 30[m] deep homogenous soil deposits considered are modeled by 8 nodes 3D solid elements with displacements and pressure (in saturated case) DOFs. The foundation is supposed to be rigid and modeled also by 8 node 3D volume elements with very stiff mechanical properties. In saturated condition, the ground water level is assumed to be at surface (z=0[m]). The so-called $u-p$ formulation used in this case is described in §1.2. We assume impervious condition for both foundation and bedrock. At the bottom of the mesh, paraxial elements described in Appendix A are used to impose the incident motion and ensure damping by radiation. Lateral limits of the mesh are considered to be far enough from the structure so that periodic condition are verified on them. Consequently, tied condition discussed in §1.4 have been imposed on the lateral limits of the meshes. the lateral boundaries are considered water tight too. The dimensions of each mesh have been chosen controlling the cleanness of the responses in frequency domain at an approximate free field control point. Details about the numerical validation of the used FE models by comparison with a substructure frequency-domain

approach (Appendix G) are provided in §1.4.2. As expected, the size of the required mesh grows with the mass of the superstructure. The DSSI FE meshes corresponding to C1L and C1M superstructures are shown in Fig.4.4 and Fig.4.5, respectively.

(a) C1M on dry soil   (b) C1M on saturated soil
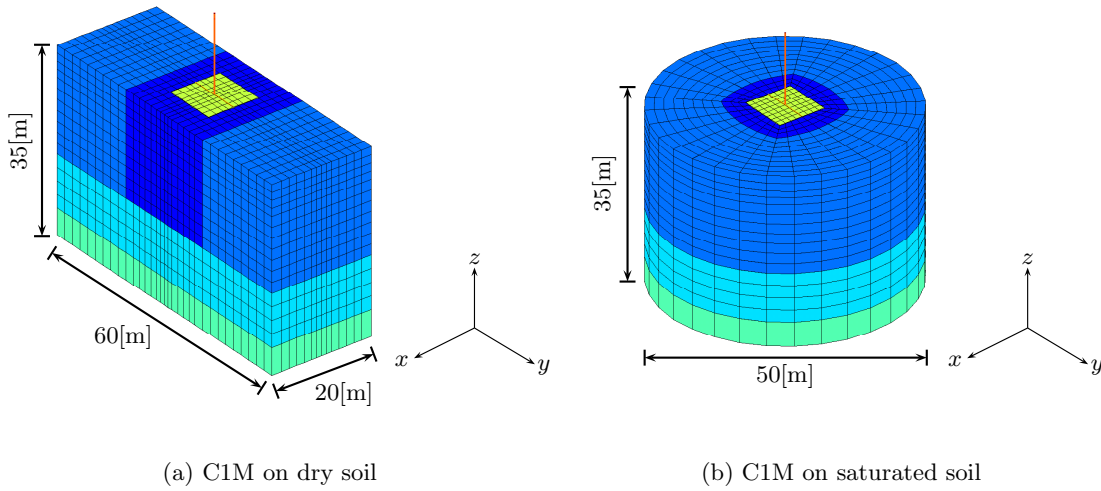
Figure 4.5: Finite element meshes for FE DSSI models corresponding to C1M superstructure

Colors displayed on meshes of these figures are related to different vertical dimension of elements. Darker colors close to the foundations correspond to a finer mesh zone used to compute some non-linear behavior indicators. It can be noticed that box soil geometries are used for dry cases and cylindrical ones are used for saturated cases. Indeed, hydraulic boundary conditions at the corners of a box mesh are delicate to model when the water table coincides with the free surface level in dynamics. In these corners, null normal flow must be ensured for lateral boundaries and free surface condition ($p = 0$) has to be imposed at $z = 0$ level. In the static initialization and superstructure construction steps, no particular difficulties were encountered. Nevertheless, under dynamical load, a flow from the superficial corners to the interior of the mesh takes place inducing unsaturation in these zones. Due to this induced flow, the soil near to the mesh corners dilates unrealistically. Several tests varying the geometry and the flow equation form were conducted in order to encompass these effects. Among these tests, the best results were obtained when the corners are eliminated using a cylindrical mesh for the soil (Fig.4.4b and Fig.4.5b).

(a) Boundary conditions for static analysis

(b) boundary conditions for dynamic analysis
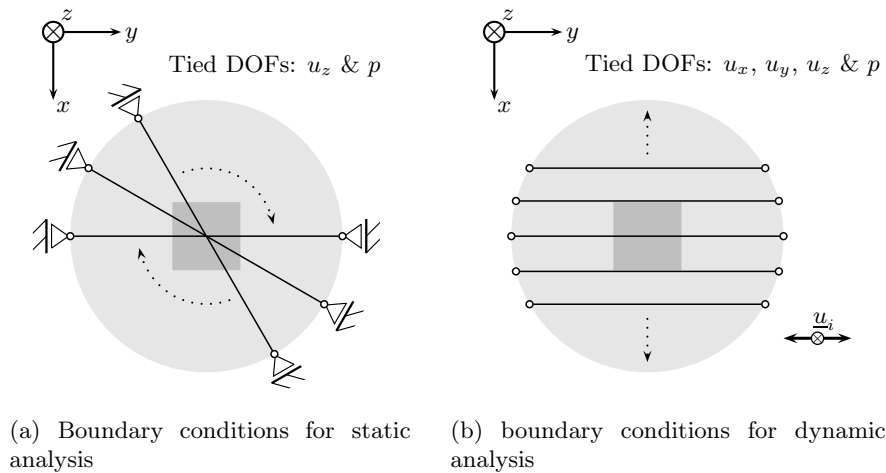
Figure 4.6: Tied nodes approach for cylindrical meshes

For these cylindrical meshes, the tied nodes approach described in §1.4 have been slightly adapted in both static and dynamic analyses. The static configuration is shown in Fig.4.6a. In this part of

the computation, we impose radial tied constraint as if the problem was axi-symmetric. Indeed, even if the problem is not perfectly axi-symmetrical in statics due to the square form of the foundation, we select lateral limits far enough to avoid border effects. In dynamic case, we impose tied nodes across the direction of the imposed shaking in order to impose shear-beam-like kinematics. We impose incident motions normal to one of the sides of square foundation for the sake of simplicity. Tied conditions for box-type meshes are shown in Fig.1.10b. Dynamic part of the analysis is conducted from the equilibrated state obtained in the static part of the analysis. Consequently, displacements, deformations, velocities and accelerations field correspond to a dynamic perturbation field around the static equilibrium.

4.2.5 Strong motion selection

Analogously to other studies conducted in this work for the strong motion, we use the selection criteria described in §3.5. Due to significant time consumption of the full soil-superstructure 3D models used in the analyses described in this chapter, each experiment was repeated only two times, thus a total of 16 runs for each structure on each soil profile have been conducted. The corresponding motions are the first two selections provided in Appendix J.1 compatible with Metropolitan France.

4.3 Elastic DSSI

In order to highlight the influence of the elastic DSSI on the elastic dynamic response of the studied SDOFs, this section presents some spectral ratio amplitudes computed for C1L and C1M superstructures on both, dry and saturated homogenous sandy soils. We use the convention depicted in Fig.1.11 to indicate spectral ratios between free field and bedrock (ff/bd) and between the top of the structure and free field (tp/ff). The free field (ff) and bedrock (bd) control points are placed as far as possible from the superstructure, depending on the corresponding FE mesh. Indeed, the curves presented below were used to control the cleanness of the free field responses obtained in order to define a suitable mesh with a reasonable degree of wave reflections on its lateral borders.

(a) ff/bd spectral ratio for dry soil   (b) ff/bd spectral ratio for saturated soil
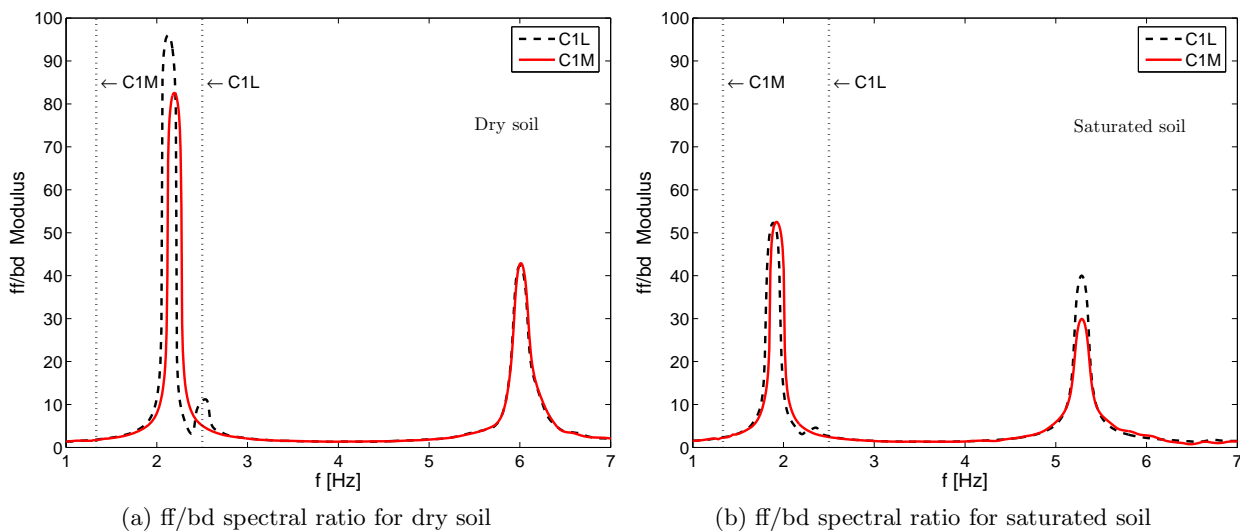
Figure 4.7: Elastic spectral ratio modulus between free field and vertical projection on bedrock

The obtained spectral ratio modulus between a free field control point and its vertical projection on the bedrock are displayed in Fig.4.7. In dry soil condition (Fig.4.7a), some evidences of the superstructure is found at the free field for the C1L SDOF structure. No perturbation appears for the C1M superstructure. This result is related to the relative position of the fixed base fundamental frequency of the superstructure compared to the elastic frequencies of the soil profile. In C1L case, its

fundamental frequency is relatively close to first elastic period of the soil, thus some resonance between both systems takes place. In the contrary, the first fixed base frequency of the C1M SDOF structure is relatively far from the first elastic frequency of the soil profile. Similarly, in the saturated soil case, some perturbations around the fundamental fixed base frequency of the C1L superstructure are found. No effect of the C1M SDOF structure is noticed. Differences between spectral ratio amplitudes computed for dry and saturated case are associated to the reduction of effective stresses due to the presence of pore water. Some small frequency shifts of the first elastic mode as well as amplitude variations can be noticed depending on the superstructure considered. This shift might be related to local confinement variation below the superstructure foundation. However, as meshes used in both cases are not identical, these variations could be also associated to wave dispersion and reflections. Additionally, as computations are carried out in time domain, spectral ratio computations in frequency domain involve interpolations, filtering and smoothing procedures. These numerical procedures could also induce some shift in main frequencies and variation of amplitudes.

(a) ff/bd spectral ratio for dry soil (b) ff/bd spectral ratio for saturated soil
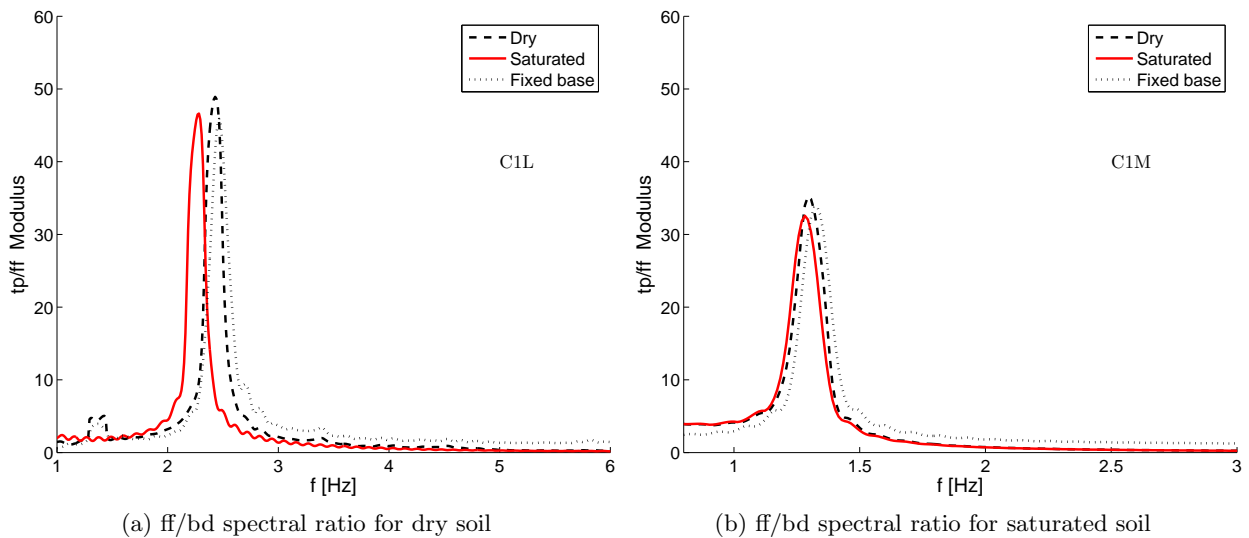
Figure 4.8: Elastic spectral ratio modulus between free field and vertical projection on bedrock

Spectral ratio amplitudes between the top of the structure and the free field control point (tp/ff) computed for both structures, in dry and saturated soils, are shown in Fig.4.8. According to Fig.4.8a for the C1L SDOF structure, no significative interaction is found for dry soil. In the saturated case, a more important shift in the fundamental frequency is found. No important modifications on the amplitudes due to radiative damping is noticed for both soils. Regarding the C1M SDOF, relatively reduced DSSI effects are found in both, dry and saturated cases. Nevertheless, in saturated soil condition, a slightly larger shift in fundamental frequency can be noticed. Concerning the added damping, a very small reduction in the amplitude of the spectral ratio is found in saturated condition.

4.4 Soil response

In order to define the input motion for TS-E and TS-N approaches, the wave propagation part of the problem is solved using a 1D FE column. Fig.4.9 shows the responses for both soils in terms of the amplitude of the acceleration at free field (PGA) and the amplitude of the acceleration imposed at outcrop (a_{out}) for the 16 motions considered in this part of the work.

When the elastoplastic behavior of the soil is taken into account, the amplification of the soil deposit decays with the amplitude. Consequently, for strong motions, large accelerations are obtained when the elastic model is used. At low amplitude, as the response is essentially elastic, responses computed using both models are equivalent. The limit between elastic and non-linear behavior depends on the soil. For dry case, motions having an a_{out} large than $0.1g$ induce non-linearities that attenuate

(a) Dry soil   (b) Saturated soil
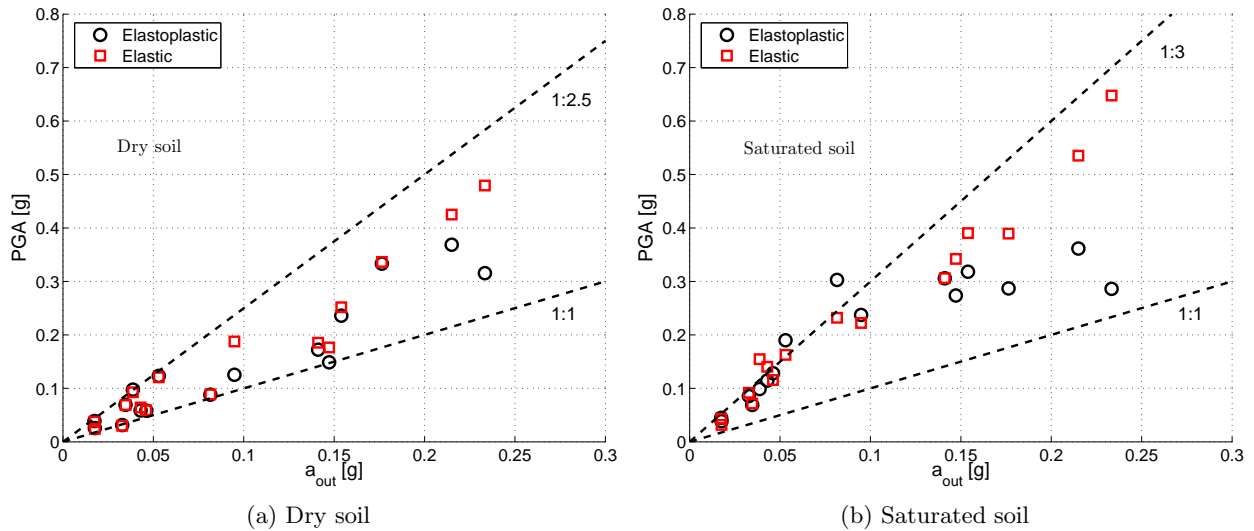
Figure 4.9: Computed PGA as a function of the acceleration amplitude imposed at outcropping bedrock a_{out}

the amplification. This limit is reduced when the soil is saturated. In this last case, for a_{out} larger than $0.03g$ the non-linear behavior takes place. The variation in this limit is related to the initial stiffness of the soil. Assuming that a similar shear stress is imposed by an earthquake independently of the soil properties, smaller strains are obtained for stiffer soils. Consequently, the saturated soil undergoes larger shear strain producing more hysteretic behavior for small levels of imposed shear stress compared to dry case. Differences between elastic and inelastic soil acceleration amplification grow in general with the amplitude. In dry case, relatively small variations are obtained for $a_{out} < 0.2g$. For larger outcrop amplitudes, significant differences are noticed between two behaviors. In saturated case, large differences start at $0.15g$. In this last hydraulic condition, there are three moderate motions ($0.05g < a_{out} < 0.1g$) exhibiting larger amplification in the inelastic case compared to the elastic one. This behavior might be related to the frequency content of the motion relative to inelastic transfer function of the soil profile during the motion. As discussed in §3.6 in terms of free field response spectra, the pore pressure build-up during the earthquake can acts as a frequency filter modifying significantly the frequency characteristic of the obtained motion at free field. When an elastic behavior model is considered, shear strains do not induce volumetric strains. Consequently, pore pressure build up does not take place and the filter effect vanishes.

In order to illustrate differences of the soil amplification in frequency domain, Fig.4.10 shows the envelopes of response spectra computed at free field for both soils, using the elastoplastic model and the elastic one. In dry soil condition, large differences in spectral ordinates can be noticed between 0.2 and 0.6[s] approximately. For large periods, spectral amplitudes are equivalent. Consequently, the effective motion transmitted to C1L SDOF in dry soil will be significantly different if an elastic or a plastic model is used. For the C1M SDOF, spectral ordinates are similar for both soil constitutive models in a practical point of view. For saturated soil, strong variations of spectral ordinates can be noticed for periods small than 0.7[s] on Fig.4.10b. In this case, when the elastoplastic constitutive model is used, large ordinates are computed in the range of $0.7 - 1.5$[s]. Thus, large structural responses are expected for C1L when the soil is assumed to behave elastically, but equivalent or even large structural responses will be obtained when the soil behaves in a non-linear manner for the C1M superstructure. Consequently, according to spectral envelopes displayed in Fig.4.10, neglecting non-linear soil behavior is in principle non conservative for superstructures lying in the range of $0.7 - 1.6$[s] in terms of seismic demand.

(a) Envelopes of response spectra for dry soil

(b) Envelopes of response spectra for saturated soil
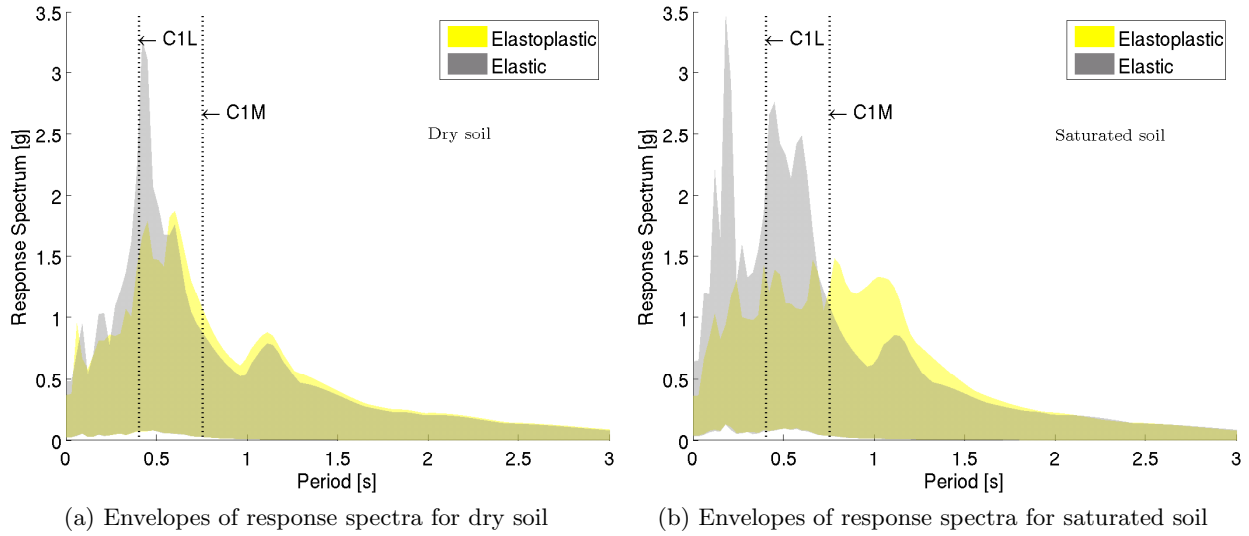
Figure 4.10: Comparison between response at free field for dry and saturated soil using elastic an elastoplastic constitutive models

4.5 Effect of DSSI on the seismic displacement demand

In order to study the influence of the elastic and inelastic DSSI on the superstructure, this section presents computed displacement demand for different combinations of soil, superstructure and soil constitutive models according to two-step and full 3D approaches described in §4.2. Results are presented in the form of scatter plots of the computed ductility ratio demand μ defined as:

$$\mu = \frac{1}{D_y} \max_t \left\{ u^{top}(t) - u^{base}(t) - h.\theta(t) \right\} \tag{4.1}$$

where $u^{top}(t)$ and $u^{base}(t)$ are the nodal displacement time histories computed at the top and at the base of the SDOF in the direction of the seismic loading, respectively. $\theta(t)$ is the rigid body rotation (tilt) time history of the superstructure in full 3D models and h is its height. D_y is the corresponding yield displacement shown in Fig.4.2. If the obtained value of μ is less than 1, the structure behaves elastically and a value of $\mu = 1$ is imposed. For two-step computations, the base displacement u^{base} and the rigid body rotation θ are equal to zero, thus the ductility ratio is directly computed with the maximum top displacement and D_y.

In order to use a common reference for different type of computations, we use motion's severity measures at outcropping. Nevertheless, the effective motion transmitted to superstructure varies in each case due to local soil condition and DSSI effects. As discussed in previous chapters, measures of energy of the input motion show better correlation with the dynamic responses than pure amplitude measures. Consequently, we use Arias intensities at outcropping AI_{out} hereinafter. Concerning the used strong motion database, unrealistic displacement demands were obtained for the record number 2 of Appendix J.1. Even if this motion has been reported as recorded on very stiff soil, an approximatively two-times larger AI_{out} is associated to this motion compared to other records in the selection, suggesting some site effects. As results of these observations, we decide to remove this motion from the set of results.

4.5.1 C1L SDOF structure on dry soil

Fig.4.11 shows the obtained ductility ratios for the C1L SDOF on dry soil, for both elastic and inelastic soil constitutive models. Results displayed in Fig.4.11a correspond to SSI-N and TS-N computations, thus considering hysteretic soil behavior. Those corresponding to elastic soil behavior are presented

(a) Elastoplastic soil behavior   (b) Elastic soil behavior
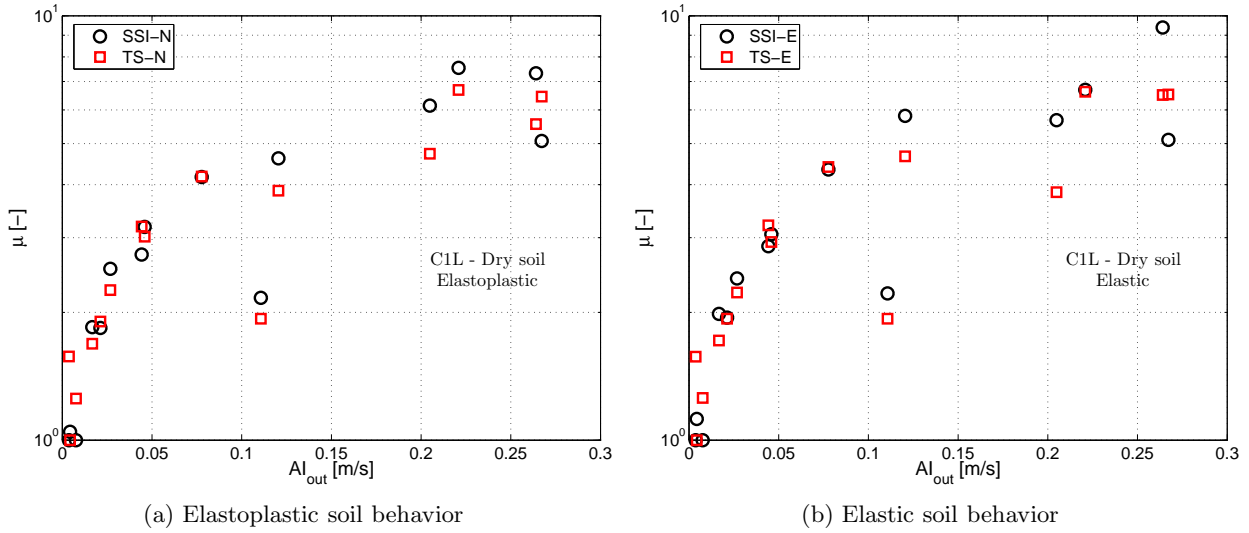
Figure 4.11: Computed ductility demand μ in terms of Arias intensity at outcropping bedrock for C1L SDOF on the dry soil

in Fig.4.11b. We use logarithmic scale in μ axis to appreciate differences at low values of ductility ratios. In both cases, for very weak motions ($AI_{out} < 0.03$[m/s]), large ductility ratios are obtained when DSSI effects are neglected, thus μ obtained in TS-N or TS-E approaches are larger than those obtained for SSI-N or SSI-E computations. In the intermediary range ($0.03 < AI_{out} < 0.1$), variations are erratic, so that depending on the motion, DSSI has a favorable or a detrimental effect on the computed ductility ratios. Clearer differences between two-step and full DSSI computations appear for motions having $AI_{out} > 0.1$. In this range, DSSI has, in general, a detrimental effect independently of the constitutive model used for the soil.

(a) Motion number 10   (b) Motion number 13
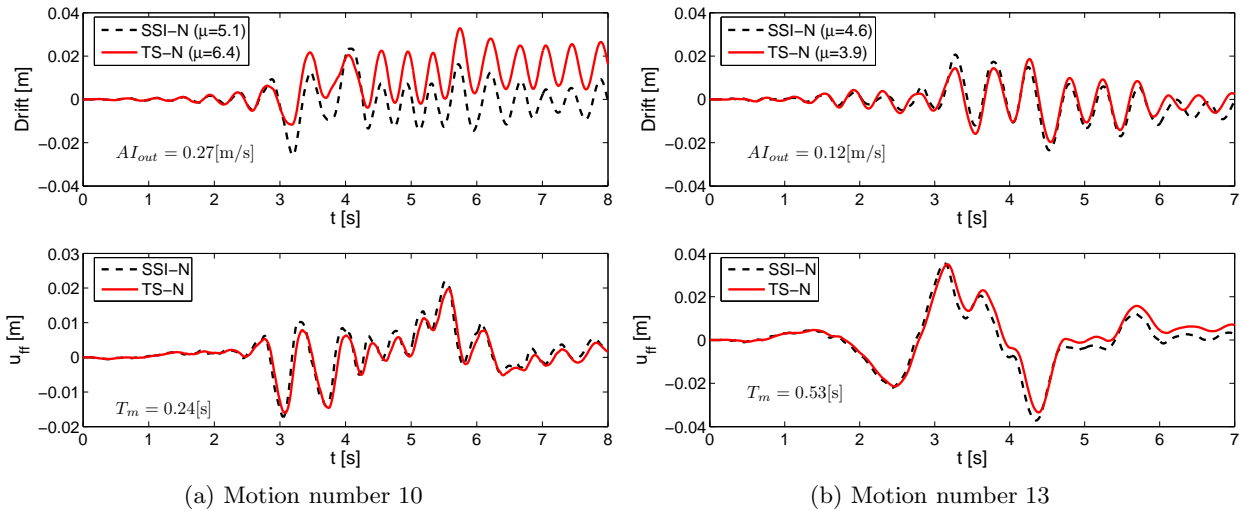
Figure 4.12: Structural drift and free field displacement u_{ff} of the C1L SDOF for some motions assuming elastoplastic behavior for the soil

The reduction of μ for severe motions is in opposite to the tendency found in the others part of this work. This unexpected behavior might be related to the modification of the properties of the local soil below the foundation and the relative position of the fundamental frequencies of the superstructure and the soil compared to the frequency content of the motions. In order to investigate these explanations, Fig.4.12 and 4.13 show some time responses in terms of the structural drift and the

free field displacement u_{ff}. We select two motions exhibiting opposite tendencies in terms of ductility ratio but having an AI_{out} larger than 0.1[m/s]. The free field displacements are provided to control the clearness of the dynamic response of the complete 3D models.

(a) Motion number 10   (b) Motion number 13
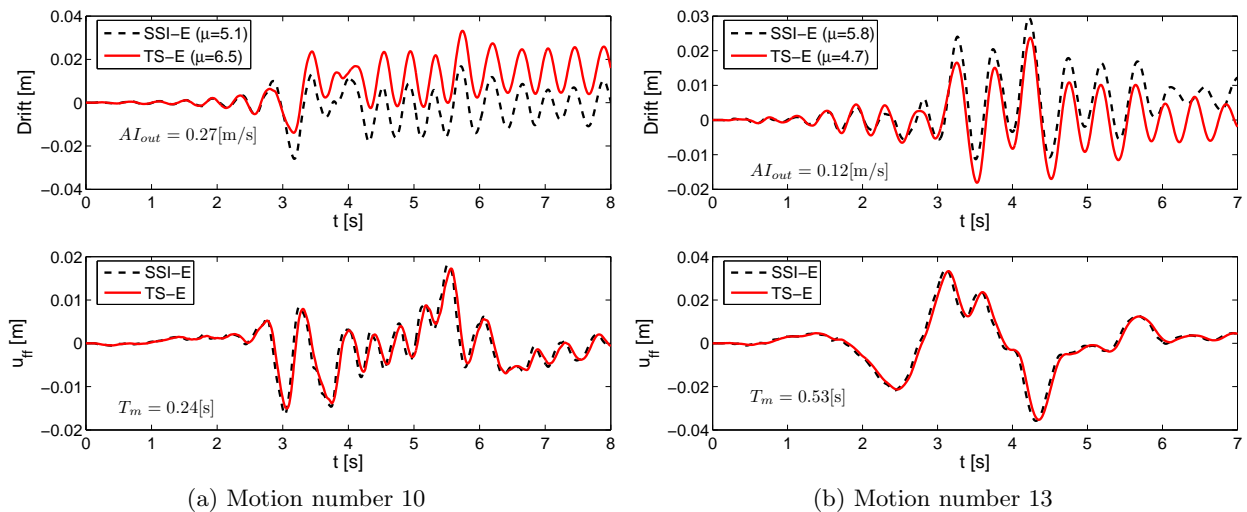
Figure 4.13: Structural drift and free field displacement u_{ff} for some motions assuming elastic behavior for the soil. C1L SDOF

Fig.4.12 and 4.13 show the computed displacements for motions number 10 and 13 of Appendix J.1 using elastoplastic and elastic soil constitutive models, respectively. For motion number 10, DSSI has a favorable effect, whereas DSSI has detrimental influence for motion number 13. For both motions, the computed free field displacement using a simple column (TS-N or TS-E) is similar to those obtained at free field control points of the full 3D computations (SSI-N or SSI-E). Due to the severity of the motion number 10 ($AI_{out} = 0.27$[m/s]), the soil undergoes plastic deformations when the elastoplastic model is considered. Comparing the free field response for this motion between SSI-N/TS-N and SSI-E/TS-E, a good agreement is in general found. However, the agreement is better in elastic cases. Consequently, when soil's non-linear behavior is taken into account, some influence of the superstructure takes place at free field control point. Similar conclusions can be derived for motion number 13. These effects might be reduced by increasing the size of the FE model with a consequent increase in the run time consumption, nevertheless free field responses seem accurate enough from a practical point of view.

Concerning the structural drift, responses are clearly different in Figs.4.12a and 4.13a when DSSI effects are taken into account for motion number 10. In these figures, differences in the structural response appear at 2.8[s] approximately. This effect appears independently of the adopted model for the soil, suggesting a pure DSSI influence. In this time step of analysis, it seems that strong non-linearities take place in the superstructure modifying its subsequent dynamic response. Regarding the motion number 13, differences between fixed base computations and fully 3D models are visible mainly in peaks of time-drift response. As the main period of the motion $T_m = 0.53$[s] is close to the first elastic period of the soil of 0.46[s], these differences could be associated to some resonance between the input and the soil neglected when the analysis is decoupled in two steps.

4.5.2 C1L SDOF structure on saturated soil

Results in terms of the computed ductility ratio following SSI-N/TS-N and SSI-E/TS-E approaches for the saturated soil are shown in Fig.4.14. Similar tendency as the one observed in dry case can be noticed for very weak motions ($AI_{out} < 0.03$[m/s]), thus a reduction of the computed ductility demand ratio. As concerns the range $0.03 < AI_{out} < 0.1$[m/s], the responses are erratic, hence depending on the motion an increase or a reduction in ductility demand is observed. For moderate to severe motion ($AI_{out} > 0.1$[m/s]) different conclusions can be derived depending on the assumption taken for the soil

(a) Elastoplastic soil behavior   (b) Elastic soil behavior
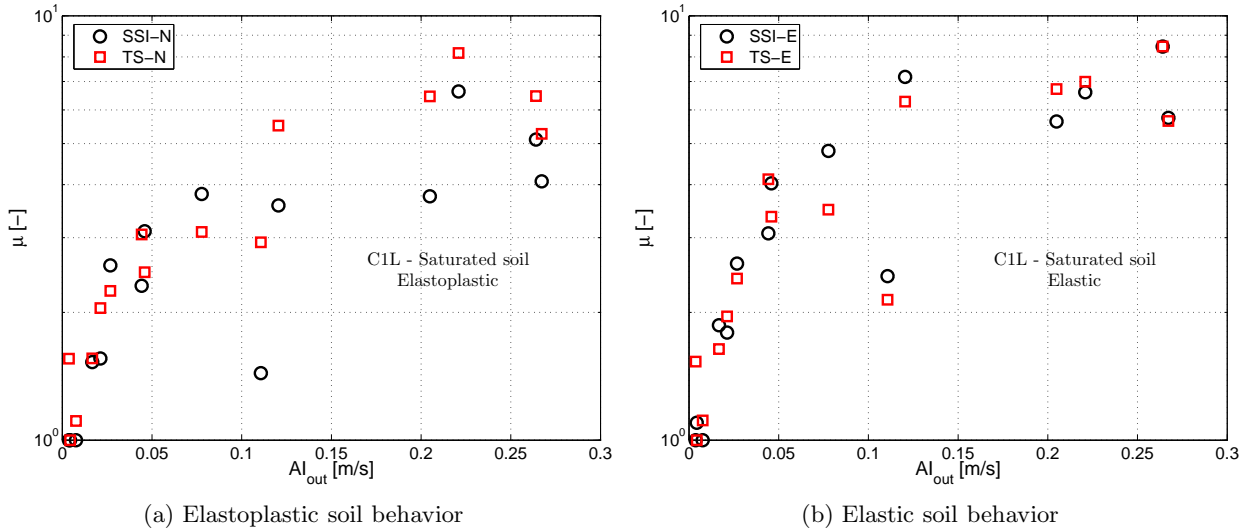
Figure 4.14: Computed ductility demand μ in terms of Arias intensity at outcropping bedrock for C1L SDOF on saturated soil

(a) Elastoplastic soil model   (b) Elastic soil model
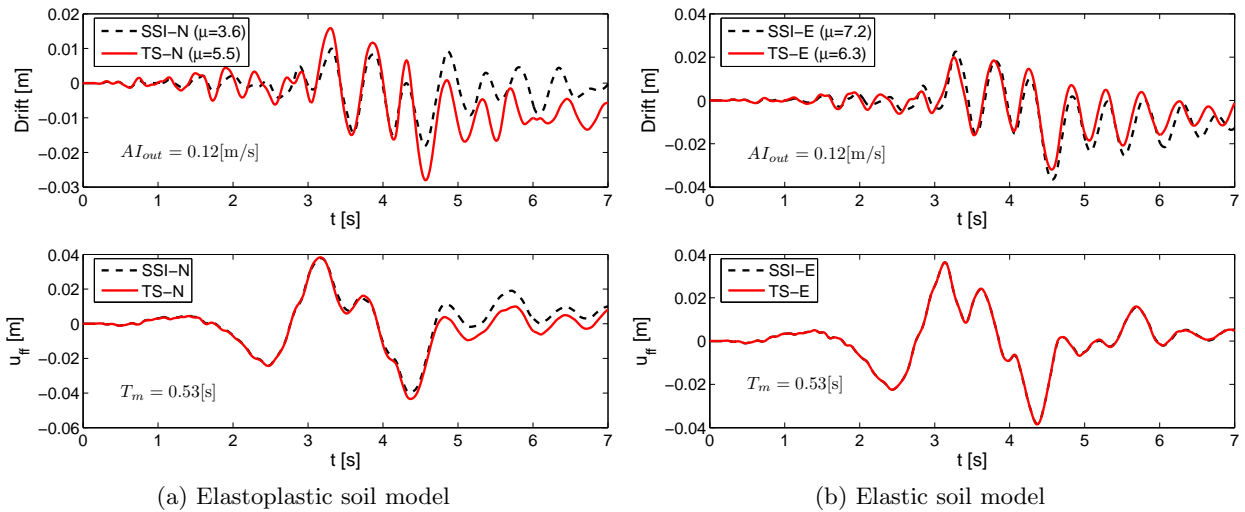
Figure 4.15: Structural drift and free field displacement u_{ff} obtained using motion number 13 for C1L SDOF structure and saturated soil

behavior. In the inelastic soil case (Fig.4.14a), all the considered cases show a reduction on the ductility demand when DSSI effects are taken into account. These results agree with the observations presented in others chapters, when significative reductions of seismic displacement were found DSSI are included in saturated soils. Under elastic soil assumption, this reduction is only noticed for motions for which $AI_{out} > 0.2[m/s]$. In fact, when the soil is modeled as a two-phase media and the inelastic soil's skeleton deformations are taken into account, volumetric deformations take place under dynamic loading. When the soil is assumed to behave elastically, pure shear strains do not induce volumetric variations and consequently the pore pressure build up does not take place. This pore pressure evolution contributes hardly to soil stiffness degradation and to hysteric soil damping. Consequently, the elastic soil behavior assumption is a crude hypothesis for the two-phase case. Additional details about the soil hysteretic behavior during the load are provided in §4.6 in terms of some energy dissipation measures. In general, comparing SSI versus TS responses, results are relatively close in elastic case (Fig.4.14b) compared to the inelastic one (Fig.4.14a). Thus, for this particular case, pure elastic DSSI considerations can not explain differences found for ductility demands when the inelastic soil behavior is taken into account

in the DSSI problem.

Time responses of structural drift and free field displacement computed for the motion number 13 in saturated soil case are shown in Fig.4.15, for both inelastic and elastic soil models. Under elastoplastic soil behavior assumption, DSSI are benefic in terms of ductility demand, whereas they are detrimental when elastic behavior is assumed for the soil. Similarly to the dry case, a good agreement is found between free field responses found in full 3D computation and 1D wave propagation model. In fact, when the soil behaves elastically free field responses match perfectly. In inelastic case, some slight differences are found. Regarding the structural response, large differences are found when the soil behaves inelastically. In elastic case, variations are mainly associated to peak amplitudes. The increment of the structural drift when DSSI effects are included might be related to some resonance between the frequency content of the ground motion ($T_m = 0.53$[s]) and the first elastic period of the soil (0.54[s] in saturated case). These effects do not take place when inelastic behavior is included probably due to stiffness degradation of the soil and the filter effect of the water. Indeed, these effects induce a reduction of the ductility demand when non-linear DSSI is included.

4.5.3 C1M SDOF structure on dry soil

As concerns mid-rise SDOF (C1M), obtained ductility demand ratios for dry soil case are shown in Fig.4.16a and b, for elastoplastic and elastic soil models, respectively. The non-linear structural behavior is developed for motions having a severity $AI_{out} > 0.03$[m/s] approximately. The ductility demand ratio grows in general monotonically with AI_{out}, proving that this parameter is a suitable measure to relate the input motion with the expected structural damage. Only the motion number 6 ($AI_{out} = 0.11$[m/s]) does not show structural damage despite its severity. Indeed, this motion has a mean period T_m of 0.23[s], hence the major part of the energy is delivered in a spectral range relatively far from the fundamental period of the superstructure ($T_0 = 0.75$[s]). This explanation is confirmed by the motion number 13 ($AI_{out} = 0.13$[m/s]), having $T_m = 0.53$[s] relatively close to fixed base fundamental period of the C1M SDOF structure. For this last motion, inelastic structural behavior takes place and the general tendency is confirmed.

(a) Elastoplastic soil behavior   (b) Elastic soil behavior
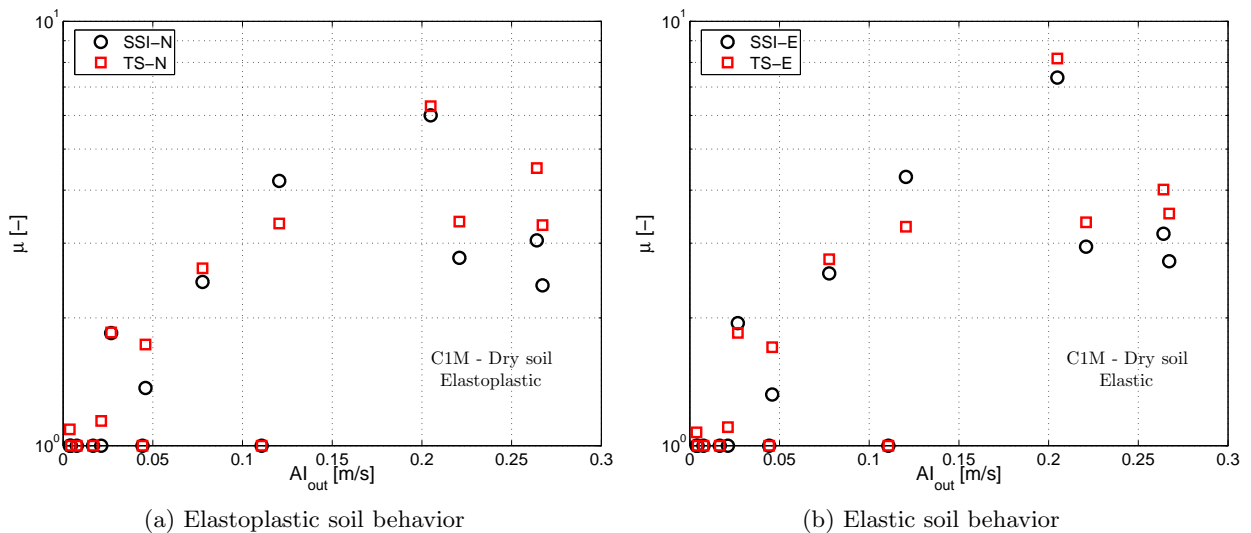
Figure 4.16: Computed ductility demand μ in terms of Arias intensity at outcropping for C1M SDOF structure on dry soil

Regarding the effects of the DSSI on the superstructure response, the results depicted in Fig.4.16 agree with the tendency found in other parts of this work, thus a general reduction of the seismic demand when DSSI are included. In contrast with responses obtained for C1L SDOF in dry soil (Fig.4.11), only one motion exhibits a clear detrimental effect of DSSI. Time responses in terms of structural drift and free field displacements are provided in Fig.4.17 for both, inelastic and elastic

(a) Elastoplastic soil model   (b) Elastic soil model
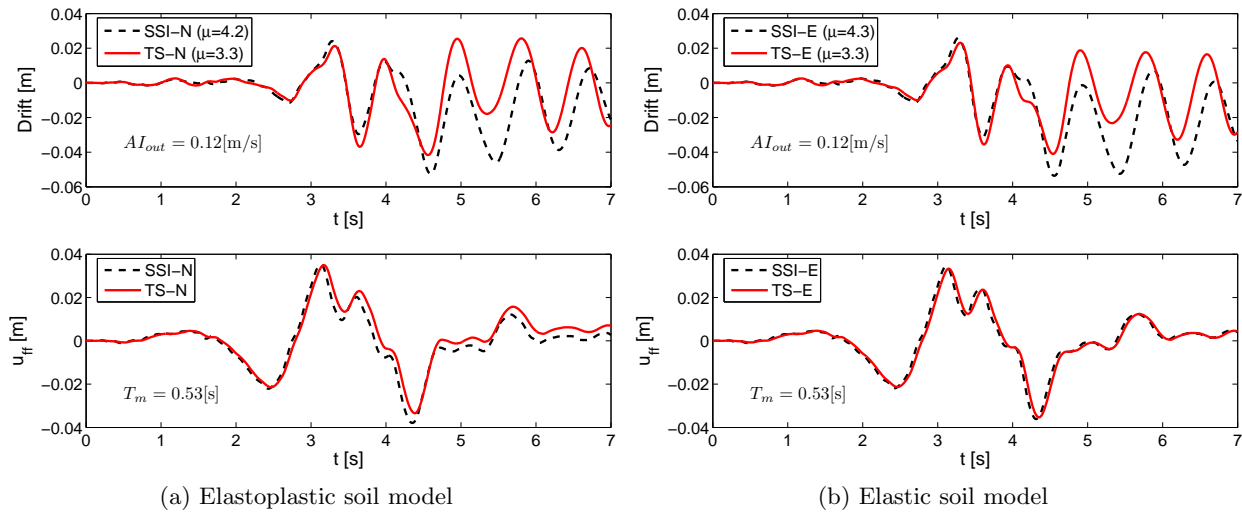
Figure 4.17: Structural drift and free field displacement u_{ff} for motion number 13 in dry soil. C1M SDOF

models. In both figures, responses at free field between 1D soil column and complete 3D models are equivalent, thus no domain truncation effects seem to take place. As the mean period of this motion ($T_m = 0.53[\text{s}]$) is relatively close to the first elastic period of the soil ($0.46[\text{s}]$), some resonance phenomena between soil and input motion might explain these differences.

On the basis of the responses displayed in Fig.4.16 and Fig.4.11, the non-linear soil behavior has a negligible effect on the superstructure's dynamic response when the soil is in dry condition. Indeed, the effect of the DSSI on the computed ductility demand is similar if the soil is assumed to behave elastically or inelastically regardless of the soil behavior. Consequently, for this soil and in the range of motion severities studied in this work, an elastic DSSI analysis seems to be accurate enough to take into account interaction effects. Moreover, the effect of neglecting DSSI can be conservative or may not depend on the considered motion as noticed for C1L SDOF structure. As C1M is more slender and massive than C1L, larger dynamic soil-structure interaction effects seem to take place due to the superstructure rocking.

4.5.4 C1M SDOF structure on saturated soil

Concerning C1M SDOF structure on saturated soil, Fig.4.18 shows seismic ductility demand ratios computed following SSI-N/TS-N and SSI-E/TS-E approaches. Similarly to responses obtained for C1L structure on saturated soil, when inelastic soil behavior is taken into account DSSI is benefic, thus a reduction of μ is noticed for almost all the considered motions. When the soil is assumed to behave elastically, the effect of DSSI can be beneficial or detrimental depending on the motion characteristics. Consequently, in contrast with the tendency observed for dry soil, elastic soil behavior assumption is a crude approximation to asses DSSI effects in this case. As previously indicated for elastic soil cases, no coupling between shear and volumetric strains is obtained for pure cyclic shear loading. Hence, variations on pore pressure during dynamic loading are neglected. In practice, depending on the soil contraction/dilation characteristics, strong pore pressure build-up might take places inducing large reductions in soil effective stresses which can result in soil stiffness degradation.

(a) Elastoplastic soil behavior

(b) Elastic soil behavior
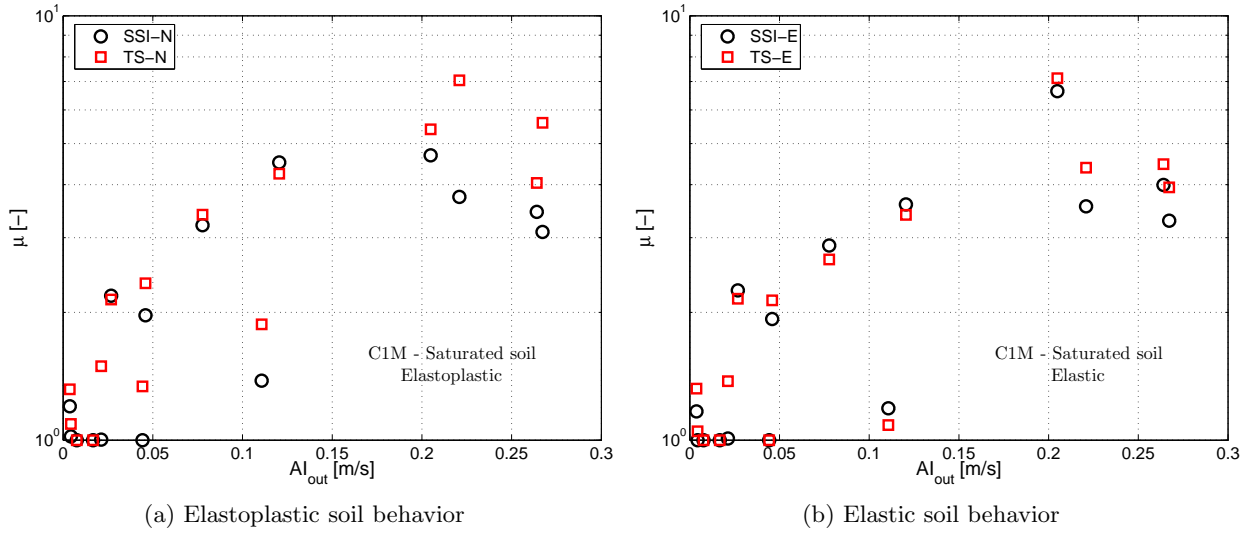
Figure 4.18: Computed ductility demand μ in terms of Arias intensity at outcropping for C1M SDOF structure on saturated soil

4.5.5 Effect of the DSSI on the displacement ductility demand ratio

In order to summarize the effect of taking into account or neglecting inelastic soil behavior on the seismic demand, we compute the ratio:

$$\frac{\mu_{SSI}}{\mu_{TS}} \tag{4.2}$$

where μ_{SSI} and μ_{TS} are the displacement ductility demands obtained from SSI-N or SSI-E and TS-N or TS-E, respectively. A value of this ratio larger than one means detrimental DSSI effects, and the opposite when the value is inferior to the unity.

(a) Variation in terms of AI_{out}

(b) Variation in terms of T_m
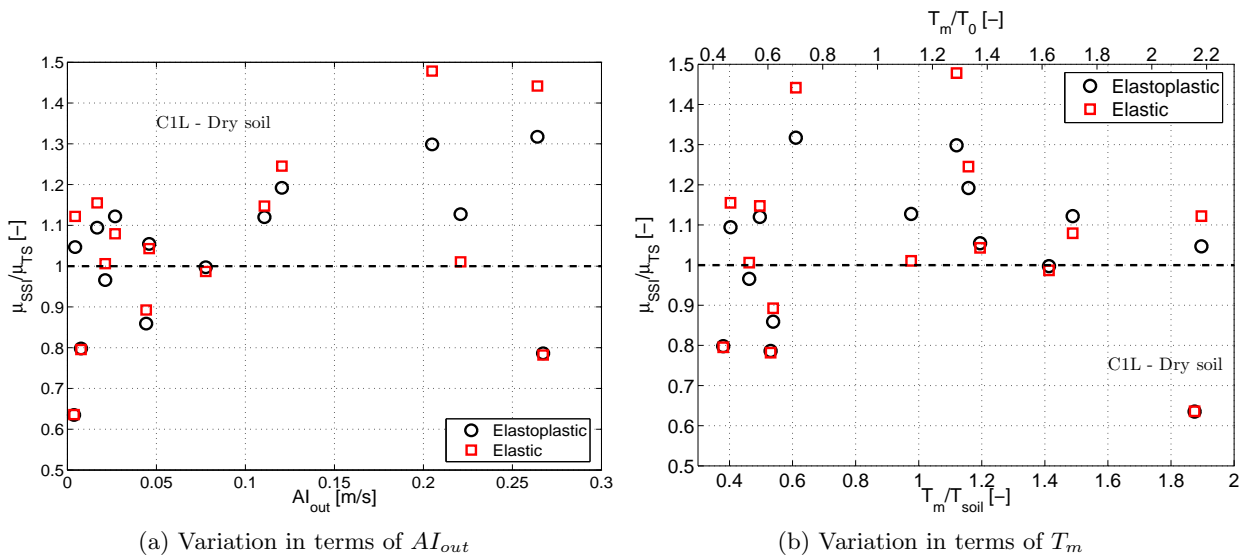
Figure 4.19: Scatter plots of μ ratios for the C1L SDOF on dry soil

Fig.4.19 displays the ductility ratio for dry soil for the C1L SDOF, assuming elastoplastic or elastic soil behaviors. According to this figure, assuming elastic or inelastic soil behavior does not modify the general tendency of the DSSI. Hence, motions exhibiting values larger than one for elastic soil, are also larger than one for inelastic soil. For this SDOF on dry soil, variations are inferior to ±25% for the

major part of motions. In terms of the input motion severity (Fig.4.19a), the beneficial or detrimental effect of the DSSI are erratic for motions with $AI_{out} < 0.1$[m/s]. For stronger motions, the tendency of the DSSI effect is in general detrimental except for the most severe motion considered (number 10). In order to highlight the effect of the frequency content, Fig.4.19b shows the μ ratio in terms of the T_m normalized by the first elastic soil period T_{soil} (bottom horizontal axis) or the fixed base fundamental period T_0 (top horizontal axis). For relatively large T_m ($\frac{T_m}{T_0}$ or $\frac{T_m}{T_{soils}}$ large than 1.8), taking into account DSSI tends to be beneficial. For short T_m periods ($\frac{T_m}{T_0}$ or $\frac{T_m}{T_{soils}}$ inferior to 0.8) the effect of DSSI is beneficial or detrimental depending on the considered motion. In the approximate resonance range between motion and soil ($\frac{T_m}{T_{soil}}$ relatively close to 1), the DSSI is detrimental or negligible. According to our computations, results for C1L structure on dry soil are extremely erratic in general, consequently, more motions should be analyzed before any general tendencies could be derived.

(a) Variation in terms of AI_{out}

(b) Variation in terms of T_m
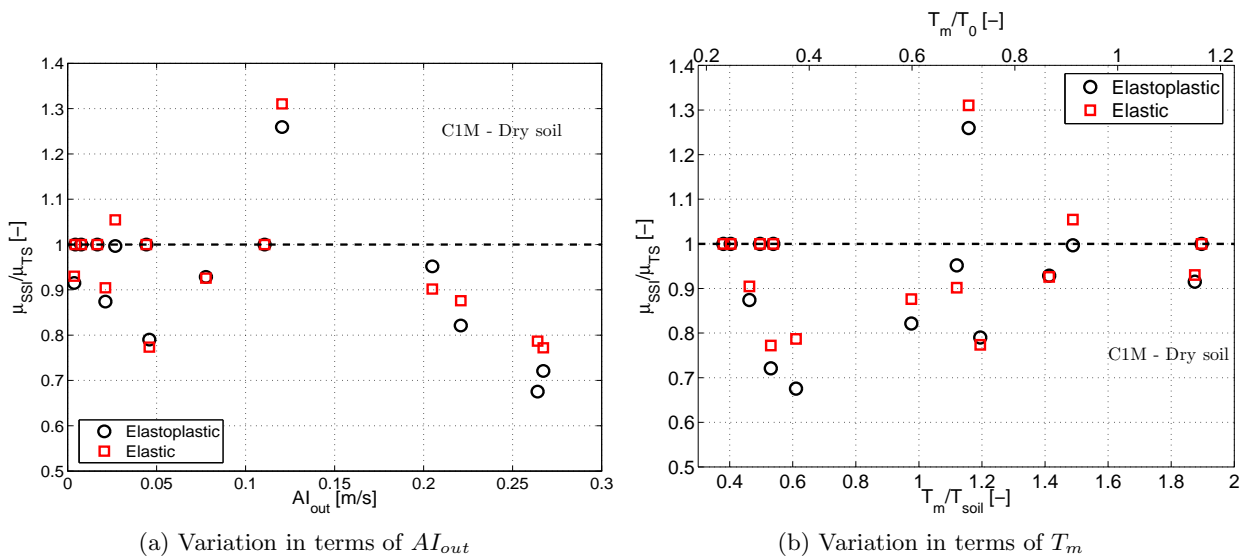
Figure 4.20: Scatter plots of μ ratios for the C1M SDOF structure on dry soil

Concerning the mid-rise superstructure (C1M), obtained values of μ ratios for dry and saturated soil cases are displayed in Fig.4.20. In this case, DSSI has a beneficial influence for the major part of considered motions. Thus, damage in the superstructure is reduced when DSSI effects are included, regardless if the soil behaves elastic or inelastically expect for one motion. According to Fig.4.20b, the frequency content of this motion is very close to T_{soil} ($\frac{T_m}{T_{soil}}$ close to 1). Thus, some resonance between the input and the soil might take place. The tendency concerning the beneficial or detrimental influence of DSSI on the dynamic response is unaltered by the constitutive soil model used for the soil. Nevertheless, numerical values of μ vary significantly when DSSI is included. Indeed, reductions of μ down to 30% can be noticed for strong motions. For both C1L and C1M structures on dry soil, it can be noticed that variations appear between elastic and inelastic soil computations. In other words, points do not coincide in previous μ ratio scatter plots for several motions. Thus, radiation damping and soil flexibility associated to elastic DSSI can not explain completely differences observed on the computed structural responses. However, as the effective motion transmitted to the structure is not exactly the same in both elastic and inelastic soil cases, part of this differences could be related to the non-linear behavior of the superstructure.

When the soil is saturated for the C1L SDOF structure case (Fig.4.21), the general reduction tendency of the superstructure damage when inelastic DSSI is included is confirmed for moderate to strong motions. Nevertheless, some weak motions ($AI_{out} < 0.1$[m/s] in Fig.4.21a) show a detrimental effect of DSSI. According to Fig.4.21b, motions exhibiting detrimental effect have a mean period T_m close to T_{soil}, thus some resonance between the input motion and the soil deposit might have taken place. The computed ratios are quite erratic when the soil is assumed to behave elastically. In contrast

(a) Variation in terms of AI_{out} (b) Variation in terms of T_m
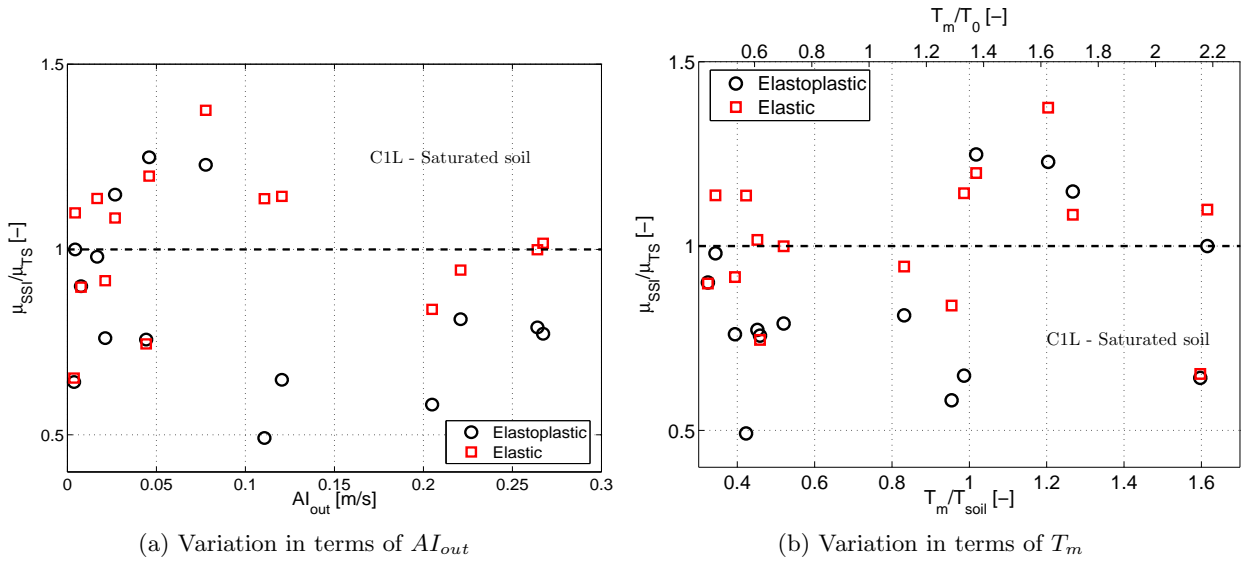
Figure 4.21: Scatter plots of μ ratios for the C1L SDOF on saturated soil

with dry case, in saturated condition the same tendency is not always kept between elastic and inelastic soil approaches. Additionally, variations of μ are significantly larger when the soil is inelastic. Thus, linear elastic soil behavior assumption is quite conservative for seismic damage evaluation purposes of this superstructure on the saturated sandy soil.

Similarly to the C1L SDOF structure case, elastic DSSI considerations are reasonably accurate for the C1M on dry soil, but are not suitable when the soil is in saturated condition. According to Fig.4.22, DSSI is invariantly favorable or negligible when the inelastic soil behavior is taken into account. This tendency is not, in general, adequately predicted under elastic soil considerations. Additionally, large differences are found in the computed μ ratio for the major part of motions, even if the detrimental/favorable tendency is correctly predicted by the elastic soil approach.

(a) Variation in terms of AI_{out} (b) Variation in terms of T_m
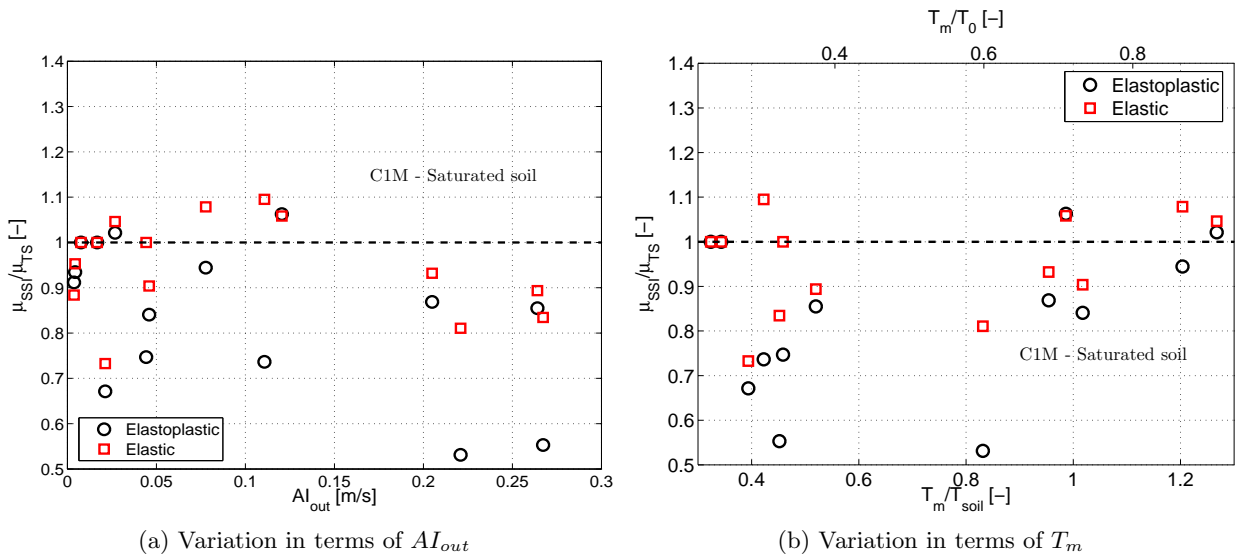
Figure 4.22: Scatter plots of μ ratio for the C1M SDOF structure on saturated soil

In summary the inelastic soil behavior seem to be not important for the structural dynamic response of C1L SDOF in dry soil. In this case, a traditional elastic DSSI analysis seems to be accurate enough to take into account interaction effects. For C1M SDOF on dry soil, some significant variation in

structural damage are found when the soil behaves inelastically, and consequently, an inelastic soil behavior evaluation is desirable for this structure in this soil. For both superstructures, large variations on μ are found when the soil is saturated. Thus, a more precise assessment of the soil behavior might alters significantly the DSSI contribution evaluation to superstructure dynamic response.

4.6 Energy oriented analysis of the results

Similarly to analyses presented in §3.8, a study of the role of the DSSI effects on the hysteretic energy dissipation mechanisms in the system is conducted in this section.

The energy dissipated by the considered SDOF can be assessed in terms of a mean value computed across each superstructure model. In this regard, the expression (3.6), introduced in Chapter 3, to compute the amount of energy dissipated in the superstructure by inelastic behavior, must be adapted to the constitutive model used in this case. Thus, the indicator of the energy dissipated by the superstructure I_{str} can be computed as:

$$
\begin{aligned}
I_{str} &= \frac{1}{m}\int_{\Omega_b}\int_t \underline{\underline{\Delta\sigma}} : d\underline{\underline{\varepsilon}}\, dV + 1 \times 10^{-3} \\
&= \frac{1}{m}\int_{\Omega_b}\int_t \Delta\sigma_{rr}(\underline{x},t)\, d\varepsilon_{rr}(\underline{x},t)\, dV + 1 \times 10^{-3} \quad [\text{J/kg}]
\end{aligned}
\tag{4.3}
$$

where m denotes the mass of the SDOF, Ω_b is the volume of the superstructure, $\underline{\underline{\Delta\sigma}}$ and $\underline{\underline{\varepsilon}}$ are the stress and strain tensor associated to dynamic perturbation. According to beam-kinematics and the the constitutive model described in Appendix C, the energy dissipated by the superstructure can be computed in terms of the axial stress $\Delta\sigma_{rr}$ and the axial strain ε_{rr}, hence, only flexural dissipated energy is considered.

Similarly to analyses presented in §3.8, we will compute an average indicator of the energy dissipated by hysteretic damping in the soil to asses the modification in the dynamic soil behavior. We use the definition provided in (3.7) to compute I_{soil} over a control volume Ω. As the problem is 3D in this case, this expression takes the form:

$$
\begin{aligned}
I_{soil} &= \frac{1}{\Omega}\int_{\Omega}\int_t \left[\Delta\sigma'_{xx}\, d\varepsilon_{xx} + \Delta\sigma'_{yy}\, d\varepsilon_{yy} + \Delta\sigma'_{zz}\, d\varepsilon_{zz}\right](\underline{x},t)\ dV \\
&+ \frac{1}{\Omega}\int_{\Omega}\int_t \left[\Delta\tau_{xz}\, d\gamma_{xz} + \Delta\tau_{xy}\, d\gamma_{xy} + \Delta\tau_{yz}\, d\gamma_{yz}\right](\underline{x},t)\ dV \quad [\text{J/m3}]
\end{aligned}
\tag{4.4}
$$

where $\Delta\tau_{ij}$ and $\Delta\sigma_{ij}$ are the shear and normal stresses in ij plane according to axis shown in Fig.4.4. γ_{ij} and ε_{ij} are the corresponding distortions and normal strains. As the earthquake is imposed across yz plane, the major part of energy dissipated by the soil hysteresis takes place in this plane (92% of I_{soil} approximately). The contribution of the shear over the plane xz and xy are negligible. The integration is performed over a domain Ω.

The integration is performed over an approximate cubic domain Ω, as defined in Fig.3.30b adding an out-of plane dimension $2a$. Hence, the total volume Ω is equal to $8a^3 [\text{m3}]$. For cylindrical meshes, we use the cylindrical domain closest to the desired cube. These integration domains correspond to darker zones in meshes displayed in figures 4.4 and 4.5. Verifications on the suitability of this volume to capture the local soil behavior modification due to the presence of the superstructure have been conducted, and are omitted here for the sake of simplicity.

With the purpose to highlight differences of the initial soil confinement, Fig.4.23 shows the distribution of effective vertical overstress under the foundation of the C1L SDOF structure. We select a window equal to domain of integration Ω for these plots. According to Fig.4.23, the effective vertical overstress is approximately homogenous and equal to 20[kPa] under the foundation. Nevertheless, some stress concentration takes place in the borders. In the saturated case, slightly larger values than

(a) C1L on dry soil

(b) C1L on saturated soil
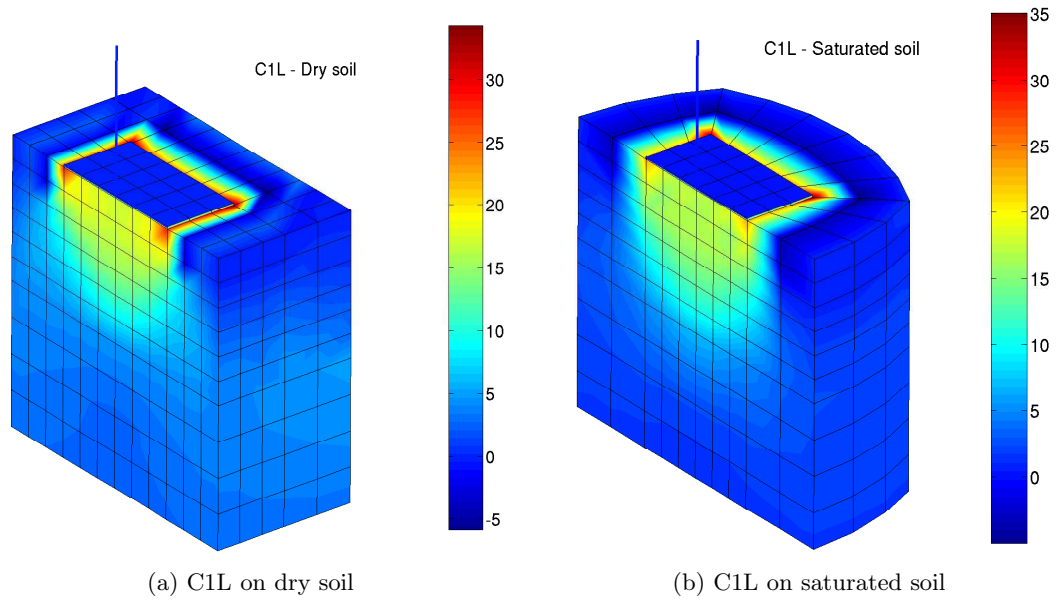
Figure 4.23: Vertical overstress $\Delta\sigma'_{zz}$[kPa] distribution for C1L superstructure

those obtained in the dry case can be noticed near the corner of the foundation. Additionally, some tensile stresses appear at the surface in the second row of solid elements starting from the foundation border. Indeed, in this case, no interface elements have been used between soil and interface surfaces. Hence, the apparition of this tensile zone due to foundation settlement was expected. Nevertheless, this reduced traction zone should not influence the general dynamic responses. Concerning the vertical extension of the confinement zone, it can be noticed that for this superstructure and for depth larger than $6-7$[m] (i.e. the foundation characteristic length a), the overstress imposed by the superstructure vanishes at the center of the foundation.

(a) C1M on dry soil

(b) C1M on saturated soil
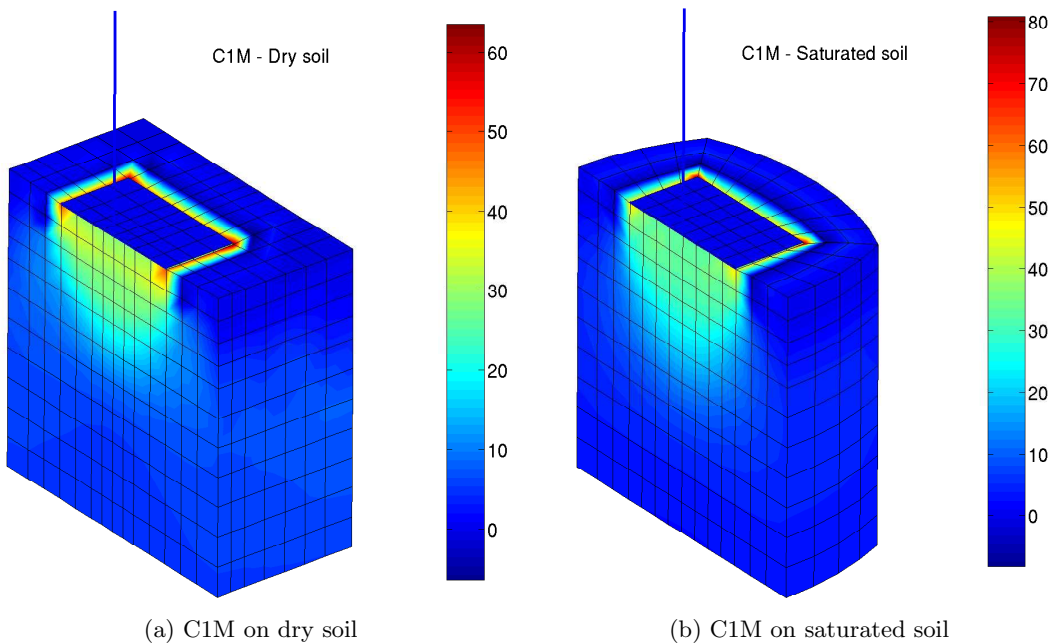
Figure 4.24: Vertical overstress $\Delta\sigma'_{zz}$[kPa] distribution for C1M superstructure

Concerning the C1M SDOF structure, Fig.4.24 shows the corresponding effective vertical overstress distribution $\Delta\sigma'_{zz}$ for both dry and saturated soil cases. Similarly to the C1L case, stress concentration zones take places across the border of the foundation and specially at the corners. The values of

these stress concentrations are slightly larger in saturated case compared to dry case. However, the concentration is more localized at the corners when the soil is saturated. These differences are related to the used meshes. Indeed, in approximately cylindrical meshes used for the saturated soil there are only two solid soil elements connected to the corners outside the foundation. In dry cases (box meshes), there are three elements in these singularities. Hence, a better stress distribution is reached in dry situation. Similar to meshes for C1L SDOF, first row of soil elements outside the foundation shows some tensile stresses at surface due to structure settlement. Nevertheless, no particular influence of these overloaded zones are expected on the structural response under the dynamic part of the loading. For the mid-rise structure, the mean overstress under the foundation is approximately of 35[kPa] and its influence vanishes approximately for a depth equivalent to the foundation characteristic's length. These values agree with the standard results of influence factors for stresses, derived assuming elastic soil behavior (e.g. Poulos and Davis (1974)).

The purpose of displaying the additional confinement imposed by the superstructure is to illustrate differences in the initial state of the soil for SSI-N/SSI-E computations, in comparison to the free field situation used to define the input for TS-N/TS-E approaches. However, differences in the dynamic inelastic soil behavior are not only due to this initial state difference. When the superstructure is included, the waves reflected by the foundation and induced by the superstructure's motion also modify the response of the soil. In this regard, it is interesting to provide a global measure of the soil behavior to make the comparison between the free field state and the one in the neighboring soil close to the foundation possible.

4.6.1   Energy dissipated by the superstructure

(a) Elastoplastic soil behavior   (b) Elastic soil behavior
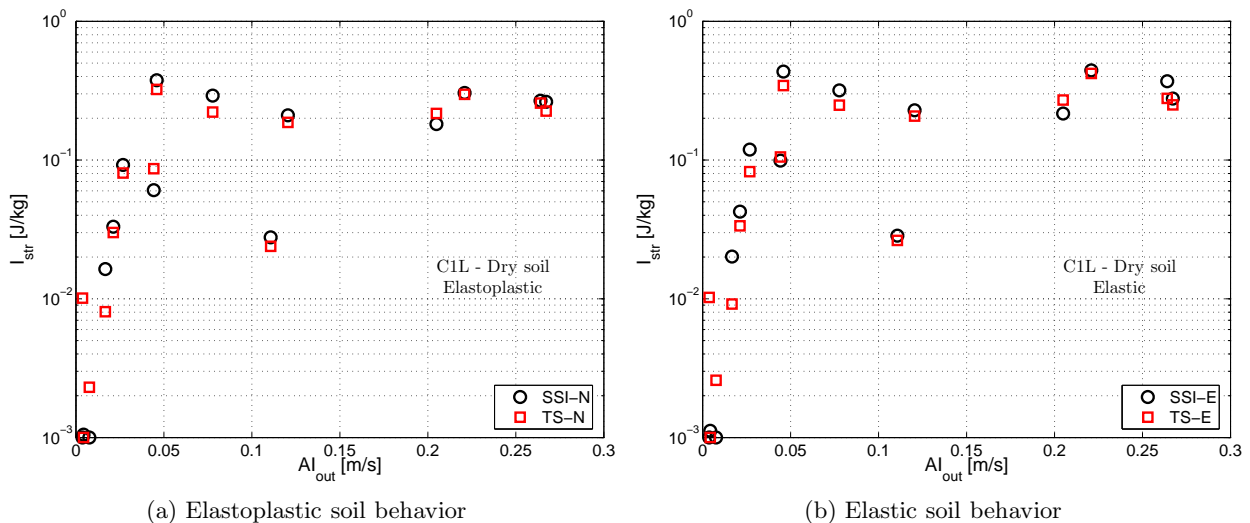
Figure 4.25: Scatter plots of energy dissipated by the C1L SDOF on dry soil

The structural energy dissipation index I_{str} obtained for the C1L SDOF structure on dry soil using both soil models is shown in Fig.4.25. In this figure, values of I_{str} equal to 1×10^{-3} corresponds to elastic structural behavior. The results show the same tendency as the one obtained in terms of the ductility ratio demand illustrated in Fig.4.11, thus a detrimental effect of the DSSI on the expected seismic damage. As discussed previously in terms of some time responses, this phenomenon might be related to frequency content of the motion relative to the fixed base fundamental period. Similarly to variations observed before, between inelastic and elastic soil conditions, elastic soil assumption provides results accurate enough in terms of the influence of the DSSI. Nevertheless, larger effective motion is transmitted to the superstructure due to lack of energy dissipation in the soil. It is interesting to note that the ductility demand ratio computed as described in expression (4.1) provides an accurate enough measure of the damage reached by the superstructure. This expression includes a rigid-body rotation

and translation to avoid including components that do not induce strain in the superstructure. Other propositions to compute ductility ratios for SDOF systems on flexible support have been provided by Priestley and Parck (1987) or Ciampoli and Pinto (1995) and have been critically reviewed by Gazetas and Mylonakis (2001). This definition of μ is computed only with maximum instantaneous responses, hence it can be computed straightforwardly. The indicator introduced here (I_{str}), includes the complete time history response at different sections of the superstructure and requires spatial and temporary integrations. Consequently it is significantly more difficult to compute. Nevertheless, both measures provide equivalent information in this case as the considered superstructure is a SDOF. For general multi-degree of freedom structures, the information provided by a simple instantaneous measure of an equivalent SDOF as μ could give an erroneous damage state evaluation. From this point of view, the use of I_{str} might provide a better description of damage for more general systems. The computation of this index for the C1M superstructure does not provide additional information than that obtained for the ductility demand analysis provided in the previous section, and is omitted here for the sake of conciseness.

4.6.2   Energy dissipated by the soil

In order to complete the study of the role of the inelastic soil behavior on the structural seismic demand, we present in this section a study in terms of the I_{soil} indicator of the energy dissipated in the soil during the dynamic loading.

(a) Dry soil   (b) Saturated soil
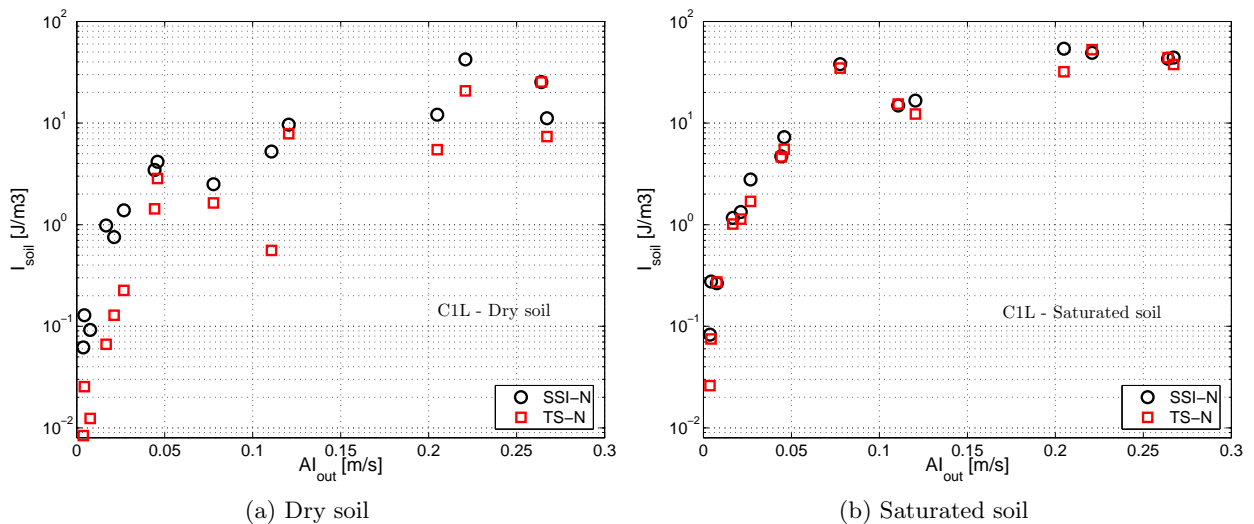
Figure 4.26: Scatter plots of energy dissipated in the soil in terms of I_{soil}[J/m3] for C1L SDOF

Scatter plots of the hysteretic energy dissipation I_{soil} for C1L superstructure are shown in Fig.4.26 for dry and saturated soil cases. Results using the control volume defined above for SSI-N cases are compared to the one obtained in the 1D column model used to compute the free field for TS-N approach. The integration is performed over a depth $z = 2a$ for 1D column cases. As expected, the evolution of I_{soil} is well correlated with the increase of the Arias intensity at outcrop AI_{out}. According to this figure, the general tendency is an increase of the energy dissipated in the soil when DSSI effect are accounted for in the dry soil case. Nevertheless, it can be noticed that some motions exhibit approximatively the same value of I_{soil}. Hence, in this case, the superstructure's oscillations contribute to increase strains in the soil and consequently the hysteretic damping. Thus, the stiffness effect due to additional confinement under the foundation is compensated by the soil deformations induced by the superstructure's oscillation increase. Concerning saturated soil case, no significant variations can be noticed comparing the analyses carried out with the superstructure or the to free field situation. Hence, the additional strains imposed by the inertial soil-structure interaction are approximately compensated by the supplementary confinement around the foundation. To complete this analysis it is interesting

to compare the numerical values of the I_{soil} index. Generally speaking, it is clear that larger values of hysteretic energy dissipation are found when the soil is saturated. As described in other parts of this work, reduction of effective stress in soil induces a soil stiffness degradation and consequently an increase of material damping.

(a) Dry soil   (b) Saturated soil
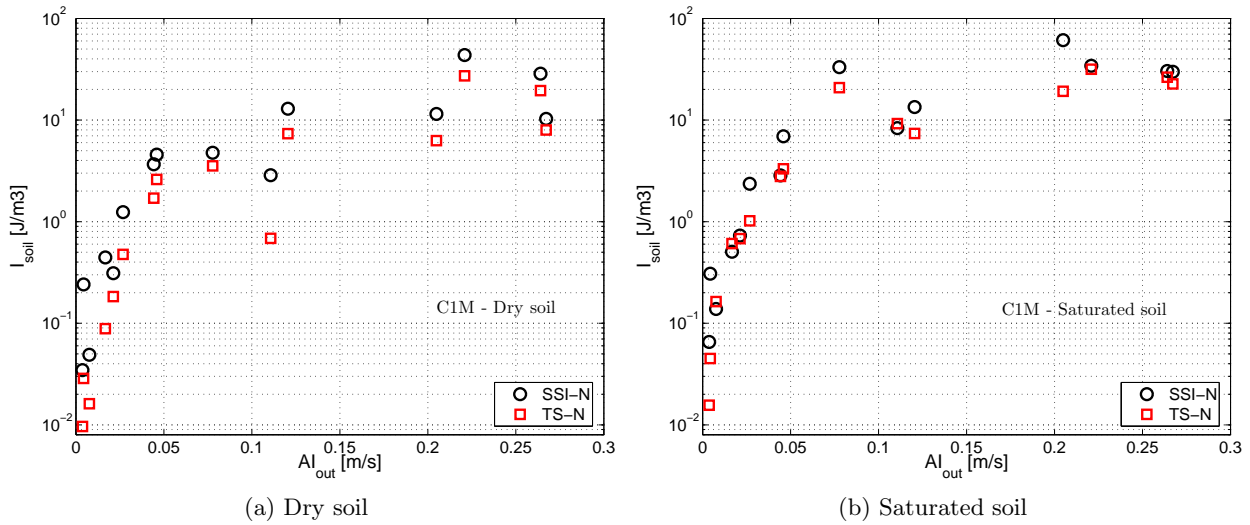
Figure 4.27: Scatter plots of energy dissipated in the soil in terms of I_{soil}[J/m3] for C1M SDOF

As concerns the C1M superstructure, the general tendency depicted in Fig.4.27 coincides with observations regarding C1L SDOF. Thus, for dry soil condition the computed values of I_{soil} are larger to those obtained for free field case. For saturated case, differences seem to be smaller. As a general reduction of seismic structural demand has been noticed for this mid-rise SDOF, it is possible to conclude that this increase of energy dissipation contributes to the reduction of the structural damage. Indeed, as previously noted, differences of computed structural response are significative when elastic soil is assumed. In this last case, no hysteretic dissipation takes place in the soil. Consequently, these variations of I_{soil} confirm that the elastic soil assumption is not adequate for the C1M SDOF in dry soil. In comparison with the C1L SDOF on saturated soil case, relative larger differences are found for I_{soil} when the considered motion is relatively weak ($AI_{out} < 0.1$[m/s]). However, for moderate to strong motions, the computed values of I_{soil} for saturated soil case are equivalent for practical purposes.

In order to highlight the modification of the soil response near the foundation, Fig.4.28 shows some time responses under the foundation for both considered structures compared to the ones obtained in the free field case. Results are presented in terms of the local index of energy dissipation i_{soil}, computed as:

$$
\begin{aligned}
i_{soil}\left(\underline{x}, t\right) &= \int_t \left[\Delta\sigma'_{xx}\,d\varepsilon_{xx} + \Delta\sigma'_{yy}\,d\varepsilon_{yy} + \Delta\sigma'_{zz}\,d\varepsilon_{zz}\right]\left(\underline{x}, t\right) \\
&+ \int_t \left[\Delta\tau_{xz}\,d\gamma_{xz} + \Delta\tau_{xy}\,d\gamma_{xy} + \Delta\tau_{yz}\,d\gamma_{yz}\right]\left(\underline{x}, t\right) \quad \text{[J/m3]} \quad (4.5)
\end{aligned}
$$

with the same definitions provided for the expression (4.4). We choose an arbitrary point under the foundation, placed approximately at 2[m] depth under the center of the superstructure. We select this point in order to highlight both, the effects of the increase in the confinement and the strains induced by the superstructure's oscillations. We present in this figure responses corresponding to motion number 3 as listed in Appendix J, as example. According to Fig.4.28 for dry soil case, an increase of the energy dissipated by hysteretic soil behavior takes place when the mid-rise superstructure is placed on the soil. For the C1L SDOF, the energy dissipated is larger than the one obtained in the free field situation.

(a) Dry soil   (b) Saturated soil
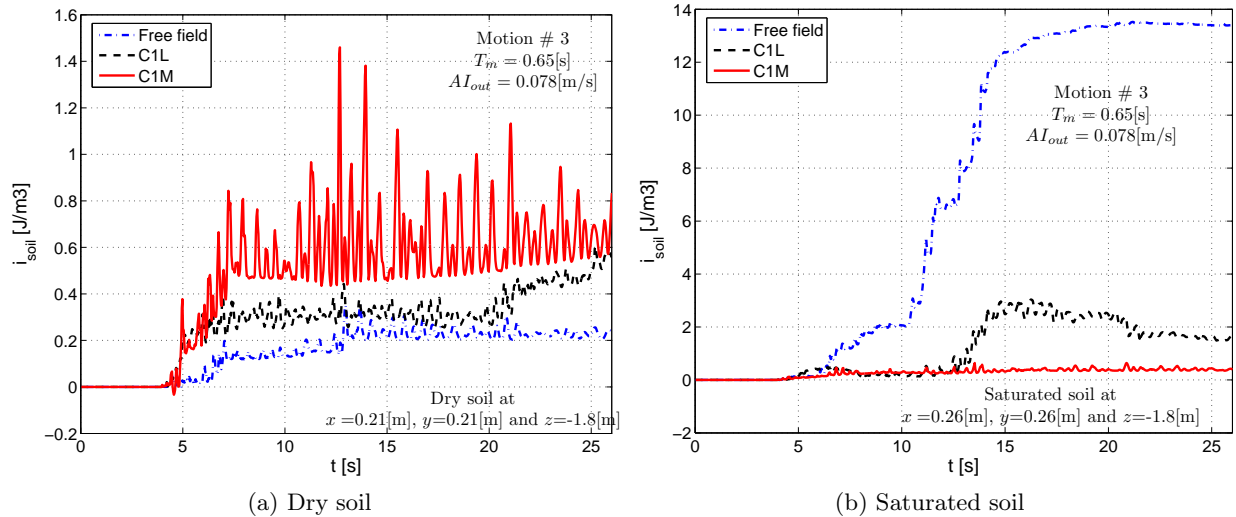
Figure 4.28: i_{soil} evolution at 2[m] depth under the center of foundation for two motions

The tendency is completely inverted for the saturated case shown in Fig.4.28b. In fact, in this case, due to reduction of effective stresses, larger values of i_{soil} are found for the free field case compared to the DSSI models. At 2[m] depth, large confinement provided by the mid-rise SDOF structure increases significantly the soil stiffness compared to the free field or the C1L structure model, and consequently reduces the induced shear strains and energy dissipation. Indeed, at free field the situation is close to liquefaction, and locally the induced hysteretic damping grows drastically. Nevertheless this situation is local, the averaged effect over the control volume Ω has been shown in previous figures. However, the implications of this local effects can be important in terms of settlements as discussed in §3.10.2.2. The purpose of introducing this energy analysis was to complete the description of the superstructure responses in order to relate detected variations with the soil inelastic state. In this regard, increases in hysteretic damping highlighted for mid-rise SDOF structure in both dry and saturated soil cases, might explain general reduction of expected structural damage. Concerning the low-rise SDOF structure, results shown in this section suggest that DSSI effects are fundamentally elastic in dry case, and only in saturated case an influence of inelastic soil behavior is clear.

4.7   Concluding remarks

This chapter was devoted to identify the contribution of the inelastic soil behavior to the general non-linear DSSI problem. With this purpose, a comparative analysis between elastic and inelastic soil behavior assumptions was presented. In order to make as general as possible our results, we selected two generic SDOF structures taking generic values suggested in some design codes. As the general problem of a shallow rigid foundation with SDOF structure is essentially three-dimensional, we used 3D FE models to analyze this problem. A homogenous medium dense sand soil profile in two hydraulic conditions (dry and saturated) has been used.

The results point out that, in general, inelastic soil behavior plays a decisive role only when the soil is saturated. When the soil is in dry condition, an elastic DSSI approach seems to be accurate enough to take into account the modification of the structural response due to dynamic interaction effects. Nevertheless, when the soil is saturated, large variations between elastic and inelastic DSSI approaches are found. As noted, these differences are related to pore pressure generation induced in the inelastic case which is neglected when elastic soil behavior is assumed.

Concerning the role of the DSSI on the dynamic response of both studied superstructures, the influence of interaction phenomena for the low-rise SDOF structure is quite erratic. Hence, depending on the characteristics of the ground motion DSSI effects are beneficial or detrimental in dry soil case. In

saturated case, inelastic DSSI effects are in general beneficial. Regarding the mid-rise superstructure, in both dry and saturated soil cases, the effects of the DSSI are favorable in reducing the expected structural damage. These differences are probably due to the slenderness and mass of the mid-rise structure. Hence, larger interaction effects take place due to the rotation component of this slender superstructure.

To complete the presentation, an analysis in terms of some measures of energy dissipation was conducted. For the superstructure, the simple use of global responses as ductility ratio demand probes to be accurate enough to describe the damage state of this kind of structures. Concerning the soil energy dissipation indicators, these measures contribute to clarify the observed responses for mid-rise superstructures. In this case, the large amount of energy dissipated in the soil coincides with the reduction of structural demand. For the low-rise structure, the same tendency is found regarding the increase of soil energy dissipation in the DSSI case. However, structural demands also increase for some motions when DSSI effects are included. Consequently, we can conclude that for the studied superstructures and in dry soil, the DSSI phenomenon is mainly controlled by elastic effects, where the frequency content of the motion with respect to the elastic frequencies of the soil and the structure seem to define the role of the DSSI on the dynamic response of the structure system.

Chapter 5

Effect of the dynamical soil-structure interaction on the seismic vulnerability assessment

Contents

5.1   Introduction

The assessment of seismic fragility of structures is a requirement for seismic loss estimation and risk management. Although some fragility databases as ATC 13 (1985) or HAZUS-MH MR3 (2003) are available, these earthquake motion-damage relations are developed for general types of structures with several assumptions, strong simplifications and large uncertainties. Regarding soil effects, for example HAZUS-MH MR3 (2003) takes into account the local soil conditions in terms of amplification factors to be applied to the response spectra characterizing the ground shaking. This document also includes guidelines to evaluate three types of ground failure: liquefaction, landsliding and surface fault rupture. These ground failures are quantified by permanent ground deformations. Nevertheless, dynamic soil-structure interaction phenomena are assumed benefic and neglected.

In order to assess the seismic fragility of general buildings, HAZUS-MH MR3 (2003) proposes a methodology to develop functions for estimating building damage due to ground shaking in terms of fragility curves. These curves are an illustrative way of expressing the probability of exceeding a certain degree of structural response as a function of the load severity. This document also provides reference building capacity curves to be used to determine peak building responses.

According to Shinozuka et al. (2000), the development of fragility curves will require synergistic use of the following methods: (1) Professional judgement; (2) quasi-static and design code consistent analysis; (3) utilization of damage data associated with past earthquakes; and (4) numerical simulation of the seismic response of structures based on dynamic analysis. However, damage data in most high seismicity regions are too scarce to provide sufficient statistical information. Additionally, fragility curves derived from engineering judgement may not be reliable, because the opinions of a few experts may dominate the results (Hwang and Huo, 1994). Consequently, fragility curves generated from well-calibrated analytical approaches may be an adequate alternative.

Several analytical methods have been proposed to generate fragility curves of structures. The traditional strategy in earthquake engineering consists in five steps: (1) probability-based scenario establishment from a seismic hazard analysis, (2) earthquake generation based on a seismologically base model, (3) definition of a numerical model for the target building, (4) non-linear seismic analysis of the model and (5) reliability analysis to establish fragility curves. In Shinozuka et al. (2000) and Shinozuka (1998), the authors introduce a statistical procedure appropriate for the reliability analysis step under the assumption that they can be represented by two-parameter lognormal distribution functions. They apply this technique to develop empirical and analytical fragility curves for bridges. Other authors use a Monte Carlo approach for the reliability analysis step (Hwang and Huo, 1994; Kafali and Grigoriu, 2007).

In general, fragility curves can include several sources of uncertainties: in the seismic loading, the soil site and the structural parameters defining the system. Hwang and Huo (1994) include in their work uncertainties in the seismic motion and in the structural parameters as viscous damping ratio, strength and stiffness of structural materials. Shinozuka et al. (2000) also include variability in structural model and input ground motion. Choi et al. (2004) use a similar strategy to generate fragility curves for bridges, but using first-order reliability principles to combine component fragility curves to generate the entire bridge system fragility curve. Popescu et al. (2005) use the method presented by Shinozuka et al. (2000) to develop fragility curves in order to summarize the effect of the variability of soil properties in the seismic liquefaction. In this work, as a first approach, only the aspect of uncertainties in the seismic ground motion is addressed.

This chapter concentrates on the development of analytical fragility curves according to Method 4 as described above including DSSI effects, hence by numerical simulation of seismic response of systems performing non-linear transient SSI-FE analysis. As recalled before, Shinozuka et al. (2000) introduce a statistical procedure to develop fragility curves on the basis that they can be represented by two-parameter lognormal distribution functions. These authors also present a procedure to test the goodness of fit and to estimate interval of confidence for the two parameters controlling the shape of the fragility curve. Unfortunately, this last step is often omitted by several authors. Frequently, fragility curves are computed using a fixed database size and no statistical justifications are provided

regarding the statistical confidence of the obtained fragility curve. The sensibility of the two parameters defining the fragility curve on the database is studied in terms of the amount of information provided by the ground motion selection. With this purpose, we develop analytical expression of the Fisher's information for a given soil and structure configuration. We present a study of the evolution of this information measure in terms of the used database and the structural response level selected. With these analytical results, we provide a geometrical interpretation and lower-bounds of the variance of the parameters describing fragility curves.

5.2 Studied case description

In order to investigate the effect of DSSI on seismic demand evaluation, a comparative dynamic analysis as described in §3.3 is conducted for a target building.

The studied building corresponds to a public building built in 1970 and placed in French Antilles. The building has 8 levels and a total height of 28m. The lateral-force-resisting system is constituted by moment resistant frames in longitudinal direction y and moment resistant frames and shear walls in transversal sense x (Fig.5.1). The building is geometrically regular in plane, but some differences exist in element dimensions and reinforcements between axes A, B, C and D, depending on the level. Detailed information about geometry, element dimensions and reinforcement can be found in Appendix I. These irregularities in stiffness distribution induce some torsion when the building is loaded following y direction. Despite these irregularities, an equivalent two-dimensional model for the structure is accurate enough to represent its dynamic response when the ground motion is imposed in y direction (§5.2.2).
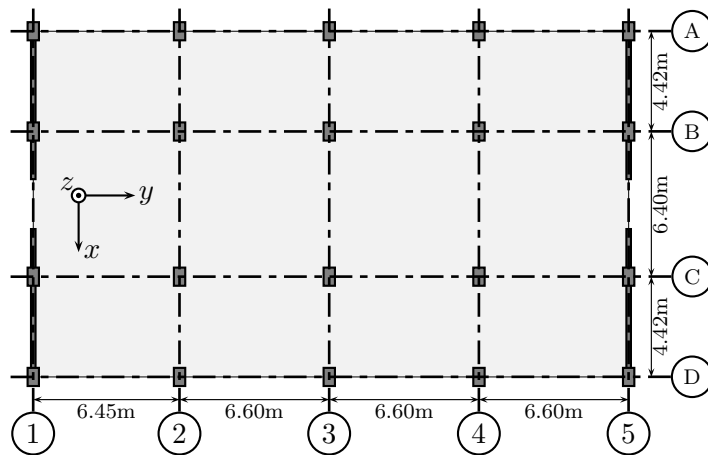
Figure 5.1: Plane of a typical floor of the target building

Two different kinds of numerical analyses are carried out. The first one, consists in a complete 3D model for both superstructure and soil. The second one corresponds to a modified plane-strain approach (§3.2). This second approach reduces significantly the required CPU-time modeling with a reasonable degree of accuracy the dynamic nonlinear behavior of the superstructure and the soil.

5.2.1 Soil characterization

In order to identify the mechanical properties of the soil profile from the seismic response point of view, we use some H/V measures available at several points of this soil deposit (Douglas et al., 2005). According to these tests, the soil profile shows site effect for a frequency near to 1.7[Hz]. On the other hand, concerning the mechanical properties of the soil, neither geotechnical tests nor a complete geotechnical description were found. However, according to the geological information, the soil profile must be composed of a mixture of sandy and clayey soils. According to the same study, the bedrock or the rigid soil seems to be found at 30 or 35[m] depth.

Due to lack of geotechnical information to identify the elastoplastic model parameters, we choose a set of parameters representing a sandy soil profile, which gives a first natural frequency of the soil profile near to the measured one. This can be justified because the scope of this chapter is only to illustrate the effects that the presence of a soil foundation has on the seismic response of a structure. The generalized typical layered soil/rock model parameters considered in this section are summarized in Appendix H.3.

5.2.2 Finite element models for 2D and 3D cases

The superstructure's FE models are constructed with one-dimensional beam-column elements and thick plates (3D case). The fixed base fundamental period of the superstructure is near to 1s. The foundation is modelled using solid infinitely stiff elements. Frictional interface elements with tension cut-off properties are placed between foundation and soil. The 30[m] homogenous soil deposit is modeled by solid linear elements. In the bottom, a layer of 5m of elastic bedrock is added to the model. The finite element meshes used for modeling this problem are shown in Fig.5.2a. Colors in this figure are associated to different vertical size of elements. A finer mesh is used in the neighborhood of the foundation to improve the approximation of non-linear behavior in this zone. The characteristic lengths of solid elements have been chosen small enough to prevent numerical dispersion problems. The time integration is carried-out using an explicit-implicit split operator strategy (Hughes and Liu, 1977b,a) associated to Newmark method. Some algorithmic damping is used to remove spurious high-frequencies. At each time step, the non-linear problem is solved by Newton-Raphson type iterations.

(a) 3D approach   (b) 2D modified plane-strain approach
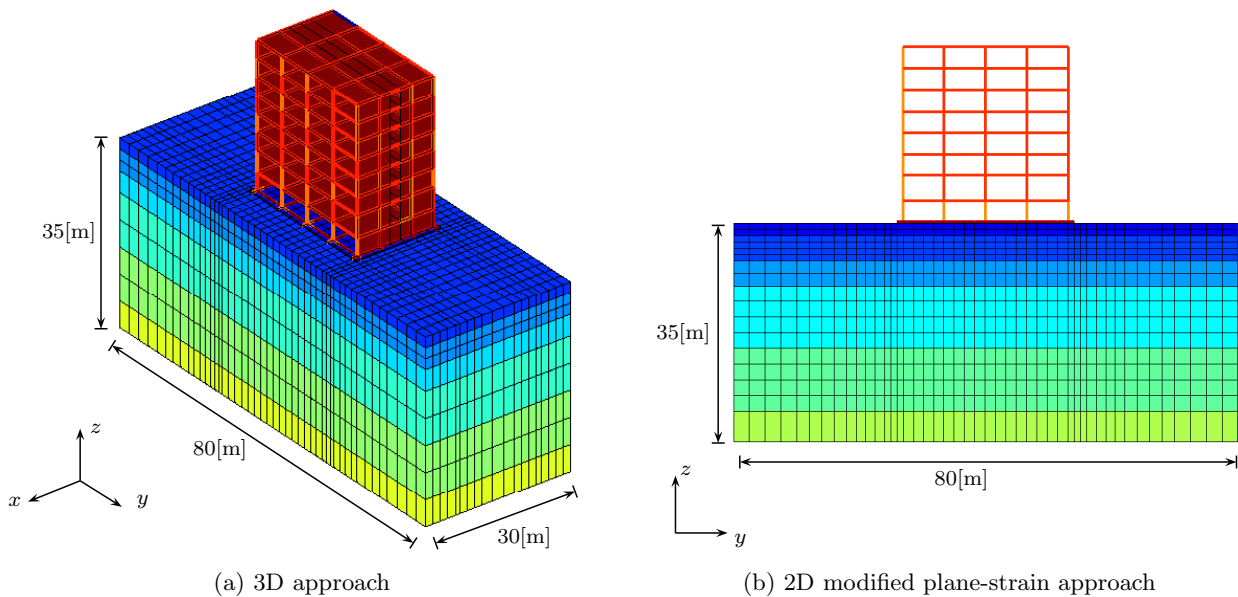
Figure 5.2: Finite element meshes

Each numerical computation is conducted in two whole steps: a static computation that permits to initialize the internal stress and internal constitutive model's variables of both soil and superstructure, followed by a dynamic perturbation analysis around the stress state and internal material memory obtained in static step. For SSI-FE approach, the static whole step includes geostatic initialization of stresses and level-by-level sequential construction of the superstructure.

Assuming an input motion across the y axis, the construction of the 2D model displayed in Fig.5.2b starts from one of the longitudinal axes of the complete 3D model. As the building is reasonably regular for loading in y sense, we take for example the axis A in Fig.5.1 to develop the equivalent 2D structural model. We add to this structural axis, a tributary distributed mass/weight over $0.5 \times (6.40 + 4.42) = 5.41$m in x sense. The contribution of out-plane structural elements (walls, slabs and beams) are introduced adding dummy elastic parallel elements to non-linear structural columns of 2D model. The equivalent two-dimensional model must respect dynamic properties and non-linear behavior of the

original 3D model. In order to verify these requirements, elastic dynamical analyses and pushover tests have been conducted to calibrate structural properties of the dummy parallel elements.

(a) Elastic fixed base transfer function modulus   (b) Capacity curve
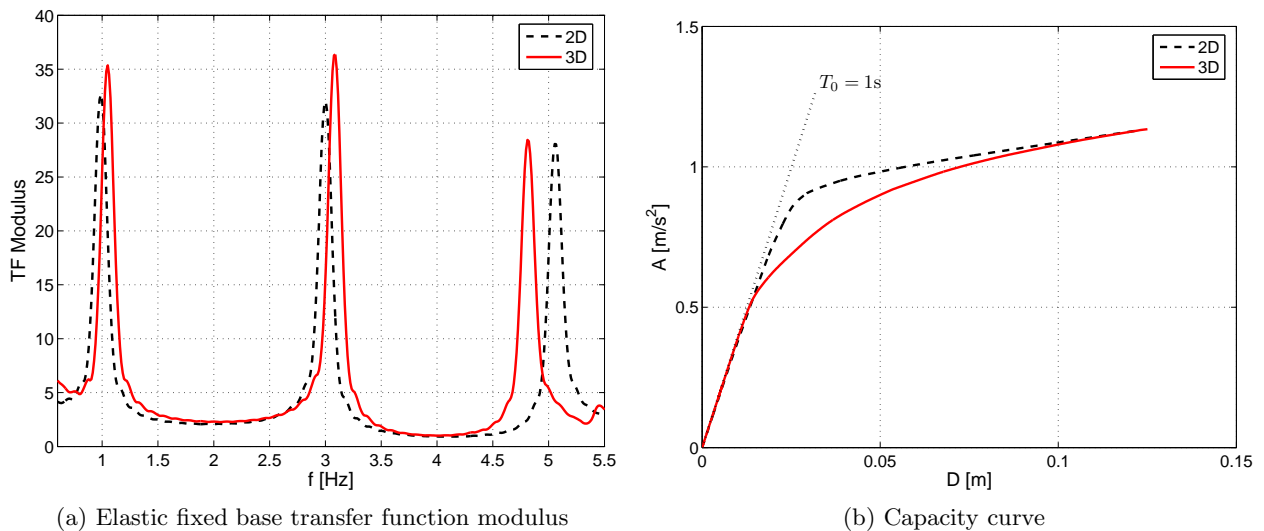
Figure 5.3: Verification of 2D equivalent model

Fig.5.3 displays elastic fixed base transfer function amplitudes of both models, obtained for to a seismic loading following y direction. The first two elastic modes of the 3D model correspond to approximately in-plane motion, thus, a satisfactory agreement is found in frequencies and amplitudes for the two 2D and 3D models. Differences found for the third mode are associated to some torsion in the original 3D model unable to be modelled in the 2D case. Modal analysis gives that approximately 76% and 11% of translational mass is associated to first and second modes, respectively. Consequently, a good approximation of two first modes is accurate enough. Regarding non-linear structural behavior, Fig.5.3b shows the computed capacity curve obtained for an incremental pushover loading using the force distribution corresponding to the first elastic mode. A good agreement is found in elastic range and near the ultimate load limit. As 3D model is more redundant in structural elements than the 2D model, a more gradually yielding of the structural system is found.

Regarding the complete SSI-FE models in 2D or 3D, several verifications were conducted in order to identify differences between both approaches. Concerning the static initialization phase, contours of the distribution of the increase in the effective vertical stress $\Delta\sigma'_{zz}$ due to the superstructure's weight are displayed in Fig.5.4. The distribution displayed in Fig.5.4b corresponds to a vertical section across the longitudinal axis C of Fig.5.1. It can be noticed that stress distributions are similar in both cases. Nevertheless, concentration of stress near the foundation corners is slightly larger for the 3D model (up to 120[kPa]) compared to the equivalent plane-strain 2D case (up to 85[kPa]). Values under the foundation are equivalent in both cases (40 to 50[kPa]). The attenuation of the increment with the depth is faster in 3D case compared to the 2D model due to the imposed plane-strain condition. Thus, at the bottom of the mesh (depth of 35[m]) and at the center of the superstructure, 3D model predicts an increment of 10[kPa] compared to 25[kPa] computed in the 2D approach. Despite these differences, the initial state for the dynamic computations are equivalent from a practical point of view.

The influence of the modeling approach on the DSSI phenomenon is studied in terms of the low-stain responses in frequency domain. Obtained spectral amplitude modulus between free field (ff) and its vertical projection over the bedrock (bd), and between the top of the building (tp) and free field according to definitions of Fig.1.11 are shown in Fig.5.5. An excellent agreement is found between both computations for the ff/bd spectral ratio. Nevertheless some frequency components of the second and third structural fixed base modes appear near 3[Hz] and 5[Hz] according to Fig.5.3. Some small differences in amplitude are found for this spectral ratio, specially for the second elastic mode. This might be related to the constructive coherency of the reflected waves in the lateral boundaries for the 2D model. In the 3D case, this effect vanishes increasing the apparent damping.

(a) Equivalent 2D model   (b) Vertical section across axis C for the complete 3D model
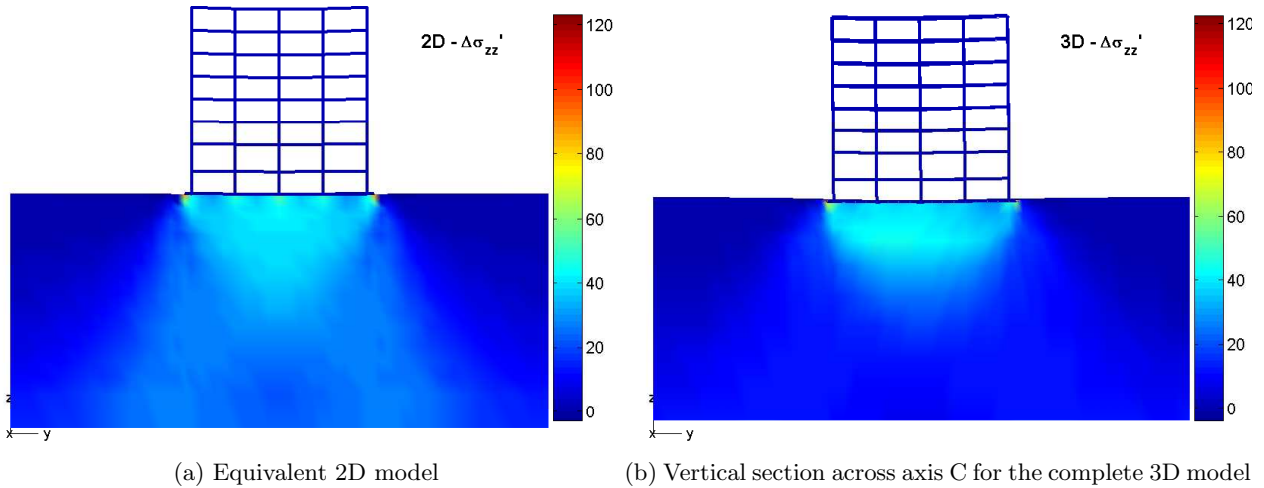
Figure 5.4: Vertical overstress $\Delta\sigma'_{zz}$ due to superstructure's weight distribution in [kPa]. Deformation magnification factor=100

(a) Spectral ratio modulus between free field and bedrock (b) Spectral ratio modulus between the top of the super-
structure and free field
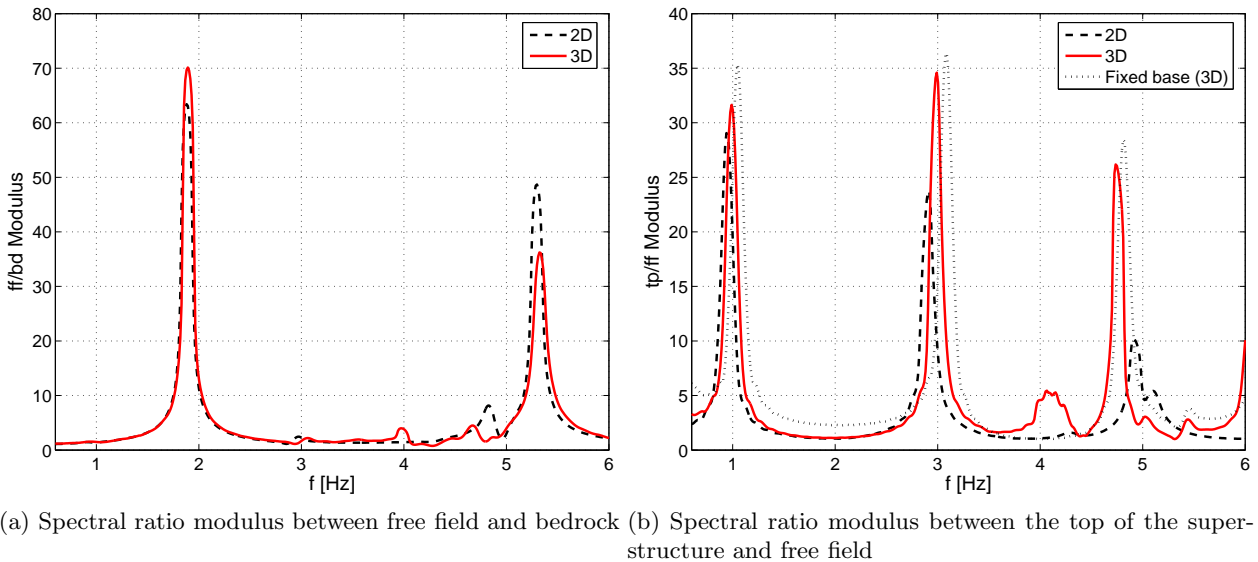
Figure 5.5: Frequency domain responses using equivalent 2D plane-strain and 3D models

Concerning the spectral ratio tp/ff displayed in Fig.5.5b, a satisfactorily agreement is found for the first three fixed base modes. Fixed base transfer function modulus for the 3D model has been added to this plot to simplify the comparison. The same shift regarding the third fixed base mode (associated to a torsional component) is highlighted on this figure. Nevertheless, an additional peak appears around 4[Hz]. This peak might be associated to a vertical mode of vibration activated by the rocking of the superstructure-foundation system. This effect is not visible in 2D plane-strain model. However, as almost 85% of the translational mass is associated to the first and second modes, these short period modes seem not introduce significant modification of the dynamical non-linear response as will be shown in §5.5.3.

As the purpose of this chapter is to study the role of the non-linear DSSI on the seismic vulnerability, we will use global indicators of seismic response as maximum inter-story drift or damage index. For this kind of indicators, the 2D model is accurate enough. Nevertheless, for a detailed study of the damage of the superstructure a complete 3D model is more convenient. The main advantage of the proposed equivalent 2D model lies in the reduction of computer runtime. Two-dimensional SSI-FE

model has approximately 3000 degrees of freedom (DOFs), while full 3D model has approximately 30000 DOFs.

5.3   Definition of input motions for dynamic analyses

One of the major issues related to nonlinear dynamical analysis is to define appropriate input motions. There are three basic options to define suitable time histories to represent seismic excitation. The first approach is to use synthetic accelerogram generators producing realistic energy, duration and frequency content motions compatible with some physical conditions. A second category of methods for simulating ground-motion records are obtained by convolving the source, path and site effect (Aki and Richards, 2002). However, these methods demand high computational resources and carry a high-degree of uncertainty due to lack of information regarding parameter values. The third strategy is to select real motions recorded during earthquakes. The increasing availability of strong-motion accelerograms makes the use of real records an interesting alternative. Some guidelines to select and scale real records are provided for example in Bommer and Acevedo (2004). In this study, we use the first and the third options. Real motion selection strategy is adopted to define input to 3D dynamical analyses. For modified 2D plane-strain approach, we use a stochastic synthetic ground motion generator due to large amount of analyses to be conducted and the lack of real records available satisfying all requirements.

5.3.1   Real earthquake accelerograms selection strategy

The adopted strategy is based on the methodology proposed by Douglas (2006) in the framework of the VEDA (Seismic Vulnerability of structures: a Damage mechanics Approach) research project in whose framework this part of the work was done.

   The geographical scope of this study is the French Antilles. According to Douglas (2006), buildings in French Antilles are subjected to shaking from earthquakes related to the neighboring subduction zone, which generates two types of events interface (shallow dipping thrust events) and intraslab (deep generally normal-faulting events). In addition, large crustal events can occur. The results of the disaggregation conducted by Martin et al. (2002) were used to define the most important earthquake scenarii for sites of this geographical zone.

   Based on the criteria described in §3.5, Table 5.1 lists the ranges of the low and high bins chosen to undertake the selection of records. The ranges of the low and high bins were chosen in order to have sufficient numbers of records within each bin for each type of event. In this table, $S_d(\zeta = 5\%)$ corresponds to 5% damped displacement response spectra at 0.1s and 1.0s and t_{SR} is the significant duration (Trifunac and Brady, 1975).

Table 5.1: Strong-motion parameters and ranges of low and high bins used for selecting records

Parameter	Interface events		Intraslab events		Crustal events	
	Low bin range	High bin range	Low bin range	High bin range	Low bin range	High bin range
$S_d(\zeta = 5\%)$ at 0.1s	≤ 0.03cm	> 0.03cm	≤ 0.03cm	> 0.03cm	≤ 0.10cm	> 0.10cm
$S_d(\zeta = 5\%)$ at 1.0s	≤ 1.0cm	> 1.0cm	≤ 0.5cm	> 0.5cm	≤ 1.5cm	> 1.5cm
t_{SR}	≤ 14s	> 14s	≤ 10s	> 10s	≤ 10s	> 10s

   An experiment is constituted by $2^3 = 8$ records (or runs). Each experiment was repeated five times (5 earthquake selections), thus a total of 40 runs were conducted for the studied building. Additional details about strong-motion parameters values of 40 used records as well earthquake magnitudes, epicentral distance and focal depth can be found in Appendix J.2.

5.3.2   Synthetic ground motion generation

There are many engineering methods for simulating ground motions. For example, procedures based on random-vibration theory proposed by Saragoni and Hart (1974) or Nau et al. (1982) range from filtering and windowing Gaussian noise to generate accelerograms. As these methods are disconnected from specific geophysical parameters, the resulting time histories are poorly correlated in terms of earthquake scaling parameters. Other approaches generate seismic ground motion time histories that are compatible with a prescribed response spectra (e.g. Gasparini and Vanmarcke, 1979; Deodatis, 1996). The intrinsic problem of this kind of procedure is that in general the matching procedure may generate an excessive number of cycles of strong motion, producing an unrealistic high energy content.

In the present work, we adopt the empirical strategy developed by Pousse et al. (2006) that improves the stochastic model introduced by Sabetta and Pugliese (1996). In the method proposed by Sabetta and Pugliese (1996), the simulation of ground motion is achieved through an empirical method where time and frequency features of motion are derived from the signal spectogram $PS(t, f)$ and depend on few strong-motion indicators, such as Arias intensity (AI) (Arias, 1970) and the significant duration. According to Sabetta and Pugliese (1996), the spectogram can be factorized as,

$$PS(t, f) = PS_\tau(f) \, Pa(t) \tag{5.1}$$

where $PS_\tau(f)$ is the power spectral density function at time τ and $Pa(t)$ is the instantaneous average power. In the original work of Sabetta and Pugliese (1996), $PS_\tau(t)$ is represented by a collection of power spectral densities described in terms of spectral moments. Pousse et al. (2006) propose to replace this expression by the following function:

$$PS_\tau(f) = \frac{\frac{(2\pi f)^2}{1 + \left(\frac{f}{f_c}\right)^2}}{\max\{S(f)\} \sqrt{1 + \left(\frac{f}{\log f_c(\tau)}\right)^8}} \, e^{-F_c(\tau)} \tag{5.2}$$

where $S(f)$ is the Fourier spectra, f_c is the corner frequency and $F_c(\tau)$ is the time evolution of the central frequency. The original lognormal shape for $S(f)$ introduced by Sabetta and Pugliese (1996) was modified to a $\omega-$square model to correct the deficit of energy in the low-frequency part of the Fourier spectra. Additionally, Pousse et al. (2006) propose to model the instantaneous power as:

$$Pa(t) = \frac{1}{25} \frac{AI}{t\sqrt{2\pi}\sigma_p} e^{-\frac{1}{2\sigma_p^2}(\log t - \mu_p)^2} + \frac{24 \, AI}{25} \begin{cases} \frac{1}{t\sqrt{2\pi}\sigma_s} e^{-\frac{1}{2\sigma_s^2}(\log t - \mu_s)^2} & t \leq T_{coda} \\ \frac{A}{t+T} e^{-\frac{2\pi f(t+T)}{Q_c}} & t \geq T_{coda} \end{cases} \tag{5.3}$$

in order to take into account the arrival time, energy, and broadening of the P and S pulses with distance, as well as the existence of scattered waves that produce the coda of the accelerogram. In the previous expression, μ_p, μ_s, σ_p and σ_s are the expected mean values and standard deviation of the distribution of parameter t for the P and S pulses, respectively. The constant T and A are fixed by the continuity condition of the function and its derivative at $t = T_{coda}$. In equation (5.3), Q_c is the frequency dependent coda $Q-$value associated to coda decay.

Finally, the simulation of the ground motion is then performed summing Fourier series with time-dependent coefficients derived from $PS(f_n, t)$:

$$a(t) = 2 \sum_{n=1}^{N} \sqrt{2\pi f_0 \, PS(f_n, t)} \cos\left(n 2\pi f_0 t + \phi_n\right) \tag{5.4}$$

where $a(t)$ is the acceleration, f_0 is the fundamental frequency and ϕ_n the phases. In the original Sabetta and Pugliese (1996) model the difference among the simulated accelerograms was only due to random phase ϕ_n. To better capture the variability of the observed ground motion, a Monte Carlo exploration of the strong-motion indicators (e.g. t_{SR} and AI), source parameters and envelope form (σ_s and $Q(f)$) was introduced to the model by Pousse et al. (2006).

In the original work of Sabetta and Pugliese (1996), the model was calibrated using predictive equation from Italian strong-motion dataset. In the paper of Pousse et al. (2006), the model was calibrated with Japanese data recorded by the K-net array. The generation tool used here corresponds to a calibration of the model conducted by the same authors, using the suitable west eurasia database described in Fukushima et al. (2003).

Due to lack of near-fault records in the west Eurasian database, Fukushima et al. (2003) add data from other tectonic regions. However, added records are associated with the same earthquake category, i.e. shallow crustal earthquakes in active regions. According to Douglas (2006), suitable crustal records for the French Antilles must be chosen conform to moment magnitude M_w between 5.3 and 7.5 and focal depth inferior to 30km. As earthquake records included in the database used to calibrate synthetic generator satisfy these criteria, obtained motions agrees with expected crustal motions for French Antilles.

5.4   Analytical fragility curves

This section describes the adopted methodology to construct fragility curves on the basis of nonlinear dynamic analysis. The procedure used here for establishing the fragility curves for seismic structural response follows that proposed by Shinozuka et al. (2000). A strategy to estimate the amount of information provided by an earthquake selection to construct fragility curves is developed and presented in the following.

A Bernoulli experiment is a random experiment in which the outcome can be classified in one of two mutually exclusive ways: success or failure. If $F(\theta)$ denote the probability of success on each trial and Y the random variable itself, the probability density function (pdf) can be written as:

$$f(y, \underline{\theta}) = [F(\underline{\theta})]^y \left[1 - F(\underline{\theta})\right]^{1-y} \tag{5.5}$$

where y is a realization of the random variable Y and is equal to 1 for a success and equal to 0 for a failure. $\underline{\theta}$ regroups the parameters describing $F(\underline{\theta})$. A sequence of Bernoulli trials occurs when a Bernoulli experiment is performed several independent times and that the probability of success remains the same from trial to trial. For a sample $y_1, y_2, \ldots y_n$ of n values from Y, the multivariate probability density associated with our observed data $f(y_1, \ldots, y_n; \underline{\theta})$ as a function of $\underline{\theta}$ with $y_1, \ldots, y_n$ fixed, is the likelihood function:

$$\mathcal{L}\left(\underline{y}; \underline{\theta}\right) = \prod_{k=1}^{N} [F(\underline{\theta})]^{y_k} \left[1 - F(\underline{\theta})\right]^{1-y_k} \tag{5.6}$$

$F(\cdot)$ can be interpreted as the probability of exceeding a specific value d of a response (usually damage) for a given earthquake severity a_k, thus the fragility curve $F(d|a_k; \underline{\theta})$. Consequently, $y_k = 1$ or 0 depending on whether or not the structure sustains the state d for an earthquake severity a_k. Under the log-normal assumption of Shinozuka et al. (2000), $F(\cdot)$ takes the analytical form:

$$F(d|a_k; \alpha, \beta) = \Phi\left[\frac{1}{\beta} \ln\left(\frac{a_k}{\alpha \, \bar{a}}\right)\right] = F(a_k) \tag{5.7}$$

in which $\Phi[\cdot]$ is the standardized normal distribution function. α and β are two parameters describing the fragility curve. We introduce here a normalization parameter $\bar{a}$ to obtain a non-dimensional value of α, for example, the mean value of AI_{out} of the considered ground motions.

The method of maximum likelihood estimates α and β by finding the values that maximize $\mathcal{L}(\underline{y}; \alpha, \beta)$. Since maxima are unaffected by monotonous transformations, the problem is equivalent to maximize:

$$\ln \mathcal{L} = \sum_{k=1}^{n} \left[y_k \ln F(a_k) + (1 - y_k) \ln\left(1 - F(a_k)\right)\right] \tag{5.8}$$

hence, solving:

$$\frac{\partial \ln \mathcal{L}}{\partial \alpha} = \frac{\partial \ln \mathcal{L}}{\partial \beta} = 0 \qquad (5.9)$$

Thus, after some algebra, the maximum condition can be expressed by:

$$\sum_{k=1}^{n} \frac{\Phi'(a_k)}{\alpha\,\beta} \left[-\frac{y_k}{F(a_k)} + \frac{1 - y_k}{1 - F(a_k)} \right] = \sum_{k=1}^{n} I_\alpha(y_k) \quad = \quad 0 \qquad (5.10)$$

$$\sum_{k=1}^{n} \frac{\Phi'(a_k)}{\beta^2} \ln\left(\frac{a_k}{\alpha\,\bar{a}}\right) \left[-\frac{y_k}{F(a_k)} + \frac{1 - y_k}{1 - F(a_k)} \right] = \sum_{k=1}^{n} I_\beta(y_k) \quad = \quad 0 \qquad (5.11)$$

The previous system of equations can be solved straightforwardly using standard optimization algorithms. The amount of information of Fisher provided by a n-sample about the set of parameters $\underline{\theta}$ can be written as:

$$\mathcal{I}_{i,j}(\underline{\theta}) = \mathrm{Cov}\left[\frac{\partial \ln \mathcal{L}}{\partial \theta_i}, \frac{\partial \ln \mathcal{L}}{\partial \theta_j} \right] = E\left[\frac{\partial \ln \mathcal{L}}{\partial \theta_i} \cdot \frac{\partial \ln \mathcal{L}}{\partial \theta_j} \right] - E\left[\frac{\partial \ln \mathcal{L}}{\partial \theta_i} \right] E\left[\frac{\partial \ln \mathcal{L}}{\partial \theta_j} \right] \qquad (5.12)$$

where $\mathcal{I}_{i,j}$ is the general term of the symmetrical positive-definite Fisher information matrix, $\mathrm{Cov}[\cdot]$ denotes the covariance and $E[\cdot]$ the expectation. This matrix corresponds to a measure of the ability of the data to estimate the set of parameters α and β. Developing for the expectation value of the partial derivative with respect to α:

$$
\begin{aligned}
E\left[\frac{\partial \ln \mathcal{L}}{\partial \alpha}\right] &= E\left[\sum_{k=1}^{n} I_\alpha(Y_k)\right] \\
&= \int_{y_1} \dots \int_{y_n} \sum_{k=1}^{n} I_\alpha(y_k)\, f(y_1)dy_1 \dots f(y_n)dy_n \\
&= \int_{y_1} I_\alpha f(y_1)dy_1 \underbrace{\int_{y_2} \dots \int_{y_n} f(y_2)dy_2 \dots f(y_n)dy_n}_{=1} + \dots \\
&\quad + \int_{y_n} I_\alpha f(y_n)dy_n \underbrace{\int_{y_1} \dots \int_{y_{n-1}} f(y_1)dy_1 \dots f(y_{n-1})dy_{n-1}}_{=1} \\
&= n\, E\left[I_\alpha(Y)\right]
\end{aligned}
\qquad (5.13)
$$

Now, using the properties of the pdf $f(y)$ and assuming that the sample size n is a large value, the expectation can be approximated by the mean:

$$E\left[I_\alpha(Y)\right] \approx \frac{1}{n} \sum_{k=1}^{n} I_\alpha(y_k; \alpha, \beta) \qquad (5.14)$$

If the estimators $\hat{\alpha}$ and $\hat{\beta}$ values of the fragility curve are used, right-hand term of the previous expression is approximatively equal to zero. Similar analysis can be conducted for the expected value of the partial derivative with respect to β. Consequently, assuming a large number of sampling and using maximum likelihood estimators, the general term of the Fisher information matrix can be estimated as:

$$\hat{\mathcal{I}}_{i,j}(\underline{\theta}) \approx E\left[\frac{\partial \ln \mathcal{L}}{\partial \theta_i} \cdot \frac{\partial \ln \mathcal{L}}{\partial \theta_j} \right] \qquad (5.15)$$

Developing for example the cross parameter term $\hat{\mathcal{I}}_{\alpha,\beta}$:

$$
\begin{aligned}
E\left[\frac{\partial \ln \mathcal{L}}{\partial \alpha} \cdot \frac{\partial \ln \mathcal{L}}{\partial \beta}\right] &= \int_{y_1} \cdots \int_{y_n} \left(\sum_{k=1}^{n} I_\alpha(y_k)\right) \cdot \left(\sum_{k=1}^{n} I_\beta(y_k)\right) f(y_1)dy_1 \ldots f(y_n)dy_n \\
&= \int_{y_1} I_\alpha(y_1)I_\beta(y_1)f(y_1)dy_1 \underbrace{\int_{y_2} \cdots \int_{y_n} f(y_2)dy_2 \ldots f(y_n)dy_n}_{=1} + \ldots \\
&\quad + \int_{y_1} I_\alpha(y_1)f(y_1)dy_1 \int_{y_n} I_\beta(y_n)dy_n \underbrace{\int_{y_2} \cdots \int_{y_{n-1}} f(y_2)dy_2 \ldots f(y_{n-1})dy_{n-1}}_{=1} + \ldots \\
&\quad \ldots + \int_{y_n} I_\alpha(y_n)I_\beta(y_n)f(y_n)dy_n \underbrace{\int_{y_2} \cdots \int_{y_{n-1}} f(y_2)dy_2 \ldots f(y_{n-1})dy_{n-1}}_{=1} \\
&= n\, E\left[I_\alpha(Y)\, I_\beta(Y)\right] + \frac{n!}{(n-2)!} E\left[I_\alpha(Y)\right].E\left[I_\beta(Y)\right]
\end{aligned}
\tag{5.16}
$$

where $\cdot!$ denotes the factorial. In a similar manner, assuming a large number of sampling and using maximum likelihood estimators, it is easy to probe that terms of estimators of Fisher information matrix can be computed as:

$$
\hat{\mathcal{I}}_{\alpha,\alpha} = \sum_{k=1}^{n} \left(\frac{\Phi'(a_k)}{\hat{\alpha}\,\hat{\beta}}\right)^2 \left[-\frac{y_k}{F(a_k)} + \frac{1-y_k}{1-F(a_k)}\right]^2
\tag{5.17}
$$

$$
\hat{\mathcal{I}}_{\alpha,\beta} = \sum_{k=1}^{n} \frac{(\Phi'(a_k))^2}{\hat{\alpha}\,\hat{\beta}^3} \ln\frac{a_k}{\hat{\alpha}\,\bar{a}} \left[-\frac{y_k}{F(a_k)} + \frac{1-y_k}{1-F(a_k)}\right]^2
\tag{5.18}
$$

$$
\hat{\mathcal{I}}_{\beta,\beta} = \sum_{k=1}^{n} \left(\frac{\phi'(a_k)}{\hat{\beta}^2}\right)^2 \left(\ln\frac{a_k}{\hat{\alpha}\,\bar{a}}\right)^2 \left[-\frac{y_k}{F(a_k)} + \frac{1-y_k}{1-F(a_k)}\right]^2
\tag{5.19}
$$

In order to obtain a bound of the variance associated to estimators of parameters, it is possible to use the Cramér-Rao inequality or the information inequality. For an estimator of a scalar parameter θ, the variance of any unbiased estimator $\hat{\theta}$ of θ is lower-bounded by the inverse of the Fisher information $\mathcal{I}(\theta)$:

$$
\text{Var}\left[\hat{\theta}\right] \geq \frac{1}{\mathcal{I}(\theta)}
\tag{5.20}
$$

where $V[\cdot]$ denotes the variance. For the multi-parameter case, if $\underline{\Theta}$ denotes the estimator of a function of the parameters $\underline{\theta}$ and $E[\underline{\Theta}] = \underline{\psi}(\underline{\theta})$, the Cramér-Rao bounds of the covariance matrix of $\underline{\Theta}$ satisfies:

$$
\text{Cov}\left[\underline{\Theta}\right] \geq \frac{\partial \underline{\psi}(\underline{\theta})}{\partial \underline{\theta}} [\mathcal{I}(\underline{\theta})]^{-1} \left(\frac{\partial \underline{\psi}(\underline{\theta})}{\partial \underline{\theta}}\right)^t
\tag{5.21}
$$

where the upperscript t denotes the transpose. If $\underline{\Theta}$ is an unbiased estimator of $\underline{\theta}$, i.e. $\psi(\underline{\theta}) = \underline{\theta}$, then the Cramér-Rao bound reduces to:

$$
\text{Cov}\left[\underline{\theta}\right] \geq [\mathcal{I}(\underline{\theta})]^{-1}
\tag{5.22}
$$

thus, the inverse of the Fisher information matrix provides the Cramér-Rao bounds, i.e. the relative covariances of the simultaneous estimation of different parameters from a set of realizations. Under certain weak regularity conditions, the maximum likelihood method is asymptotically optimal. Hence, the bias of the estimator tends to zero as the sample size increase to infinity. Additionally, the method

achieves the Cramér-Rao lower bound asymptotically. In practice, these properties are approximately true when the sample size is moderately large (van der Vaart, 2000). Hence, assuming that the number of observations is large enough to satisfy asymptotic properties, the Fisher information matrix can be estimated by the observed information matrix.

Fisher information matrix is used in this chapter to control the amount of information provided by a selection of ground motions to construct the fragility curve associated to the probability of exceeding a specific value of a response. For example, if the studied response is a level of damage, intuitively a large collection of ground motions is required to explore higher levels of damage (relative rare events) in comparison to low levels of damage. Studying the evolution of the amount of information provided with the increasing of the number of motions considered, some guidelines regarding the size of the database required to obtain a reliable fragility curve for a specific level of damage can be derived.

5.5 Numerical results

As previously described, two kinds of dynamic analyses were carried out: a complete soil-foundation SSI-FE approach and a two-step T-S strategy. Additionally, in order to reduce the CPU-runtime, equivalents 2D models were constructed for both SSI-FE and T-S approaches. Full 3D models were studied using the earthquake selection described in §5.3.1, thus a total of 40 dynamical analyses were carried out for each SSI-FE and T-S approaches. Equivalents 2D models for both SSI-FE and T-S approaches were subjected to synthetic ground motions. A total of 200 input motions were generated using the nonstationary stochastic procedure described in §5.3.2. This number is justified below, in terms of the amount of information provided to generate reliable fragility curves.

5.5.1 Input motions

In order to highlight the differences of the frequency contents between both earthquake collections at outcropping level, Fig.5.6 displays 5% damped elastic response spectra shapes (normalized to ground acceleration). Computed spectra for 40 selected real motions, spectra envelopes and reference spectrum for soil class S_0 in seismic zone III (French Antilles) according to French seismic design guidelines defined in PS-92 (1999) are presented in Fig.5.6a. Fig.5.6b shows the spectral shape envelope, mean shape, one standard deviation and code reference spectrum for the 200 generated motions.

(a) Real earthquake selection   (b) Synthetic ground motions
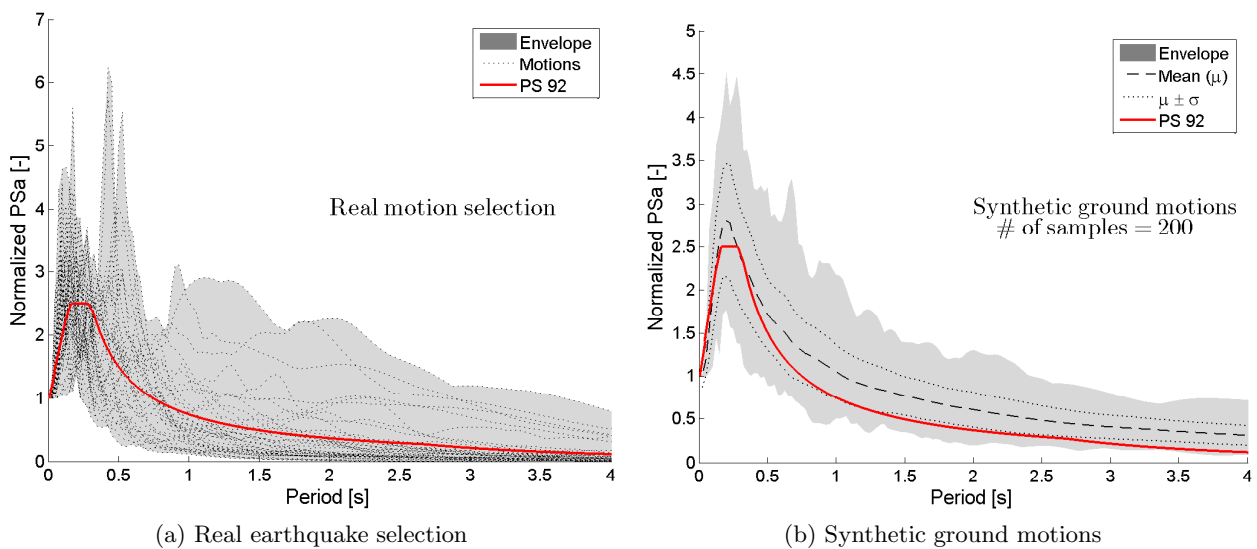
Figure 5.6: 5% damped elastic response spectra shapes.

Most of the spectra shapes presented in Fig.5.6a are compatible with the French seismic design spectrum. Nevertheless, some of them exhibit large long-period spectral ordinates. As described in

§5.3.1, real earthquakes were selected from stations placed in geological conditions compatible with French Antilles on the basis of strong-motion indicator values. Additionally, as site effects are explicitly taken into account in our computations, only records on rock or stiff soil were used. Nevertheless, long-period content noticed in some motions might indicate some site effect associated to the recording site. In order to prevent strong incompatibilities between selected ground motions and a target design spectrum, a spectral ordinates matching criteria can be added to the selection procedure as suggested by Bommer and Acevedo (2004).

Generated ground motions shape spectra displayed in Fig.5.6b agrees satisfactorily with the French design spectra. Indeed, spectral ordinates of mean spectrum for periods smaller than 0.5s approximately coincide with those of design spectrum. For periods large than 0.5s, spectral ordinates are in general larger than those of the design spectrum, specially for periods larger than 1s.

5.5.2   Soil response

In order to define the input motion for the T-S approach (corresponding to the first step), a free field dynamic analysis of the soil profile was performed. Figure 5.7 shows the simulation values representing the peak ground acceleration (PGA) obtained at free field with respect to maximum acceleration amplitude at outcropping bedrock (a_{out}) for both, earthquake selections and synthetics motions. It is possible to see that for weak base acceleration the amplification is near to 3 times the acceleration imposed at outcropping. It is noted that due to soil non-linearity the amplification of the ground response decays with the amplitude. For very strong motions in Fig.5.7a, the amplification vanishes and de-amplification appears for two cases. A second order tendency curve is fitted by least-squares to data and added to Fig.5.7a. This tendency curve has been plotted in Fig.5.7b too.

(a) Real earthquake selection   (b) Synthetic ground motions
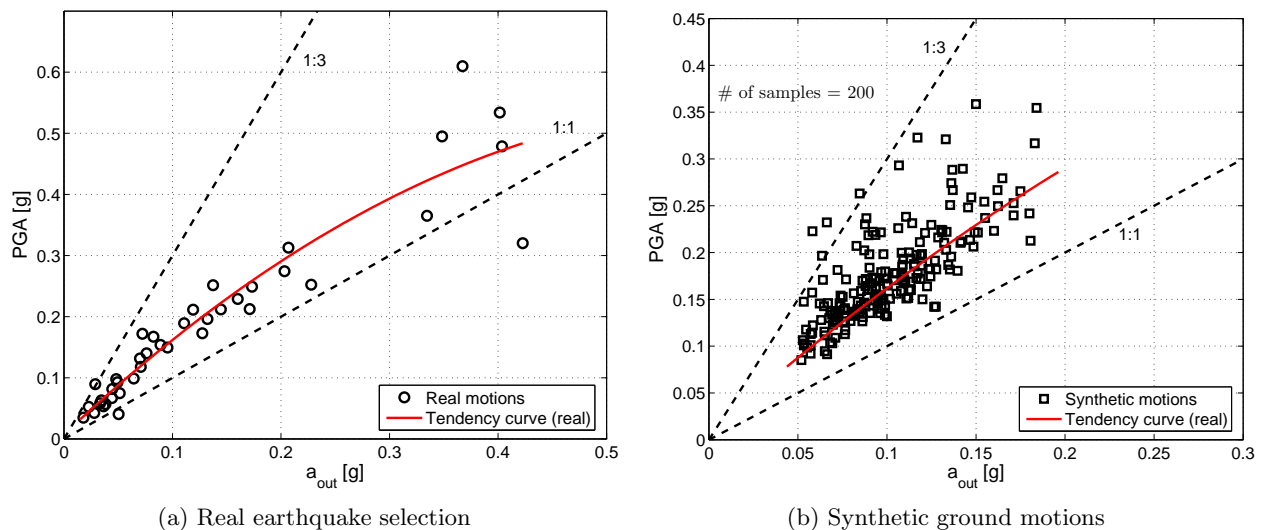
Figure 5.7: Computed PGA in terms of the acceleration amplitude imposed at outcropping bedrock a_{out}

Concerning the acceleration amplitudes of both studied databases, outcropping acceleration of synthetic ground motions lay approximately between $0.05g$ and $0.2g$. In this range, the computed PGA agrees satisfactorily with the tendency curve obtained from real ground motion selection. Dispersions displayed in Fig.5.7b are related to variation of the frequency content of the input motion. Consequently, in this interval, the observed soil response for synthetic ground motions agrees in this interval with the responses obtained for the earthquake selection. For real motion selection, the acceleration amplitude imposed at outcropping varies between $0.05g$ and $0.9g$. Consequently, large variation of the non-linear soil behavior is expected for this database.

5.5.3   Effect of the DSSI on the dynamic response of the system

In order to assess the influence of the DSSI effects on the dynamic non-linear structural response, the results of the two approaches (SSI-FE and T-S) for the studied building are shown in Fig.5.8a for the full 3D model. Results are presented in the form of scatter plots of the maximum value of the computed inter-story drift $ISD_{max,\%}$ normalized by the inter-story height that was observed for each record as a function of the severity parameter of the earthquake. In order to use a common reference for both T-S and SSI-FE approaches, severity measures at outcrop are used for these figures on the x-axis. In general, it is accepted that the use of a pure acceleration amplitude as the measure of severity of earthquakes is not ideal because it does not contain information about duration and the frequency content. This aspect is critical for systems involving stiffness degradation, where the duration and frequency content of strong motion have an important effect on the response of the system (Koutsourelakis et al., 2002). Hereinafter, we use the Arias intensity of acceleration at outcrop AI_{out} as the ground motion severity measure.

(a) Normalized maximum inter-story drift $ISD_{max,\%}$ (b) Overall damage index DI_{ov}
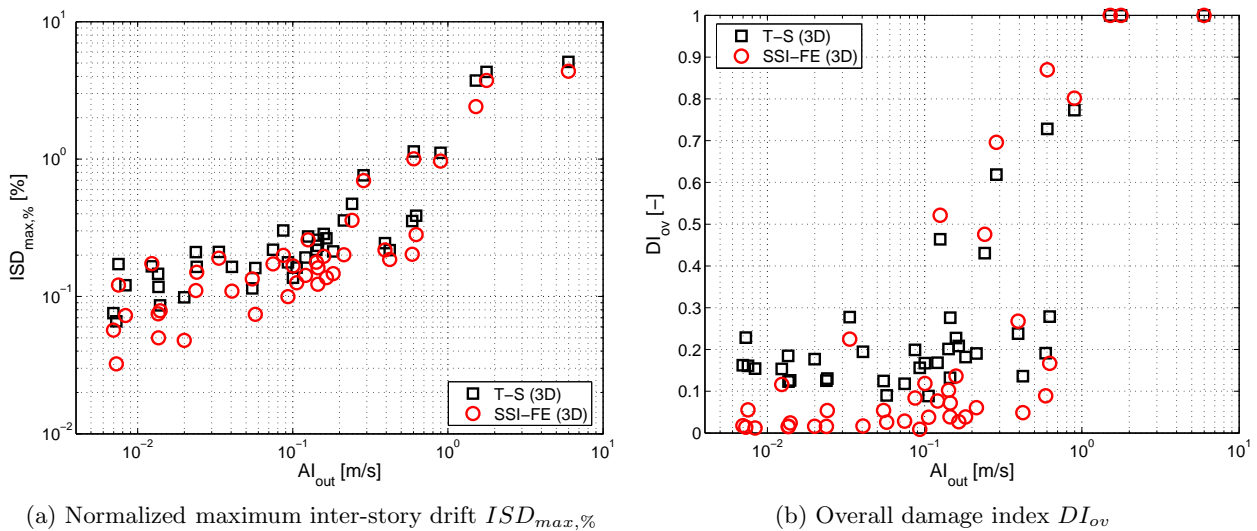
Figure 5.8: Effect of the DSSI on the dynamical response for the full 3D model under real ground motion selection

Fragility curves usually express the probability of reaching a damage state for a given ground motion severity. Similarly to §2.4.3, the damage index used in this chapter to evaluate the structural damage of the structures is based on the damage model for reinforced concrete introduced by Park and Ang (1985). Since the inelastic behavior is confined to plastic zones near the ends of some members, the relation between element and overall structure integrity is not direct. According to the used structural non-linear model, for each potential hinge i, it is possible to compute a local index of damage $DI_{loc,i}$:

$$DI_{loc,i} = \frac{\theta_{m,i}^p}{\theta_u^p} + \lambda_p \frac{1}{M_{y,i}^p \theta_u^p} \int_t M_i^p \, d\theta_i^p \tag{5.23}$$

where $\theta_{m,i}^p$ is the maximum rotation reached during the load history in the plastic component, θ_u^p is the ultimate rotation capacity, $M_{y,i}^p$ is the yield moment of the plastic component and the integral corresponds to the energy dissipated in the section. λ_p is a model constant parameter. For nominal strength deterioration of reinforced concrete sections a value of 0.1 for this parameter has been suggested by Park and Ang (1985). Finally, the θ_u value corresponds to the largest cumulated plastic rotation of the hinges at the end of incremental pushover analysis.

Similarly to §2.4.3 and Hwang and Huo (1994), the overall damage index is computed using weighting factors based on dissipated hysteretic energy at each potential hinge i:

$$DI_{ov} = \sum_i \lambda_i \, DI_{loc,i} \quad \text{with} \quad \lambda_i = \frac{\int_t M_i^p \, d\theta_i^p}{\sum_i \int_t M_i^p \, d\theta_i^p} \tag{5.24}$$

where λ_i is the energy weighting factor of the potential hinge i. This parameter was calibrated in terms of ultimate plastic hinge rotations observed during incremental pushover test. Hence, the value of DI_{ov} corresponds to a relative damage to pushover collapse damage state.

Fig.5.8b displays the computed overall damage index of the building for SSI-FE and T-S computations using the 3D model. When DSSI effects are taken into account, in general a reduction of damage index is found. Assuming that a threshold limit for slight structural damage can be fixed at $DI_{ov} < 0.2$ (Hwang and Huo, 1994), the SSI-FE computations show that this limit is reached only if AI_{out} is larger than 0.1m/s. Furthermore, only for $AI_{out} > 1$m/s the total collapse is found, i.e. a DI_{ov} near to 1. For some motions in the intermediary range $0.1 < AI_{out} < 1$m/s, T-S approach provides a conservative prediction of the expected damage. However, results given by two approaches are relatively close.
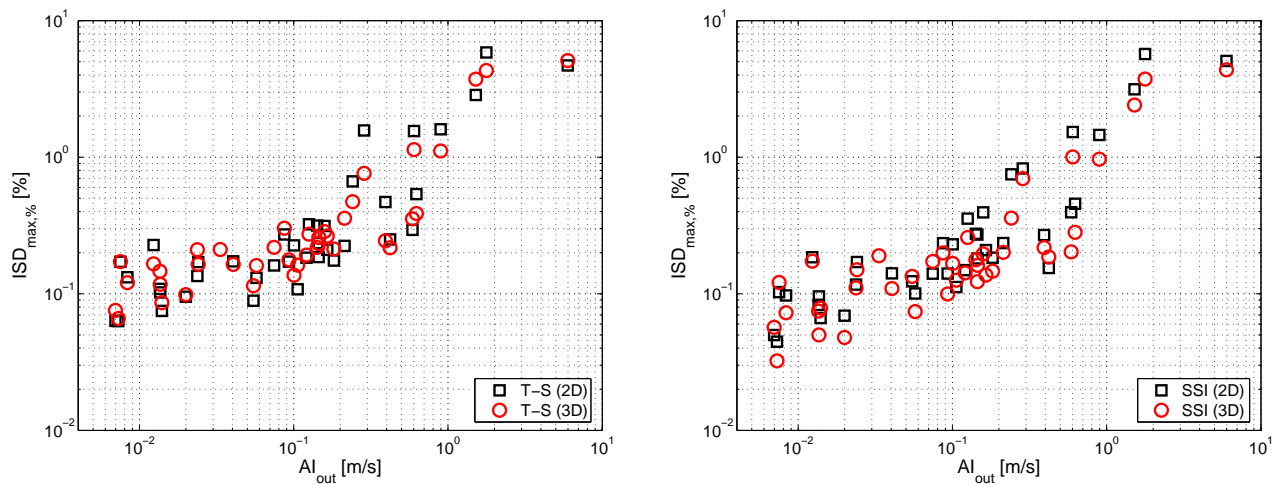
(a) Computed normalized maximum inter-story drift $ISD_{max,\%}$ following T-S approach

(b) Obtained normalized maximum inter-story drift $ISD_{max,\%}$ following SSI-FE approach

Figure 5.9: Comparison of dynamical non-linear responses using equivalent 2D and 3D models

In order to complete validations of the equivalent 2D model constructed for the target building, Fig.5.9 shows the non-linear dynamical responses associated to 40 real motions in terms of the normalized maximum interstory-drift $ISD_{max,\%}$. Fig.5.9a displays the results obtained following T-S approach, thus associated to fixed base structural model. In general, results follow the same tendency with variable differences depending on the considered motion. Fig.5.9b presents the same comparison for the SSI-FE computations. Similarly to T-S computations, results are relatively close, providing over or under estimations of the $ISD_{max,\%}$ depending on the input motion. It can be concluded that the accuracy of the proposed 2D equivalent models is more dependent on the frequency content than the amplitude of the input motion. Indeed, depending on the frequency characteristics of the motion, low period torsional modes (neglected in 2D models) might be activated. Nevertheless, responses are in general accurate enough for the seismic vulnerability assessment sensibility analysis presented in §5.5.5.

5.5.4 Fragility curves for real motions

Fragility curves generated describe the probability of reaching or exceeding a damage state as a function of Arias intensity at outcropping AI_{out}. In this study, two damage states are quantified in terms of DI_{ov}: slight to minor ($DI_{ov} \leq 0.2$) and moderate ($0.2 < DI_{ov} \leq 0.4$), that agrees with the ranges suggested by Hwang and Huo (1994).

(a) Overall damage index $DI_{ov} > 0.2$ (b) Overall damage index $DI_{ov} > 0.4$
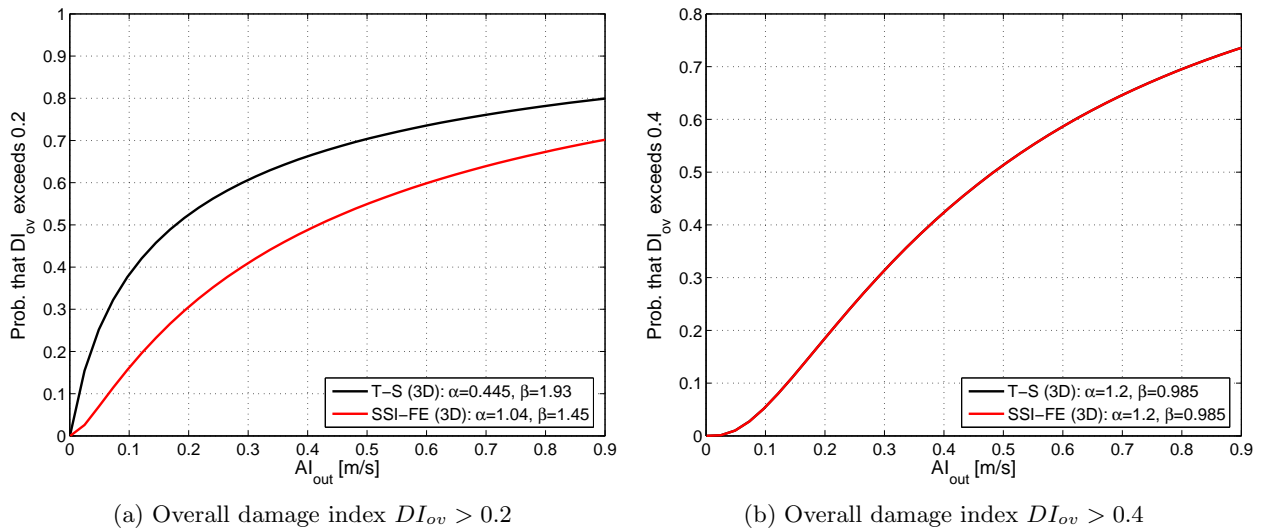
Figure 5.10: Computed fragility curves following both approaches for full 3D models

Fig.5.10 displays the computed fragility curves for the damage states related to the damage index defined above for full 3D computations using the selection of 40 real motions. Fig.5.10a shows the computed fragility curves for the first damage index threshold ($DI_{ov} \geq 0.2$) obtained following T-S and SSI-FE approaches. The fragility curves reflect the variations of the computed damage index obtained for each case (Fig.5.8b), thus a general reduction of seismic demand tendency is observed when DSSI effects are included. Indeed, during dynamic loading soil dissipates energy by both wave radiation and material damping, reducing the effective energy transmitted to superstructure. In contrast in T-S approach only material damping is included in the analysis. Nevertheless, the state of soil in the vicinity of the foundation is not the same in both cases. When the superstructure is included in the model, the effective stress under the foundation grows resulting into an increase of the soil stiffness. This modification of stiffness alters hysteretic dissipation during the dynamic loading, inducing in general, a reduction of material damping compared to free field situation. In this case, for weak to moderate severity motions, added radiative damping compensates the stiffness-increase effect producing a beneficial effect over the seismic response. Whereas, for strong motions, the benefic effect of DSSI seems to vanish. Indeed, according to Fig.5.8b, predicted damage index for both T-S and SSI-FE approaches are closer for severe motions compared to weak or moderate earthquakes. Fixing second threshold at $DI_{ov} = 0.4$, responses are split in the same groups for both T-S and SSI-FE approaches, consequently the same fragility curve is obtained (Fig.5.10b).

5.5.5   Fragility curves for synthetic motions

Fragility curve derived from 3D computations were constructed using a fixed data base of 40 motions. However, from a statistical point of view, it is desirable to evaluate the reliability of these curves. To reach this goal, we study the amount of information provided by the motion sample about the set of parameters α and β controlling the shape of the fragility curve. Due to large number of realizations required to conduct this analysis, we develop the equivalent 2D model described in §5.2.2. Each realization consists in the non-linear time history analysis of the 2D plain-strain model for a synthetic motion.

In order to highlight the effects of the DSSI on the dynamic response, Fig.5.11 shows the computed normalized maximum interstory drift $ISD_{max,\%}$ and the overall damage index DI_{ov} obtained following T-S and SSI-FE approaches. As for the 3D computations and real motions selection, the general tendency is a reduction in $ISD_{max,\%}$ and consequently in damage. The beneficial effect of the DSSI coincides with the previous observation (3D case) for the same range of Arias intensities. Similarly, combined effect of radiative damping, modification of vibrating modes and hysteretic soil dissipation

(a) Normalized maximum inter-story drift $ISD_{max,\%}$ (b) Overall damage index DI_{ov}
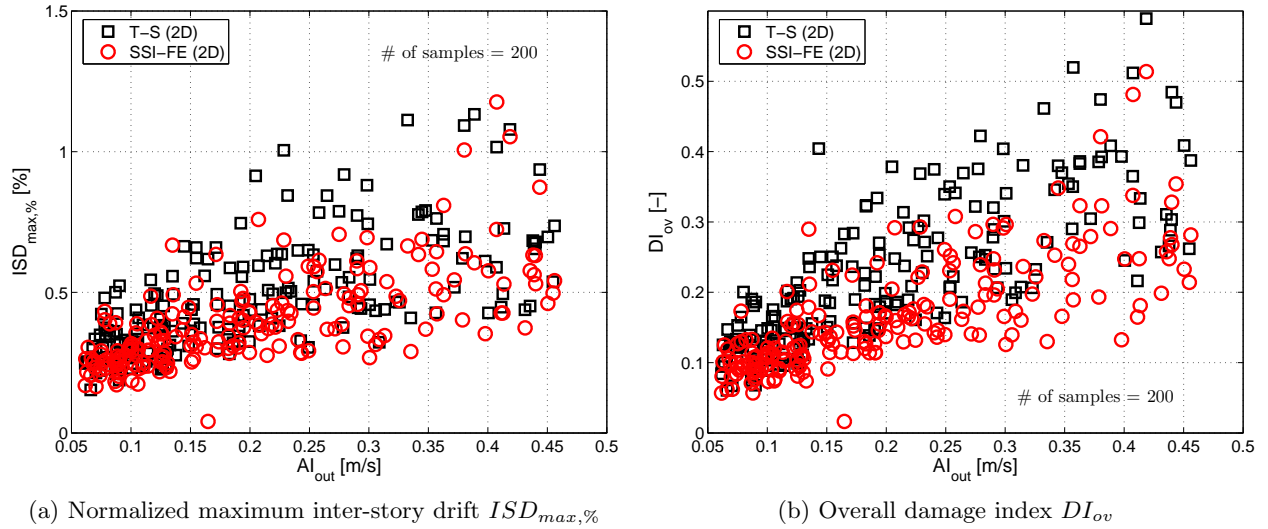
Figure 5.11: Effect of the DSSI on the dynamical response for the equivalent 2D models using synthetic ground motions

due to its non-linear behavior, produces a general reduction of the structural seismic demand. Different effects regarding the DSSI role on the dynamic response of systems have been extensively treated in previous chapters and are omitted here. The problem addressed in this section is the construction of a reliable fragility curve including DSSI effects. However, the statistical study described in the following can be carried out for any other fragility analysis.

(a) Overall damage index $DI_{ov} > 0.2$ (b) Overall damage index $DI_{ov} > 0.4$
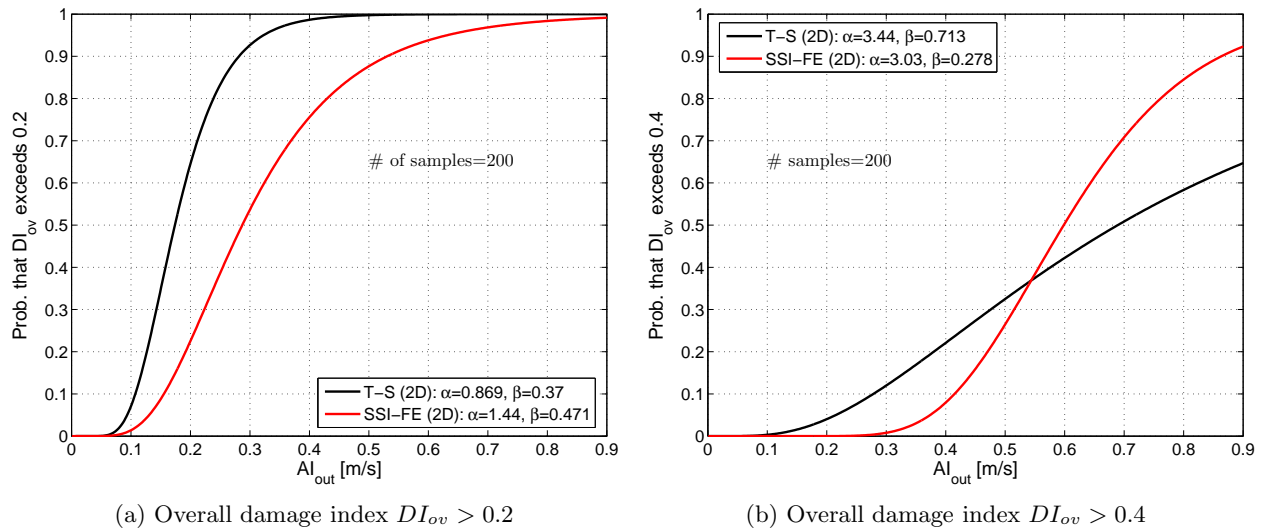
Figure 5.12: Computed fragility curves following both approaches for equivalent 2D models

Assuming that the 200 synthetic motions provide enough information to estimate in a reliable way the parameters defining the fragility curve, the maximum likelihood method can be used to compute numeric values of the estimators $\hat{\alpha}$ and $\hat{\beta}$. Using the procedure described in §5.4, Fig.5.12 shows computed fragility curves for two levels of damage $DI_{ov} = 0.2$ and 0.4 for both T-S and SSI-FE approaches. It should be noted that an Arias intensity range of $0.05 - 0.47 \text{m/s}$ is explored by synthetic ground motions, while log-normal assumption allows extrapolation beyond this range. Doubtlessly, the accuracy of computed fragility curve for large motion severity range is reduced. The obtained fragility curve for the first level of damage ($DI_{ov} > 0.2$) agrees with the tendencies of the dynamical responses, i.e. a general reduction when DSSIs are included. However, for the second level of damage, obtained

fragility curves have an unexpected shape showing a crossing near $AI_{out} = 0.5\,[\text{m/s}]$. In principle, this abnormality might be attributed to a lack of information relative to this level of damage. In order to quantify this aspect, we will study the evolution of the information provided by a variable size of motion database over the parameters α and β describing the fragility curve.

The effect of parameters α and β on the shape of the fragility curve, can be highlighted by developing the logarithmic argument of the corresponding analytical expression (5.7):

$$F(d|a_k; \alpha, \beta) = \Phi\left[\frac{1}{\beta}\ln a_k - \frac{1}{\beta}\ln\left(\alpha\,\bar{a}\right)\right] \tag{5.25}$$

consequently α controls the relative position of the curve on the a_k axis (AI_{out} in Fig.5.12), and β defines both the slope and the position. We repeat the computation of estimators of these parameters for a motion database size increasing from 105 to 200 (Fig.5.13). The number of 105 was selected to ensure at least one case surpassing the second level of damage for SSI-FE computation. Of course, as synthetic motions are randomly generated, this minimum database size is controlled by the intrinsic randomness of the synthetic generator. The normalization variable $\bar{a}$ has been computed as the mean of the 200 AI_{out} values and kept constant for this analysis.

(a) Overall damage index $DI_{ov} > 0.2$ (b) Overall damage index $DI_{ov} > 0.4$
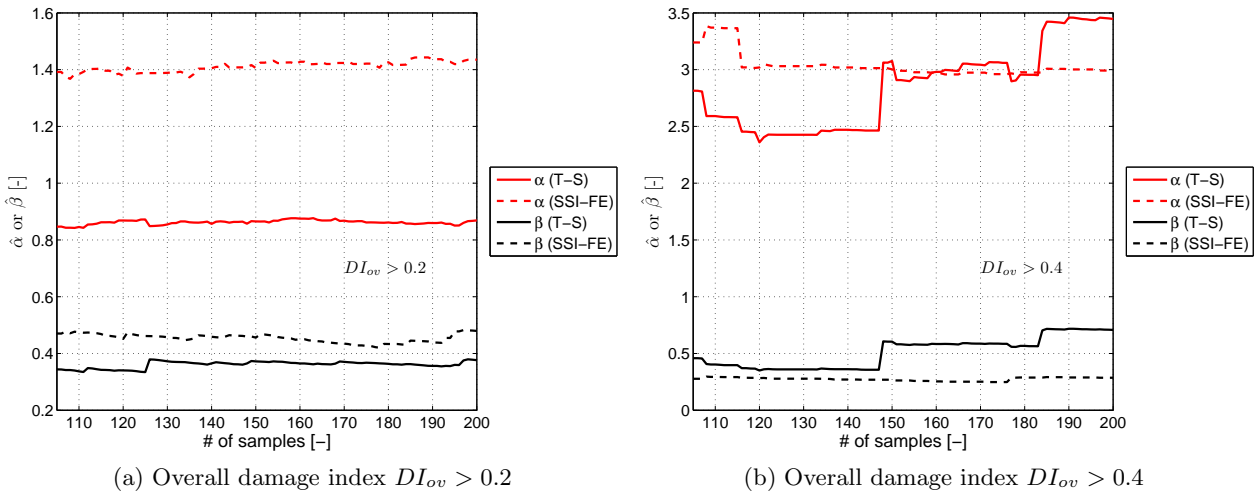
Figure 5.13: Evolution of parameters α and β with the number of samples considered

According to Fig.5.13, both α and β estimators have stable values after 105 realizations for the first level of damage. In contrast with $DI_{ov} > 0.2$ level, the second level of damage shows strong variation of estimated values for these parameters. When DSSI is included, estimated values of α and β are approximately stable after 120 realization. For T-S approach two jumps can be noticed, close to 150 and 180 realizations. These realizations corresponds to additional cases showing $DI_{ov} > 0.4$. Consequently, for this size of database, general tendencies of the parameters are extremely sensible to additional cases sustaining the studied level of damage. It can be concluded that despite relative stability of the numeric values of the estimators, the study of the evolution with the number of realizations can provide an erroneous idea of convergency.

Stoping the number of realizations at 140, the obtained fragility curves for the second level of damage are displayed in Fig.5.14. These curves have a more reasonably shape than those in Fig.5.12b, nevertheless, they include less information regarding α and β. According to expression (5.25), the increase of the value in β for SSI-FE case close to realization number 150 reduces the slope of the fragility curve and, combined with the increase of the value of α, shifts the fragility curve to the left.

In order to study the evolution of the information with the number of realizations, it is convenient to introduce a geometric interpretation of the Fisher information matrix. Indeed, Fisher information is the negative of the expectation of the second derivative of $\ln\mathcal{L}$ (5.8) with respect to parameters. Thus, it can be seen as a measure of the sharpness of $\ln\mathcal{L}$ near the maximum likelihood estimate of
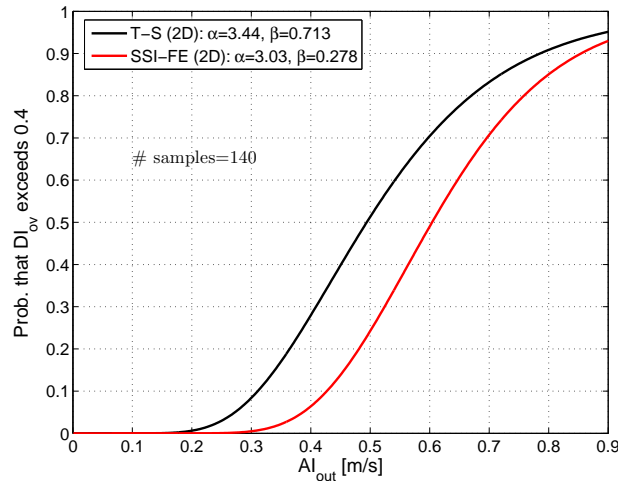
Figure 5.14: Computed fragility curves following both approaches for $DI_{ov} > 0.4$ using 140 realizations

the parameters. In this case, $\ln \mathcal{L}$ corresponds to a surface in the $\alpha - \beta$ plane. Consequently, a blunt surface has low expected second derivative (low information), while a sharp one has a high expected second derivatives (high information). In order to illustrate this geometrical interpretation in this case, Fig.5.15 presents iso-values of $\ln \mathcal{L}$ around the estimators $\hat{\alpha}$ and $\hat{\beta}$ over a window of ± 0.3 and ± 0.2 for α and β axes, respectively. Ten contours are plotted in each case, thus relative separations between successive iso-values indicate the sharpness of the surface $\ln \mathcal{L}$. Optimal value satisfying (5.9) is represented by a red cross. It can be noticed that a sharper surface, i.e. with more associated information, is found for T-S approach compared to SSI-FE approach for the same level of damage. Thus, for the same number of realizations, T-S fragility curve is in some sense more reliable than the one for SSI-FE approach.

(a) Two-step approach

(b) SSI-FE approach
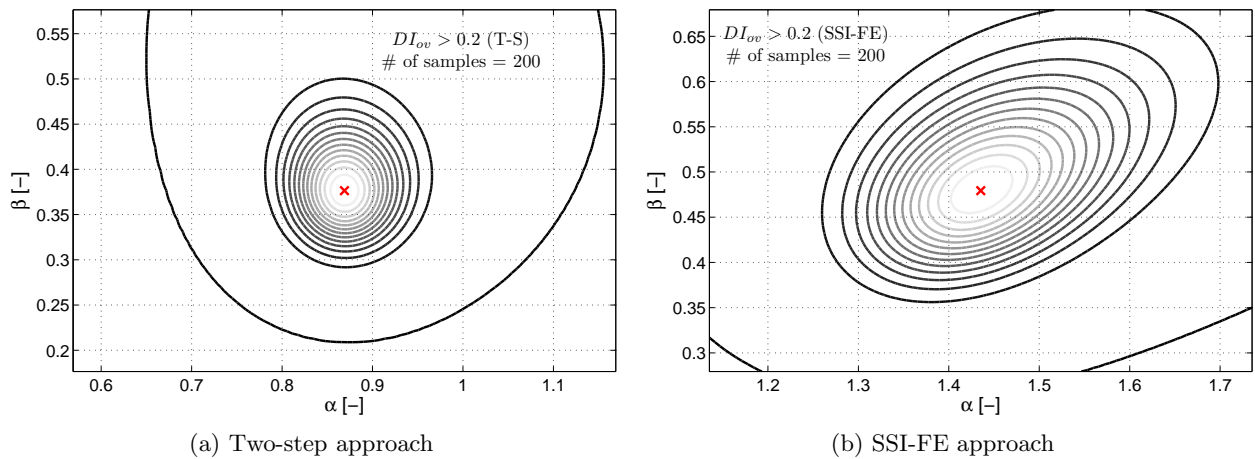
Figure 5.15: Contours of $\ln \mathcal{L}$ around $\hat{\alpha} \pm 0.3$ and $\hat{\beta} \pm 0.2$ for the level of damage $DI_{ov} > 0.2$

In order to associate this surface sharpness with a variability of the parameters α and β, Fig.5.16a displays the evolution of the eigenvalues of the Fisher information matrix $\mathcal{I}_{i,j}(\alpha, \beta)$ associated to the first damage level as a function of the number of realizations (i.e. $DI_{ov} > 0.2$). Fig.5.16b shows the corresponding orientation of eigenvectors using a polar reference in terms of the angle θ with respect to the axis α.

Computed eigenvalues agree with the iso-values represented in Fig.5.15. Thus, for the first level of damage, T-S provides more information (larger values of λ_1 and λ_2) compared to SSI case. Additionally, values of both eigenvalues are of the same order after 130 realizations, that agrees with the approximate round shape of contours of $\ln \mathcal{L}$. In SSI-FE case, first eigenvalue (λ_1) is approxi-

(a) Eigenvalues

(b) Orientation in $\alpha - \beta$ plane
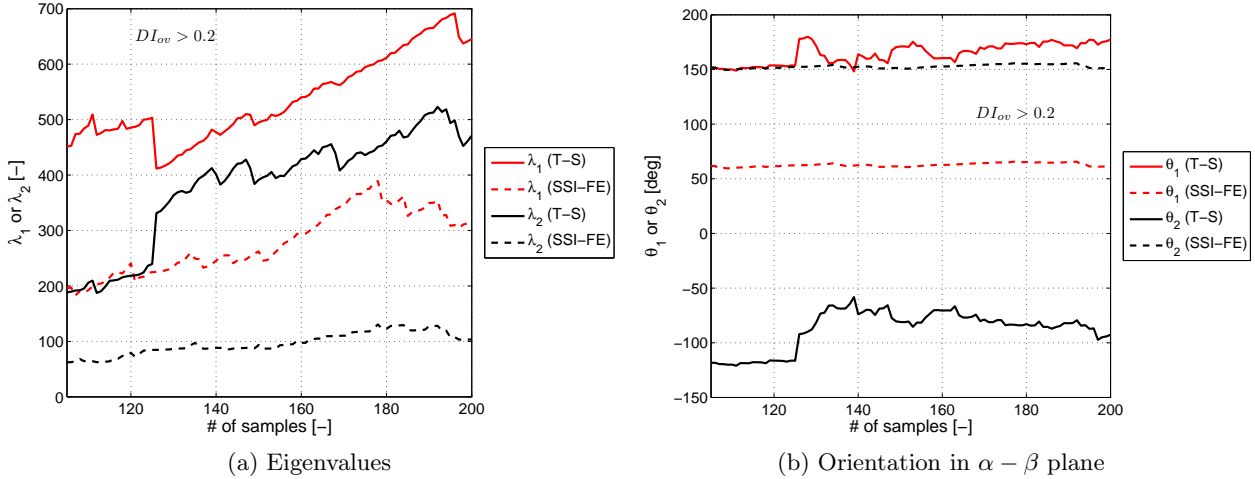
Figure 5.16: Eigenvalues and eigenvectors of Fisher information matrix evolution for $DI_{ov} > 0.2$

mately three times larger than λ_2, producing approximately elliptic iso-values around the optimal. It is also interesting to analyze the orientation of eigenvectors. In T-S approach, orientation of the first eigenvector is close to α axis ($\theta_1 \approx 180°$), thus a better description of this parameter is provided by the database. In this case, the second eigenvector approximately coincides with β axis ($\theta_2 \approx -90°$). While, for SSI-FE approach, eigenvectors are rotated approximately $60°$ with respect to $\alpha - \beta$ axes. Thus, there is a strong covariance between α and β in this case.

(a) Standard deviation of parameters in eigenvalue directions

(b) Covariance of parameters α and β
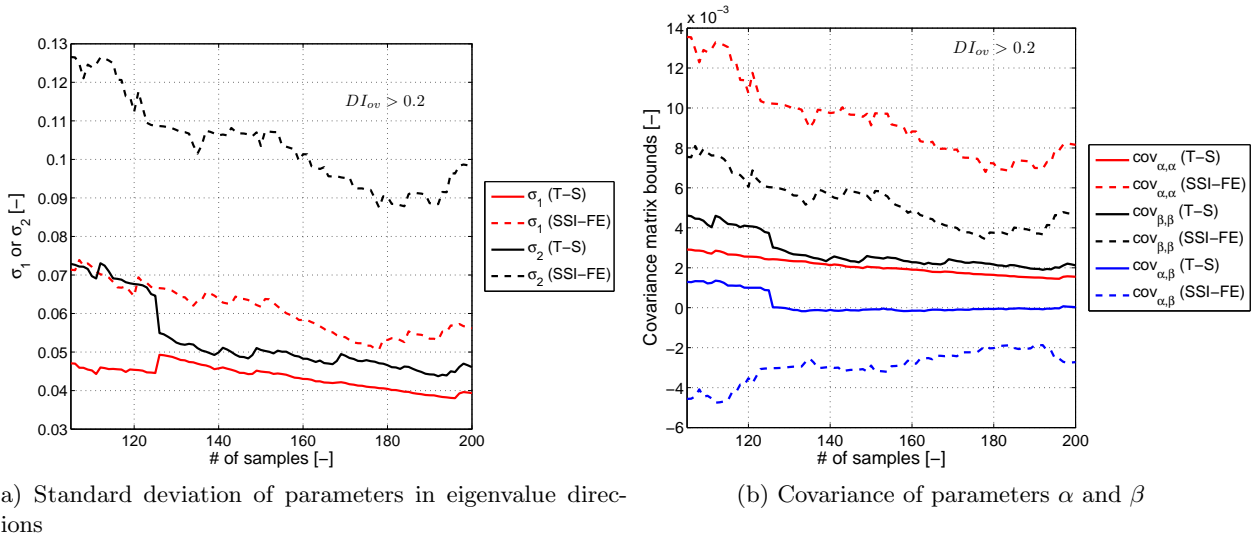
Figure 5.17: Evolution of lower-bounds of parameters for the overall damage index $DI_{ov} > 0.2$

Concerning the evolution of eigenvalues, it can be noticed that eigenvalues grow linearly after 130 realizations in T-S case. That means that the amount of information grows with the same rate as that of the number of samples n, i.e. $\frac{\lambda}{n}$ is approximately constant. A better way to study the evolution of the information with the number of samples can be conducted in terms of the variance or the standard deviation of the parameters. According to Cramér-Rao bound, the variance of any unbiased estimator is at least as high as the inverse of the Fisher information. In terms of the eigenvalues, the variance of the parameters following the direction of the eigenvectors i can be lower-bounded by $\frac{1}{\lambda_i}$. Or by $\frac{1}{\sqrt{\lambda_i}}$ for the standard deviation.

Fig.5.17 shows the evolution of the lower bound of standard deviation of the parameters σ_i in the eigenvalue direction i. Due to orientation of eigenvalues for T-S approach and for $DI_{ov} > 0.2$ damage

level, the values of σ_1 and σ_2 can be interpreted directly as lower-bound of the standard deviation of α and β, respectively. Thus, according to Fig.5.17a and Fig.5.12a, the value of α obtained with 200 realizations is approximately equal to 0.86 with a standard deviation of at least 0.04, similarly, 0.37 for β with a standard deviation of at least 0.045. Consequently, coefficients of variation of at least 5% and 12%, for α and β respectively are obtained. This information might be used to construct confidence intervals for α and β and define families of fragility curves by varying the confidence on the parameters for example. However, the strategy described before gives a lower-bound of standard deviation of parameters defining fragility curve. Consequently, the use of this information to estimate confidence intervals requires judgement.

Due to the orientation of eigenvectors for SSI-FE approach, the analysis of the variance of the estimated parameters is conducted directly with the inverse of the Fisher information matrix according to expression (5.22). Thus, Fig.5.17b displays the evolution of the lower-bounds of the covariance matrix terms for both approaches associated to the first level of damage. It can be noticed that the cross term $\text{Cov}_{\alpha,\beta}$ is near to zero after 130 samples in T-S case, while it is negative and of the same order as the diagonal terms for the SSI-FE approach. These curves confirm the evolution of orientations shown in Fig.5.16. Regarding the diagonal terms of the bound covariance matrix, large uncertainty is associated to α parameter in comparison to β for SSI-FE case, that is the opposite of $T-S$ case. Additionally, variances in SSI-FE approach are significantly larger than those in the T-S approach. Consequently, larger uncertainties are associated to the position rather than to the slope of the fragility curve. These conclusions can not be derived directly from the evolution of $\hat\alpha$ or $\hat\beta$ with the number of samples (Fig.5.13). Thus, it can be concluded that the apparent stabilization of estimators must not to be interpreted as a convergency of the fragility curves. In this case, curves associated to SSI-FE are less reliable on a statistically point of view compared to those derived from T-S results.

(a) Two-step approach

(b) SSI-FE approach
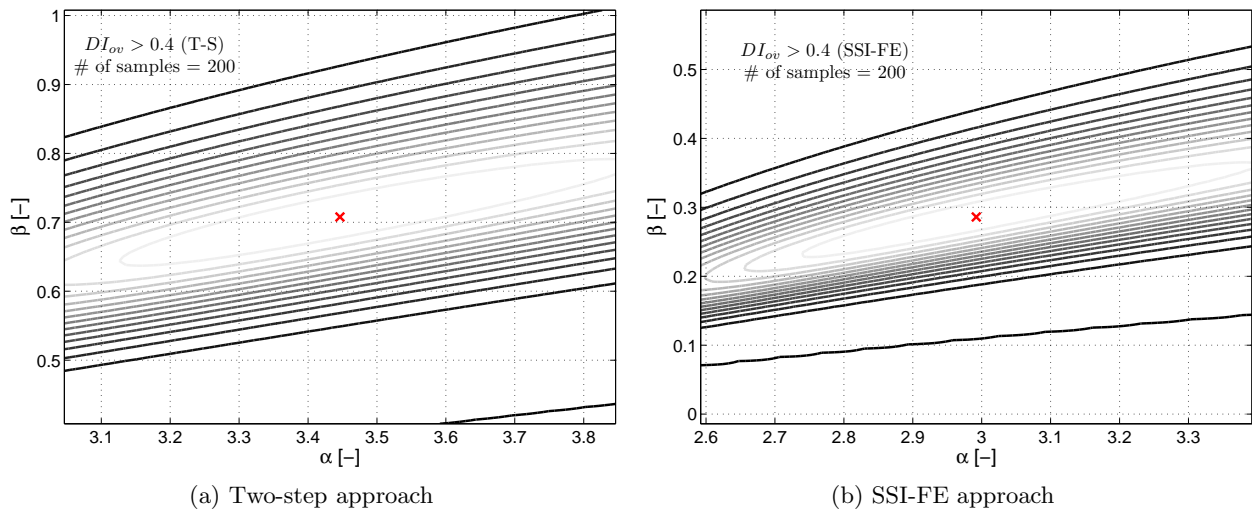
Figure 5.18: Contours of $\ln\mathcal{L}$ around $\hat\alpha \pm 0.4$ and $\hat\beta \pm 0.3$ for the level of damage $DI_{ov} > 0.4$

Concerning the second level of damage ($DI_{ov} > 0.4$), Fig.5.18 shows the iso-values of $\ln\mathcal{L}$ for 200 realizations, around the optimal values of $\hat\alpha$ and $\hat\beta$ for a window of ± 0.4 and ± 0.3 in α and β axes, respectively. Ten contours are plotted in each case, to make comparisons between both approaches possible. According to this figure, there are large uncertainties regarding one of the principal directions (large separation in iso-values). Fig.5.19 shows the corresponding eigenvectors and eigenvalues.

It can be noticed that the first eigenvalue (λ_1) is very close to β axis in both cases ($\theta_1 \approx 80°$). Consequently, second eigenvector corresponds approximately to α value. According to the numerical value of λ_2, there is very few information regarding α, i.e. the relative position of the fragility curve in the AI_{out} axis (Fig.5.12b). Additionally, according to the evolution of λ_1 with the number of samples, information provided by the motions in T-S case is very erratic, while λ_1 for SSI-FE grows monotonically with the number of samples. Indeed, there is an abrupt broke near to 150 realizations

(a) Eigenvalues

(b) Orientation in $\alpha - \beta$ plane
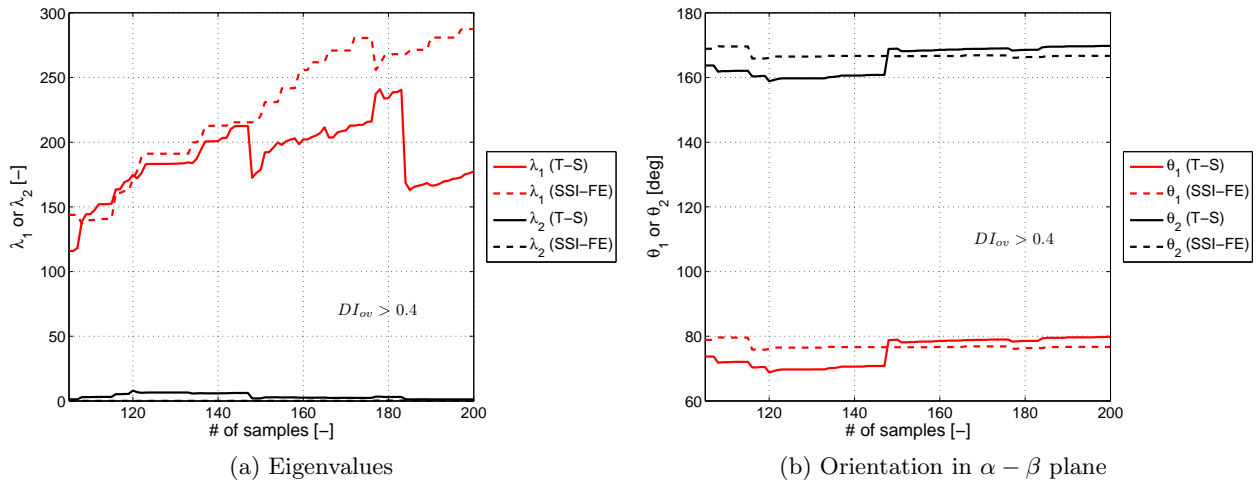
Figure 5.19: Eigenvalues and eigenvectors of Fisher information matrix evolution for $DI_{ov} > 0.4$

in T-S case due to the apparition of realizations satisfying the damage criterion. Thus, for this level of damage, the database is not large enough and there is a great sensibility to additional cases sustaining the studied level of damage. Even if evolution of λ_1 for the SSI-FE analysis seems stabilized ($\frac{\lambda_1}{n}$ approximately constant), the second eigenvalue λ_2 is close to zero. Assuming that λ_1 corresponds approximately to the lower-bound of variance of β in SSI-FE case, for 200 realizations we obtain that $\hat{\beta} = 0.278$ with a variance of at least $\frac{1}{\sqrt{\lambda_1}} \approx 0.06$, thus a coefficient of variation of 20%. For the second parameter α, as λ_2 is close to zero we have a very large lower-bound standard deviation. In conclusion, there is not enough information to construct fragility curves for this level of damage. On the basis of these arguments, we need to increase significantly the number of realizations and/or to add stronger records exploring a larger range of motion severity in order to increase data sustaining the second level of damage.

Table 5.2: Eigenvalues and eigenvectors for real ground motion selection used for 3D models

Parameter	T-S		SSI-FE	
	$DI_{ov} > 0.2$	$DI_{ov} > 0.4$	$DI_{ov} > 0.2$	$DI_{ov} > 0.4$
λ_1	66	21	50	33
θ_1	$-80°$	$-60°$	$-80°$	$-70°$
λ_2	5	3	6	4
θ_2	$-170°$	$-150°$	$-170°$	$-160°$

To complete this analysis, it is interesting to estimate the information provided by real ground motion collection used to compute fragility curves for 3D models (§5.5.4). Rounded values of eigenvalues and eigenvectors for T-S and SSI-FE approaches are summarized in Tab.5.2 for the 40 real motions selected, and for the two levels of damages explored. According to eigenvector orientations, for all combinations the first eigenvector is close to β axis ($\theta_1 \approx 80°$) and the second eigenvector is close to α axis, i.e. associated to the position of the fragility curve. In general, eigenvalues are significantly smaller than those obtained for the synthetic motion study. For example, for the first level of damage of T-S case, the lower bound of the standard deviation can be obtained as $\frac{1}{\sqrt{\lambda_1}} \approx 0.12$. According to the value of $\hat{\beta}$ in Fig.5.10b, the corresponding coefficient of variation is at least of 33%. Performing the same computation for the other parameters we obtain larger coefficients of variation. Consequently, this 40 real motions selection give a poor description in a statistically point of view of the parameters describing the fragility curve. This conclusion is not evident from the fragility curves, highlighting the importance of the provided information analysis presented in this section.

5.6   Concluding remarks

A study on the influence of DSSI on the assessment of the seismic vulnerability of buildings was presented in this chapter. Two major aspects have been exposed. The first one consists in the development of reasonably equivalent two-dimensional models for a given approximately regular building. The model constructed is accurate enough for practical purposes and represents an important economy in consumption run-time. The second point is related to the development of fragility curves to summarize results from dynamic time history analyses. A strategy to quantify the sufficiency of the information provided by a data collection for the construction of fragility curves was introduced. This strategy points out the importance to conduct a statistical analysis to verify the validity of the set of parameters defining an analytical fragility curve. Unfortunately, this statistical analysis is often neglected by many authors. Strategies exposed in this chapter were applied to a particular case of DSSI, but they are flexible enough to be used for general situations involving soil-foundation-structure interaction problems and fragility analyses.

Concerning the effect of the DSSI on the vulnerability assessment, according to our computations, there is in general a reduction of seismic demand or damage when DSSI phenomena are included. This reduction can be associated fundamentally to two phenomena: radiative damping and hysteretic damping due to non-linear soil behavior. The two-step approach used here neglects radiation damping but includes the non-linear soil behavior in order to modify the effective motion applied to the superstructure. Nevertheless, both effects take place simultaneously during the dynamic load and it is extremely difficult to separate the contribution of each part in reducing seismic demand. Indeed, effective motion transmitted to the superstructure does not correspond to the free field response because of the geometrical and inertial interactions as well as the local modification of soil behavior, specially due to the supplementary confinement imposed by the superstructure. In summary, due to beneficial effect of DSSI highlighted in this chapter, there is an economic justification to include DSSI effects on seismic vulnerability analyses.

——-Conclusions

Conclusions

Summary

In the preceding chapters we have investigated various aspects of the dynamical non-linear SSI. Even if this problem has been the subject of numerous investigations, no simple realistic solution exists for the introduction of the non-linear soil behavior. The major goal of this thesis was to contribute to the understanding of the role of the non-linear soil behavior over the complete problem.

Chapter 1 provides theoretical basis for non-linear DSSI modeling using Finite Element Method. Special developments in the used FE code *GEFDyn* were done, in order to increase the performance of the code and enhance its capabilities to model structural non-linear behavior. The major issue related to numerical modeling is the treatment of the lateral boundaries and damping. Modeling issues associated to the treatment of the lateral boundaries and damping were explored in the form of several numerical validations, in order to justify different adopted choices.

In Chapter 2 we looked into the influence of DSSI effects on the seismic performance evaluation of structures. A parametric study concerning the structure, the input signal and the soil was conducted. The main conclusion of this chapter was that the soil-structure interaction with a non-linear soil model can vary significantly the response of the considered set of structures with respect to those with fixed base condition. In terms of the Capacity Spectrum Method, this chapter points out that the major challenge to quantify the non-linear SSI effects in seismic demand evaluation is to predict an accurate global damping, able to be used in simpler approaches. Three important aspects of the problem were detected: limitations associated to a 2D plane-strain approach, contribution of the elastic part of the soil behavior to the DSSI and the influence of the seismic database on the obtained fragility curves. Each aspect was studied in detail in the other chapters of this document.

In Chapter 3, a modified formulation of standard plane-strain model suitable for regular buildings was presented. The main advantage of the proposed approach lies in the CPU time consumption reduction. The approach was validated and successfully applied to two buildings on three different soils. The effects of the non-linear DSSI result in a variation of the computed structural response compared to that obtained with fixed base condition, even if the non-linear behavior of the soil is taken into account to estimate the imposed free field motion. The evaluation of some energy dissipation measure has been done to highlight the influence of the initial state modification induced by the self weight of the superstructure. Though the self weigh contributes to increase the stiffness of the soil below the foundation, this additional confinement reduces hysteretic behavior under dynamic loading, compensating strain field generated by the superstructure oscillations. In the case of liquefiable soil, severe motions inducing extensive pore pressure build-up result into approximately elastic structural response. In these case, structure responds essentially as a rigid block compared to extensively stiffness degraded soil. Generalization of DSSI effects on displacement demand for a given building on a defined soil was unsuccessful. Large dispersion of results can be associated to the complexity of several non-linear inter-dependant phenomena.

Chapter 4 describes the investigation conducted in order to define the contribution of the pure elastic DSSI effects in the complete non-linear DSSI problem. With this purpose, a comparative analysis between elastic and inelastic soil behavior assumptions for two SDOF structures and two soils is carried out. The results point out that, in general, inelastic soil behavior plays a decisive role only when the soil is saturated. When the soil is in dry condition, an elastic DSSI approach seems to be

accurate enough to take into account the modification of the structural response due to DSSI. Differences in structural dynamics responses are related to pore pressure generation induced in the inelastic case and neglected when elastic soil behavior is assumed. The influence of interaction phenomenon for the low-rise SDOF structure considered is quite erratic. Hence, depending on the characteristics of the ground motion DSSI effects are beneficial or detrimental in dry soil case. In saturated case, inelastic DSSI effects are in general beneficial. Regarding the studied mid-rise superstructure, in both dry and saturated soil cases, the effects of the DSSI are favorable in reducing the expected displacement ductility demand.

Finally, the Chapter 5, is devoted to the development of analytical fragility curves including DSSI effects. Major attention is focused in the statistical confidence of the obtained fragility curve. With this purpose, a strategy to study the sensibility of the two parameters defining the fragility curve on the database in terms of the amount of information provided by the ground motion selection is developed. A set of analytical expressions are derived in order to provide a geometrical interpretation of the parameters describing fragility curves. Strategies presented in this chapter were applied to a particular case of DSSI, but they are flexible enough to be used for general situations involving seismic fragility analyses. The strategy presented points out the importance of conducting a statistical analysis to verify the validity of the set of parameters defining an analytical fragility curve.

Overall conclusions

According to the investigation conducted in this work, except for some cases described in Chapter 4, there is in general a reduction of seismic demand or structural damage when non-linear DSSI phenomenon is included. This reduction can be associated fundamentally to two phenomena: radiative damping and hysteretic damping due to non-linear soil behavior. The two-step approach used as reference throughout this work, neglects radiation damping but includes the non-linear soil behavior in order to modify the effective motion applied to the superstructure. Nevertheless, both effects take place simultaneously during the dynamic load and it is extremely difficult to separate the contribution of each part in reducing seismic demand. Indeed, effective motion transmitted to the superstructure does not correspond to the free field response because of the geometrical and inertial interactions as well as the local modification of soil behavior, specially due to the supplementary confinement imposed by the superstructure's weight. Large efforts have been made in order to generalize findings with a limited success. A series of strong-motion severity measures, structural damage measures and energy dissipation indicators have been introduced and studied for this purpose. Nevertheless, results are in general erratic and consequently, generalization was extremely difficult.

The results of the work illustrate clearly the importance of accounting for the non-linear soil behavior. In this case, the major part of non-linear DSSI effects are beneficial related to decreasing the maximum seismic structural demand. However, the non-linear DSSI could increase or decrease the expected structural damage depending on the type of the structure, the input motion, and the dynamic soil properties. Furthermore, there is an economic justification to take into account the modification effects due to non-linear soil behavior. Further investigations in this direction are needed in order to obtain more general conclusions for diverse structure and soil typologies.

Further research

The current seismic design philosophy is based on non-linear behavior of structures. Thus, design base shear provided by design codes are intentionally much lower than the lateral strength required to ensure an elastic structural behavior. The ratio between the lateral yielding strength required to avoid inelastic behavior and the lateral yield required to sustain a ductility ratio demand μ is usually known as strength reduction factor R_{μ}. During the last decades, several investigations have been conducted in order to improve the reliability of the reduction factors in design provisions. Later, some investigations were conducted in order to point out the effect of the soil conditions (e.g. Miranda and Vertero 1994).

More recent investigations on site-dependent strength reduction factors for soil-structure interacting systems (Ciampoli and Pinto, 1995; Rodriguez and Montes, 2000; Ghannad and Jahankhah, 2007; Avilés and Pérez-Rocha, 2003) have shown the effects of the DSSI. Nevertheless, these studies have been developed using standard approximations for linear elastic DSSI, thus, the effects of the non-linear DSSI has not been considered yet. Findings presented in this work have illustrated the importance of accounting for the non-linear soil behavior. Consequently, the development of R_μ including non-linear site and non-linear DSSI effects can lead to a more reliable seismic design of structures. The use of the methodology presented in this work can contribute to a better understanding of the DSSI effects on the seismic structural design. Of course, the development of this kind of relations needs an extensive parametric investigation on diverse soils, structures and foundations typologies. In addition, the modified plane-strain approach presented in this work might considerably contribute to reduce the CPU time required for such large parametric studies.

The assessment of building damage caused by ground motions requires the definition of building's capacity and vulnerability as a function of the demand. In this problem, there are several sources of uncertainty: the earthquake (demand), the soil and the building itself. Only the problem of the demand variability has been addressed in Chapter 5. Nevertheless in practice the properties of the soil vary as much, exhibiting strong inhomogeneities very difficult to estimate. The risk of damage in soil-structure systems including variability in both, soil and earthquake, has been studied for liquefiable soils (Koutsourelakis et al., 2002; Popescu, 2002; Popescu et al., 2006). However, in these studies, structural damage is estimated using foundation responses (settlement or tilt). Indeed, in these studies the effect of the structural damage in the DSSI has been neglected assuming elastic structures. This simplification is satisfactory for liquefiable soils when structure responds essentially as a rigid block. However, for more general cases, the inelasticity of the superstructure must be included in the analysis. The vulnerability assessment strategy developed in this work can be extended straightforwardly to take into account soil variability. Indeed, the statistical confidence strategy presented in this work is still valid for several sources of uncertainties. Consequently, this aspect could be easily studied.

Concerning the numerical modeling of the DSSI problem, this work was conducted using the so-called direct method. The substructure method in frequency domain was employed as a tool for numerical validation in elastic case. Nevertheless, there are methods that combine advantages of both the direct and substructure method called hybrid method. Usually, a bounded soil domain (near-field) is treated with FEM, while the unbounded soil domain (far-field) is treated with BEM. When material non-linearities are taken into account in near-field, an iterative procedure is carried out to compute interaction forces between both domains. Other sub-structuring methods as the Domain Reduction Method (Bielak et al., 2003) can be used. These kinds of techniques are compatible with the problem addressed in this work and might reduce some wave reflections detected when a tied lateral approach is used. Similarly, other possible improvements to our computations are associated to absorbing boundary conditions. In this work, we use paraxial approximation to compute time domain impedances. This approximation is exact only for normal incident waves. Currently, better approximations for this problem exist (e.g. Bérenger 1994; Basu and Chopra 2003). Therefore, some reduction of wave reflections could be obtained by implementing these absorbing boundaries in *GEFDyn* .

Finally, the main drawback of the adopted strategy is related to the large amount of parameters associated to each FE model. The good performance of each model has been studied by numerical validations under elastic assumption. The calibration of the soil constitutive model parameter has been carried out using reference laboratory test results when available. Nevertheless, no experimental calibrations of the complete non-linear FE models have been done. Doubtlessly, validations against instrumented sites or physical experiments performed in a shaking table or in a centrifuge in inelastic range are desirable.

Appendices

Appendix A

Paraxial approximation

In order to establish the paraxial approximation at the boundary Σ (Fig.1.3), the displacement $\underline{u}_s$ is decomposed on a local coordinate system $(\underline{e}_1, \underline{e}_2, \underline{e}_3)$ over a plane tangent to Σ (Fig. A.1a):

$$\underline{u}_s = \underline{u}_{s'} = u_1 \underline{e}_1 + u_2 \underline{e}_2 + u_3 \underline{e}_3 \tag{A.1}$$
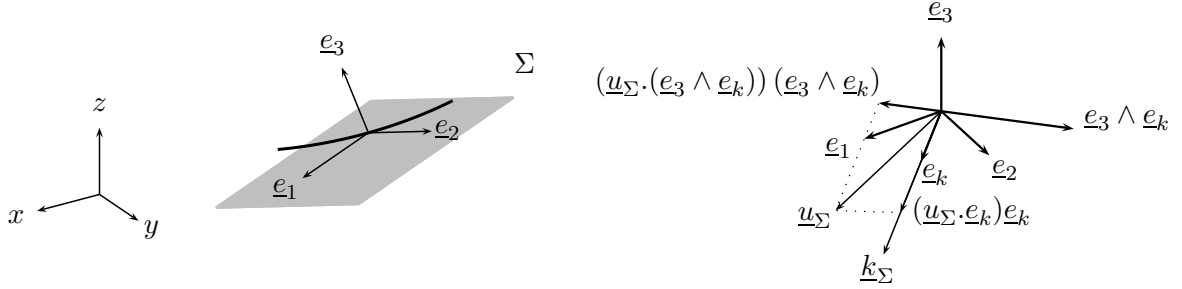
(a) Local displacement decomposition on a tangent plane to the boundary Σ

(b) Definition of local coordinate system to decompose tangent displacement on the basis $(\underline{e}_k, \underline{e}_3 \wedge \underline{e}_k, \underline{e}_3)$

Figure A.1: Local decomposition over a plane tangent to the boundary Σ

Using this local system, the elastodynamics equation (1.34) can be written as:

$$
\begin{aligned}
\left(c_p^2 - c_s^2\right)\left(\partial_{11}u_1 + \partial_{12}u_2 + \partial_{13}u_3\right) + c_s^2\left(\partial_{11}u_1 + \partial_{22}u_1 + \partial_{33}u_3\right) - \partial_{tt}u_1 &= 0 \\
\left(c_p^2 - c_s^2\right)\left(\partial_{12}u_1 + \partial_{22}u_2 + \partial_{23}u_3\right) + c_s^2\left(\partial_{11}u_2 + \partial_{22}u_2 + \partial_{33}u_2\right) - \partial_{tt}u_2 &= 0 \\
\left(c_p^2 - c_s^2\right)\left(\partial_{13}u_1 + \partial_{23}u_2 + \partial_{33}u_3\right) + c_s^2\left(\partial_{11}u_3 + \partial_{22}u_3 + \partial_{33}u_3\right) - \partial_{tt}u_3 &= 0
\end{aligned}
\tag{A.2}
$$

where the Lamé coefficients have been replaced by the P-waves and S-waves propagation velocities $c_p = \sqrt{\frac{\lambda + \mu}{\rho}}$ and $c_s = \sqrt{\frac{\mu}{\rho}}$. Taking the Fourier transform defined by:

$$\hat{u} = F(u) = \int_{-\infty}^{\infty} u(t)e^{-i(k_1 x_1 + k_2 x_2 + \omega t)}dt \tag{A.3}$$

the equation (A.2) in frequency domain can be rewritten as:

$$
\begin{aligned}
\left(c_p^2 - c_s^2\right)\left(-k_1^2\hat{u}_1 - k_1 k_2 \hat{u}_2 + ik_1 \partial_3 \hat{u}_3\right) + c_s^2\left(-k_1^2\hat{u}_1 - k_2^2\hat{u}_1 + ik_2 \partial_3 \hat{u}_3\right) + \omega^2 \hat{u}_1 &= 0 \\
\left(c_p^2 - c_s^2\right)\left(-k_1 k_2 \hat{u}_1 - k_2^2\hat{u}_2 + ik_2 \partial_3 \hat{u}_3\right) + c_s^2\left(-k_1^2\hat{u}_2 - k_2^2\hat{u}_2 + \partial_{33}\hat{u}_2\right) + \omega^2 \hat{u}_2 &= 0 \\
\left(c_p^2 - c_s^2\right)\left(ik_1 \partial_3 \hat{u}_1 + ik_2 \partial_3 \hat{u}_2 + \partial_{33}\hat{u}_3\right) + c_s^2\left(-k_1^2\hat{u}_3 - k_2^2\hat{u}_3 + \partial_{33}\hat{u}_3\right) + \omega^2 \hat{u}_3 &= 0
\end{aligned}
\tag{A.4}
$$

A.1   P, SV and SH wave decomposition

If the vector $\underline{u}_\Sigma$ regroups the tangential motion:

$$\underline{u}_\Sigma = u_1\underline{e}_1 + u_2\underline{e}_2 \quad \text{and} \quad \underline{k}_\Sigma = k_1\underline{e}_1 + k_2\underline{e}_2 \tag{A.5}$$

an equivalent form of (A.4) is:

$$\left(c_p{}^2 - c_s^2\right)\left(-\underline{k}_\Sigma.\hat{\underline{u}}_\Sigma + i\partial_3\hat{u}_3\right).\underline{k}_\Sigma + c_s^2\left(-\left|\underline{k}_\Sigma\right|^2 + \partial_{33}\right)\hat{\underline{u}}_\Sigma + \omega^2\hat{\underline{u}}_\Sigma = \underline{0}$$

$$\left(c_p{}^2 - c_s^2\right)\left(i\underline{k}_\Sigma.\partial_3\hat{\underline{u}}_\Sigma + \partial_{33}\hat{u}_3\right) + c_s^2\left(-\left|\underline{k}_\Sigma\right|^2 + \partial_{33}\right)\hat{u}_3 + \omega^2\hat{u}_3 = 0 \tag{A.6}$$

The previous equations form a linear system for $\hat{u}_3$ that can be solved directly by diagonalization using an appropriate change of variables. For example, using the standard decomposition of the tangent displacement $\underline{u}_\Sigma$ into P, SV and SH waves (Fig.A.1b):

$$\begin{aligned}
\underline{u}_\Sigma &= \left(\underline{u}_\Sigma.\underline{e}_k\right)\underline{e}_k + \left(\underline{u}_\Sigma.\left(\underline{e}_3 \wedge \underline{e}_k\right)\right)\left(\underline{e}_3 \wedge \underline{e}_k\right) \\
&= \left(\underline{u}_\Sigma.\frac{\underline{k}_\sigma}{|\underline{k}_\Sigma|}\right)\frac{\underline{k}_\Sigma}{|\underline{k}_\Sigma|} + \left(\underline{u}_\Sigma.\frac{\underline{e}_3 \wedge \underline{k}_\Sigma}{|\underline{k}_\Sigma|}\right)\frac{\underline{e}_3 \wedge \underline{k}_\Sigma}{|\underline{k}_\Sigma|} \\
&= u_1^{PSV}\underline{e}_k + u_2^{SH}\left(\underline{e}_3 \wedge \underline{e}_k\right)
\end{aligned} \tag{A.7}$$

where $\underline{k}_\Sigma = |\underline{k}_\Sigma|\,\underline{e}_k$. Replacing the tangent displacement decomposition in (A.6), and after some simplifications we obtain:

$$\begin{aligned}
\left(\left(\omega^2 - c_s^2\left|\underline{k}_\Sigma\right| + c_p^2\partial_{33}\right)\hat{u}_1^{PSV} + i\left|\underline{k}_\Sigma\right|\left(c_p^2 - c_s^2\right)\partial_3\hat{u}_3^{PSV}\right)\underline{e}_k + \\
\underbrace{\left(c_s^2\left(-\left|\underline{k}_\Sigma\right|^2 + \partial_{33}\right)\hat{u}_s^{SH} + \omega^2\hat{u}_2^{SH}\right)}_{\text{SH component}}\left(\underline{e}_3 \wedge \underline{e}_k\right) &= 0
\end{aligned} \tag{A.8}$$

$$\left(\left(\omega^2 - c_p^2\left|\underline{k}_\Sigma\right|^2 + c_s^2\partial_{33}\right)\hat{u}_3^{PSV} + i\left|\underline{k}_\Sigma\right|\left(c_p^2 - c_s^2\right)\partial_3\hat{u}_1^{PSV}\right)\underline{e}_3 = 0 \tag{A.9}$$

The vectors $\underline{e}_k$ and $\underline{e}_3 \wedge \underline{e}_k$ are orthogonal, therefore the equation (A.8) is equivalent to two equations. The underbraced term on (A.8) correspond to SH component and can be solved explicitly:

$$\partial_{33}\hat{u}_2^{SH} = -\left(\frac{\omega^2}{c_s^2} - \left|\underline{k}_\Sigma\right|^2\right)\hat{u}_2^{SH} \tag{A.10}$$

The expressions for the components P and SV form a coupled system:

$$\begin{aligned}
\partial_{33}\hat{u}_1^{PSV} &= \frac{c_p^2\left|\underline{k}_\Sigma\right|^2 - \omega^2}{c_s^2}\hat{u}_1^{PSV} - i\left|\underline{k}_\Sigma\right|\left(c_p^2 - c_s^2\right)\partial_3\hat{u}_3^{PSV} \\
\partial_{33}\hat{u}_3^{PSV} &= \frac{c_s^2\left|\underline{k}_\Sigma\right|^2 - \omega^2}{c_s^2}\hat{u}_3^{PSV} - i\left|\underline{k}_\Sigma\right|\left(c_p^2 - c_s^2\right)\partial_3\hat{u}_1^{PSV}
\end{aligned} \tag{A.11}$$

Using the following notation:

$$\xi_p^2 = \frac{\omega^2}{c_p^2} - \left|\underline{k}_\Sigma\right|^2 \quad \text{and} \quad \xi_s^2 = \frac{\omega^2}{c_s^2} - \left|\underline{k}_\Sigma\right|^2 \tag{A.12}$$

the above equations become:

$$\partial_{33}\hat{u}_2^{SH} = 0$$

$$\partial_{33}\hat{u}_1^{PSV} = -\frac{c_p^2}{c_s^2}\xi_p^2\hat{u}_1^{PSV} - i\frac{|\underline{k}_\Sigma|\left(c_p^2 - c_s^2\right)}{c_s^2}\partial_3\hat{u}_3^{PSV}$$

$$\partial_{33}\hat{u}_3^{PSV} = -\frac{c_s^2}{c_p^2}\xi_s^2\hat{u}_2^{PSV} - i\frac{|\underline{k}_\Sigma|\left(c_p^2 - c_s^2\right)}{c_p^2}\partial_3\hat{u}_1^{PSV} \tag{A.13}$$

The solution of the previous differential system can be easy carried out by replacing test solutions of the form $u_i = e^{\lambda x_i}$. This substitution leads to a characteristic polynomial in terms of λ. As we are interested only in the solutions propagating downwards (outgoing waves following $-\underline{e}_3$), only the $Im(\lambda) < 0$ solutions are kept. Imposing these considerations, the solution for the displacement components are:

$$\hat{u}_1^{PSV} = A_P\, e^{-i\xi_p x_3} + A_{SV}\, e^{-i\xi_s x_3}$$

$$\hat{u}_2^{SH} = A_{SH}\, e^{-i\xi_s x_3}$$

$$\hat{u}_3^{PSV} = -\frac{\xi_p}{|\underline{k}_\Sigma|}A_P\, e^{-i\xi_p x_3} + \frac{|\underline{k}_\Sigma|}{\xi_s}A_{SV}\, e^{-i\xi_s x_3} \tag{A.14}$$

In order to compute the constants A_P, A_{SH} and A_{SV} we suppose to know the displacement $\underline{u}_s(x_3 = 0)$ over the boundary Σ. Evaluating the system (A.14) for $x_3 = 0$, and imposing the known displacement values $\hat{u}_2^{SH}(x_3 = 0)$, $\hat{u}_1^{PSV}(x_3 = 0)$ and $\hat{u}_3^{PSV}(x_3 = 0)$, we obtain:

$$A_{SH} = \hat{u}_{2_0}^{SH}$$

$$A_P = \frac{|\underline{k}_\Sigma|^2}{\xi_p\xi_s + |\underline{k}_\Sigma|^2}\hat{u}_{1_0}^{PSV} - \frac{\xi_s\,|\underline{k}_\Sigma|}{\xi_p\xi_s + |\underline{k}_\Sigma|^2}\hat{u}_{3_0}^{PSV}$$

$$A_{SV} = \frac{\xi_p\xi_s}{\xi_p\xi_s + |\underline{k}_\Sigma|^2}\hat{u}_{1_0}^{PSV} + \frac{\xi_s\,|\underline{k}_\Sigma|}{\xi_p\xi_s + |\underline{k}_\Sigma|^2}\hat{u}_{3_0}^{PSV} \tag{A.15}$$

A.2 Spectral impedance approximation

In order to construct the impedance over the boundary Σ, we need to evaluate the stress vector $\underline{t}(\underline{x}, t)$ applied on the plane perpendicular to $\underline{e}_3$. As it is assumed that the domain $\Omega_{s'}$ (and Ω_{st}) is elastic:

$$\underline{t}(\underline{x}, t) = \left(\lambda\,\mathrm{div}\,(\underline{u}_{s'})\,\underline{\underline{I}} + 2\mu\underline{\underline{\varepsilon}}\right).\underline{e}_3 \quad \forall \underline{x} \in \Sigma \tag{A.16}$$

The corresponding expression in frequency domain is:

$$\begin{aligned}\hat{\underline{t}}(\underline{x}, \omega) &= \rho c_s^2\left(\partial_3\hat{u}_1 + ik_1\hat{u}_3\right)\underline{e}_1 + \rho c_s^2\left(\partial_3\hat{u}_2 + ik_2\hat{u}_3\right)\underline{e}_2 \\ &\quad + \rho c_p^2\left(\partial_3\hat{u}_3\rho\left(c_p^2 - 2c_s^2\right)(ik_1\hat{u}_1 + ik_2\hat{u}_2)\right)\underline{e}_3 \\ &= \rho c_s^2\left(\partial_3\hat{\underline{u}}_\Sigma + i\hat{u}_3\underline{k}_\Sigma\right) + \left(i\rho\left(c_p^2 - 2c_s^2\right)\underline{k}_\Sigma.\hat{\underline{u}}_\Sigma + \rho c_p^2\partial_3\hat{u}_3\right)\underline{e}_3 \quad \forall \underline{x} \in \Sigma\end{aligned} \tag{A.17}$$

The previous expression can be written in terms of the decomposition into P, SV and SH waves:

$$\begin{aligned}\hat{\underline{t}}(\underline{x}, \omega) &= \rho c_s^2\left(\partial_3\hat{u}_1^{PSV} + i\hat{u}_3^{PSV}|\underline{k}_\Sigma|\right)\underline{e}_k + \rho c_s^2\partial_3\hat{u}_2^{SH}\left(\underline{e}_3 \wedge \underline{e}_k\right) \\ &\quad + \left(i\rho\left(c_p^2 - 2c_s^2\right)|\underline{k}_\Sigma|\hat{u}_1^{PSV} + \rho c_s^2\partial_3\hat{u}_3^{PSV}\right)\underline{e}_3\end{aligned} \tag{A.18}$$

Using the displacement expressions previously obtained (A.14), it is possible to compute directly the partial derivatives and replace them in (A.18):

$$\hat{\underline{t}}\,(\underline{x},\omega) \quad = \quad \frac{i\rho}{\xi_p \xi_s + |\underline{k}_\Sigma|^2} \left(-\xi_p \omega^2 \hat{u}_{1_0}^{PSV} + c_s^2 \,|\underline{k}_\Sigma| \left(|\underline{k}_\Sigma|^2 + 2\xi_p \xi_s - \xi_s^2 \right) \hat{u}_{3_0}^{PSV} \right) \underline{e}_k$$

$$- i\rho c_s^2 \xi_s \hat{u}_{2_0}^{SH} \left(\underline{e}_3 \wedge \underline{e}_k \right) + \frac{i\rho}{\xi_p \xi_s + |\underline{k}_\Sigma|^2} \left(|\underline{k}_\Sigma| \left(\omega^2 - 2c_s^2 \left(\xi_p \xi_s + |\underline{k}_\Sigma|^2 \right) \right) \hat{u}_{1_0}^{PSV} - \xi_s \omega^2 \hat{u}_{3_0}^{PSV} \right) \underline{e}_3$$

$$(A.19)$$

The previous equation can be written in terms of a linear operator over the displacements at the boundary:

$$\hat{\underline{t}}\,(\underline{x},\omega) = \underline{\underline{A}}\,(|\underline{k}_\Sigma|\,,\omega)\,.\hat{\underline{u}}_0\,(\underline{k}_\Sigma,\omega) \tag{A.20}$$

where $\underline{\underline{A}}\,(|\underline{k}_\Sigma|\,,\omega)$ is the global impedance operator. By using an inverse Fourier transform, the corresponding expression in time domain is:

$$\underline{t}\,(\underline{x},t) = \frac{1}{8\pi^3} \int_{-\infty}^{\infty} \underline{\underline{A}}\,(|\underline{k}_\Sigma|\,,\omega)\, \hat{\underline{u}}_0\,(\underline{k}_\Sigma,\omega)\, e^{i(\underline{k}_\Sigma \cdot \underline{x}_\Sigma + \omega t)} d\underline{k}_\Sigma\, d\omega \tag{A.21}$$

The equation (A.21) represents the spectral action imposed by outgoing waves propagating in $-\underline{e}_3$ direction from the boundary Σ. This action is nonlocal since depends on the displacements $\hat{\underline{u}}_0\,(\underline{k}_\Sigma,\omega)$, i.e., the Fourier transform of $\underline{u}\,(\underline{x}_\Sigma, t)$ over the time t and the space $\underline{x}_\Sigma$. In order to obtain a local approximation of the impedance Engquist and Majda (1977) proposed to expand the variables ξ_p and ξ_s as a series of $\frac{|\underline{k}_\Sigma|}{\xi}$. For example, using a Taylor's expansion for ξ_p:

$$\xi_p = \frac{\omega}{c_p} \sqrt{1 - \frac{c_p^2}{\omega^2}\,|\underline{k}_\Sigma|^2} = \frac{\omega}{c_p} \left(1 - \left(\frac{c_p}{\omega}\,|\underline{k}_\Sigma| \right)^2 \frac{1}{2} + \ldots \right) \tag{A.22}$$

Thus, the zero order and first order approximations are given by:

$$\text{Zero order approximation} \quad : \quad \xi_p = \frac{\omega}{c_p} + \mathcal{O}\left(c_p^2 \frac{|\underline{k}_\Sigma|^2}{\omega^2} \right) \tag{A.23}$$

$$\text{First order approximation} \quad : \quad \xi_p = \frac{\omega}{c_p} \left(1 - \frac{1}{2}\frac{c_p^2}{\omega^2}\,|\underline{k}_\Sigma|^2 \right) + \mathcal{O}\left(c_p^4 \frac{|\underline{k}_\Sigma|^4}{\omega^4} \right) \tag{A.24}$$

The zero order approximation is the familiar solution for the one-dimensional wave propagation problem and could be easily derived from physical considerations (Wolf, 1985; Wolf and Song, 1996). For the three-dimensional case, the zero order approximation is accurate for high frequency waves and for waves approximately normal to the boundary Σ ($\underline{k}_\Sigma$ small). Some numerical instabilities are found for high-order Taylor expansions (Engquist and Majda, 1977). An expansion using Padé series encompasses this problem (Clayton and Engquist, 1977), in this case the series follows the recursive form:

$$\xi_p^j = \frac{\omega}{c_p} \left(1 - \frac{\left(\frac{c_p |\underline{k}_\Sigma|}{\omega} \right)^2}{1 + \frac{c_p}{\omega}\xi_p^{j-1}} + \ldots \right) \quad \text{with} \quad \xi_p^1 = \frac{\omega}{c_p} \tag{A.25}$$

In order to construct the paraxial approximation for the spectral impedance on the boundary Σ, the expansions for ξ_p and ξ_s can be replaced in (A.19). After some simplifications, we obtain for the zero order $|\underline{k}_\Sigma|$ expansion:

$$\hat{\underline{t}}\,(\underline{x},\omega) \quad = \quad -i\rho c_s \omega \left(\hat{u}_{1_0}^{PSV} \underline{e}_k + \hat{u}_{2_0}^{SH} \left(\underline{e}_3 \wedge \underline{e}_k \right) \right) - i\rho c_p \omega \hat{u}_{3_0}^{PSV} \underline{e}_3 \quad \forall \underline{x} \in \Sigma \tag{A.26}$$

In the local reference system at the boundary $(\underline{e}_1, \underline{e}_2, \underline{e}_3)$, the previous expression becomes:

$$\hat{\underline{t}}(\underline{x}, \omega) = -i\rho c_s \omega \hat{u}_{1_0} \underline{e}_1 - i\rho c_s \omega \hat{u}_{2_0} \underline{e}_2 - i\rho c_p \omega \hat{u}_{3_0} \underline{e}_3 \quad \forall \underline{x} \in \Sigma \qquad (A.27)$$

Taking inverse Fourier transform, the corresponding expression in time domain is:

$$\underline{t}(\underline{x}, t) = -\rho c_s \dot{u}_{1_0} \underline{e}_1 - \rho c_s \dot{u}_{2_0} \underline{e}_2 - \rho c_p \dot{u}_{3_0} \underline{e}_3 \quad \forall \underline{x} \in \Sigma \qquad (A.28)$$

If a first order $|\underline{k}_\Sigma|$ expansion is used, the corresponding stress vector in frequency domain can be written as:

$$\begin{aligned}
\hat{\underline{t}}(\underline{x}, t) = &\left(-i\rho c_s \omega \hat{u}_{1_0} + i\rho c_s \left(2c_s - c_p \right) \hat{u}_{3_0} k_1 \right) \underline{e}_1 + \left(-i\rho c_s \omega \hat{u}_{2_0} + i\rho c_s \left(2c_s - c_p \right) \hat{u}_{3_0} k_2 \right) \underline{e}_2 \\
&+ \left(-i\rho c_p \omega \hat{u}_{3_0} - i\rho c_s \left(2c_s - c_p \right) \left(\hat{u}_{1_0} k_1 + \hat{u}_{2_0} k_2 \right) \right) \underline{e}_3 \quad \forall \underline{x} \in \Sigma
\end{aligned} \qquad (A.29)$$

The corresponding expression in time domain is:

$$\begin{aligned}
\underline{t}(\underline{x}, t) = &\left(-\rho c_s \dot{u}_{1_0} + \rho c_s \left(2c_s - c_p \right) \partial_1 u_{3_0} \right) \underline{e}_1 + \left(-\rho c_s \dot{u}_{2_0} + \rho c_s \left(2c_s - c_p \right) \partial_2 u_{3_0} \right) \underline{e}_2 \\
&\left(-\rho c_p \dot{u}_{3_0} - \rho c_s \left(2c_s - c_p \right) \left(\partial_1 u_{1_0} + \partial_2 u_{2_0} \right) \right) \underline{e}_3 \quad \forall \underline{x} \in \Sigma
\end{aligned} \qquad (A.30)$$

It can be noticed that the previous expression is developed using only the first term of the expansion (A.22) for ξ_p and ξ_s. In the last expression, the spatial derivatives lead to some numeric instabilities. In this case, high order finite elements must be used to avoid strong discontinuities in the evaluation of these terms. A detailed studied of the numerical dispersion of the paraxial approximation depending on the order of the approximation can be found in Modaressi (1987); de Martin and Aochi (2008).

In a symbolic way, the previous relations in time domain can be summarized in terms of an operator $\underline{A}_n$ for the n-order approximation over the displacement field $\underline{u}_s$ at the boundary Σ of the Ω_s domain:

$$\underline{t}(\underline{x}, t) = \underline{A}_0 \left(\dot{\underline{u}}_s \right) \qquad (A.31)$$

$$\underline{t}(\underline{x}, t) = \underline{A}_1 \left(\dot{\underline{u}}_s, \partial_{\underline{x}} \underline{u}_s \right) \qquad (A.32)$$

Usually, the total displacement field on the unbounded domain $\Omega_{s'}$ is decomposed into an incident field $\underline{u}_i$ and into a radiant field $\underline{u}_r$:

$$\underline{u}_{s'} = \underline{u}_i + \underline{u}_r \qquad (A.33)$$

where the radiant field must vanish far enough from the boundary Σ:

$$\lim_{\|\underline{x}\| \to \infty} \underline{u}_r = \underline{0} \qquad (A.34)$$

At the boundary, the stress vector due to the diffraction can be computed as:

$$\underline{t}(\underline{u}_r, t) = \underline{A}_0 \left(\dot{\underline{u}}_r \right) \quad \text{or} \quad \underline{t}(\underline{u}_r, t) = \underline{A}_1 \left(\dot{\underline{u}}_r, \partial_{\underline{x}} \underline{u}_r \right) \qquad (A.35)$$

Using the continuity of the stress tensor at Σ and the assumption of linear elastic behaviour around the boundary, the zero-order approximation for the total stress vector can be summarized as:

$$\begin{aligned}
\underline{t}(\underline{u}_s, t) &= -\underline{t}(\underline{u}_{s'}, t) \\
&= -\underline{t}(\underline{u}_i, t) - \underline{t}(\underline{u}_r, t) \\
&= -\underline{t}(\underline{u}_i, t) - \underline{A}_0 \left(\dot{\underline{u}}_r \right) \\
&= -\underline{t}(\underline{u}_i, t) - \underline{A}_0 \left(\dot{\underline{u}}_s \right) + \underline{A}_0 \left(\dot{\underline{u}}_i \right)
\end{aligned} \qquad (A.36)$$

The extension for the case of saturated porous media is presented in Modaressi and Benzenati (1994) for the $u-p$ simplified dynamic Biot formulation. The extension of paraxial absorbing boundary for a MESHLESS approach is extensively treated by Aubert (1997).

Appendix B

Mechanical interfaces

The model takes into account the normal and the tangential discontinuities over the interface Σ_{bs} between both solid domains Ω_b and Ω_s. It is assumed that both solid domains are in contact at initial state and small-strains applies. Let $\underline{n}$ the normal vector over the interface oriented from Ω_b to Ω_s. The jump of displacement defined in (1.33) can be decomposed into a normal component (gap $[u_N]$) and a relative tangential jump (slide $[\underline{u_T}]$):

$$
\begin{aligned}
[u_N] &= [\underline{u}].\underline{n} \\
[\underline{u_T}] &= [\underline{u}] - [u_N]\underline{n}
\end{aligned}
\tag{B.1}
$$

If $\underline{\sigma}$ is the stress tensor of Ω_s or Ω_b, the normal stress σ_N and the tangential stress vector $\underline{\sigma_T}$ over Σ_{bs} can be written as (Fig.B.1):

$$
\begin{aligned}
\sigma_N &= \underline{n}.\underline{\sigma}.\underline{n} \\
\underline{\sigma_T} &= \underline{\sigma}.\underline{n} - \sigma_N\underline{n}
\end{aligned}
\tag{B.2}
$$
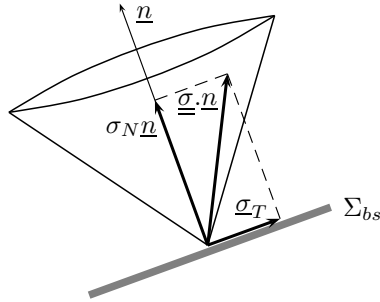
Figure B.1: Stress vector decomposition over the interface Σ_{bs}

According to action-reaction principle, the stress vector must be continuous over the interface even if uplift or slide appears during the loading (1.32). Therefore, only displacement discontinuities are allowed. Assuming a Mohr-Coulomb frictional behaviour, three different criteria must be satisfied:

1. No interpenetration criterion:
$$[u_N] \geq 0$$

2. Uplift and free surface criterion:
$$\text{If } [u_N] > e_{ini} \rightarrow \underline{\sigma}.\underline{n} = \underline{0}$$

where e_{ini} is the initial thickness of the interface.

3. Contact-compression criterion:

$$\text{If } [u_N] \leq e_{ini} \rightarrow \sigma_N \leq 0 \quad \text{and} \quad |\underline{\sigma}_T| \leq |\sigma_N| \tan\phi + c$$

where ϕ is the friction angle of the interface

- No sliding:

$$\text{If } |\underline{\sigma}_T| \leq |\sigma_N| \tan\phi + c \quad \rightarrow \quad [\underline{\dot{u}}_T] = \underline{0}$$

- Sliding:

$$\text{If } |\underline{\sigma}_T| = |\sigma_N| \tan\phi + c \quad \rightarrow \quad [\underline{\dot{u}}_T] = \dot{\lambda}^p \frac{\underline{\sigma}_T}{|\underline{\sigma}_T|} \quad \text{with} \quad \dot{\lambda}^p \geq 0$$

where $\dot{\lambda}^p$ is the plastic multiplier and c is the cohesion of the joint.

In the previous expressions $|\cdot|$ means the absolute value for scalars or modulus for vectors. The condition $\dot{\lambda}^p \geq 0$ means that if sliding occurs, it must follow the direction of the tangent stress vector. The previous criteria are summarized graphically on the Fig. B.2a. in terms of the jump of displacements and stresses. The uniqueness are not satisfied in these formulations, therefore as a numerical point of view, these relations must be regularized. This regularization can be carried out introducing an elastoplastic formulation for the jump-stress relation at the interface.

(a) Mohr-Coulomb friction model   (b) Regularized Mohr-Coulomb friction model
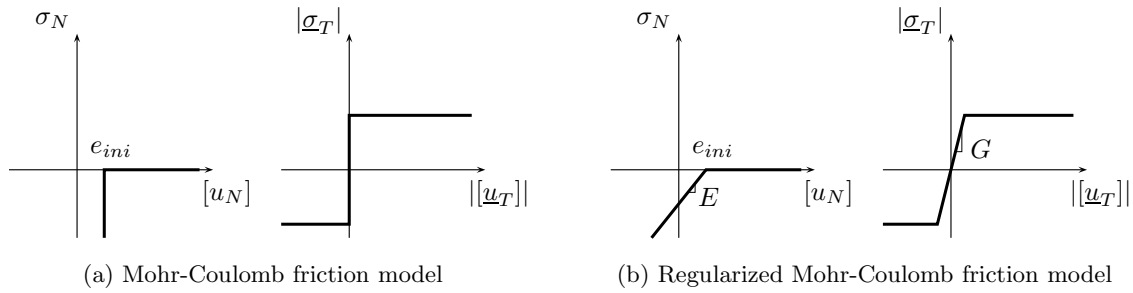
Figure B.2: Graphical representation of interface model

The jump-stress relations can be regularized introducing a set of penalization parameters E and G related to the elastic stiffness of the interface to the normal and tangential relative displacement (Fig.B.2b). According to general assumptions of an elastoplastic model, the normal and tangential jump increments can be decomposed into an elastic and a plastic contribution:

$$
\begin{aligned}
\left[\underline{\dot{u}}_T\right] &= \left[\underline{\dot{u}}_T^e\right] + \left[\underline{\dot{u}}_T^p\right] \\
\left[\dot{u}_N\right] &= \left[\dot{u}_N^e\right] + \left[\dot{u}_N^p\right]
\end{aligned}
\tag{B.3}
$$

where the upperscript e and p denote elastic and plastic contributions respectively. The evolution of the stress vector is only related to elastic jump increments:

$$
\begin{aligned}
\underline{\dot{\sigma}}_T &= G\left[\underline{\dot{u}}_T^e\right] \\
\dot{\sigma}_N &= E\left[\dot{u}_N^e\right]
\end{aligned}
\tag{B.4}
$$

The third criterion is now written in terms of plastic tangential jump:

- No plastic sliding:

$$\text{If } |\underline{\sigma}_T| < |\sigma_N| \tan\phi + c \quad \rightarrow \quad [\underline{\dot{u}}_T^p] = \underline{0} \quad \text{and} \quad [\dot{u}_N^p] = 0$$

- Plastic sliding:

$$\text{If} \quad |\underline{\sigma}_T| = |\sigma_N| \tan\phi + c \quad \rightarrow \quad \exists \, \dot{\lambda}^p \geq 0 \ \text{t.q.}$$

$$
\begin{aligned}
\left[\dot{\underline{u}}_T^p\right] &= \dot{\lambda}^p \frac{\underline{\sigma}_T}{|\underline{\sigma}_T|} \\
\left[\dot{u}_N^p\right] &= \dot{\lambda}^p \tan\psi
\end{aligned}
$$

where ψ is the angle of dilatancy of the joint, which relates the plastic normal uplift with the plastic sliding. For a zero value for ψ, the dilatancy vanishes and the formulation is equivalent to a Coulomb pure friction model. When $\phi = \psi$, the elastoplastic friction model is associated.

The computation of the plastic multiplier $\dot{\lambda}^p$ can be easy carried out with the compatibility equation derived from the friction threshold:

$$\frac{1}{|\underline{\sigma}_T|} (\underline{\sigma}_T \cdot \dot{\underline{\sigma}}_T) + \dot{\sigma}_N \tan\phi = 0 \tag{B.5}$$

Injecting the jump-stress relations (B.4), the previous expression becomes:

$$\frac{G}{|\underline{\sigma}_T|} (\underline{\sigma}_T \cdot [\dot{\underline{u}}_T^e]) + E[u_N^e] \tan\phi = 0 \tag{B.6}$$

Therefore, the plastic multiplier can be computed as:

$$\dot{\lambda}^p = \frac{\frac{G}{|\underline{\sigma}_T|} (\underline{\sigma}_T \cdot [\dot{\underline{u}}_T]) + E[\dot{u}_N] \tan\phi}{G + E \tan\phi \tan\psi} \tag{B.7}$$

Finally, the total stress increment at the joint is given by:

$$
\begin{aligned}
\dot{\underline{\sigma}}_T &= G[\dot{\underline{u}}_T] - \dot{\lambda}^p G \frac{\underline{\sigma}_T}{|\underline{\sigma}_T|} \\
\dot{\sigma}_N &= E[\dot{u}_N] - \dot{\lambda}^p E \tan\psi
\end{aligned}
\tag{B.8}
$$

B.1 Numerical integration

The integration of the constitutive model is carried out following an explicit strategy. During a load step $n+1$, the total jump increment is divided in two parts: the first one correspond to elastic part before reaching the limit of elasticity, and the second one is plastic increment. For an iteration $k+1$ of the loading step n, the jump increments can be written as:

$$
\begin{aligned}
[\dot{\underline{u}}_T] &= \frac{1}{\Delta t}\left[\underline{u}_{T_{n+1}}^{k+1} - \underline{u}_{T_n}\right] &= \frac{1}{\Delta t}[\Delta \underline{u}_T] \\
[\dot{u}_N] &= \frac{1}{\Delta t}\left[u_{N_{n+1}}^{k+1} - u_{N_n}\right] &= \frac{1}{\Delta t}[\Delta u_N]
\end{aligned}
\tag{B.9}
$$

where the time step increment Δt is assumed to be constant during the analysis. Afterward, the step increment is divided in two parts: $\gamma \Delta t$ and $(1-\gamma)\Delta t$. The first one is the elastic part of the increment and second one the corresponding plastic part. The value of γ is computed as:

$$f\left(\underline{\sigma}_{T_n} + \gamma \Delta \underline{\sigma}_T, \sigma_{N_n} + \gamma \Delta \sigma_N\right) \leq 0 \tag{B.10}$$

where:

$$
\begin{aligned}
f(\underline{\sigma}_T, \sigma_N) &= |\underline{\sigma}_T| - |\sigma_n| \tan\phi \\
\Delta \underline{\sigma}_T &= G[\Delta \underline{u}_T] \\
\Delta \sigma_n &= E[\Delta u_n]
\end{aligned}
$$

With γ, the elastic part of stress increment is known. Next, the plastic multiplier $\dot{\lambda}^p$ is computed with (B.7) using the plastic part of the jump increment:

$$
\begin{aligned}
[\Delta \underline{u}_T^*] &= (1-\gamma)[\Delta \underline{u}_T] \\
[\Delta u_N]^* &= (1-\gamma)[\Delta u_N]
\end{aligned}
\tag{B.11}
$$

for stress state:

$$
\begin{aligned}
\underline{\sigma}_T^* &= \underline{\sigma}_{T_n} + \gamma \Delta \underline{\sigma}_T \\
\sigma_N^* &= \sigma_{N_n} + \gamma \Delta \sigma_N
\end{aligned}
\tag{B.12}
$$

After the evaluation of the plastic multiplier, the stress increment can be written in a matrix form:

$$
\left\{ \begin{array}{c} \Delta \underline{\sigma}_T \\ \Delta \sigma_N \end{array} \right\} =
\left[\begin{array}{cc} G - \frac{(1-\gamma)G^2}{H} & -\frac{(1-\gamma)EG\tan\phi}{H} \\ -\frac{(1-\gamma)EG\tan\phi}{H} & E - \frac{(1-\gamma)E^2\tan\phi\tan\psi}{H} \end{array} \right]
\left\{ \begin{array}{c} [\Delta \underline{u}_T]^* \\ [\Delta u_N]^* \end{array} \right\}
\tag{B.13}
$$

where $H = G + E\tan\phi\tan\psi$. Finally, the stress tensor at the interface for the iteration $k+1$ of the load step $n+1$ is obtained by:

$$
\begin{aligned}
\underline{\sigma}_{T_{n+1}}^{k+1} &= \underline{\sigma}_{T_n} + \Delta \underline{\sigma}_T
\end{aligned}
\tag{B.14}
$$

$$
\begin{aligned}
\sigma_{N_{n+1}}^{k+1} &= \sigma_{N_n} + \Delta \sigma_N
\end{aligned}
\tag{B.15}
$$

The model parameters for the mechanical joint element are summarized in Table B.1.

Table B.1: Parameters for the Mohr-Coulomb joint constitutive model

Parameter	Description
E	normal stiffness modulus
G	tangent stiffness modulus
ϕ	friction angle
ψ	dilatancy angle
e_{ini}	joint thickness
c	joint cohesion

Appendix C

Continuous beam constitutive model

According to beam kinematics introduced in §1.2, assuming the transverse stresses are small with respect to axial stress $\underline{\underline{\sigma}}_b\,\underline{e}_r$ and the material is isotropic and elastic, the axial stress vector can be computed as:

$$
\begin{aligned}
\underline{\underline{\sigma}}_b\,\underline{e}_r &= \left(\underline{\underline{\underline{C}}} : \underline{\underline{\varepsilon}} \right) \underline{e}_r \\
&= \left(\underline{\underline{\underline{C}}} : (\partial_r u_{0_r}\,\underline{e}_r + \partial_r \underline{u}_1 \wedge \underline{x}^*) \otimes_s \underline{e}_3 \right) \underline{e}_r
\end{aligned}
\tag{C.1}
$$

where $\underline{\underline{\underline{C}}}$ is the elastic tensor of the material. In this work we are interested in material non-linear behaviour, in this case, the axial stress vector can be written symbolically as:

$$
\underline{\underline{\sigma}}_b\,\underline{e}_r = \underline{\underline{\sigma}}_b \left(\underline{\underline{\varepsilon}} \right) \underline{e}_r = \underline{\underline{\sigma}}_b \left((\partial_r u_{0_r}\,\underline{e}_r + \partial_r \underline{u}_1 \wedge \underline{x}^*) \otimes_s \underline{e}_3 \right) \underline{e}_r
\tag{C.2}
$$

It can be noticed that according to the this kinematics, the stress tensor can be written as:

$$
\underline{\underline{\sigma}}_b = \sigma_{rr}\,\underline{e}_r \otimes \underline{e}_r + \sigma_{rs}\,\underline{e}_r \otimes_s \underline{e}_s + \sigma_{rt}\,\underline{e}_r \otimes_s \underline{e}_t
\tag{C.3}
$$

C.1 Non-linear constitutive model

The non-linear material behavior is modelled by a Prandtl-Reuss elastoplastic constitutive model (Lemaitre and Chaboche, 2001; Chen and Mizuno, 1990) with a Von Mises yield criterion and isotropic hardening. Plastic incompressibility is assumed, i.e. the yield function f depends only of the invariants of the deviatoric stress tensor $\underline{\underline{s}}$:

$$
f\left(\underline{\underline{\sigma}}_b, \epsilon^p \right) = \sigma_{eq} - R - \sigma_y = \sqrt{3J_2\left(\underline{\underline{s}} \right)} - k(\epsilon^p) - \sigma_y
\tag{C.4}
$$

where J_2 is the second invariant of $\underline{\underline{s}}$, $R = k(\epsilon^p)$ is the isotropic hardening rule in terms of the cumulative plastic strain ϵ^p:

$$
\epsilon^p = \int_0^t \sqrt{\underline{\underline{\dot{\varepsilon}}}^p(\tau) : \underline{\underline{\dot{\varepsilon}}}^p(\tau)}\, d\tau
$$

and σ_y is the initial elastic limit stress. An associated flow rule and a normal hardening rule are used:

$$
\begin{aligned}
\underline{\underline{\dot{\varepsilon}}}^p &= \dot{\lambda}^p \frac{\partial f}{\partial \underline{\underline{\sigma}}_b} = \frac{3}{2\sigma_{eq}} \dot{\lambda}^p\, \underline{\underline{s}} \\
\dot{\epsilon}^p &= -\dot{\lambda} \frac{\partial f}{\partial R} = \dot{\lambda}^p
\end{aligned}
\tag{C.5}
$$

According to Bernouilli beams kinematics, the explicit form of $\underline{\underline{s}}$ is given by:

$$\underline{\underline{s}} = \frac{2}{3}\sigma_{rr}\,\underline{e}_r \otimes \underline{e}_r - \frac{1}{3}\sigma_{rr}\,\underline{e}_s \otimes \underline{e}_s - \frac{1}{3}\sigma_{rr}\,\underline{e}_t \otimes \underline{e}_t + \sigma_{rs}\,\underline{e}_r \otimes_s \underline{e}_s + \sigma_{rt}\,\underline{e}_r \otimes_s \underline{e}_t \tag{C.6}$$

When plasticity is activated, the consistency condition gives directly the plastic multiplier $\dot{\lambda}^p$:

$$\dot{f} = \dot{\sigma}_{eq} - k'(\epsilon^p).\dot{\epsilon}^p = 0 \quad \rightarrow \quad \dot{\lambda}^p = \dot{\epsilon}^p = \frac{1}{k'(\epsilon^p)}\dot{\sigma}_{eq} \tag{C.7}$$

Using the previous computed value of the plastic multiplier, the total incremental form can be summarized as:

$$\begin{aligned}
\dot{\underline{\underline{\varepsilon}}} &= \dot{\underline{\underline{\varepsilon}}}^e + \dot{\underline{\underline{\varepsilon}}}^p \\
\dot{\underline{\underline{\varepsilon}}}^e &= \frac{1+\nu}{E}\dot{\underline{\underline{\sigma}}}_b - \frac{\nu}{E}\,tr\left(\dot{\underline{\underline{\sigma}}}_b\right)\underline{\underline{I}} \\
\dot{\underline{\underline{\varepsilon}}}^p &= \frac{3}{2}\frac{1}{k'(\epsilon^p)\sigma_{eq}}\dot{\sigma}_{eq}\,\underline{\underline{s}}
\end{aligned} \tag{C.8}$$

The expression for the hardening relation $k(\epsilon^p)$ can be easily derived from simple traction tests. In this condition, the only non-zero component of the stress tensor is $\sigma_1 = \sigma$, and the non null components of the deviatoric stress tensor are $s_{11} = \frac{2}{3}\sigma$ and $s_{22} = s_{33} = -\frac{1}{3}\sigma$. The total plastic strain is $\epsilon^p = \varepsilon^p$ and $\sigma_{eq} = \sigma$. In this case, the flow rule is:

$$\dot{\varepsilon}^p = \frac{1}{k'(\varepsilon^p)}\dot{\sigma} \quad \rightarrow \quad k'(\varepsilon^p) = \frac{\partial\sigma}{\partial\varepsilon^p} \tag{C.9}$$

According to the previous expression, the function R can be computed as:

$$R = k(\varepsilon^p) = \int_0^\varepsilon k'(\varepsilon^p)d\varepsilon^p = \int_{\sigma_y}^\sigma d\sigma = \sigma - \sigma_y \tag{C.10}$$

Assuming a bilinear stress-strain relation (Fig.C.1), the tangent modulus $k'(\epsilon^p)$ can be expressed by:

$$R = k(\epsilon^p) = \frac{E\,E_t}{E - E_t}\,\varepsilon^p \quad \rightarrow \quad k'(\epsilon^p) = \frac{E\,E_t}{E - E_t} \tag{C.11}$$
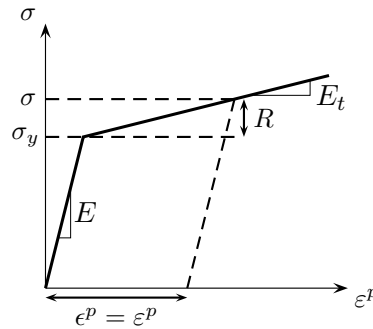
Figure C.1: Graphical representation of a simple traction test and interpretation of hardening parameter $R = k(\epsilon^p)$ and $k'(\epsilon^p)$

As explained in (§B.1), the numerical integration is carried out following and explicit strategy. The strain increment predictor is divided into an elastic part and into a plastic part. Let $\Delta\underline{\underline{\varepsilon}}^*$ the plastic part of the total increment. By inverting the incremental relations (C.8), the stress increment associated to $\Delta\underline{\underline{\varepsilon}}^*$ can be computed as:

$$\Delta\underline{\underline{\sigma}}^* = \underline{\underline{\underline{\underline{C}}}}^{ep}\left(\underline{\underline{s}}, \sigma_{eq}\right) : \Delta\underline{\underline{\varepsilon}}^* \tag{C.12}$$

as the elastoplastic tensor $\underline{\underline{C}}^{ep}$ is a function of the deviatoric stress tensor, the equivalent stress σ_{eq} and its derivative, the plastic increment is subdivided in several steps and the elastoplastic tensor evaluated for the updated values of $\underline{s}$, σ_{eq} and $d\sigma_{eq}$ for each step.

The model parameters for the continuous beam element are summarized in the Table C.1. As previously explained, these parameters are related to experimental results of a simple traction test. The numerical used values are given for each example in the corresponding section.

Table C.1: Parameters for the Prandtl-Reuss constitutive model

Parameter	Description
E	elastic modulus
ν	Poisson's modulus
σ_y	initial yield stress
E_t	hardening modulus

Appendix D

Plastic hinges beam column elements

Beam column elements may be arbitrarily oriented in the global system. Each element must be assigned an axial stiffness plus a major axis flexural stiffness. Torsional and minor axis flexural stiffness may also be specified if necessary. Elements of variable cross section can be considered by specifying appropriate flexural stiffness coefficients. Flexural shear deformations and the effects of eccentric end connections can be taken into account too.

Yielding may take place only in concentrated plastic hinges at the element ends. Hinge deformation is affected by the axial force and major axis bending moment only. That is, an element may be placed in a three-dimensional frame, but is yield mechanism is only two-dimensional, in the plane of major bending axis. The yield moments may be specified to be different at the two element ends, and for positive and negative bending. The interaction between axial force and moment in producing yield is taken into account approximately.

The model consists of a linear component and an ideally elastoplastic component (Fig. D.1a), so that each beam can have only bilinear hysteresis loops at each end as a result of the nature of the model. For this model, the initial slope on the moment-curvature diagram is determined from the sum of the stiffness of both components while the second slope is determined by the stiffness of only the linear component of the beam (Fig. D.1b). Plastic hinges that yield to constant moment form an elastic-plastic component. The moments in the elastic component continue to increase, simulating strain hardening.

| (a) Parallel components | (b) Moment-curvature relationships |
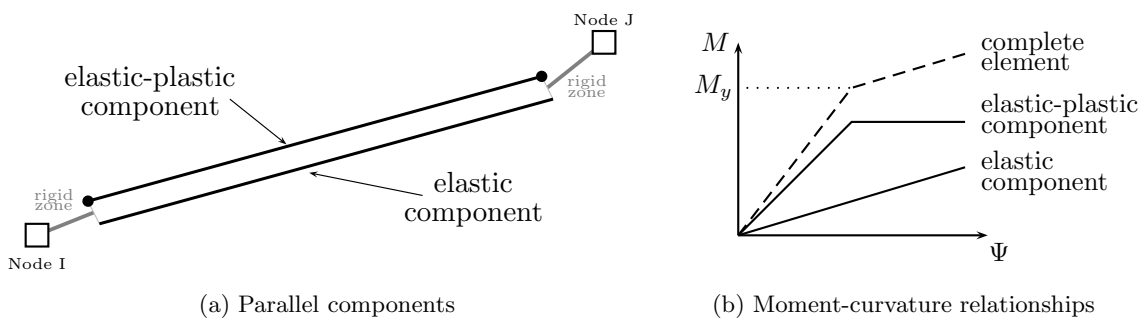
Figure D.1: Two-component model

D.1 Elastic stiffness matrix

An equivalent expression for the assumed displacement field $\underline{u}$ (1.15) is:

$$
\begin{aligned}
u_r &= u_{0_r} - s\, u_{1_t} + t\, u_{1_s} \\
u_s &= u_{0_s} - t\, u_{1_r} \\
u_t &= u_{0_t} + s\, u_{1_r}
\end{aligned}
\tag{D.1}
$$

where u_{1_r}, u_{1_s} and u_{1_t} are the rotations around the local directions $\underline{e}_r$, $\underline{e}_s$ and $\underline{e}_t$ respectively (Fig.D.2) with the sign convention of the right-hand rule. We assume a homogenous isotropic material:
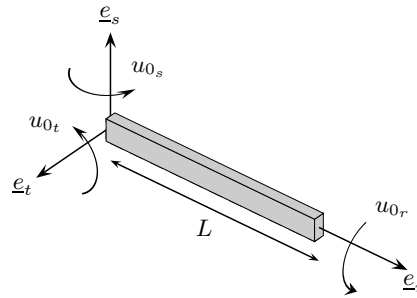
Figure D.2: Sign convention for displacements and rotations fields

$$
\underline{\sigma} = \lambda\, tr\left(\underline{\varepsilon}\right) \underline{I} + 2\mu \underline{\varepsilon}
\tag{D.2}
$$

with the usual notation for the Lamé constants. According to beams kinematics, the previous relation can be reduced to:

$$
\sigma_{rr} = E\varepsilon_{rr} \quad ; \quad \sigma_{rs} = 2\mu\varepsilon_{rs} \quad \text{and} \quad \sigma_{rt} = 2\mu\varepsilon_{rt}
\tag{D.3}
$$

Similarly, the strain-displacements equations can be summarized as:

$$
\begin{aligned}
\varepsilon_{rr} &= \partial_r u_{0_r} - s\, \partial_r u_{1_t} + t\, \partial_r u_{1_s} \\
\varepsilon_{rs} &= \frac{1}{2}\left(\partial_r u_{0_t} + s\, \partial_r u_{1_r} + u_{1_s}\right) \\
\varepsilon_{rt} &= \frac{1}{2}\left(\partial_r u_{0_s} - t\, \partial_r u_{1_r} - u_{1_s}\right)
\end{aligned}
\tag{D.4}
$$

According to (D.4), the shear strains γ_{rs} and γ_{rt}, the axial strain ε_{rr} and the twist ψ can obtained as follows:

$$
\begin{aligned}
\gamma_s &= \partial_r u_{0_t} + u_{1_s} \\
\gamma_t &= \partial_r u_{0_s} - u_{1_t} \\
\varepsilon_r &= \partial_r u_{0_r} \\
\psi &= \partial_r u_{1_r}
\end{aligned}
\tag{D.5}
$$

We also assume the local system of axes (r, s, t) are geometrical principal axes:

$$
\int_S s\, dS = \int_S t\, dS = \int_S s\, t\, dS = 0
\tag{D.6}
$$

With the definitions (D.5) for strains and twist, the components of the internal forces $\underline{q}$ and moments $\underline{m}$ can be expressed as:

$$
\begin{aligned}
q_r &= \int_S \sigma_{rr}\, dS = \int_S \partial_r u_{0_r} - s\partial_r u_{1_t} + t\partial_r u_{1_s}\, dS = EA\varepsilon_r \\
q_s &= \int_S \sigma_{sr}\, dS = \mu \int_S \partial_r u_{0_t} + s\partial_r u_{1_r} + u_{1_s}\, dS = \mu A\gamma_s \\
q_t &= \int_S \sigma_{st}\, dS = \mu \int_S \partial_r u_{0_s} - t\partial_r u_{1_r} - u_{1_t}\, dS = \mu A\gamma_t \\
m_r &= \int_S \sigma_{rt}s - \sigma_{rs}t\, dS = \mu \int_S (\partial_r u_{0_t} + s\partial_r u_{1_r} + u_{1_s})\, s - (\partial_r u_{0_s} - t\partial_r u_{1_r} - u_{1_t})\, t\, dS = \mu J\psi \\
m_s &= \int_S \sigma_{rr}t\, dS = E \int_S (\partial_r u_{0_r} - s\partial_r u_{1_t} + tu_{1_s})\, t\, dS = EI_s\kappa_s \\
m_t &= \int_S \sigma_{rr}s\, dS = E \int_S (\partial_r u_{0_r} - s\partial_r u_{1_t} + tu_{1_s})\, s\, dS = -EI_t\kappa_t
\end{aligned}
\tag{D.7}
$$

with the standard definitions for area A, moments of inertia I_s and I_t and polar moment of inertia J:

$$
I_s = \int_S t^2\, dS \quad ; \quad I_t = \int_S s^2\, dS \quad \text{and} \quad J = I_s + I_t
$$

Decomposing the field test $\underline{w}$ in a similar manner, it is possible to compute the same expression for $\bar{\gamma}_{rs}$, $\bar{\gamma}_{rt}$, $\bar{\varepsilon}_{rr}$, $\bar{\psi}$, $\bar{\kappa}_s$ and $\bar{\kappa}_t$ (denoted with a bar to differentiate with these associated to the real field $\underline{u}$). Injecting these definition in (1.42) we obtain for a linear elastic isotropic beam:

$$
\int_\Omega \underline{\underline{\sigma}} : \bar{\underline{\underline{\varepsilon}}}\, dV = \int_L \left(\bar{\gamma}_s \mu A_s^s \gamma_s + \bar{\gamma}_t \mu A_t^s \gamma_t + \bar{\kappa}_s EI_s \kappa_s + \bar{\kappa}_t EI_t \kappa_t + \bar{\varepsilon}_r EA\varepsilon_r + \bar{\psi}EJ\psi \right)\, dl
\tag{D.8}
$$

where A_s^s and A_t^s are effective shear area for the s and t directions, respectively. Introducing the finite element approximation $\underline{u}_0^h$ and $\underline{u}_1^h$ (1.49), the elastic stiffness matrix can be computed straightforward (Hughes, 2000).

D.2   Two-component stiffness matrix

Applying static condensation with respect to bending rotations in the local stiffness matrix defined by (D.8), the local element bending stiffness relationships in $r-s$ plane for the elastic element are:

$$
\left\{ \begin{array}{c} m_t^{I,e} \\ m_t^{J,e} \end{array} \right\} = \frac{EI_t}{L} \left[\begin{array}{cc} k_{II} & k_{IJ} \\ k_{IJ} & k_{JJ} \end{array} \right] \left\{ \begin{array}{c} \theta_t^I \\ \theta_t^J \end{array} \right\}
\tag{D.9}
$$

where $m_t^{I,e}$ and $m_t^{J,e}$ are the elastic end bending moments at nodes I and J in $r-s$ plane (vectors in $\underline{e}_t$ direction), θ_t^I (or $u_{1_{I3}}$) and θ_t^J (or $u_{1_{J3}}$) are the corresponding total end node rotations.

For a linear elastic uniform cross section element, the flexural stiffness coefficients are:

$$
k_{II} = k_{JJ} = 4 \quad \text{and} \quad k_{IJ} = 2
\tag{D.10}
$$

Usually it is assumed that the beam has a uniform cross section throughout the length, but elements of variable cross section can be considered by specifying appropriate flexural stiffness coefficients for the elastic beam. Elastic shear deformations can be included by specifying an effective shear area A_t^s.

A plastic hinge forms when the moment in the inelastic component of the element reaches its yield value. A hinge is then introduced into this component, the elastic component remaining unchanged. The measure of flexural plastic deformation is the plastic hinge rotation.

In order to obtain incremental moment-rotation equations, the total end rotation increments must be related to rotations in both elastic and elastic-plastic components (Fig.D.3). In this figure m_t^I and m_t^J are the total bending moment at the ends I and J, $m_t^{I,p}$ and $m_t^{J,p}$ are the bending moments at the

(a) Two-component

(b) Elastic component

(c) Elastic-plastic component
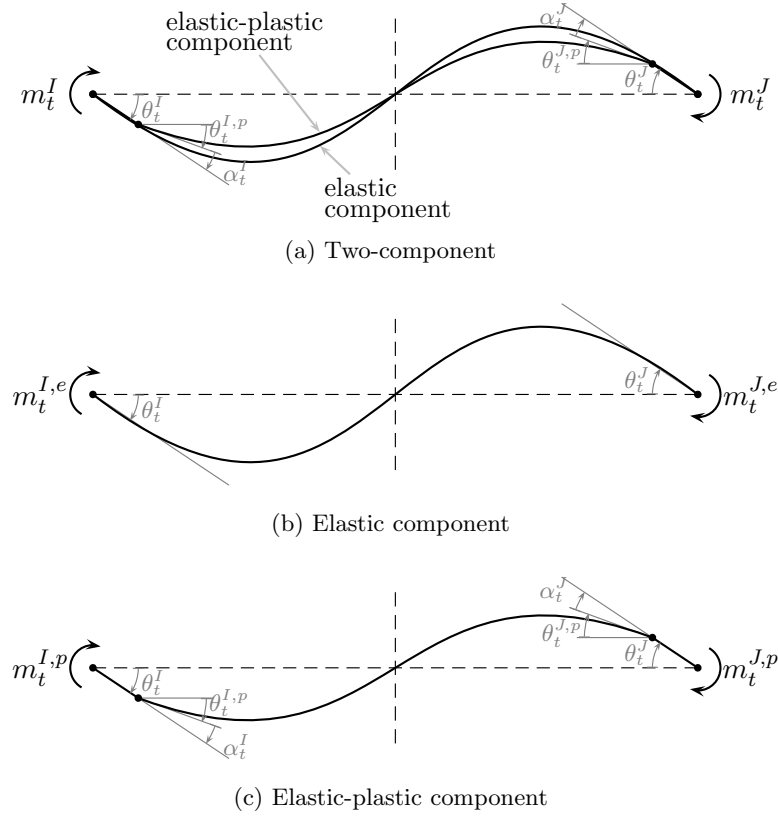
Figure D.3: Two-component notation

ends of the elastic-plastic component, $\theta_t^{I,p}$ and $\theta_t^{J,p}$ the end rotations of the elastic-plastic component, α_t^I and α_t^J the incurred plastic angle at the ends of the elastic-plastic component.

The rotational stiffness $k_t = \frac{4E_t I}{L}$ (uniform cross section) of the total beam is divided into two components:

$$k_t^e = \tilde{p}\,k_t \quad ; \quad k_t^p = \tilde{q}\,k_t \quad ; \quad \tilde{p} + \tilde{q} = 1 \tag{D.11}$$

where k_t^e is the stiffness of the linear elastic component and k_t^p the stiffness of the elastic-plastic component. The parameters $\tilde{p}$ and $\tilde{q}$ govern the stiffness distribution, usually $\tilde{p} \approx 0.05$.

From (D.9), the fundamental bending moment-end rotations equations for both components are:

$$m_t^{I,e} = \tilde{p}k_t \left(\theta_t^I + \frac{1}{2}\theta_t^J \right) \quad ; \quad m_t^{J,e} = \tilde{p}k_t \left(\frac{1}{2}\theta_t^I + \theta_t^J \right) \qquad \text{(Elastic)}$$

$$m_t^{I,p} = \tilde{q}k_t \left(\theta_t^{I,p} + \frac{1}{2}\theta_t^{J,p} \right) \quad ; \quad m_t^{J,p} = \tilde{q}k_t \left(\frac{1}{2}\theta_t^{I,p} + \theta_t^{J,p} \right) \quad \text{(Elastic-plastic)} \tag{D.12}$$

From Fig.D.3:

$$\theta_t^{I,p} = \theta_t^I - \alpha_t^I \quad ; \quad \theta_t^{J,p} = \theta_t^J - \alpha_t^J \tag{D.13}$$

Combining (D.12) and by substitution of (D.13), the incremental form of the bending-moment relation can be written as:

$$\begin{aligned}
\dot{m}_t^{I,e} &= \tilde{q}k_t \left(\left(\dot{\theta}_t^I - \dot{\alpha}_t^I \right) + \frac{1}{2} \left(\dot{\theta}_t^J - \dot{\alpha}_t^J \right) \right) \\
\dot{m}_t^{J,e} &= \tilde{q}k_t \left(\frac{1}{2} \left(\dot{\theta}_t^I - \dot{\alpha}_t^I \right) + \left(\dot{\theta}_t^J - \dot{\alpha}_t^J \right) \right)
\end{aligned} \tag{D.14}$$

The addition of bending moments at the ends of the elastic and the elastic-plastic components gives the total bending moment:

$$m_t^I = m_t^{I,e} + m_t^{I,p} \quad ; \quad m_t^J = m_t^{J,e} + m_t^{J,p} \tag{D.15}$$

Finally, the fundamental bending-end rotation equations for the complete element are obtained:

$$
\begin{aligned}
\dot{m}_t^I &= k_t \left(\left(\dot{\theta}_t^I - \tilde{q}\dot{\alpha}_t^I \right) + \frac{1}{2} \left(\dot{\theta}_t^J - \tilde{q}\dot{\alpha}_t^J \right) \right) \\
\dot{m}_t^J &= k_t \left(\frac{1}{2} \left(\dot{\theta}_t^I - \tilde{q}\dot{\alpha}_t^I \right) + \left(\dot{\theta}_t^J - \tilde{q}\dot{\alpha}_t^J \right) \right)
\end{aligned} \tag{D.16}
$$

Assuming that the state of yield remains constant throughout each time increment, the incremental bending moments $\dot{m}_t^I$ and $\dot{m}_t^J$ are related to both incremental rotations $\dot{\theta}_t^I$ and $\dot{\theta}_t^J$, and the incremental plastic angles $\dot{\alpha}_t^I$ and $\dot{\alpha}_t^J$. Now, for any state of yield which is held constant throughout a time increment, it is possible to establish equations of the form $\dot{\alpha}_t = \dot{\alpha}_t \left(\dot{\theta}_t^I, \dot{\theta}_t^J \right)$ relating the incremental plastic angles to the incremental end rotations. With these equations it is possible to eliminate the incremental plastic angles from the incremental moment-rotation equations resulting in equations of the form $\dot{m}_t = \dot{m}_t \left(\dot{\theta}_t^I, \dot{\theta}_t^J \right)$.

When the state of yield is linear at end I or end J, or both, the corresponding incremental plastic angle must be zero: $\dot{\alpha}_t^I = \dot{\alpha}_t^J = 0$.

When the state of yield is non-linear at end I or end J, or both, the corresponding incremental total bending moments equals the incremental bending moment of the linear component, and the incremental bending moment in the elastoplastic component is zero: at end I, $\dot{m}_t^I = \dot{m}_t^{I,e}$ and $\dot{m}_t^{I,p} = 0$; or at end J, $\dot{m}_t^J = \dot{m}_t^{J,e}$ and $\dot{m}_t^{J,p} = 0$; or both.

On the other hand, $\dot{m}_t^{I,e}$ and $\dot{m}_t^{J,e}$ are dependent upon the same stiffness parameter $\tilde{p}$. Consequently, this model can have hysteresis loops at the ends with only two slopes k_t and $\tilde{p}k_t$ although the yields levels may be different.

There are four possible states of yield for a beam:

(a) Linear at ends I and J.

(b) Non-linear at end I and linear at end J.

(c) Linear at end I and non-linear at end J.

(d) Non-linear at ends I and J.

Because the incremental bending moment-end rotation equations have a regular pattern for all four states of yield, the following matrix equations using the effective stiffness parameters S_A, S_B and S_C can be established (Table D.1):

$$
\left\{ \begin{array}{c} \dot{m}_t^I \\ \dot{m}_t^J \end{array} \right\} = \left[\begin{array}{cc} S_A & S_B \\ S_B & S_C \end{array} \right] \left\{ \begin{array}{c} \dot{\theta}_t^I \\ \dot{\theta}_t^J \end{array} \right\} \tag{D.17}
$$

Even if the beam element can be placed arbitrarily in 3D, this two-component approach is taken into account only in the local $r-s$ plane (primary flexural plane), therefore the model is bidimensional in a non-linear sense. The minor axis flexural stiffness (plane $r-t$) can be obtained by multiplying the primary elastic stiffness by a specified factor α. The torsional deformation is related to torque m_r by:

$$\dot{m}_r = \frac{\mu J}{L} \dot{\alpha} \tag{D.18}$$

Table D.1: Effective stiffness coefficients

State	S_A	S_B	S_C
(a)	k_t	$\frac{1}{2}k_t$	k_t
(b)	$\tilde{p}k_t$	$\frac{1}{2}\tilde{p}k_t$	$\left(1-\frac{\tilde{q}}{4}\right)k_t$
(c)	$\left(1-\frac{\tilde{q}}{4}\right)k_t$	$\frac{1}{2}\tilde{p}k_t$	$\tilde{p}k_t$
(d)	$\tilde{p}k_t$	$\frac{1}{2}\tilde{p}k_t$	$\tilde{p}k_t$

in which it is assumed that $\mu = 0.4E$ and:

$$J = \alpha\left(k_{II} + k_{JJ}\right)\frac{I_t}{8} \tag{D.19}$$

in which k_{II} and k_{JJ} are the primary flexural stiffness factors, after any modification for shear deformations.

D.3   Yield surfaces

The effect of axial force on bending strength is taken into account by specifying P-M yield surfaces. Yield interaction surface of three types may be specified for the ends of the beam element:

- Beam type (Fig.D.4a) This type of surface should be specified where axial forces are small or are ignored. Yielding is affected by bending moment only.

- Steel column type (Fig.D.4b) This type of surface is intended for use with steel columns.

- Concrete column type (Fig.D.4c). This type of surface is intended for use with concrete columns.

(a) Beam type   (b) Steel column type   (c) Concrete column type
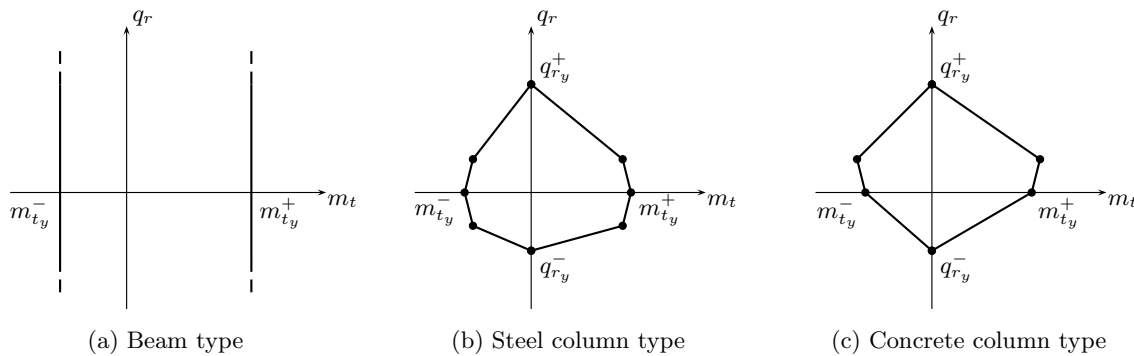
Figure D.4: Yield interaction surfaces

For any combination of axial force and bending moment within a yield surface, the cross section is assumed to be elastic. If the force-moment combination lies on or outside the surface, a plastic hinge is introduced. Combinations outside the yield surface are permitted only temporarily, being compensated by applying corrective loads in the succeeding step. This procedure is not strictly correct because the axial and flexural deformations interact after yield, and it is therefore wrong to assume that only the flexural stiffness changes whereas the axial stiffness remains unchanged.

If a force-moment combination goes from the elastic range to beyond the yield surface in any load substep; an equilibrium correction is made as shown in Fig.D.5a. Because the axial stiffness is assumed

to remain unchanged, in subsequent substeps the force-moment combination at a plastic hinge will generally move away from the yield surface within any substep, as shown in Fig.D.5b. An equilibrium correction, as shown, is therefore made.

(a) Yield at an existing hinge   (b) Formation of a new hinge
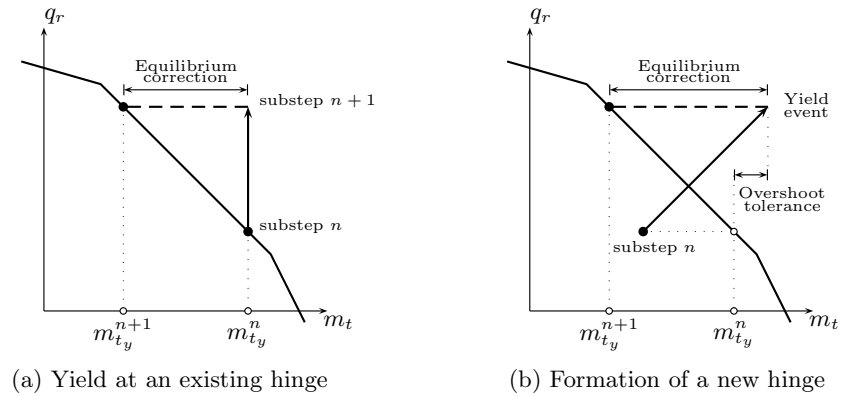
Figure D.5: Equilibrium correction for yield surface overshoot

The axial force in an element with a column-type interaction surface can, never exceed the yield value for zero moment. However, because of the computational procedure which is used, axial forces in excess of yield can be computed. For axial forces in excess of yield, the yield moment are assumed to be zero.

Appendix E

ECP multimechanism model

E.1 General hypotheses and characteristics of the model

E.1.1 Hypothesis 1

We assume that small-strains hypothesis is valid, i.e. the strain tensor increment can be decomposed into an elastic part and a plastic part:

$$\dot{\underline{\underline{\varepsilon}}} = \dot{\underline{\underline{\varepsilon}}}^e + \dot{\underline{\underline{\varepsilon}}}^p \tag{E.1}$$

consequently, the decomposition is also valid for volumetric ε_v and deviatoric strains $\dot{\underline{\underline{\bar{\varepsilon}}}}$ increments:

$$\dot{\varepsilon}_v = \dot{\varepsilon}_v^e + \dot{\varepsilon}_v^p \quad \text{and} \quad \dot{\underline{\underline{\bar{\varepsilon}}}} = \dot{\underline{\underline{\bar{\varepsilon}}}}^e + \dot{\underline{\underline{\bar{\varepsilon}}}}^p \tag{E.2}$$

E.1.2 Hypothesis 2

The effective stress principle applies.

E.1.3 Hypothesis 3

The elastic part of the behavior is isotropic:

$$
\begin{aligned}
\dot{\varepsilon}_v^e &= \frac{1}{K\,(p')}\dot{p}' \\
\dot{\underline{\underline{\bar{\varepsilon}}}}^e &= \frac{1}{2\,G\,(p')}\dot{\underline{\underline{s}}}
\end{aligned}
\tag{E.3}
$$

where the bulk $K = K(p')$ and shear $G = G(p')$ moduli are function of the mean effective compressive stress p' by a non-linear relation:

$$
\begin{aligned}
K &= K_{ref}\left(\frac{p'}{p'_{ref}}\right)^{n_e} \\
G &= G_{ref}\left(\frac{p'}{p'_{ref}}\right)^{n_e}
\end{aligned}
\tag{E.4}
$$

where K_{ref} and G_{ref} are the bulk and shear moduli measured at the mean effective pressure p'_{ref} and n_e is the degree of non-linearity. Therefore, there is no-coupling effect between the volumetric and deviatoric elastic strain rates, i.e. $\dot{\varepsilon}_v^e$ is independent of $\dot{\underline{\underline{\bar{\varepsilon}}}}^e$, but $\dot{\underline{\underline{\bar{\varepsilon}}}}^e$ depends on $\dot{\varepsilon}_v^e$.

E.1.4   Hypothesis 4

The behavior is divided in four sub-domains:

1. **Elastic domain**: no energy dissipation and reversible deformations

2. **Hysteretic or pseudo-elastic domain (stabilized)**: energy dissipation by plastic deformation appears, but the volumetric plastic strain variation is neglected ($\dot{\varepsilon}_v^p = 0$).

3. **Intermediate domain (hysteretic unstabilized)**: the volumetric plastic strain variation is no longer neglected.

4. **Mobilized domain**: the shear stress mobilizes completely the shear resistance of the solid phase.

E.1.5   Hypothesis 5

The deviatoric plastic behavior is decomposed into three plane-strain elementary mechanisms, over three orthogonal planes. The plastic energy dissipation is related to variations of Mohr circles in the corresponding orthogonal plane. Each elementary deviatoric mechanism is equivalent to a Mohr-Coulomb type criterion relative to its corresponding plane. The critical state into a plane corresponds to the limit Mohr circle of each mechanism.

The yield surface of each deviatoric mechanism is a circle in a normalized deviatoric plane, constructed by a normalization factor. In this normalized plane, the flow rule is associated. The mobilization of each deviatoric mechanism is progressive and depends on the behavior sub-domains (§E.1.4). The hardening variable in the normalized plane is the degree of friction mobilization of the mechanism.

The material stores the historic loading by a double memory approach: the maximum primary loading (historic memory) and the last load-reversal change (instantaneous memory).

The decomposition is constructed into a basis defined by the unitary vectors $\underline{e}_i$, $\underline{e}_j$ and $\underline{e}_k$ for the deviatoric mechanism k. For all planes oriented by the normal vector $\underline{e}_k$, the plastic strains increments exist only in the directions defined by $\underline{e}_i$ and $\underline{e}_j$. These plastic strains increments are function only of the stress state in this $k-$plane associated to the deviatoric mechanism k. Thus, the effective stress tensor in the $k-$plane $\underline{\underline{\sigma}}'_k$ can be written as:

$$\underline{\underline{\sigma}}'_k = \sigma'_{ii}\,\underline{e}_i \otimes \underline{e}_i + \sigma'_{jj}\,\underline{e}_j \otimes \underline{e}_j + \sigma'_{ij}\,\underline{e}_i \otimes_s \underline{e}_j \tag{E.5}$$

The stress state in the $k-$plane is defined by its effective mean pressure p'_k and its deviatoric stress tensor $\underline{s}_k$ (Fig.E.1a):

$$
\begin{aligned}
p'_k &= \frac{1}{2}\,tr\left(\underline{\underline{\sigma}}'_k\right) \\
\underline{s}_k &= \underline{\underline{\sigma}}'_k - \frac{1}{2}\,tr\left(\underline{\underline{\sigma}}'_k\right)\underline{\underline{I}}_k
\end{aligned}
\tag{E.6}
$$

where $\underline{\underline{I}}_k = \underline{e}_i \otimes \underline{e}_i + \underline{e}_j \otimes \underline{e}_j$. The tensor $\underline{\underline{s}}_k$ can be seen as a deviatoric stress vector $\underline{s}_k$ in the $k-$plane of components and norm:

$$
\begin{aligned}
s_{k_1} &= \frac{\sigma'_{ii} - \sigma'_{jj}}{2} \\
s_{k_2} &= \sigma'_{ij} \\
|\underline{s}_k| &= \sqrt{\frac{1}{4}\left(\sigma'_{ii} - \sigma'_{jj}\right)^2 + {\sigma'_{ij}}^2} = q_k
\end{aligned}
\tag{E.7}
$$

where q_k is the radius of the Mohr circle. The plane associated to deviatoric stress vector $\underline{s}_k$ is the diviatoric plane of the mechanism k (Fig.E.1b).

(a) Mohr's representation of the stress state in the $i-j$ plane of the mechanism k ($k-$plane)

(b) Stress state of the deviatoric plane of the mechanism k
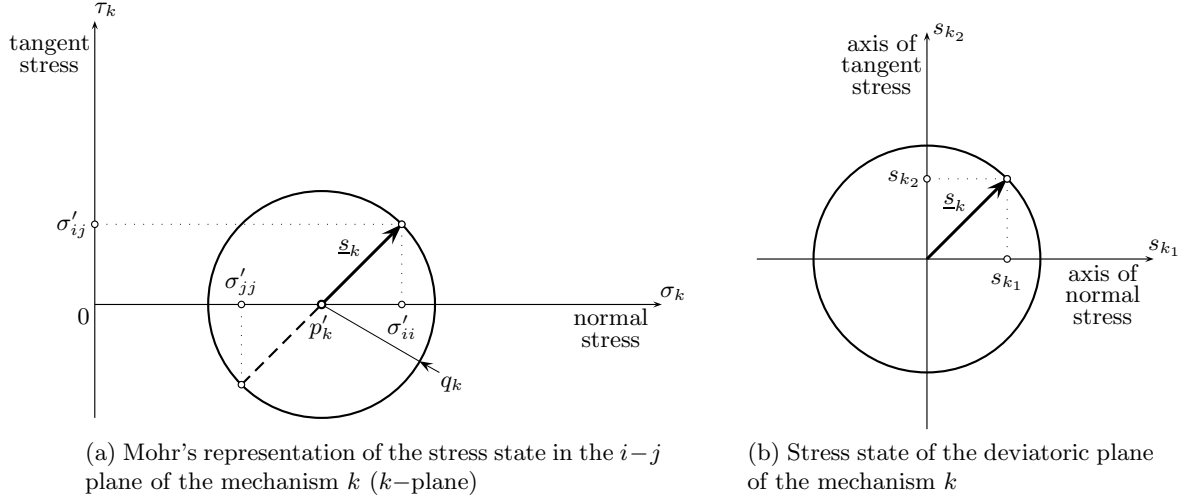
Figure E.1: Stress state representations for deviatoric mechanism k

In a similar way, the strain stain in the plane of the mechanism k is defined by the volumetric strain ε_{v_k} and the deviatoric strain tensor $\bar{\bar{\varepsilon}}_k$:

$$
\begin{aligned}
\underline{\underline{\varepsilon}}_k &= \varepsilon_{ii}\,\underline{e}_i \otimes \underline{e}_i + \varepsilon_{jj}\,\underline{e}_j \otimes \underline{e}_j + \varepsilon_{ij}\,\underline{e}_i \otimes_s \underline{e}_j \\
\bar{\underline{\underline{\varepsilon}}}_k &= \underline{\underline{\varepsilon}}_k - \frac{1}{2}tr\left(\underline{\underline{\varepsilon}}_k\right)\underline{\underline{I}}_k \\
\varepsilon_{v_k} &= tr\left(\underline{\underline{\varepsilon}}_k\right)
\end{aligned}
\tag{E.8}
$$

Similarly, the deviatoric strain tensor can be represented as a deviatoric strain vector $\bar{\underline{\varepsilon}}_k$ of components and norm:

$$
\begin{aligned}
\bar{\varepsilon}_{k_1} &= \varepsilon_{ii} - \varepsilon_{jj} \\
\bar{\varepsilon}_{k_2} &= 2\varepsilon_{ij} \\
|\bar{\underline{\varepsilon}}_k| &= \gamma_k
\end{aligned}
\tag{E.9}
$$

where γ_k is the distortion of the mechanism k and its value corresponds to two-times the radius of the circle in Mohr's representation (centered in $\frac{1}{2}\varepsilon_{v_k}$ Fig.E.2).
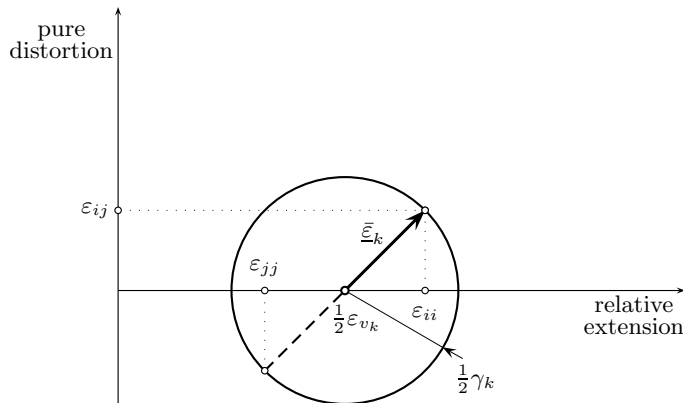
Figure E.2: Mohr's representation of the strain state in the $i-j$ plane of the mechanism k

Adopting the soil mechanics sign convention (compression positive), the deviatoric primary yield surface f_k of the k plane is given by:

$$f_k \left(p_k', \underline{s}_k, r_k, \varepsilon_v^p \right) = q_k - \sin \phi_{pp}' \, p_k' \, r_k \, F \left(p', \varepsilon_v^p \right) \tag{E.10}$$

where:

$$
\begin{aligned}
F \left(p', \varepsilon_v^p \right) &= 1 - b \log \frac{p'}{p_c} \\
p_c &= p_{c_0} e^{\beta \varepsilon_v^p}
\end{aligned}
\tag{E.11}
$$

in which ϕ_{pp}' is the friction angle at the perfect plasticity, p_{c_0} is the critical mean effective stress that corresponds to the initial state (defined by the initial void ratio), β is the plastic compressibility modulus that introduces the influence of the densification of the material in the final resistance. Both parameters are similar to the ones used in Cam-Clay model (Schofield and Wroth, 1968). The parameter b controls the form of the yield surface in the $p_k' - q_k$ plane and varies from $b = 0$ to 1 passing from a Coulomb type surface to a Cam-Clay type one (Fig. E.3). The parameter b governs the influence of the density or the overconsolidation, thus its value is near to one for clays and very small for sands. The function F, through the plastic volumetric strain ε_v^p, introduces volumetric hardening or softening with respect to the critical state due to plastic strains.
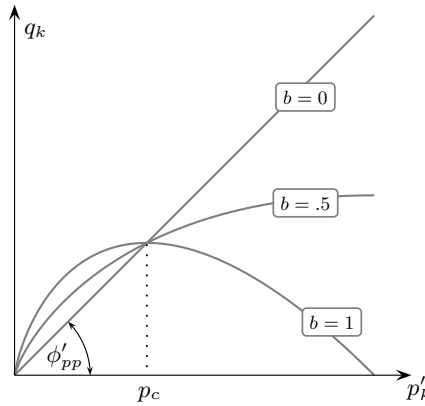
Figure E.3: Influence of parameter b on the yield surface shape

The deviatoric primary yield surface of each k mechanism can be interpreted in the normalized deviatoric plane of the mechanism $\tilde{s}_{k_1} - \tilde{s}_{k_2}$:

$$\tilde{s}_{k_1} = \frac{1}{\eta_k} s_{k_1} \quad \text{and} \quad \tilde{s}_{k_2} = \frac{1}{\eta_k} s_{k_2} \tag{E.12}$$

the normalization factor η_k is given by:

$$\eta_k \left(p_k', \varepsilon_v^p \right) = \sin \phi_{pp}' \, p_k' \, F \left(p', \varepsilon_v^p \right) \tag{E.13}$$

In this plane, the deviatoric yield surfaces are circles of radius r_k. This hardening variable r_k can be interpreted as the degree of mobilization of the deviatoric mechanism k, i.e. the degree of friction mobilization:

$$r_k = \frac{q_k}{\eta_k} = \frac{q_k}{p_k'} \frac{1}{\sin \phi_{pp}' \, F} \tag{E.14}$$

The hardening variable r_k corresponds to progressive plasticity evolution due to plastic shear distortions γ_k^p of the k mechanism. Thus, it accounts for the isotropic hardening generated by plastic deviatoric strains $\underline{\tilde{\varepsilon}}_k^p$ or γ_k^p. This variable varies from r_k^{el} (elastic domain) to its limit unit value in the perfect plasticity.

Under primary loading (superscript m to indicate monotonic loading), the surfaces associated to deviatoric yield functions are the circles of radius r_k^m centered at the origin (Fig.E.5a):

$$
\begin{aligned}
f_k^m\left(p_k', \underline{s}_k, r_k^m, \varepsilon_v^p\right) &= \left|\underline{\tilde{s}}_k\right| - r_k^m \\
r_k^m &= r_k^{el} + \left(\frac{\gamma_k^p}{a + \gamma_k^p}\right)^{n_p} \\
\gamma_k^p &= \int_0^t \dot{\gamma}_k^p\, dt
\end{aligned}
\tag{E.15}
$$

where the parameter a controls the hardening evolution. The parameter n_p controls the evolution of the degree of friction mobilization with the plastic strain. If $n_p = 1$ the evolution is hyperbolic as some strain-stress curves, but it can be modified to take into account experimental data. The hardening evolution rule can be derived from (E.15):

$$
\dot{r}_k^m = \dot{\lambda}_k^p \frac{n_p \left(r_k^m\right)^{n_p-1}}{a}\left(1 - (r_k^m)^{\frac{1}{n_p}}\right)^2
\tag{E.16}
$$

where $\dot{\lambda}_k^p$ is the plastic multiplier of the deviatoric k mechanism.

The parameter a in equation (E.15) is an important parameter of the model because it controls the rigidity when the soil is in plastic domain. The simpler way is to use a constant value, but it is also possible to modify its value as a function of the deviatoric plastic strains. Hujeux (1985) defined a through the following relation:

$$
a = a_1 + (a_2 - a_1)\,\alpha\left(r_k\right)
\tag{E.17}
$$

where $\alpha\left(r_k\right)$ is defined through the behavior domains (§E.1.4) described below:

$$
\alpha\left(r_k\right) = \begin{cases}
0 & \text{if } r_k < r_k^{hys} & \text{pseudo-elastic domain} \\
\left(\frac{r_k - r_k^{mob}}{r_k^{mob} - r_k^{hys}}\right)^m & \text{if } r_k^{hys} < r_k < r_k^{mob} & \text{hysteretic domain} \\
1 & \text{if } r_k^{mob} < r_k < 1 & \text{mobilized domain}
\end{cases}
\tag{E.18}
$$

in which r_k^{hys} and r_k^{mob} are the thresholds friction mobilization sub-domains associated to mechanism k. According to Hujeux (1985), $\alpha\left(r_k\right)\dot{\gamma}_k^p$ can be interpreted as the portion of the plastic shear strain increment related to relative tangent displacement between grains with total friction strength mobilization. The portion of the increment induces a rearrangement of the grains and plastic volumetric strain. On the contrary, $(1 - \alpha\left(r_k\right))\dot{\gamma}_k^p$ is the portion of the relative tangent displacements of grains with partial friction mobilization, therefore without inducing volumetric plastic strains. Consequently, the parameter $\alpha\left(r_k\right)$ allows that for drained conditions, there is no volume variations until a certain level of shearing is achieved. In addition, for undrained conditions, it allows that the evolution of the pore pressure will depend on the level of deformations (Modaressi, 2003). The evolution into the hysteretic domain is controlled by the value of m (Fig.E.4).

Concerning the cyclic loading (superscript c to indicate cyclic loading), the surfaces associated to deviatoric yield functions are the circles of radius r_k^c interior to circles of primary loading, both tangent at the point $\underline{d}_k^h$ of exterior normal $\underline{n}_k^h$:

$$
f_k^c\left(p_k', \underline{s}_k, r_k^c, \varepsilon_v^p, \underline{d}_k^h, \underline{n}_k^h\right) = \left|\underline{\tilde{s}}_k - \left(\underline{d}_k^h - r_k^c \underline{n}_k^h\right)\right| - r_k^c
\tag{E.19}
$$

where the point $\underline{d}_k^h$ corresponds to the last load reversal h of the mechanism k:

$$
\underline{d}_k^h = \frac{q_k^h}{p_k'^h} \frac{1}{\sin\phi_{pp}'\, F\left(p'^h, \varepsilon_v^{p^h}\right)} \quad \text{and} \quad \underline{n}_k^h = \frac{\underline{\tilde{s}}_k^h}{\left|\underline{\tilde{s}}_k^h\right|}
\tag{E.20}
$$
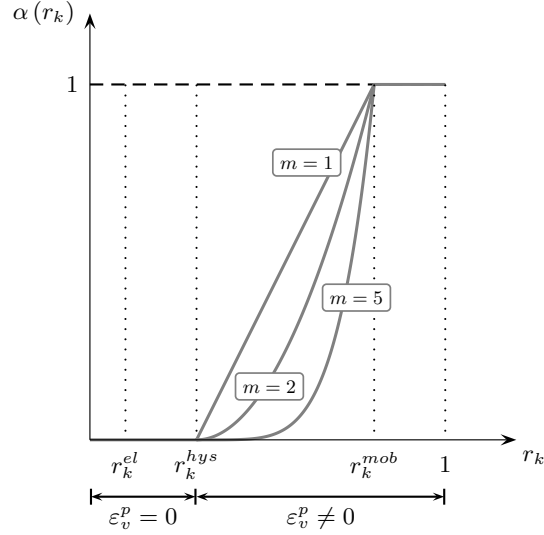
Figure E.4: Graphic representation of $\alpha\left(r_k\right)$ controlling the evolution of deviatoric mechanism k

The vector $\underline{d}_k^h - r_k^c \underline{n}_k^h$ corresponds to the vector going from the origin of the normalized deviatoric plane to the center of the cyclic circle (Fig.E.5b). The hardening variable r_k^c can be expressed in terms of the position of the current stress state with respect to the position of the last load reversal. Its initial value is r_k^{el}:

$$r_k^c = r_k^{el} + \left(\frac{\left| \gamma_k^p - \gamma_k^{p^h} \right|}{a + \left| \gamma_k^p - \gamma_k^{p^h} \right|} \right)^{n_p} \tag{E.21}$$

in which $\gamma_k^{p^h}$ is the plastic distortion of the mechanism k at the last load reversal h. The variable a obeys the same relations as in monotonic loading (E.17). The vectors $\underline{d}_k^h$ and $\underline{n}_k^h$ are discontinuous parameters introducing kinematic hardening to the model.

(a) Evolution of deviatoric yield surface for monotonic loading

(b) Evolution of deviatoric yield surface for cyclic loading
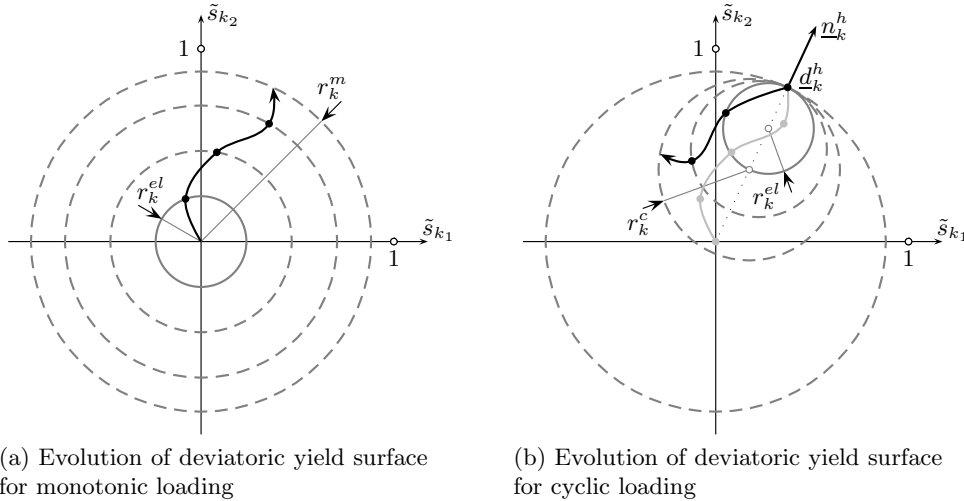
Figure E.5: Evolution of deviatoric threshold in the normalized deviatoric plane of the k mechanism

In summary, the model keeps the memory by two ways:

1. The maximum friction mobilization reached with r_k^m.

2. The last load reversal with $\underline{d}_k^h$ and $\underline{n}_k^h$. For each sign reversal, the value of $\underline{d}_k^h$ is reset to the current value of $\underline{\tilde{s}}_k$, additionally r_k^c is reset to the limit of the elastic domain r_k^{el}.

Concerning the evolution of the plastic strains and the hardening variables, it is supposed that the evolution of the plastic deviatoric deformations follow an associated flow rule:

$$\dot{\underline{\varepsilon}}_k^p = \dot{\lambda}_k^p \frac{\partial f_k}{\partial \underline{s}_k} = \dot{\lambda}_k^p \frac{\underline{s}_k}{|\underline{s}_k|} \tag{E.22}$$

where $\dot{\lambda}_k^p$ is the plastic multiplier for the mechanism k, and can be obtained writing the consistency relationships $\dot{f}_k = 0$ over all active mechanisms. The evolution of the volumetric plastic strains is controlled by a flow rule based on a Roscoe-type dilatancy rule (Schofield and Wroth, 1968):

$$
\begin{aligned}
\dot{\varepsilon}_k^p &= \dot{\lambda}_k^p \Psi_k \\
\Psi_k &= \alpha_\psi \, \alpha\left(r_k\right) \left(\sin\psi - \frac{q_k}{p_k}\right)
\end{aligned} \tag{E.23}
$$

in which ψ is the characteristic angle (Luong, 1980) defining the limit between dilatancy ($\dot{\varepsilon}_v^p < 0$) and contractancy ($\dot{\varepsilon}_v^p > 0$) of the material (Fig.E.6) and α_ψ is a constant parameter.
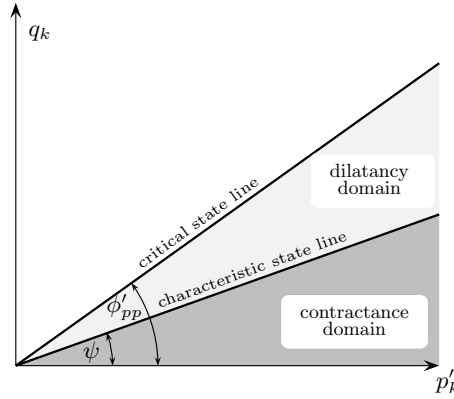
Figure E.6: Critical state and characteristic state lines

E.1.6 Hypothesis 6

In order to model an isotropic path, a pure elato-plastic volumetric mechanism is included in the model. In this consolidation mechanism, the mobilization is progressive using a hardening variable related to plastic volumetric strain $\varepsilon_{v_{iso}}^p$ associated to this mechanism. In a similar way as that of the deviatoric mechanisms, the yield function can be related to a normalized space. The flow-rule is also associated. The memory of the mechanism is also controlled by a double-memory approach, storing the monotonic loading and the last sign-reversal. This mechanism is only activated under isotropic part of the loading and it produces just volume changes.

The expression for the yield function is:

$$f_{iso}\left(p', r_{iso}, p_c\right) = \left|p'\right| - d\, p_c\, r_{iso} \tag{E.24}$$

with r_{iso} the degree of mobilization of the mechanism, varying from the limit of elastic domain r_{iso}^{el} to the unity according to:

$$r_{iso} = r_{iso}^{el} + \frac{\varepsilon_{v_{iso}}^p}{c\frac{p_c}{p_{ref}^r} + \varepsilon_{v_{iso}}^p} \tag{E.25}$$

where the volumetric plastic strain associated to isotropic mechanism can be computed as $\varepsilon_{v_{iso}}^p$:

$$\varepsilon_{v_{iso}}^{p} = \int_{0}^{t} \dot{\varepsilon}_{v_{iso}}^{p} \, dt \tag{E.26}$$

The degree of mobilization r_{iso} starts from the elastic threshold r_{iso}^{el} to the unity when the mechanism is completely activated, i.e. $p' = d\,p_c$. The evolution of this degree of mobilization can be written as:

$$\dot{r}_{iso} = \dot{\varepsilon}_{v_{iso}}^{p} \frac{(1 - r_{iso})^{2}}{c\dfrac{p_c}{p_{ref}}} \tag{E.27}$$

The parameter c governs the evolution of the mobilization of this mechanism, i.e. the isotropic hardening. The flow rule is associated, the compatibility equation can be written as:

$$\dot{p} = \underline{d\,p_c \frac{(1 - r_{iso})^{2}}{c\dfrac{p_c}{p_{ref}}} \dot{\varepsilon}_{v_{iso}}^{p}} - r_{iso}\,d\,p_c\,\beta\,\dot{\varepsilon}_{v}^{p} = 0 \tag{E.28}$$

The underlined term in the previous expression can be interpreted as the intrinsic hardening modulus. According to this expression, the initial plastic modulus is independent of the initial value of p_c. Under isotropic loading, when the elastic threshold r_{iso}^{el} is surpassed a generation of volumetric plastic strain appears ($\dot{\varepsilon}_{v}^{p} > 0$) and consequently the isotropic mechanism is mobilized ($\dot{r}_{iso} > 0$) and the critical mean effective stress grows ($\dot{p}_c > 0$). When this mechanism is entirely mobilized: $r_{iso} = 1$ and $p = d\,p_c$. This evolution matches with the experimental observations of consolidation curves, thus an initial curve who tends to a straight isotropic consolidation line in the plane $e - \log p'$. The parameter d defines the distance of the isotropic consolidation line to the critical state line in this plane $e - \log p'$ (Fig.E.7). As these curves are parallel, it is possible to relate both curves by:

$$\dot{\varepsilon}_{v}^{p} = \frac{1}{\beta} \frac{\dot{p}'}{p'} = \frac{1}{\beta} \frac{\dot{p}_c}{p_c} \tag{E.29}$$
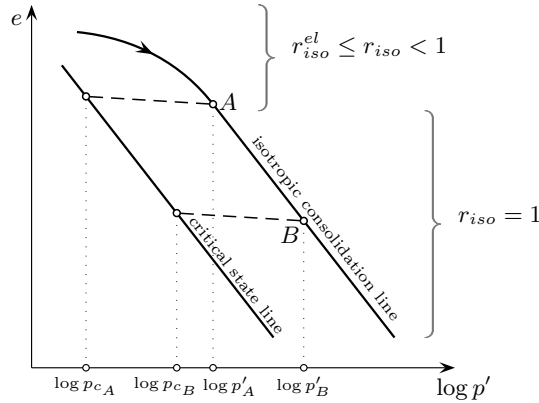
Figure E.7: Progressive mobilization of the isotropic mechanism

As for the deviatoric mechanism, the isotropic mechanism can be described in a normalized isotropic axis $\tilde{p}'$ defined as:

$$\tilde{p}' = \frac{p'}{\eta_{iso}} \quad \text{with} \quad \eta_{iso} = d\,p_c \tag{E.30}$$

where η_{iso} denotes the normalization factor. For primary loading, the threshold surface is orthogonal plane to the axis $\tilde{p}'$, of a distance from the origin r_{iso}^{m} (Fig.E.8a):

$$f_{iso}^{m}\left(\tilde{p}', r_{iso}^{m}, p_c\right) = \left|\tilde{p}'\right| - r_{iso}^{m} \tag{E.31}$$

As for cyclic deviatoric cyclic mechanisms, the isotropic mechanism uses a double memory approach. Thus, under cyclic loading, the successive consolidation thresholds are orthogonal planes to the axis $\tilde{p}'$ at a distance r_{iso}^c of the load reversal point r_{iso}^h in the normalized space (Fig.E.8b):

$$f_{iso}^c\left(\tilde{p}', r_{iso}^c, p_c, r_{iso}^h\right) = \left|\tilde{p}' - r_{iso}^h\right| - r_{iso}^c \tag{E.32}$$

The variable r_{iso} can be also interpreted as the degree of mobilization of the consolidation mechanism.

(a) Evolution of isotropic threshold for monotonic loading

(b) Evolution of isotropic threshold for cyclic loading
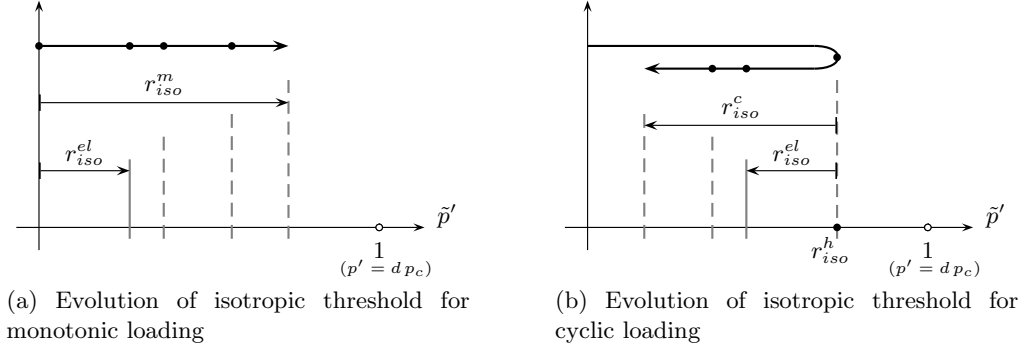
Figure E.8: Evolution of isotropic threshold in the normalized axis of consolidation mechanism $\tilde{p}'$

E.1.7 Hypothesis 7

The four mechanisms are coupled through the hardening variable ε_v^p. The critical effective stress is common for the four mechanisms, thus the density hardening couples the mechanisms:

$$\varepsilon_v^p = \sum_{k=1}^3 \varepsilon_{v_k}^p + \varepsilon_{v_{iso}} = \frac{1}{\beta}\log\frac{p_c}{p_{c_0}} \tag{E.33}$$

where ε_v^p is the variation of the plastic volumetric strain between the initial state ($p_c = p_{c_0}$) and the final state (p_c). In general the four mechanisms can be active. In this case, the plastic multipliers are the solution of a 4×4 non-linear system. The hardening is characterized by hardening modulus matrix in which deviatoric terms appear only in the diagonal while the volumetric hardening appears in all terms:

- the softening is related to a global dilative behaviour: $\dot{p}_c < 0$ and $p_{c_0} > p_c$

- the hardening is related to a global contractive behaviour: $\dot{p}_c > 0$ and $p_{c_0} < p_c$

E.1.8 Tensile stress

The natural stress state of the soil is in compression. Nevertheless, during the numerical integration procedure or due to loading the soil can reach a tensional stress state locally in time or space. Thus, a tension stress behavior must be defined for cohesionless materials in order to ensure the non-resistance to tensile stresses.

The adopted criteria is a perfect elastoplastic yield function:

$$f_{tr}\left(\underline{\sigma}'\right) = \max\left\{\sigma_I', \sigma_{II}', \sigma_{III}'\right\} = \sigma_I' \geq 0 \tag{E.34}$$

where σ_I', σ_{II}' and σ_{III}' are the principal effective stresses of the tensor $\underline{\sigma}'$. The flow rule is associated:

$$\underline{\dot{\varepsilon}}_{tr}^p = \dot{\lambda}_{tr}^p \, \underline{e}_I \otimes \underline{e}_I \tag{E.35}$$

where $\underline{e}_I$ is the unitary vector associated to the maximum principal stress direction.

E.2   Numerical integration

As extensively described in the previous section, each mechanism has its own yielding function f_j, flow rule $\underline{\underline{\Psi}}_j$ and plastic multiplier $\dot{\lambda}_j^p$. The evolution of some hardening variables are specific to each mechanism r_j or common to the four mechanisms ε_v^p. Thus, a non active mechanism can have evolution of its hardening variables even if it is not active. The flow rule of each mechanism can be written in a general form:

$$\dot{\underline{\underline{\varepsilon}}}_j^p = \dot{\lambda}_j^p \, \underline{\underline{\Psi}}_j \quad j = \{1, 2, 3, iso\} \tag{E.36}$$

where the volumetric part of the plastic strain is controlled by the dilatancy law:

$$\dot{\varepsilon}_{v_j}^p = \dot{\lambda}_j^p \, \Psi_{v_j} \tag{E.37}$$

The following relation is still valid, defining the conditions of plastic state for each mechanism:

$$\dot{\lambda}_j^p \geq 0 \quad ; \quad f_j\left(\underline{\underline{\sigma}}', r_j, \varepsilon_v^p\right) \leq 0 \quad ; \quad \dot{\lambda}_j^p \, f_j\left(\underline{\underline{\sigma}}', r_j, \varepsilon_v^p\right) = 0 \tag{E.38}$$

The evolution of the hardening variables are given by their evolution laws:

$$\dot{r}_j = \dot{\lambda}_j^p \, L_{r_j} \tag{E.39}$$

and (E.37). The total increment of ε_v^p is computed over the active mechanisms:

$$\varepsilon_v^p = \sum_i \varepsilon_{v_i}^p \quad i \in M_{act}^p \tag{E.40}$$

where M_{act}^p is the set of activated mechanisms. We make the difference between the set of potentially active mechanism M_{pact}^p and the set of active mechanism M_{act}^p:

$$
\begin{aligned}
M_{pact}^p &= \{a \,|\, f_a = 0\} \\
M_{act}^p &= \left\{b \in M_{pact}^p \,|\, \dot{\lambda}_b > 0\right\}
\end{aligned}
\tag{E.41}
$$

In the case of multimechanism plasticity, the denomination of the total load is used if all the mechanisms are active, the denomination of partial load is used when not all mechanisms are activated and the denomination of elastic regime when no mechanisms are activated.

The total strain increment can be written in terms of the contribution of active mechanisms:

$$\dot{\underline{\underline{\varepsilon}}} = \dot{\underline{\underline{\varepsilon}}}^e + \sum_b \dot{\underline{\underline{\varepsilon}}}_b^p \quad b \in M_{act}^p \tag{E.42}$$

The active plastic multipliers are the solution of the non-linear system obtained using the compatibility equations of the potentially active mechanism ($\dot{f}_a = 0$). We write for each potentially active mechanism a, keeping only the terms of the active mechanism b ($\dot{\lambda}_b^p > 0$):

$$\sum_b \left(\frac{\partial f_a}{\partial \underline{\underline{\sigma}}'} : \underline{\underline{\underline{C}}} : \underline{\underline{\Psi}}_b - \partial_{r_a} f_a : L_{r_a} \delta_{ab} - \partial_{\varepsilon_v^p} f_a : \Psi_{v_b}\right) \dot{\lambda}_b = \frac{\partial f_a}{\partial \underline{\underline{\sigma}}'} : \underline{\underline{\underline{C}}} : \dot{\underline{\underline{\varepsilon}}} \tag{E.43}$$

Similarly to the previous constitutive models, an explicit integration approach with variable time step is adopted to perform the numerical integration of the soil constitutive model. For a load step t_n, the material state is characterized by the stress state $\underline{\underline{\sigma}}'_n$ and the hardening internal variables regrouped in the vector $\underline{\eta}_n$. The goal is to compute the state of the material for the load step t_{n+1} characterized by $\underline{\underline{\sigma}}'_{n+1}$ and $\underline{\eta}_{n+1}$ due to a strain increment $\dot{\underline{\underline{\varepsilon}}}_{n+1}$. The strain increment is approximated by the relation:

$$\dot{\underline{\underline{\varepsilon}}}_{n+1} \approx \frac{\underline{\underline{\varepsilon}}_{n+1} - \underline{\underline{\varepsilon}}_n}{\Delta t_{n+1}} \tag{E.44}$$

assumed to be constant during the interval $\Delta t_{n+1} = t_{n+1} - t_n$. The previous increment is calculated iteratively, thus for an iteration k the approximation of the increment becomes:

$$\dot{\underline{\underline{\varepsilon}}}_{n+1}^{k+1} \approx \frac{\underline{\underline{\varepsilon}}_{n+1}^{k+1} - \underline{\underline{\varepsilon}}_n}{\Delta t_{n+1}} \tag{E.45}$$

As high non-linearities can appear during the loading, the time step increment Δt_{n+1} is subdivided into a set of substeps δt_m to improve the integration procedure:

$$\Delta t_{n+1} = \sum_m \delta t_m \tag{E.46}$$

If the set of variables defining the material state is denoted by E ($E = \left\{ \underline{\underline{\sigma}}', \underline{\eta}_n \right\}$), the initial values for the iteration procedure is taken from the converged values of the previous load step: $E_{n+1}^0 = E_n$. For a substep m associated to an iteration k of the load step $n+1$, thus to a strain increment $\dot{\underline{\underline{\varepsilon}}}_{n+1}^k$, the set of variables defining the state of the material $E_{n+1}^{m^k}$ can be obtained according to:

$$
\begin{aligned}
f_j^{m^k} \left(\underline{\underline{\sigma}}'^{m^k}_{n+1}, \underline{\eta}_{n+1}^{m^k} \right) &\leq 0 \\
\delta A_{n+1}^{m^k} &= A_{n+1}^{m^k} - A_{n+1}^{m-1^k} \quad \forall\, A \in E
\end{aligned}
\tag{E.47}
$$

where:

$$\Delta A_{n+1}^{m^k} = \sum_m \delta A_{n+1}^{m^k} \tag{E.48}$$

The total increment of the load step for the variables which describe the state of the material can be computed according to:

$$
\begin{aligned}
\Delta \underline{\underline{\sigma}}'^{k}_{n+1} &= \sum_m \underline{\underline{\underline{\underline{C}}}} \left(\underline{\underline{\sigma}}'^{m^k}_{n+1} \right) : \left(\dot{\underline{\underline{\varepsilon}}}_{n+1}^k - \sum_j \sum_m \dot{\lambda}_j^{p^m} \underline{\underline{\Psi}}_j^{m^k} \right) \\
\Delta \eta_{j_{n+1}}^k &= \sum_m \dot{\lambda}_j^{p^m} L_{\eta_j}^k \quad \forall\, j \in M_{act}^p
\end{aligned}
\tag{E.49}
$$

in order to compute the updated state of the material for the iteration k:

$$A_{n+1}^k = A_n + \Delta A_{n+1}^k \tag{E.50}$$

Appendix F

One-dimensional linear elastic ground response

The general solution of the equation of elastodynamics in time domain (1.34) can be obtained by decomposition of the displacement field $\underline{u}_s$ into an irrotational field from a scalar potential ϕ and a rotational field from a vectorial potential $\underline{\chi}$:

$$\underline{u}_s = \underline{\text{grad}}\,\phi + \underline{\text{rot}}\,\underline{\chi} \tag{F.1}$$

with $\text{div}\,\underline{\chi} = 0$. With this decomposition, the displacement field can be decoupled into two partial difference equations:

$$\begin{aligned}
\triangle \phi &= \frac{1}{c_p^2}\frac{\partial^2 \phi}{\partial t^2} \\
\triangle \underline{\chi} &= \frac{1}{c_s^2}\frac{\partial^2 \underline{\chi}}{\partial t^2}
\end{aligned} \tag{F.2}$$

with the standard notation for the P-waves and S-waves wave propagation velocities. For a stationary monochromatic wave of circular frequency ω, a general solution of F.2 is given by:

$$\begin{aligned}
\phi = A e^{\frac{i\omega}{c_p}(c_p t - \underline{l}.\underline{x})} &= A f_p \\
\underline{\chi} = \underline{B} e^{\frac{i\omega}{c_s}(c_s t - \underline{l}.\underline{x})} &= \underline{B} f_s
\end{aligned} \tag{F.3}$$

where $\underline{l}$ is the unit director vector if all of the components are real and $\underline{l}.\underline{B} = 0$. Replacing in (F.1) we obtain:

$$\underline{u}_s = -\frac{i\omega A}{c_p} f_p \underline{l} + \frac{i\omega}{c_s} f_s \underline{B} \otimes \underline{l} = A_p f_p \underline{l} + \frac{i\omega}{c_s} f_s \underline{B} \otimes \underline{l} \tag{F.4}$$

The previous expressions show that for the P-waves the motion follows the direction of propagation and that for the S-waves the motion takes place in a plane orthogonal to this direction. In this plane, the S-waves can be decomposed into a SH and a SV component according to:

$$A_{SH} = \frac{i\omega}{c_s}\frac{B_z}{\sqrt{l_x^2 + l_y^2}} \qquad A_{SV} = \frac{i\omega}{c_s}\frac{l_x B_y - l_y B_x}{\sqrt{l_x^2 + l_y^2}} \tag{F.5}$$

where A_{SH} and A_{SV} are the amplitudes of displacements of SH and SV waves. The general earthquake wave propagation problem is tridimensional, but in earthquake engineering context (near to the surface) the problem can be treated as bidimensional assuming that the waves propagates parallel to

a vertical plane (yz for instance), thus the motion is independent of the x coordinate. In this case, the general solution can be written as ($l_x = 0$):

$$\underline{u}_s = A_{SV} f_s l_z \underline{e}_x + \left(A_p f_p l_y + A_{SH} f_s l_z\right) \underline{e}_y + \left(A_p f_p l_z - A_{SH} f_s l_y\right) \underline{e}_z \tag{F.6}$$

The previous expression shows that for plane waves, the motion following x is decoupled from the motion in the plane yz. The motion in this plane is governed by the P and S-waves. If the incident field is vertical ($l_x = l_y = 0$), the problems becomes one-dimensional and the displacement field can be written as:

$$\underline{u}_s = A_{SV} f_s \underline{e}_x + A_{SH} f_s \underline{e}_y + A_p f_p \underline{e}_z \tag{F.7}$$
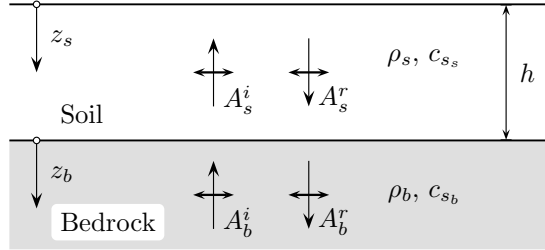
Figure F.1: Homogenous elastic soil layer overlying a half-space bedrock

We consider now a homogenous elastic soil layer overlying a half-space elastic rock (Fig.F.1). The horizontal displacement following y due to a vertically incident SH-waves in each material can be written as:

$$
\begin{aligned}
u_s &= A_s^i e^{\frac{i\omega}{c_{s_s}}(c_{s_s} t + z_s)} + A_s^r e^{\frac{i\omega}{c_{s_s}}(c_{s_s} t - z_s)} \\
u_b &= A_b^i e^{\frac{i\omega}{c_{s_b}}\left(c_{s_b} t + z_b\right)} + A_b^r e^{\frac{i\omega}{c_{s_b}}\left(c_{s_b} t - z_b\right)}
\end{aligned}
\tag{F.8}
$$

where the upperscript i and r refer to incident and reflected field, and the subscript s and b refer to soil and bedrock. The free surface condition ($\sigma_{yz} = 0$) imposes that $A_s^r = A_s^i = A_s$. The compatibility of displacement and continuity of shear stress at the soil-bedrock interface require that:

$$A_s \left(e^{\frac{i\omega}{c_{s_s}}h} - e^{-\frac{i\omega}{c_{s_s}}h}\right) = A_b^i + A_b^r \tag{F.9}$$

According to the definition of shear stress ($\tau_{yz} = \mu \frac{\partial u}{\partial z}$), the relation between the amplitudes can be summarized as (Pecker, 1984; Kramer, 1996):

$$
\begin{aligned}
A_b^i &= \frac{1}{2} A_s \left[(1 + \alpha)\, e^{\frac{i\omega}{c_{s_s}}h} + (1 - \alpha)\, e^{-\frac{i\omega}{c_{s_s}}}\right] \\
A_b^i &= \frac{1}{2} A_s \left[(1 - \alpha)\, e^{\frac{i\omega}{c_{s_s}}h} + (1 + \alpha)\, e^{-\frac{i\omega}{c_{s_s}}}\right]
\end{aligned}
\tag{F.10}
$$

where α is the impedance ratio defined by

$$\alpha = \sqrt{\frac{\rho_s c_{s_s}}{\rho_b c_{s_b}}} \tag{F.11}$$

Defining the transfer function $T(\omega)$ as the ratio of the ground movement amplitude to a hypothetic outcrop bedrock movement:

$$T(\omega) = \frac{2A_s}{2A_b^i} = \frac{1}{\cos \frac{i\omega}{c_{s_s}}h + i\alpha \sin \frac{i\omega}{c_{s_s}}h} \quad \rightarrow \quad |T(\omega)| = \frac{1}{\sqrt{\cos^2 \frac{i\omega}{c_{s_s}}h + \alpha^2 \sin^2 \frac{i\omega}{c_{s_s}}h}} \tag{F.12}$$

Appendix G

Substructure SSI approximation in frequency domain

Starting from the definition of the complete system shown in Fig.G.1, Aubry and Clouteau. (1992) and Clouteau and Aubry (2003) developed an analytical formulation of the dynamic SSI phenomenon, based on the substructure technique. This approach was integrated in the numerical code MISS3D, performing SSI analysis in the linear elastic or viscoelastic domain. The physical domain is decomposed into three subdomains: the unbounded soil denoted by Ω_s, the bounded foundation denoted by Ω_f and the bounded structure Ω_b. In comparison with the decomposition shown in Fig.1.1, there are two main differences: the soil domain Ω_s is unbounded and the superstructure is decomposed into a rigid domain Ω_f and a flexible domain Ω_b. The interfaces are denoted respectively by Σ_{bf} and Σ_{sf}. Free field conditions are assumed into the other part of their boundary Γ_s and Γ_b.
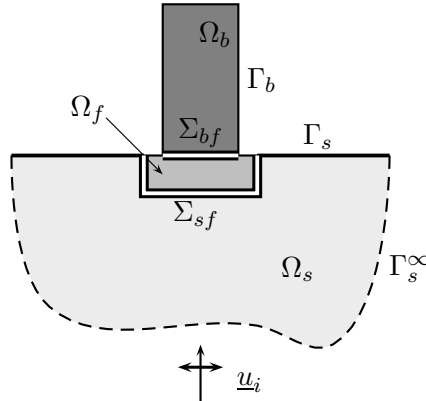
Figure G.1: Definition of the global system for substructure approach

The permanent displacements fields on Γ_s and Γ_b due to static loads (weight and dead and/or live loads) are assumed to be known in the following. We keep the notation for the dynamic perturbations fields due to dynamic loads $\underline{u}_s(\underline{x},t)$ and $\underline{u}_b(\underline{x},t)$. In this case, they are assumed to be small enough to satisfy linear elastic hypothesis around the equilibrated static state. The corresponding elastic stress tensors due to dynamic perturbation are denoted by $\underline{\underline{\sigma}}_s$ and $\underline{\underline{\sigma}}_b$.

The seismic loading is taken into account defining an incident field $\underline{u}_i$ inside Ω_s, defined as the displacement field in the soil without superstructure and foundation due to seismic motion. Assuming small deformations, the displacements fields $\underline{u}_s$ and $\underline{u}_i$ verify elastodynamic equations in the soil:

$$
\begin{aligned}
\underline{\mathrm{div}}\,\underline{\underline{\sigma}}_s\,(\underline{u}_s) &= \rho_s \underline{\ddot{u}}_s \quad \forall\,\underline{x} \in \Omega_s \\
\underline{\mathrm{div}}\,\underline{\underline{\sigma}}_s\,(\underline{u}_i) &= \rho_s \underline{\ddot{u}}_i \quad \forall\,\underline{x} \in \Omega_s
\end{aligned}
\tag{G.1}
$$

while $\underline{u}_b$ satisfies elastodynamic equation in the superstructure domain:

$$\underline{\text{div}}\,\underline{\underline{\sigma}}_b\,(\underline{u}_b) = \rho_b \underline{\ddot{u}}_b \quad \forall\,\underline{x} \in \Omega_b \tag{G.2}$$

Assuming that no uplift appears between soil and foundation, and no loss of contact takes place between the structure and its foundation, the following kinematic conditions are verified over the interfaces:

$$\underline{u}_b = \underline{u}_f \quad \forall\,\underline{x} \in \Sigma_{bf} \quad \text{and} \quad \underline{u}_s = \underline{u}_f \quad \forall\,\underline{x} \in \Sigma_{sf} \tag{G.3}$$

and continuity of traction over these interfaces. Free field conditions are also verified in Γ_s and Γ_b.

Due to linearity of equations (G.1) and (G.2) a Fourier transform can be applied to solve the problem in the frequency domain. Thus, the superstructure field displacement verifies:

$$\underline{\text{div}}\,\underline{\underline{\sigma}}_b\,(\underline{\hat{u}}_b) + \rho_b \omega^2 \underline{\hat{u}}_b = 0 \quad \forall\,\underline{x} \in \Omega_b \tag{G.4}$$

Using the same definition for the set of kinematically acceptable fields of §1.2.4, the weak formulation can be written as:

$$\int_{\Omega_b} \underline{\underline{\sigma}}_b\,(\underline{\hat{u}}_b) : \underline{\underline{\varepsilon}}_b\,(\underline{w}_b)\,dV - \omega^2 \int_{\Omega_b} \rho_b \underline{\hat{u}}_b . \underline{w}_b\,dV = \int_{\Sigma_{bf}} \underline{t}_b\,(\underline{\hat{u}}_b)\,.\underline{w}_b\,dS \tag{G.5}$$

Choosing a rigid body mode $\underline{\psi}_n$ as kinematical acceptable field, the following equation is obtained:

$$-\omega^2 \int_{\Omega_b} \rho_b \underline{\hat{u}}_b . \underline{\psi}_n\,dV = \int_{\Sigma_{bf}} \underline{t}_b\,(\underline{\hat{u}}_b)\,.\underline{\psi}_n\,dS \tag{G.6}$$

for each rigid body mode $\underline{\psi}_n$. Previous expression takes into account the fact that rigid body modes do not induce deformations.

G.1   Rigid foundation

Assuming a rigid foundation Ω_f, the corresponding displacement field $\underline{u}_f$ can be written in terms of the rigid body modes $\underline{\psi}_m\,(\underline{x})$:

$$\underline{\hat{u}}_f\,(\underline{x},\omega) = \sum_{m=1}^{6} \hat{c}_m\,(\omega)\,\underline{\psi}_m\,(\underline{x}) \quad \forall\,\underline{x} \in \Omega_f \tag{G.7}$$

where the six rigid body modes are three translational and three rotational modes passing by the three principal axis of the foundation. $\hat{c}_m$ are the participation factors depending on the frequency. As the foundation is rigid, the equilibrium in moments and forces in terms of test functions $\underline{\hat{w}}_f$ can be written as:

$$\int_{\Sigma_{sf}} \underline{t}_s\,(\underline{\hat{u}}_s)\,.\underline{w}_f\,dS + \int_{\Sigma_{bf}} \underline{t}_b\,(\underline{\hat{u}}_b)\,.\underline{w}_f\,dS - \omega^2 \int_{\Omega_f} \rho_f \underline{\hat{u}}_f . \underline{w}_f\,dV = 0 \tag{G.8}$$

Similarly to (G.6), by choosing rigid body modes $\underline{\psi}_n$ as kinematical acceptable field, the previous expression becomes:

$$\int_{\Sigma_{sf}} \underline{t}_s\,(\underline{\hat{u}}_s)\,.\underline{\psi}_n\,dS + \int_{\Sigma_{bf}} \underline{t}_b\,(\underline{\hat{u}}_b)\,.\underline{\psi}_n\,dS - \omega^2 \int_{\Omega_f} \rho_f \underline{\hat{u}}_f . \underline{\psi}_n\,dV = 0 \tag{G.9}$$

for each rigid body mode $\underline{\psi}_n$.

G.2 Decomposition of the displacement in the superstructure

The displacement field in the superstructure $\underline{\hat{u}}_b$ can be decomposed in two modal basis: the rigid body modal basis $\underline{\hat{u}}_f$ due to rigid body modes of the foundation, and the flexible modal part $\underline{\hat{u}}_{b0}$ of the structure under fixed base condition:

$$\underline{\hat{u}}_b = \underline{\hat{u}}_f + \underline{\hat{u}}_{b0} \quad \forall\, \underline{x} \in \Omega_b \tag{G.10}$$

The flexible modal field $\underline{\hat{u}}_{b0}$ can be expressed in terms of the natural fixed base modes $\underline{\phi}_j$:

$$\underline{\hat{u}}_{b0}\left(\underline{x}, \omega\right) = \sum_{j \geq 1} \hat{q}_j\left(\omega\right) \underline{\phi}_j\left(\underline{x}\right) \quad \forall\, \underline{x} \in \Omega_b \tag{G.11}$$

where $\hat{q}_j$ are the frequency-dependent modal participation factors. Using decompositions (G.7 and (G.11), the total displacement field of the superstructure is given by:

$$\underline{\hat{u}}_b\left(\underline{x}, \omega\right) = \sum_{m=1}^{6} \hat{c}_m\left(\omega\right) \underline{\psi}_m\left(\underline{x}\right) + \sum_{j \geq 1} \hat{q}_j\left(\omega\right) \underline{\phi}_j\left(\underline{x}\right) \quad \forall\, \underline{x} \in \Omega_b \tag{G.12}$$

Introducing (G.12) in the variational formulation (G.6) and the equilibrium equation (G.9), we obtain:

$$\int_{\sigma_{sf}} \underline{t}_s\left(\underline{\hat{u}}_s\right) . \underline{\psi}_n \, dS = \omega^2 \left(\sum_{m=1}^{6} \hat{c}_m \int_{\Omega_f} \rho_f \underline{\psi}_m . \underline{\psi}_n \, dV + \sum_{m=1}^{6} \hat{c}_m \int_{\Omega_b} \rho_b \underline{\psi}_m . \underline{\psi}_n \, dV + \sum_{j \geq 1} \hat{q}_j \int_{\Omega_b} \rho_b \underline{\phi}_j . \underline{\psi}_n \, dV \right) \tag{G.13}$$

As the previous expression is still valid for each rigid body mode $\underline{\psi}_n$, it can be written in an equivalent matrix form in frequency domain:

$$\int_{\Sigma_{sf}} \underline{t}_s\left(\underline{\hat{u}}_s\right) . \underline{\underline{\Psi}} \, dS - \omega^2 \left([M_f] + [M_b] + [M_b^*\left(\omega\right)] \right) \{c\} = \{0\} \tag{G.14}$$

where $\underline{\underline{\Psi}}$ regroups the rigid body modes and $\{c\}$ the participation factors. $[M_f]$ and $[M_b]$ are the mass matrix of the foundation and the superstructure, respectively. Their components can be computed as:

$$[M_f]_{mn} = \int_{\Omega_f} \rho_f\, \underline{\psi}_m . \underline{\psi}_n \, dV$$

$$[M_b]_{mn} = \int_{\Omega_b} \rho_b\, \underline{\psi}_m . \underline{\psi}_n \, dV$$

The third matrix in (G.14) represents the equivalent added structural mass matrix $[M_b^*]$ due to the vibration of the flexible superstructure. It can be deduced by replacing the expression of mode participation factors q_j in frequency domain for the SSI case (assuming mass normalized modes: $\int_{\Omega_b} \rho_b\, \underline{\phi}_j . \underline{\phi}_j \, dV = 1$):

$$\sum_{j \geq 1} q_j \int_{\Omega_b} \rho_b\, \underline{\phi}_j . \underline{\psi}_n \, dV = \sum_{m=1}^{6} \hat{c}_m \left(\sum_{j \geq 1} \frac{\omega^2}{\omega_j^2 + 2i\zeta_j \omega \omega_j - \omega^2} \int_{\Omega_b} \rho_b\, \underline{\psi}_m . \underline{\phi}_j \, dV \int_{\Omega_b} \rho_b\, \underline{\phi}_j . \underline{\psi}_n \, dV \right) \tag{G.15}$$

where ω_j and ζ_j are the natural frequency and modal damping associated to fixed base mode j. Thus, each component of the $[M_b^*]$ matrix can be computed as:

$$[M_b^*]_{mn} = \sum_{j \geq 1} \frac{\omega^2}{\omega_j^2 + 2i\zeta_j \omega \omega_j - \omega^2} \int_{\Omega_b} \rho_b\, \underline{\psi}_m . \underline{\phi}_j \, dV \int_{\Omega_b} \rho_b\, \underline{\phi}_j . \underline{\psi}_n \, dV \tag{G.16}$$

This matrix is complex and highly dependent on the frequency. When ω approaches a modal frequency value ω_j, this matrix is purely complex and acts as a dashpot pumping energy to resonance modes. For $\omega > \omega_j$ this term is approximately a pure negative real reducing the effective mass of the system. For $\omega < \omega_j$ the matrix is real and positive and tends towards zero for very low frequency (static case).

G.3 Decomposition of the displacement in the soil

The kinematic continuity over the interface Σ_{bf} in frequency domain can be written as:

$$\hat{\underline{u}}_d\left(\underline{x},\omega\right) = \hat{\underline{u}}_f\left(\omega\right) - \hat{\underline{u}}_i\left(\underline{x},\omega\right) = \sum_{m=1}^{6} \hat{c}_m\left(\underline{x},\omega\right)\underline{\psi}_m\left(\underline{x}\right) - \hat{\underline{u}}_i\left(\underline{x},\omega\right) \qquad \forall\, \underline{x} \in \Sigma_{bf} \tag{G.17}$$

where $\hat{\underline{u}}_d$ is the displacement field due to total diffracted waves. This diffracted displacement field, can be decomposed as follows:

$$\hat{\underline{u}}_d\left(\underline{x},\omega\right) = \sum_{m=1}^{6} \hat{\underline{u}}_{dm}\left(\underline{x},\omega\right) + \hat{\underline{u}}_{d0}\left(\underline{x},\omega\right) \qquad \forall\, \underline{x} \in \Sigma_{bf} \tag{G.18}$$

The displacement field $\hat{\underline{u}}_{d0}$ is the displacement due to local diffraction of the incident wave field on the foundation assumed fixed. It verifies the elastodynamics equation in the soil domain Ω_s and free field conditions at the boundary Γ_s:

$$
\begin{aligned}
\underline{\mathrm{div}}\underline{\underline{\sigma}}_s\left(\hat{\underline{u}}_{d0}\right) + \rho_s\omega^2\hat{\underline{u}}_{d0} &= \underline{0} & \text{in } \Omega_s \\
\underline{t}_s\left(\hat{\underline{u}}_{d0}\right) &= \underline{0} & \text{on } \Gamma_s \\
\hat{\underline{u}}_{d0} &= \hat{\underline{u}}_i & \text{on } \Sigma_{sf}
\end{aligned} \tag{G.19}
$$

The second component $\hat{\underline{u}}_{dm}$ corresponds to displacement due to radiation caused by a unitary foundation movement along the rigid base mode m. Each component m also verifies:

$$
\begin{aligned}
\underline{\mathrm{div}}\,\underline{\underline{\sigma}}_s\left(\hat{\underline{u}}_{dm}\right) + \rho_s\omega^2\hat{\underline{u}}_{dm} &= \underline{0} & \text{in } \Omega_s \\
\underline{t}_s\left(\hat{\underline{u}}_{dm}\right) &= \underline{0} & \text{on } \Gamma_s \\
\hat{\underline{u}}_{dm} &= \underline{\psi}_m & \text{on } \Sigma_{sf}
\end{aligned} \tag{G.20}
$$

Injecting decomposition (G.18) in (G.14) we obtain the general system of equations of soil-structure interaction:

$$\left([K_s\left(\omega\right)] - \omega^2\left[M_f\right] + [M_b] + [M_b^*\left(\omega\right)]\right)\{c\} = \{f_s\} \tag{G.21}$$

where $[K_s]$ is the generalized dynamic impedance of the soil and $\{f_s\}$ is the vector of induced seismic forces introduced at the foundation level. Their components can be computed as:

$$
\begin{aligned}
\left[K_s\right]_{mn} &= \int_{\Sigma_{sf}} \underline{t}_s\left(\hat{\underline{u}}_{dm}\right).\underline{\psi}_n \, dS \\
\{f_s\}_n &= -\int_{\Sigma_{sf}} \underline{t}_s\left(\hat{\underline{u}}_i + \hat{\underline{u}}_{d0}\right).\underline{\psi}_n \, dS
\end{aligned}
$$

The resolution of the previous system for each frequency ω gives the frequency-dependent modal participation factors regrouped in vector $\{c\}$. These values allow to compute displacement fields in the superstructure, foundation and soil. Compared to standard fixe base analysis, the previous expression includes the soil stiffness associated to impedance $[K_s]$ and the interface forces $\{f_s\}$ induced by the

ground motion. Even if the solution procedure is straightforward, its direct application involves assembling matrices and vectors depending on the solution of boundary value problems (G.19) and (G.20). Thus, the Boundary Element Method is particulary well suited to these fields. Details about the numerical approximation of these equations in the case of layered half-spaces implanted in MISS3D are beyond of the scope of this presentation and can be found in Clouteau and Aubry (2001, 2003); Clouteau (1990, 2000, 2003).

Appendix H

Numerical simulation of laboratory soil test using ECP multimechanism model

The purpose of this section is complete the information concerning the set of parameter used for the ECP multimechanism model described in §1.3.4 used in each case. Several soil mechanics test are modelled in order to show both a global view of the response of the constitutive model and the coherence of the set of parameters proposed to simulate the non-linear soil behaviour.

The purpose of this section is complete the information concerning the set of parameter used for the ECP multimechanism model described in §1.3.4 used in each case. Several soil mechanics test are modelled in order to show both a global view of the response of the constitutive model and the coherence of the set of parameters proposed to simulate the non-linear soil behaviour.

H.1   Toyoura sand, $D_r = 38\%$

For this material, the simulated soil mechanics test concern both undrained monotonic triaxial test and cyclic shear test at different consolidation pressures p_0'. The available curves provided by Ishihara (1993) for monotonic loading and by Iwasaki et al. (1978) and Yamashita et al. (2001) for cyclic loading have been used as reference response path. According with these work, the main characteristics of the Toyoura sand are:

- $d_{50} = 0.19$ [mm]

- $d_{10} = 0.12$ [mm]

- $U_c = 1.3$ [mm]

- $e_{min} = 0.597$ [mm]

- $e_{max} = 0.997$ [mm]

- $\phi_{pp}' = 31°$

- $\psi = 31°$

whit the standard notation for grain diameter characteristics d_{50}, d_{10} and U_c, minimum and maximum void ratio e_{min} and e_{max}. ϕ_{pp}' is the perfect plasticity friction angle and ψ the dilatancy angle. These values are used as starting data for identification parameter strategy proposed by Lopez-Caballero (2003), in order to define some key parameters of the model as the plastic compressibility modulus β. Other parameters related to hardening and threshold domain are obtained using reference curves.

The simulations conducted for monotonic test correspond to an initial relative density of $D_r = 38\%$. Four initial confinement pressures p_0' (i.e. 0.1, 1, 2 and 3 [MPa]) are used for the triaxial undrained tests. The simulation results are presented in both planes $q - \varepsilon_1$ and $q - p'$. Figure H.1 show the

response obtained for the sets of parameters given in Table H.1. It can be noticed that the simulations agrees with the experimental data. Concerning the values of the parameters, those related to elastic properties and to yield functions remains unchanged for the different values of confinement pressure p'_0. We accept a small reduction of the initial void ratio during the isotropic consolidation test phase. This variation is introduced by a small augmentation of the initial critical pressure p_{c_0} value with p'_0. The hardening variables have been slightly modified for each p'_0 to improve the agreement between experimental and simulated data. The threshold domain values remain unchanged with p'_0. For the homogenous Toyoura sandy soil deposits used in the FE models described in Chapters 2 and 3, we neglect these variations on initial critical pressure and hardening variables. Thus, the set of parameter computed for $p'_0 = 0.1$ [MPa] is retained for the entire soil deposit. This hypothesis has a negligible effect on the global response of the FE model and on the SSI effects studied in this work.

(a) Response on $q - \varepsilon_1$ plane

(b) Response on $q - p'$ plane
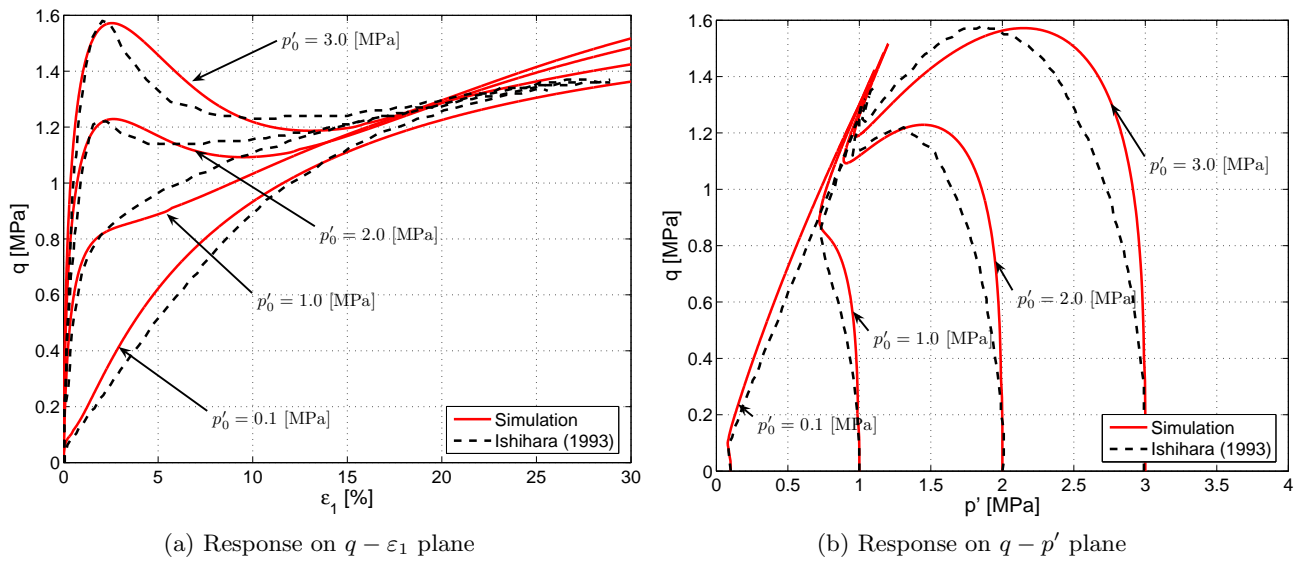
Figure H.1: Simulated undrained triaxial test using ECP constitutive model compared to references curves provided by Ishihara (1993) for Toyoura sand ($D_r = 38\%$)

(a) Modulus degradation curve

(b) Damping increasing curve
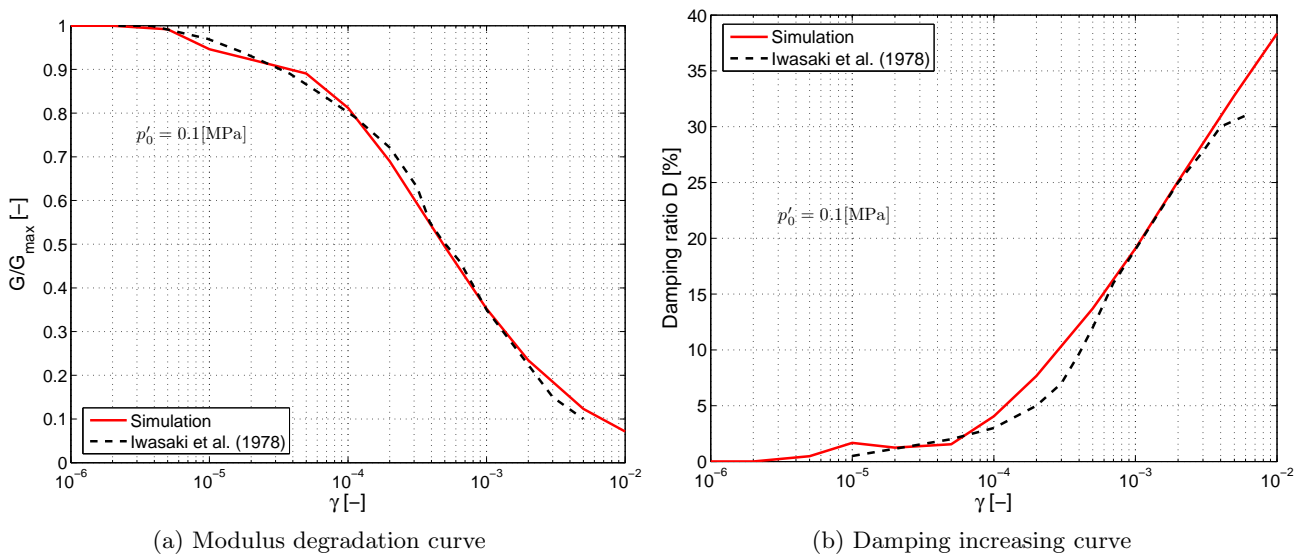
Figure H.2: Simulated drained cyclic shear test using ECP constitutive model compared to references curves provided by Iwasaki et al. (1978) for Toyoura sand ($D_r = 38\%$)

In order to verify the model's parameters under cyclic loading, the behaviour of the sand must be studied by simulating drained cyclic shear (DCS) tests. Fig.H.2 shows the responses of a DCS test obtained by the model of the Toyoura sand at a initial confinement of $p'_0 = 100$[kPa]. The test results are compared with the reference curves given by Iwasaki et al. (1978). We can notice that the obtained modulus degradation curve $\frac{G}{G_{max}} - \gamma$ curves match satisfactorily. The damping increasing curve $D - \gamma$ agrees with the experimental data for strains less than 0.5%, while for large strains the damping is overestimated.

Table H.1: Parameters of ECP model for Toyoura sand, $D_r = 38\%$

D_r [%]	38			
p' [MPa]	0.1	1.0	2.0	3.0
	Model parameters			
Elasticity				
K_{ref} [MPa]	444	444	444	444
G_{ref} [MPa]	222	222	222	222
n_e	0.4	0.4	0.4	0.4
p'_{ref} [MPa]	1.0	1.0	1.0	1.0
Yield function				
ϕ'_{pp}	31	31	31	31
β	43	43	43	43
d	3.5	3.5	3.5	3.5
b	0.2	0.2	0.2	0.2
Initial state				
p_{c_0} [MPa]	1.80	1.82	1.92	1.95
$\frac{p_{c_0}}{p'_0}$	18	1.82	0.91	0.65
Hardening				
a_1	1×10^{-4}	3×10^{-4}	3×10^{-4}	2×10^{-3}
a_2	4×10^{-3}	9×10^{-3}	1.8×10^{-2}	2.3×10^{-2}
c^m	6×10^{-2}	6×10^{-2}	3×10^{-2}	1.8×10^{-2}
c^c	3×10^{-2}	3×10^{-2}	1.5×10^{-2}	9×10^{-3}
m	1.0	1.0	1.0	1.0
n_p	1.0	1.0	1.0	1.0
Threshold domains				
r_k^{el}	5×10^{-3}	5×10^{-3}	5×10^{-3}	5×10^{-3}
r_k^{hys}	3×10^{-2}	3×10^{-2}	3×10^{-2}	3×10^{-2}
r_k^{mob}	8×10^{-1}	8×10^{-1}	8×10^{-1}	8×10^{-1}
r_{iso}^{el}	1×10^{-3}	1×10^{-3}	1×10^{-3}	1×10^{-3}

H.2 Liquefiable sand

The model parameters of each layer were determined with the methodology suggested by Lopez-Caballero et al. (2007); Lopez-Caballero and Modaressi-Farahmand Razavi (2008) and they are given in Tab.H.2 for each layer.

In order to verify the model's parameters and to characterize the liquefaction resistance of sand placed between 3.5 and 9[m] depth, the behaviour of the sand must be studied by simulating drained cyclic shear (DCS) tests and undrained stress controlled cyclic shear tests. Fig.H.3 shows the responses of these DCS tests obtained by the model of the loose sand at $p'_0 = 40$ and 70[kPa]. The test results are compared with the reference curves provided by Seed et al. (1986). We can notice that the obtained modulus degradation curves match satisfactorily for strains less than 0.01%. The damping increasing curve is underestimated for small strains ($\gamma < 10^{-5}$), while for large strains it is overestimated.

(a) Modulus degradation curve   (b) Damping increasing curve
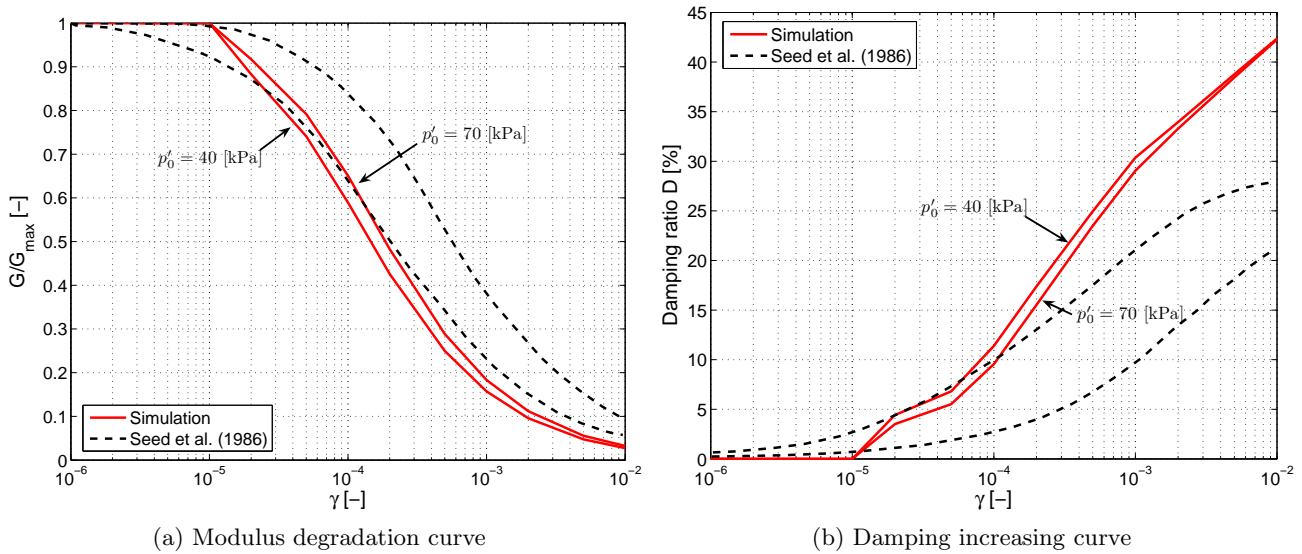
Figure H.3: Simulated drained cyclic shear test using ECP constitutive model compared to references curves provided by Seed et al. (1986)

The obtained curve of cyclic stress ratio $\frac{\tau_d}{p'_0}$ as a function of the number of loading cycles to produce liquefaction (N) for an initial confinement of $p'_0 = 40$[kPa] is shown in Fig.H.4. The modelled test result is compared with the reference curves given by Seed and Idriss (1982) for sands at different densities (i.e. SPT values). It can be noticed that the obtained curve agrees with the reference curve corresponding to SPT of $N_{60} = 5$.
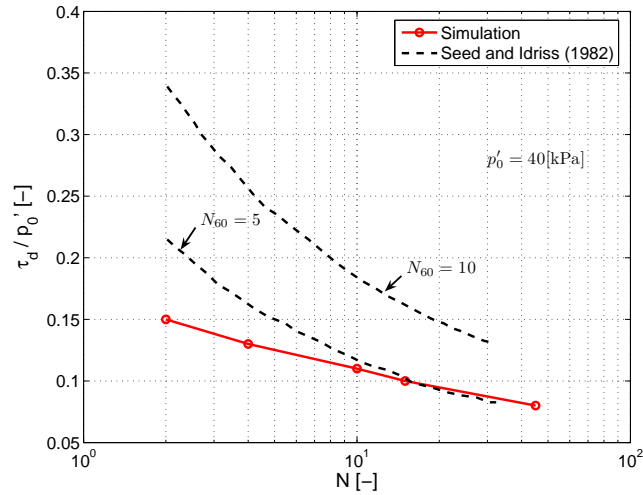
Figure H.4: Comparison of simulated liquefaction curve with cyclic strength relations provided by Seed and Idriss (1982)

Table H.2: Parameters of ECP model for all soil profile layers

Layers	$0-2$[m]	$2-9$[m]	$9-16$[m]	$16-22$[m]	$22-29$[m]
	Model parameters				
Permeability					
k_s [m/s]	1×10^{-3}	1×10^{-5}	1×10^{-5}	1×10^{-4}	1×10^{-4}
Elasticity					
K_{ref} [MPa]	90	628	628	628	444
G_{ref} [MPa]	45	290	290	290	22.4
n_e	0.0	0.5	0.5	0.5	0.4
p'_{ref} [MPa]	1.0	1.0	1.0	1.0	1.0
Yield function					
ϕ'_{pp} °	31	30	30	30	31
β	20	33	33	33	43
d	2.0	2.0	2.0	2.0	3.5
b	0.2	0.2	0.2	0.2	0.2
Initial state					
p_{c_0} [MPa]	1.86	0.04	0.05	0.08	1.80
Hardening					
ψ°	31	30	30	30	31
a_1	1×10^{-4}	1×10^{-4}	1×10^{-4}	1×10^{-4}	1×10^{-4}
a_2	2×10^{-4}	5×10^{-3}	5×10^{-3}	5×10^{-3}	5×10^{-3}
c^m	1×10^{-3}	4×10^{-3}	4×10^{-3}	4×10^{-3}	6×10^{-2}
c^c	5×10^{-4}	2×10^{-3}	2×10^{-3}	2×10^{-3}	3×10^{-2}
m	1.0	1.5	1.5	1.5	1.0
Threshold domains					
r_k^{el}	1.3×10^{-2}	3×10^{-2}	3×10^{-2}	3×10^{-2}	5×10^{-3}
r_k^{hys}	2.2×10^{-1}	4×10^{-2}	4×10^{-2}	4×10^{-2}	3×10^{-2}
r_k^{mob}	8×10^{-1}	8×10^{-1}	8×10^{-1}	8×10^{-1}	8×10^{-1}
r_{iso}^{el}	4×10^{-3}	2×10^{-2}	2×10^{-2}	2×10^{-2}	1×10^{-3}

H.3   French Antilles soil

The model parameters of each layer were selected from the material library of ECP and are given in Tab.H.3 for each layer. We use the same set of parameters for layers between 2 and 30[m] depth for the sake of simplicity.

Table H.3: Parameters of ECP model for all soil profile layers

Layers	$0 - 2$[m]	$2 - 6$[m]	$6 - 10$[m]	$10 - 20$[m]	$20 - 30$[m]
	Model parameters				
Elasticity					
K_{ref} [MPa]	90	399	399	399	399
G_{ref} [MPa]	45	184	184	184	184
n_e	0.0	0.4	0.4	0.4	0.4
p'_{ref} [MPa]	1.0	1.0	1.0	1.0	1.0
Yield function					
ϕ'_{pp} °	31	33	33	33	33
β	20	17	17	17	17
d	2.0	2.5	2.5	2.5	2.5
b	0.2	0.2	0.2	0.2	0.2
Initial state					
p_{c_0} [MPa]	1.86	7.20	7.20	7.20	7.20
Hardening					
ψ°	31	33	33	33	33
a_1	1×10^{-4}	2×10^{-4}	2×10^{-4}	2×10^{-4}	2×10^{-4}
a_2	2.1×10^{-4}	1.8×10^{-2}	1.8×10^{-2}	1.8×10^{-2}	1.8×10^{-2}
c^m	1×10^{-3}	1×10^{-4}	1×10^{-4}	1×10^{-4}	1×10^{-4}
c^c	5×10^{-4}	5×10^{-5}	5×10^{-5}	5×10^{-5}	3×10^{-5}
m	1.0	1.0	1.0	1.0	1.0
Threshold domains					
r_k^{el}	1.3×10^{-2}	1×10^{-2}	1×10^{-2}	1×10^{-2}	1×10^{-3}
r_k^{hys}	2.2×10^{-1}	5×10^{-2}	5×10^{-2}	5×10^{-2}	5×10^{-2}
r_k^{mob}	8×10^{-1}	9×10^{-1}	9×10^{-1}	9×10^{-1}	9×10^{-1}
r_{iso}^{el}	4×10^{-3}	1×10^{-4}	1×10^{-4}	1×10^{-4}	1×10^{-4}

In order to verify the model's parameters under cyclic loading, the behaviour of the soil is studied by simulating drained cyclic shear (DCS) tests. Fig.H.5 shows the responses of a DCS test obtained by the model for the set of parameter used between $2-30[\text{m}]$ depth, for three different initial confinement p_0.

(a) Modulus degradation curve   (b) Damping increasing curve
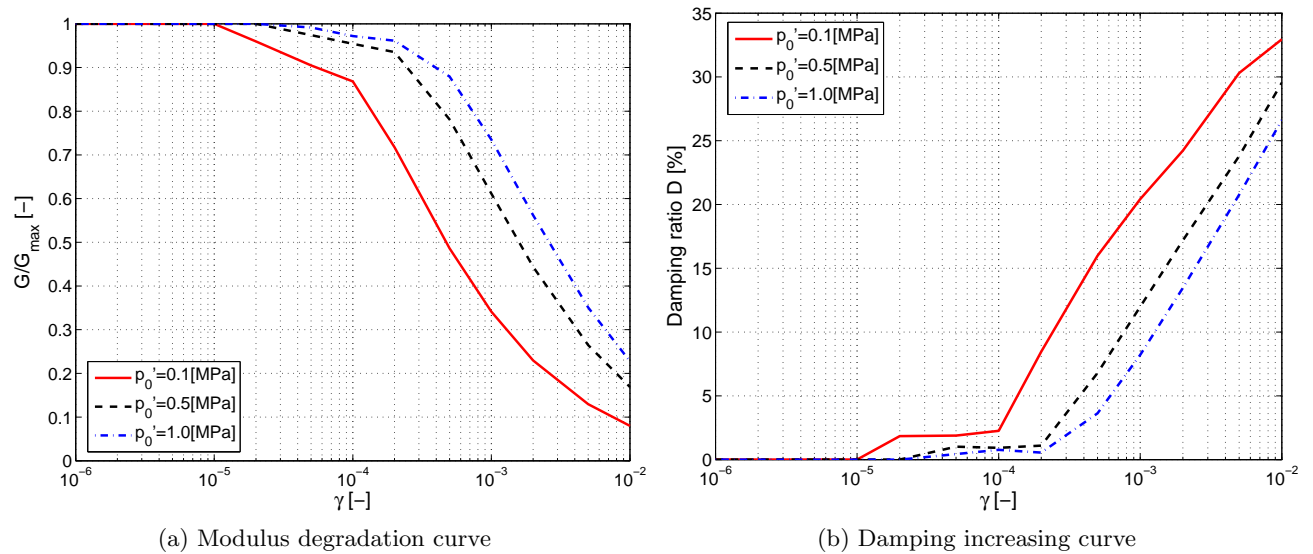
Figure H.5: Simulated drained cyclic shear test using ECP constitutive model $(2-30[\text{m}]$ depth)

Appendix I

Description of studied buildings

This appendix gives additional details concerning buildings studied in this work. General geometry and reinforcement description are provided with the degree of detail required to be used in plastic-hinge beam column elements of *GEFDyn* . Additional details concerning reinforcement diameters and transversal reinforcement dispositions are omitted here for sake of simplicity.

I.1 Two-level building: b01

I.1.1 Geometry

The two-level b01 building extracted from Marante et al. (2005) corresponds to an adaption of a true-scale model performed by Vecchio and Emara (1992). The general geometry, label identification of sections and a schema of transversal properties required for plastic-hinge elements are shown in FigI.1.
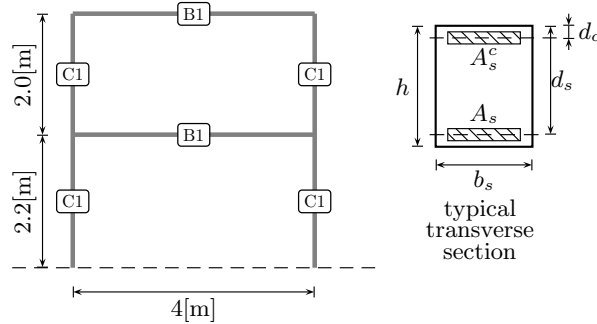
Figure I.1: Geometry and transverse section descriptions of b01 building

I.1.2 Transverse sections

Table I.1 shows dimension of transverse sections, steel reinforcement area and unitary mass ρ. This unitary mass takes into account the self weight of the frame and the tributary weight/loading across l_a according to Fig.3.2. Last value is used to compute body forces due to gravity for static initialization analysis and assemble the mass matrices for dynamic computations.

Table I.1: Transverse section properties

Label	h[m]	b_s[m]	d_c[m]	d_s[m]	A_s[cm2]	A_s^c[cm2]	ρ[kg/m3]
B1	0.4	0.3	0.03	0.37	11.4	11.4	42473
C1	0.4	0.4	0.02	0.38	11.4	11.4	-

I.1.3   Materials

Numerical values of different mechanical properties are indicated in Tab.I.2, extracted from Marante et al. (2005).

Table I.2: Mechanical properties of material for b01 building

Mechanical property	Symbol	Value
Resistance to compressive stresses	f_c	30[MPa]
Yield stress of steel	f_y	418[MPa]
Ultimate stress of steel	f_{s_u}	596[MPa]
Elastic modulus of steel	E_s	210[GPa]
Elastic modulus of concrete	E_c	26.5[GPa]
Crushing strain of concrete	ε_c	0.0034

I.1.4   Axial load-moment interaction diagrams

Figure I.2 displays axial force-moment interaction diagrams that control non-linear behavior of plastic-hinge beam elements of b01 building, computed using a resistance factor of $\phi = 0.9$. It can be noticed that no interaction is supposed for beams B1, thus plastic hinge apparition depends only on the bending moments for these elements.

(a) Beams (B1)   (b) Columns (C1)
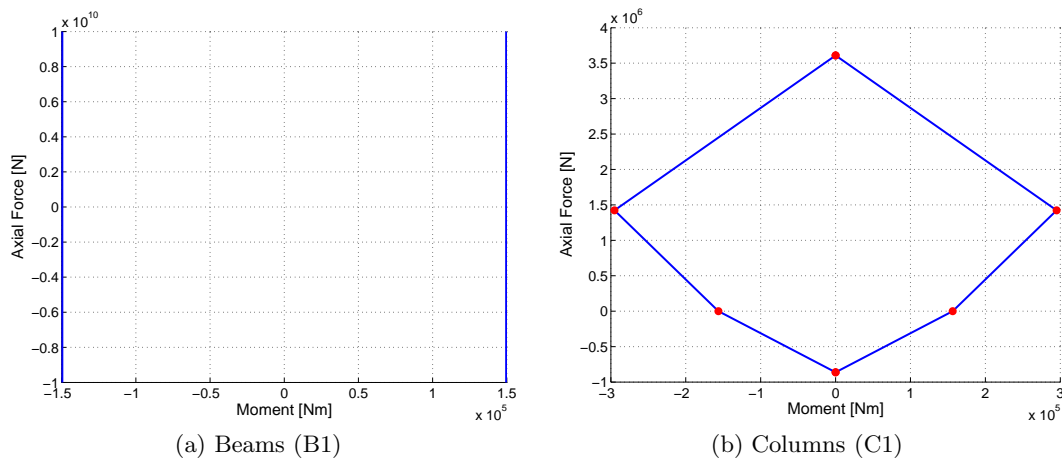
Figure I.2: Axial force-moment interaction diagrams used for plastic-hinge beam-column elements of b01 building

I.2 Seven-level building: b02

I.2.1 Geometry

The seven-level b02 building extracted from Marante et al. (2005) corresponds to a residential building placed in Mérida city, Venezuela. This building was designed according to seismic recommendations of this country. The general geometry, label identification of sections and a schema of transversal properties required for plastic-hinge elements are shown in Fig.I.3.
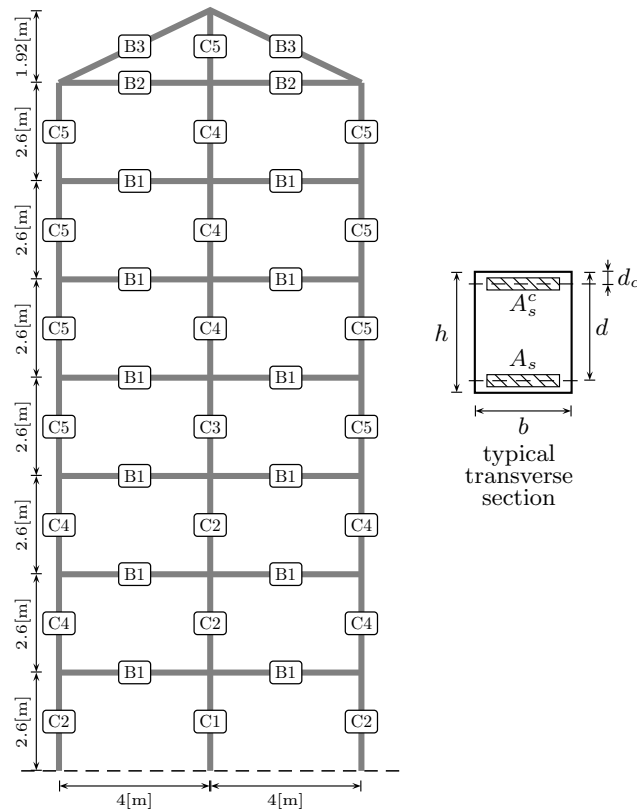
Figure I.3: Geometry and transverse section descriptions of b02 building

I.2.2 Transverse sections

Table I.3 shows dimensions of transverse sections, steel reinforcement area and unitary mass ρ. This unitary mass takes into account the self weight of the frame and the tributary weight/loading across l_a according to Fig.3.2. Last value is used to compute body forces due to gravity for static initialization analysis and assemble the mass matrices for dynamic computations.

I.2.3 Materials

Numerical values of different mechanical properties are indicated in Tab.I.4, extracted from Marante et al. (2005).

I.2.4 Axial load-moment interaction diagrams

Figure I.4 displays axial force-moment interaction diagrams that control non-linear behavior of plastic-hinge beam elements of b02 building, computed using a resistance factor of $\phi = 0.9$. It can be noticed that no interaction is supposed for beams, thus plastic hinge apparition depends only on the bending moments of these elements.

Table I.3: Transverse section properties

Label	h[m]	b_s[m]	d_c[m]	d_s[m]	A_s[cm2]	A_s^c[cm2]	ρ[kg/m3]
B1	0.6	0.3	0.04	0.56	25.34	25.34	34900
B2	0.7	0.3	0.04	0.66	11.40	11.40	30285
B3	0.3	0.2	0.04	0.26	8.55	8.55	70500
C1	0.6	0.5	0.04	0.56	40.54	40.54	-
C2	0.6	0.5	0.04	0.56	30.95	30.95	-
C3	0.6	0.4	0.04	0.56	40.54	40.54	-
C4	0.6	0.4	0.04	0.56	30.95	30.95	-
C5	0.6	0.4	0.04	0.56	14.41	14.41	-

Table I.4: Mechanical properties of material for b01 building

Mechanical property	Symbol	Value
Resistance to compressive stresses	f_c	25[MPa]
Yield stress of steel	f_y	440[MPa]
Ultimate stress of steel	f_{s_u}	596[MPa]
Elastic modulus of steel	E_s	200[GPa]
Elastic modulus of concrete	E_c	25.5[GPa]
Crushing strain of concrete	ε_c	0.003

(a) Beams B1   (b) Beams B2   (c) Beams B3

(d) Columns C1   (e) Columns C2   (f) Columns C3

(g) Columns C4   (h) Columns C5
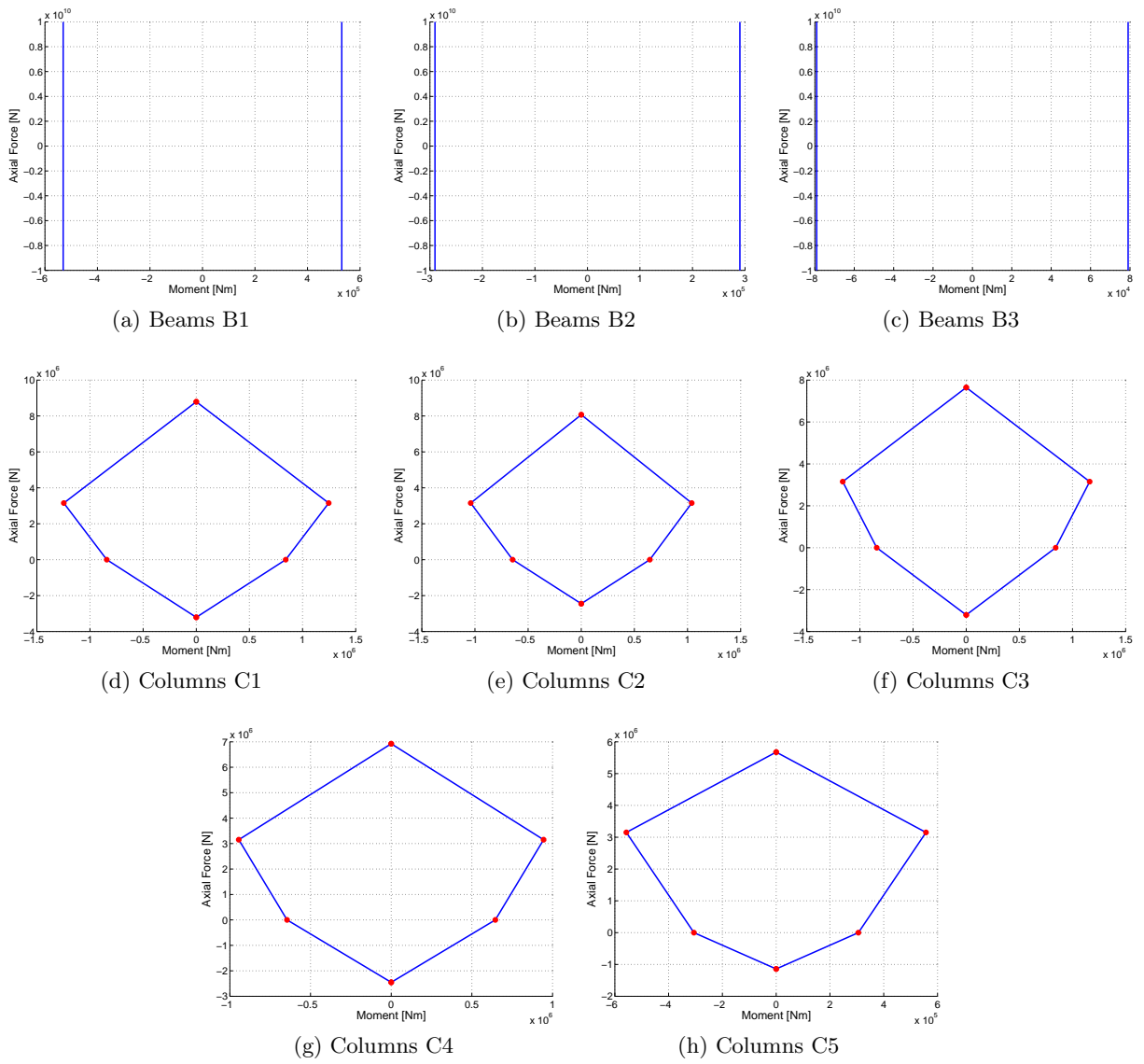
Figure I.4: Axial force-moment interaction diagrams used for plastic-hinge beam-column elements of b02 building

I.3 Public building

I.3.1 Geometry

The public building considered in this work was built in 1970 and it is placed in French Antilles. The general geometry, label identification of sections and a schema of transversal properties required for plastic-hinge elements are shown in Fig.I.5 and I.6.


(a) Axis A

(b) Axis B

(c) Axis C

(d) Axis D
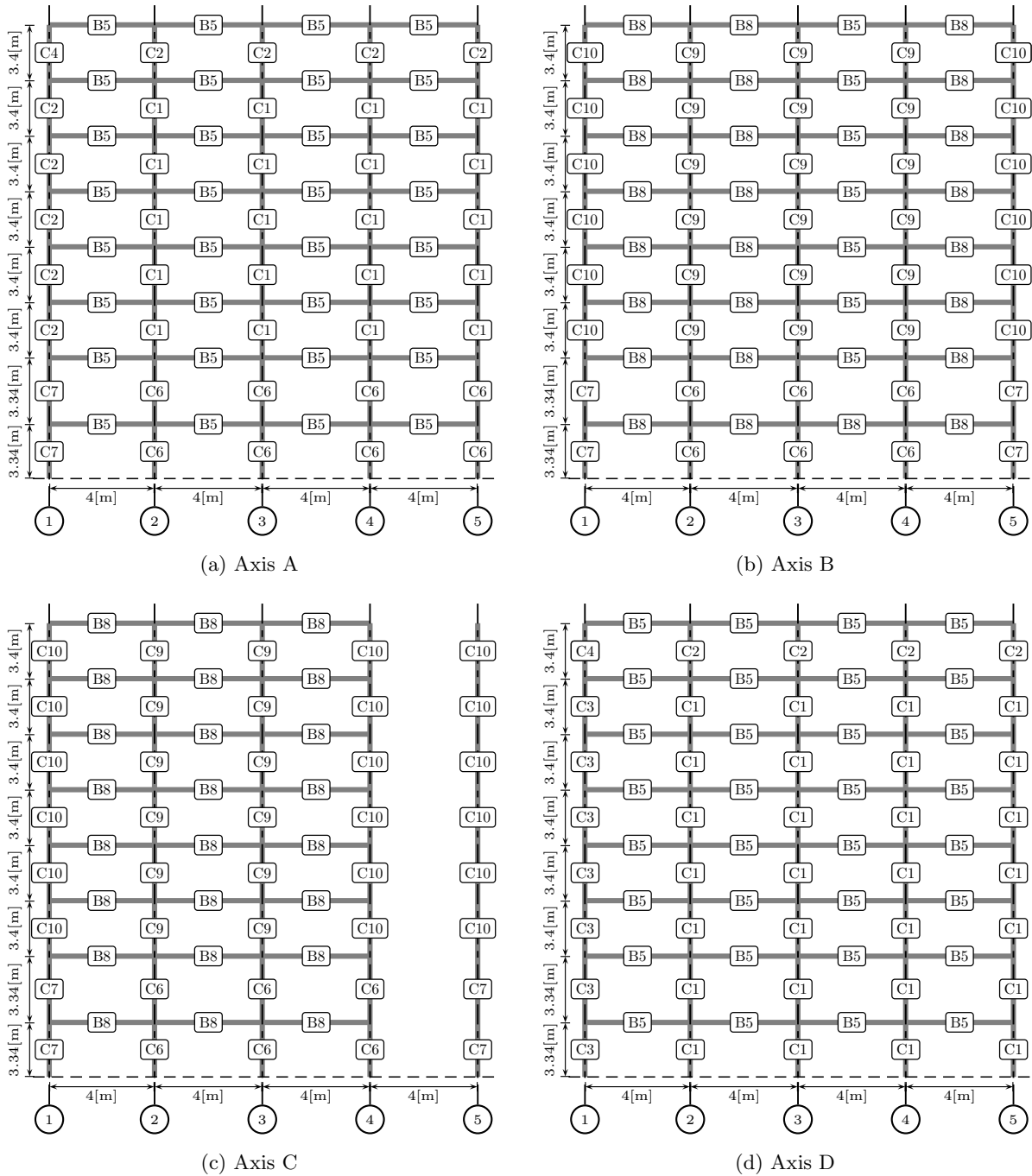
Figure I.5: Geometry and transverse section descriptions of public building: longitudinal axes

I.3.2 Transverse sections

In the real building, some of the columns have an irregular cross section. They were approximated by rectangular sections in order to compute axial force-bending interaction diagrams according to

the geometry described in Fig.I.3. Table I.5 shows transverse sections properties: transverse area A, transverse primary inertia I, factor α defining minor flexural properties (§D.2), reinforcement according and unitary mass ρ. This unitary mass takes into account the self weight of the frame and a part of the dead and live loads. Last value is used to compute body forces due to gravity for static initialization analysis and assemble the mass matrices for dynamic computations.

Table I.5: Transverse section properties

Label	A[m2]	I[m4]	α	h[m]	b_s[m]	d_c[m]	d_s[m]	A_s[cm2]	A_s^c[cm2]	ρ[kg/m3]
C1	0.44	0.014	1.5	0.6	0.8	0.02	0.58	25.1	25.1	2400
C2	0.44	0.014	1.5	0.6	0.8	0.02	0.58	15.7	15.7	2400
C3	0.21	0.002	6.19	0.3	0.8	0.03	0.28	15.7	12.6	7000
C4	0.21	0.002	6.19	0.3	0.8	0.03	0.28	10.1	8.0	7000
B5	0.31	0.013	0.41	0.7	0.45	0.66	0.04	10.8	10.8	7000
C6	0.48	0.014	1.77	0.45	0.3	0.02	0.44	4.5	4.5	2400
C7	0.24	0.002	7.11	0.3	0.8	0.02	0.58	25.1	25.1	14000
B8	0.18	0.005	0.25	0.6	0.3	0.02	0.58	10.8	10.8	14000
C9	0.14	0.002	0.44	0.45	0.3	0.02	0.44	4.5	4.5	14000
C10	0.11	0.001	0.73	0.35	0.3	0.02	0.33	4.5	4.5	14000
B11	0.08	0.002	0.09	0.5	0.15	0.02	0.48	8.0	9.6	2400
B12	0.024	0.007	0.44	0.6	0.4	0.02	0.58	10.8	10.8	2400

I.3.3 Materials

Numerical values of different mechanical properties are indicated in Tab.I.6.

Table I.6: Mechanical properties of material for public building

Mechanical property	Symbol	Value
Resistance to compressive stresses	f_c	27.5[MPa]
Yield stress of steel	f_y	420[MPa]
Ultimate stress of steel	f_{s_u}	596[MPa]
Elastic modulus of steel	E_s	200[GPa]
Elastic modulus of concrete	E_c	24.8[GPa]
Crushing strain of concrete	ε_c	0.003

(a) Axis 1   (b) Axis 2   (c) Axis 3

(d) Axis 4   (e) Axis 5
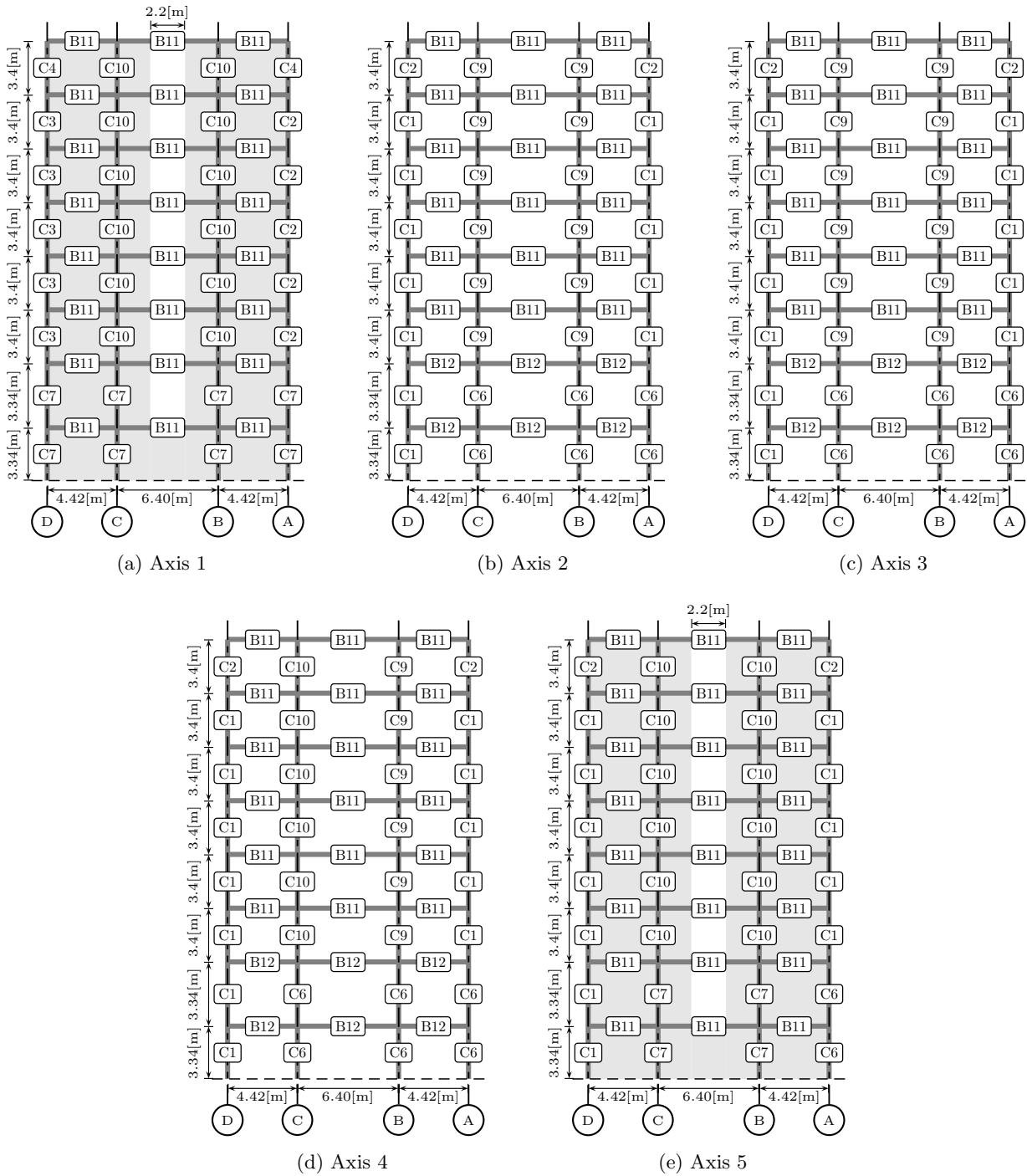
Figure I.6: Geometry and transverse section descriptions of public building: transverse axes

Appendix J

List of strong-motion records selected

This appendix lists the sets of records chosen as input to the FE models.

J.1 List of records compatible with Metropolitan France

Table J.1: Strong-motion selection #1

Number	Station	Soil	$V_{s,30}$[m/s]	Waveform	M_w	T_{SR}[s]	AI[m/s]	T_m[s]
1	San Rocco	stiff	600	000147y	6.08	2.82	0.221	0.4504
2	Kalamata-Prefecture	stiff	486	000413x	5.9	5.48	0.559	0.6103
3	Bevagna	stiff	> 600	000595y	5.72	22.31	0.078	0.6574
4	Preveza-OTE Building	stiff	–	000582y	5.4	14.24	0.025	0.6409
5	Monte Fegni	rock	–	000598y	6.04	10.86	0.008	0.1736
6	Atina-Pretura Terrazza	rock	–	000990y	5.53	15.22	0.111	0.2289
7	Argostoli-OTE	stiff	405	001862y	5.35	7.50	0.017	0.1845
8	Irafoss	rock	–	005085y	5.45	7.77	0.004	0.8688

(a) Motion number 1

(b) Motion number 2

(c) Motion number 3

(d) Motion number 4

(e) Motion number 5

(f) Motion number 6

(g) Motion number 7

(h) Motion number 8

Figure J.1: Time-histories and computed response spectra at outcropping bedrock. Strong-motion selection #1

Table J.2: Strong-motion selection #2

Number	Station	Soil	$V_{s,30}$[m/s]	Waveform	M_w	T_{SR}[s]	AI[m/s]	T_m[s]
9	Forgaria-Cornio	stiff	441	000114x	5.33	4.25	0.044	0.2455
10	Cascia	rock	–	000242x	5.8	5.47	0.257	0.2393
11	Valsamata-Seismograph Station	rock	–	000428y	5.3	15.16	0.251	0.2574
12	Bevagna	stiff	> 600	000595x	5.72	24.47	0.046	0.5572
13	San Rocco	stiff	600	000147x	6.08	4.99	0.118	0.5198
14	Matelica	stiff	> 600	000601x	5.72	11.63	0.021	0.2114
15	Cassino-Sant'Elia	alluvium	–	000378x	5.9	12.74	0.202	0.5044
16	Reykjavik Heidmork	rock	–	005089x	5.45	8.16	0.004	0.8811

Table J.3: Strong-motion selection #3

Number	Station	Soil	$V_{s,30}$[m/s]	Waveform	M_w	T_{SR}[s]	AI[m/s]	T_m[s]
17	Akhalkalaki	rock	–	000487x	5.48	8.83	0.007	0.2346
18	Preveza-OTE Building	stiff	–	000582x	5.4	16.43	0.022	0.5649
19	Villeta-Borrea	rock	–	000384x	5.53	3.64	0.132	0.1870
20	Valsamata-Seismograph	rock	–	000428x	5.3	15.78	0.138	0.2521
21	Kalamata-Prefecture	stiff	486	000413y	5.9	7.04	0.841	0.5354
22	Bevagna	stiff	> 600	000596y	6	20.27	0.190	0.6177
23	Vasiliki-Town	stiff	490	001990y	5.42	10.90	0.066	0.3877
24	Irafoss	rock	–	005085x	5.45	9.36	0.003	0.6974

(a) Motion number 9

(b) Motion number 10

(c) Motion number 11

(d) Motion number 12

(e) Motion number 13

(f) Motion number 14

(g) Motion number 15

(h) Motion number 16

Figure J.2: Time-histories and computed response spectra at outcropping bedrock. Strong-motion selection #2

(a) Motion number 17

(b) Motion number 18

(c) Motion number 19

(d) Motion number 20

(e) Motion number 21

(f) Motion number 22

(g) Motion number 23

(h) Motion number 24
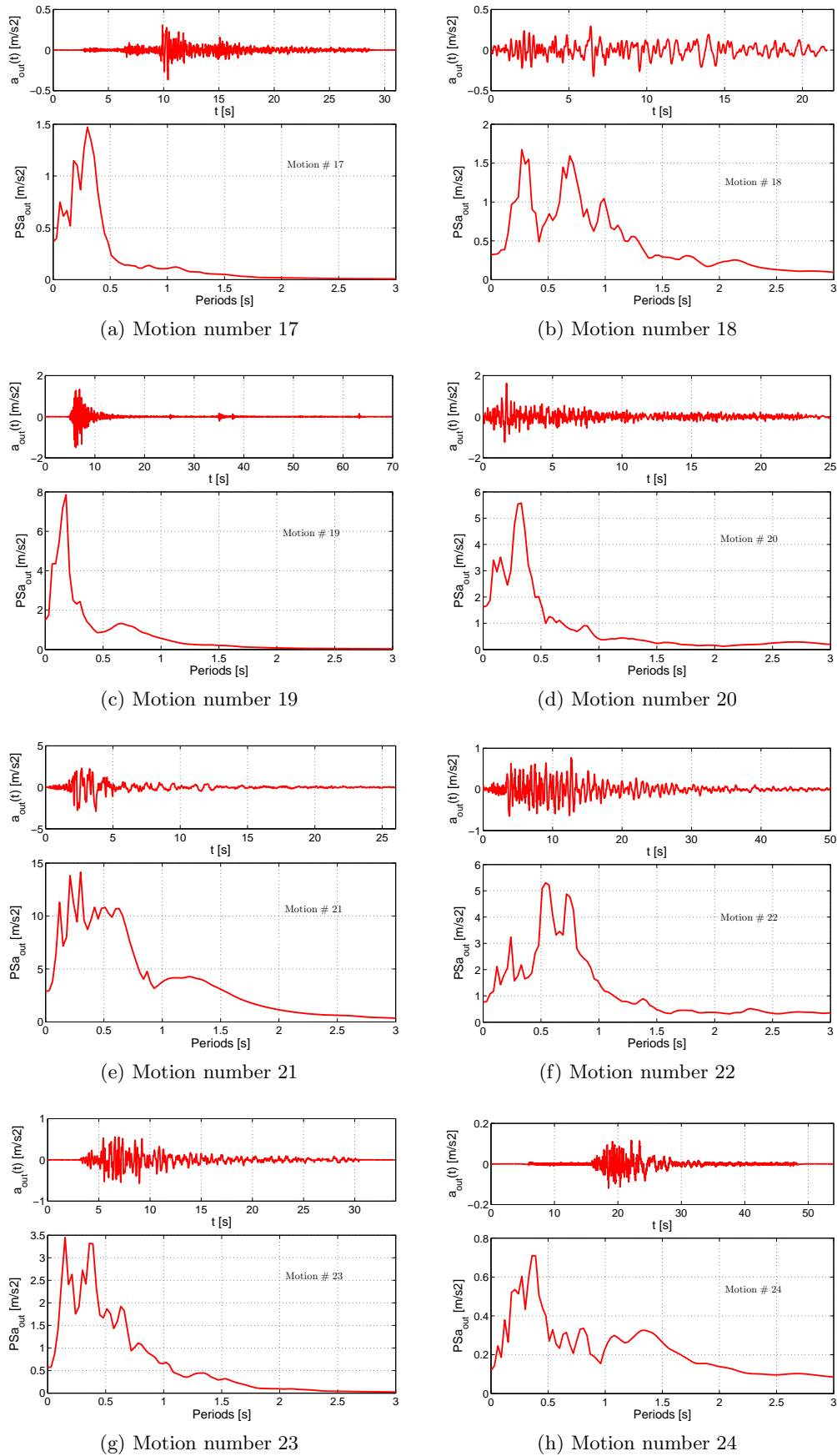
Figure J.3: Time-histories and computed response spectra at outcropping bedrock. Strong-motion selection #3

Table J.4: Strong-motion selection #4

Number	Station	Soil	$V_{s,30}$[m/s]	Waveform	M_w	T_{SR}[s]	AI[m/s]	T_m[s]
25	Oseyrabru	rock	–	005090x	5.4	12.75	0.008	0.4806
26	Athens-Syntagma	stiff	372	001713y	6.04	5.91	0.059	0.5443
27	Bevagna	stiff	> 600	000620y	5.5	19.31	0.046	0.5828
28	Kalamata-OTE Building	stiff	399	000414y	5.9	6.21	0.742	0.5251
29	Bevagna	stiff	> 600	000596x	6	21.61	0.146	0.6063
30	Colfiorito-Casermette	rock	–	000651x	5.58	5.42	0.209	0.2383
31	Atina-Pretura Terrazza	rock	–	000990x	5.53	10.21	0.145	0.2130
32	Kyparrisia Agriculture	rock	862	001900x	5.36	5.00	0.016	0.2745

(a) Motion number 25

(b) Motion number 26

(c) Motion number 27

(d) Motion number 28

(e) Motion number 29

(f) Motion number 30

(g) Motion number 31

(h) Motion number 32
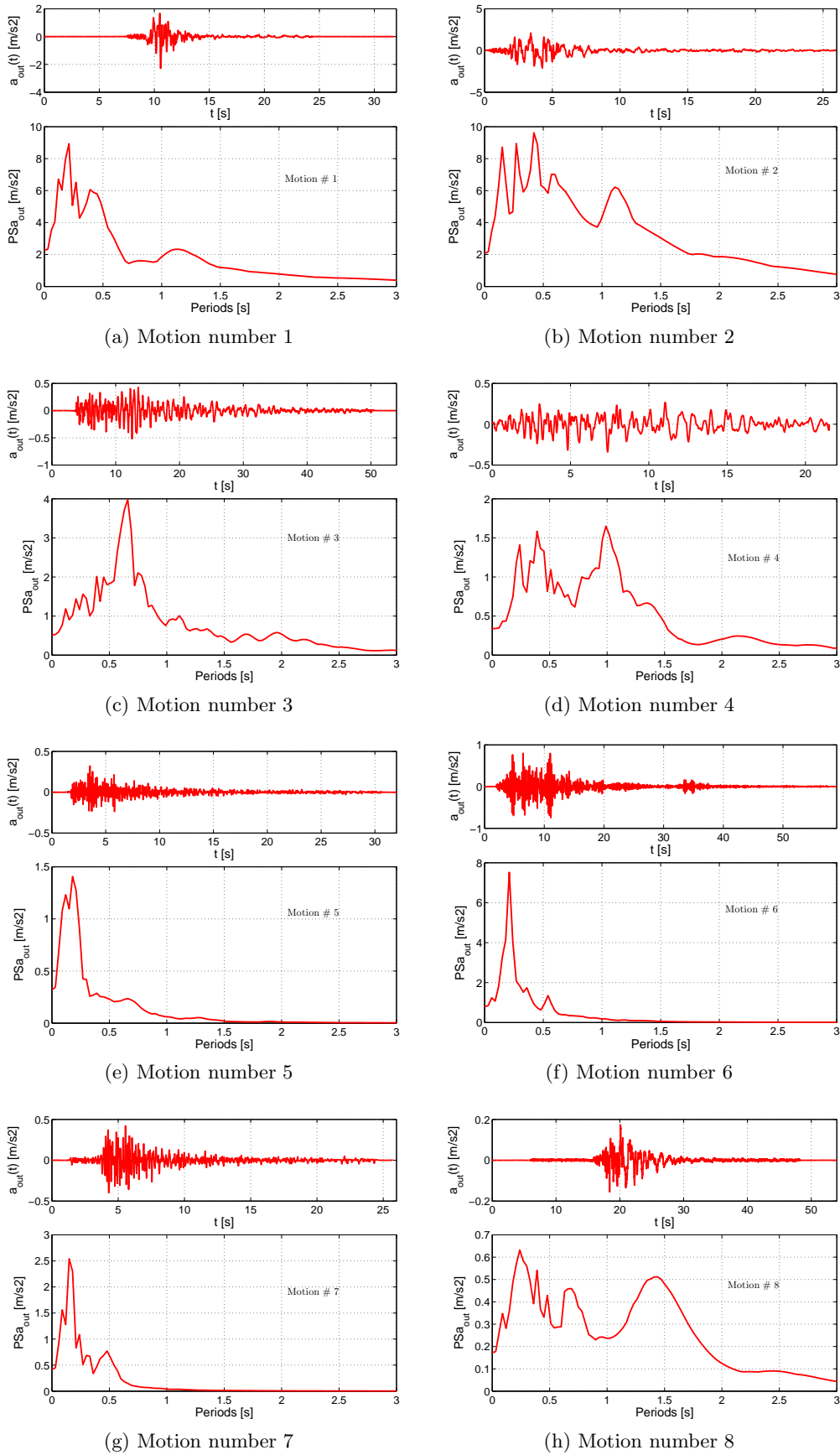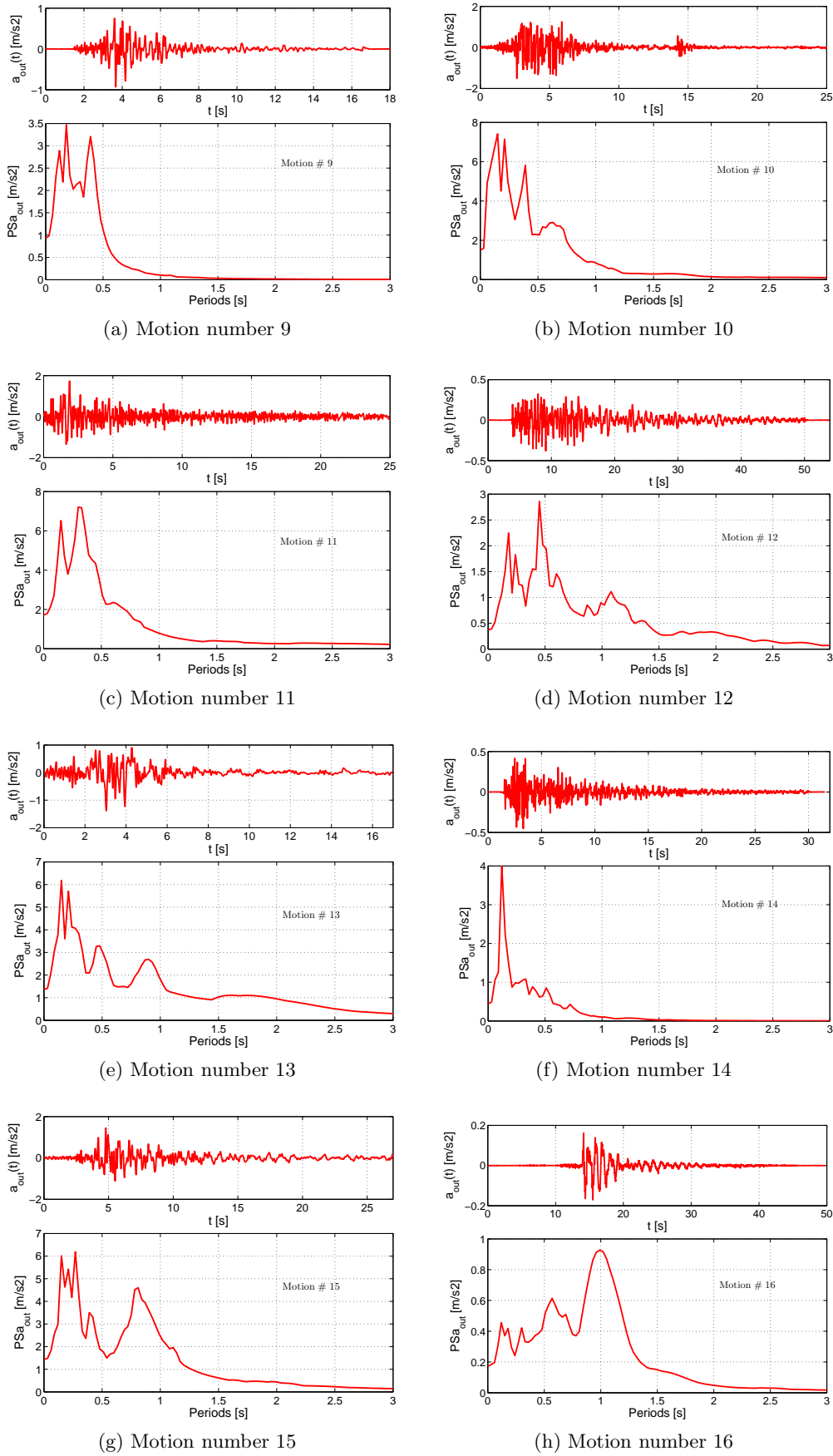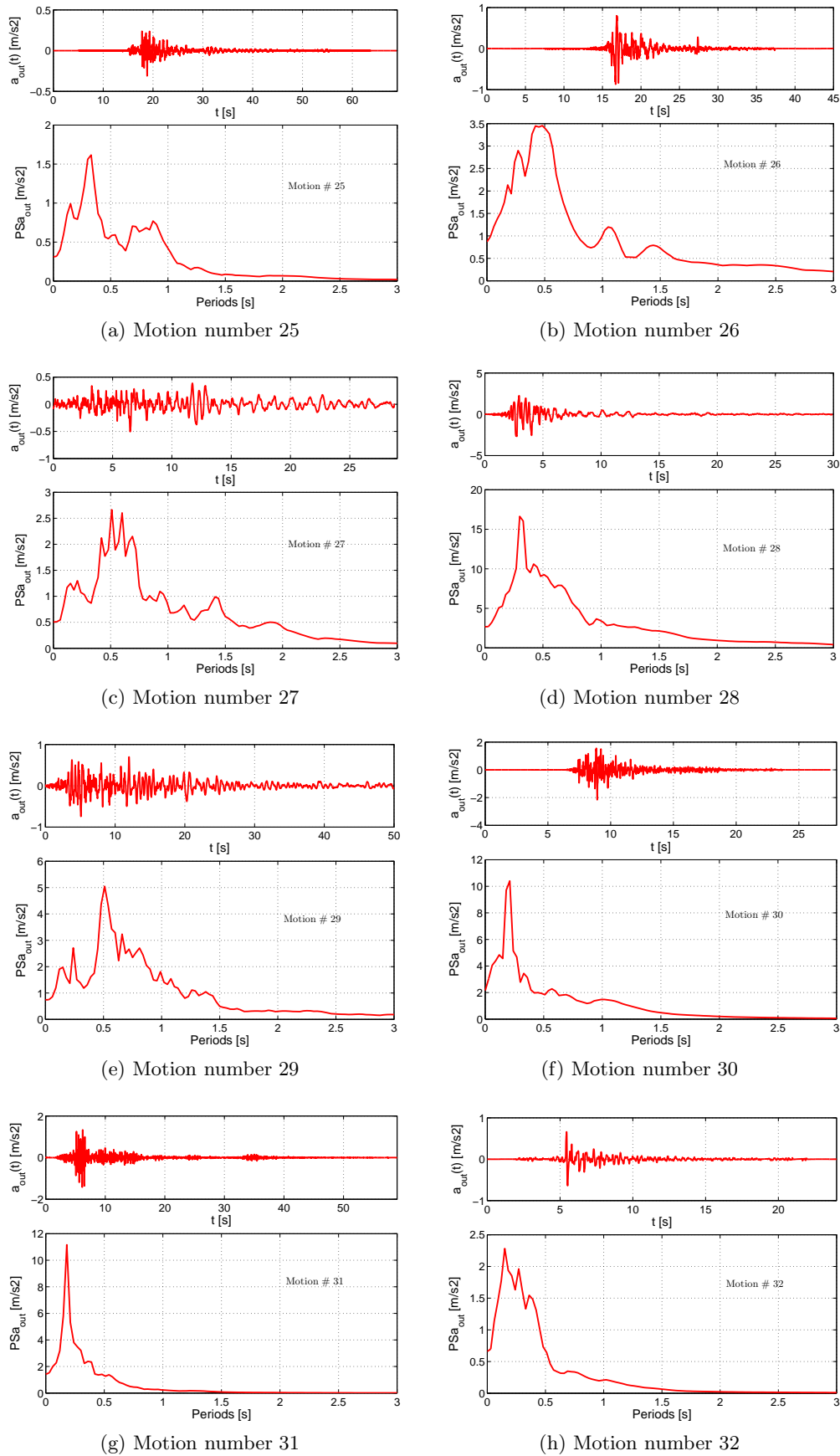
Figure J.4: Time-histories and computed response spectra at outcropping bedrock. Strong-motion selection #4

J.2   List of records compatible with French Antilles

Table J.5: Strong-motion selection #1: Interface records

Number	Station	Soil	$V_{s,30}$[m/s]	Waveform	M_w	$S_{d,\zeta=5\%}$ at 0.1s bin	$S_{d,\zeta=5\%}$ at 1s bin	t_{SR} bin
1	Palma sur	rock	–	007786y	6.4	low	low	low
2	Corinto Muelle Norte	alluvium	–	005387x	6.5	low	low	high
3	Savegre	stiff	–	007933x	6.2	low	high	low
4	Erimo	–	–	009161x	8.3	low	high	high
5	Quepos	rock	–	007927y	5.9	high	low	low
6	Chinandega bomberos	soft	–	007725y	6.5	high	low	high
7	Quepos	rock	405	007932x	6.2	high	high	low
8	Toyokoro	–	–	011362y	8.3	high	high	high

Table J.6: Strong-motion selection #2: Interface records

Number	Station	Soil	$V_{s,30}$[m/s]	Waveform	M_w	$S_{d,\zeta=5\%}$ at 0.1s bin	$S_{d,\zeta=5\%}$ at 1s bin	t_{SR} bin
9	Savegre	stiff	–	007928x	5.9	low	low	low
10	Savegre	stiff	–	007933x	6.2	low	low	high
11	Golfito	rock	–	007785y	6.4	low	high	low
12	Corinto Muelle Norte	alluvium	–	005387x	6.5	low	high	high
13	Corinto Muelle Sur	soft	–	007733x	6.5	high	low	low
14	Corinto Adm. building	alluvium	–	005385x	6.5	high	low	high
15	Guayabo	stiff	–	007886y	5.3	high	high	low
16	Infiernillo	–	–	003291y	8.0	high	high	high

Table J.7: Strong-motion selection #3: Intraslab records

Number	Station	Soil	$V_{s,30}$[m/s]	Waveform	M_w	$S_{d,\zeta=5\%}$ at 0.1s bin	$S_{d,\zeta=5\%}$ at 1s bin	t_{SR} bin
17	Golfito	rock	–	007918y	5.6	low	low	low
18	Tacuba	alluvium	–	005326x	6.0	low	low	high
19	San Salvador NGI	soft	–	005348y	5.6	low	high	low
20	San Salvador Seismic Observatory	–	–	005403y	5.7	low	high	high
21	Managua Inst. Sísmico	soft	–	007758y	5.9	high	low	low
22	Managua Coca-Cola	soft	–	007759x	5.9	high	low	high
23	León Col. Calazans	soft	–	007753x	5.9	high	high	low
24	Atina-Pretura Terrazza	rock	–	000990x	5.5	high	high	high

Table J.8: Strong-motion selection #4: Crustal records

Number	Station	Soil	$V_{s,30}$[m/s]	Waveform	M_w	$S_{d,\zeta=5\%}$ at 0.1s bin	$S_{d,\zeta=5\%}$ at 1s bin	t_{SR} bin
25	Gilroy Gavilan College	stiff	–	001040x	6.5	low	low	low
26	Uttarkasi	rock	–	007685y	6.8	low	low	high
27	Kobe Port Island Array (surface)	soft	–	002057x	6.9	low	high	low
28	Los Angeles 1100 Wilshire Bd.	stiff	–	002198y	6.7	low	high	high
29	San Vicente Hospital	alluvium	–	004654x	6.5	high	low	low
30	Muika (surface)	–	–	010156y	6.6	high	low	high
31	Nahanni Station 2	rock	–	001143x	6.7	high	high	low
32	Chi-Chi TAP065	stiff	> 750	–	7.6	high	high	high

Table J.9: Strong-motion selection #5: Crustal records

Number	Station	Soil	$V_{s,30}$[m/s]	Waveform	M_w	$S_{d,\zeta=5\%}$ at 0.1s bin	$S_{d,\zeta=5\%}$ at 1s bin	t_{SR} bin
33	Hella	stiff	–	006330x	6.4	low	low	low
34	Los Angeles- 3620 South Vermont	soft	–	002664y	6.7	low	low	high
35	San Jose IBM Build. 12	rock	–	001043x	6.5	low	high	low
36	Brawley Airport Hangar	soft	–	001016y	6.5	low	high	high
37	Superstition Mountain Camera Site 8	soft	–	001109x	6.5	high	low	low
38	Glendale 3320 Las Palmas Av.	–	–	002678y	6.7	high	low	high
39	Tsunan	–	–	008667y	6.6	high	high	low
40	El Centro Array Station 6	soft	–	001022x	6.5	high	high	high

(a) Motion number 1

(b) Motion number 2

(c) Motion number 3

(d) Motion number 4

(e) Motion number 5

(f) Motion number 6

(g) Motion number 7

(h) Motion number 8

Figure J.5: Time-histories and computed response spectra at outcropping bedrock. Strong-motion selection #1: Interface records

(a) Motion number 9

(b) Motion number 10

(c) Motion number 11

(d) Motion number 12

(e) Motion number 13

(f) Motion number 14

(g) Motion number 15

(h) Motion number 16

Figure J.6: Time-histories and computed response spectra at outcropping bedrock. Strong-motion selection #2: Interface records

(a) Motion number 17

(b) Motion number 18

(c) Motion number 19

(d) Motion number 20

(e) Motion number 21

(f) Motion number 22

(g) Motion number 23

(h) Motion number 24

Figure J.7: Time-histories and computed response spectra at outcropping bedrock. Strong-motion selection #3: Intraslab records

(a) Motion number 25

(b) Motion number 26

(c) Motion number 27

(d) Motion number 28

(e) Motion number 29
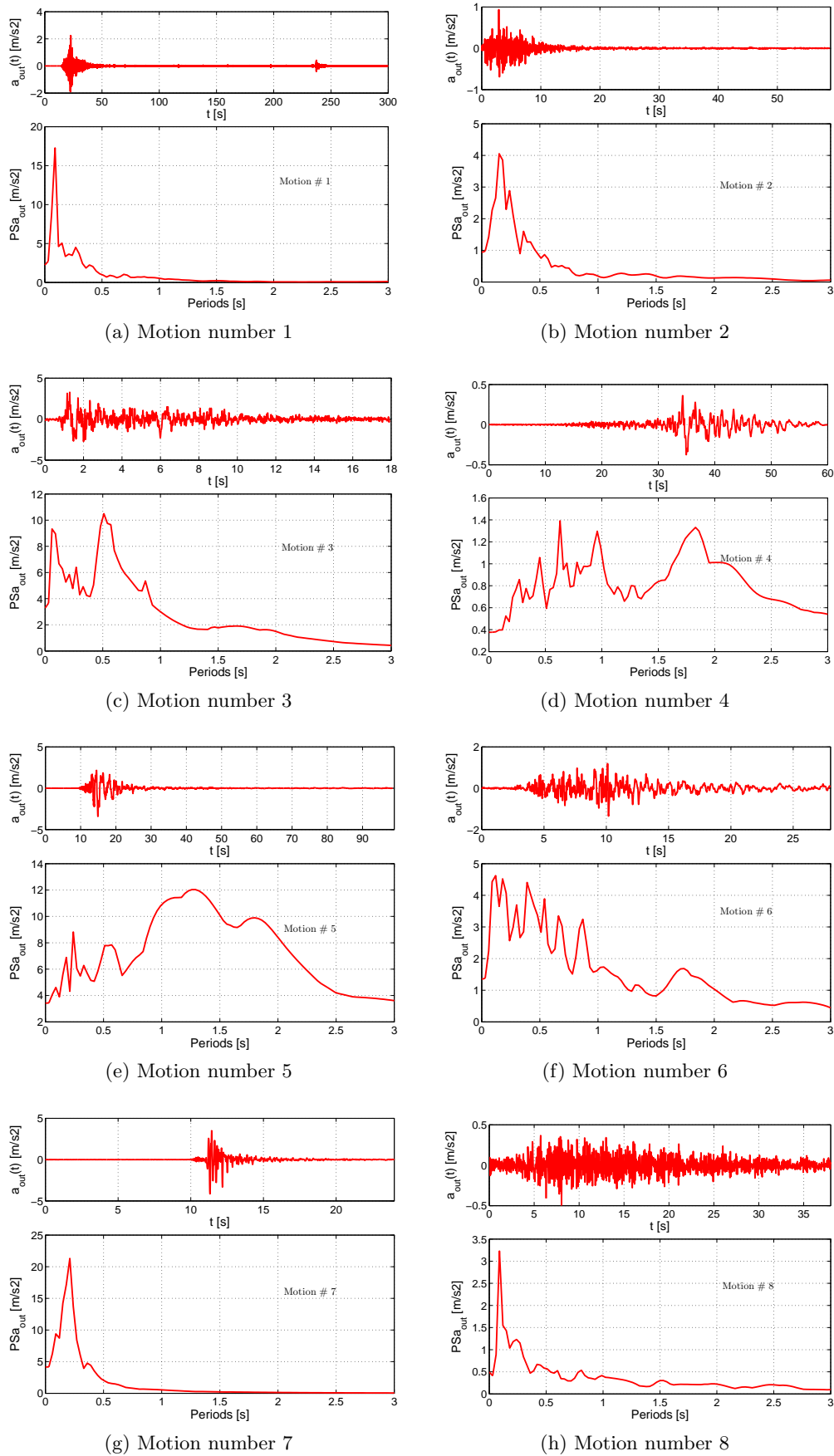
(f) Motion number 30

(g) Motion number 31

(h) Motion number 32

Figure J.8: Time-histories and computed response spectra at outcropping bedrock. Strong-motion selection #4: Crustal records

(a) Motion number 33

(b) Motion number 34

(c) Motion number 35

(d) Motion number 36

(e) Motion number 37
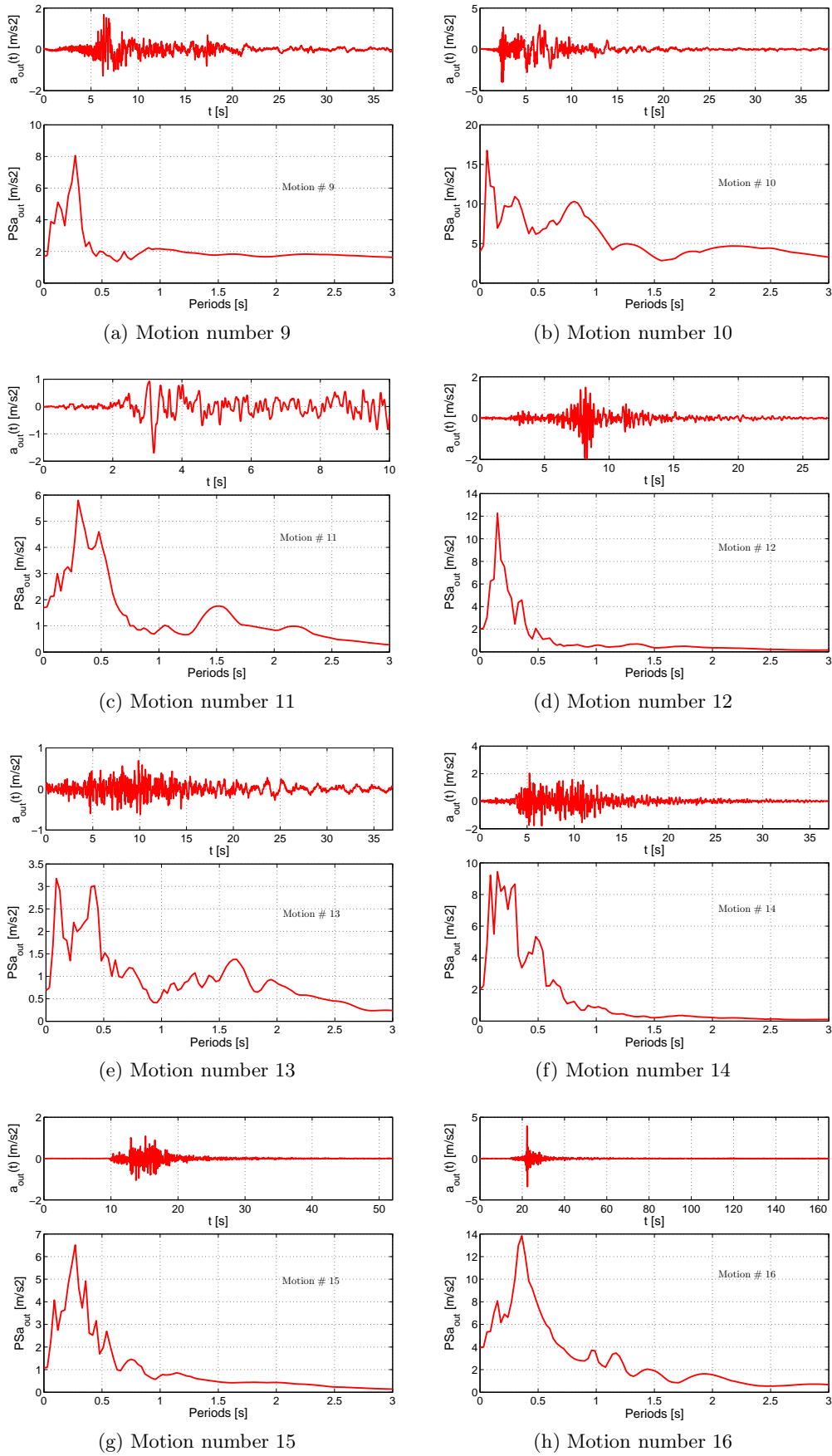
(f) Motion number 38

(g) Motion number 39

(h) Motion number 40
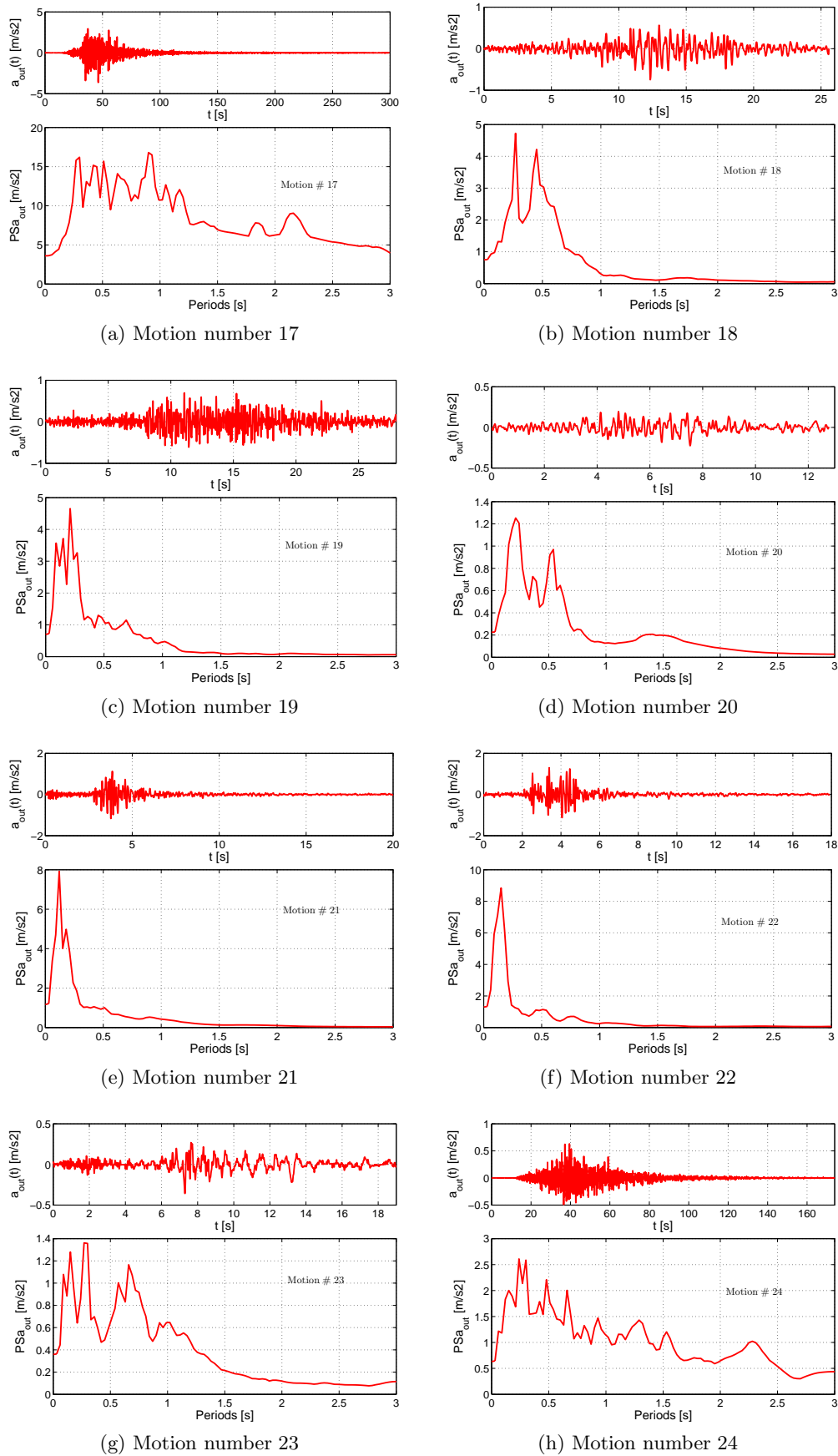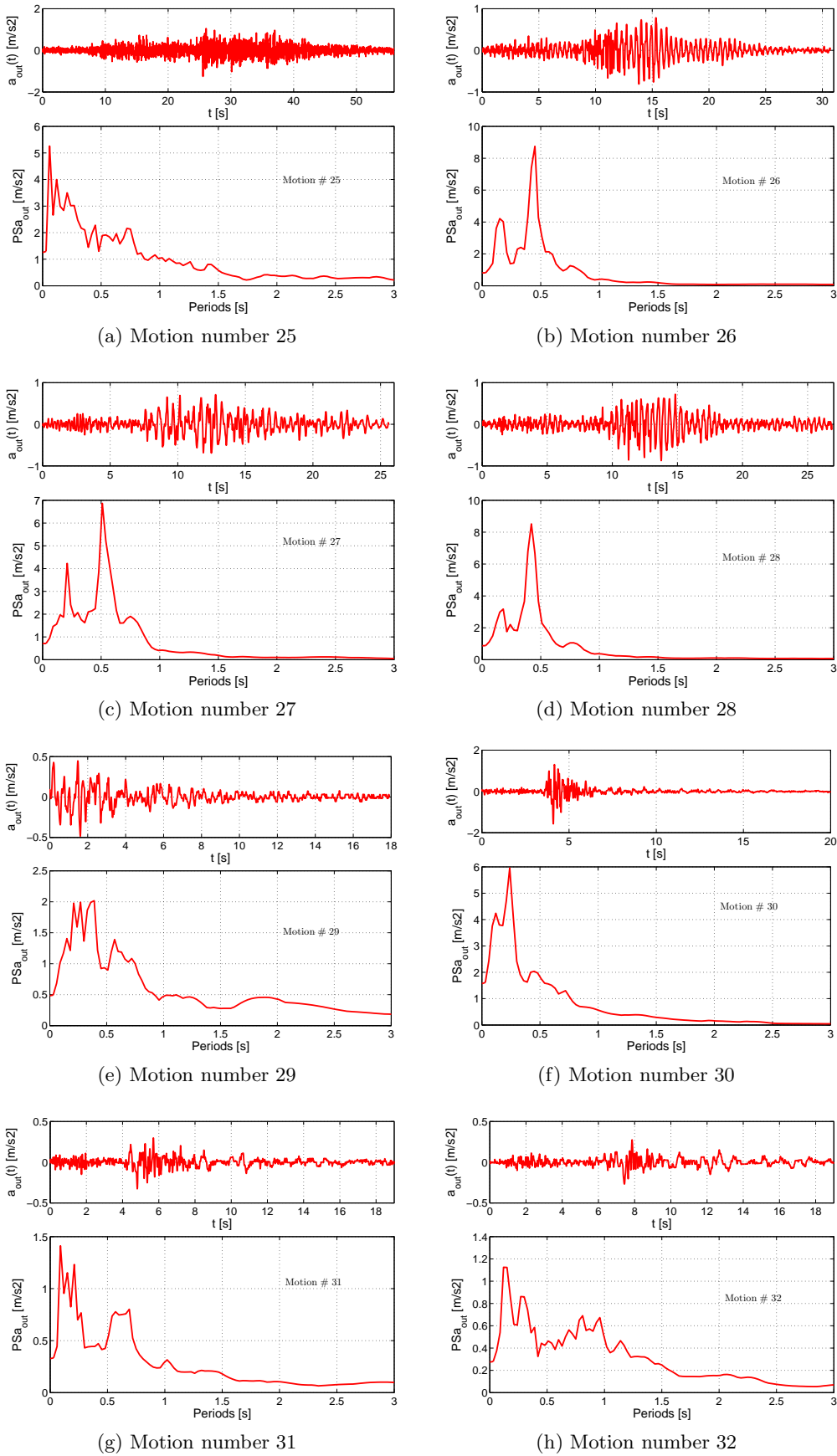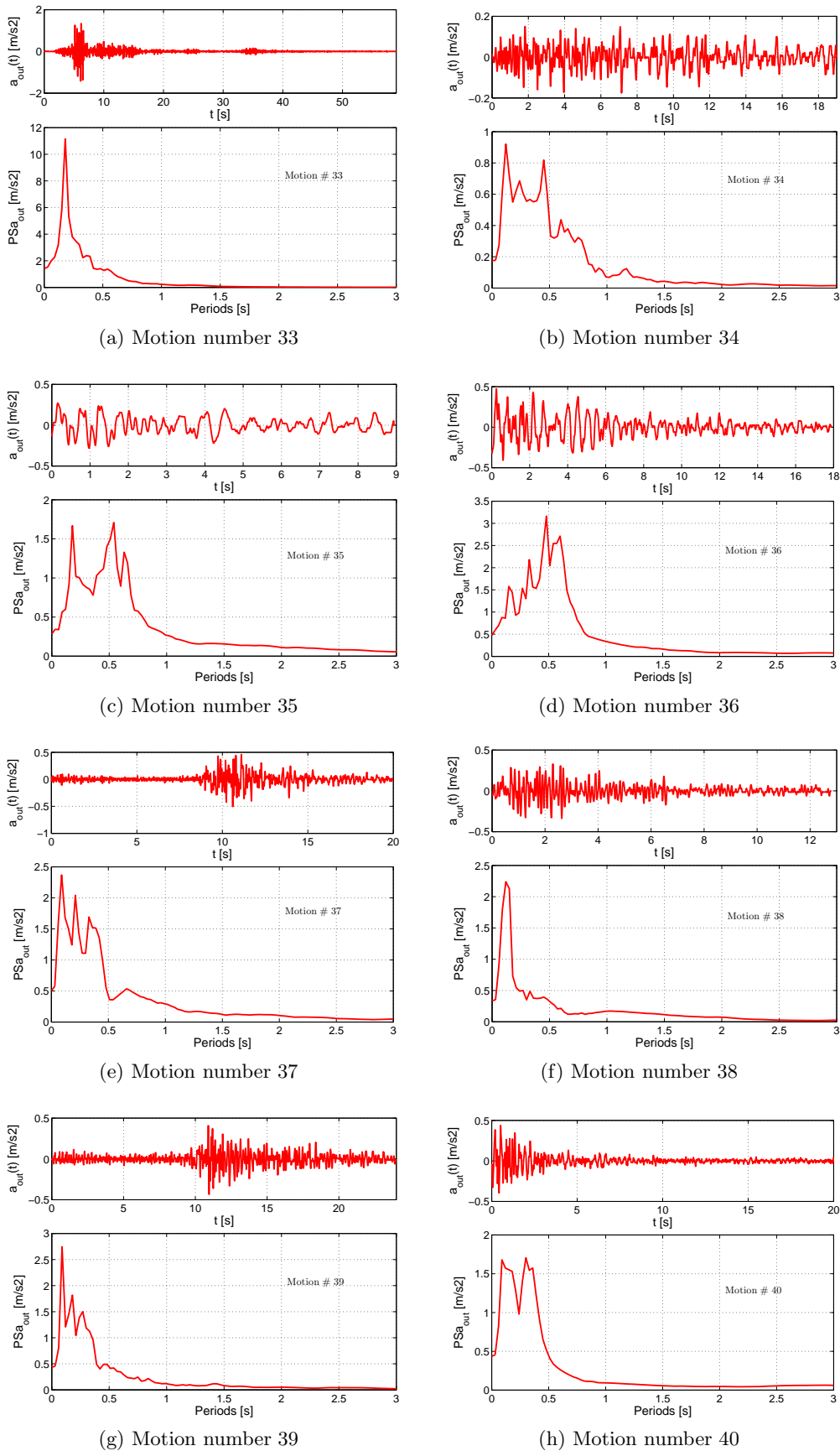
Figure J.9: Time-histories and computed response spectra at outcropping bedrock. Strong-motion selection #5: Crustal records

Bibliography

Aki, K. and Richards, P. (2002). *Quantitative Seismology: Theory and Methods.* University Science Books, Sausalito, California, USA, second edition edition.

Ambraseys, N., Douglas, J., Sigbjörnsson, R., Berge-Thierry, C., P. Suhadolc, P., Costa, G., and Smit, P. (2004). Dissemination of european strong- motion data, vol. 2, using strong-motion datascape navigator. Cd-rom collection, Engineering and Physical Sciences Research Council, United Kingdom.

Arias, A. (1970). A measure of earthquake intensity. In *Seismic design for nuclear power plants*, pages 438–483. R.J. Hansen. MIT Press. Cambridge, Mass.

ATC 13 (1985). Erathquake damage evaluation data for california. Report atc, Applied Technology Council.

ATC 40 (1996). Seismic evaluation and retrofit of concrete buildings. Report atc, Applied Technology Council.

Aubert, P. (1997). *Méthodes MESHLESS en Géomécanique.* Thèse de doctorat, École Centrale Paris.

Aubry, D., Chouvet, D., Modaressi, A., and Modaressi, H. (1985). GEFDYN 5*, Logiciel d'analyse du comportement statique et dynamique des sols par éléments finis avec prise en compte du couplage sol-eau-air.*

Aubry, D. and Clouteau., D. (1992). *Recent Advances in Earthquake Engineering and Structural Dynamics*, chapter A Subdomain Approach to Dynamic Soil-Structure Interaction, pages 251–272. Ouest Editions/AFPS, Nantes, France.

Aubry, D., Hujeux, J., Lassoudière, F., and Meimon, Y. (1982). A double memory model with multiple mechanisms for cyclic soil behaviour. In *Int. Symp. Num. Mod. Geomech.*, pages 3–13. Balkema.

Aubry, D. and Modaressi, A. (1992a). Strain localization in multipotential elastoplasticity. *International Journal for Numerical Methods in Engineering*, 3(34):349–363.

Aubry, D. and Modaressi, A. (1996). GEFDYN,*Manuel Scientifique.*

Aubry, D., Modaressi, A., and Modaressi, H. (1990). A constitutive model for cyclic behaviour of interfaces with variable dilatancy. *Computers and Geotechnics*, 9(1):47–58.

Aubry, D. and Modaressi, H. (1989). Un modèle de sols saturés en dynamique non linéaire. *Revue Française de Géotechnique*, (46):43–75.

Aubry, D. and Modaressi, H. (1992b). Seismic wave propagation in soils including non-linear and pore pressure effects. *In: Recent Advances in Earthquake Engineering and Structural Dynamics, V. Davidovici (ed.), Ouest Editions*, pages 209–224.

Avilés, J. and Pérez-Rocha, L. (1996). Evaluation of interaction effects on the system period and the system damping due to foundation embedment and layer depth. *Soil Dynamics and Earthquake Engineering*, 15:11–21.

Avilés, J. and Pérez-Rocha, L. (2003). Soil-structure interaction in yieding systems. *Earthquake Engineering and Structrual Dynamics*, 32:1749–1771.

Basu, U. and Chopra, A. (2003). Perfectly matched layers for time-harmonic elastodynamics of unbounded domains: theory and finite-element implementation. *Computer Methods in Applied Mechanics and Engineering*, 192(11-12):1337–1375.

Bathe, K. (1996). *Finite Element Procedures.* Pretince-Hall, New Jersey, USA.

Benzenatti, I. (1992). *Modélisation du comportement dynamique des sols saturés appliquée aux barrages et effets de site.* Thèse de doctorat, École Centrale Paris.

Bérenger, J. (1994). A perfectly matched layer for the absorption of electromagnetic waves. *Journal of Computational Physics archive*, 114(2):185–200.

Bielak, J., Loukakis, K., Hisada, Y., and Yoshimura, C. (2003). Domain reduction method for three-dimensional earthquake modeling in localized regions. part i: Theory. *Bulletin of the Seismological Society of America*, 93(2):817–824.

Biot, M. (1962). Theory of propagation of elastic waves in a fluid-saturated porous solid. ii.- higher frequency range. *The Journal of Acoustical Society of America*, 28(2):168–178.

Bommer, J. and Acevedo, A. (2004). The use of real earthquake accelerograms as input to dynamic analysis. *Journal of Earthquake Engineering*, 8(1):43–91.

Chan, A. (1988). *A unified Finite Element solution to Static and Dynamic Geomechanics.* Ph.d. dissertation, University College of Swansea.

Chen, W. and Mizuno, E. (1990). *Nonlinear analysis in soil mechanics.* Elsevier, New York.

Choi, E., DesRoches, R., and Nielson, B. (2004). Seismic fragility of typical bridges in moderate seismic zones. *Engineering Structures*, 26(2):187–199.

Ciampoli, M. and Pinto, P. (1995). Effects of soil-structure interaction on inelastic seismic response of brdige piers. *Journal of Structural Engineering ASCE*, 121(5):806–814.

Clayton, R. and Engquist, B. (1977). Absorving boundary conditions for acoustic and elastic wave equations. *B.S.S.A.*, 67(6):1529–1540.

Clouteau, D. (1990). *Propagation d'ondes dans des milieux héérogègenes, Application à la tenue d'ouvrages sous séismes.* Thèse de doctorat, Ecole Centrale Paris.

Clouteau, D. (2000). *ProMiss 0.2: Manuel Scientifique.*

Clouteau, D. (2003). *Miss 6.3: Manuel Utilisateur.*

Clouteau, D. and Aubry, D. (2001). *Computational Soil-Structure Interaction.*

Clouteau, D. and Aubry, D. (2003). *Boundary Element Methods for Soil-Structure Interaction*, chapter Computational Soil-Structure Interaction, pages 61–126. Kluwer Academic Publishers.

de Martin, F. and Aochi, H. (2008). Radiation boundary condition using paraxial approximation. Report BRGM, BRGM.

Deodatis, G. (1996). Non-stationary stochastic vector processes: seismic ground motion applications. *Probabilistic Enineering Mechanics*, 11(149-168).

Dickenson, S. and Seed, R. (1996). Nonlinear dynamic response of soft and deep cohesive soil deposits. In *Proc. of the International Workshop on Site Response Subjected to Strong Earthquake Motions.* Yokosuka, Japan.

Douglas, J. (2006). Selection of strong-motion records for use as input to the structural models of veda. Report BRGM BRGM/RP-54584-FR, BRGM.

Douglas, J., Roulle, A., Dominique, P., Maurin, C., and Dunand, F. (2005). Traitement des données accélérométriques du conseil général de la martinique. rapport final. Report BRGM BRGM/RP-53906-FR, BRGM.

Engquist, B. and Majda, A. (1977). Absorbing boundary conditions for the numerical simulation of waves. *Mathematics of Computation*, 31(139):629–651.

EUROCODE 8 (2003). Design of structures for earthquake resistance, prEN 1998-1:200X. European Standard, European Committee for Standardization.

FEMA 356 (2000). Prestandard and commentary for the seismic rehabilitation of buildings. Report fema, Federal Emergency Management Agency.

FEMA 450 (2003). NEHRP recommended provisions for seismic regulations for new buildings and other structures. provisions. commentary. Report fema, Federal Emergency Management Agency.

Fukushima, Y., Berge-Thierry, C., Volant, P., Griot-Pommera, D.-A., and Cotton, F. (2003). Attenuation relation for west Eurasia determined with recent near-fault records from California, Japan and Turkey. *Journal of Earthquake Engineering*, 7(4):573–598.

Gasparini, D. and Vanmarcke, E. (1979). Simulated earthquake motions compatible with prescribed response spectra. Technical report, Departement of Civil Engineering, Massachusetts Institute of Technology, Cambridge, Massachusetts.

Gazetas, G. and Mylonakis, G. (2001). Soil-structure interaction effects on elastic and inelastic structures. In *Fourth International Conference on Recent Adavances in Geotechnical Earthquake Engineering and Soil Dynamics. Symposium in Honor of Professor W.D. Liam Finn*. San Diego, California.

Ghannad, M. and Jahankhah, H. (2007). Site-dependent strength reduction factors for soil-structure systems. *Soil Dynamics and Earthquake Engineering*, 27:99–110.

Ghosh, B. and Madabhushi, S. P. G. (2003). Effects of localised soil inhomogenity in modyfyng seismic soil structure interaction. In *16th ASCE Engineering Mechanics Conference*. University of Washington, Seattle.

Giberson, M. (1969). Two nonlinear beams with definitions of ductility. *Journal of Structural Division, ASCE*, 95(2):137–157.

Hajal, T. (1984). *Modélisation élasto-plastique des sols par une loi multimécanismes. Application au calcul pressiométrique*. Thèse de doctorat, École Centrale Pais, France, Châtenay-Malabry.

Hicher, P. and Rahma, A. (1994). Micro-macro correlations for granular media. Application to the modelling of sands. *European Journal of Mechanics. A/Solids*, 13(6):763–781.

Hughes, T. (1983). *Computational Methods for Transient Analysis*, chapter Analysis of Transient Algorithms with Particular Reference to Stability Behavior, pages 67–155. North-Holland, Amsterdam.

Hughes, T. (2000). *The Finite Element Method, Linear Static and Dynamic Finite Element Analysis*. Dover Publications, Mineola, New York.

Hughes, T. and Liu, W. (1977a). Implicit explicit finite elements in transient analysis: Implementation and numerical examples. *Journal of Applied Mechanics*, (45):375–378.

Hughes, T. and Liu, W. (1977b). Implicit explicit finite elements in transient analysis: Stability theory. *Journal of Applied Mechanics*, (45):371–374.

Hughes, T., Pister, K., and Taylor, R. (1979). Implicit explicit finite elements in nonlinear transient analysis. *Computer Methods in Applied Mechanics and Engineering*, (17/18):159–182.

Hujeux, J. (1979). *Calcul numérique de problèmes de consolidation élastoplastiques*. Thèse de doctorat, École Centrale Paris, France.

Hujeux, J. (1985). Une loi de comportement pour le chargement cyclique des sols. In *Génie Parasismique*, pages 287–302. Presse ENPC.

Hwang, H. and Huo, J.-R. (1994). Generation of hazard-consistent fragility curves. *Soil Dynamics and Earthqauke Engineering*, 13(5):34–354.

Ishihara, K. (1993). Liquefaction and flow failure during earthquakes. 33*rd* Rankine lecture. *Géotechnique*, 43(3):351–415.

Iwasaki, T., Tatsuoka, F., and Takagi, Y. (1978). Shear moduli of sands under cyclic torsional shear loading. *Soils and Foundations*, 18(1):39–55.

Jennings, P. and Bielak, J. (1973). Dynamics of building-soil interaction. *Bulletion of the Seismological Society of America*, 63:9–48.

Juang, C., Yuan, H., Li, D., Yang, S., and Christopher, R. (2005). Estimating severity of liquefaction-induced damage near foundation. *Soils Dynamics and Earthquake Engineering*, 25(5):403–11.

Kafali, C. and Grigoriu, M. (2007). Seismic fragility analysis: Application to simple linear and non-linear systems. *Earthquake Engineering and Structural Dynamics*, 36(13):1885–1900.

Kordjani, M. (1995). *Caractérisation et modélisation du comportement en petites déformations des sols sur des chemins de sollicitation monotone et cyclique*. Thèse de doctorat, École Centrale Paris, France.

Koutsourelakis, S., Prévost, J., and Deodatis, G. (2002). Risk assessment of an interacting structure-soil system due to liquefaction. *Earthqauke Enginnering and Structural Dynamics*, (31):851–879.

Kramer, S. (1996). *Geotechnical Earthquake Engineering*. Prentice Hall, New Jersey.

Lebrat, L., Morineau, A., and Piron, M. (2004). *Statistique exploratoire multidimensionnelle*. Dunod, Paris, 3ème édition edition.

Lemaitre, J. and Chaboche, J. (2001). *Mécanique des matériaux solides*. Dunod, Paris, 2ème édition edition.

Lopez-Caballero, F. (2003). *Influence du comportement non linéaire du sol sur les mouvements sismiques induits en géo-structures*. Thèse de doctorat, École Centrale Paris.

Lopez-Caballero, F. and Modaressi, A. (2002). Identification des paramètres pour la modélisation de la liquéfaction des sables. In *Symposium International- Identification et détermination des paramètres des sols et des roches pour les calculs géotechniques*, pages 189–198. Paris, Ed. J.P. Magnan, Presses de l'École Nationale des Ponts et Chaussées.

Lopez-Caballero, F., Modaressi, A., and Elmi, F. (2003). Identification of an elastoplastic model parameters using laboratory and in-situ tests. In *Deformation Characteristics of Geomaterials ISLyon 03*, pages 1183–1190.

Lopez-Caballero, F., Modaressi, A., and Modaressi, H. (2007). Nonlinear numerical method for earthquake site response analysis i- elastoplastic cyclic model & parameter identification strategy. *Bulletin of Earthquake Engineering*, 5(3).

Lopez-Caballero, F. and Modaressi-Farahmand Razavi, A. (2008). Numerical simulation of liquefaction effects on seismic ssi. *Soil Dynamics and Earthquake Engineering*, 28(2):85–98.

Luco, J. (1980). Soil-structure interaction and identification of structural models. In *Proceedings of the ASCE Specially Conference in Civil Engineering and Nuclear Power*. Tennessee.

Luong, M. (1980). Phénomènes cycliques dans les sols pulvérulents. *Revue Française de Géotechnique*, 10(1):39–53.

Maison, F. (1992). *PC-ANSR: A Computer program for Nonlinear Structural Analysis*.

Marante, M., Suárez, L., Quero, L., j. Redondo, Vera, J., Uzcátegui, M., Delgado, S., León, L., nez, L. N., and Florez, J. (2005). Portal of damage: a web-based finite element program for the analysis of framed structrues subjected to overloads. *Advances in Engineering Software*, 36:346–358.

Marin, S., Avouac, J., Nicolas, M., and Schlupp, A. (2004). A probabilistic approach to seismic hazard in metropolitan france. *Bulletin of the Seismological Society of America*, 94(6):2137–2163.

Martin, C., Combes, P., Secanell, R., Lignon, G., Fioravanti, A., Carbon, D., Monge, O., and Grellet, B. (2002). Revision du zonage sismique de la france : Etude probabiliste. Rapport de Phase 3 Affaire no. 1601, Report GTR/MATE/0701-150.

Mellal, A. (1997). *Analyse des effets du comportement non linéaire des sols sur le mouvement sismique*. Thèse de doctorat, École Centrale Paris, France.

Michali, A. (1994). *Méthode pour l'identification des paramètres d'une loi élastoplastique à partir d'essais de laboratoire et in-situ*. Thèse de doctorat, École Centrale Paris, France.

Michalski, E. and Rahma, A. (1989). Modélisation du comportement des sols en élastoplasticité : définition des paramètres des modèles Hujeux- Cyclade et recherche des valeurs des paramètres pour différents sols. 89 SGN 117 GEG, Bureau de Recherches Géologiques et Minières BRGM.

Miranda, E. and Vertero, V. (1994). Evaluation of strength reduction factors for earthquake-resistant design. *Earthquake Spectra*, 10(2):357–379.

Modaressi, A. (2003). *Modélisation des milieux poreux sous chargements complexes*. Diplôme d'habilitation à diriger des recherches, Institut National Polytechnique de Grenoble, Grenoble.

Modaressi, A. and Lopez-Caballero, F. (2001). Global methodology for soil behavior identification and its application to the study of site effects. In *4th International Conference on recent Advances in Geotechnical Earthquake Engineering and Soil Dynamics*, page 1.08. San Diego, California. Eds. Prakash.

Modaressi, H. (1987). *Modélisation numérique de la propagation des ondes dans les milieux poreux anelastiques*. Thèse de doctorat, École Centrale Paris.

Modaressi, H. and Aubry, D. (1989). On the dynamic behaviour of an elastoplastic constitutive model for soils. In *Soil Dynamics and Liquefaction, Proceedings of the Fourth International Conference on Soil Dynamics and Earthquake Engineering, Mexico City, Mexico*, pages 53–60. Computational Mechanics Publications, Southampton, England and Boston.

Modaressi, H., Aubry, D., Faccioli, E., and Noret, C. (1995). Numerical modelling approaches for the analysis of the earthquake triggered landslides. In *3rd International Conference on recent Advances in Geotechnical Earthquake Engineering and Soil Dynamics*, volume II, pages 833–843. St. Louis, Missouri. Eds. Prakash.

Modaressi, H. and Benzenati, I. (1994). Paraxial approximation for poroelastic media. *Soil dynamics and Earthquake Engineering*, 13(2):117–129.

Modaressi, H. and Foerster, E. (2000). CyberQuake. User's manual, BRGM, France.

Nau, R., Oliver, R., and Pister, K. (1982). Simulating and analyzing artificial nonstationary earthquake ground motions. *Bulletin of the Seismological Society of America*, 72:615–636.

NIST/SEMATECH (2006). Nist/sematech e-handbook of statistical methods. http://www.itl.nist.gov/div898/handbook/.

Park, Y. and Ang, A. (1985). Mechanistic seismic damage model for reinforced concrete. *Journal of Structural Engineering, ASCE*, 111(4):722–739.

Pecker, A. (1984). *Dynamique des sols.* Presses de ÉCOLE Nationale des Ponts et Chaussées, Champs sur Marne.

Pianka, C. (1998). *Contribution to soil/structure and user interfaces in geomechanics.* Thèse de doctorat, École Centrale Paris.

Piccuezzu, E. (1991). *Lois de Comportement en Géomécanique; Modélisation, Mise en oeuvre, Identification.* Thèse de doctorat, École Centrale Paris.

Pitilakis, D. (2006). *Soil-Structure Interaction Modeling Using Equivalent Linear Soil Behavior In The Substructure Method.* Thèse de doctorat, École Centrale Paris.

Popescu, R. (2002). Finite element assessment of the effects of seismic loading rate on soil liquefaction. *Canadian Geotechnical Journal*, 39(2):331–344.

Popescu, R., Prévost, J., and Deodatis, G. (2005). 3d effects in seismic liquefaction of stochastically variable soil deposits. *Géotechnique*, 55(1):21–31.

Popescu, R., Prévost, J., Deodatis, G., and Chakrabortty, P. (2006). Dynamics of nonlinear porous media with applications to soil liquefaction. *Soil Dynamics and Earthquake Engineering*, 26(2):648–665.

Poulos, H. and Davis, E. (1974). *Elastic Solutions for Soil and Rocks Mechanis.* Wiley, New York.

Pousse, G., Bonilla, L., Cotton, F., and Margerin, L. (2006). Nonstationary stochastic simulation of strong ground motion time histories including natural variability: application to the K-Net Japanese database. *Bulletin of the Seismological Society of America*, 96(6):2103–2117.

Prakash, V., Powel, G., and Campbell, S. (1993). DRAIN 2D-X, *Base program description and User Guide.*

Priestley, M. and Parck, R. (1987). Strength and ductility of concrete bridges columns under seismic loading. *ACI Structural JOURNAL*, 84(1):61–76.

PS-92 (1999). Règles PS applicables aux bâtiments - PS-92. Règles de construction parasismique., Norme Française NF P 06-013.

Rahma, A. (1988). *Modélisation probabiliste des paramètres de lois élasto-plastiques - Modèle Cyclade.* Thèse de doctorat, École Centrale Paris.

Rathje, E., Abrahamson, N., and Bray, J. (1998). Simplified frequency content estimates of earthquake ground motions. *Journal of Geotechnical and Geoenvironmental Engineering*, 124(2):150–159.

Rodriguez, M. and Montes, R. (2000). Seismic response and damage analysis of building supported on flexible soils. *Earthquake Engineering and Structural Dynamics*, 29:647–665.

Sabetta, F. and Pugliese, A. (1996). Estimation of response spectra and similation of nonstationary earthquake ground motions. *Bulletin of Seismological Society of America*, 86(2):337–352.

Sáez, E. (2005). Prise en compte de la non-linéarité du comportement du sol sur les effets de l'interaction sol structure en dynamique. Mémoire de master, École Nationle des Ponts et Chaussées.

Sáez, E. (2007). Poutre 33 v1.1. Gefdyn technical note, École Centrale Paris.

Saez, E., Lopez-Caballero, F., and Modaressi, A. (2006). Effects of ssi on the capacity spectrum method. In *Proc. First European Conference on Earthquake Engineering and Seismology*, page id 1073.

Saez, E., Pitilakis, D., Lopez-Caballero, F., and Modaressi, A. (2007). Evaluation of non linear ssi effects following an equivalent linear approach. In *Proc. 5th International Conference on Seismology and Earthquake Engineering*, page SF65. Tehran, Iran.

Saporta, G. (2006). *Probabilités, analyse des données et statistique*. TECHNIP, Paris, 2ème édition edition.

Saragoni, G. and Hart, G. (1974). Simulation of artificial earthquakes. *Earthquake Engineering and Soil Dynamics*, 2:249–267.

Schnabel, P., Lysmer, J., and Seed, H. (1972). Shake: a computer program for earthquake response analysis of horizontally layered sites. Report EERC-72-12, Earthquake Engineering Research Center, University of California, Berkeley, CA.

Schofield, A. and Wroth, C. P. (1968). *Critical State Soil Mechanics*. McGraw-Hill, London.

Seed, H. B. and Idriss, I. M. (1982). Ground motion and soil liquefaction during earthquakes. Monograph series, earthquake engineering research institute, University of California, Berkeley, CA.

Seed, H. B., Wong, R. T., Idriss, I. M., and Tokimatsu, K. (1986). Moduli and damping factors for dynamic analyses of cohesionless soils. *Journal of Geotechnical Engineering - ASCE*, 112(11):1016–1032.

Seekins, L., Brady, A., Carpenter, C., and Brown, N. (1992). Digitized strong-motion accelerograms of north and central american earthquakes 1933-1986. Cd-rom, Digital Data Series DDS-7.

Shinozuka, M. (1998). Statical analysis of bridge fragility curves. In *Proceedings of the US-Italy Workshop on Protective Systems for Bridges*. New York, N.Y.

Shinozuka, M., Feng, Q., Lee, J., and Naganuma, T. (2000). Statistical analysis of fragility curves. *Journal of Engineering Mechanics*, 126(12):1224–1231.

Sica, S. (2001). *Analisi del comportamento dinamico di dighe in terra*. Dottorati di ricerca, Università degli Studi di Napoli Federico II, Italia.

Tokimatsu, K., Mizuno, K., and Kakurai, H. (1996). Building damage associated with geotechnical problems. *Soils Found - Special Issue*, (1):219–32.

Trifunac, M. and Brady, A. (1975). A study on the duration of strong earthquake ground motion. *Bulletin of the Seismological Society of America*, 65(3):581–626.

HAZUS-MH MR3 (2003). Multi-hazard Loss Estimation Methodology. Technical Manual. Report FEMA, Federal Emergency Management Agency.

van der Vaart, A. (2000). *Asymptotic Statistics (Cambridge Series in Statistical and Probabilistic Mathematics)*. Cambridge University Press.

Vecchio, F. and Emara, M. (1992). Shear deformation in reinforced concrete frames. *ACI Structural Journal*, 89(6):45–56.

Veletsos, A. (1977). *Structural and Geotechnical Mechanics*, chapter Dynamic of structure-foundation systems, pages 333–361. Prentice-Hall, Englewood Cliffs, NJ.

Veletsos, A. and Meek, J. (1974). Dynamic behavior of building-foundation systems. *Earthquake Engineering and Structural Mechanics*, 3:121–138.

Veletsos, A. and Nair, V. (1975). Seismic interaction of structures on hysteretic foundations. *Journal of the Structural DIVISION (ASCE)*, 101:109–129.

Wolf, J. (1985). *Dynamic Soil-Structure Interaction*. Prentice Hall, Englewood Cliffs, New Jersey.

Wolf, J. and Song, C. (1996). *Finite-element modelling of unbounded media*. John Wiley & Sons, Baffins Lane, England.

Yamashita, S., Kohata, Y., Kawaguchi, T., and Shibuya, S. (2001). International round-robin test organized by TC-29. In *Advanced Laboratory Stress-Strain Testing of Geomaterials*, pages 60–82. Tatsuoka, Shibuya & Kuwano (eds), Balkema Publishers.

Zienkiewicz, O., Bicanic, N., and Shen, F. (1988). Earthquake input definition and the transmitting boundary conditions. In Doltsinis, I. S., editor, *Advances in Computational Nonlinear Mechanics*, pages 109–138. Springer-Verlag.

Zienkiewicz, O., Chan, A., Pastor, M., Schrefler, B., and Shiomi, T. (1999). *Computational Geomechanics with Special Reference to Earthquake Engineering*. Wiley, Baffins Lane, Chichester, England.

Zienkiewicz, O., Chang, C., and Bettless, P. (1980). Drained, undrained, consolidating and dynamic behaviour assumption in soils; limits of validity. *Géotechnique*, (30):385–395.

Zienkiewicz, O. and Shiomi, T. (1984). Dynamic behaviour of saturated porous media: The generalized biot formulation and its numerical solution. *International Journal of Numerical and Analytical Methods of Geomechanics*, (8):71–96.